ANL-7100

ARGONNE NATIONAL LABORATORY

ATOMIC ENERGY COMMISSION
UNITED STATES OF AMERICA
NATIONAL AERONAUTICS AND SPACE ADMINISTRATION
U.S.A.

FACILITY FORM 602

N66 31671 (ACCESSION NUMBER)
667 (PAGES)
CR-76450 (NASA CR OR TMX OR AD NUMBER)

N66 31700 (THRU)
1
(CODE)
33 (CATEGORY)

PROCEEDINGS OF THE CONFERENCE ON APPLICATION OF HIGH TEMPERATURE INSTRUMENTATION TO LIQUID-METAL EXPERIMENTS

SEPTEMBER 28-29, 1965

31690

GPO PRICE $ _____

CFSTI PRICE(S) $ 6.75

Hard copy (HC) _____

Microfiche (MF) 2.25

ff 653 July 65

ANL-7100
Engineering and Equipment
(TID-4500)
AEC Research and
Development Report

ARGONNE NATIONAL LABORATORY
9700 South Cass Avenue
Argonne, Illinois 60439

PROCEEDINGS OF THE CONFERENCE ON APPLICATION OF HIGH TEMPERATURE INSTRUMENTATION TO LIQUID-METAL EXPERIMENTS

September 28-29, 1965

Program Committee

Paul A. Lottes, ANL
R. M. Scroggins, USAEC
Ruth Weltmann, NASA

Sponsored by
United States Atomic Energy Commission
and the
National Aeronautics and Space Administration

Operated by The University of Chicago
under
Contract W-31-109-eng-38
with the
U. S. Atomic Energy Commission

Page

WELCOMING ADDRESS
R. M. Scroggins, USAEC 1

WELCOMING REMARKS ON BEHALF OF NASA
Martin Gutstein, NASA Lewis Research Center 5

SESSION 1

September 28, 1965

THERMODYNAMICS AND HEAT TRANSFER MEASUREMENTS
Chairman: R. P. Stein, Argonne National Laboratory

HEATING TECHNIQUES FOR LIQUID METAL LOOPS
R. E. Holtz, Argonne National Laboratory. 9

ELECTRICAL HEATER FOR LIQUID METALS AT ELEVATED TEMPERATURES
L. G. Hays, Jet Propulsion Laboratory. 23

FLOW INSTRUMENTATION AND OPERATING EXPERIENCE IN A CONDENSING ALKALI METALS TEST LOOP
C. R. Fisher and J. H. Moskowitz, Jr., Aerojet-General Nucleonics 45

HEAT TRANSFER AND PRESSURE DROP MEASUREMENTS FOR HIGH TEMPERATURE BOILING POTASSIUM IN FORCED CONVECTION
J. A. Bond, J. R. Peterson, and F. E. Tippets, General Electric Company 53

MEASUREMENTS OF FORCED CONVECTION CONDENSING POTASSIUM HEAT TRANSFER
S. G. Sawochka, General Electric Company. 97

DEVELOPMENT OF EFFLUX MEASURING DEVICE FOR PERFORMANCE EVALUATION OF POTASSIUM VAPOR TURBINE
G. C. Wesling, R. J. Rossbach, and W. M. Shaffernocker, General Electric Company 127

PRESSURE TRANSDUCER FOR LIQUID METAL APPLICATIONS
A. J. Cassano and R. E. Engdahl, Consolidated Controls Corporation. 165

SESSION 2

September 28, 1965

QUALITY AND VOID FRACTION MEASUREMENTS
Chairman: M. Gutstein, NASA

FORCED CONVECTION BOILING SODIUM STUDIES AT LOW PRESSURE
J. B. Heineman, Argonne National Laboratory 189

X-RAY MEASUREMENT OF VOID DYNAMICS IN BOILING LIQUID METALS
L. B. Wentz, L. G. Neal, and R. W. Wright, TRW Systems 195

INSTRUMENTATION FOR TWO PHASE METALLIC FLOWS
R. E. Balzhiser and L. R. Smith, The University of Michigan 217

Session 2 (Contd.) Page

AN ACCURATE ONE-SHOT GAMMA ATTENUATION TECHNIQUE FOR MEASURING VOID FRACTIONS
J. K. Ferrell and J. W. McGee, North Carolina State University 247

DEVELOPMENT OF ALKALI METAL QUALITY METER
P. Tauson and R. L. Ammon, Westinghouse Electric Corporation 271

SESSION 3

September 28, 1965

BEARING FILM MEASUREMENTS
Chairman: J. Couch, NASA

LIQUID-METAL LUBRICATED BEARING INSTRUMENTATION
D. R. Grieser, Battelle Memorial Institute, and J. L. Morris, Air Force Aero Propulsion Laboratory (WPAFB). 291

DEVELOPMENT OF PERFORMANCE-MEASURING INSTRUMENTATION FOR A LIQUID-METAL TURBINE-DRIVEN BEARING TEST RIG
L. W. Stillwell and R. Herman, AiResearch Manufacturing Company of Arizona. . 307

APPROACHES TO THE MEASUREMENT OF THE STEADY STATE AND DYNAMIC PERFORMANCE CHARACTERISTICS OF LIQUID-METAL LUBRICATED BEARINGS
E. B. Arwas, F. K. Orcutt, and B. Sternlicht, Mechanical Technology Inc. 331

SESSION 4

September 29, 1965

LIQUID LEVEL AND IMPURITY MEASUREMENTS
Chairman: P. A. Lottes, Argonne National Laboratory

LIQUID-METAL LEVEL DETECTOR AND INDICATOR
L. W. Stillwell, AiResearch Manufacturing Company of Arizona 367

EXPERIENCES AND DEVELOPMENTS IN INSTRUMENTATION FOR LIQUID METAL EXPERIMENTS
H. J. Metz and M. M. Yarosh, Oak Ridge National Laboratory 379

IMPURITY AND LIQUID LEVEL MEASUREMENTS FOR THE FARET LOOP
A. G. Hosler, USAEC-COO, and F. A. Smith, Argonne National Laboratory. 413

THE LIQUID METAL OXYGEN METER
B. Minushkin, United Nuclear Corporation 427

AN INERT GAS PURITY TESTER
J. McKee, United Nuclear Corporation 443

INSTRUMENTATION FOR EVALUATING CAVITATION DAMAGE RESISTANCE AND HIGH FREQUENCY FATIGUE OF REFRACTORY ALLOYS IN HIGH TEMPERATURE LIQUID ALKALI METALS
H. S. Preiser and A. Thiruvengadam, Hydronautics, Inc. 455

SESSION 5

September 29, 1965

HEAT TRANSFER
Chairman: R. M. Scroggins, USAEC

Page

A METHOD FOR THE DETERMINATION OF LOCAL HEAT FLUXES IN LIQUID METAL HEAT EXCHANGERS
R. P. Stein, Argonne National Laboratory 483

EXISTENCE OF NON-EQUILIBRIUM, INVERSE TEMPERATURE PROFILE IN BOILING TWO-PHASE FLOW
J. C. Chen, Brookhaven National Laboratory 499

EXPERIMENTAL STUDIES OF BOILING OF SODIUM AND CONDENSING OF POTASSIUM
J. P. Lewis, National Aeronautics and Space Administration. 513

SUPERHEAT WITH BOILING ALKALI METALS
J. A. Edwards and H. W. Hoffman, Oak Ridge National Laboratory 515

PRESSURE DROP WITH FORCED-CONVECTION BOILING OF POTASSIUM
R. P. Wichner and H. W. Hoffman, Oak Ridge National Laboratory 535

SODIUM BOILING HEAT TRANSFER AND HYDRODYNAMICS
H. Lurie, Atomics International 549

RECENT DEVELOPMENTS IN HEAT TRANSFER AND DEVELOPMENT OF THE MERCURY BOILER FOR THE SNAP-8 SYSTEM
A. J. Sellers and M. K. Wong, Aerojet-General Corporation, and
G. M. Thur, National Aeronautics and Space Administration. 573

X-RAY MOVIE FILM REPORT OF FLOW PATTERNS IN A ONCE-THROUGH FORCED CIRCULATION NaK HEATED MERCURY BOILER
R. J. Ziobro, TRW Equipment Laboratories 633

HIGH TEMPERATURE LIQUID METAL INSTRUMENTATION AT ATOMICS INTERNATIONAL FOR: (1) THE SNAP 10A FLIGHT SYSTEM, (2) BOILER CONDITIONING EXPERIMENTS AND MERCURY VAPOR QUALITY MEASUREMENT FOR MERCURY RANKINE SYSTEMS
H. H. Hanlin, Atomics International. 641

WELCOMING ADDRESS

by

R. M. Scroggins
Division of Reactor Development and Technology
U. S. Atomic Energy Commission

It is my pleasure to welcome you gentlemen on behalf of the U. S. Atomic Energy Commission to the Joint AEC/NASA Conference on the Application of High Temperature Instrumentation to Liquid Metal Experiments. As most of you know, the Atomic Energy Commission sponsored three High-Temperature Liquid-Metal Heat Transfer Technology meetings during the period 1961 through 1963 at the Argonne, Brookhaven and Oak Ridge National Laboratories. These meetings were attended by all prime investigators in this field, and the appropriate government project supervisors. While these symposia were sponsored by the Commission, NASA and the Department of Defense were active participants in establishing the need and programs for these meetings. Official proceedings of each symposium were published.

One of the prime objectives of these early meetings was to acquaint all of those in industry and Government, engaged in this rapidly expanding field, with each other's programs and philosphy, in order to establish a general coordination of effort and exchange of information. We believe that this objective has been met. For example, in addition to wide distribution of all progress reports of work in this area among the principal investigators, the Commission sponsors the Bimonthly High-Temperature Liquid-Metal Technology Review published by the Brookhaven National Laboratory which was initiated as a result of the aforementioned meetings. We do not believe that further general information exchange meetings of the previous type are necessary; however, we do believe that technical symposia on specific subject items be held as determined by necessity, attended by those invited persons who can contribute to a technical working group discussion and evaluation.

It was therefore agreed by NASA and AEC to jointly sponsor a series of liquid-metal technology meetings which would delve into these specific items of interest to the investigators concerned with liquid-metal technology.

This is the first such Conference in the new Joint Liquid-Metal Technology Meeting series. While many subjects could have been chosen for this inaugural symposium, it was decided to delve into the subject of high temperature instrumentation for application to high temperature liquid metal experimental loops and systems. One rationale for this choice could be that there is a suspicion among most government program directors that liquid metal experimental loops and systems (primarily for corrosion and heat transfer purposes) can now be constructed and successfully operated by competent organizations within a "reasonable" length of time. However, we are not quite sure, if one considers the proposal for development of instrumentation and measurement techniques, that any useful data can be obtained from such systems.

The purpose therefore of this meeting is to attempt to establish, on an overall industry basis: first, the status of existing available instrumentation and pertinent system equipment; secondly, operating experience with such equipment; and finally, the necessity for additional instrumentation and equipment for future systems. Since the instrumentation techniques are so closely tied to the purpose of obtaining the information in question, and because of the need to establish the desirability for either more reliable, higher response, more accurate instruments or development of techniques for data not now obtainable, the majority of those present are engineers experienced in this field of endeavor who must answer the question of need before and in addition to how.

Since the previous meetings were concerned with heat transfer and fluid dynamics of high temperature boiling, condensing, and

sub-cooled liquid metals and it has been two years since the last meeting, many investigators have requested a forum to present new developments since that time in this area. Therefore, we have scheduled one session on heat transfer at the end of this meeting to present these papers. It is possible that some of the results discussed in this session may point the need for further instrument development.

In closing, I would like to thank the Argonne National Laboratory, Dr. Lottes and Dr. Koch and their associates for arranging a most interesting conference that I am sure will go a long way in answering the questions which form the purpose for this gathering. Since we are planning to hold future meetings in this liquid metal technology series, we (the AEC and NASA) welcome any suggestions from those present as to the subject matter for the next conference. Thank you.

WELCOMING REMARKS ON BEHALF OF NASA

Martin Gutstein, NASA Lewis
Research Center

Good morning.

My function this morning is to welcome the attendees to the Conference on Application of High Temperature Instrumentation to Liquid-Metal Experiments on behalf of both the National Aeronautics and Space Administration and your co-chairman, Miss Ruth Weltmann of the Lewis Research Center. Unfortunately, Miss Weltmann was unable to attend this Conference and I am pinch-hitting for her.

This is the first time this Conference is being co-sponsored by NASA. NASA's interest in liquid-metal technology has extended over a period of many years and over a wide range of topics. In the field of liquid-metal heat transfer alone, these topics have included the estimation of thermodynamic and physical properties, the measurement of single phase and two-phase phenomena of both the alkali metals and mercury, and the development of instrumentation for the ever increasingly difficult environments which our work demands. Many of the papers to be presented at this Conference will discuss work done in-house or represent NASA sponsorship and technical direction. It is therefore not at all strange to have the Space Administration co-sponsor this series of meetings.

Indeed, in extending a welcome to you all on behalf of NASA, Miss Weltmann and myself, I hope we may see you all at the next Liquid-Metal Technology Conference which I hope will be held at the Lewis Research Center.

May you all have a most successful meeting.

PRECEDING PAGE BLANK NOT FILMED.

SESSION 1

THERMODYNAMICS AND HEAT TRANSFER MEASUREMENTS

Tuesday, September 28, 1965

CHAIRMAN: R. P. Stein
Argonne National Laboratory

PRECEDING PAGE BLANK NOT FILMED.

N66 31672

Heating Techniques for Liquid Metal Loops

by

Robert E. Holtz
Argonne National Laboratory
Argonne, Illinois

Operated by The University of Chicago
under
Contract W-31-109-eng-38
with the
U. S. Atomic Energy Commission

PRECEDING PAGE BLANK NOT FILMED.

INTRODUCTION

One of the more severe problems involved in obtaining experimental boiling liquid metal heat transfer information is the design and construction of a satisfactory heater section. Many of the difficulties in liquid metal heat transfer experiments stem from the inability of the heater sections to function properly. Most of these heater failures have been caused by material expansions at higher temperatures.

The primary objective of the Boiling Liquid Metal Program in the Reactor Engineering Division at Argonne is to obtain experimental information pertinent to the boiling and fluid flow behavior of the alkali metals, especially sodium. Associated with obtaining this experimental information is the design of a heated section capable of supplying high relatively uniform heat fluxes to flowing liquid metals. It appears that heat fluxes well above one million Btu/hr-ft^2 may be required for studying the boiling characteristics of the alkali metals up to the critical heat flux. Temperatures up to and in many cases beyond 2100^{o}F must be anticipated. The basic heat transfer measurements to be taken in the heated section are the heat flux and the difference between the inside tube wall temperature and the fluid saturation temperature, and these measurements must be made as accurately as possible.

A variety of possible heating techniques have been examined and thermal radiation heating and electron-bombardment heating appear promising. The remainder of this report will be used to examine these two heating methods.

THERMAL RADIATION HEATING

Initial experiments at Argonne using thermal radiation heating used a small scale, forced convection loop. A schematic diagram of the thermal radiation heat transfer loop is shown in Figure 1. The loop was constructed primarily from type 316 Stainless Steel tubing. Sodium-potassium alloy (NaK-78) was used as the heat transfer fluid.

The thermal radiation heated section consisted of a 0.500 inch outside diameter, 0.035 inch wall, type 316 Stainless Steel tube containing flowing NaK. The tube was surrounded by two one-half cylindrically shaped tantalum elements which were electrically heated. The 0.003 inch thick tantalum elements were 1-1/4 inch in diameter and had a heated length of sixteen-inches. The heated section had a L/D ratio of thirty-seven. Al_2O_3 was used as both

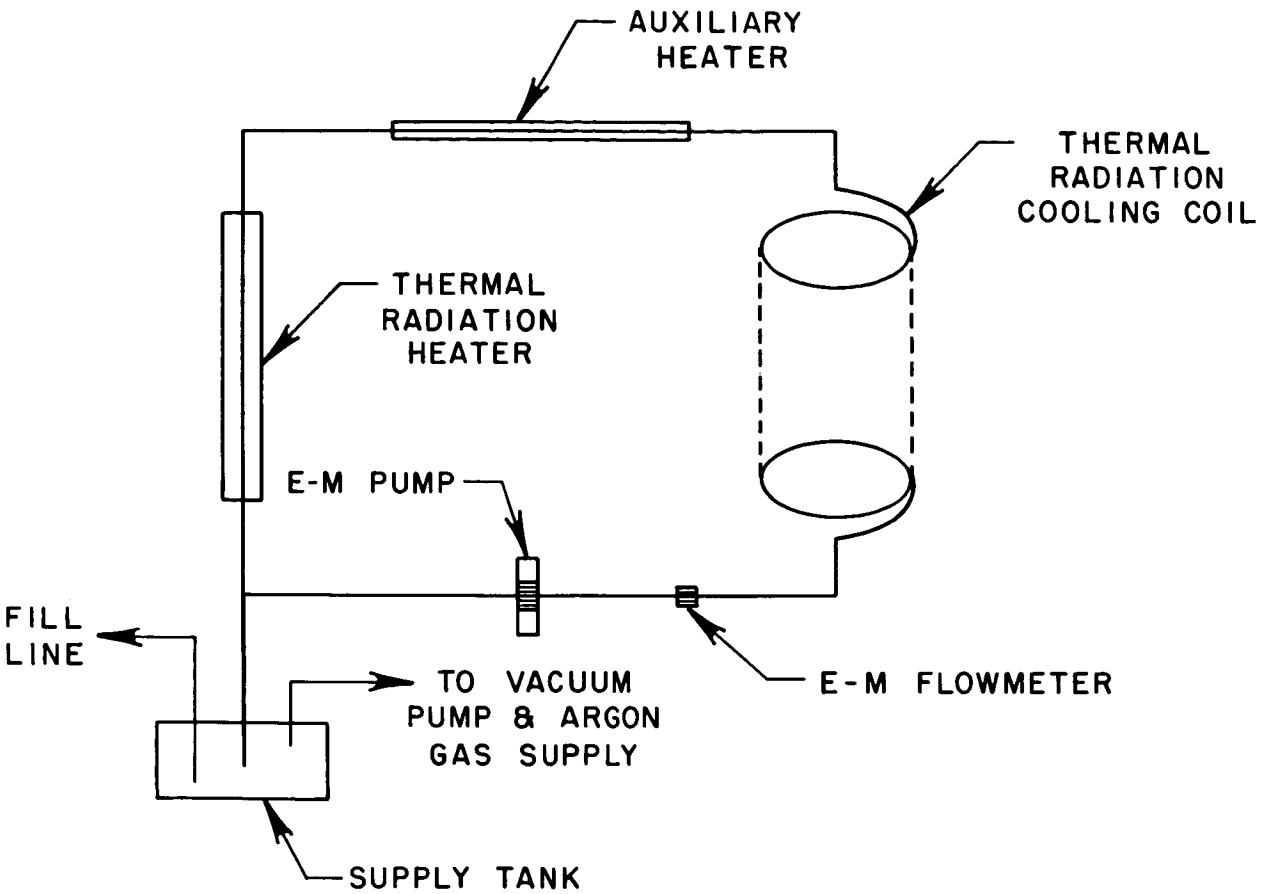


Fig. 1. Schematic Diagram of Thermal Radiation Heated Loop

electrical and thermal insulation between the tantalum heating elements and the tube containing the flowing NaK. The Al_2O_3 insulation also served to support and position the tantalum heating elements. Heat was transferred from the heating elements to the tube by thermal radiation. The heat was then conducted through the tube wall to the liquid metal flowing inside the tube. A photograph showing the thermal radiation heater before installation into the loop is shown in Figure 2. Thermal radiation shields surrounded the heated section to reduce heat losses. Heat was removed from the loop by means of a thermal radiating cooling coil. An electromagnetic pump was used for circulating the NaK, and an electromagnetic flowmeter was used for obtaining flow rates. The loop was pressurized by utilizing an argon gas blanket on the NaK surface in the supply tank.

The loop was contained within an evacuated enclosure. This enclosure was used as a safety precaution; in case of a rupture in the system, no injuries or fire would result. Also, the enclosure was necessary to extend the life of the tantalum heating elements.

Three chromel-alumel thermocouples were attached to the tube wall at the center of the sixteen-inch heated section. One of these thermocouples was beaded at the outside wall. The other two thermocouples were unbeaded, each wire being individually spot welded to the outside tube wall. These three thermocouples were brought into the heated section through holes in the bottom Al_2O_3 insulator. Also, two chromel-alumel thermocouples were located both at the inlet and the outlet of the thermal radiation heated section to measure the NaK temperature at these points in the loop.

During the period of loop operation, three thermal radiation heaters operated a total of 750 hours. Of this time, approximately 500 hours of heater operation were used to obtain single-phase heat transfer data, while the remaining time was utilized to investigate boiling heat transfer. Heat fluxes ranging up to 62,000 Btu/hr-ft^2 were investigated. Flow rates ranging up to 416 lb/hr and liquid metal temperatures ranging up to 1400°F were obtained.

The operation of the thermal radiation heater has shown the feasibility of thermal radiation techniques for supplying fairly high and uniform heat fluxes to a high temperature liquid metal. Also, the data obtained from this experiment for a single-phase liquid flowing upward in a vertical tube under

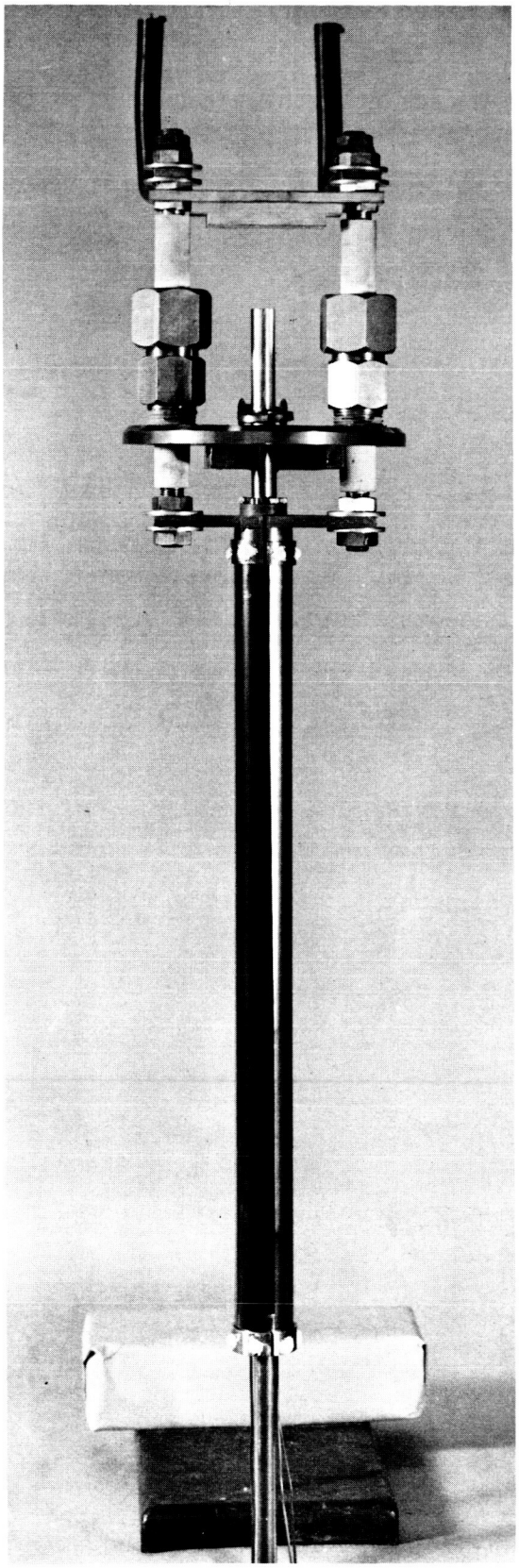


Fig. 2. Thermal Radiation Heater

constant heat flux conditions shows agreement with the expressions presented by Lyon[1] and Dwyer.[2] These results are shown in Figure 3. The boiling observations in this investigation have resulted in the same basic conclusions found by other investigations.[3] It was observed that the initiation of boiling at low pressures (less than one atmosphere) is generally accompanied by a "bumping" noise and flow instabilities. A more elaborate discussion of this experiment may be found in Reference 4.

ELECTRON-BOMBARDMENT HEATING

Electron-bombardment heating may be applied in an experimental loop for the study of the heat transfer phenomena of the liquid metals. Taylor and Steinhaus[5] have shown that electron-bombardment heating is a satisfactory technique for this application, in both forced-convection and natural-convection systems.

The basic electron-bombardment heating system may be utilized either with a system studying flow through a tube or with a system investigating annular flow.

The basic system for studying heat transfer in annular flow consists of two concentric tubes with heat applied to the inside surface of the inner tube while the liquid metal flows in the annulus between the tubes (see Figure 4). The heating is accomplished by placing an electron emitter (cathode) inside the evacuated inner tube, heating the cathode, and drawing the electrons to the inner tube (anode) with an accelerating voltage. The generated heat then flows through the tube wall to the liquid metal inside the annulus.

The arrangement for using electron-bombardment to supply heat to a liquid metal flowing in a circular tube consists of the electron emitter (cathode) surrounding the flow tube (anode). The cathode consists of many vertically positioned wires, equally spaced around the flow tube. This heating arrangement is surrounded by shielding. A cross-section of this system is shown in Figure 5.

Three of the most commonly used electron emitters are tungsten, thoriated-tungsten, and oxide coated cathodes. Because of the high voltages associated with the high heat fluxes required in boiling liquid metal studies, it appears that tungsten and thoriated-tungsten emitters may be more desirable than

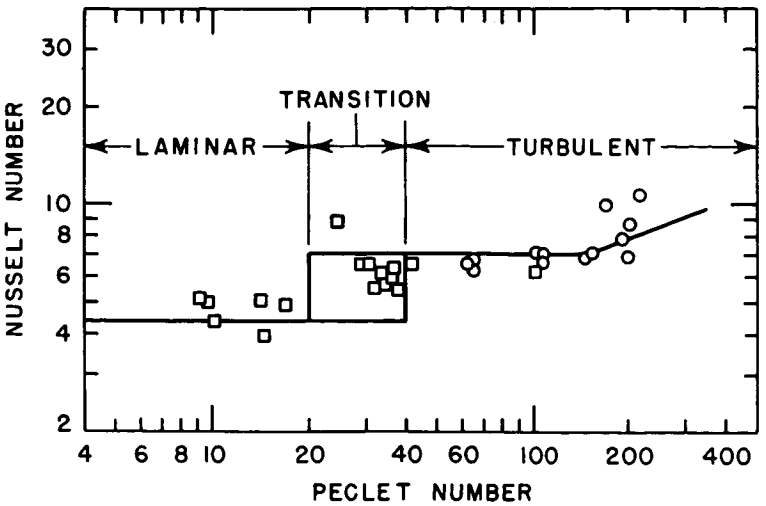


Fig. 3

Plot of Nusselt Number versus Peclet Number

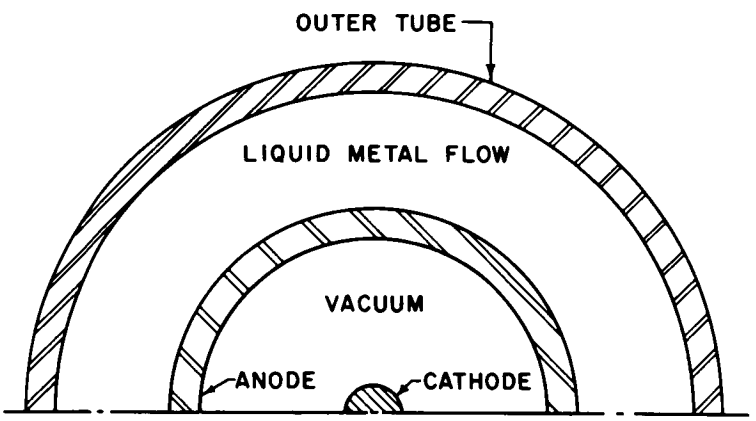


Fig. 4

Electron-Bombardment Heating Arrangement for Annular Flow

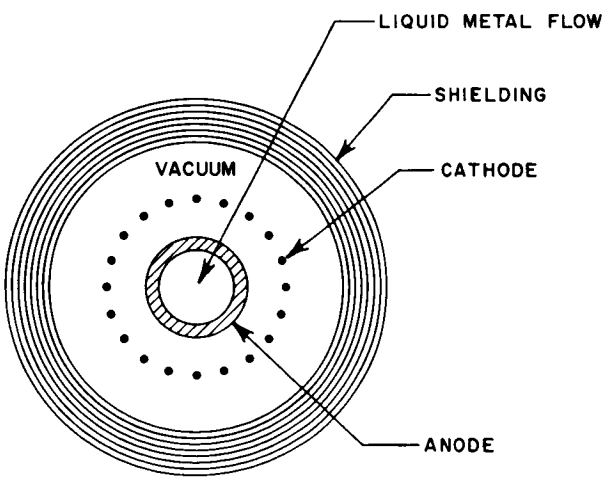


Fig. 5

Electron-Bombardment Heating Arrangement for Tube Flow

oxide-coated emitters for this application. Figure 6 shows the emission characteristics of both tungsten and thoriated-tungsten as predicted by Richardson's Equation. It is seen that the electron emission per unit area increases with increasing temperature; thus, the larger the area emitting electrons, the lower the cathode temperature required for a given heat flux. Additional information concerning the application of electron-bombardment heating for boiling liquid metals may be found in Reference 6.

A small scale electron-bombarding heating experiment was constructed at Argonne to verify the uniform heat fluxes expected. This model consisted of a 0.020 inch diameter, thoriated-tungsten cathode surrounded by a one-half inch outside diameter, type 316 Stainless Steel tubular anode of a 0.035 inch wall thickness. The heated length was four inches. Thermocouples were placed one-half inch from the ends of the heated length and in the center of the anode on the outside surface. It was found that the thermocouple at the center and the thermocouples at the ends gave identical readings at given heat fluxes. Heat fluxes ranging up to approximately 8000 Btu/hr-ft^2 at the outside anode surface were obtained. Limitations of the available power supply caused termination of testing at these power levels.

In order to gain experience with electron-bombardment heating at higher power levels than the previous experiment allowed and to check out the high voltage power supply required, another experiment has been designed. This system has the cathode placed inside a vertical tube (anode) with the liquid metal surrounding the tube. The system, schematically shown in Figure 7, is a sodium pool boiling experiment with a sixteen-inch electron-bombardment heated length. A 0.030 inch thoriated-tungsten wire is being used as the cathode. Chromel-alumel thermocouples are placed in the tube wall to obtain temperature measurements. Heat is removed from the system by means of cooling coils placed above the liquid sodium level on which the sodium vapors will condense. The system is pressurized by means of an argon gas blanket. A photograph of the electron-bombardment heating experiment is shown in Figure 8.

The power supply which is being used with this system is variable from 440 to 20,000 volts. The supply is capable of delivering 200 KW at 10 amperes. A remote control station is available so that control of the voltage and the necessary measurements may be effected at a safe distance from the high voltage region.

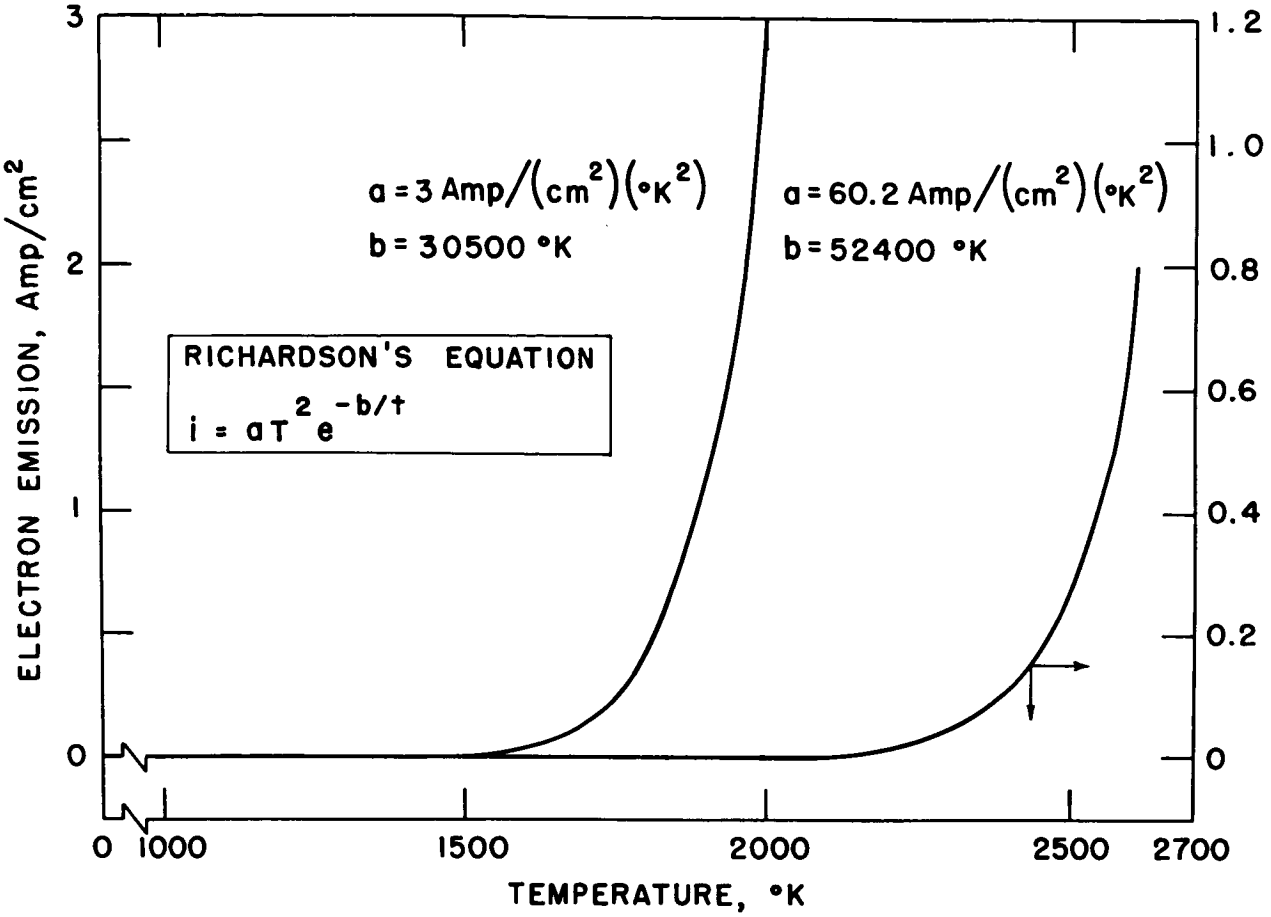


Fig. 6. Electron Emission of Tungsten (a = 60.2 amp/cm^2K^2, b = 52400°K) and Thoriated Tungsten (a = 3 amp/cm^2K^2, b = 30500°K)

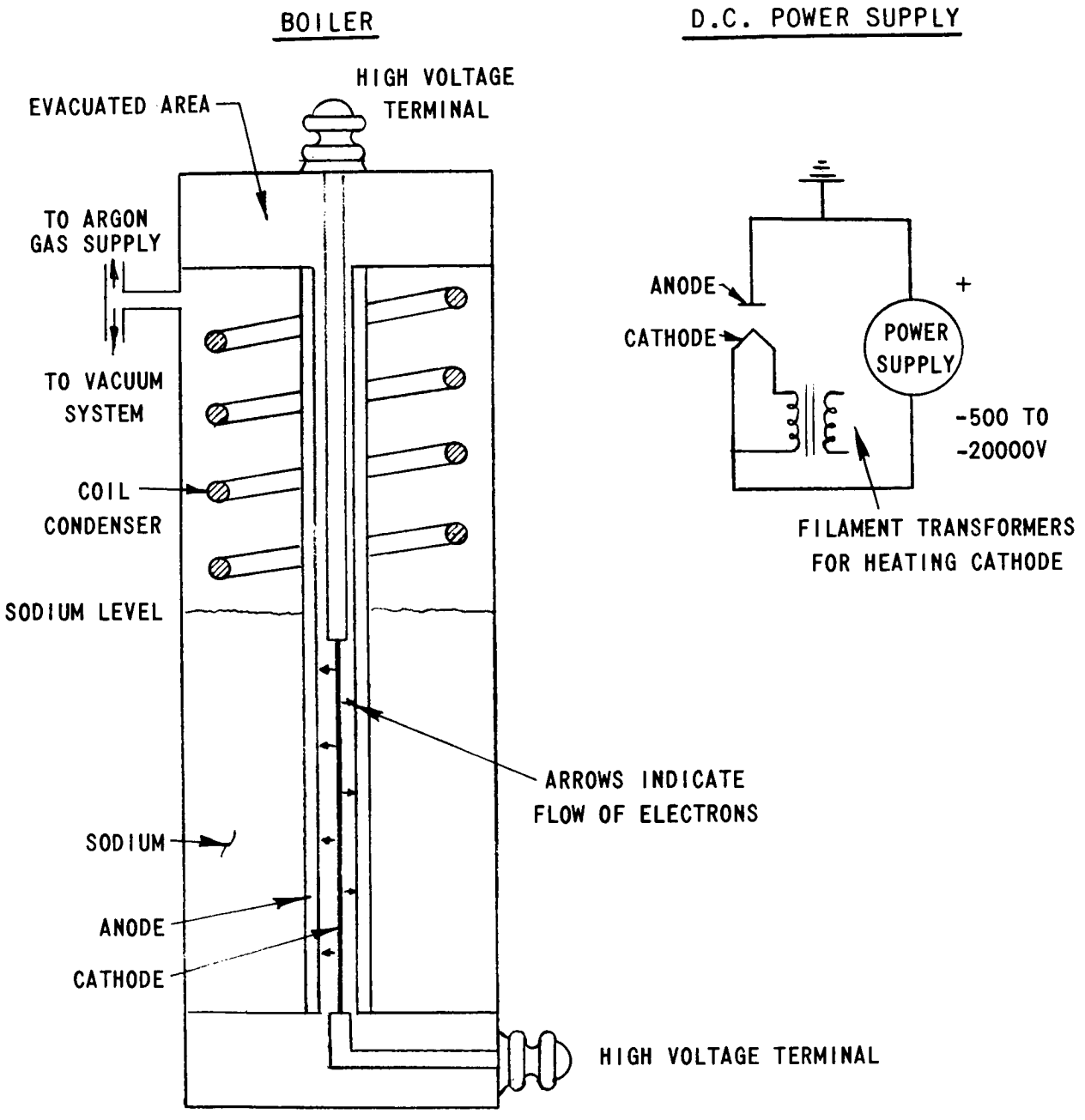


Fig. 7. Schematic Diagram of Electron-Bombardment Heating Experiment

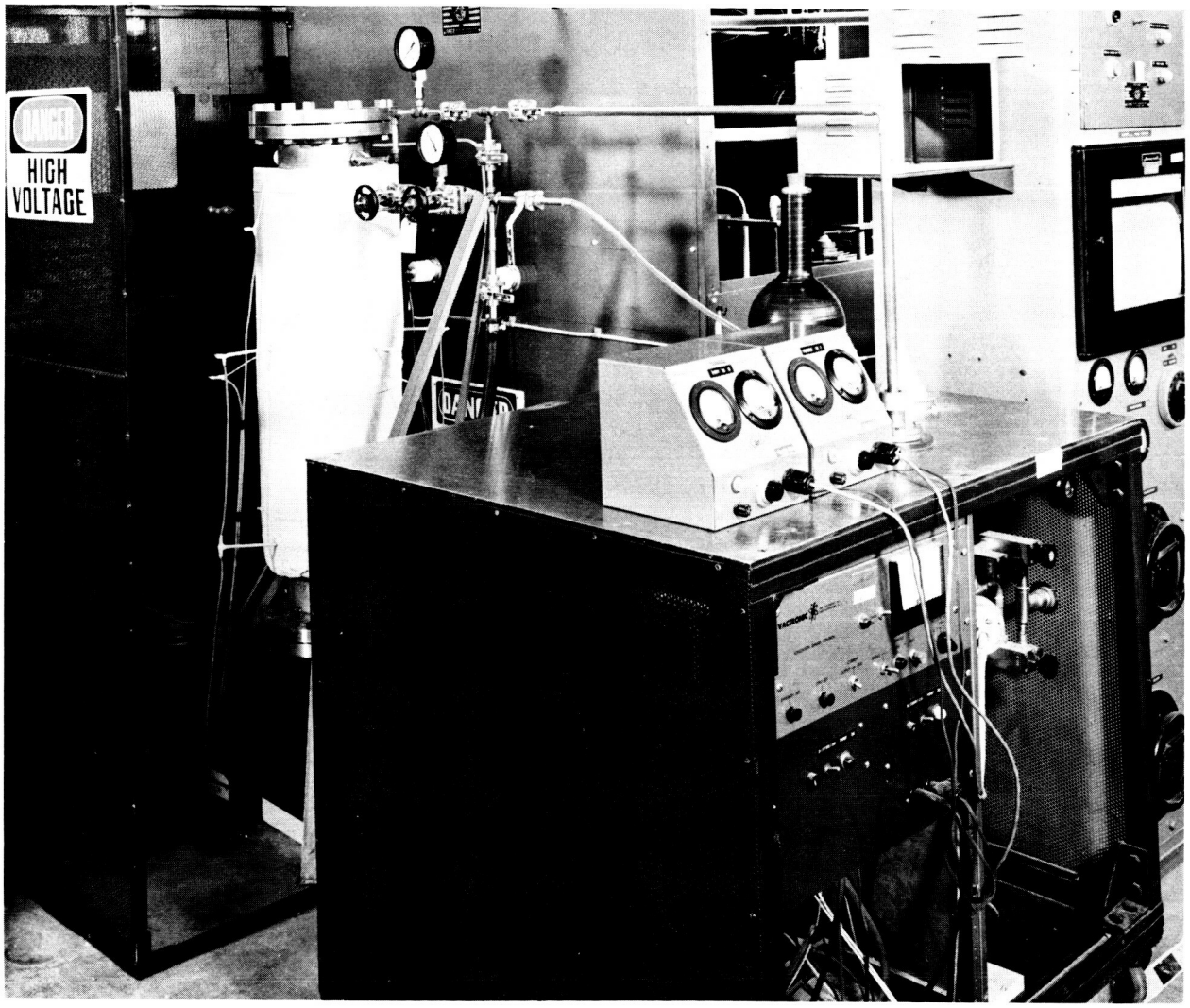


Fig. 8. Electron-Bombardment Heating Experiment

Although the data obtained from this experiment will be used mainly for the design of a high temperature electron-bombardment heater, basic information pertaining to the pool boiling of sodium from a vertical cylinder may also be available.

Operation of this electron-bombardment heated sodium pool boiler began March 30, 1965. Since then the operation of the system has been continually interrupted by several difficulties. These problems involve the design of a sufficiently flexible extension lead which will allow for thermal expansion of the cathode and still have adequate current carrying capacity, the breakdown of the Al_2O_3 high voltage insulators which appear to contain sufficient impurities such that their use as a high voltage insulator is marginal, and the development of leaks in the vacuum system.

However, during the short term operations of the electron-bombardment heated experiment, voltages ranging up to 20,000 volts and currents ranging up to one ampere have been obtained. Heat fluxes ranging up to 20,000 Btu/hr-ft^2 on the outside anode surface have been supplied. During these tests, the sodium surrounding the anode was sufficiently subcooled so that no boiling occurred. Thermocouples in the anode wall recorded temperature increases ranging up to 8°F/sec during these heating periods.

NIOBIUM-1% ZIRCONIUM LOOP HEATERS

A niobium-1% zirconium loop was designed to investigate the heat transfer and two-phase flow characteristics of boiling sodium up to a temperature of 2100°F, a pressure of approximately eight atmospheres. Among the variables to be investigated are boiling heat flux and temperature difference up to the critical heat flux occurrence, boiling and adiabatic two-phase pressure drop, vapor volume fraction, slip ratio, and boiling stability parameters.

A thermal radiation boiler section is to be used initially in the niobium-1% zirconium loop. The boiler section consists of a thick walled Nb-1% Zr tube having a length of twenty-four inches, an outside diameter of two inches, and an inside diameter nominally of 5/16 inch. This tube is surrounded by closely spaced tungsten wires which are Joulean heated. Heat is transferred from these electrically heated wires to the thick walled boiler tube by thermal radiation. This heat is then conducted through the tube wall to the liquid metal flowing inside

the tube. Thermocouples are placed at various radial and axial locations in the tube wall so that both the heat flux and the inside tube wall temperature may be determined. The tungsten heating elements are surrounded by twelve cylindrically shaped thermal radiation shields constructed of tantalum.

This loop also contains a thermal radiation pre-heater section. The pre-heater section is built basically the same as the boiler section except that it does not utilize the thick wall to increase the heat flux at the inside tube wall.

By utilizing the thick walled section with the thermal radiation heater, it is expected that heat fluxes ranging up to one million Btu/hr-ft^2 may be obtained at the 5/16 inch inside diameter of the thick walled Nb - 1% Zr tube. This high a heat flux is possible because the heat flux at the inside tube wall is 6.4 times the heat flux at the outside tube wall.

An electron-bombardment heated boiler section is also being designed for use in the niobium - 1% zirconium loop. This heater section will consist of a Nb - 1% Zr tube (anode) containing flowing sodium and surrounded by either tungsten or thoriated-tungsten emitters (cathode). This heating arrangement (see Figure 5) will then be surrounded by shielding. The inner shield will be at the same electrical potential as the cathode. The emitted electrons will be drawn to the anode by an accelerating voltage. It is expected that heat fluxes well above one million Btu/hr-ft^2 may be obtained by using this technique. The factors limiting the heat flux are the size of the 200 KW power supply and the thermal stresses in the tube (anode) wall.

REFERENCES

1. R. N. Lyon, "Liquid Metal Heat Transfer Coefficients," AIChE Trans., 47, pp. 75-79 (1951).

2. O. E. Dwyer, "Eddy Transport in Liquid-Metal Heat Transfer," AIChE Journal, Vol. 9, No. 2 (March, 1963).

3. W. M. Rohsenow, "Heat Transfer to Liquid Metals," Developments in Heat Transfer, The MIT Press (1964).

4. R. E. Holtz, "A Liquid Metal Heat Transfer Experiment," ANL-7038 (July, 1965).

5. C. E. Taylor and J. F. Steinhaus, "High Flux Boiling Heat Transfer from a Flat Plate," UCRL-5414 (November 25, 1958).

6. R. E. Holtz, "Application of Electron-Bombardment Heating for Boiling Liquid Metals," ANL-6869 (March, 1964).

N66 31673

ELECTRICAL HEATER FOR LIQUID METALS AT ELEVATED TEMPERATURES *

Lance G. Hays
Jet Propulsion Laboratory
Pasadena, California

1. Introduction

An advanced development feasibility investigation of a liquid metal MHD space power concept is currently being conducted at the Jet Propulsion Laboratory (Ref. 1). A future phase of this investigation is expected to involve a five megawatt (thermal) system test using a cesium-lithium working fluid combination. A key component in this test, as in other high temperature liquid metal systems, is the liquid metal heater. In recent programs heater failure has been a prominent operating difficulty encountered in experimental liquid metal loops. A particularly severe set of requirements exist for the MHD system heater. The heater for this application must transfer five megawatts to lithium flowing at a maximum flow rate of 100 pounds per second. Maximum temperature for the lithium may be as high as 2000°F in the eventual application, requiring refractory metal construction.

Direct resistance heating of a liquid metal has been used quite successfully in recent high temperature investigations (Ref. 2, 3, 4). However, for large power levels the use of expensive low voltage, high current power sources are required to avoid excessive heater geometric size and fluid pressure loss. Because of the high currents in larger installations, bus problems may be encountered. Also d.c. power is desirable to avoid skin effect and fatigue due to fluctuating magnetic force fields.

* This work presents the results of one phase of research carried out at the Jet Propulsion Laboratory, California Institute of Technology, under Contract NAS 7-100, sponsored by the National Aeronautics and Space Administration.

Radiant heating has also been proven successful for high temperature applications (Ref. 5). This method allows the use of medium voltage power sources and moderate current levels. However, for large power inputs the required heat transfer area may become excessive and necessitate fabrication of large, complex refractory metal structures.

The third type of heater, that which was selected for use, is the conduction heater. Heat is generated in the current element and transferred by conduction across an electrical insulator and metal sheath to the liquid metal stream. Conduction heaters have been used extensively for liquid metal heating (Ref. 6, 7, 8), but at lower power and temperature levels than those of interest for the liquid MHD system. This type of heater enables the use of medium voltage, moderate current power sources and results in a compact component. However, the attainable level of reliability is not known for higher temperatures.

The three most important failure modes for conduction heaters at elevated temperatures were felt to be electrical breakdown of the insulator, degradation of the ceramic in the region of sheath weldments, and local over-heating in the region of center conductor attachment to the bus. The method of approach has been to use a simple configuration which was amenable to analysis and to select materials and fabrication methods which are compatible at the predicted temperatures.

The sequence adopted for development of the five megawatt heater is as follows:

1. Analysis and preliminary sizing of the five megawatt heater based on existing high temperature electrical breakdown data for fired ceramics.

2. Testing of geometrically similar heater elements in lithium at elevated temperatures to determine breakdown strength and insulator leakage currents for swaged ceramics, and to verify design and fabrication methods.

3. Operation of a geometrically similar heater in a 100 kilowatt cesium-lithium erosion loop to determine reliability and verify design.

4. Final design of the five megawatt heater incorporating test data from (2) and (3).

This paper presents some results from (1) and (2) and discusses fabrication details of the 100 kilowatt lithium heater for the erosion loop.

2. Heater Design

The starting point in the heater design was to examine the relationship between center conductor temperature, geometry, and electrical characteristics as a function of the allowable insulator field strength and material properties.

In this analysis the leakage currents, axial temperature variation and contact resistances were neglected. Consider the geometry of Fig. 1. If a total of N heating elements are used with n elements connected in series, the total power is given by Ohm's law as:

$$P_e = \frac{23.9\ V^2\ N\ d_c^{\,2}}{\rho\ n^2\ L} \tag{1}$$

(where the quantities and units are defined in Nomenclature).

The temperature difference from sheath to center is obtained by considering conduction through concentric cylinders. If the surface heat flux is related to the geometry and total power, the temperature difference is given by:

$$\theta_c = \frac{0.543\ P_e}{NL}\left[\frac{\ln\ (d_i/d_c)}{k_i} + \frac{\ln\ (d_t/d_i)}{k_t}\right] \tag{2}$$

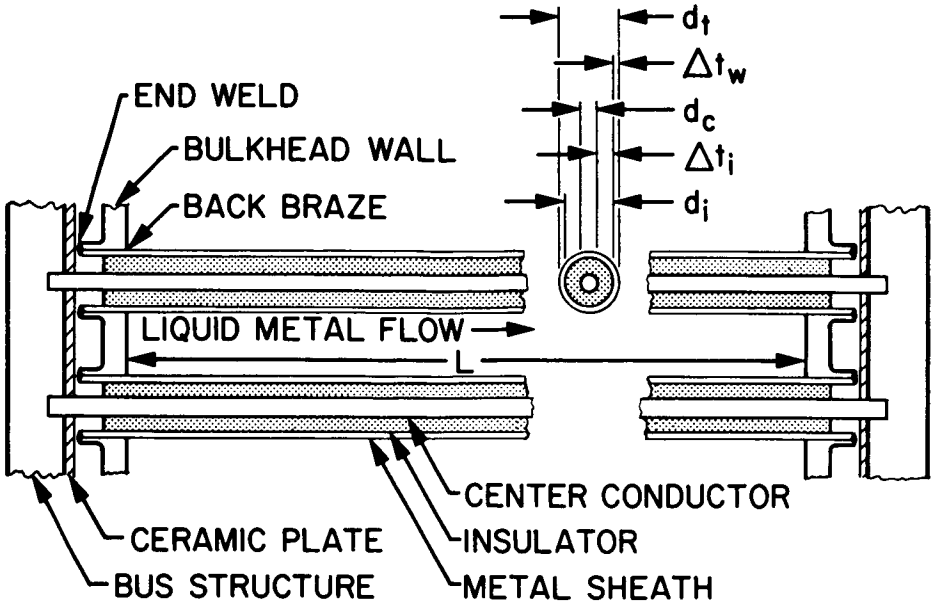


Fig. 1. Schematic of Conduction Heater Geometry

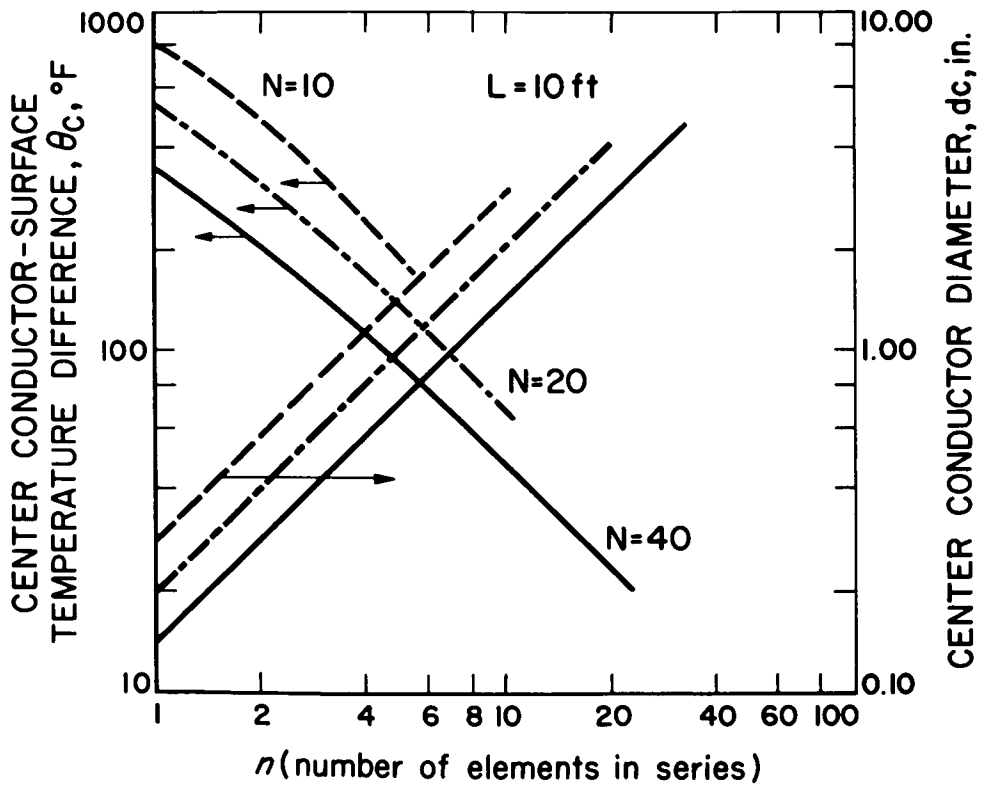


Fig. 2. Temperature Difference and Center Conductor Diameter versus Number of Heating Elements Connected in Series

If the design field strength on the ceramic is E then the minimum insulator thickness which can be used is simply:

$$\Delta t_i \approx \frac{V}{E} \tag{3}$$

and (2) becomes

$$\theta_c = \frac{0.543\ P_e}{NL}\left[\frac{1}{k_i}\ln\left(1+\frac{9.8\ V^2\ N^{\frac{1}{2}}}{nE\ P_e^{\frac{1}{2}}\rho^{\frac{1}{2}}L^{\frac{1}{2}}}\right)+\frac{1}{k_t}\ln\left(1+\frac{\Delta t_w}{\frac{0.102nP_e^{\frac{1}{2}}\rho^{\frac{1}{2}}L^{\frac{1}{2}}}{VN^{\frac{1}{2}}}+\frac{V}{E}}\right)\right] \tag{4}$$

This expression can be used for a specified power output P_e, and power source voltage V, to determine the influence of element length L, total number N, and series connection number n, on the sheath-center conductor temperature difference, θ_c, and the center conductor diameter, d_c.

For example, figures 2 and 3 were calculated for an output power, P_e, of 5000 kw, a voltage, V, of 150 volts and an allowable gradient, E, of 3 volts/mil. The value of 3 volts/mil for the ceramic insulator was based on a measured breakdown strength of 4 volts/mil reported in reference 9 for alumina and magnesia at 1200° C (2650°R) and beryllia at 1000°C. Beryllia was chosen as the insulator for these calculations due to its compatibility with refractory metals at elevated temperatures and high thermal conductivity. The sheath was Cb-1Zr, with a wall thickness of .030 in., chosen for lithium compatibility and fabricability. The center conductor was tantalum, chosen for its high resistivity, and ductility in the recrystallized condition. Properties were evaluated at average temperatures, assuming a sheath temperature of 2000°F and a design center conductor temperature of 2400°F.

As shown in Figure 2, increasing the number of heating elements results in lower centerline temperatures and larger center conductor diameters. The same

effect is produced as more elements are operated in series. For example, for 40 elements, operating groups of 2 in series, instead of all in parallel, lowers the centerline temperature difference from 350°F to 200°F. For parallel operation decreasing the number of elements from 40 to 10 would increase the centerline temperature from 350° to 800°F, exceeding the design value.

The influence of varying element length is shown in Figure 3. For 40 elements operating in parallel changing the length from 10 ft to 5 ft would increase the centerline temperature difference from 350°F to 900°F. This length decrease would require a decrease in center conductor diameter from about 0.15 in. to 0.10 in. to satisfy the voltage and power requirements.

On the basis of these calculations, a reasonable heater geometry which should satisfy reliability considerations by having a moderate centerline temperature would be comprised of 40 elements of 10 ft length. This would produce a centerline temperature difference of about 350°F with a conductor diameter of 0.16 in. The sheath or outer diameter would be 0.32 in. and the insulator thickness,0.050 in.

Arrangement of these heaters in a square array with s/d = 2 would result in a heater shell of 4.5 in. i.d. by 10 ft length for the five megawatt unit. Application of liquid metal heat transfer relations for in-line rod bundles (Ref. 10) yields a temperature drop of about 20°F from the sheath wall to the coolant bulk temperature for 100 lb/sec lithium flow at about 1975° average bulk temperature and the required heat transfer rate. For a maximum lithium temperature of 2000°F this would result in a centerline temperature of about 2400°F, which is certainly consistent with the assumptions of the analysis and compatible with available materials and fabrication techniques.

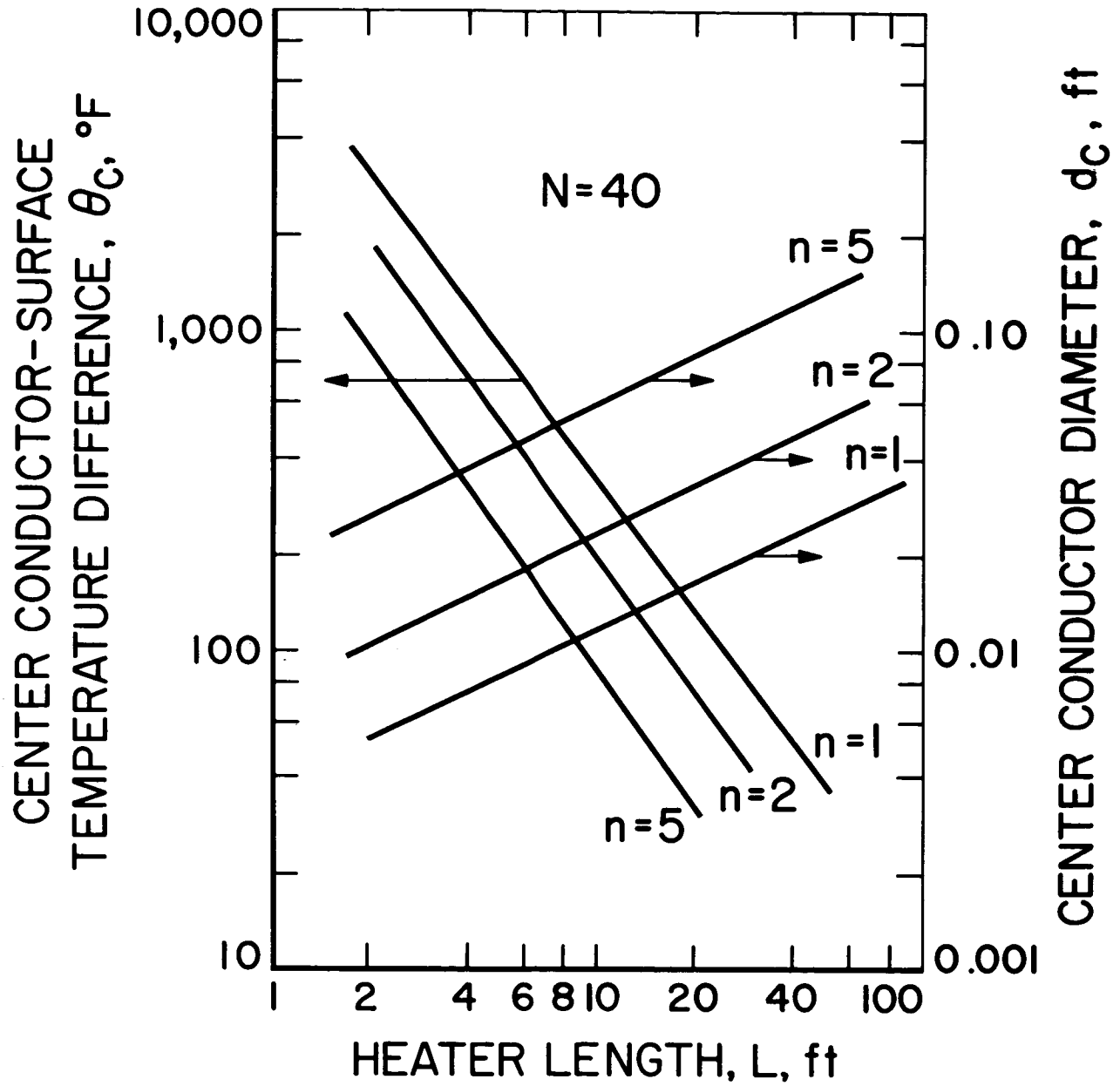


Fig. 3. Temperature Difference and Center Conductor Diameter versus Heater Length for 40 Heating Elements

The moderate current levels (~30,000 amps) enable radiantly cooled buses to be used to supply power to the heater with the attendent simplicity and reliability. The method of attachment of the sheaths to the heater shell is to recess the ceramics and then weld, followed by a zirconium back braze (cf. Fig. 1). The exposed center conductor (cf. Fig. 1) will generate a significant amount of heat which must be removed and dissipated by the bus to avoid excessive temperature in this region. In the following discussions, the recessed length, L_1, is the length from the bus to the beginning of the ceramic (cf. Fig. 1). In order to determine the influence of the recessed length on the minimum bus length, L_2, a simplified analysis was performed to guide the design of test geometries. The following assumptions were made for the analysis:

1. The exposed conductor is insulated in the radial direction.
2. The maximum temperature allowable is the centerline heater temperature (2400°F in the example above).
3. One dimensional heat flow.

With these assumptions the bus dimensions can be determined. For example, for the cylindrical conductor:

$$T_b = T_c - \frac{q''' L_1^2}{2k_1} \tag{5}$$

where q''' = volumetric heat release $= 0.181 \frac{I^2 \rho}{d_1^4}$ (6)

The heat transferred by radiation from a cylindrical bus heated at one end is:

$$Q_r = \sigma \epsilon \eta_f \pi d_2 L_2 T_b^4 \tag{7}$$

(neglecting the bus I^2R heating since it is small compared to the end heating)

where:

$$\eta_f = f\left(\frac{2\sigma\epsilon T_b^3 L_2^2}{k_2 d_2}\right) \tag{8}$$

The relation between η_f and "radiation modulus" for a cylindrical fin is given in Fig. 4 (after Ref. 11).

It is now desired to find the value of bus length, L_2, which will reject the required heat. Solving for L_2 using (5) and (7) gives

$$L_2 = 0.0454 \frac{I^2 \rho L_1}{\sigma \epsilon \eta_f d_1^2 d_2 T_b^4} \tag{9}$$

Equation (9) can be solved by trial and error for the value of L_2 which will reject the required heat. Fig. 5 presents the results of such a calculation for one of the test geometries. The bus length, L_2, required to maintain the exposed conductor temperature at a value less than the centerline temperature, T_c, is plotted as a function of the exposed conductor length. The particular values of I, d, and T_c were 400 amperes, 0.150 in. and 2370°F. The influence of different bus diameters is also shown. As can be seen, beyond a recess of about 1/8 in. to 1/4 in. the required bus length increases very rapidly. For these parameters no solution exists to the equations beyond a recess of about 3/8 in., indicating that radiant cooling could not be used without increasing the bus diameter, emissivity, or maximum allowable temperature. The recessed distance of the test geometry is 1/8 in. From the curve, for a bus diameter of 1/2 in. a minimum bus length of about 1/4 in. is required to dissipate the heat. Hence, any bus length in excess of this value would clearly be acceptable. Further increases in L_2 will simply lower the maximum temperature of the exposed center conductor.

Similar calculations can be performed for a planar bus with multiple conductors by assigning an area to each conductor and using relations for circular fin efficiencies based on circular fins with the equivalent area of the assigned area.

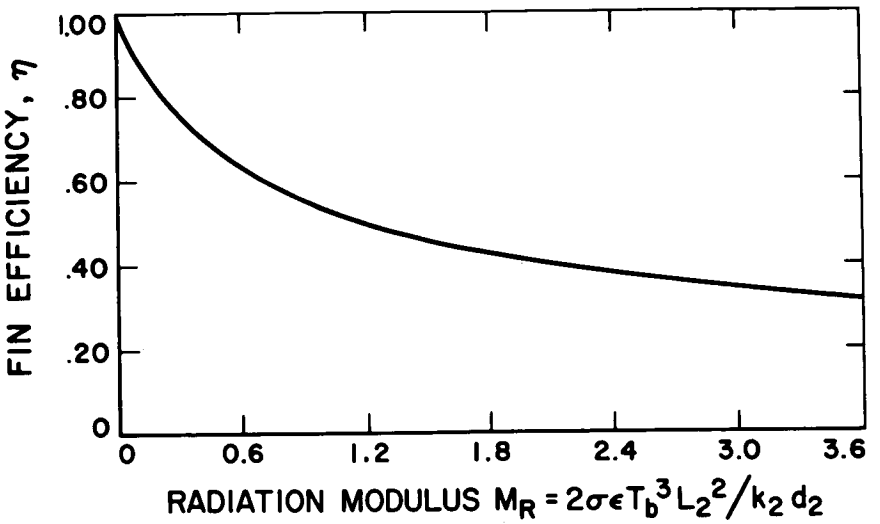


Fig. 4. Fin Efficiency versus Radiation Modulus for a Cylindrical Conductor

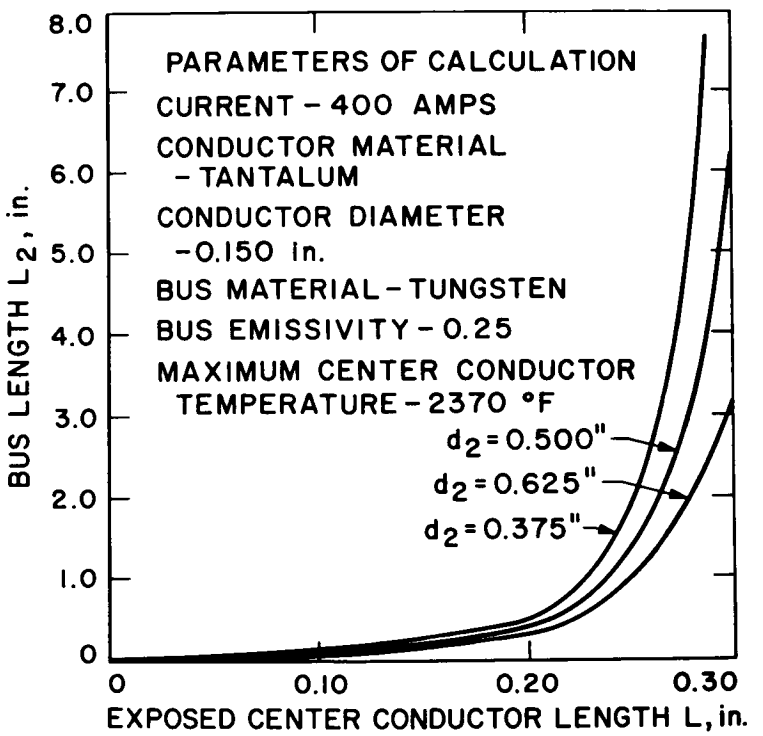


Fig. 5. Minimum Bus Length Required for Radiant Cooling of Exposed Center Conductor in a Test Geometry

3. Test Geometry and Experimental Arrangement

An initial test geometry was fabricated and tested in lithium which had a tantalum center conductor of .125 in. diameter, .070 in. of swaged alumina insulation, and a Cb-1% Zr sheath with a diameter of .380 in. The swaging on this unit was performed by Temptron, Inc. of North Hollywood, California, to JPL specifications. This geometry is shown schematically in Figures 6 and 7 as it was installed in a lithium container with expansion chamber. W5Re vs W26Re thermocouples were attached, but the primary temperature measurement was an optical pyrometer.

As noted, the ceramic was recessed by 1/4 in. in this initial geometry to ensure good heater weldments. Welding and zirconium brazing were performed in an inert gas dry box (Ref. 12) and the unit was subsequently annealed at 2200^{o}F for one hour in a vacuum furnace. Boron nitride spacers and supports were used which provided an increased path for heat flow from the exposed conductor.

After filling the container with lithium from a filtered stainless steel loading system, the basic heater capsule was mounted on the end flange of an ion-pumped, water-cooled, vacuum chamber as shown in Fig. 8. During operation in the chamber, the heat generated in the heater was conducted through the lithium and container wall and transferred to the vacuum chamber wall by radiation. The wall of the Cb-1%Zr container was grit blasted to enhance the emissivity.

A silicon rectifier d.c. power supply was used to supply the heater current through brazed vacuum feedthroughs. Several small d.c. power supplies were connected in parallel to apply voltage to the heater sheath to determine ceramic resistivity and breakdown. Fig. 9 shows the final test setup with the heater at temperature.

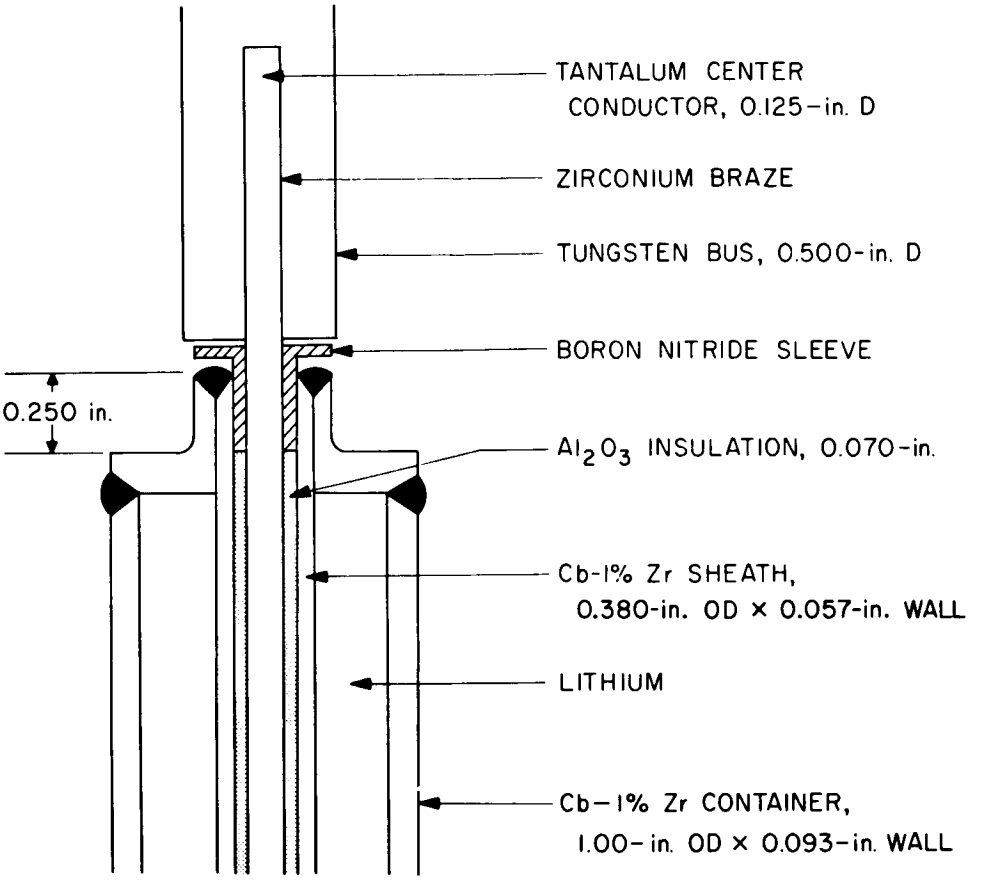


Fig. 6. End Detail of Lithium Heater

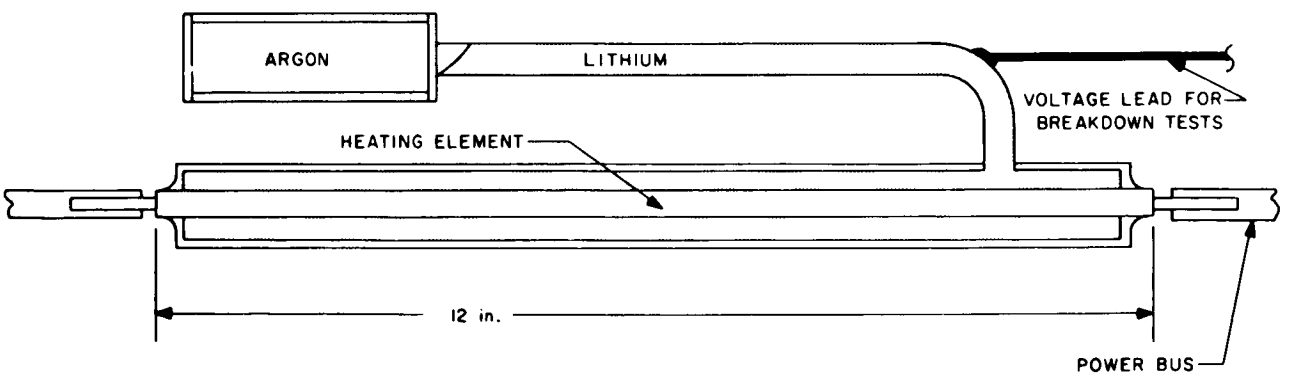


Fig. 7. Schematic of Heater Test Geometry

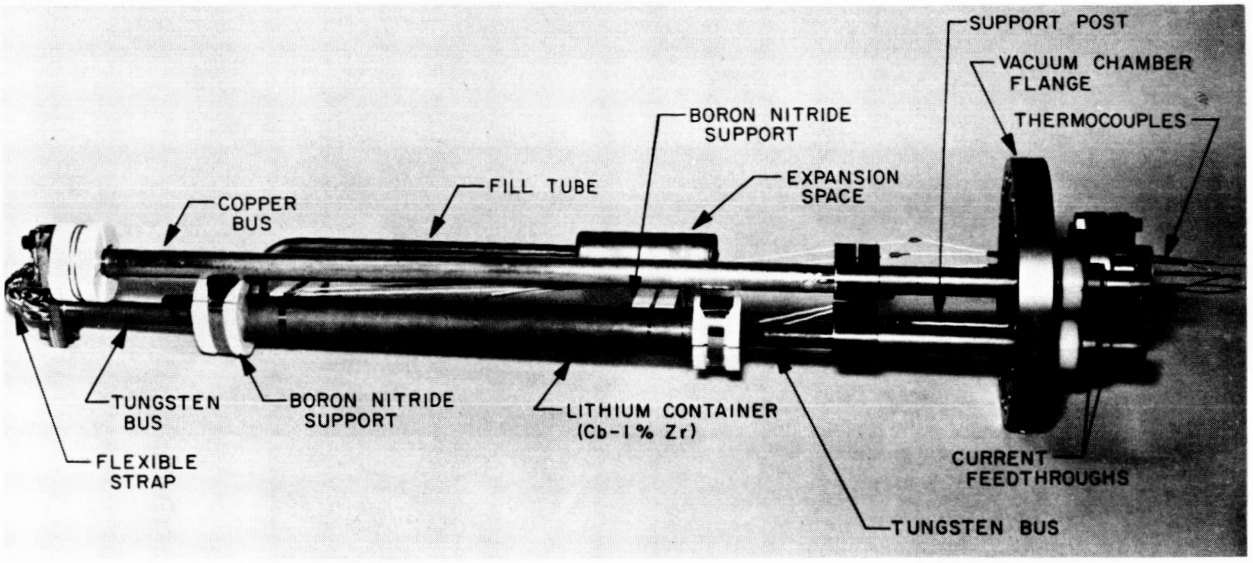


Fig. 8. Lithium Heater Experiment Mounted on Flange

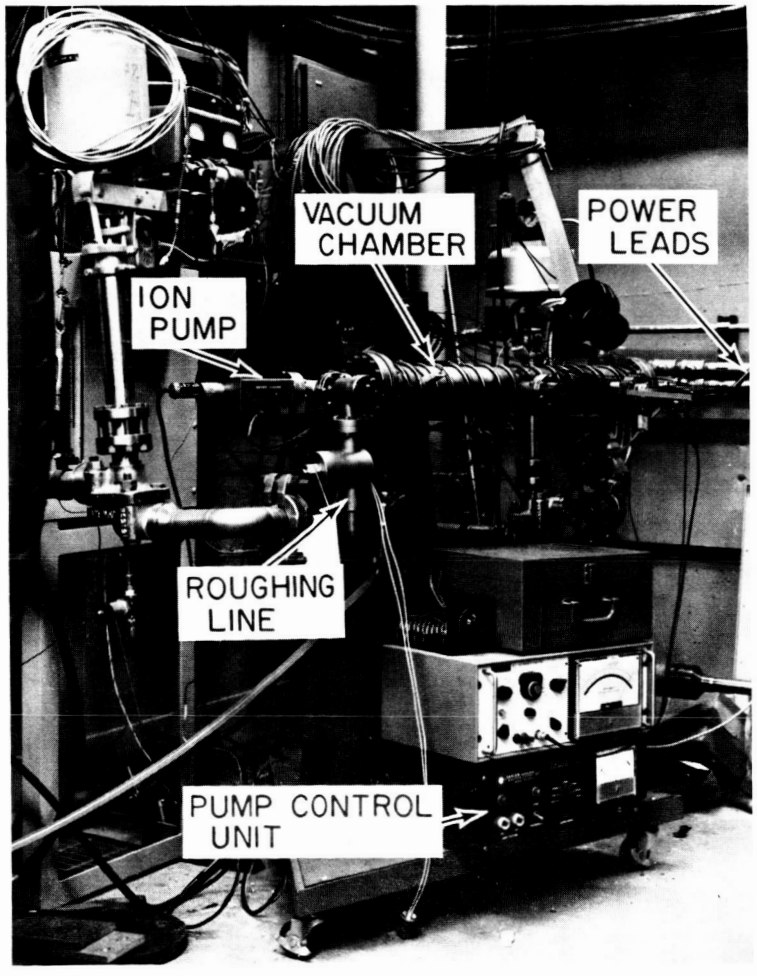


Fig. 9. Lithium Heater Test during Operation

4. Initial Test Results

After the outgassing, the lithium heater was operated continuously for 500 hours maintaining a bulk lithium temperature of approximately 2080°F. This is a corrected pyrometer temperature based on a surface emissivity of 0.4 which was determined by a heat balance. (The uncorrected reading was 1940°F). During the course of the test the temperature varied at times between 2000°F and 2100°F because of drift in the power supply but at no time was less than 2000°F. As shown in Fig. 10, approximately 2 kw were required to maintain the heater at its peak temperature. The heat flux during this test was 130 watts/in.^{2} at the heater surface. The center conductor temperature was between 2360°F (calculated from the surface temperature and heat flux) and 2540°F (estimated from the measured increase in resistance of the tantalum). The low bus temperatures measured (~500°F) qualitatively confirmed the radiant cooling calculations discussed under heater design.

After the operation for 500 hours, a d. c. potential was applied to the sheath to determine resistivity of the alumina in the swaged condition and the maximum field strength it could support. Fig. 11 presents the results of these tests.

A linear relation between leakage current and potential existed up to about 3 volts/mil. The average resistivity for this region was measured at 0.25×10^5 ohm-cm. for the swaged alumina at an average temperature of about 2270°F. This can be compared to a value of 1×10^5 ohm-cm. reported in the literature for fired alumina at this temperature (Ref. 9). Above an applied voltage of 3 volts/mil the leakage current showed a sharp increase which may have been due to the beginning of breakdown in the ceramic. However, the heater current had to be decreased as the leakage current increased to maintain

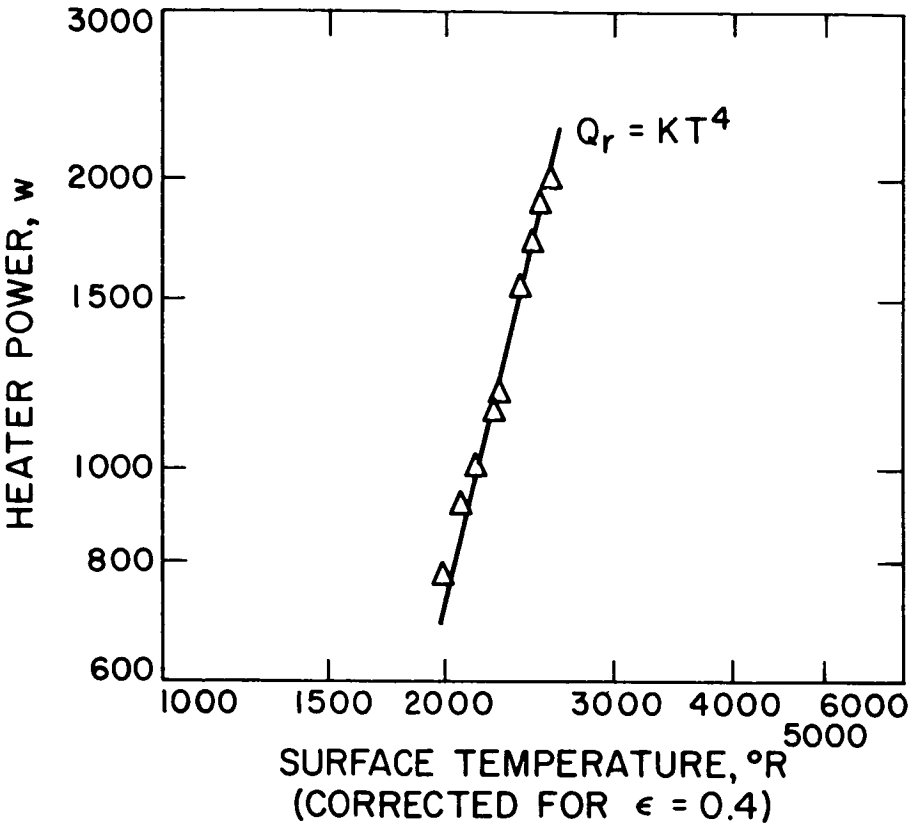


Fig. 10. Lithium Heater Power versus Surface Temperature of Lithium Container

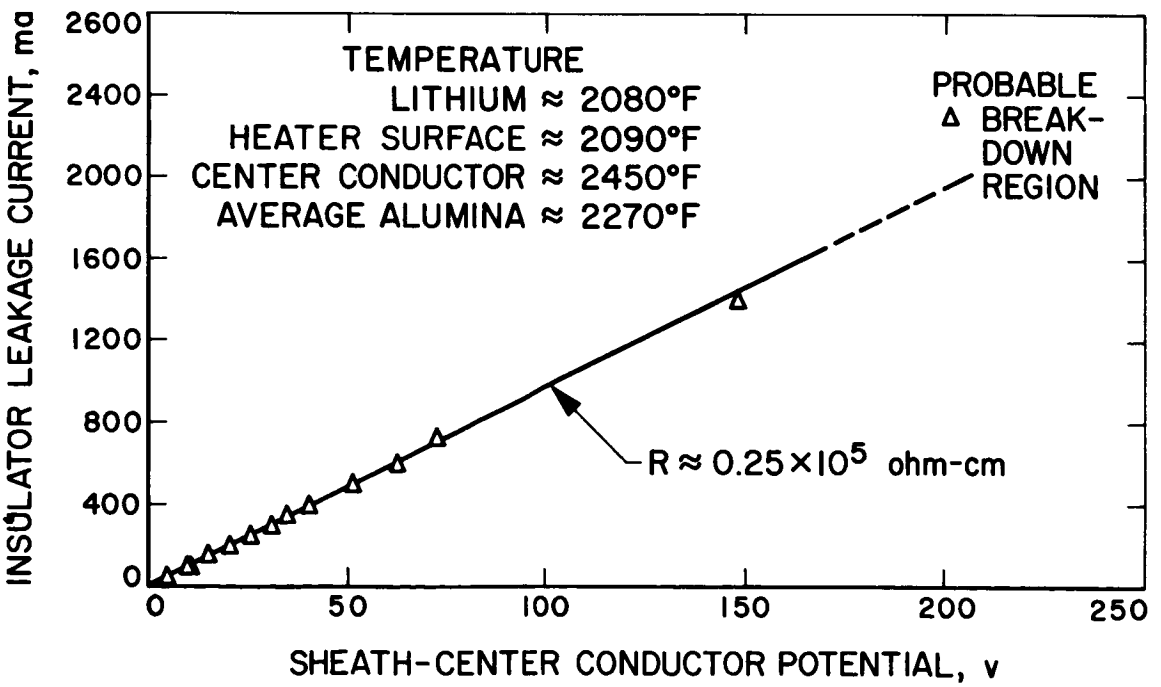


Fig. 11. Alumina Insulator Leakage Current for the Lithium Heater as a Function of Applied Potential

a constant ceramic temperature. The decrease in resistivity may, therefore, have been due to local temperature increases which resulted from the difficulty in coordinating these two power inputs. In any case, it was felt the tests demonstrated the basic feasibility of using swaged conduction heaters at elevated temperatures with field strengths of up to 3 volts/mil across the ceramic.

Post-test examination of the heater revealed slight reactions between the alumina and tantalum and the boron nitride and Cb-1%Zr in the region of the end weldment. These reactions are known and were expected but are not serious at the temperatures of interest. It is not anticipated that a similar reaction will occur between the beryllia and tantalum at the temperatures of interest. No lithium penetration occurred in the weld regions and the end weldments appeared mechanically sound after test.

5. Future Experiments

Static testing of heater geometries similar to the above will continue in the future. A total of five units with beryllia insulation and five with alumina have been fabricated for this purpose. The primary emphasis during these tests will be determination of ceramic electrical properties (breakdown strength and resistivity) at elevated temperatures. A secondary goal will be the demonstration of increased heat fluxes (1000 watts/in^2 max.) with the beryllia heaters. Figure 12 shows a beryllia heater ready for testing in the vacuum system described above. For this test, cylindrical fins of Cb-1%Zr are used to achieve a satisfactory level of heat flux. A black-body hole is provided for pyrometer temperature measurements and several different thermocouple attachment methods will be compared. Other tests are planned, using lithium reflux systems, to enable the attainment of still higher heat fluxes.

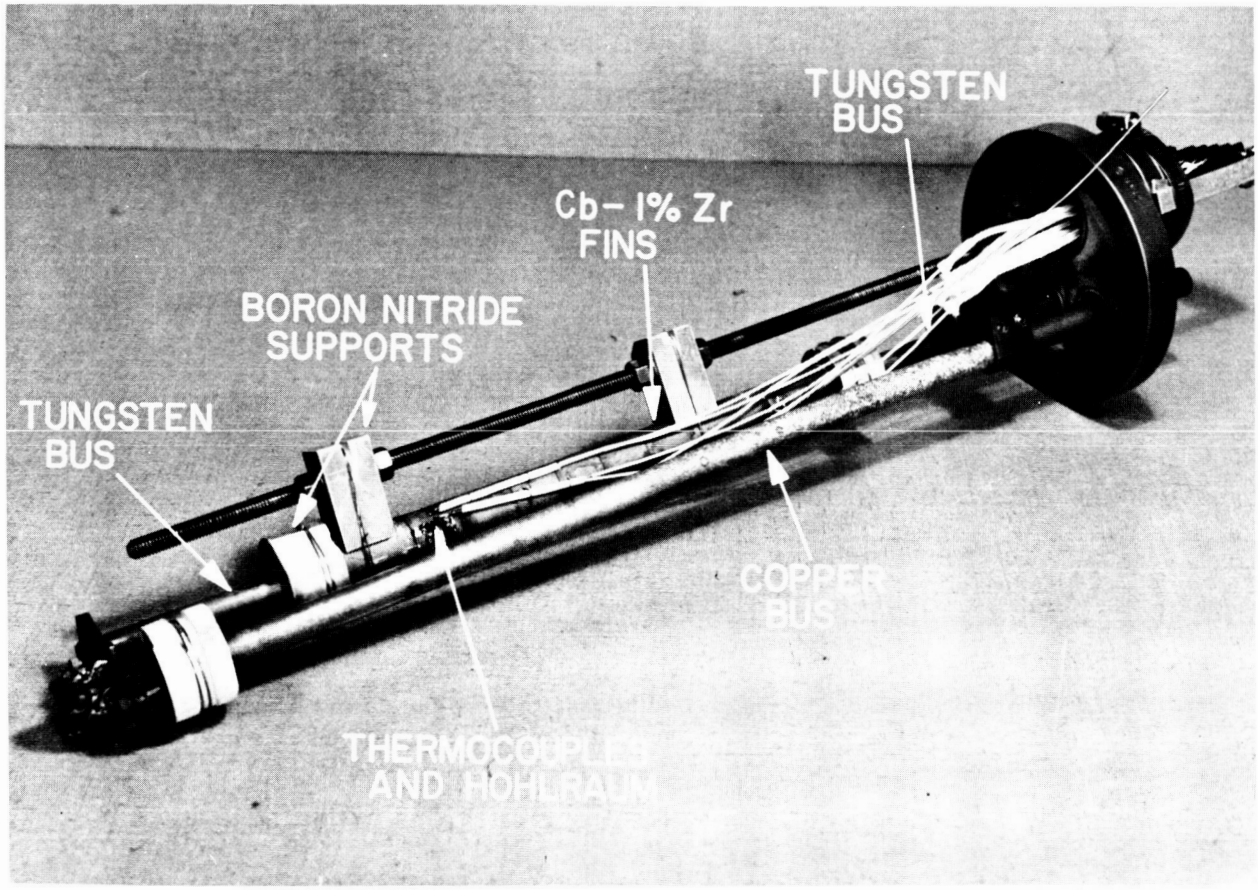


Fig. 12. Beryllia Heater Test Setup

Tests in a flowing lithium system are also planned for the near future. The heater for this cesium-lithium erosion loop (Ref. 1) is shown prior to welding in Fig. 13. It consists of four heating elements of 2½ ft length in a Cb-1%Zr shell. The heating elements have tantalum center conductors with swaged beryllia insulation and Cb-1%Zr sheaths. A stress analysis on the heater indicated a need for a curved configuration to relieve thermal expansion stresses. The design conditions on this heater are 300 watts/in.^{2} with the resulting temperature difference from center conductor to sheath of about 100^{o}F.

Completion of the tests described above (in addition to providing basic information on electrical properties of ceramics at elevated temperatures) should result in sufficient data for final design of a five megawatt lithium heater. A satisfactory degree of reliability, a compact geometry and an inexpensive system appear to be attainable with the conduction type of heater.

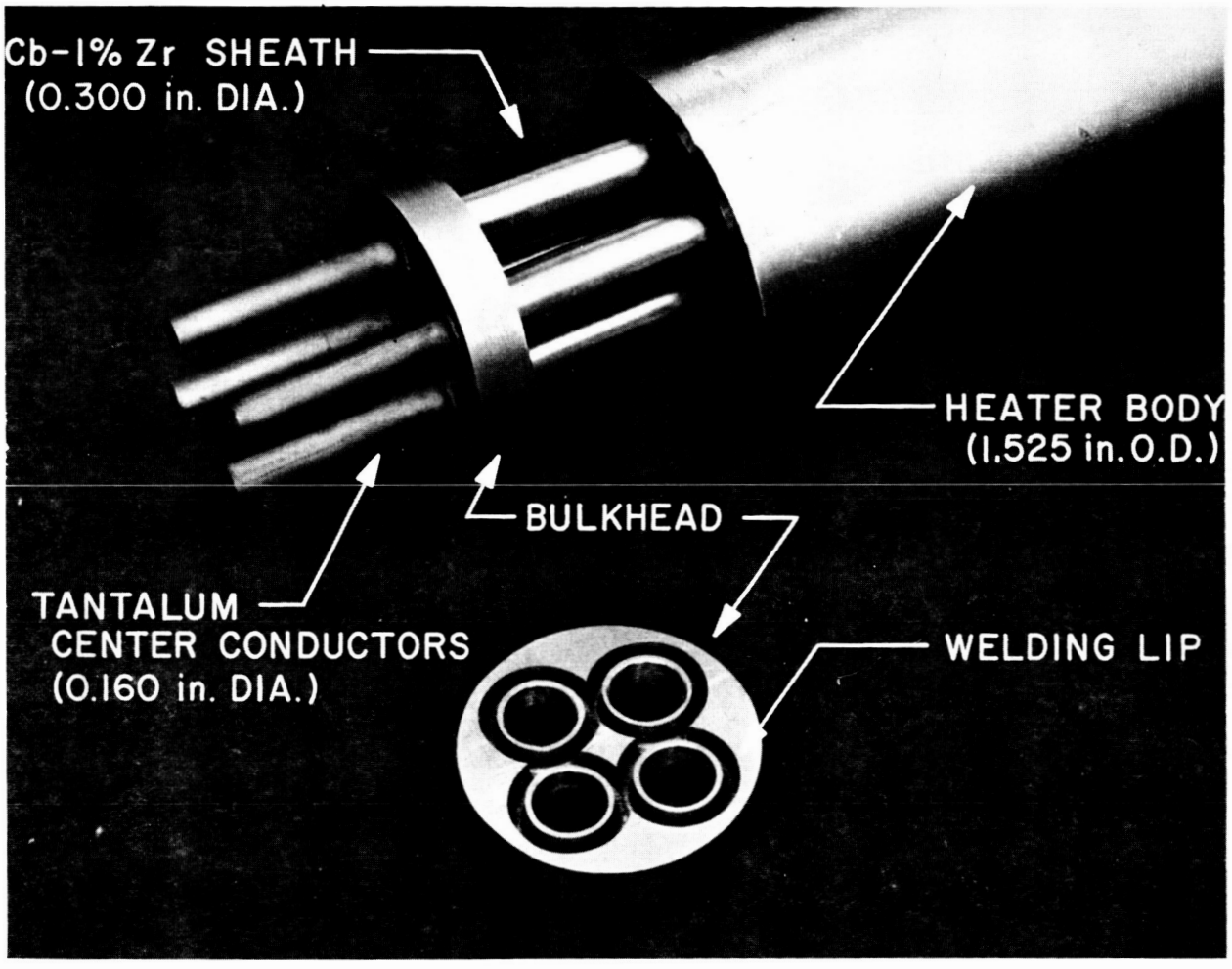


Fig. 13. End Detail of Erosion Loop Heater Components

NOMENCLATURE

d_c, d_1 = center conductor diameter (ft)

d_i = outer diameter of insulation (ft)

d_t = outer diameter of sheath (ft)

d_2 = bus diameter (ft)

E = maximum allowable ceramic gradient (volts/ft)

I = current in conductor (amp)

k_1 = thermal conductivity of center conductor (Btu/hr ft ^{o}F)

k_i = average thermal conductivity of insulator (Btu/hr ft ^{o}F)

k_t = average thermal conductivity of sheath (Btu/hr ft ^{o}F)

L_1 = length of exposed center conductor (ft)

L_2 = minimum bus length (ft)

N = total number of heaters

n = number of heaters connected in a series connection (n = 1 if all heaters in parallel)

P_e = electrical power output (kw)

q''' = volumetric heat release in bus (Btu/hr ft^3)

T_b = temperature of bus at point of heater attachment (^{o}R)

T_c = temperature of center conductor (^{o}R)

Δt_i = minimum allowable insulator thickness (ft)

V = power supply voltage (volts)

θ_c = temperature difference from center conductor to sheath surface (^{o}F)

ρ = resistivity of center conductor (ohm-cm)

σ = Stefan-Boltzmann constant ($.1714 \times 10^{-8}$ Btu/hr ft^2 ^{o}R^4)

ϵ = emissivity of bus

η_f = radiation or fin efficiency of bus

REFERENCES

1. Elliott, D., Cerini, D., Hays, L., O'Connor, D., and Weinberg, E., "Liquid MHD Power Conversion," JPL Space Programs Summary No. 37-28 Vol. IV, Supporting Research and Advanced Development, Jet Propulsion Laboratory, Pasadena, California, Aug. 1964.

2. Lithium Corrosion Investigation of a High Power Columbium Alloy System, Report No. PWAC-381, Pratt and Whitney Aircraft, Canel, Middletown, Connecticut, Feb. 1963.

3. Nichols, L., et al.,"Design and Operational Performance of a 150-kilowatt Sodium Flash Vaporization Facility," NASA TN-D-1661, National Aeronautics and Space Administration, Washington, D. C., May 1963.

4. Hoffman, E. and Holowach, J., "New Components for Refractory Metal - Alkali Metal Corrosion Test Systems," Preprint, AEC-NASA Liquid Metals Information Meeting, Gatlinburg, Tenn., Apr. 1965.

5. Tippets, F., and Converse, G., "Alkali Metals Boiling and Condensing Investigations," NASA-CR-54215 prepared for the National Aeronautics and Space Administration on Contract NAS3-2528, General Electric Co., Evandale, Ohio, Oct. 1964.

6. Noyes, R., "Boiling Studies for Sodium Reactor Safety" Report No. NAA-SR-7909, prepared for the Atomic Energy Commission under Contract AT(11-1)-GEN-8, Atomics International Division of North American Aviation, Inc., Canoga Park, Calif., Aug. 1963.

7. Hays, L., "Investigation of Condensers Applicable to Space Power Systems" Report No. EOS 1588-F prepared for the National Aeronautics and Space Administration under Contract No. NAS7-11, Electro Optical Systems, Inc., Pasadena, Calif., Nov. 1962.

8. Fraas, A., et al, "Medium Power Reactor Experiment," Report No. ORNL-3748, Oak Ridge National Laboratory, Oak Ridge, Tenn., Sept., 1964.

9. Goldsmith, A., Waterman, T., and Hirschhorn, H., "Handbook on Thermophysical Properties of Solid Materials," The Macmillan Co., New York, N. Y., 1960.

10. Dwyer, O., "Eddy Transport in Liquid Metal Heat Transfer," A.I.Ch.E. Journal, Vol. 9 No. 2 pp 261-268, March 1963.

11. Mackay, D., and Bacha, C., "Space Radiator Analysis and Design," Technical Documentary Report No. ASD-TDR-61-30, Aeronautical Systems Division, Wright-Patterson Air Force Base, Ohio, Oct. 1961.

12. Davis, J., et al, "Lithium-Boiling Potassium Refractory Metal Loop Facility," Technical Report No. 32-508, Jet Propulsion Laboratory, Pasadena, Calif. Aug. 1963.

N66 31674

FLOW INSTRUMENTATION AND OPERATING EXPERIENCE IN A CONDENSING ALKALI METALS TEST LOOP

by

C. R. Fisher
and
J. H. Moskowitz, Jr.

(Paper presented by C. R. Fisher)

Aerojet-General Nucleonics
San Ramon, California

(This paper also bears the number AGN-TP-157)

Aerojet-General Nucleonics is conducting the Alkali Metals Program for the U. S. Atomic Energy Commission, to determine the transport behavior and thermophysical properties of the alkali metals. This paper is concerned with recent work in which the condensing heat transfer characteristics of rubidium and cesium were investigated for both horizontal and vertical flow in a straight, round duct.

A schematic diagram of the condensing test apparatus is shown in Figure 1. It is constructed of 316 SS with the exception of the test section which is nickel. Liquid metal evaporation is accomplished in two steps. The first step occurs in the boiler in a tube immersed in a NaK bath, heated by electrical immersion heaters. Fifty to sixty percent of the evaporation takes place in the boiler. The metal is then completely evaporated and slightly superheated in the dryer-superheater consisting of a sixty foot long tube, heated directly by the passage of an electrical current through the tube wall. A magnetic flowmeter is used to measure the flow rate of the liquid metal. A manipulation of valves causes the full flow through the flowmeter to be diverted into a calibration tank where the time for filling a known volume can be determined. The calibration tank is fitted with electrical liquid level probes. The volume between probes was determined by filling with mercury prior to starting the experiment.

The test section is shown in Figure 2. It consists of two nickel bars of 4.0 in. O.D. and 0.4 in. I.D. The bars are arranged in series and each bar is fitted with four sheathed, ungrounded thermocouples at each end, arranged to have different radial spacings. The thermocouples are brazed into holes 2.0 in. deep in the test section bars. The readings from these thermocouples are extrapolated to determine the inside surface temperature,and the slope of a temperature vs. log radius plot is used to determine the local heat flux. It is estimated that the inside surface temperature can be determined to $\pm$ 3^{o}F. The temperature of the liquid

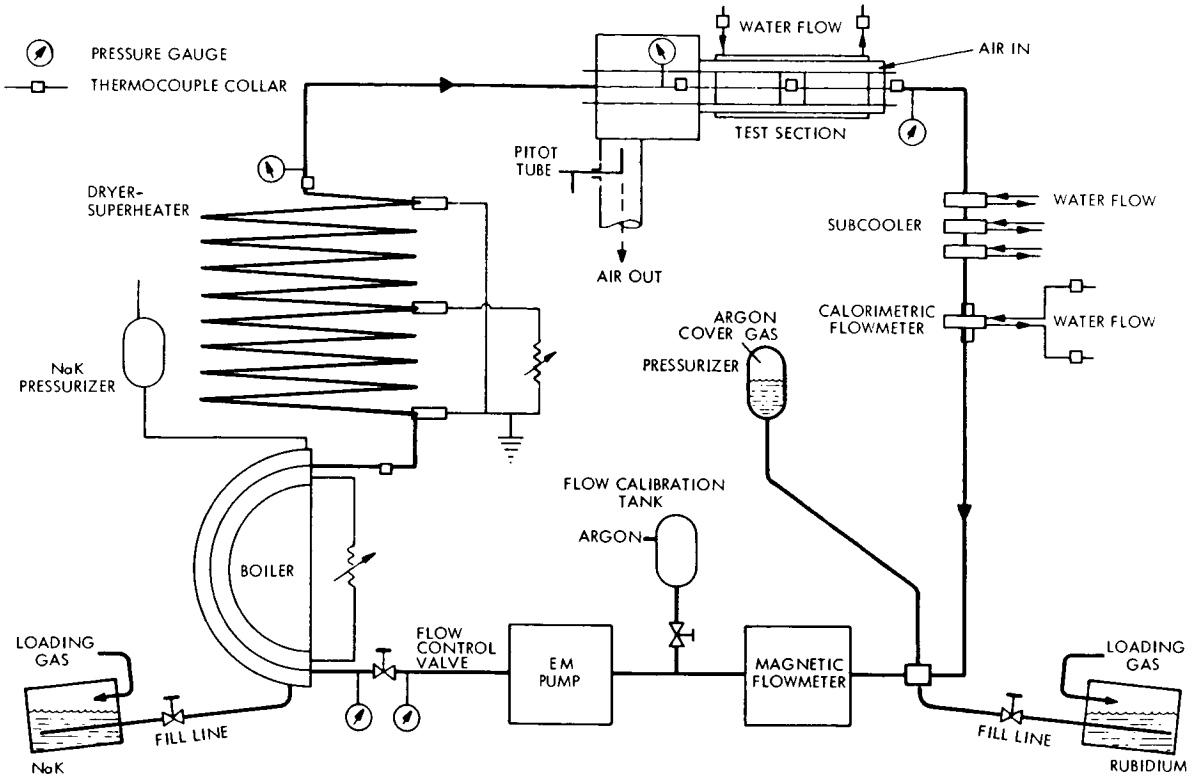


Fig. 1. Loop Diagram for Rubidium/Cesium Condensing Tests

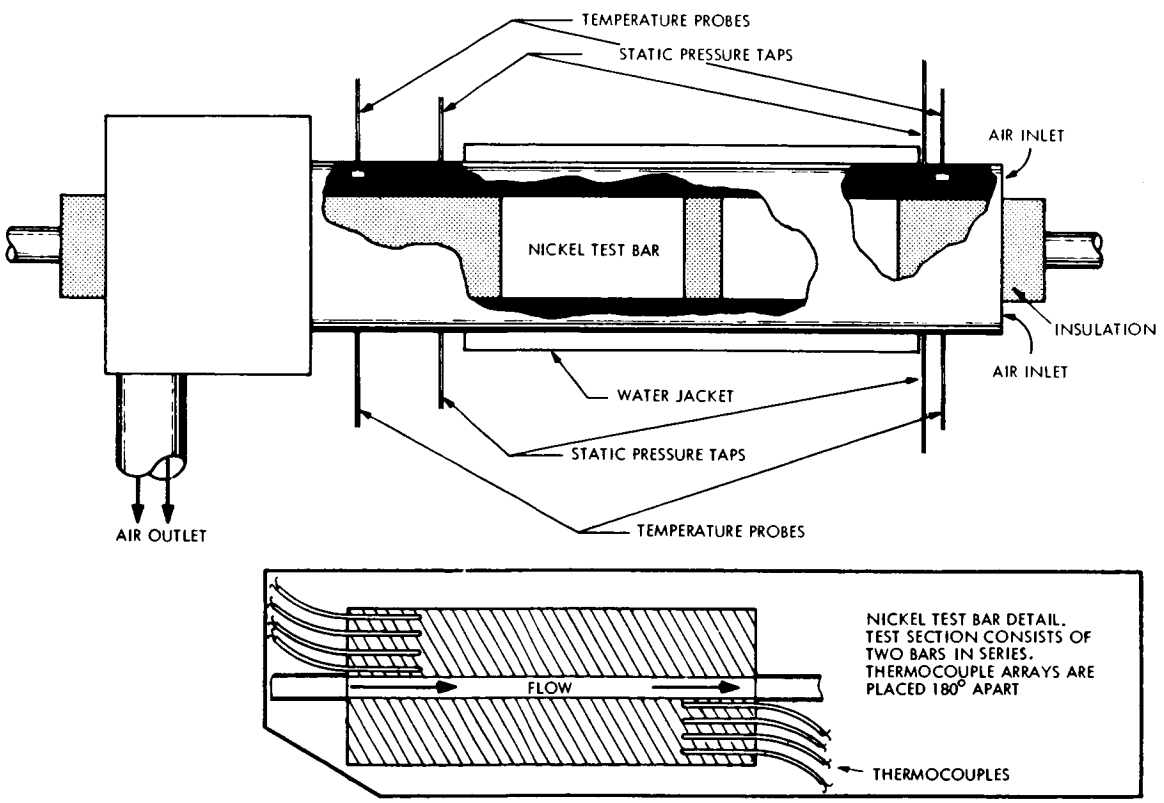


Fig. 2. Rubidium/Cesium Condensing Test, Test Section

metal is measured by placing sheathed thermocouples in conduction wells placed around the loop tubing at the entrance and exit of the test section and between the two test section bars. Heat removal is effected by blowing air parallel to the axis of the test section in an annular duct formed by the test section and a water-cooled jacket concentric with it. The static pressure taps shown were used to ensure a uniform velocity profile in the air at the time of assembly of the test section.

During calibration of the magnetic flowmeter, it was observed that there was an EMF developed across the flowmeter cell when there was no flow in the loop. This EMF was found to be a function of the temperature of the cell. Care was taken in construction of the cell to eliminate material inhomogeneities and temperature gradients at the connections of the flowmeter leads. Natural convection currents in the liquid metal were eliminated as the cause of this EMF because it was unchanged when closing valves which isolated the flowmeter from the loop. Changing the liquid metal in the loop produced a different calibration curve for the thermal EMF as can be seen in Figure 3. It is therefore assumed that the source of at least a portion of this effect is located on the inside wall of the flowmeter cell. One can postulate a surface film which caused this effect, although it is a very stable film, since the flowmeter calibration did not change more than 1% over a period of several hundred hours. The film would have to have essentially zero thickness since the flowmeter calibration curve, corrected for no-flow EMF, agrees within seven percent of the theoretical curve based upon a measurement of the magnet strength and cell dimensions and calculated by the method of Reference 1.

It would be surprising if the no-flow EMF generated in another experiment were to be identical to that shown in Figure 3. However, Figure 3 indicates the magnitude of what might be expected to occur, and it is suggested that other experimenters check their equipment for the presence of this effect.

Other interesting phenomena related to surface effects were observed during the course of this program. When there was only the liquid phase flowing in the loop, the voltage-current relationship for the dryer-

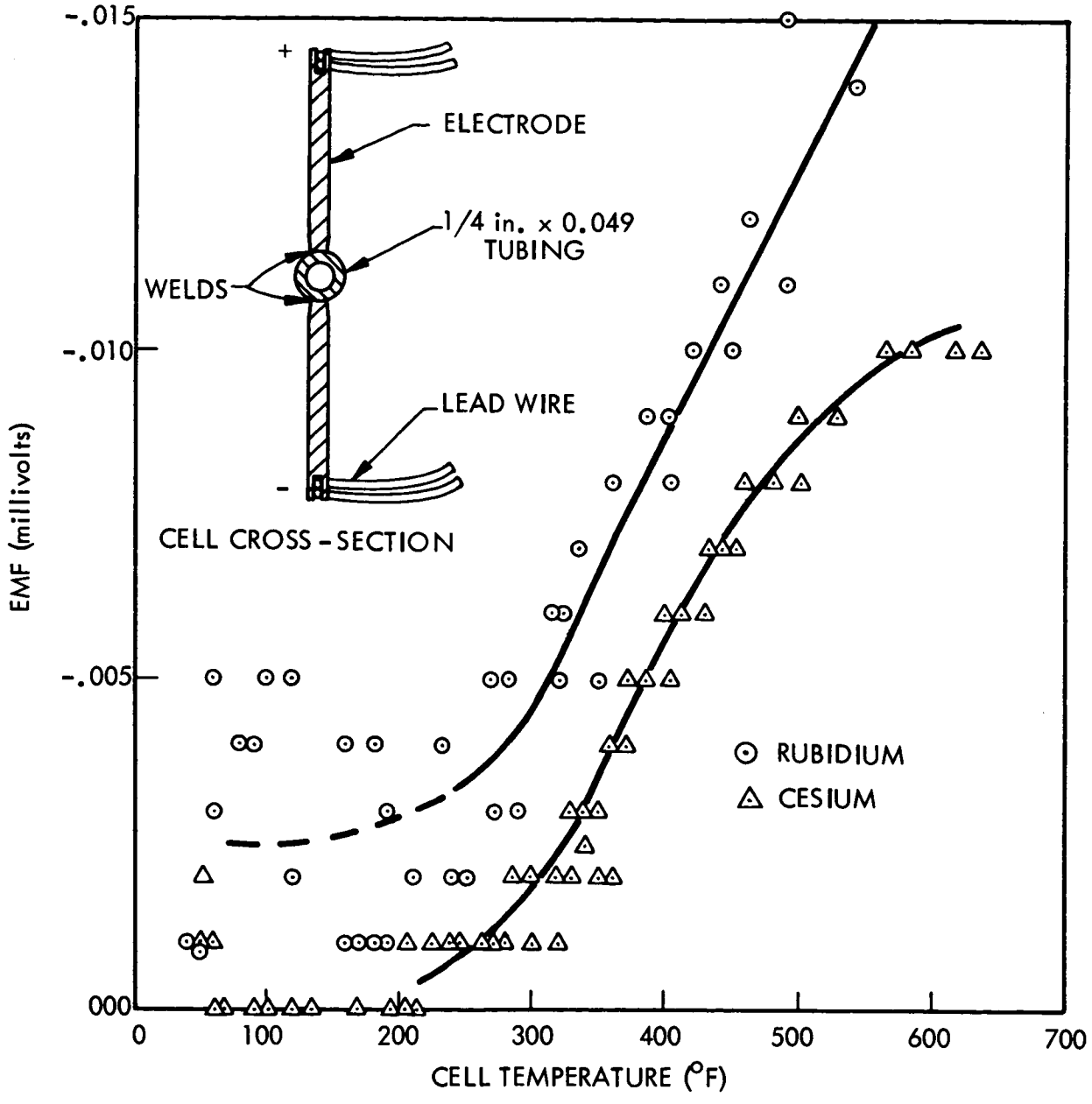


Fig. 3. Magnetic Flowmeter No-Flow Emf

superheater indicated that the stainless steel tube wall and the liquid metal shared the electrical current in inverse proportion to the calculated resistance of each material. This indicates little, if any, interfacial electrical resistance. However, in the boiling heat transfer work performed earlier in this program, (reported in References 2 & 3) which used a columbium-1 zirconium loop, a similar observation indicated that there was essentially no electrical current in the liquid metal in a section of the loop heated by direct passage of current through the loop. This indicates a significant difference in interfacial resistance between liquid metal and loop for refractory metal and stainless steel loops.

Another related observation is as follows:

There was a large difference in the time required for the magnetic flowmeters and AC conduction pumps to reach asymptotic performance for stainless steel and for refractory metal loops. Steady performance was achieved in stainless steel within half an hour of filling with liquid metal at a temperature of 300°F with the final flowmeter calibration curve falling 7% below the calculated. Achieving this condition required an eight hour soak at 800-1000°F in the refractory metal loop with the final calibration curve falling 11% below the calculated.

The design of liquid metal heaters in which Joule heating is employed should consider the possibility that the electrical resistance of the heater may be unpredictable, lying somewhere between the cases of a full tube in perfect contact with the liquid metal, and an empty tube.

It can be postulated that a difference in very high flux heat transfer results could be measured for liquid alkali metals in loops of different materials even where it appears that good wetting exists. This remains to be seen. The authors do not know of existing data whereby this idea can be tested.

In a discussion of surface effects, it is important to list the surface treatment of the containment materials and the analysis of the fluids. The inside surfaces of the loops were washed with acetone, distilled water and methanol, and were then hot outgassed at temperatures above 200°F for 24 hours with a pressure of 10^{-5} Torr at the vacuum pumping station. The liquid

metals were filtered and gettered at 1200°F with 50 zirconium - 50 titanium before loading into the loop. The oxygen content of the liquid metals varied from 50-200 ppm for the several tests.

Some preliminary results of the condensing heat transfer tests are presented here. The test work includes rubidium and cesium in both vertical and horizontal flow, with flow rates from 20,000 - 70,000 lb/hr-ft^2, saturation temperature from 1000 - 1400°F, and heat flux ranging to 140,000 Btu/hr-ft^2.

The data indicates that, over the range of parameters investigated, the temperature drop associated with the condensing process is very small, the maximum measured for any set of conditions being 13°F and less than 18% of the data greater than 5°F. This should be compared to the estimated uncertainty in ΔT of $\pm$ 5°F. Data for rubidium condensing in horizontal flow are shown in Figure 4 and are typical of all the data. With the large scatter inherent in the data, it is difficult to identify functional dependence upon the important system parameters. Attempts to do this have produced no significant results. However, the data show that, in the design of equipment in which rubidium or cesium is condensed, it is safe to assume that the controlling resistance to heat flow will not occur in the condensing film.

This work was performed for the U. S. Atomic Energy Commission on Contract AT(04-3)-368, P.A. No. 1.

References:

1. Liquid Metals Handbook-Sodium (NaK) Supplement TID 5277 (1955) pg 342
2. C. R. Fisher et al, "Forced Convection Boiling of Rubidium and Cesium-Heat Transfer and Pressure Drop", AGN-8099 (1964)
3. C. R. Fisher et al, "Swirl Flow Boiling of Alkali Metals-Heat Transfer and Pressure Drop", AGN-8127 (1965)

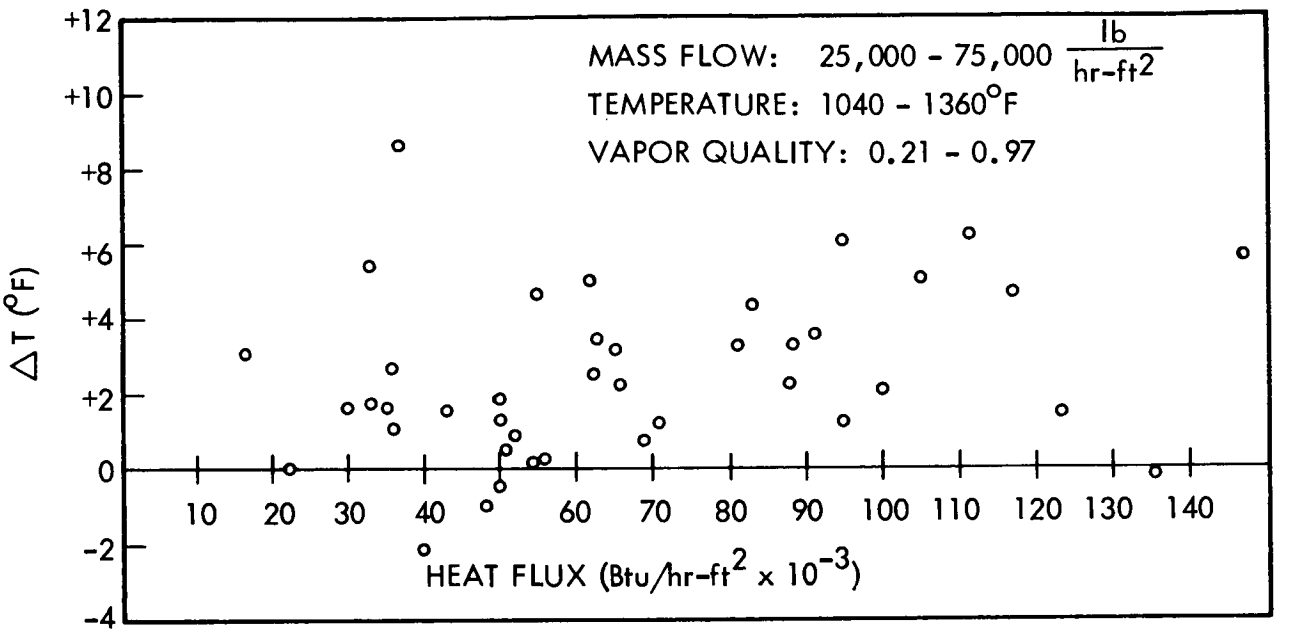


Fig. 4. Condensing Rubidium-Horizontal Flow

N66 31675

HEAT TRANSFER AND PRESSURE DROP MEASUREMENTS FOR HIGH TEMPERATURE BOILING POTASSIUM IN FORCED CONVECTION*

By

J.A. Bond
J.R. Peterson
F.E. Tippets

Space Power and Propulsion Section
Missile and Space Division
General Electric Company
Cincinnati, Ohio 45215

(Paper presented by F. E. Tippets)

ABSTRACT

Instrumentation and measurement techniques used for experiments with forced convection boiling potassium in a sodium-heated Haynes-25 alloy test facility at potassium temperatures to 1750°F and in a radiant-heated Cb-1Zr facility at temperatures to 2100°F are described. Some of the heat transfer and pressure drop results obtained are presented. The heat transfer data presented include measurements of heat transfer coefficients in the nucleate boiling and transition boiling regimes and measurements of onset of critical heat flux conditions.

*Work Performed for National Aeronautics and Space Administration under Contract Number NAS 3-2528

INTRODUCTION

An investigation of boiling and condensing potassium heat transfer is being conducted for the National Aeronautics and Space Administration by General Electric Company under Contract NAS 3-2528 to obtain two-phase heat transfer and fluid flow data for potassium under conditions of boiling and condensing at temperatures anticipated in turbo-electric Rankine cycle systems. The purpose of this paper is to present some of the results obtained from the boiling studies done under this program.

Experimental work with boiling potassium includes both "once-through" two-fluid boiler tests in Haynes-25 alloy facility with single-tube geometries at potassium temperatures to 1750°F, and complementary boiling experiments with a radiant-heated Cb-1Zr facility at potassium temperatures to 2100°F. Results from these experiments include measurements of heat transfer coefficients in the various boiling regimes from low vapor quality to superheated vapor conditions, two-phase pressure drop measurements, and some exploratory critical heat flux determinations.

EXPERIMENTAL APPARATUS AND INSTRUMENTATION

300 KW Two-Fluid Facility

The 300 KW two-fluid liquid metal test facility (Figure 1) is constructed of Haynes-25 alloy. Liquid sodium flows in the primary loop of the facility, accepting heat from a gas fired furnace at maximum sodium temperatures to 1850°F and rejecting the heat at the test section to boiling potassium in the secondary loop. Potassium flowing in the secondary loop is condensed in vertical and horizontal air-cooled single-tube condensers. The potassium vapor-liquid interface is maintained in a head tank fitted with level probes, positioned immediately downstream of the horizontal condenser. Flow rates are measured by electromagnetic flowmeters in the primary and secondary loops. Control

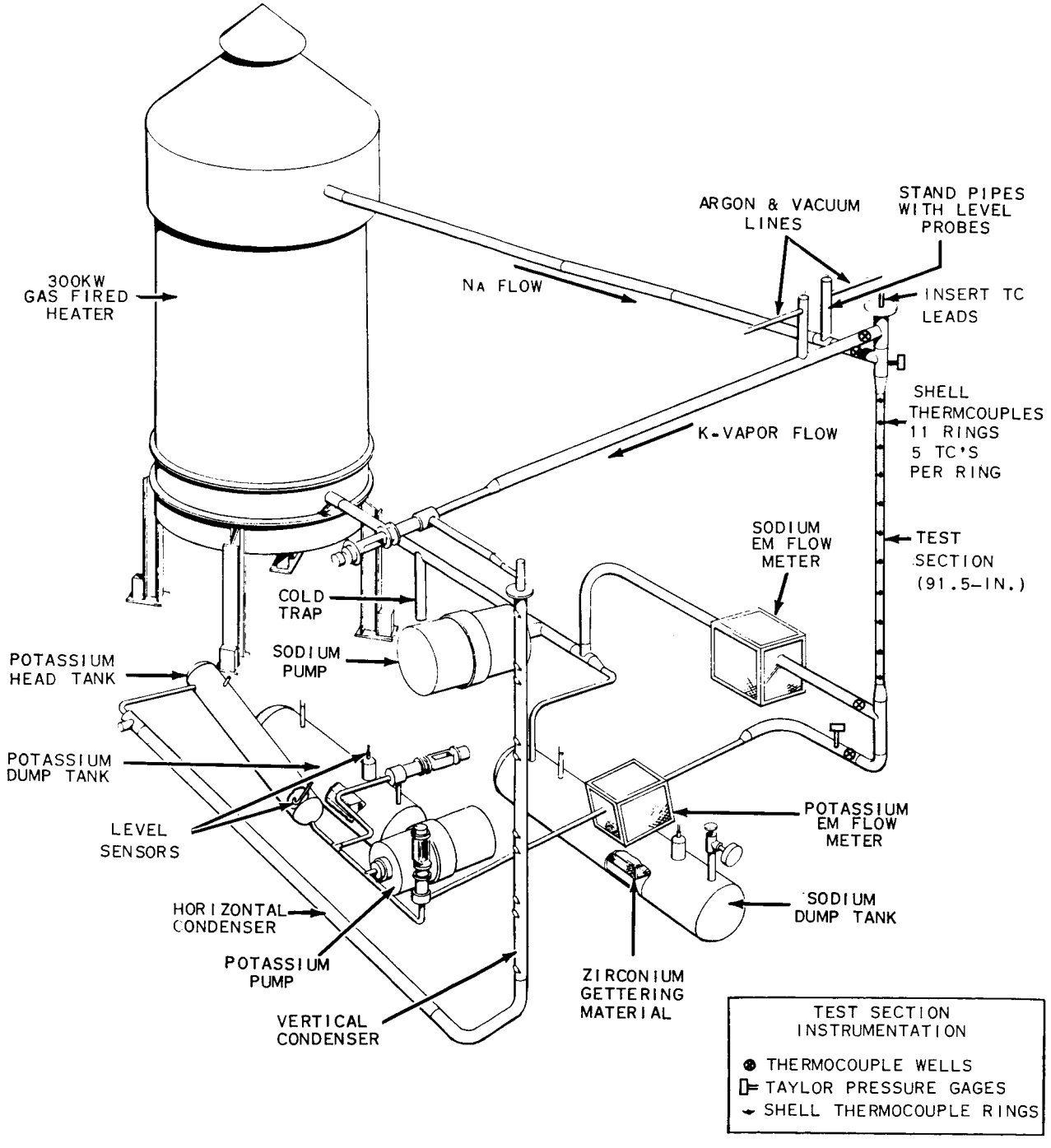


Fig. 1. 300 kW Two-fluid Heat Transfer Facility

of oxygen concentration in both loops is accomplished by zirconium gettering grids located in the dump tanks.

Figure 2 shows a disassembled view of the boiling test section, including one of the helical inserts employed. The test section is a shell and tube heat exchanger with the potassium flowing inside the boiler tube and heated by sodium flowing in the annulus. Relative expansion between the boiler tube and the shell is accommodated by a bellows located before the heated section of the tube near the potassium inlet. The helix insert consists of a 1/4-inch outside diameter support tube around which is wound a ribbon to form a helical flow path when the insert is placed in the boiler tube.

Seven 1/16-inch diameter Inconel sheathed chromel-alumel thermocouples are located in the insert support tube, entering from the outlet end, to measure potassium temperature distribution. Thermocouple wells, each containing three calibrated platinum-platinum 10% rhodium Haynes-25 alloy sheathed thermocouples, are located at the test section inlet and exit of both the sodium and the potassium streams. Inconel sheathed platinum-platinum 10% rhodium thermocouples are positioned on the outside shell of the test section in eleven rings of five thermocouples each to measure the sodium axial temperature distribution (Figure 3).

All the thermocouples in the inlet and exit wells were calibrated periodically in a melting point apparatus and were used as primary standards for the in-loop calibration of the shell and insert thermocouples. Calibration of the shell thermocouples and determination of test section heat losses were done by maintaining the primary loop at temperature with the secondary loop evacuated, under which conditions the temperature change

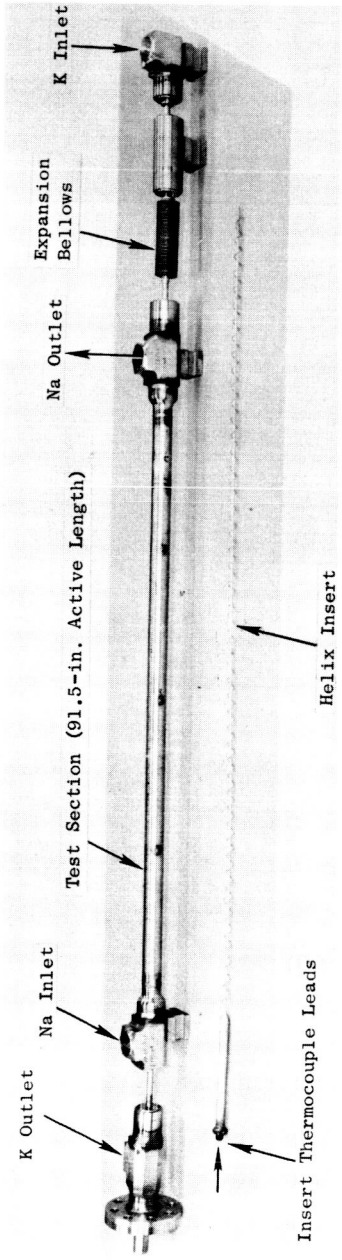


Fig. 2. 300 kW Test Section with Instrumented Helix Insert

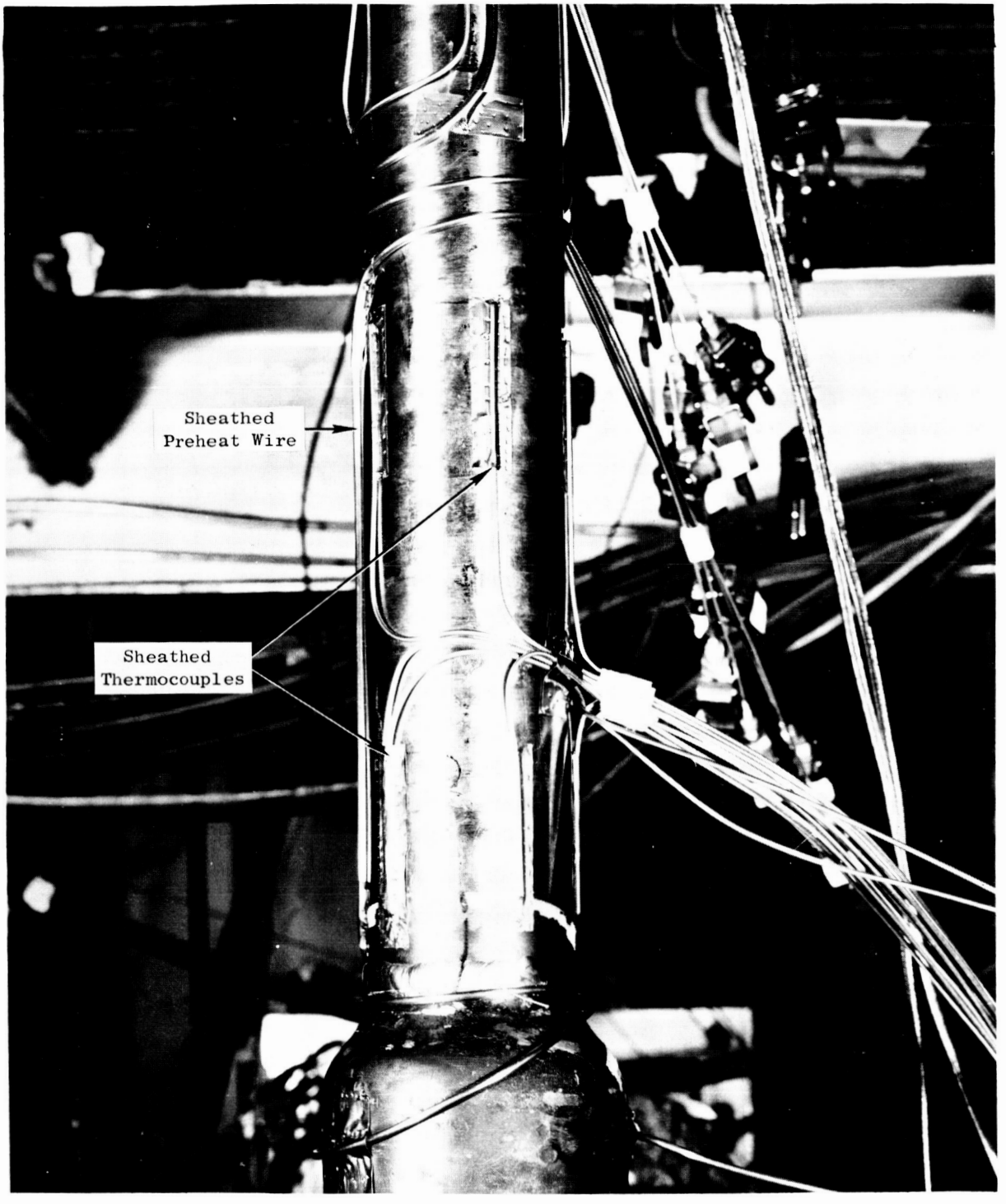


Fig. 3. Shell Thermocouple Attachment on 300 kW Test Section

between the sodium inlet and exit wells is due solely to heat loss. The heat loss determinations were made at a very low sodium flow rate in order to maximize the sodium temperature change across the test section. The shell thermocouples were calibrated relative to the primary side well thermocouples at near-isothermal conditions attained by use of the maximum sodium flow rate. The insert thermocouples were calibrated against the potassium exit well thermocouples under boiling conditions at low flow and low vapor quality, for which the temperature changes along the insert and between the insert end and the outlet well were negligible.

The thermocouple calibrations were performed at various temperature levels and the corrections obtained were then applied as functions of sodium and potassium temperatures at the test section, respectively, in the data reduction procedure. The test section heat loss, which was of the order of 1 KW was also determined as a function of sodium temperature. The thermocouple corrections were generally less than $10^{\circ}F$, and no appreciable drift was detected over the course of the experiments. The temperature measurements are believed to be accurate to within $\pm 2^{\circ}F$ with the procedures followed.

The relationship between flow rate and output signal from the electromagnetic flowmeters in both loops of the facility were obtained by calculation using the equations given in Reference 1. In order to minimize errors, measured values of the field intensity of the magnets were used for the calculations. An indication of the resulting accuracy in flow determination was obtained through intercalibration of the two flowmeters by heat balance around the test section, using liquid-

liquid runs. The disagreement obtained was 2%, which is believed to be representative of the probable error in the individual loop flow rate determinations.

The two-phase potassium pressure loss in the test section was determined by means of two slack-diaphragm pressure transducers, with pressure taps positioned at the potassium inlet and exit (Figure 1). These pressure gages were calibrated against a Wallace and Tiernan (type FA-145) standard gage by filling the potassium loop to various pressures with argon both before and after the experiments with each test section. The calibrations before and after testing generally agreed to within 1-psi; thus the error of the pressure measurements is taken to be less than 1-psi. This accuracy was attained by maintaining the diaphragm of the transducers at a constant temperature level, which was necessary since the gage calibration depends on the diaphragm temperature.

Measurements of potassium exit pressure together with exit temperature were used as one means to determine the amount of vapor superheat in the once-through boiling tests in the 300 KW Facility. Figure 4 shows the measured potassium exit pressure plotted against the measured exit temperature for several runs in which superheated vapor exit conditions were attained. Also plotted are data for which the calculated exit vapor quality was between 10% and 90%. The latter results agree generally, within 1-psi, with the saturation curve as determined by the Naval Research Laboratories (Reference 10). This is a further indication of the accuracy of the pressure measurements.

Recording of the large number of instrument readings required to define a single data point in the 300 KW Facility is accomplished through the use of a high speed digital recorder.

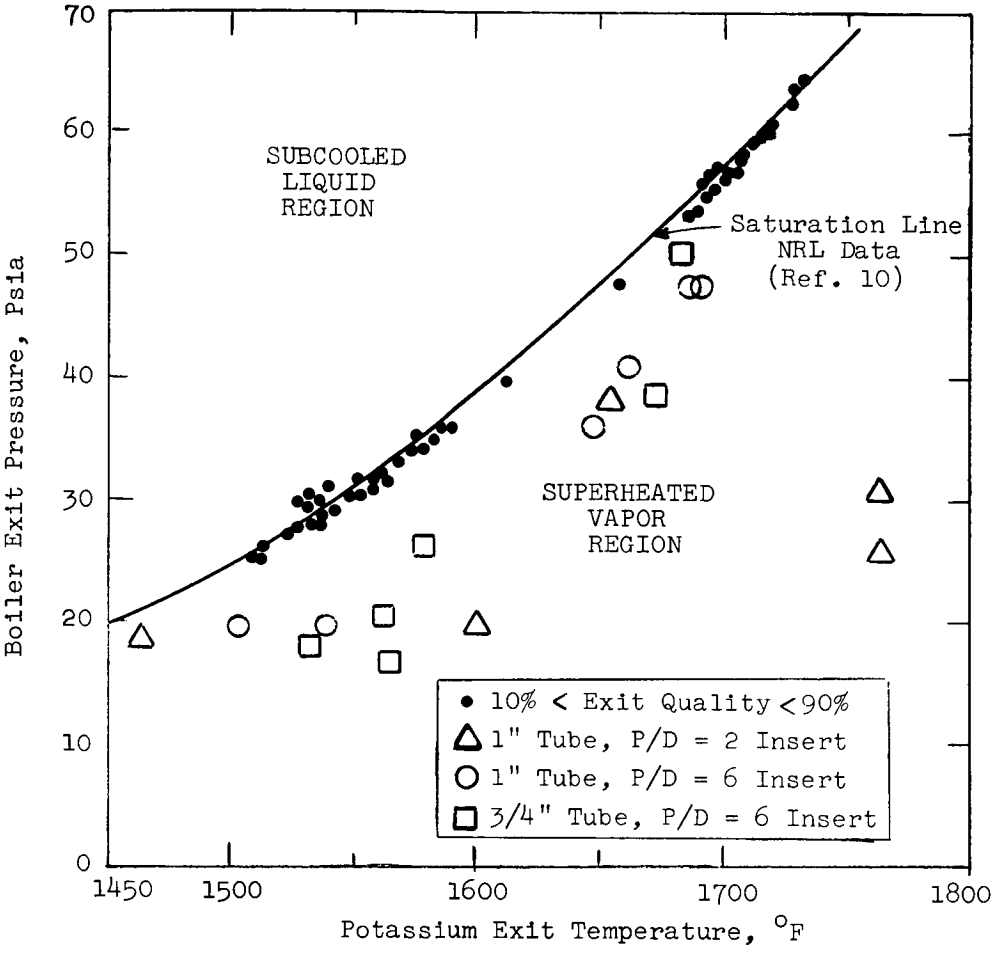


Fig. 4. Comparison of Saturation Properties with Measured Potassium Pressures and Temperatures in 300 kW Facility

Complete readout on paper tape of the approximately 150 information bits required is obtained in approximately one minute. Three complete readouts were obtained for each data point, in order to provide an indication of the presence or absence of significant fluctuations.

100 KW High Temperature Facility

The 100 KW Facility is a single loop system used to study heat transfer to boiling potassium at fluid temperatures up to 2100°F. The alkali metal containment piping is constructed from columbium-1% zirconium and is enclosed in a high-vacuum environmental chamber to avoid atmospheric contamination. Figure 5 is a schematic representation of the loop and principal instrumentation.

Liquid potassium is discharged from the electromagnetic pump and flows through an electromagnetic flowmeter to an 8 KW radiant preheater, which controls the preboiler inlet subcooling. Upon leaving the preheater the potassium flows through a throttling orifice into the preboiler, and then, in vertical up-flow, into the test section.

The preboiler consists of a helically wound section of pipe with a radiant heater element in the core of the helix, all contained in a radiation shield (Figure 6). The preboiler heater element is fabricated from coiled tungsten wire and is operated at gross electrical power levels up to 60 KW. The function of the preboiler is to control the enthalpy of the potassium in the test section independent of test section heat flux, thus permitting separation of the effects of quality and heat flux in the tests.

The test section, located downstream of the preboiler, is a vertical section of pipe with a 30-inch heated length. The

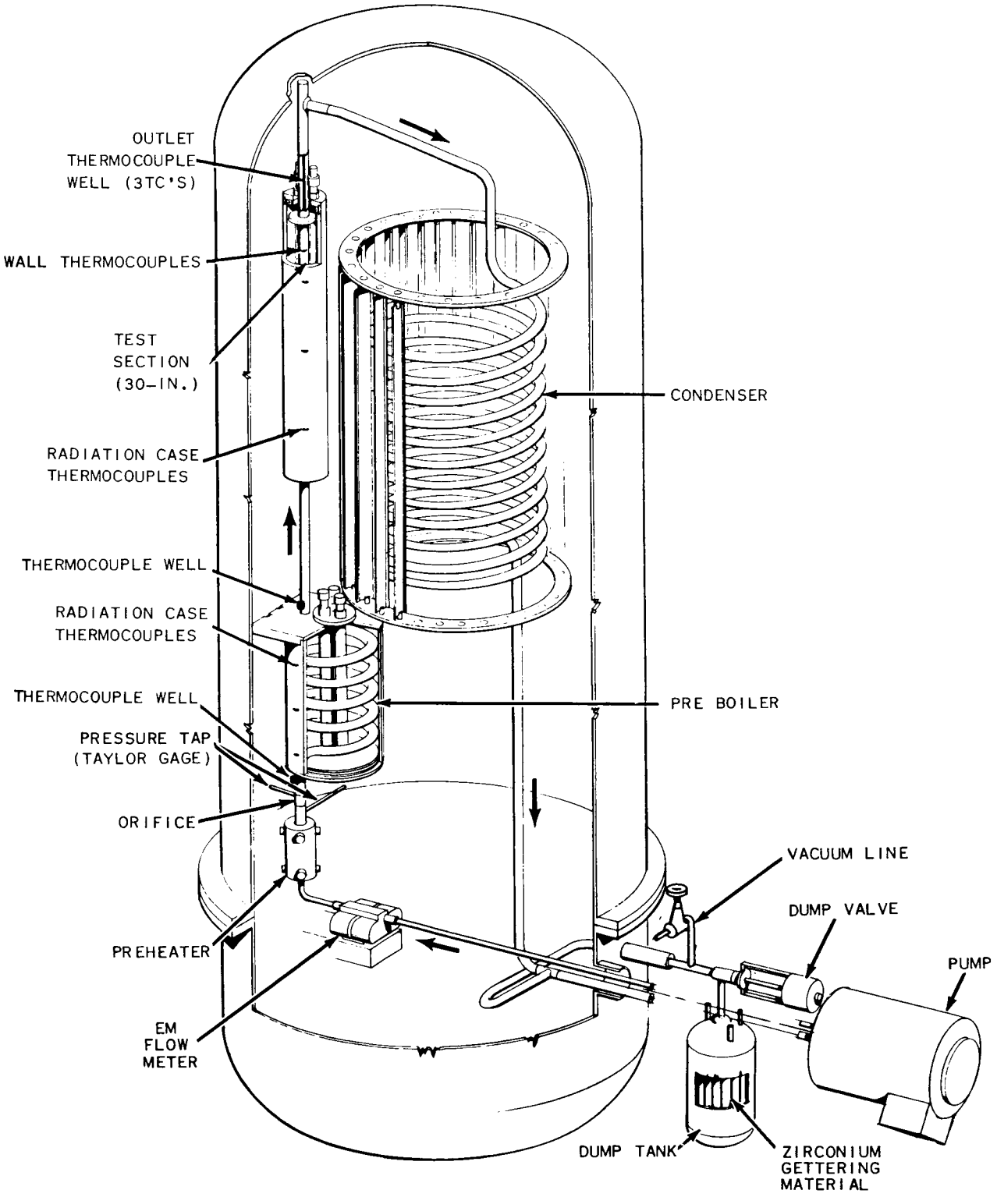


Fig. 5. 100 kW High-temperature Heat Transfer Facility

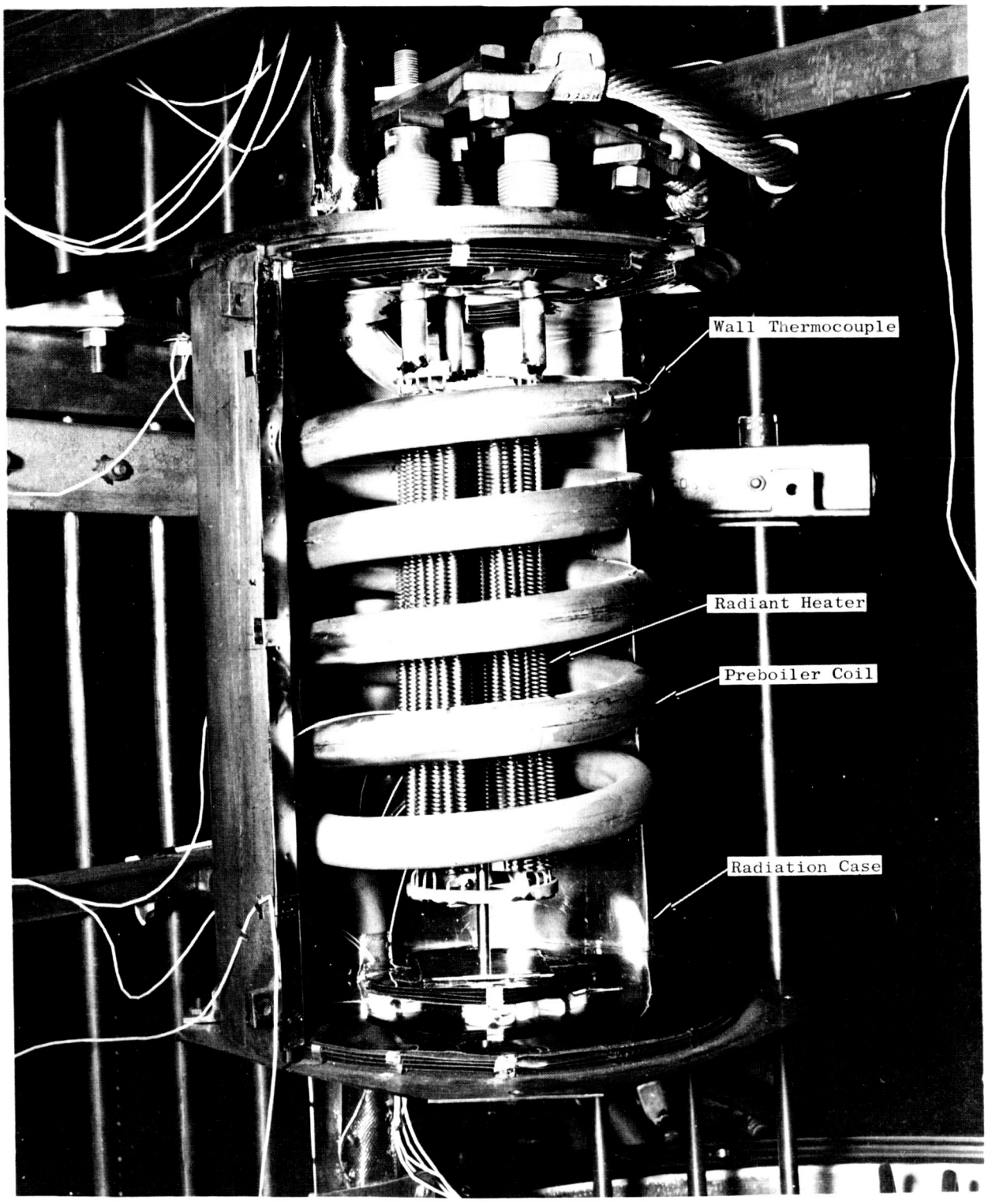


Fig. 6. Preboiler for 100 kW Facility

radiant heater for the test section consists of an array of 27 tungsten rods surrounding the test section, together with a radiation shield (Figure 7). The test section heater is operated at gross electrical power levels up to 32 KW.

Heat is rejected from the system in approximately 60 ft. of condenser piping radiating to the water-cooled walls of the environmental chamber. Some control of the heat rejection rate is accomplished with adjustable shutters which surround the condenser coil (Figure 7).

The preboiler and the test section radiation shields consist of concentric tantalum sheets enclosed in stainless steel cases. The temperature of each of these cases is measured at six locations and these temperatures are used to determine heat losses using heat loss calibration data. The heat loss calibrations are performed with the preboiler and test section piping removed. With the vacuum chamber evacuated, power is supplied to the heaters and the corresponding steady-state radiation shield case temperatures are measured. This procedure is repeated at several power levels, and since all the power supplied is lost through the shield a direct correlation of heat loss as a function of shield case temperature is obtained.

The principal measurements and corresponding instrumentation are as follows:

a) The flow rate is measured with an electromagnetic flowmeter. Calibration of the flowmeter is by the calorimetric method using an energy balance across the test section with all liquid flow. The range of error of the flow rate measurements is estimated to be within $\pm$ 10%, depending on the accuracy of the potassium liquid specific heat data used (Reference 10), which was assumed

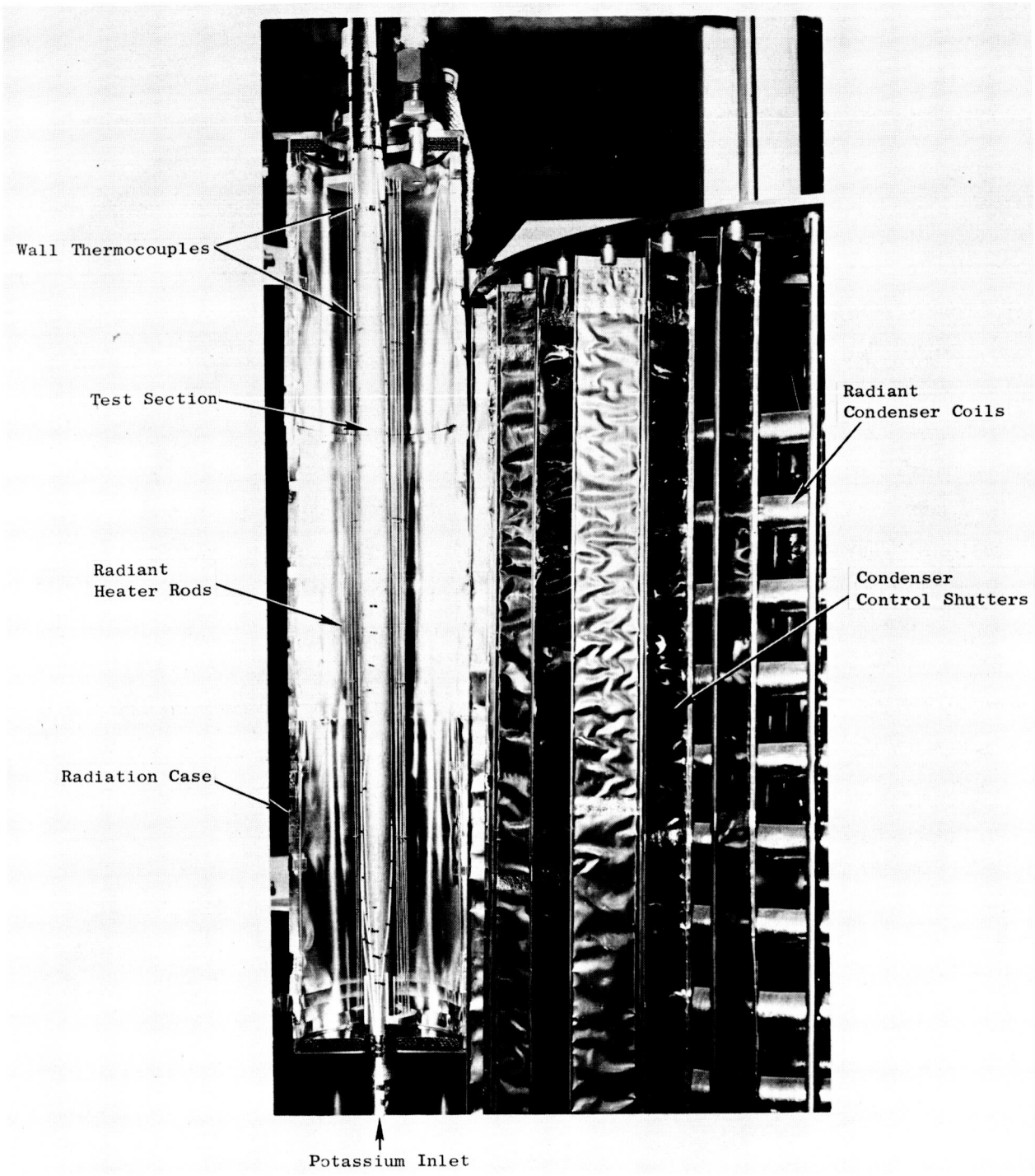


Fig. 7. 100 kW Test Section Arrangement

for this flow rate error estimation to be within ± 5%.

b) Power to the preboiler and test section is measured with polyphase wattmeters. The estimated range of error of the electrical power measurements is ± 1%.

c) Fluid temperatures at the preboiler inlet, preboiler outlet and test section outlet are measured with W-3%Re vs. W-25%Re bare-wire thermocouples located in wells (Figure 5).

c) Pipe wall temperatures are measured with W-3%Re vs. W-25%Re thermocouples. Figure 8 shows typical thermocouple junctions on the test section wall. The junction is made by resistance welding the 0.005-inch thermocouple wires to the pipe wall. A continuing problem in the 100 KW Facility has been repeated failures of the wall thermocouples. One mode of failure has been due to the W-3%Re leg of the thermocouple lifting off the pipe surface. It was found that a small tab of 0.002-inch thick tantalum foil tacked over the junction reduces the frequency of this type of failure. However, due to the severe operating conditions imposed on the test section, wall thermocouple failures remains one of the chief causes of loop "downtime".

e) System pressures are monitored with two slack-diaphragm type pressure transducers located upstream and downstream of the inlet throttling orifice. The argon pressure in the dump tank is an additional indication of system pressure, since the loop is normally operated with the dump tank valve open.

Test section thermocouples are calibrated in-loop as follows. With the test section mass velocity held constant at a relatively low value, the preboiler power is increased to a level such that the vapor quality of the potassium entering the test section is about 10%. Neglecting the small temperature changes due to pressure drop the temperature of the two-phase fluid in the test section

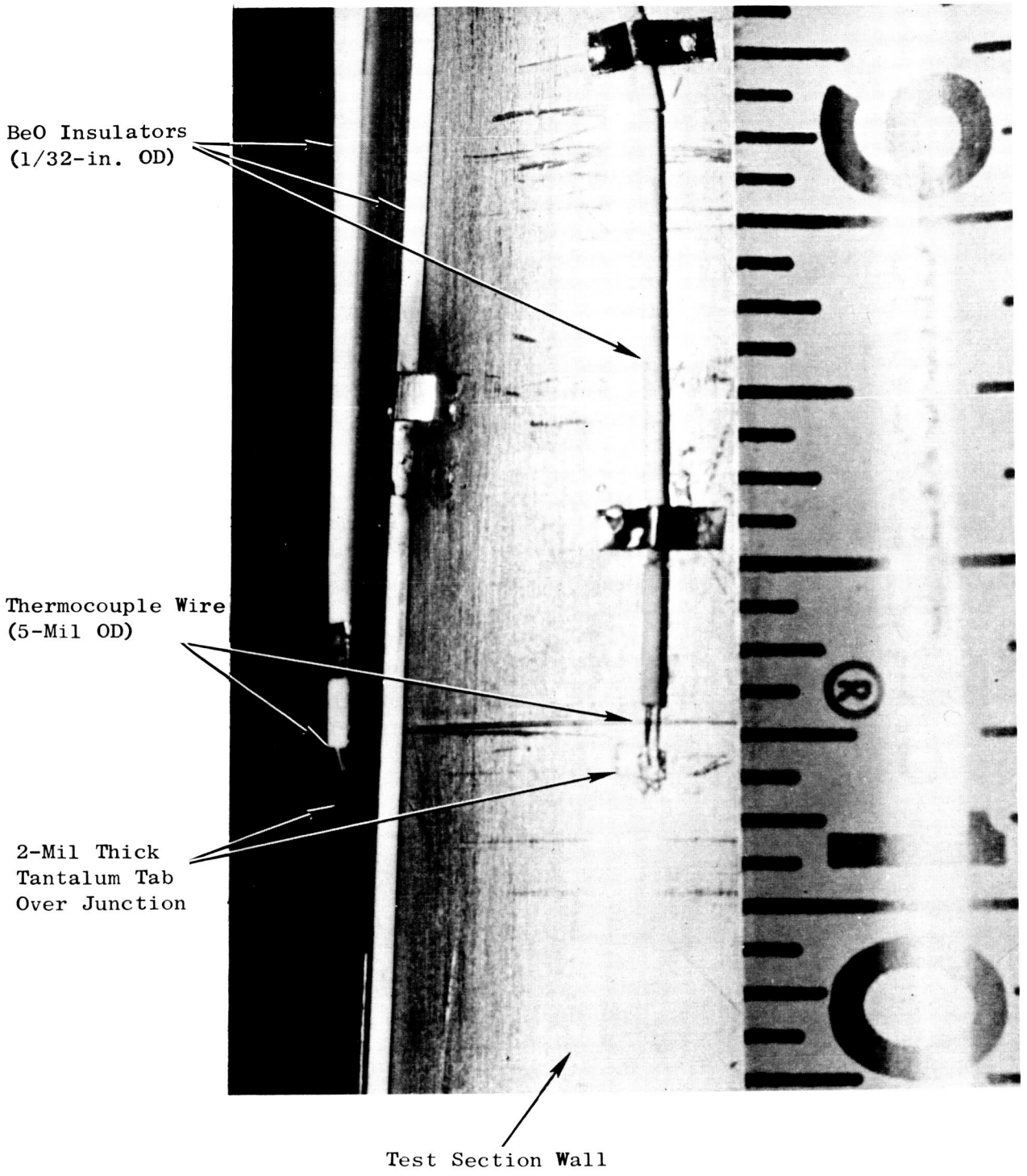


Fig. 8. Wall Thermocouple Attachment on 100 kW Test Section

is assumed to be uniform. After the system has reached a steady-state condition, the test section heat loss is determined using the radiation-case temperatures. The test section power is then increased until the electrical power input balances the heat losses. Under these very nearly isothermal, adiabatic conditions, the temperatures of all test section thermocouples closely approximate each other. Using one of the test section outlet well thermocouples as the standard, a thermocouple correction is obtained for each of the test section thermocouples by comparison with this standard thermocouple.

Since an applicable national standard EMF-temperature table has not been adopted, samples from the same spool of W-3%Re vs. W-25%Re thermocouple wire used in the 100 KW Facility are calibrated in a vacuum furnace. Initial calibrations of this kind indicated a drift of about 20°F. However, after the thermocouples were "soaked" for a few hours at 2300°F, repeatability to within $\pm$ 3°F was obtained. As part of the procedure for in-loop calibrations, newly installed thermocouples are held at 2100°F for at least five hours before taking the first calibration reading. Two additional calibration readings are then taken at one hour intervals to verify absence of drift.

DATA MEASUREMENT AND REDUCTION

It is useful at this point to define the various regimes of forced convection boiling encountered in the "once-through" boiling tests in the 300 KW Facility and in the tests in the 100 KW Facility, as the experimental techniques depend to some extent on the boiling regime being investigated.

The "nucleate" boiling regime exists in the lower range of vapor qualities extending to some upper quality level which is dependent on the heat flux for a given flow geometry, flow

rate and saturation temperature. This regime is characterized by relatively high heat transfer performance (heat transfer coefficients of the order of 10,000 Btu/hr-ft^2-^{o}F) and steady or only slightly fluctuating wall temperatures. It is believed that in the nucleate boiling regime the heated wall is entirely wetted by liquid, possibly by a continuous liquid film for forced convection bulk boiling. As heat flux or vapor quality is raised, the nucleate boiling regime is eventually terminated by onset of the "critical heat flux" condition, as characterized by beginning of substantial wall temperature fluctuations and reduction of heat transfer performance. This marks the beginning of the "transition" boiling regime, for which the wall temperature fluctuates markedly and the effective heat transfer coefficient is significantly less than for the nucleate boiling regime (heat transfer coefficients of the order of 1,000 Btu/hr-ft^2-^{o}F or less). It is thought that in the transition boiling regime the wall is only intermittently wetted by liquid. Further increases in heat flux and vapor quality result in increased fluctuations of the wall temperature until finally stable "film" boiling occurs, as characterized by relatively steady, but large wall-to-fluid temperature differences and correspondingly poorer heat transfer performance, with heat transfer coefficients comparable to those for dry vapor flow. In the film boiling regime the heated wall is believed to be completely dry with the liquid being carried along as droplets in the stream and with the heated wall in contact with locally superheated vapor.

300 KW Two-Fluid Boiling Tests

Figure 9 shows the measurements made for a typical once-through boiling run to exit superheat conditions in the 300 KW Facility using a helix insert in the test section. Four distinct heat transfer regimes may be inferred, namely: sub-cooled liquid

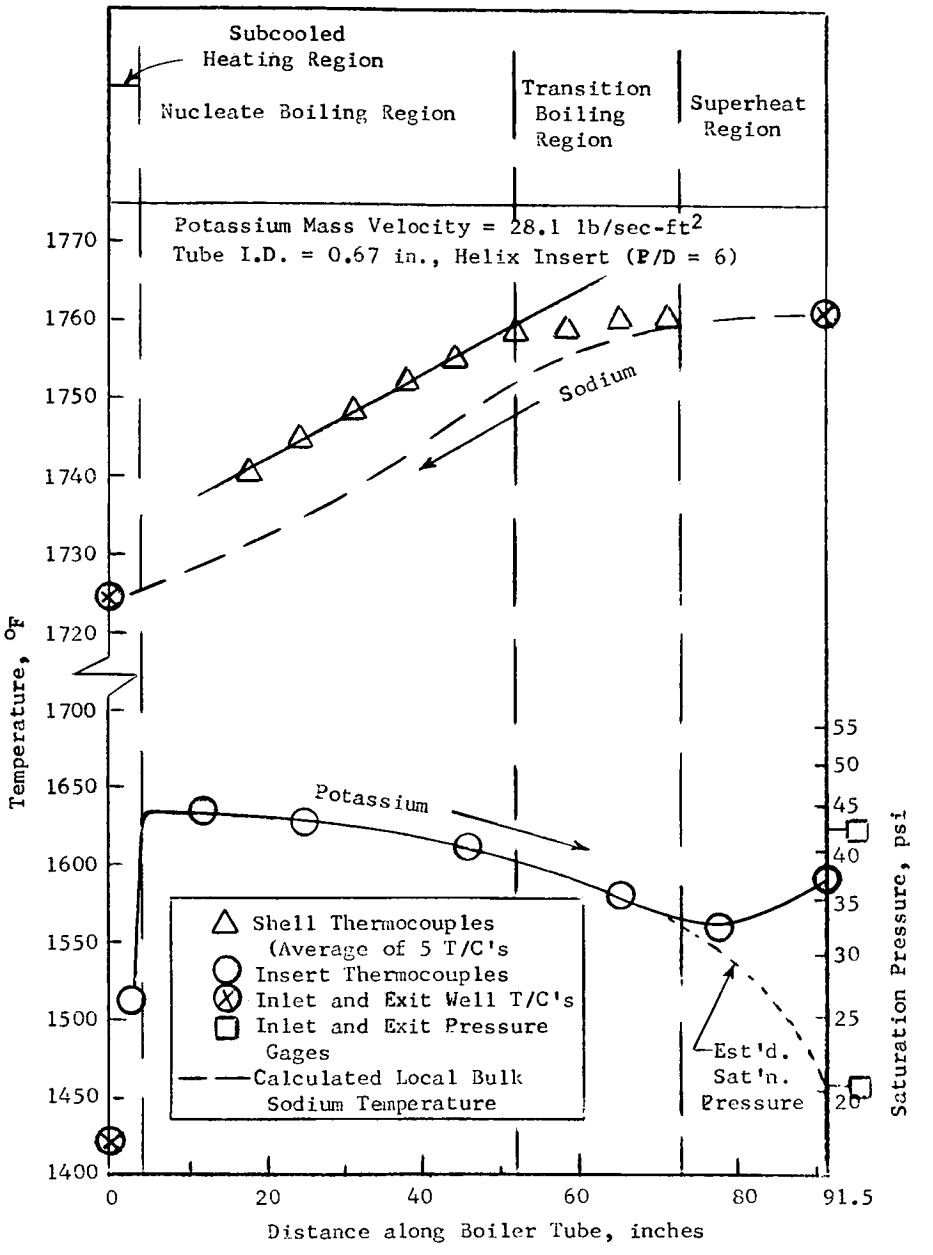


Fig. 9. Measured Fluid Temperature Profiles in 300 kW Test Section

heating, nucleate boiling, transition boiling, and vapor superheating.

The data for this typical run, as shown in Figure 9, do not provide a basis for distinguishing the film boiling regime from the transition boiling regime. It is possible that due to the controlled temperature characteristics of the two-fluid boiler, the corresponding upper limit of the wall-to-fluid temperature difference is not high enough to cause complete drying of the heated wall prior to reaching dry vapor flow conditions, as is required for onset of the film boiling regime.

The discontinuity of slope in the sodium temperature profile indicated by the shell temperature measurements shown in Figure 9 is assumed to be the critical heat flux point and the beginning of transition boiling. The position at which the potassium temperature begins to rise near the tube exit is assumed to mark the beginning of the superheated vapor region. The amount of heat transferred in the superheat region is calculated from the measured potassium temperature rise to the exit. The point of boiling inception and the amount of heat transferred in the subcooled liquid region are similarly determined from the insert thermocouples. For runs in which no insert was used superheated vapor exit conditions were not attained and, consequently, only the subcooled heating region and nucleate and transition boiling regions were present. For these runs without insert, the potassium temperature at boiling inception was obtained using the inlet pressure gage in conjunction with saturation temperature-pressure properties, and the subcooled heating length was determined by single-phase heat transfer calculations.

The average heat flux in the nucleate boiling region is

calculated from the axial shell temperature gradient in this region, which is assumed to be equal to the sodium axial bulk temperature gradient. From the average heat flux and the length of the nucleate boiling region, the amount of heat transferred in the region is calculated. The heat transferred in the transition boiling region is determined as the difference between the total heat input and that transferred in the other regions. The average heat flux in the transition region is then calculated from the estimated length of the region.

The local vapor quality and local sodium temperature at various points along the tube, including the critical heat flux point, are calculated by heat balance, employing the values of heat flux and length determined for the various regions. The local potassium temperature, obtained from the insert thermocouples, and the calculated local sodium temperatures are utilized to calculate overall heat transfer coefficients for each of the various regions. From these coefficients a potassium heat transfer coefficient for each region is obtained by subtraction of the thermal resistances of the sodium and boiler tube wall from the respective overall thermal resistances.

The average nucleate boiling heat transfer coefficients calculated in the above manner are large compared to the tube-wall and sodium coefficients and therefore represent a small fraction of the overall thermal resistance in the nucleate boiling region. This fact precludes their accurate determination in the 300 KW Facility; but correspondingly the overall heat transfer coefficient in the nucleate boiling region, which includes the average nucleate boiling heat transfer coefficient and the effective coefficients for the tube wall and the sodium, both of which are known with reasonable accuracy, can be employed to calculate with good accuracy values of the heat flux in that region. In particular, the critical heat flux is calculated as

the product of the overall heat transfer coefficient in the nucleate boiling region and the measured sodium-to-potassium temperature difference at the critical heat flux point.

The error in the critical heat flux levels calculated in the above manner is not expected to be large. The potassium nucleate boiling heat transfer coefficient should be largest just upstream of the critical heat flux point since both heat flux and vapor quality increase towards the critical point, and there is evidence from the 100 KW Facility data (treated subsequently) that the nucleate boiling heat transfer coefficient increases with both of these quantities. If, for example, the potassium heat transfer coefficient were taken to be infinite in the calculations, the corresponding critical heat flux level would be increased by less than 20% over that determined by the above procedure.

The error in the local vapor quality, including the quality at inception of critical heat flux conditions, is estimated to be about 5% from a consideration of flow and heat balance errors. As mentioned above, the error in the nucleate boiling coefficient is large since it is a small part of the overall resistance. Since the transition boiling heat transfer coefficients are smaller than the nucleate boiling coefficients, they represent a greater share of the overall thermal resistance and thus can be determined with greater accuracy. The major sources of error in the determination of the transition boiling heat transfer coefficient are the uncertainty of the transition boiling length, because of the limited number of insert and shell thermocouples, and the error in the calculation of the heat transferred in this region. An estimate of the error in the transition boiling heat transfer coefficients is $\pm$ 25%.

100 KW High-Temperature Boiling Tests

The test procedure used in the 100 KW Facility is to hold the saturation temperature, test section mass velocity and test section heat flux nearly constant while the test section vapor quality is varied by changing the preboiler power.

Heat transfer coefficients are calculated from measurements made at a station inside the heated zone about 2-inches upstream of the test section exit. The heat flux, which is assumed uniform over the heated length, is calculated from the measured electrical power input, and is corrected for heat losses. The inside wall temperature is calculated using the measured outside wall temperature and the calculated temperature drop across the pipe wall. The local fluid temperature is measured by the three well thermocouples at the test section exit.

The error in the nucleate boiling heat transfer coefficients is estimated to be within about $\pm$ 45%, due primarily to the small wall-to-fluid temperature differences, which are typically less than about $10^{\circ}F$. For the film boiling and superheated vapor heat transfer coefficients the error is estimated to be within about $\pm$ 10%.

Onset of critical heat flux conditions is detected by observing the behavior of the test section wall temperatures as they are recorded on an 8-channel oscillograph recorder. The behavior of the test section wall temperature at the onset of the critical heat flux condition was found to be of two general types, as follows. At relatively high heat fluxes, when the critical heat flux condition was reached (by slowly increasing test section inlet vapor quality) the wall temperature at the

test section exit would suddenly begin to rise on a rapid transient ($\approx 50^{\circ}F/sec.$) sharply distinguishable from the small wall temperature fluctuations ($\ll 5^{\circ}F$) typical of nucleate boiling conditions. Presumably, if no corrective action had been taken, the wall temperature would have continued to rise until stable film boiling was established— or some limit to the process occurred such as a test section failure or reduction of heat flux due to increased heat losses caused by the correspondingly higher radiant heater temperatures. Such runs were terminated by either automatic or manual reduction of the test section power after the wall temperature transient had begun, in order to protect the test section from damage.

At relatively low heat fluxes and correspondingly higher exit vapor qualities, onset of the critical heat flux condition is not so definite. Under conditions of low heat flux, when the vapor quality is raised beyond a certain critical value, which is dependent on the heat flux level, there results a corresponding increase is amplitude of wall temperature fluctuations above that characteristic of the nucleate boiling regime, as illustrated in Figure 10. Further increases in vapor quality result in corresponding increases in the amplitude of the wall temperature fluctuations and the time-average wall-to-fluid temperature difference until, at sufficiently high vapor qualities, stable film boiling occurs.

As illustrated in Figure 10, the amplitude of the wall temperature fluctuation increases continuously from nucleate boiling through transition boiling to film boiling as the vapor quality is raised. Thus, the "critical quality" corresponding to the critical heat flux condition cannot be definitely deter-

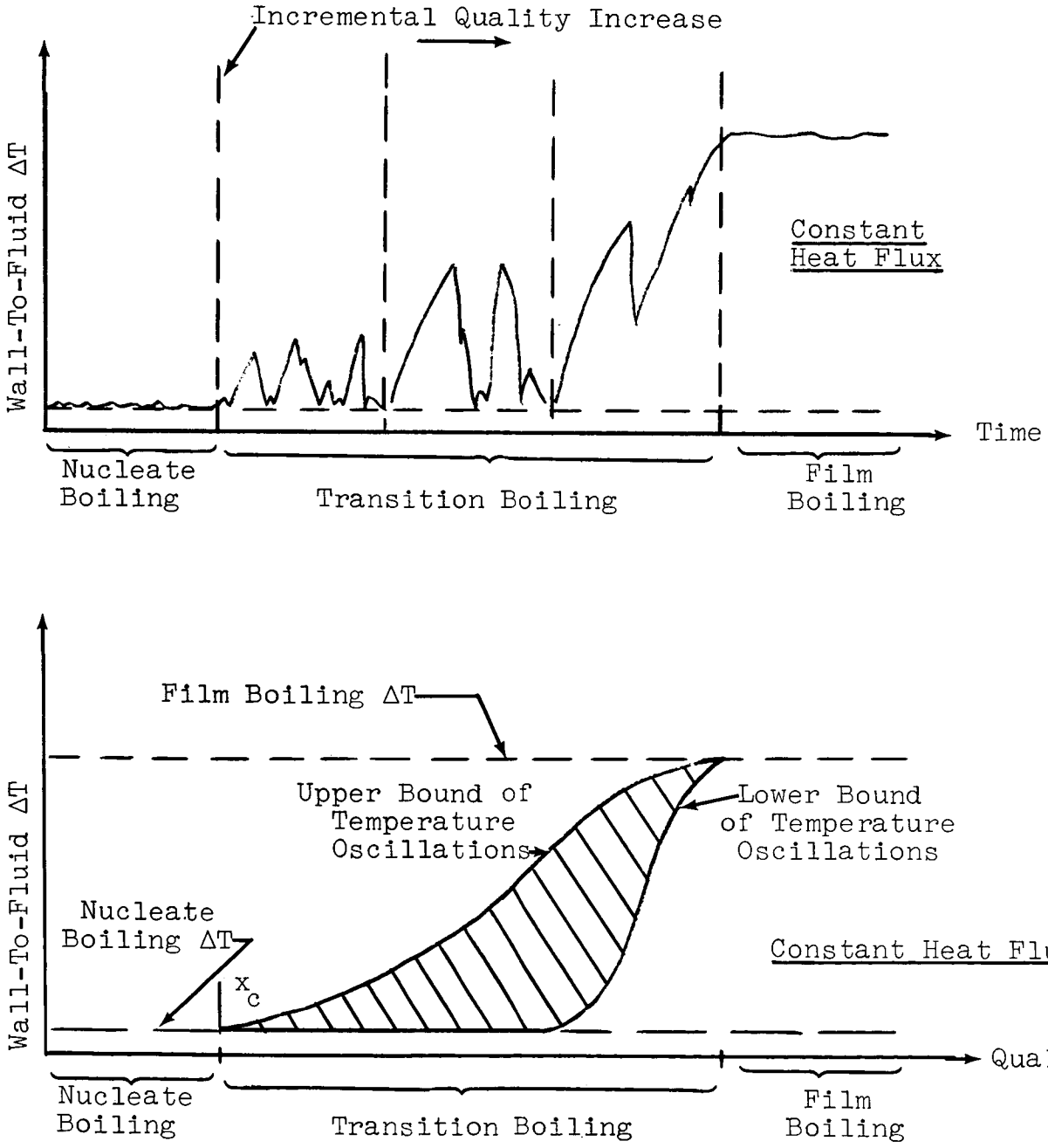


Fig. 10. Sketch of Wall Temperature Behavior in Nucleate, Transition and Film Boiling Regimes

mined. The criterion which has been arbitrarily selected as a working definition for runs in which this type of behavior occurs is that for a given heat flux the "critical quality" is that quality for which the time-average fluctuating wall-to-fluid temperature difference becomes approximately equal to twice the corresponding steady-state nucleate boiling temperature difference. For data taking purposes, the time-average fluctuating wall temperature at the critical heat flux condition is estimated directly from the oscillograph recorder charts made for each of the test runs, and a constant value of 10,000 Btu/hr-ft^2-^{o}F is taken as a representative average of the steady-state nucleate boiling heat transfer coefficient over the range of variables covered by these tests.

For runs in which an estimate of the effective heat transfer coefficient in the transition boiling regime is made, the procedure used is to calculate a time-average wall temperature from digital recorder data, taken at 3-printouts/second for about 1-minute, and to then use this in conjunction with the measured fluid temperature and test section heat flux to calculate a corresponding time-average heat transfer coefficient.

EXPERIMENTAL RESULTS

Pressure Drop Data From 300 KW Facility

The boiling pressure losses in the test section were determined from slack-diaphragm absolute pressure transducers positioned at each end of the boiler tube. Only the pressure losses in test sections with inserts were analyzed, since the pressure losses without inserts were of the same order of magnitude as the accuracy of the gages, about 1 psi. The frictional component of the boiling pressure loss was calculated by subtraction of the momentum pressure loss. The integrated two-phase frictional pressure drop multiplier

was computed as the ratio of the two-phase frictional component divided by the pressure drop for all-liquid flowing at the same total flow rate. Using the square root of the liquid to vapor density ratio as an estimate of the slip ratio (Reference 2), the calculated momentum component was generally less than 20% of the total two-phase pressure loss.

The friction factors required for the computation of the liquid potassium pressure drop, necessary for the determination of the two-phase multipliers, were obtained by water pressure drop tests performed on the boiler tubes with inserts. Typical two-phase potassium frictional pressure drop multipliers, calculated from experimental data reported in Reference 5 and 6, are presented in Figure 11. Shown for comparison on Figure 11 are predictions by the "Martinelli" and "Homogeneous" models. These two-phase frictional pressure drop models are derived and discussed in relation to application to potassium flows in Reference 4.

The agreement between theory and experiment shown in Figure 11 is typical of all the pressure drop results obtained with the 300 KW Facility. The experimental values for the potassium two-phase frictional pressure drop multipliers generally fall between the predictions of the two models.

Nucleate Boiling Data

Figure 12 is a plot of a typical set of nucleate boiling heat transfer coefficients measured with a tube without insert in the 100 KW Facility. At constant saturation temperature, mass velocity and heat flux, the heat transfer coefficient is apparently almost independent of vapor quality over the range shown. The data indicate a trend of increased heat transfer

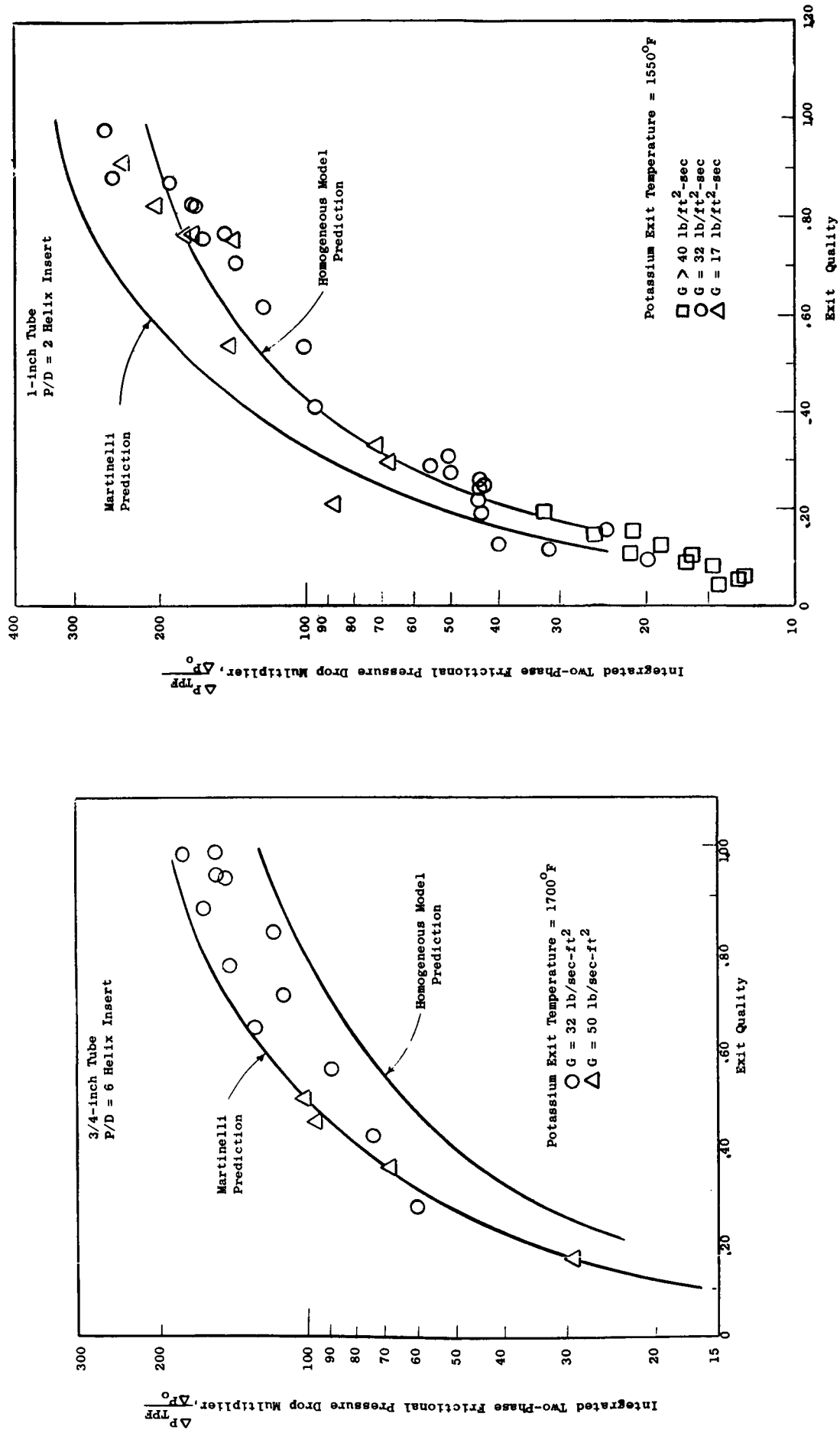


Fig. 11. Boiling Potassium Pressure Drop Data from 300 kW Facility

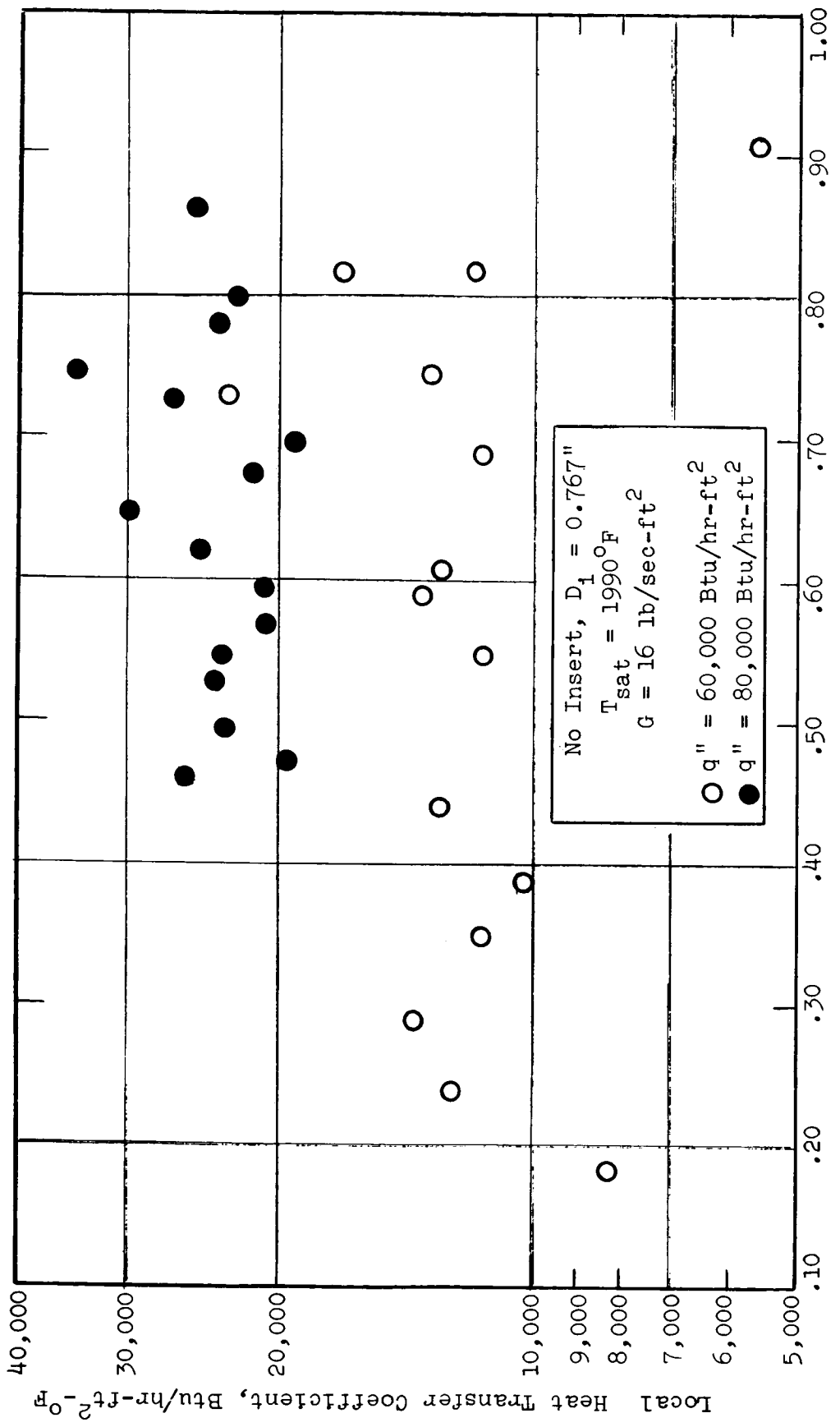


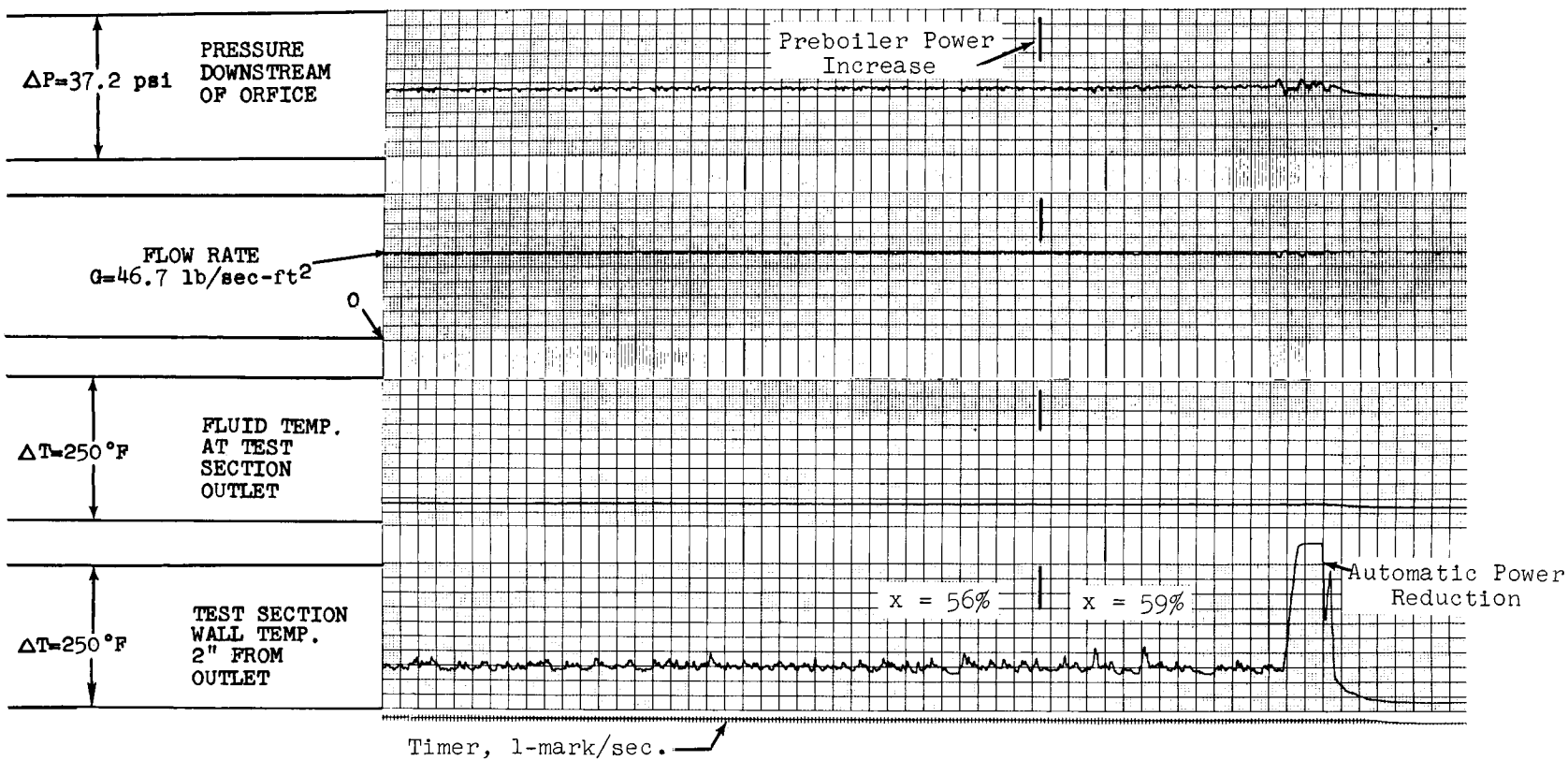
Fig. 12. Potassium Nucleate Boiling Data from 100 kW Facility

coefficient with increased heat flux. These data are reported together with other nucleate boiling data from the 100 KW Facility in Reference 7.

Measured Temperature Behavior at Post-Critical Heat Flux Conditions

Figure 13 is a segment of a typical oscillograph recorder chart obtained during a critical heat flux determination at a heat flux of 211,000 Btu/hr-ft^2 in the 100 KW Facility. Prior to the preboiler power increase (test section inlet quality increase), the pressure downstream of the orifice, the flow rate and the fluid temperature at the test section outlet were steady and the test section wall temperature had small random oscillations, characteristic of nucleate boiling. Following the power increase, the wall temperature began an abrupt, rapid transient which actuated the automatic power reduction system. This run is typical of the type of wall temperature behavior observed when the critical heat flux condition is exceeded at heat fluxes above about 150,000 Btu/hr-ft^2, in tubes without inserts.

Figure 14 shows segments of a continuous oscillograph recorder chart obtained during a run in the 100 KW Facility during which the heat flux was low, about 50,000 Btu/hr-ft^2. The time of day during the run when each segment was taken is marked on the recording in hours. This run illustrates the general behavior of the test section wall temperature as conditions are changed sequentially from the nucleate boiling regime into transition boiling, stable film boiling and finally into superheated vapor conditions. In segment-1, before the preboiler power increase, the test section is apparently in nucleate boiling although there is an occasional small excursion in the wall temperature indicating that the critical heat flux condition was imminent. Immediately following the preboiler power increase (segment-1), the amplitude of the wall temperature oscillations momentarily reached values up to about 50°F and then became more



Data taken 4/1/65

T_{sat} = 2105°F

G = 46.7 lb/sec-ft^2

q''_c = 211,000 Btu/hr-ft^2

Test Section ID = 0.423-in. (no insert)

Fig. 13. Critical Heat Flux Determination at Relatively High Heat Flux in 100 kW Facility

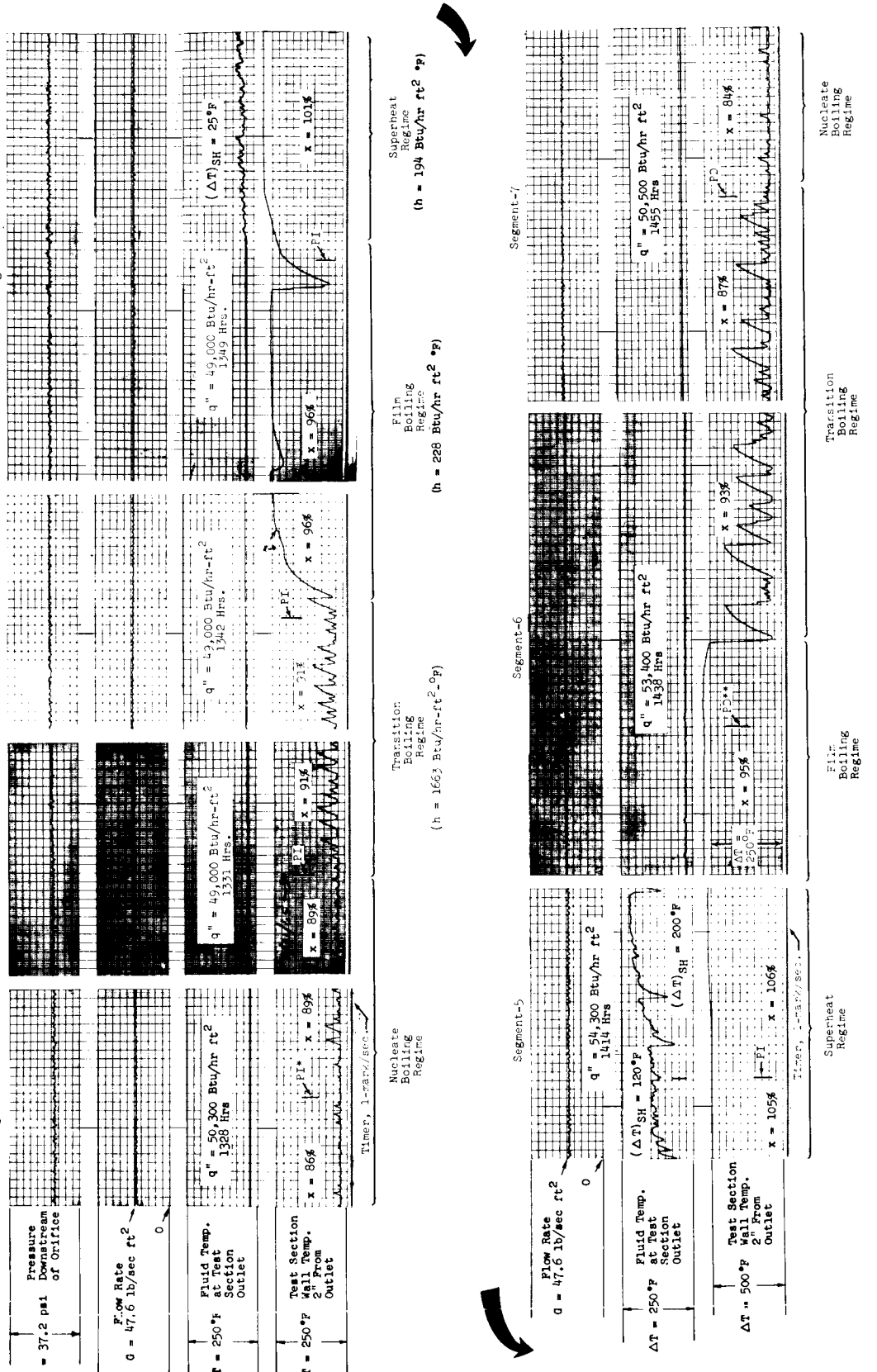
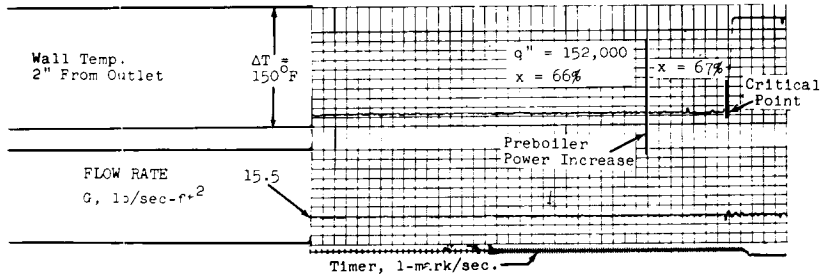


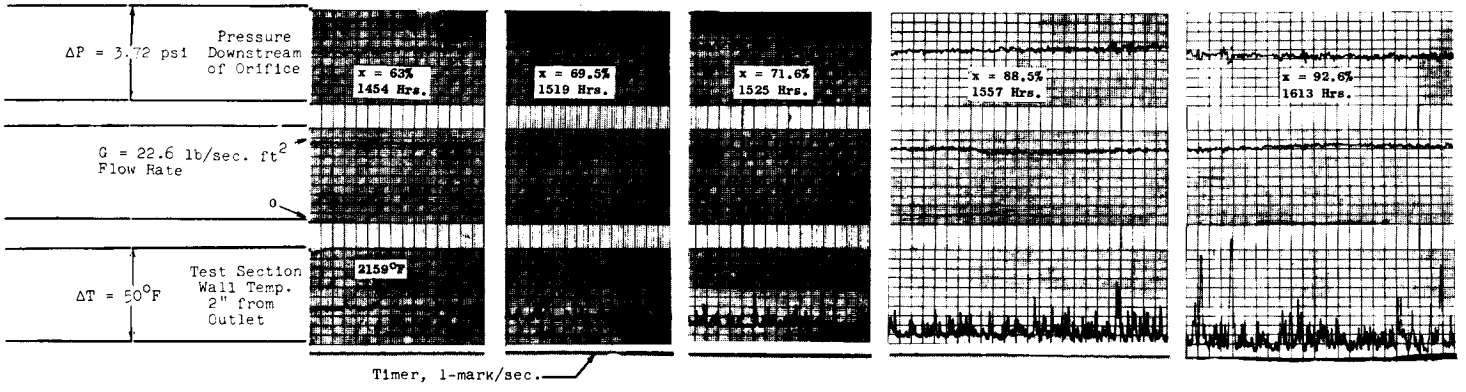
Fig. 14. Wall Temperature Behavior during Operation from Nucleate Boiling to Superheated Vapor Conditions at Low Heat Flux in 100 kW Facility

steady. In segment-2, after the next preboiler power increase, the amplitude of the wall temperature oscillations increased markedly to values of about 75°F with a peak value of almost 150°F, indicating that the test section outlet region was in transition boiling. Following a further preboiler power increase, in segment-3, the wall temperature started to rise steadily and finally reached a maximum and leveled off in stable film boiling. In segment-4, the preboiler power was again increased, resulting in slightly superheated vapor at the test section outlet, as indicated by the rise in measured bulk fluid temperature. Further increases in power (segment-5) resulted in a measured outlet vapor superheat of about 200°F. In segments-6 and -7, the preboiler power was reduced in steps to repeat in reverse the sequence of events observed when going up in preboiler power. The wall temperature behavior during the power reductions is very similar to that observed when increasing power. Heat transfer coefficients calculated from the measured wall temperatures, using the procedures described earlier, are noted under segments-2, -3 and -4 on Figure 14 at the times for which they were calculated, for the transition, film boiling and superheated vapor regimes, respectively.

Figure 15 compares the wall temperature behavior for a tube without insert with that obtained for a tube with a helical insert. The upper recorder chart in Figure 15 shows the characteristic sharp temperature rise at onset of critical heat flux conditions, for the tube without insert. The lower recorder chart segments in Figure 15 were taken with a tube containing a helical insert (P/D = 6). For this run the wall temperature began to oscillate slightly at a quality approximately equal to the critical quality in the run with no insert; but there was no sharp temperature excursion, even though the heat flux levels



No Insert
Data taken 10/22/64
T_{sat} = 2100°F
G = 15.5 lbs/sec-ft²
q" = 152,000 Btu/hr-ft²
Test Section ID = 0.767-in.



Helix Insert (P/D = 6)
Data taken 1/29/65
T_{sat} = 2100°F
G = 22 lbs/sec-ft²
q" = 150,000 Btu/hr-ft²
Test Section ID = 0.740-in.

Fig. 15. Comparison of Wall Temperature Behavior at Critical Heat Flux and Transition Boiling Conditions with and without Helix Insert - In 100 kW Facility

were the same. Further increases in quality, approaching 100%, resulted in increases in amplitude and mean level of the wall temperature fluctuations, characteristic of the transition boiling regime, but did not result in onset of stable film boiling conditions. This suggests that a helical swirl-generator insert prolongs the transition boiling regime to higher quality levels than would be obtained in a tube without insert for the same heat flux.

Critical Heat Flux Data and Correlation

Critical heat flux data for potassium in vertical up-flow in circular tubes with and without helical inserts, obtained in the 100 KW and 300 KW Facilities, are presented in Figure 16. These data were reported in References 5, 6, 7, 8 and tabulated in References 8 and 9. The data are correlated by the following empirical equation*:

$$q''_c = \frac{(1 + a_R)^{\frac{1}{4}}}{1 + 2\left(\frac{x_c}{1-x_c}\right)}, \frac{10^6 \text{ Btu}}{\text{hr-ft}^2} \qquad (1)$$

The parameter a_R in equation (1) is the radial acceleration of the fluid at the tube wall, in g's, developed by the helical insert, and is calculated using the following equation:

$$a_R = \frac{2}{D_i\, g_o} \left[\frac{x_c\, G_K\, \pi}{(P/D)\, \rho_v \sqrt{\rho_L/\rho_v}}\right]^2 \qquad (2)$$

Equation (2) is derived and discussed in some detail in Reference 8. The exponent on the quantity $(1 + a_R)$ in equation (1) was suggested by results for pool boiling, for which the critical heat flux is proportional to the fourth root of the acceleration

*Symbols are defined in the Nomenclature listed at the end

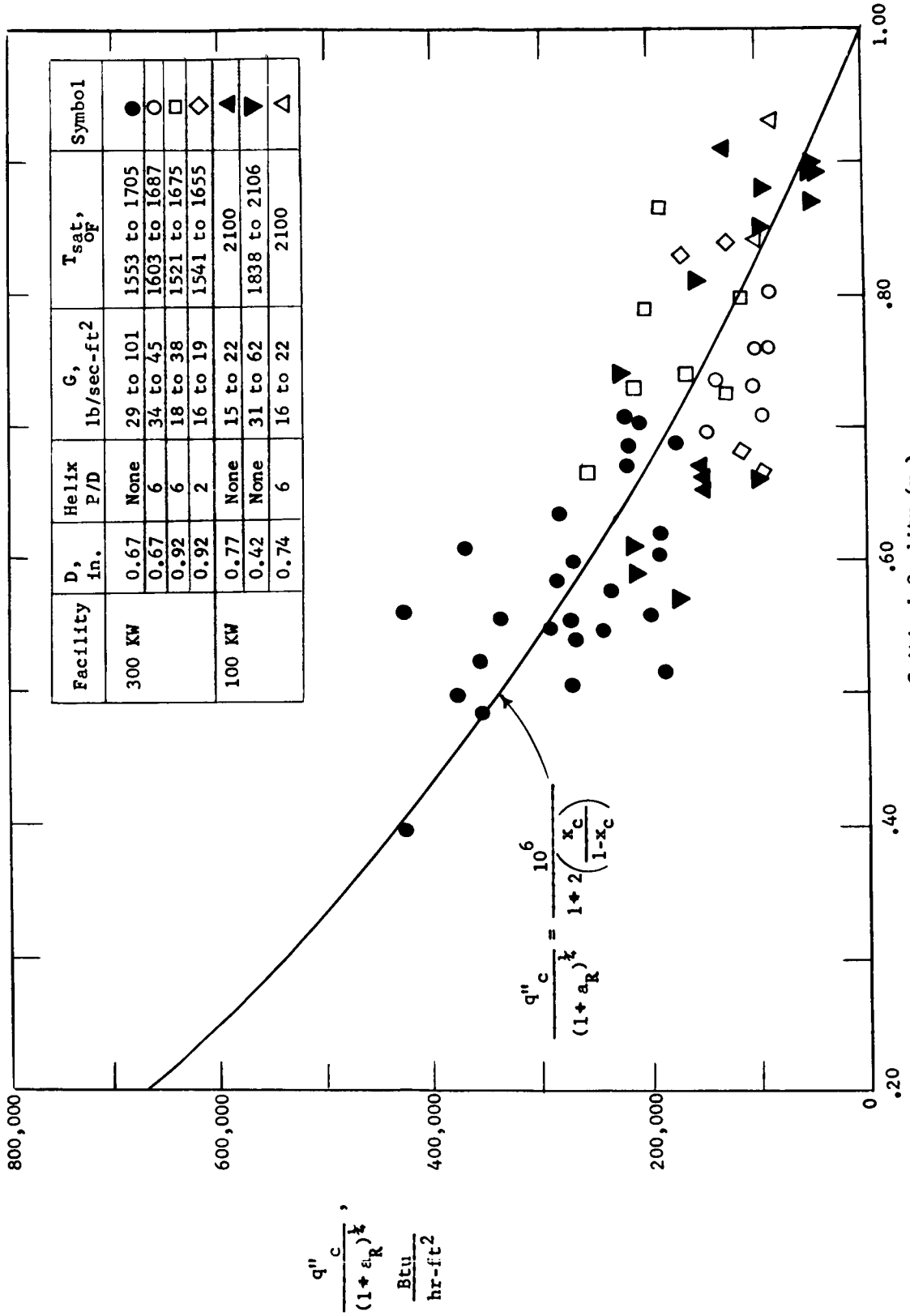


Fig. 16. Potassium Critical Heat Flux Data and Correlation

normal to the heated surface (References 12, 13, 14).

The form of equation (1) with respect to the critical quality x_c is arbitrary, and the two constants in the denominator were determined empirically by best fit to the data given in Figure 16. The trend of decreasing critical heat flux with increasing vapor quality shown by the data in Figure 16 and given by equation (1) is in agreement with the trend shown for water under stable conditions (c.f., Reference 15 and 16).

Equation (1) correlates the experimental data within an average deviation of 31%. Deviations of the individual data points from equation (1) were examined with respect to the significance of other parameters, such as mass velocity and saturation temperature. No trends were evident, indicating that the dependence of the critical heat flux on these parameters is less than the data scatter over the range of test conditions covered.

Transition Boiling Data and Correlation

Transition boiling heat transfer coefficients have been obtained for a variety of test section geometries. These data were reported in References 5, 6, 7, 8 and tabulated in References 8 and 9. The data are plotted in Figure 17 in terms of the following empirical equation:

$$\frac{\frac{h_{TB}}{h_v} - 1}{(1 + a_R)^{1/5}} = 2.55(10^5) \left(\frac{1-x}{x}\right)^{0.7} \left(\frac{1}{\Delta t}\right)^2 \qquad (3)$$

Equation (3) was derived using the following reasoning:

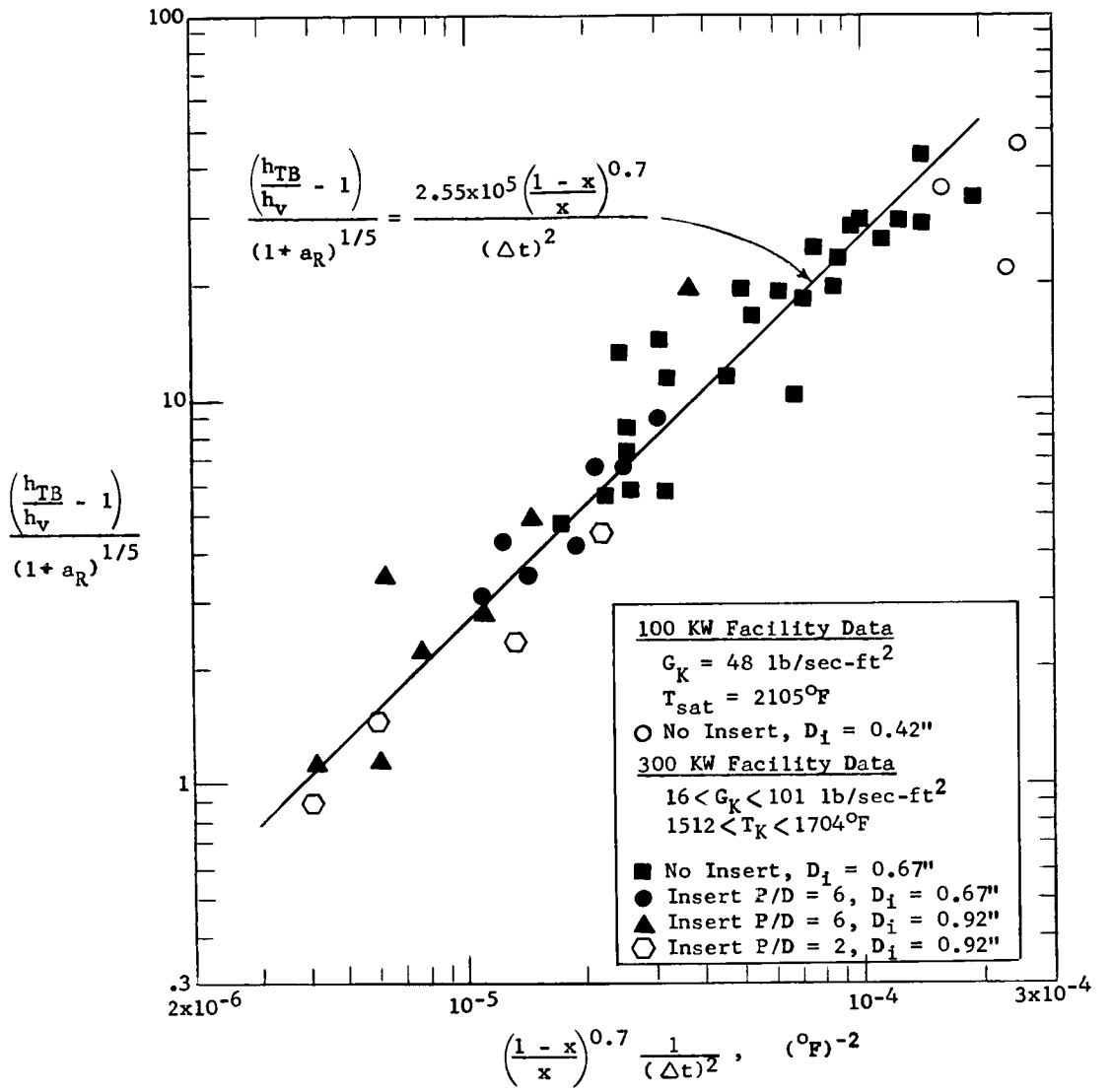


Fig. 17. Potassium Transition Boiling Data and Correlation

1) The results from potassium droplet vaporization experiments by Geoscience (Reference 11) show that the vaporization lifetimes of single droplets increase rapidly with increasing temperature difference between the heated surface and the droplet before the onset of complete film boiling. This suggested that the wall-to-fluid temperature difference Δt is an important parameter affecting the heat transfer coefficient in transition boiling.

2) The local vapor quality x is considered an important variable, because the amount of liquid which can be in contact with the heat transfer surface decreases with increasing quality.

3) The transition boiling heat transfer coefficient h_{TB} should reduce to the vapor phase heat transfer coefficient h_v at 100% quality.

4) The radial acceleration generated by a helical insert a_R, given by equation (2), should increase the transition boiling heat transfer coefficient, because the centrifugal force generated tends to increase the fraction of liquid in contact with the heat transfer surface.

The Colburn equation (Reference 18) was used to calculate the vapor phase heat transfer coefficient h_v in equation (3) for the tubes without insert. For the data taken in tubes with helical inserts h_v is calculated from the following empirical equation, which is developed in Reference 8 using Greene's data for liquid water in helical flow (Reference 19):

$$\frac{h_v D_e}{k_v} = 0.359 \left(\frac{D_e V_H \rho_v}{\mu_v}\right)^{0.563} \left(N_{Pr_v}\right)^{1/3} \qquad (4)$$

where

$$V_H = V_a \sqrt{1 + \left(\frac{\pi D_i}{P}\right)^2} \qquad (5)$$

and

$$D_e = \frac{D_i \left[1 - \left(\frac{D_{cb}}{D_i}\right)^2\right]}{1 + \frac{D_{cb}}{D_i} + \frac{1}{\pi}\left(1 - \frac{D_{cb}}{D_i}\right)} \qquad (6)$$

All exponents and constants in equation (3) were empirically determined to obtain best fit of the 300 KW Facility transition boiling data. Equation (3) correlates the data from both the 300 KW Facility and the 100 KW Facility, shown in Figure 17, with an average deviation of 24%.

SUMMARY AND CONCLUDING REMARKS

Boiling potassium heat transfer data have been obtained over a range of mass velocities, heat fluxes and qualities at temperatures up to 2100°F in single-tube test sections. These results provide a reasonable basis for thermal design of once-through potassium boilers. The experimental equipment and measurement techniques developed in the course of the work represent an advance in the technology associated with high-temperature boiling of potassium.

Results obtained in the two-fluid 300 KW Facility provide data on local heat transfer performance in the transition boiling and superheated vapor regimes at temperatures up to 1750°F. The results from the radiant-heated 100 KW Facility extend the range of test temperatures up to 2100°F for measurements of local heat

transfer coefficients.

The exploratory measurements of critical heat flux conditions and wall temperature behavior in the transition and film boiling and superheated vapor regimes, made in the 100 KW Facility, are useful for application to design and give information on the nature of the forced convection boiling process for potassium at high-temperature and high vapor qualities. It is interesting that the measured wall temperature behavior at onset of critical heat flux conditions and in the transition and film boiling regimes for forced-convection boiling potassium (Figures 13, 14, 15) is similar to the wall temperature characteristics reported for water in forced convection bulk boiling flow (References 15 and 17). This similarity suggests that the underlying physical mechanisms may be nearly the same for the two fluids.

NOMENCLATURE

a_R	Radial acceleration developed by insert, g's
D_{cb}	Diameter of insert centerbody, feet
D_e	Equivalent diameter of boiler tube with insert, feet
D_i	Inside diameter of boiler tube, feet
g_o	Acceleration due to gravity, 32.17 ft/sec^2
G_K	Potassium mass velocity, lb/(ft^2-sec)
h	Heat transfer coefficient, Btu/hr-ft^2-^{o}F
h_{TB}	Heat transfer coefficient in transition region, Btu/hr-ft^2-^{o}F
h_v	Heat transfer coefficient for the vapor, Btu/(hr-ft^2-^{o}F)
k_v	Thermal conductivity of the vapor, Btu/(hr-ft-^{o}F)
N_{Pr}	Prandtl Number, dimensionless
P/D	Twist ratio or pitch-to-diameter ratio, tube diameters for 360^o revolution of insert
q"	Local heat flux, Btu/(hr-ft^2)
$q"_c$	Critical heat flux, Btu/(hr-ft^2)
T_{sat}	Saturation temperature, ^{o}F
V_a	Axial velocity, feet/sec
V_H	Helical velocity, feet/sec
x	Local quality, dimensionless
x_c	Local quality at point of critical heat flux, dimensionless
μ	Viscosity, lb/(hr-ft)
ρ	Density, lb/ft^3
ρ_L	Liquid density, lb/ft^3
ρ_v	Vapor density, lb/ft^3
$\frac{\Delta P_{TPF}}{\Delta P_o}$	Integrated two-phase frictional pressure drop multiplier, dimensionless
Δt	Wall-to-fluid temperature difference, ^{o}F
ΔT	Temperature difference, ^{o}F
ΔT_{SH}	Bulk superheat of vapor, ^{o}F

LIST OF REFERENCES

1. Affel, R.G., Burger, G.H. and Pearce, C.L., "Calibration and Testing of 2-inch and 3½-inch Magnetic Flowmeters For High Temperature NaK Service", ORNL-2793, March 4, 1960.

2. "Alkali Metal Boiling and Condensing Investigations", Quarterly Progress Report No. 6, Contract NAS 3-2528, SPPS-MSD, General Electric Company, NASA-CR-54037, April 20, 1964.

3. "Alkali Metal Boiling and Condensing Investigations", Quarterly Progress Report No. 7, Contract NAS 3-2528, SPPS-MSD, General Electric Company, NASA-CR-54038, April 20, 1964.

4. "Alkali Metal Boiling and Condensing Investigations", Quarterly Progress Report No. 8, Contract NAS 3-2528, SPPS-MSD, General Electric Company, NASA-CR-54138, October 20, 1964.

5. "Alkali Metal Boiling and Condensing Investigations", Quarterly Progress Report No. 9, Contract NAS 3-2528, SPPS-MSD, General Electric Company, NASA-CR-54215, October 20, 1964.

6. "Alkali Metal Boiling and Condensing Investigations", Quarterly Progress Report No. 10, Contract NAS 3-2528, SPPS-MSD, General Electric Company, NASA-CR-54308, January 20, 1965.

7. "Alkali Metal Boiling and Condensing Investigations", Quarterly Progress Report No. 11, Contract NAS 3-2528, SPPS-MSD, General Electric Company, NASA-CR-54405, April 23, 1965.

8. "Alkali Metal Boiling and Condensing Investigations", Quarterly Progress Report No. 12, Contract NAS 3-2528, SPPS-MSD, General Electric Company, NASA-CR-54739, July 23, 1965.

9. "Alkali Metal Boiling and Condensing Investigations", Quarterly Progress Report No. 13, Contract NAS 3-2528, SPPS-MSD, General Electric Company, October 1965(to be issued).

10. Wesling, G.C., and McCarthy, M.E., "Thermodynamic Properties of Potassium Vapor from 1300°R - 2700°R - Using Naval Research Laboratory Experimental Data", GE Report R64SD3012, SPPS-MSD, General Electric Company, October 6, 1964.

LIST OF REFERENCES (CONT'D)

11. Poppendiek, H.F., et al., Quarterly Technical Report on High Acceleration Field Heat Transfer for Auxiliary Space Nuclear Power Systems, AEC Contract No. AT(04-3)-409, September 1 to November 30, 1964.

12. Zuber, N., "Stability of Boiling Heat Transfer", Trans. ASME April 1964.

13. Costello, C.P. and Adams, J.M., Paper No. 30, "1961 International Heat Transfer Conference", Boulder, Colorado, August 1961.

14. Usiskin, C.M. and Siegel, R., Trans. ASME, J. Ht. Trans., 83-C pp. 243-253, August 1961.

15. Janssen, E. and Kervinen , J.A., "Burnout Condition for Single Rod in Annular Geometry, Water at 600 to 1400 psia", GEAP-3899, February 1963 (OTS)

16. Tippets, F.E., "Analysis of the Critical Heat Flux Condition In High-Pressure Boiling Water Flows", Trans. ASME, J. Ht. Trans. 86-C pp. 23-33, February 1964.

17. Hench, J.E., "Transition and Film Boiling Data at 600, 1000 and 1400 psi In Forced Convection Heat Transfer To Water", GEAP-4492, February 1964 (OTS)

18. Rohsenow, W.M. and Choi, H.Y., "Heat, Mass and Momentum Transfer", Prentice-Hall, 1961.

19. Gambill, W.R. and Bundy, R.D., "An Evaluation of The Present Status of Swirl-Flow Heat Transfer", ORNL Report (central files number 61-4-61), April 1961.

N66 31676

MEASUREMENTS OF FORCED CONVECTION CONDENSING POTASSIUM HEAT TRANSFER*

By

S.G. Sawochka

Space Power and Propulsion Section
Missile and Space Division
General Electric Company
Cincinnati, Ohio 45215

ABSTRACT

A discussion of temperature and flow rate measuring techniques, which have allowed the determination of heat transfer and pressure change data for the forced convection condensation of potassium, is presented.

Intercalibration of the condensing test section thermocouples is discussed, and representative tube wall radial temperature profiles and potassium axial temperature profiles are presented.

*Work performed for National Aeronautics and Space Administration Contract Number NAS 3-2528

INTRODUCTION

An experimental and analytical program was conducted at the General Electric Company for the National Aeronautics and Space Administration to determine the thermal and fluid dynamic behavior of single tube potassium condensers for application to space power system condenser design. The primary goals of this investigation were to determine potassium condensing heat transfer coefficients and to compare them to analytical predictions (1 - 10)*. Examination of the literature (11 - 19) had shown that the experimental heat transfer coefficients of other low Prandtl number fluids were lower than predicted by analysis. Presented in this paper is a discussion of the five test geometries which were studied and also the condensing test facility with emphasis on the temperature and flow rate measurement techniques developed during the course of the program.

APPARATUS

Facility (20) - An isometric of the potassium condensing test facility is presented in Figure 1. The facility, except the test section, was constructed of Type 316 SS selected because of its high strength and compatibility with alkali metals up to 1600°F.

Potassium vapor was generated in a pot boiler which contained immersion heaters capable of 50 KW heat input. The vapor generated in the boiler flowed through a vertical 8-foot length of 2-inch Schedule 40 pipe, a 1½-inch vapor throttle valve, a horizontal 10-foot length of 1-inch Schedule 40 pipe,

*Underlined numbers in parentheses designate references listed at the end.

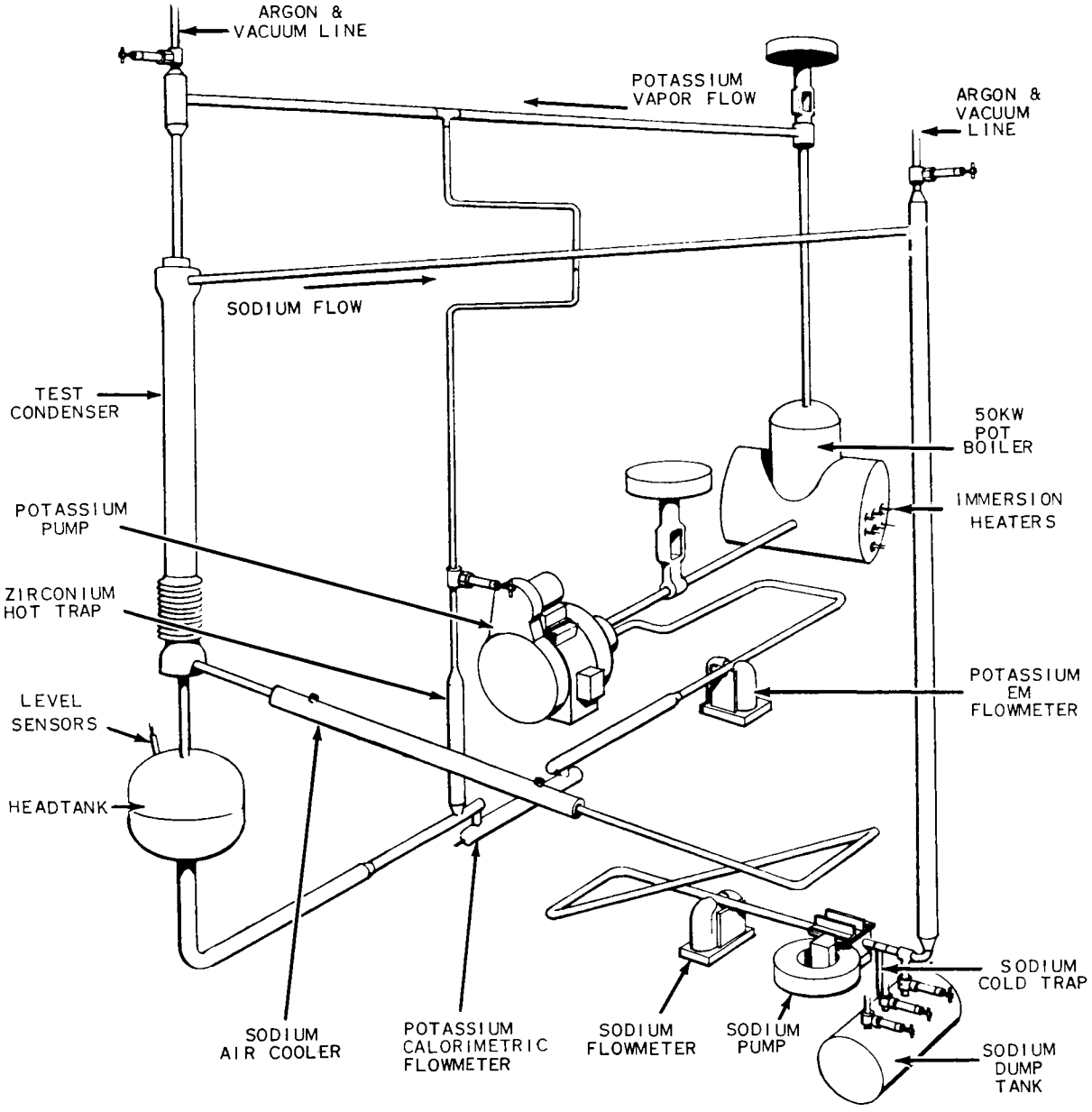


Fig. 1. 50 kW Heat Transfer Test Facility

and vertically downward into a sodium cooled test condenser. During condensing heat transfer tests, the liquid-vapor interface was maintained downstream of the active test section heat transfer length, in the head tank shown in Figure 1, to minimize the effect of boiler level oscillations on test condenser operation. The liquid exiting from the test section flowed through a thermal calorimeter, a helical induction electromagnetic pump, an electromagnetic flowmeter and back into the boiler. All lines were wrapped with Inconel sheathed Chromel "A" heating wire for preheating.

The sodium loop, an all-liquid loop, was used to cool the test condenser. The sodium passed vertically upward through the annulus of the test condenser and then through lengths of 1 and 2-inch Schedule 40 pipe, an electromagnetic conduction pump, and an electromagnetic flowmeter. The sodium then passed through an air cooler where heat was rejected and returned to the test section. A dump tank was provided for storing the sodium during shutdown.

Test Section (21) - A schematic of the condensing test section used in this series of experiments is presented in Figure 2. Potassium condensation occurred inside a thick walled nickel tube which was cooled by a countercurrent sodium flow in the surrounding annulus. Operation was with the condenser tube axis vertical and the potassium in vertical downflow.

The condenser tubes were made of 99.95% + nickel selected for its high thermal conductivity in combination with its compatability with the alkali metal test environment. Two different tube sizes were used: 5/8-inch inside diameter

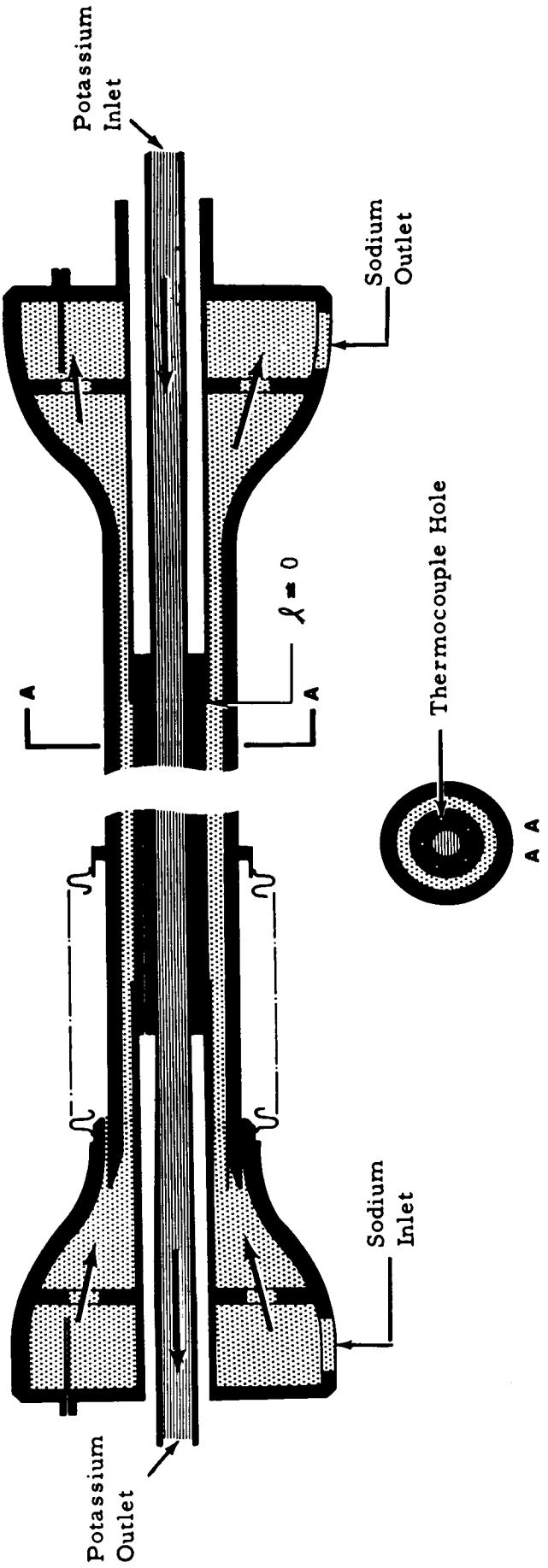


Fig. 2. Test Section Schematic

and 3/8-inch inside diameter, both with a 1.85-inch outside diameter. Both tubes were 38-inches in length, and the center holes were concentric with the outside diameter of the tube to within 0.003-inch.

To calculate the condensing heat transfer coefficients, measurements of the local heat flux, inner wall temperature and vapor temperature were required. To determine the inner wall temperature and heat flux, thermocouples were located in holes which were drilled by an electrical discharge process in the thick walled nickel tube and which ran parallel to the axis of the tube. The locations of these holes, five entering the nickel tube wall from each end, are indicated in Figure 3. The drilled thermocouple holes were 0.050-inch in diameter and 9-inches deep, and their radial location was held within 0.004-inch of the specified location over their length. The holes were located at three different radial locations thereby allowing for redundancy in temperature measurement at two radial positions. Two holes were located as close as possible to the inside diameter, one at an intermediate radius, and two near the outside diameter. Potassium vapor temperatures were measured at the test section inlet and outlet with all test section geometries. In the last two test sections, thermocouples were located in a test section insert to determine the axial potassium temperature distribution. The wall and vapor temperature measuring techniques are discussed subsequently. In addition to the thermocouples located within the nickel tube wall and potassium fluid, additional instrumentation was provided to measure the inlet and outlet sodium bulk temperature. Figure 4 shows the sodium inlet end of the test section with three thermocouple wells spaced 120^{o} apart for measuring the inlet bulk sodium temperature. A similar arrangement was

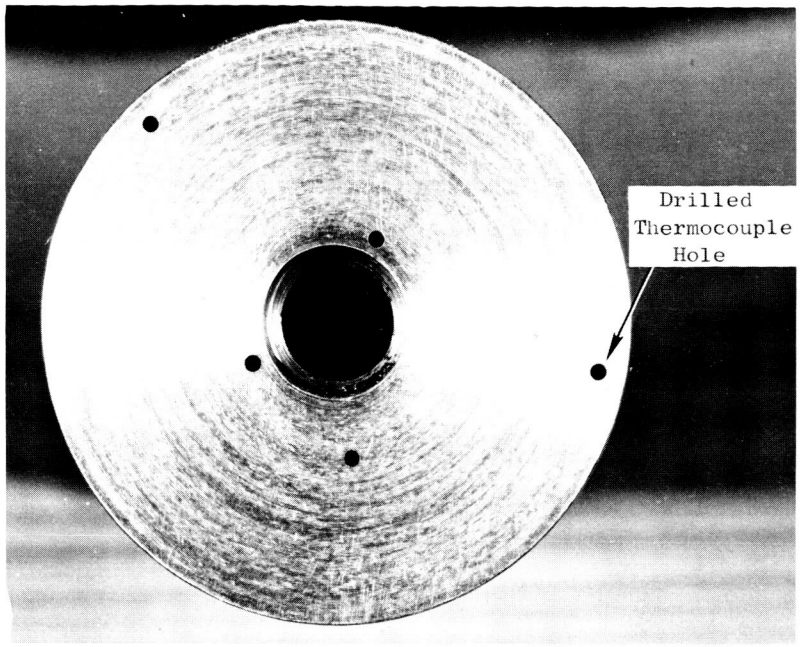


Fig. 3. End View of 3/8-inch ID Condenser Tube Showing Drilled Thermocouple Holes

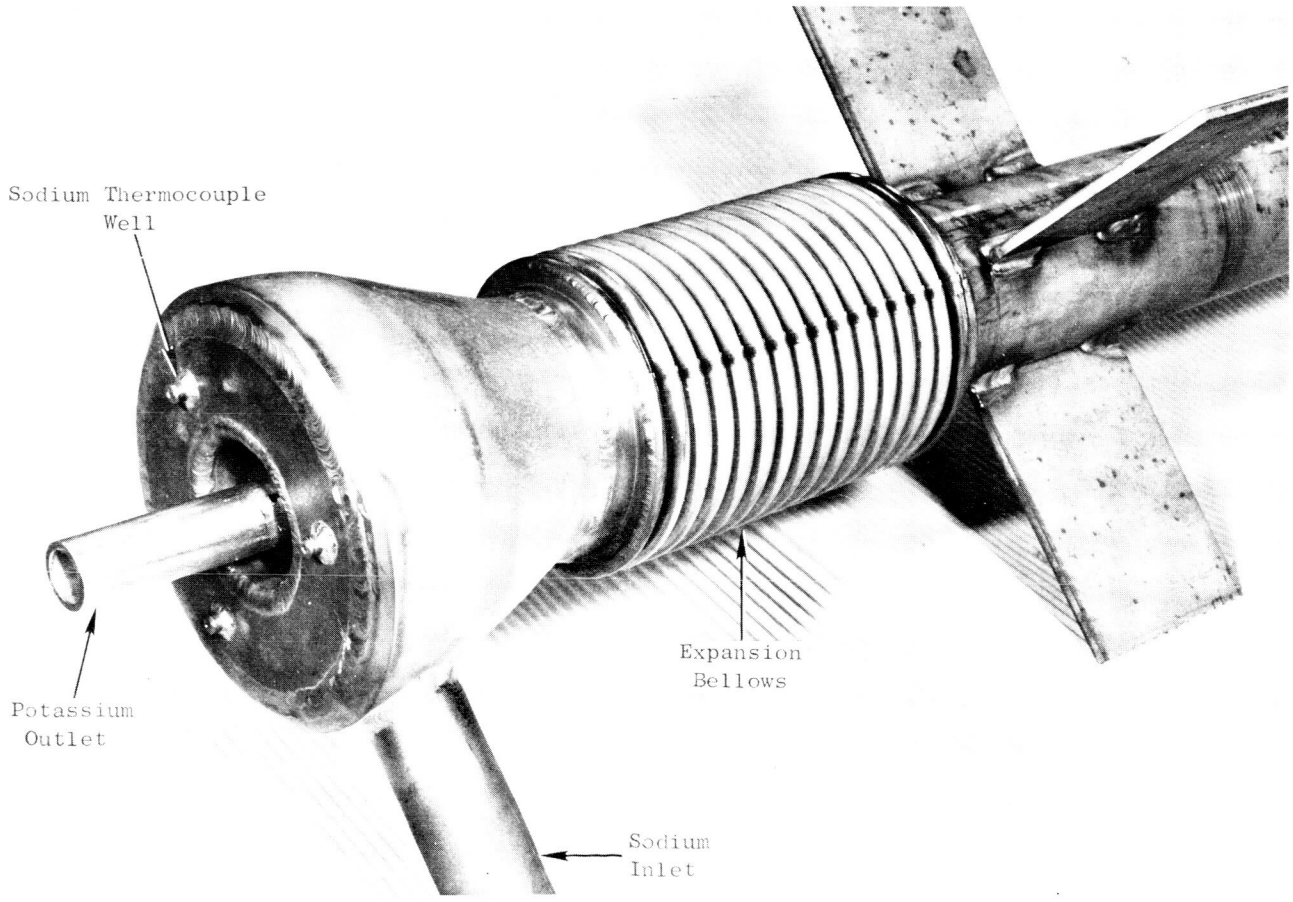


Fig. 4. End View of Test Condenser Shell Showing Inlet Sodium Thermocouple Wells

provided at the sodium exit.

Figure 5 shows one end of the 3/8-inch inside diameter test section after attachment of a stainless steel adaptor which was brazed into each end of the test piece to allow the condensing test section to be welded to the potassium loop piping. In addition to the joint shown in Figure 5, each end of the nickel tube was fitted to a 2-inch OD stainless steel tube which was welded to the outside diameter of the nickel tube at each end. This tube was used to join the nickel tube to the surrounding sodium-containing shell. The space between these two concentric tubes formed an annulus open to the atmosphere through which the tube wall thermocouples were installed. This assembly, shown in Figure 2, allowed the leads of the wall thermocouples to be taken out without crossing either the sodium or potassium streams thereby avoiding mechanical complexity and undesirable flow disturbance.

The test section outer shell was constructed of $2\frac{1}{2}$-inch Schedule 40 pipe with the two enlarged ends made from pipe reducers and flat plates. Each end was internally baffled with a perforated disc. Concentricity of the test section shell and the thick walled nickel tube was maintained by small spacers which were attached to each end of the nickel tube. Flexibility to accommodate lengthwise differential thermal expansion between the stainless steel shell and the nickel tube was provided by a guided $3\frac{1}{2}$-inch OD bellows located at the bottom end of the outer casing.

Figure 6 shows the 3/8-inch inside diameter condenser tube with its potassium loop adaptors attached and also the completed 5/8-inch inside diameter condensing test section. The 3/8-inch

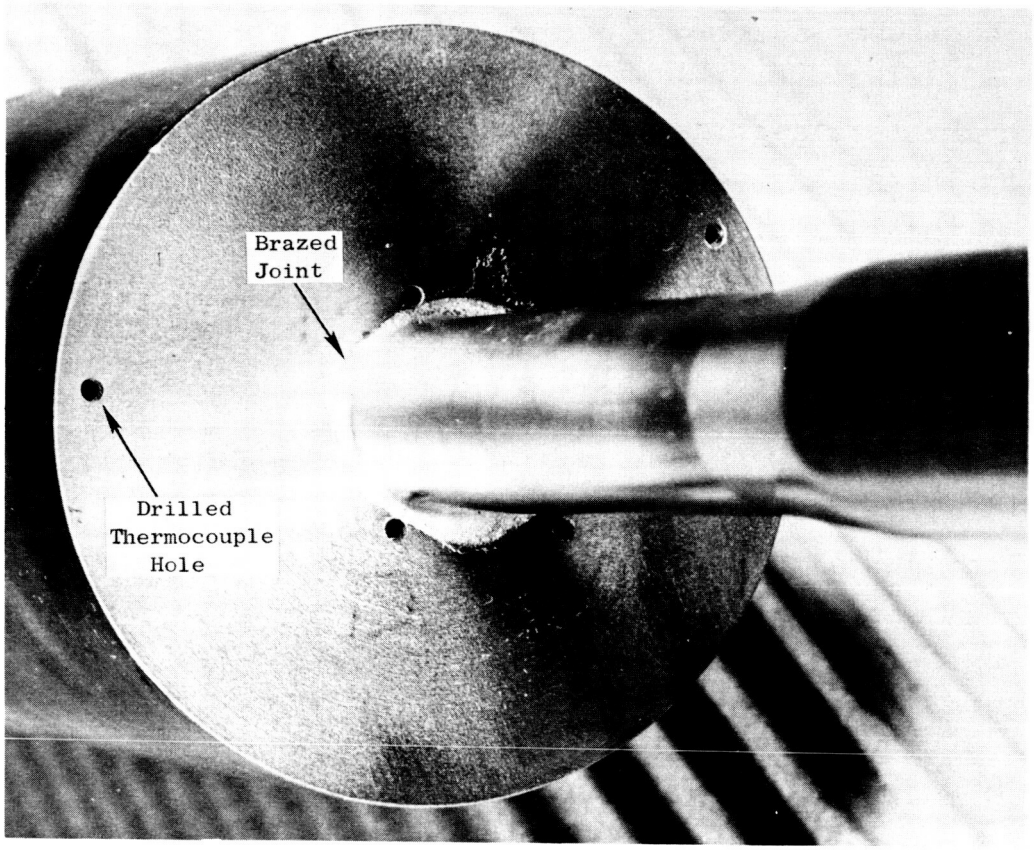


Fig. 5. End View of 3/8-inch ID Condenser Tube Showing Potassium Loop Adaptor Pipe and Wall Thermocouple Holes

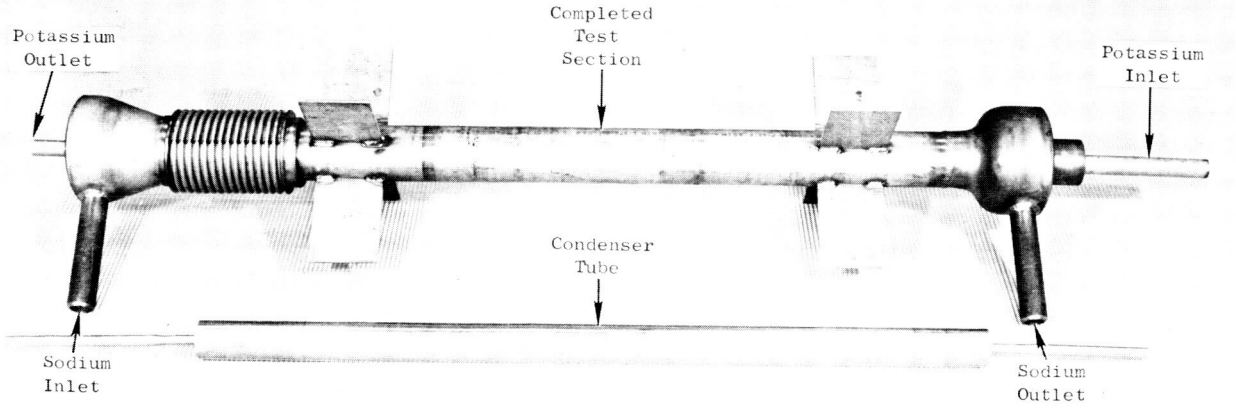


Fig. 6. 5/8-inch ID Test Condenser and 3/8-inch ID Condenser Tube

condenser tube is shown adjacent to the completed test section to indicate its relative length and location within the test section shell. Figure 7 shows the test section installed in the facility before covering it with thermal insulation. As shown, it was surrounded by a structural shell to minimize bending and to maintain a vertical orientation. The supporting structure allowed the test section to expand vertically but not to deviate from a vertical orientation more than $\pm$ 1/16-inch in the 28-inch length between the supports welded to its outer shell.

Experimental data was obtained for five condensing test sections, listed below in the order of testing.

1. 5/8-inch ID tube with no insert
2. 5/8-inch ID tube with a tapered plug insert
3. 3/8-inch ID tube with no insert
4. 5/8-inch ID tube with an instrumented helical insert
5. 5/8-inch ID tube with an instrumented 1/4-inch OD tubular insert.

The three inserts which were tested are shown in Figure 8. The primary purpose of testing the inserts was to determine their effect on condenser performance. However, the last two inserts were instrumented with internal thermocouples thereby providing a measurement of the potassium axial temperature distribution. The first of the inserts consisted of a non-instrumented tapered pin which had diameters of 1/32-inch and 3/8-inch at the test section inlet and outlet, respectively. This insert was used to simulate a tapered tube flow geometry by affording a gradually reducing flow cross-section to the condensing potassium stream.

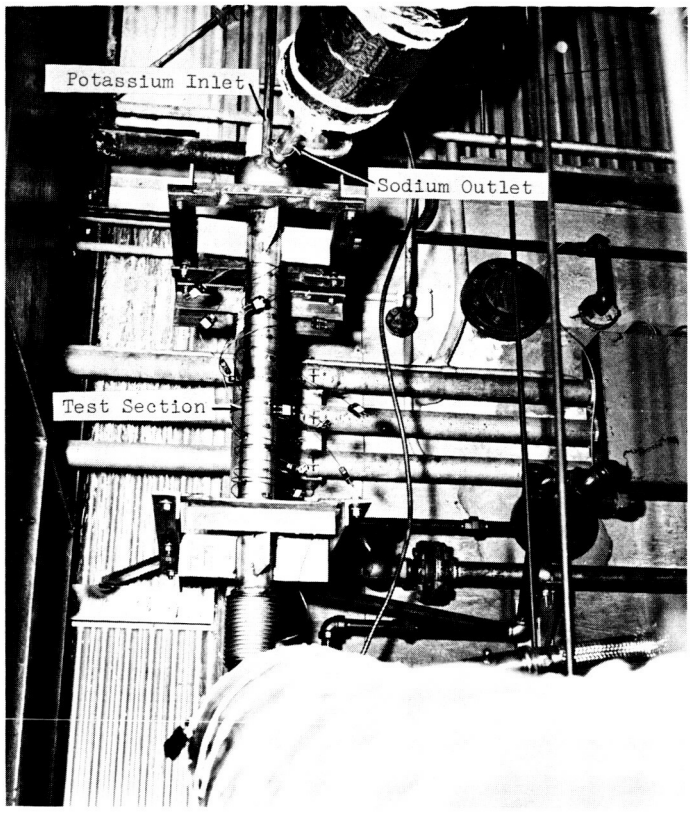
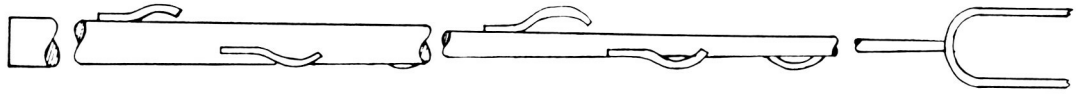


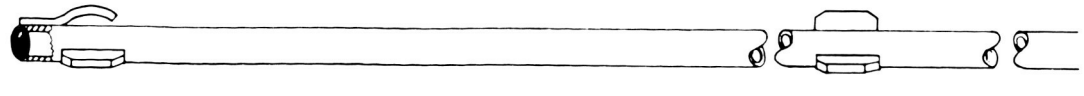
Fig. 7. Test Condenser Installed in Facility



a) Tapered Pin



b) Helix of P/D = 6
(Instrumented)



c) 1/4 - Inch OD Tube
(Instrumented)

Fig. 8. Inserts Tested in 5/8-inch ID Condenser Tube

The insert was held concentric with the inside diameter of the condensing tube by wire prongs located approximately 11 and 30 inches from the test section inlet. The tapered pin was secured in the axial direction by a hair pin-shaped yoke attached to the upstream or small diameter end of the insert and tack welded to the pipe inside diameter above the test section inlet.

The second insert used in the 5/8-inch inside diameter tube was an instrumented helical insert of pitch to diameter ratio, (P/D), equal to 6. This insert consisted of a single helical vane wound around a 1/4-inch outside diameter center tube. This center tube acted as a support for the vane and was brought out of the potassium loop above the test section inlet. Eleven thermocouples were inserted into the center support tube of the helical insert. Three of these preceded the active condensing heat transfer length; the other eight were spaced at five-inch increments from 1 to 36-inches along the active condensing heat transfer length. The loop penetration for the center support tube was made to permit a gradual long radius bend in the insert tube which made insertion and removal of the thermocouples possible without requiring bending of the thermocouples, and to provide accessibility for welding.

The third insert was a 1/4-inch outside diameter tube instrumented in a manner similar to that used for the helical insert. This insert was held concentric with the nickel tube with wire clips in the same fashion as that employed with the tapered pin insert.

EXPERIMENTAL TECHNIQUE

Temperature Measurement - Sheathed, capped 0.040-inch

diameter, chromel-alumel thermocouples were selected due to their stability and relatively high emf output in the 1100 - 1400°F temperature range. The high gain of the chromel-alumel thermocouples, approximately 23 μv/°F, minimized temperature errors due to instrumentation noise which was generally less than ± 3 μv.

When it became evident that the condensing heat transfer coefficients for potassium were relatively high, on the order of 10,000 Btu/hr-ft^2-°F, accurate calibrations of the test section thermocouples became necessary. For the calculation of the condensing heat transfer coefficient a difference between the vapor and wall temperatures is needed. Therefore, in-place intercalibrations of all test section thermocouples were obtained.

Initial calibrations indicated inhomogeneities in the chromel-alumel sheathed thermocouples which might have been caused by bending the thermocouples during installation. These inhomogeneities were detected by moving a soldering iron at about 700°F along the exposed thermocouple length after installation and observing the change in thermocouple output. It was not uncommon to obtain output changes due to inhomogeneities as great as 500 μv (20°F). All thermocouples which indicated greater than 50 μv output change during the homogeneity check were replaced. In addition an individual ice junction was provided for each thermocouple to reduce errors caused by junction emf's.

For intercalibration of the sodium inlet and outlet well thermocouples, sodium fluid temperature measurements were

obtained at one temperature and two different sodium flow rates with the potassium loop evacuated and with no heating of the test section (22). From these data the test section heat loss and also individual thermocouple corrections were determined independently as a function of average sodium temperature as shown below. For two runs under the above conditions at two different flow rates, Equations 1 and 2 are obtained*.

$$q_{LI} = (W\ c_p)_{Na1}\ (T_{NaI} - T_{NaO} + \Delta)_1 \qquad (1)$$

$$q_{L2} = (W\ c_p)_{Na2}\ (T_{NaI} - T_{NaO} + \Delta)_2 \qquad (2)$$

At the same average sodium temperature (shell temperature), the test section heat loss should be the same for both runs, i.e., $q_{L1} = q_{L2}$. Also, if each thermocouple has a systematic correction which is independent of flow rate, the systematic thermocouple correction between the sodium inlet and outlet thermocouples can be obtained from Equation 3.

$$\Delta = \frac{(T_{NaI} - T_{NaO})_1 - (T_{NaI} - T_{NaO})_2}{1 - \dfrac{(W\ c_p)_{Na1}}{(W\ c_p)_{Na2}}} + (T_{NaO} - T_{NaI})_1 \qquad (3)$$

The assumption of thermocouple corrections independent of flow rate is reasonable for this specific geometry.

This method of calibration yields only relative calibrations between the inlet and outlet sodium well thermocouples. The

*Symbols are defined in the Nomenclature listed at the end.

correction, Δ, was applied to thermocouple readings used in the calculation of the amount of heat transferred to the sodium from the potassium during condensing tests. The test section heat loss was simultaneously determined during these thermocouple calibration runs.

In a similar manner, an attempt was made to determine relative calibrations between the potassium inlet and outlet well thermocouples. However, these calibrations were unsuccessful probably due to the lack of fluid mixing at the test section inlet and outlet on the potassium side. Therefore, to obtain relative calibrations between the potassium fluid thermocouples and the nickel tube wall thermocouples, a different procedure was used. The test section annulus was evacuated, and potassium vapor was passed through the test section while the test section shell was maintained at the potassium vapor temperature by use of electrical heating. The small amount of vapor passing through the test section from the boiler was condensed by heat losses in the surge tank below the condenser. Test section thermocouple readings were obtained under these conditions for each test section at $1200^{\circ}F$ and $1300^{\circ}F$ both before and after condensing operation. From these data a systematic correction for each test section thermocouple relative to a selected standard thermocouple was obtained as a linear function of temperature. For the last two test sets, the maximum relative correction was less than $3^{\circ}F$, and agreement between the systematic corrections determined before and after condensing operation was generally better than $1^{\circ}F$.

The magnitude of the distortion of the temperature distribution in the thick walled nickel tube caused by the axial

thermocouple holes was determined (23) by using an analogue method (teledeltos paper). The maximum, minimum and average values of the potential around the circumference of each of the five thermocouple holes was determined. The average potentials were compared to the analytically predicted values for the radial position of the center of each hole and agreed within 3.5% for the hole nearest the outer radius and within 1% for the hole nearest the inner radius. Therefore, the temperature indicated by any of the wall thermocouples was assumed to be equal to the temperature at the radial position corresponding to the center of the thermocouple hole.

The precision in the measurement of the nickel tube wall temperature profile is indicated by the two radial temperature profiles of Figure 9. These two profiles were obtained with local heat fluxes of approximately $1.25(10^5)$ and $2.5(10^5)$ Btu/hr-ft^2. A least squares procedure was used to fit the measured wall temperature within the nickel tube wall with the integrated Fourier conduction equation. The local inner wall heat flux, q_i'', was obtained from the slope of the radial wall temperature profile.

In Figure 10 are shown two measured potassium axial temperature distributions (24) and corresponding saturation pressures for two mass velocities at an inlet temperature of 1150°F. The pressure profiles indicate that in both cases the frictional pressure gradient near the test section inlet exceeds the momentum pressure gradient but is less than the momentum pressure gradient near the test section exit. A net pressure increase is indicated over the condensing length for both cases. A larger pressure rise across the test section was obtained at the higher mass velocity.

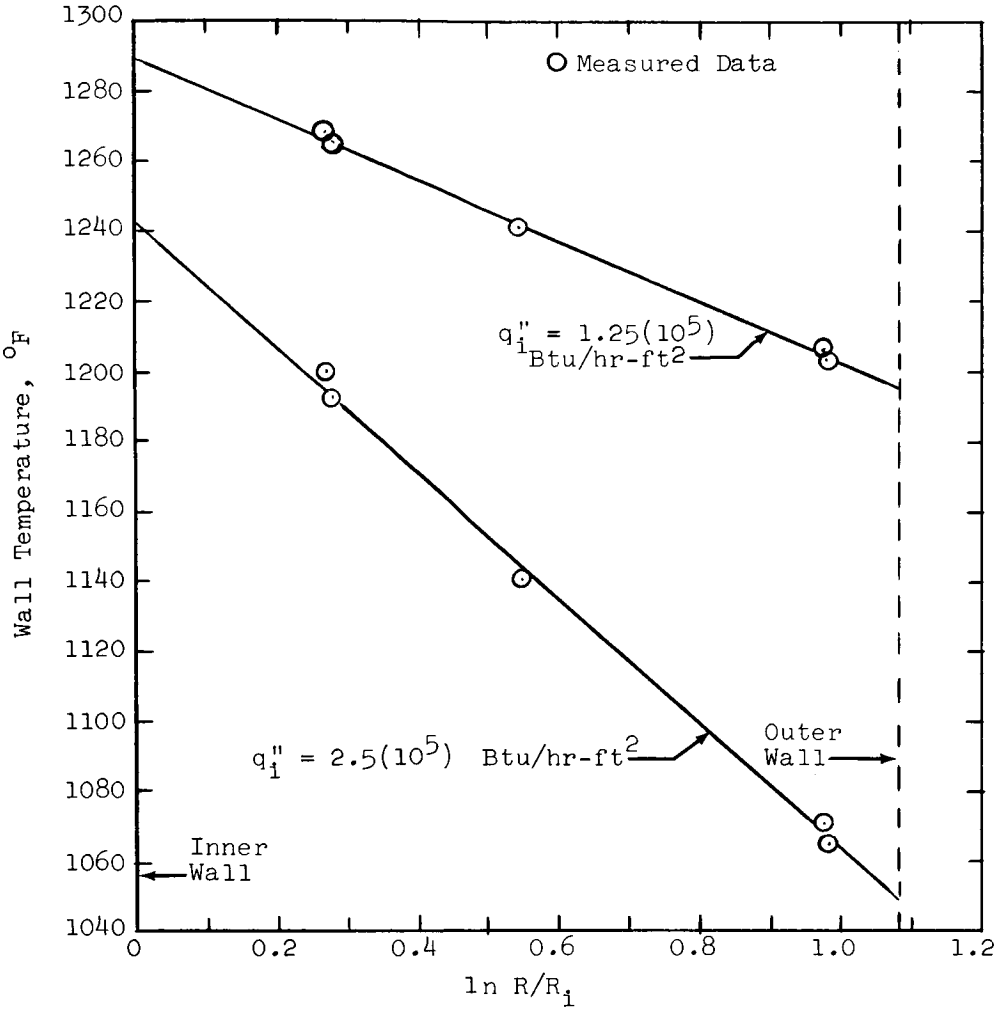


Fig. 9. Nickel Tube Wall Radial Temperature Profiles

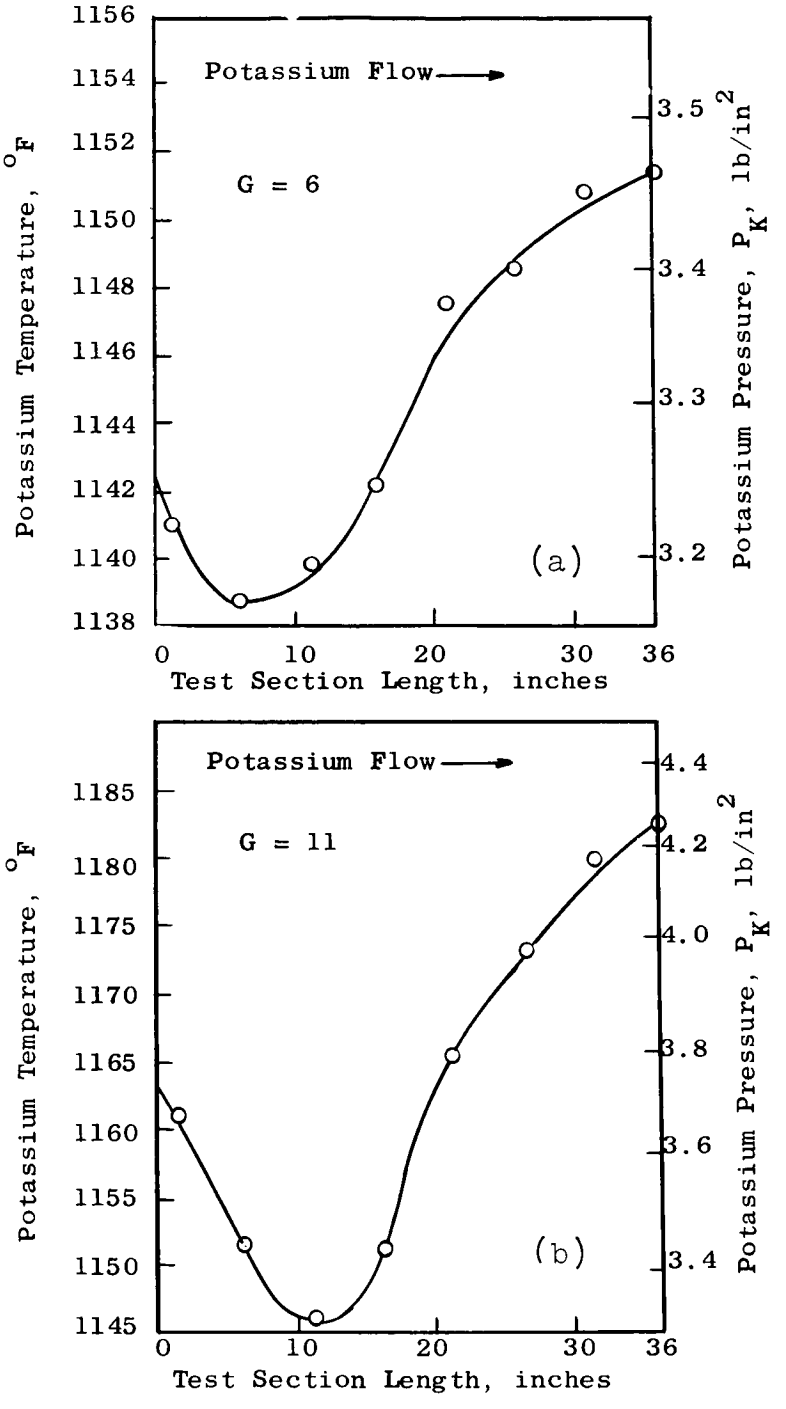


Fig. 10. Potassium Axial Temperature Distributions and Corresponding Saturation Pressures for an Inlet Temperature of 1150°F and Mass Flows of 6 and 11 lb/sec-ft^2 (5/8-inch ID tube with 1/4-inch OD Instrumented Tubular Insert)

In Figure 11 are shown two measured potassium axial temperature distributions and corresponding saturation pressures for inlet temperatures of 1300°F and 1400°F at a superficial mass velocity of approximately 13 lb/sec-ft^2. For the lower inlet temperature, a larger momentum pressure increase was obtained. This is caused by the larger inlet vapor velocity at the lower temperature and the same flow rate. The precision of the insert thermocouples is indicated by examination of Figure 11b. As can be seen, the total temperature variation between the test section inlet and outlet was less than 2°F, and the maximum scatter of the measured temperatures is less than 0.5°F at 1400°F. Included in Figure 11 are the measurements of two of the three thermocouples which precede the active condensing heat transfer length. These thermocouples give an indication of decreasing pressure as a function of length which is expected due to the friction pressure drop along the pipe preceding the test section inlet.

Flow Rate Measurement (22) - When a heat balance discrepancy of approximately 15% was noted in some liquid-liquid tests, the potassium loop electromagnetic flowmeter was calibrated. A calorimetric method was chosen for calibration since the measurement of a temperature difference in a flowing single phase alkali metal stream appeared to be possible within approximately $\pm$ 0 .5°F (22).

The design of the calorimetric flowmeter is shown in Figure 12. An immersion heater was used for heat input to the calorimeter to assure that all of the heat input to the calorimeter went into potassium sensible heat. To determine the potassium flow rate, three parameters had to be known:

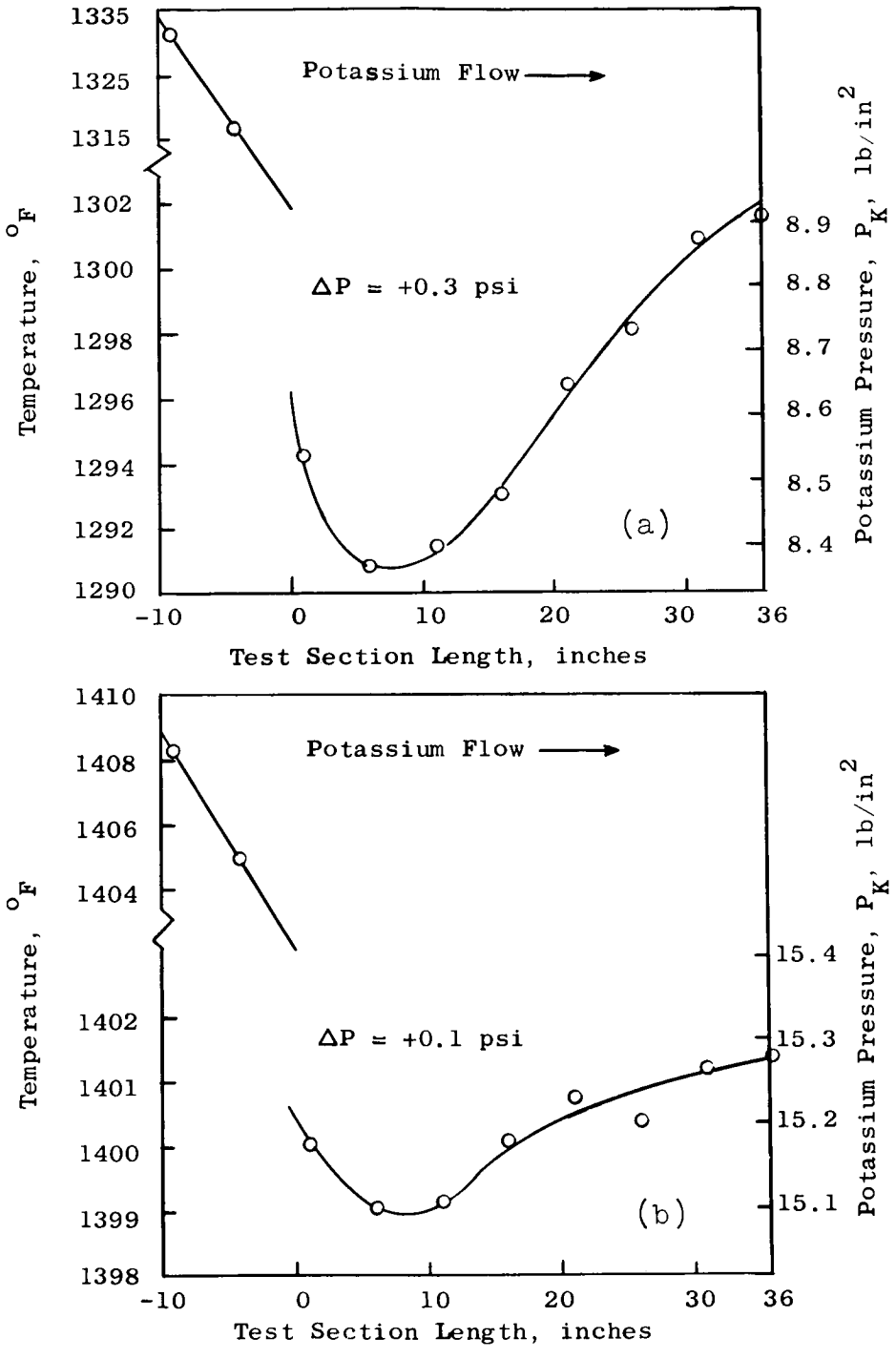


Fig. 11. Potassium Axial Temperature Distributions and Corresponding Saturation Pressures for a Superficial Mass Velocity of 13 lb/sec-ft^2 (5/8-inch ID Tube with 1/4-inch OD Instrumented Tubular Insert, average heat flux 1.4 to 1.5 x 10^5 Btu/hr-ft^2)

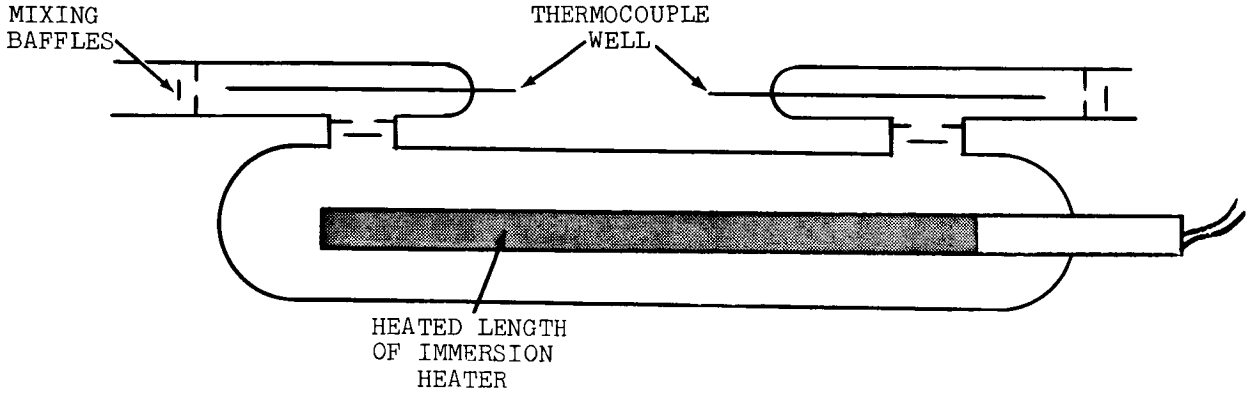


Fig. 12. Thermal Calorimeter

1. Heat input to the calorimeter, q_c, Btu/sec
2. Specific heat of liquid potassium, c_{PK}, Btu/lb-^{o}F
3. The potassium temperature increase across the calorimeter due to the heat input, $T_{KO} - T_{KI}$, ^{o}F

The heat input to the calorimeter was measured by a standardized single-phase watt meter having full scale ranges of 500, 1000, and 2000 watts and an accuracy of $\pm \frac{1}{4}\%$ of full scale. The specific heat of liquid potassium (25)is given by:

$$c_{PK} = 0.202 - .5093(10^{-4})\ T_K + 0.3385(10^{-7})\ T_K^{\,2} \qquad (4)$$

The estimated accuracy of this equation is $\pm$ 2% up to 900^{o}F (25). For a 5^{o}F error in temperature level, the error in c_{PK} is approximately $3(10^{-4})$ Btu/lb-^{o}F or 0.2% at 900^{o}F. Thus the error of c_{PK} due to temperature level uncertainties is small.

These considerations indicate that the accuracy of the calorimetric method is primarily dependent on the measurement of the potassium temperature increase due to the calorimeter heat input. For this reason the calorimeter heat loss and the systematic temperature measurement error between the inlet and outlet thermocouples were determined by a technique similar to that used in the sodium thermocouple calibrations.

With zero heat input to the calorimeter, the potassium loses heat to the surroundings as a function of temperature difference between the calorimeter case and the surroundings. This heat loss is given by:

$$q_{LI} = (W\ c_P)_{K1}\ (T_{Im} - T_{Om} + \Delta)_{K1} \qquad (5)$$

With heat input to the calorimeter, the following expression is obtained:

$$q_C - q_{L2} = (W\ c_P)_{K2}\ (T_{Om} - T_{Im} - \Delta)_{K2} \qquad (6)$$

A measurement without and with heat input to the calorimeter were obtained at the same average potassium temperature, i.e., the same calorimeter case temperature and heat loss. In this case, equations 5 and 6 can be combined to yield:

$$q_C = \left[(W\ c_P)_{K2} \right] \left[(T_{Om}-T_{Im}- \Delta)_{K2} + \frac{(W\ c_P)_{K1}}{(W\ c_P)_{K2}} (T_{Im}-T_{Om}- \Delta)_{K1} \right] \qquad (7)$$

During calibration, the electromagnetic flowmeter was used to equate the flows during the runs with and without heat input. In addition, the systematic temperature measuring error between the inlet and outlet temperatures is independent of the calorimeter neat input. For these conditions equation 7 reduces, after rearrangement, to:

$$W = \frac{q_C}{c_{PK} \left[(T_{Om} - T_{Im})_{K2} + (T_{Im} - T_{Om})_{K1} \right]} \qquad (8)$$

Equation 8 contains measured values of temperature, heat input, and the potassium specific heat, and therefore can be used to calculate the flow rate. For assumed errors in calorimeter heat input of $\pm$ 0.5%, specific heat errors of $\pm$ 2.2% and errors in temperature difference of $\pm$ 1.6%, the estimated standard error in the calculation of flow rate is 3.1%.

This technique of electromagnetic flowmeter calibration was used on the 50 KW Facility for the following conditions:

Flow rate	0.14 - 0.31 lbs/sec
Temperature Difference	11.5 - 43.4°F
Average Temperature	600 - 700°F
Calorimeter heat input	0.76 - 1.6 Btu/sec

Four sets of calibrations resulted in a ratio of the calorimeter to electromagnetic flowmeter flow rates of 1.145 with a standard error of 0.014 or 1.3%. Application of this factor to the indicated electromagnetic flowmeter flow rate brought the liquid-liquid heat balances into reasonable agreement within a standard error of 6.7% and an average error of 0.3%.

SUMMARY AND CONCLUDING REMARKS

Temperature measuring techniques developed during this program have allowed the determination of condensing heat transfer data for potassium. This data, obtained with five test section geometries at temperatures spanning the range from 1100 to 1400°F, provide a reasonable basis for the thermal design of a space power system condenser.

The heat transfer results for the 5/8-inch ID tube with helical and tubular instrumented inserts are presented in Figure 13. These data are considered the most reliable of the data obtained for the five test section geometries since the instrumented inserts provided a means of measuring the local potassium saturation temperatures.

As can be seen the data are generally lower than the Nusselt theory prediction. This discrepancy is thought to be due to the presence of a thermal resistance between the

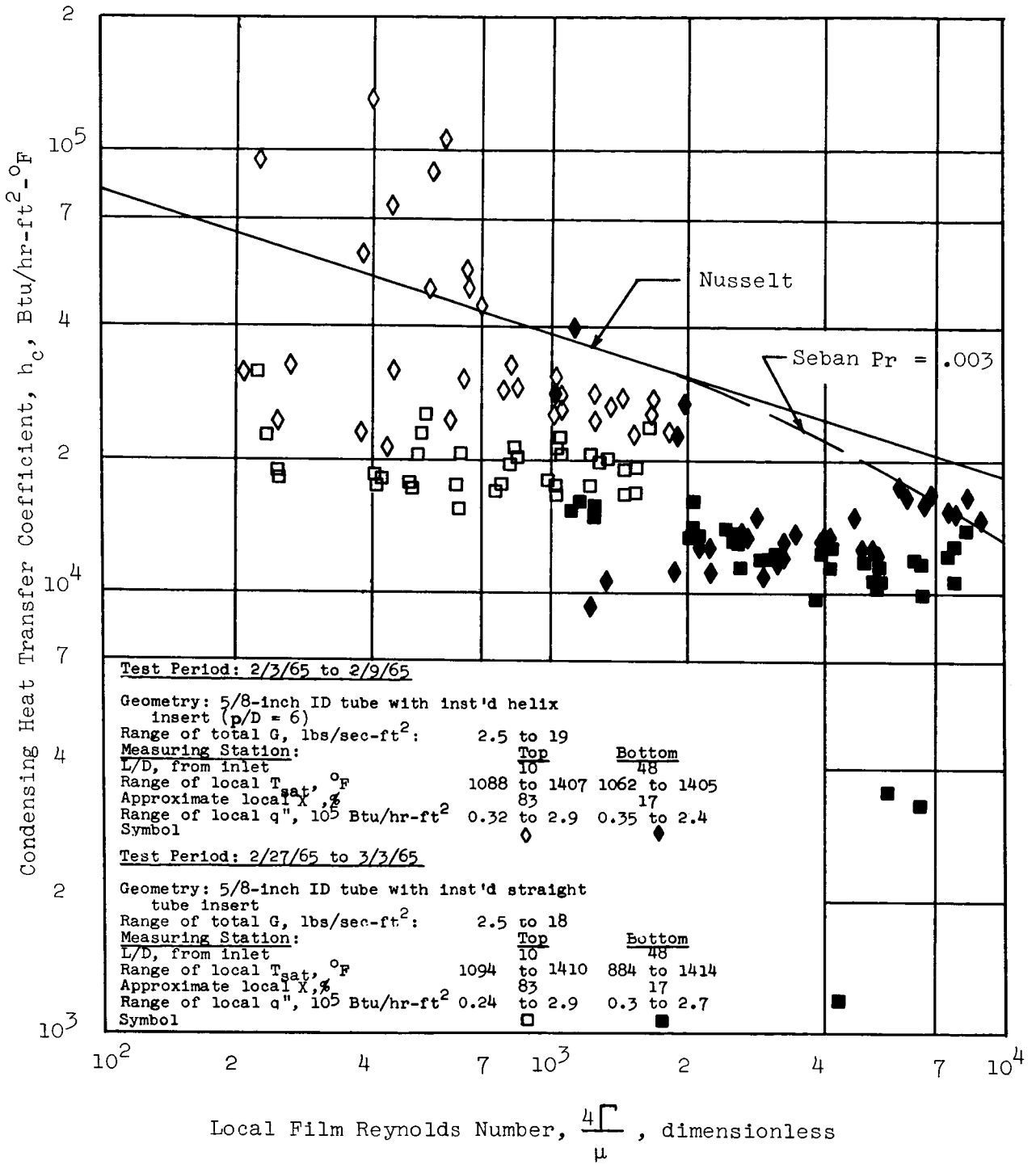


Fig. 13. Condensing Heat Transfer Results

vapor and liquid phases. The data that are presented were obtained at inlet velocities from 100 to 1700 ft/sec. temperatures from 900 to 1400°F, heat fluxes from $3.0(10^4)$ to $3.0(10^5)$ Btu/hr-ft^2, and condenser loads from 5 to 35 KW thermal.

Further details concerning the heat transfer and pressure drop results can be found in Reference 21.

ACKNOWLEDGMENTS

The work described herein was accomplished under the sponsorship of the National Aeronautics and Space Administration under Contract NAS 3-2528.

NOMENCLATURE

Symbols

c_p	Specific heat, Btu/lb-^oF
D	Diameter, ft.
G	Superficial mass velocity, lb/sec-ft^2
h	Condensing heat transfer coefficient, Btu/hr-ft^2-^oF
L	Length, ft.
P	Pitch, ft.
q	Rate of heat flow, Btu/hr.
q"	Heat Flux, Btu/hr-ft^2
R	Radius, ft.
T	Temperature, ^oF
W	Flow rate, lb/hr
x	Quality, dimensionless
Δ	Systematic temperature correction between measured inlet and outlet temperatures
μ	Potassium absolute viscosity, lb/ft-hr

Subscripts

B	Boiler
c	Calorimeter
i	Inside
I	Inlet
K	Potassium
L	Loss
m	Measured
Na	Sodium
O	Outlet
sat	Saturation
1	Run 1
2	Run 2

BIBLIOGRAPHY

1. Heat Transmission, McAdams, W.H., 3rd Edition, McGraw Hill, Inc., New York, New York, 1954.

2. "Remarks on Film Condensation with Turbulent Flow," Seban, R.A., ASME Trans., 1954, p. 299.

3. "Heat Transfer and Temperature Distribution in Laminar Film Condensation," Rohsenow, W.M., Trans. ASME, Vol. 78, pp. 1645-1648, November 1956.

4. "Effect of Vapor Velocity on Laminar and Turbulent Film Condensation," Rohsenow, W.M., Weber, J.H., and Ling, A.J., Trans. ASME, Vol. 78, pp. 1637-1643, November 1956.

5. "Laminar Condensation Heat Transfer on a Horizontal Cylinder," Sparrow, E.M., and Gregg, J.L., Trans. ASME, Series C, J. Heat Trans., Vol. 81, No. 4, pp. 291 - 296, November 1959.

6. "The Two-Phase Boundary Layer in Laminar Film Condensation," Koh, J.C.Y., Sparrow, E.M., and Hartnett, J.P., Int. J. Heat Mass Trans., Vol. 2, pp. 69-82, 1961.

7. "An Analytical Study of Laminar Film Condensation: Part I - Flat Plates, and Part 2 - Single and Multiple Horizontal Tubes", Chen, M.M., Trans. ASME, Series C, J. Heat Trans., Vol. 83, No. 1 pp. 48-54 and pp. 55-60, February 1961.

8. "Turbulent Film Condensation," Lee, Jon, AIChE Journal, pp. 540-544, July 19, 1964, Vol. 10, No. 4.

9. "Fluid Mechanics and Heat Transfer in Vertical Falling-Film Systems," Dukler, A.E., Chem. Eng. Prog. Symposium Series, No. 30, Vol. 56, 1960.

10. "Film Condensation in Forced-Convection Boundary-Layer Flow," Koh, J.C.Y., Int. J. Heat Mass Trans., Vol. 5, pp. 941-954, 1962.

11. "Heat Transfer in the Condensation of Metal Vapors: Mercury and Sodium Up to Atmospheric Pressure," Misra, B., and Bonilla, C.F., Chem. Eng. Prog. Symposium Series, Vol. 52, No. 18, 7-21-65.

12. "Heat Exchange by Drop Condensation of Mercury Vapor", Gel'man, L.I., Teploenergetika, Vol. 5, No. 3, 1958, pp. 47-50.

13. "Heat Transfer Coefficients for Condensation of Liquid Metal Vapors Inside a Vertical Tube," Cohn, P.D., M. Sc. Thesis, Dept. of Chem. Eng., Oregon State College, July 1959.

14. "Heat Transfer During Film Condensation of a Liquid Metal Vapor," Sukhatme, S.P., and Rohsenow, W.M., Technical Report No. 9167-27, Dept. of Mech. Eng., MIT, April 1964.

15. "Experimental Determination of Over-all Heat Transfer Coefficients for Condensing Sodium (1140° to 1840°F)," Roth, J.A., Proceedings of 1962 High Temperature Liquid-Metal Heat Transfer Technology Meeting, Brookhaven National Laboratory, May 1962, pp. 276-285.

16. "Condensation of Sodium and Rubidium at Low Heat Fluxes," Roth, J.A., Report No. ASD-TDR-62-738, October 1962.

17. "Heat Transfer Coefficients in the Boiling and Condensation of Liquid Metals: Potassium and Rubidium, "Englebrecht, J.C., M. Sc. Thesis, Dept. of Chem. Eng., Columbia University, October 1961.

18. "Alkali Metal - Phase Heat Transfer for Space Power - Present Status," Brooks, R.D., and Sawochka, S.G., Paper No. 2547-62, ARS Space Power Systems Conference, September 1962.

19. "Condensation of Metal Vapors: Mercury and the Kinetic Theory of Condensation," Wilhelm, D.J., ANL 6948, October 1964.

20. "Alkali Metals Boiling and Condensing Investigations", Quarterly Report No. 9, Contract NAS 3-2528, Space Power and Propulsion Section, MSD, General Electric Company, October 20, 1964, NASA CR 54215.

21. "Alkali Metals Boiling and Condensing Investigations," Quarterly Report No. 12, Contract NAS 3-2528, Space Power and Propulsion Section, MSD, General Electric Company, July 23, 1965. NASA CR 54739

22. "Alkali Metals Boiling and Condensing Investigations," Quarterly Report No. 6, Contract NAS 3-2528, Space Power and Propulsion Section, MSD, General Electric Company, April 20, 1964, NASA CR 54037.

23. "Alkali Metals Boiling and Condensing Investigations," Quarterly Report No. 4, Contract NAS 3-2528, Space Power and Propulsion Section, MSD General Electric Company, July 25, 1963.

24. "Alkali Metals Boiling and Condensing Investigations," Quarterly Report No. 11, Contract NAS 3-2528, Space Power and Propulsion Section, MSD, General Electric Company, April 20, 1965, NASA CR-54405.

25. Lemmon, A.W., (Jr.), Deem, H.W., Hall, E.H., and Walling, J.R. "The Thermodynamic and Transport Properties of Potassium, Battelle Memorial Institute. Presented at ORNL, Liquid Metals Conference, September, 1963.

N66 31677

DEVELOPMENT OF EFFLUX MEASURING DEVICE FOR PERFORMANCE EVALUATION OF POTASSIUM VAPOR TURBINE

By

G.C. Wesling, R.J. Rossbach
Space Power & Propulsion Section
Re-Entry Systems Department
General Electric Company

W.M. Shaffernocker
Applied Research & Aerodynamics Design Operation
Advanced Engine Technology Department
General Electric Company

(Paper presented by G. C. Wesling)

I. SUMMARY

In the preparation for the performance testing of a 200-horsepower potassium vapor turbine, being developed under NASA Contract NAS 5-1143, it was recognized that a device was required to measure total and static pressures before and after blade rows in a turbine having flow passages no higher than 1 inch.

Existing limp diaphragm pressure transducers which had previously been developed for alkali metal service were known to have an accuracy of about $\pm$ 1 percent and were known to require an access hole to the fluid which was at least 1/2 inch in diameter, which is impossible in a small turbine. The direct connection of the sensor line to either a pressure transducer or a manometer was ruled out because potassium vapor would condense and freeze in the sensor line, rendering the pressure measuring device inoperative.

The pressure measuring device (efflux) that was developed is based upon flowing a metered amount of an inert gas through the sensor lines into the test facility. The flow of inert gas into the test facility prevents the diffusion of potassium vapor into the sensor lines. By this technique the potassium vapors can be contained within the facility and pressure transducers which operate in an inert gas, moderate temperature environment can be used for the measurements. The device was developed

by making tests with air, steam and potassium vapor. When fully developed, the efflux measuring device was used to measure total and static pressures in the two-stage 200-horsepower potassium turbine at inlet and outlet, and the static pressures between all blade rows. In addition, an important application of this device was the measurement of potassium vapor flow rate by means of the measurement of total and static pressures in the calibrated annulus ahead of the potassium vapor turbine. The efflux pressure measuring device may work equally well in the measurement of the pressure of alkali metal vapors other than potassium.

II. INTRODUCTION

In the early phases on planning for design and evaluation of space power turbomachinery development, it was decided that about 40 pressure measurements would be required to evaluate potassium turbine performance. At that time, commercial high-temperature pressure transducers were being used for pressure measurements on alkali-metal heat transfer loops. These pressure transducers had demonstrated reliability and an accuracy of 1 to 2 percent of full scale; however, their cost was approximately ten times that of precision, moderate-temperature pressure transducers for gas service. In addition, the high-temperature transducers were connected to the test piece by means of a 0.5-inch pipe. There was no space available for nipples of this size to make detailed fluid dynamic measurements on small sized turbomachinery. In view of these considerations, it was decided under NASA Contract NAS 5-1143 to develop a pressure measuring system specifically for alkali-metal vapor turbine testing.

The pressure measuring device that was developed is based upon the continuous efflux of inert gas into the test facility through the pressure measurement lines. By this technique the potassium vapors can be contained within the facility and pressure transducers, used for the measurements, operate in an inert gas, moderate-temperature environment. The technique lends itself to the standard methods for pressure switching and the application of high-accuracy commercial transducers.

III. DESIGN

Shown in Figure 1 is a schematic diagram of the efflux system used to measure the pressure of potassium vapor in the 3000 KW test facility. To date, this facility has been used to obtain pressure distribution data in an instrumented converging-diverging nozzle and to carry out performance testing of a 200-horsepower potassium vapor turbine. In the efflux system, argon flows through a filter, an efflux system assembly, a solenoid valve, a vapor trap, and into the test vehicle. The flow of argon prevents potassium vapor from entering the pressure transducer measuring system. A lead connects the scani-valve to a tee which is between the efflux system assembly and the test vehicle. This scani-valve is a fluid switch permitting 12 separate pressures to be read on the same precision transducer. The transducer is connected to the central terminal of the scani-valve. Prior to the taking of a reading, an emergency-purge valve located in the efflux system assembly is opened permitting the argon to flow through a much larger orifice so as to flush the sensor line of any potassium vapor attempting to proceed from the test vehicle to the tee.

In designing the actual hardware for the potassium turbine measurements, one of the primary concerns was ease of maintenance. Figure 2 is a photograph of a typical efflux system assembly. The basic module will accommodate five individual pressure measurements with common continuous efflux and emergency purge manifold and individual orifices and plenum chambers. Connections on each plenum are avaiable for hooking up transducer and pressure sensing lines. The flow of argon is metered by means of a small (0.005 in. diameter) orifice in the efflux system assembly. Hypodermic needles were found to be the most economical orifice.

In order to avoid cross coupling between channels in the emergency purge manifold, it was necessary to include a check valve in each purge line. Standard tire valves were found to work reliably and are brazed to each of the emergency purge needles.

The module is designed such that it can be easily disassembled for replacement or clean out of components by removing the six assembly bolts.

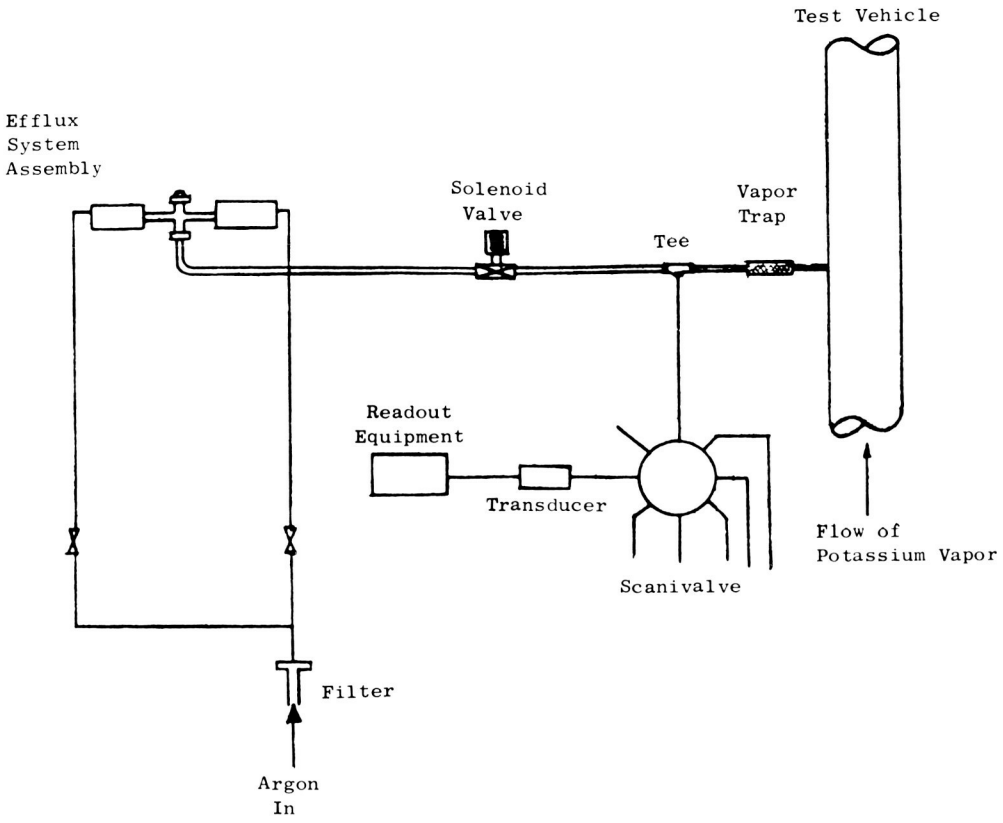


Fig. 1. Schematic Diagram of Efflux Pressure Measuring Device

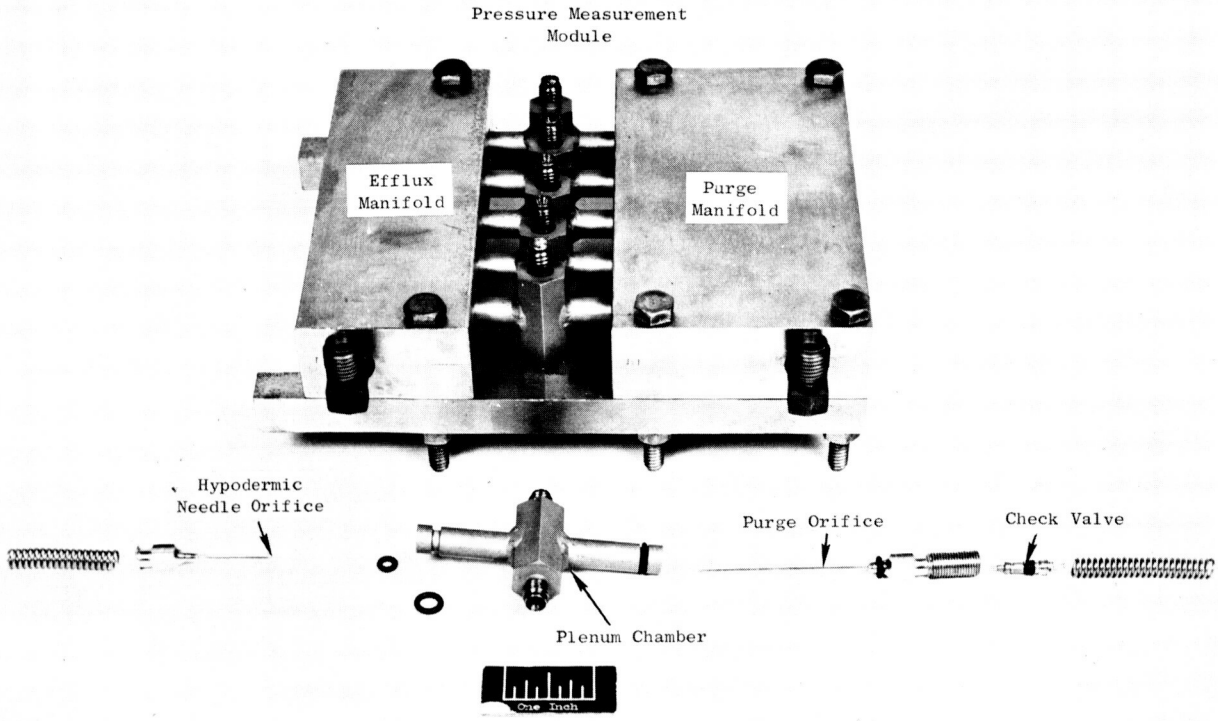


Fig. 2. Efflux System Assembly

A single plenum section disassembled is shown in Figure 2. The continuous efflux hypodermic needle and the emergency purge needle with tire valve are also shown in proper position. The springs indicated at both ends of the photograph are required to couple the section together and position the needles tightly against their seat.

IV. DEVELOPMENT

In the original concept of the efflux pressure measuring device (PMD), it was planned to operate the efflux system with the argon flowing continuously (and, therefore, the solenoid switches were not required). It was realized that for this method of operation there were certain sources of error such as line pressure drop and fluid dynamic effects at the pressure tap, but after some analysis, it was felt that these errors could be determined by calibration.

Tests were conducted to determine the reliability and accuracy of the efflux PMD. One of the developmental tests was the operation of the efflux device in the 50 KW potassium heat transfer facility. The objectives of this test were:

1. To determine whether the efflux device is acceptable from an operational standpoint in a potassium vapor facility.
2. To compare the response and actual values of pressure with those of the limp diaphragm pressure transducer.

Shown in Figure 3 is a schematic diagram of the 50 KW two-phase potassium loop with the efflux system installed. The flow through the loop is by natural convection. The loop consists of a boiler, condenser, dump tank and an argon removal subsystem. The vertical boiler has limp diaphragm gauges at the upper and lower ends. These gauges give the boiling pressure in addition to the liquid level in the boiler.

Shown in Figure 4 is a plot of the efflux pressure readings against those of the adjacent limp diaphragm gauge taken in the 50 KW potassium loop. These data extend over a range of pressures from about 5 to 16 psia. In this pressure range, the deviations of the efflux readings from

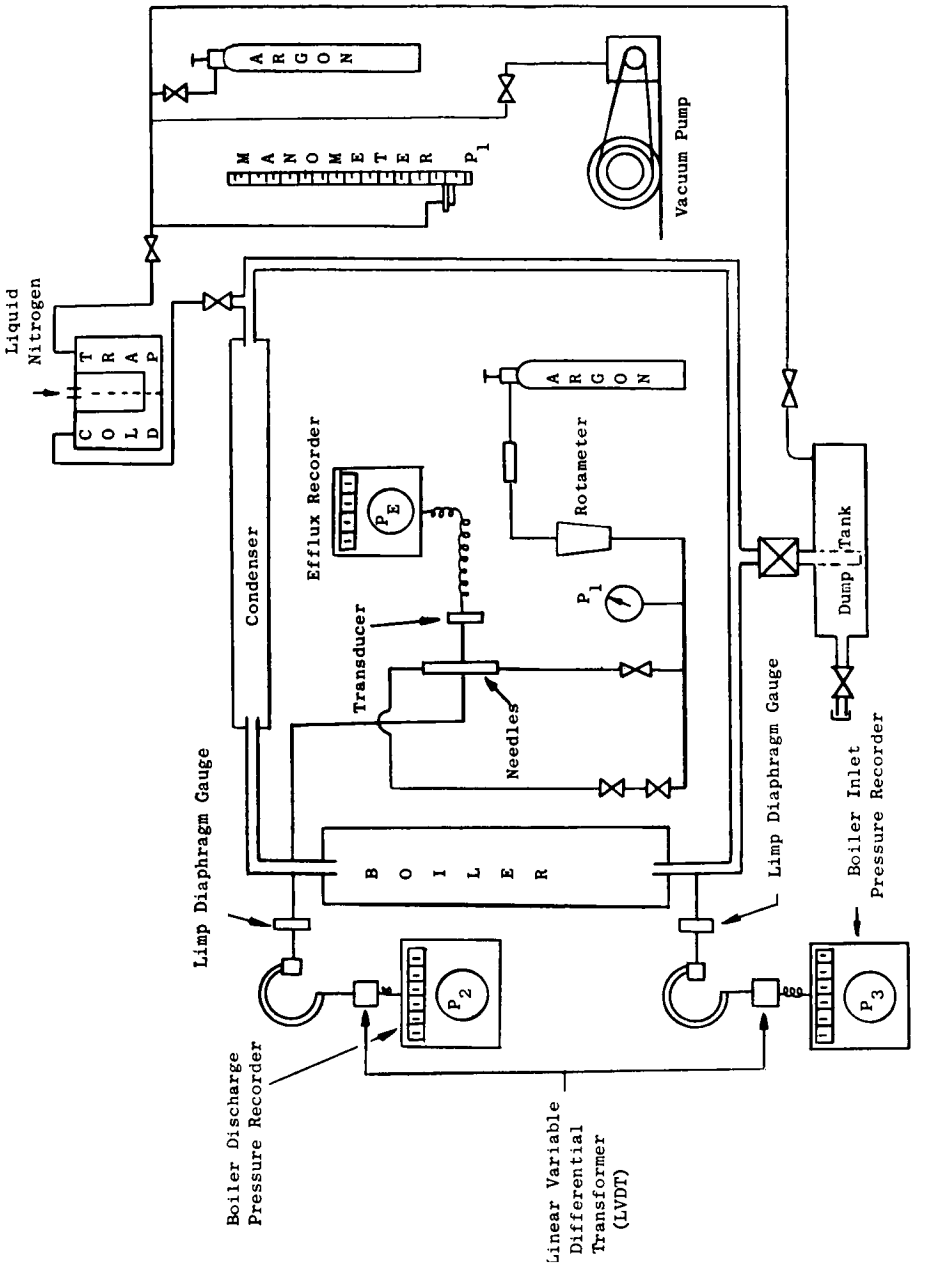


Fig. 3. Schematic of Efflux System Installed in the 50 kW Two-Phase Potassium Loop

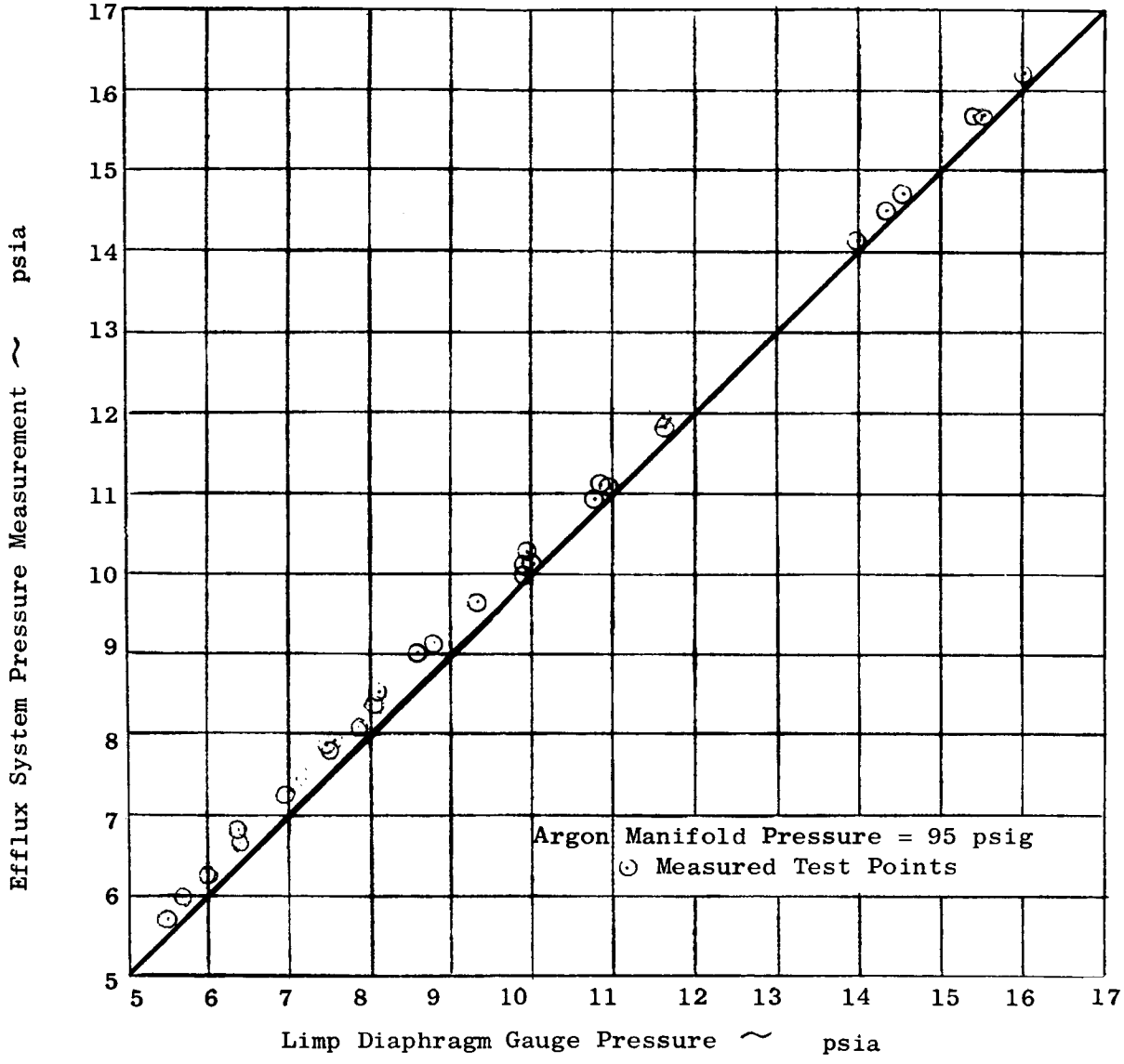


Fig. 4. Efflux Pressure Measurement versus Limp Diaphragm Gauge

the limp diaphragm gauge are in the range of 0.1 to 0.4 psi. The agreement is considered good in consideration of two facts:

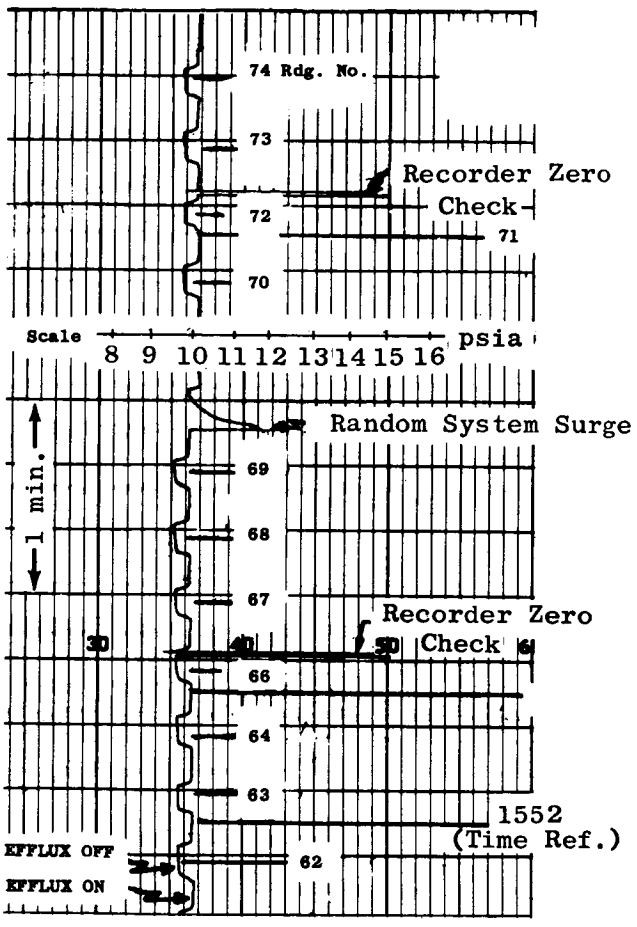
1. The accuracy of the limp diaphragm gauge is about $\pm$ 0.5 psi.
2. Calibrations in steam on the efflux device indicated that over the pressure range of 5 to 16 psia, the deviation of the efflux measurements from the true value are 0.1 to 0.4 psi.

Reference to Figure 4 indicated that the maximum pressure attained in the 50 KW facility was about 16 psia. This pressure corresponded to a vapor temperature of 1400°F, which is the limit of the 50 KW loop. During potassium testing the efflux device would be subjected to a pressure of 37.5 psia, which corresponds to a vapor temperature of 1600°F (Reference 1). During the testing of the flow nozzle in steam, the efflux device was used up to a pressure of 39 psia. Subsequent inspection revealed no moisture had diffused back to the hypodermic needle chambers.

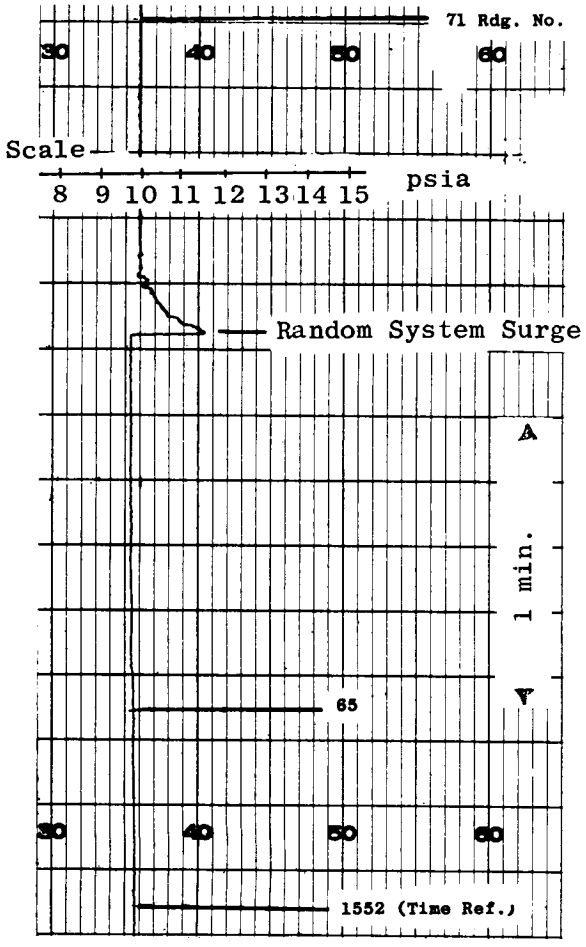
Shown in Figure 5 is a typical time-dependent trace of efflux-system measured pressure during which time the efflux gas flow was periodically shut off 28 times for nine-second intervals. The corresponding limp diaphragm gauge trace is also shown in Figure 5. A random system surge is marked along with the paper position corresponding to numbered readings. The pressure scale is also shown. Unfortunately, the two charts were run at different speeds, making detailed comparisons awkward.

Reference to Figure 5 indicates that the pressure read by the efflux system dropped to the facility pressure when the argon gas was turned off and returned to the original level when turned on. The significant point, however, is that in spite of turning the efflux gas off 28 times, no malfunction of the efflux system occurred.

The test demonstrated that the efflux system is acceptable from an operational standpoint for use with potassium vapor. This is substantiated by the facts that neither artificial surges nor periodically turning off the gas in the efflux system caused plugging of the system. In addition, the test demonstrated that the response of the efflux system is better than that of the limp diaphragm gauge. (Reference 2)



50 kW Boiler Outlet Efflux System Pressure Trace



50 kW Boiler Outlet Limp Diaphragm Gauge Pressure Trace

Figure 5

A converging-diverging flow nozzle was tested prior to the turbine testing to check out the operation of the 3000 KW facility and to obtain some basic data on the expansion of potassium vapor (Reference 3). This converging-diverging nozzle was first calibrated in the Flow Analysis Calibration Test (FACT) stand, to determine the effective flow areas through the nozzle.

During air tests of the converging-diverging nozzle an attempt was made to obtain calibration data for the error in pressure reading, which changes with stream Mach number by taking readings with and without the argon flowing. On the average, this difference resulted in an error of about 2 percent at a Mach number of unity and decreases to zero at vanishing values of Mach number. However, the Mach number effect contained a considerable amount of scatter, indicating that no precise correlation could be made. Therefore, in the interest of removing potentially unknown errors during nozzle testing in potassium, where pressure readings were required to an accuracy of 0.25 psi, it was decided to shut off the argon efflux flow by means of solenoid valves while the readings were taken, thereby eliminating the source of error. The efflux pressure measuring device had been utilized in this manner during tests conducted in the 50 KW loop and no system plugging was experienced. The solenoid valves as well as the scani-valve for each pressure measuring line are controlled by the digital data handling system circuitry so that the transducer is vented to the test vehicle for approximately 4 seconds before the digital data handling system secures a reading.

An efflux solenoid valve control permits the selection of the efflux channels for which the solenoid valves are to be closed. Normally, all solenoid valves are open, permitting argon to flow through the instrument lines into the facility. (The flow rate is about 1.3×10^{-5} lb/sec for each sensor line.) This condition is signalled by a "ready" light. On pushing the "start" button, the selected (or all of the) solenoid valves close, and after a predetermined time interval for pressure stabilization, scanning of the pressure lines commences. Lights signal which of four scanners is being read. After scanning, the solenoids are all opened and an emergency argon purge of about 3.5×10^{-5} lb/sec for each line is actuated for a few seconds to clear the pressure lines of any potassium vapor. Then the device returns to the ready position or normal argon efflux.

Shown in Figure 6 is an interior view of the cabinet which houses the equipment for the efflux system, showing the following equipment:

- 4 pressure scanning modules - upper left and right
- 8 (2 not shown) efflux blocks - back and side walls
- 40 solenoid valves - floor
- reference pressure transducer - center
- argon pressure controller - center

The empty compartment at upper center is for the pressure module control.

The efflux system equipment cabinet is connected to the turbine or nozzle test piece by pressure leads. Cables connect this cabinet to the terminal box at the digital data handling system location. The required sequencing of the various channels is accomplished by making the required connections on programming panels.

The terminal box just described is connected to the digital data handling system. This system is capable of scanning between any two channels from 1 to 600 and recording the results in decimal format with 4 digits on paper tape beside a data channel number and/or recording on punched tape using a 6-character word compatible with IBM and other standard reading devices. When the printer is used the maximum recording rate is 5 bits of data per second. When only the punch is used the recording rate is increased to 9 bits per second. The punched tape includes a 20-character word which can be used for fixed data. The analog-to-digital converter has an accuracy of 0.01 percent and the gain accuracy is 0.02 percent of full scale. The gain can be changed three times per scan and 10-volts, 100-millivolt and 10-millivolt ranges are available.

Four scanner modules are controlled by a matrix from 48 control inputs originating in the digital system. While one scanner is being moved to the next point, the remaining three are in various phases of stabilization which takes two seconds. The scanners are read sequentially at the rate of 1 per second. Each scanner module has its own precision transducer (accurate to 0.1 percent of full scale or 0.1 psi).

During the checkout of the 3000 KW two-phase potassium turbine test facility, some difficulty was encountered with the efflux pressure measuring system. The 1/8-inch O.D. tubes which sense the loop pressure became plugged

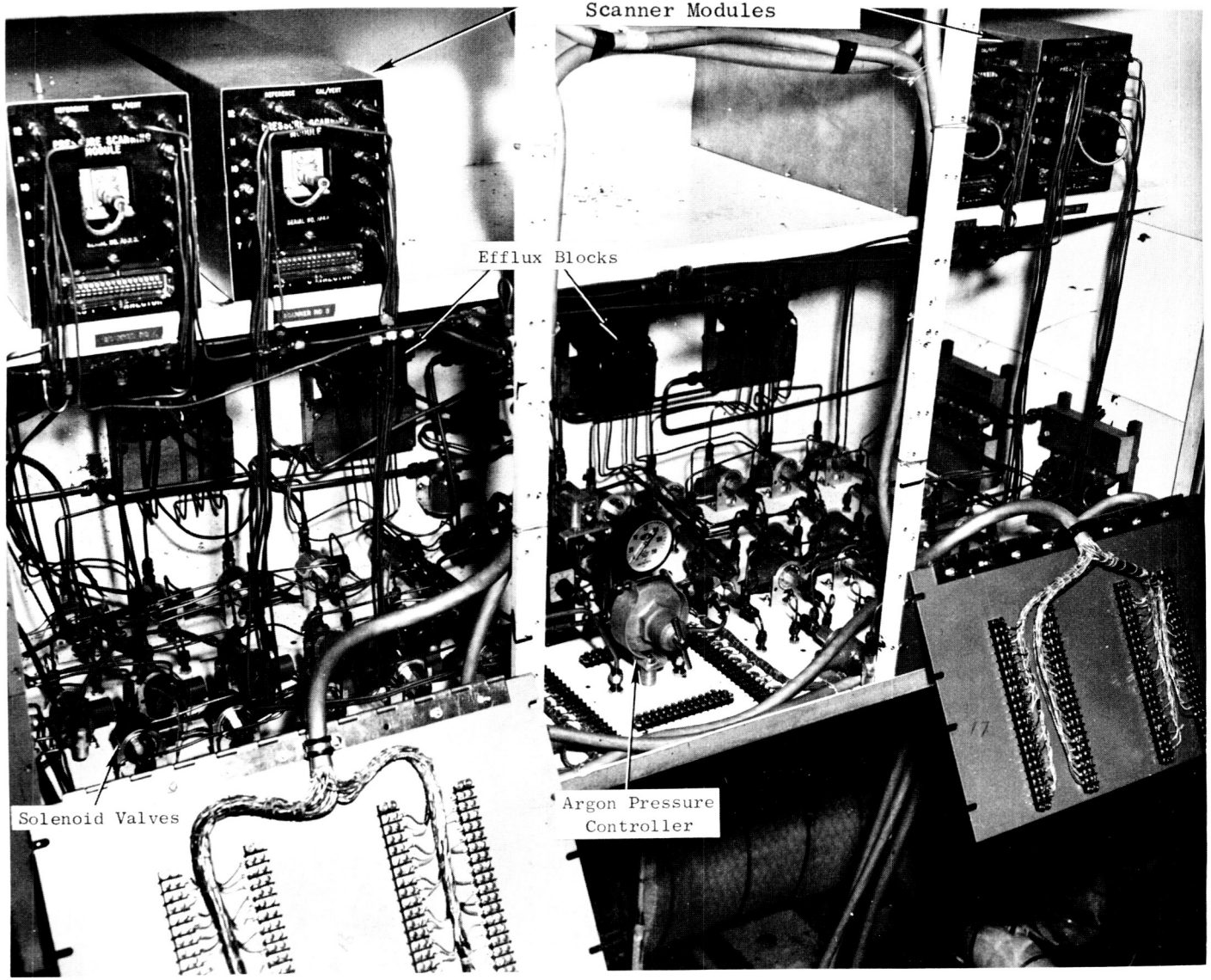


Fig. 6. Efflux System Equipment

several times. Potassium vapor had apparently diffused to the cooler regions of the sensing tubes where it froze. The efflux system was modified to include the installation of vapor traps in eight of the efflux lines. The efflux pressure measuring device with the vapor trap installed is shown schematically in Figure 1.

Figure 7 shows the general construction of the demister trap used in this facility. A thermocouple was attached to the side of the 1.0-inch pipe section and the entire demister capsule and part of the 3/8-inch tube was traced with heating wire. In operation, the demister capsule was heated to 200-300°F, and held at that temperature. The theory of operation is that as the potassium vapor tends to back diffuse or migrate into the cold efflux line, it will condense on the extensive surface of the wire demister. At 200°F, the potassium remains liquid, and as the liquid accumulates, it will eventually drain back into the potassium loop. Drainage is aided by the constant inflow of argon into the top of the demister capsules and gravity.

During the facility checkout, nearly all efflux pressure lines without demisters in the line plugged repeatedly. The 8 efflux pressure taps that contained demisters remained open during this test. Consequently, demister traps were installed in all efflux lines. All efflux lines were changed to 3/8-inch O.D. x 0.125 wall tubing in the hot region instead of 1/8-inch O.D. x 0.030 wall tubing. All efflux tube connections were made by welding instead of brazing. Figure 8 shows the installation of the demister capsules on the potassium turbine. In subsequent test runs (boiling between 1450°F - 1580°F for a period of 75 hours), only one sensor line out of 36 plugged.

In conjunction with the use of these traps, the efflux control system was modified to shut off the argon flow to each of the sensing lines sequentially, as the pressures are scanned. Since the settling time of the pressure measuring device has been established as approximately 1.5 seconds, the argon flow is shut off for four seconds prior to reading the pressure. Thus, each sensing line is open directly to the potassium environment for a shorter period of time, although enough time is allowed for adequate pressure stabilization during scanning.

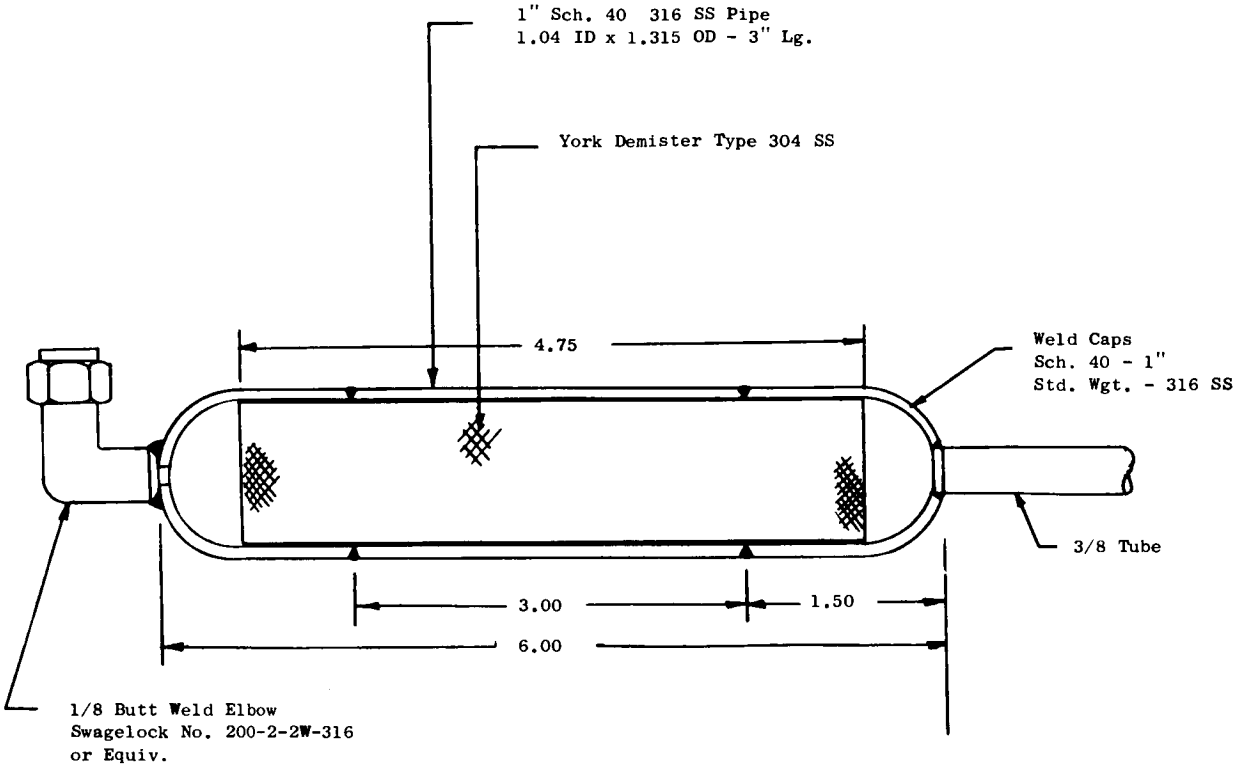


Fig. 7. Efflux Vapor Trap

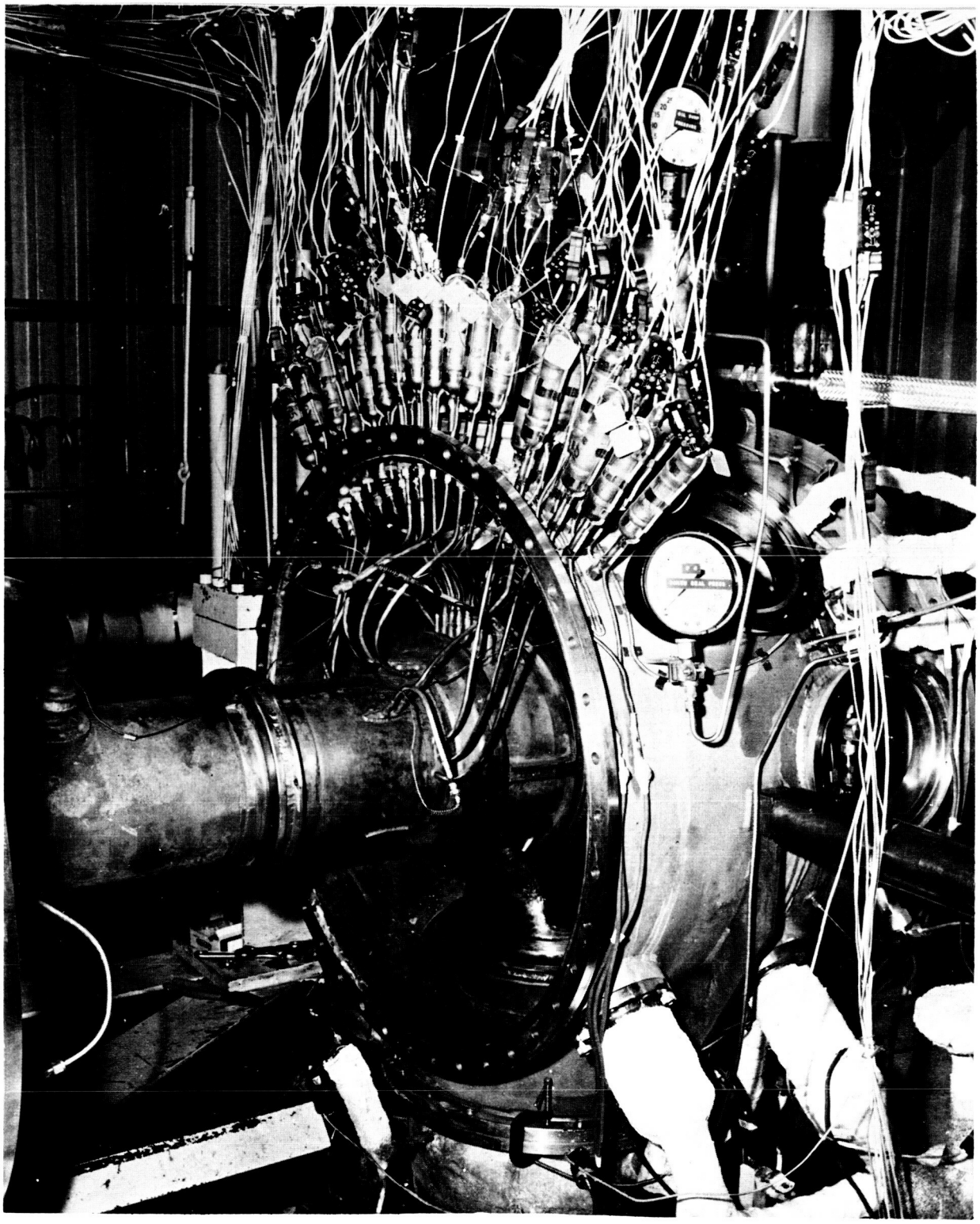


Fig. 8. Installation of the Demister Capsules on the Potassium Turbine

V. EVALUATION

A. POTASSIUM TURBINE TESTING - PRESSURE MEASUREMENTS

Shown in Figure 9 is a schematic diagram of the test turbine performance instrumentation stations. For overall performance, the primary stations are 1, 3, 7 and 8. Stations 4, 5 and 6 in the figure are internal to the turbine and provide information useful in finding load distribution and stage reaction. Shown in Figures 10 and 11 are schematic diagrams showing the location and number of sensors in each of the instrumentation stations. There are temperature measurements and total and static pressure measurements at stations 1, 3, 7 and 8, but only static pressure measurements at stations 4, 5 and 6.

Pressure measurements affect the turbine efficiency calculation because the measured pressures are used to calculate the ideal enthalpy change which is the basis for turbine efficiency. A measurement error of 1 psi out of 20 psia at the turbine inlet will cause an error of 5 percent ideal enthalpy change and efficiency. An error of 1 psi out of 7 psia at the turbine exit will cause an error of 10 percent in turbine efficiency. Thus, calculated efficiency is very sensitive to pressure measurement errors, particularly at the turbine exit.

Before each period of performance testing, the efflux pressure measuring system was calibrated over a range of 0 to 50 psia, by pressurizing the loop with argon, with repeatability and accuracy of better than 1/2 percent being obtained.

Pressure measurements taken during performance testing of the potassium vapor turbine have been plotted against the vapor pressures corresponding to the measured temperatures to determine how well the efflux system worked. Shown in Figure 12a (inlet temperature, 1550°F) and 12b (inlet temperature 1450°F) is a comparison of measured pressure and temperature at station 1, upstream of the turbine. On the abscissa is the vapor pressure of potassium at the measured temperature. The good correlation lends credence to the measurements. The correlation is not quite as good at station 3, the turbine inlet, shown in Figure 13a (inlet temperature, 1550°F) and 13b (inlet temperature, 1450°F). The 1.0 psi deviation of the measured pressure from the vapor pressure corresponds to 7.5 to 11°F temperature error. (The thermocouple

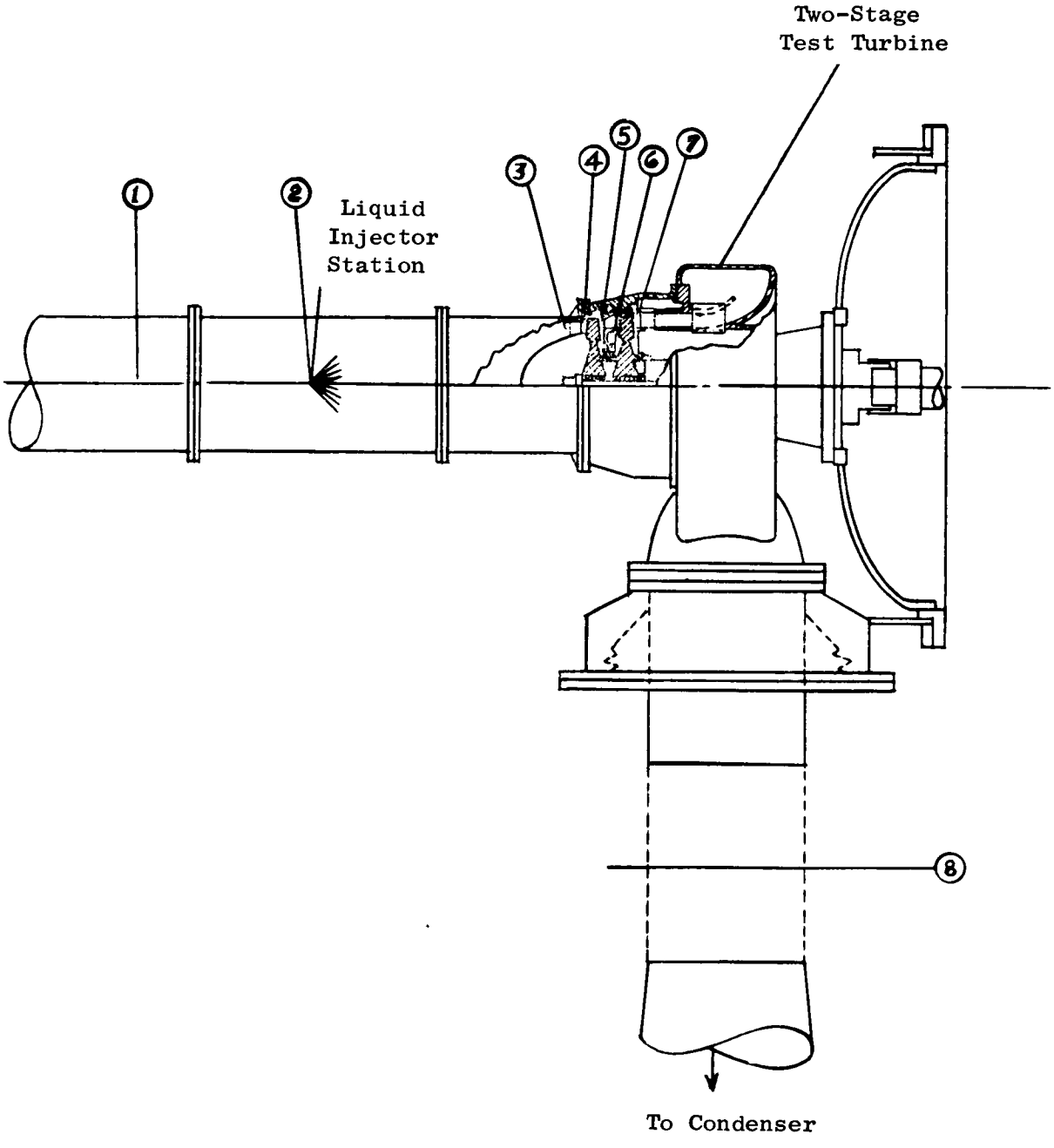


Fig. 9. Instrumentation Stations

Note: All total pressure and total temperature sensors arranged in equal area annuli.

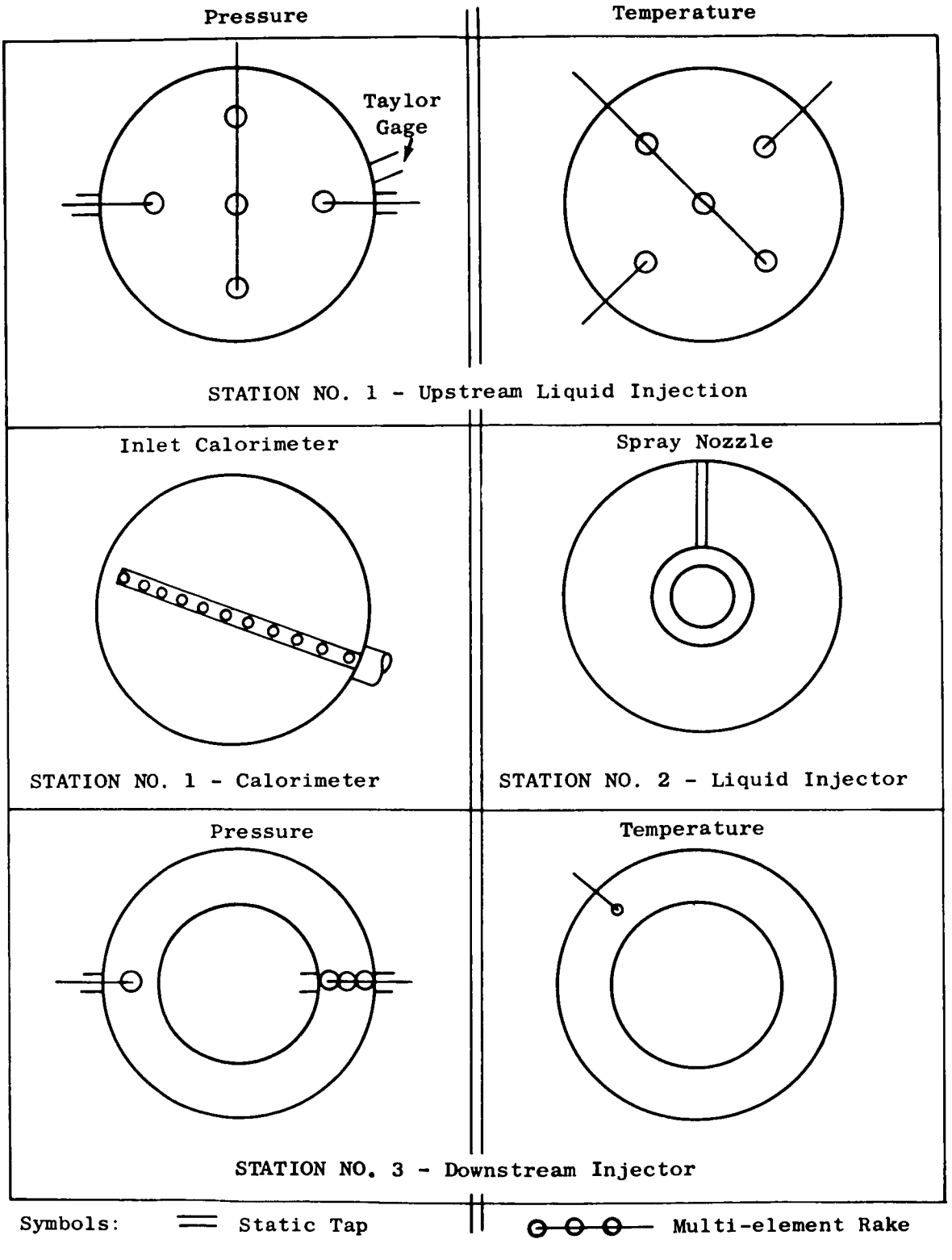


Fig. 10. Potassium Test Turbine Instrumentation Location

Note: All total pressure and total temperature sensors arranged in equal area annuli.

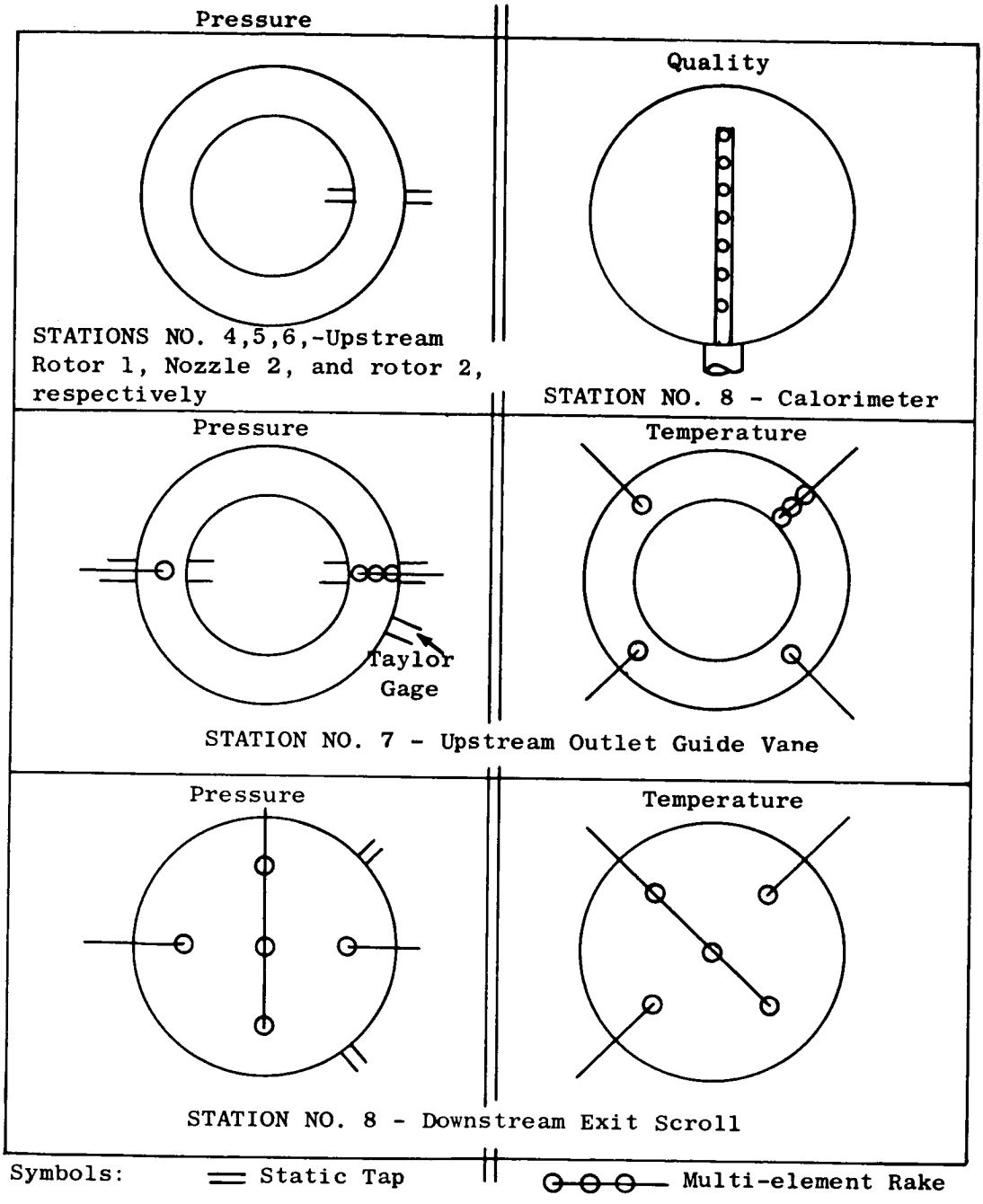


Fig. 11. Potassium Test Turbine Instrumentation Location

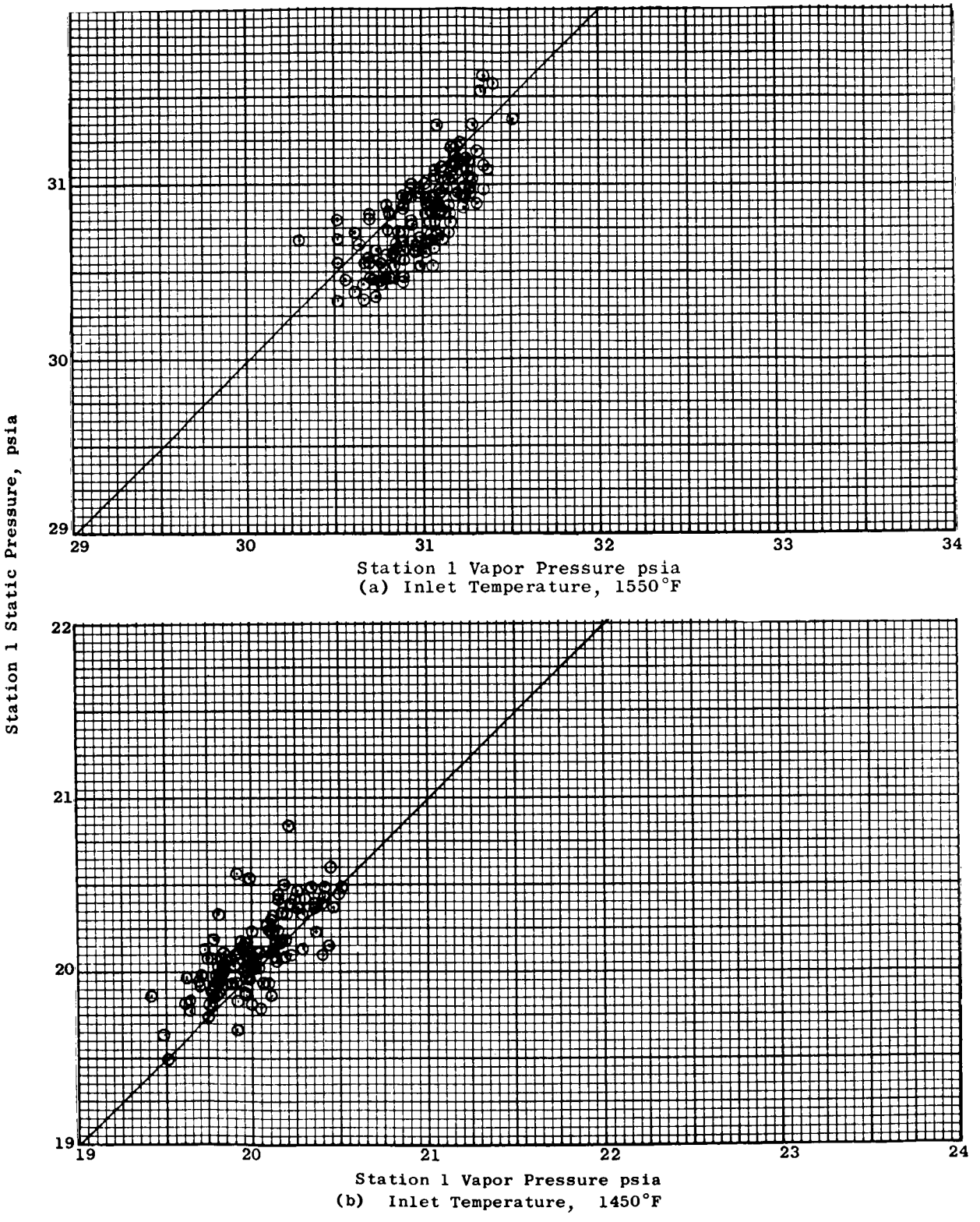


Fig. 12. Comparison of Measured Pressure with Vapor Pressure at Station 1

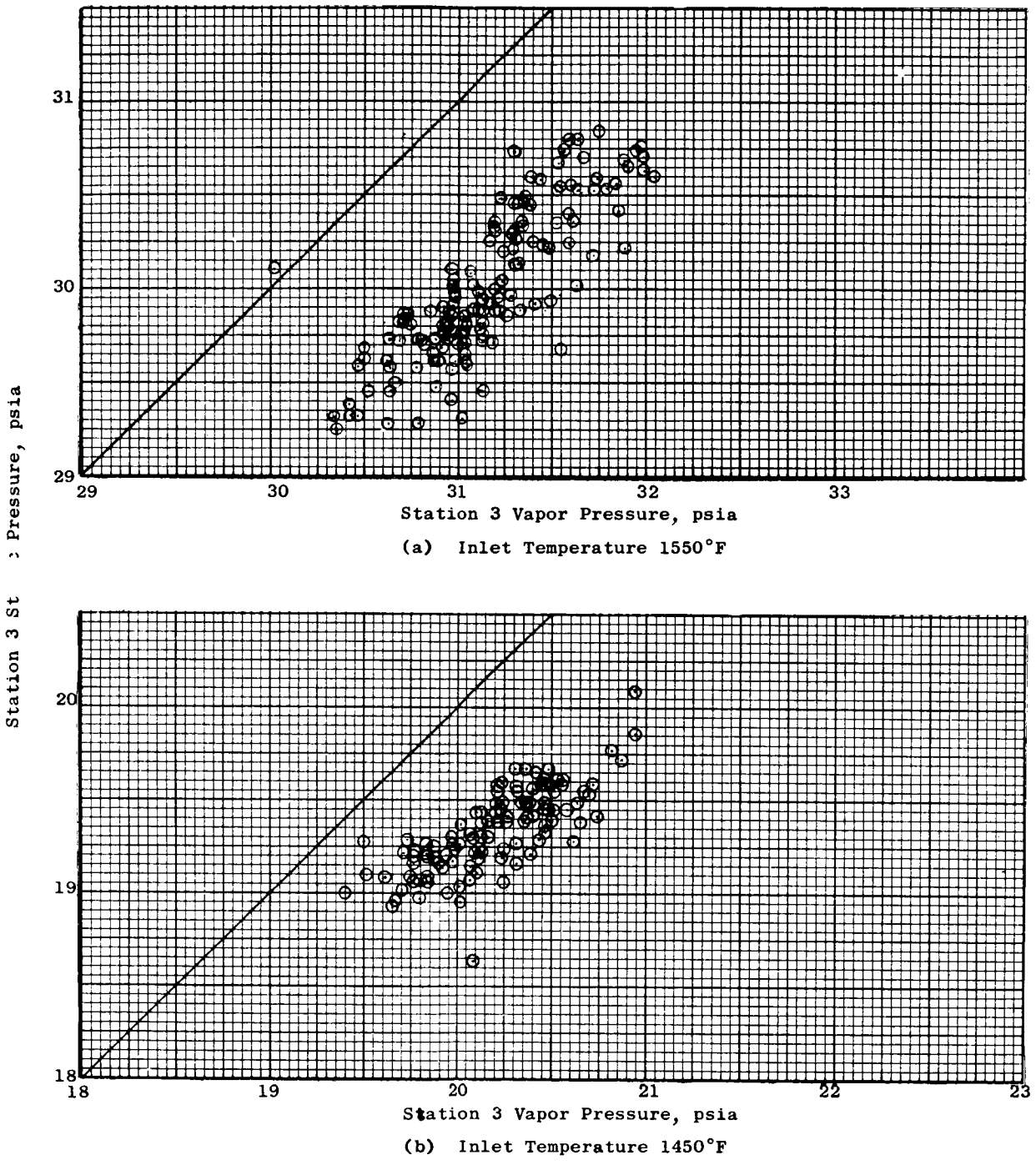


Fig. 13. Comparison of Measured Pressure with Vapor Pressure at Turbine Inlet

accuracy is ± 3/4 percent or about 11°.) The error could be in the pressure measuring device; however, since it is calibrated immediately before the test whereas the thermocouples are calibrated at much longer intervals, it is more likely that it is a thermocouple error. The four static pressure measurements had a maximum spread of 0.4 psi and usually less. There was only one thermocouple at station 3 and it indicated virtually the same temperature as at station 1. However, since the flow area is smaller at station 3 than at station 1, a higher velocity, 400 ft/sec vs. 100 ft/sec at station 1, and lower temperature would be expected at station 3. Therefore, the pressure measurement appears to be more reliable.

Shown in Figure 14 is a comparison of measured total pressure with the vapor pressure corresponding to the measured temperature. The correlation is much better than it was for static pressure, indicating that the thermocouple may be reading closer to a total temperature. It also seems possible that what appears to be scatter in the pressure measurements is at least partially attributable to other factors such as velocity. For instance, the difference between measured total and static pressure was used to calculate the vapor flow rate through the turbine with good results, as discussed later in this paper. The velocity head is about 0.75 psi for a velocity of 400 ft/sec.

For comparison, the static pressures at station 1, measured with a limp diaphragm gauge, are shown in Figure 15. The limp diaphragm pressure measurements seem to have a little less scatter than the efflux measurements, although the correlation with vapor pressure is not as good at 1450°F inlet temperature.

Shown in Figure 16 is a pressure-temperature comparison at station 7, the turbine exit station. At the higher pressures shown, the correspondence between the measured pressures and the saturated vapor pressure is quite good. As lower pressures are approached, however, the discrepancy between the two pressures increased. One explanation is that the efflux system is measuring the aggregate of the potassium and argon partial pressures while the thermocouple is measuring a temperature corresponding to the partial pressure of the potassium. This, however, is contravened in Figure 17 where the measured pressure at the station downstream of the turbine exit is plotted against the vapor pressure corresponding to the temperature at the

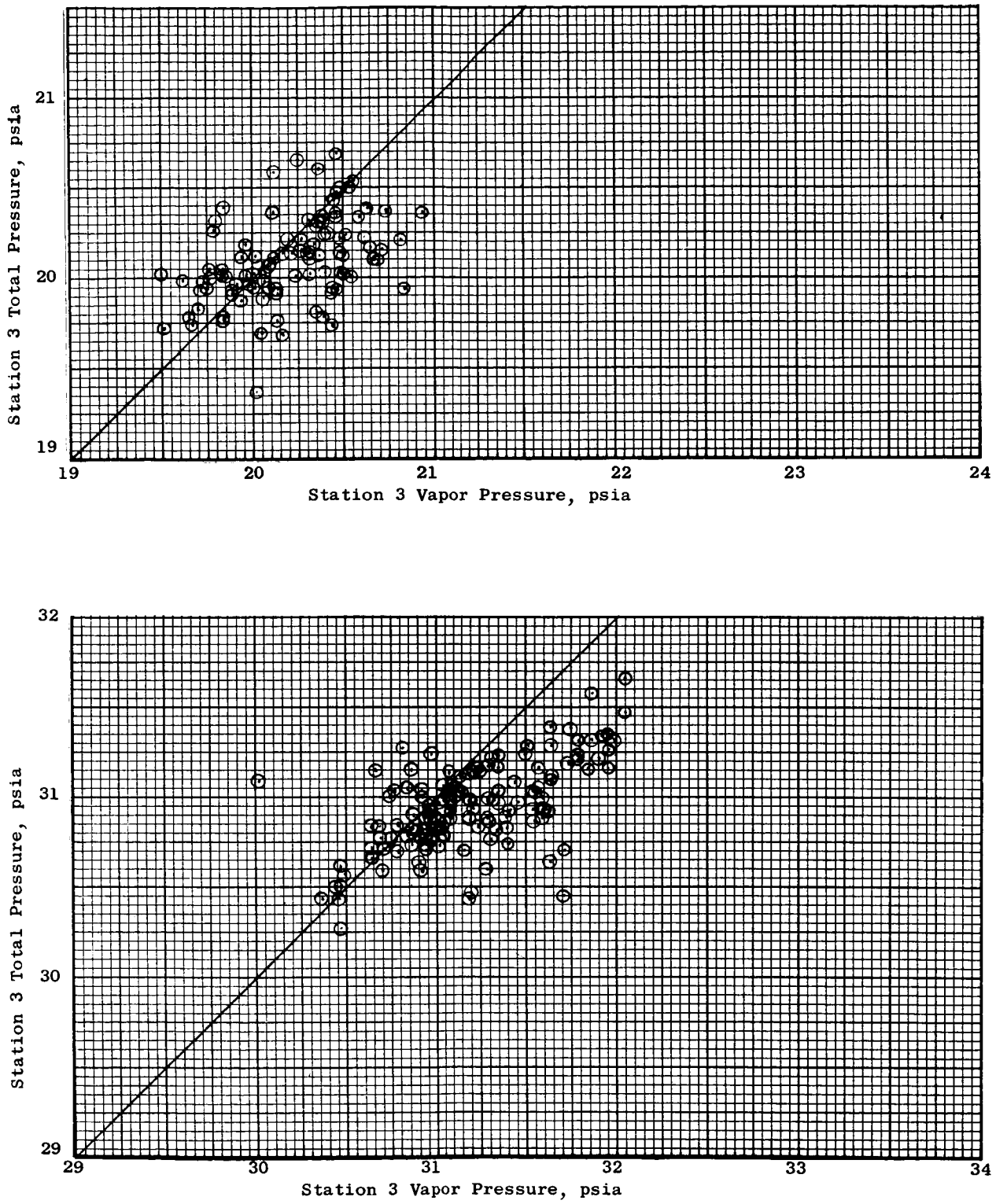
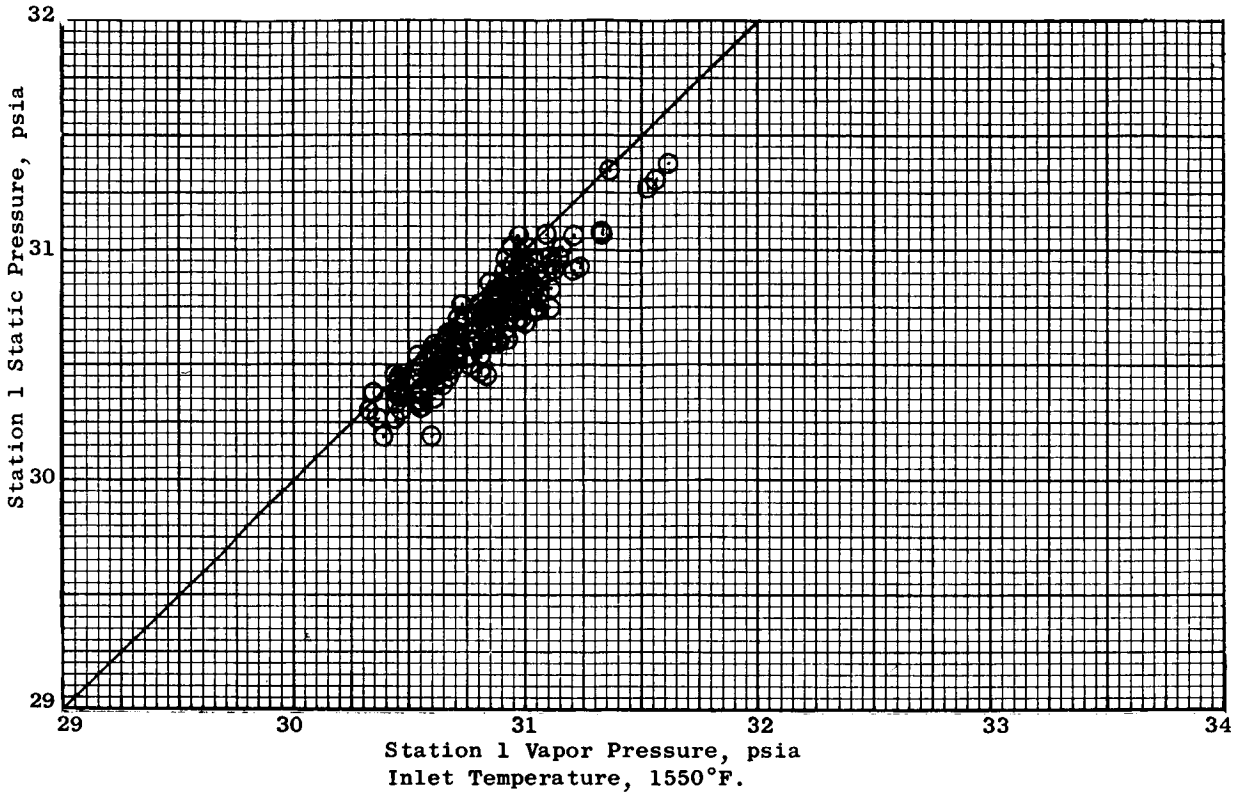


Fig. 14. Comparison of Measured Total Pressure with Vapor Pressure at Turbine Inlet



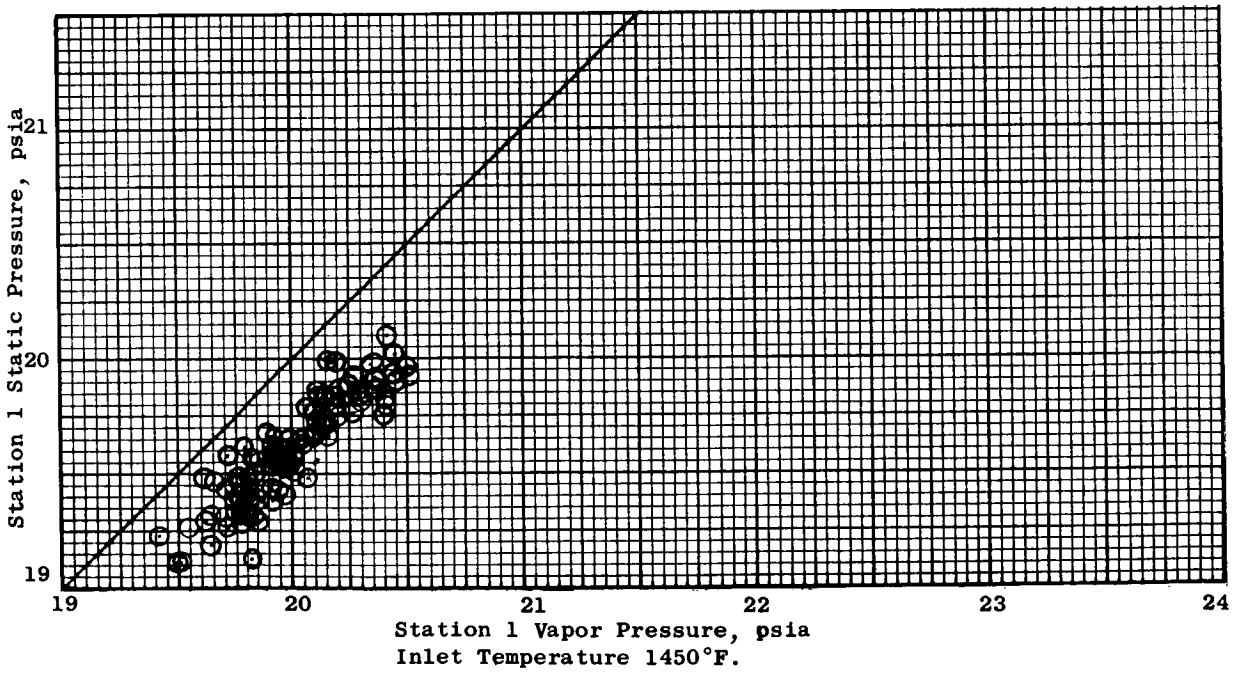


Fig. 15. Comparison of Limp Diaphragm Gauge Pressure with Vapor Pressure Upstream of Turbine

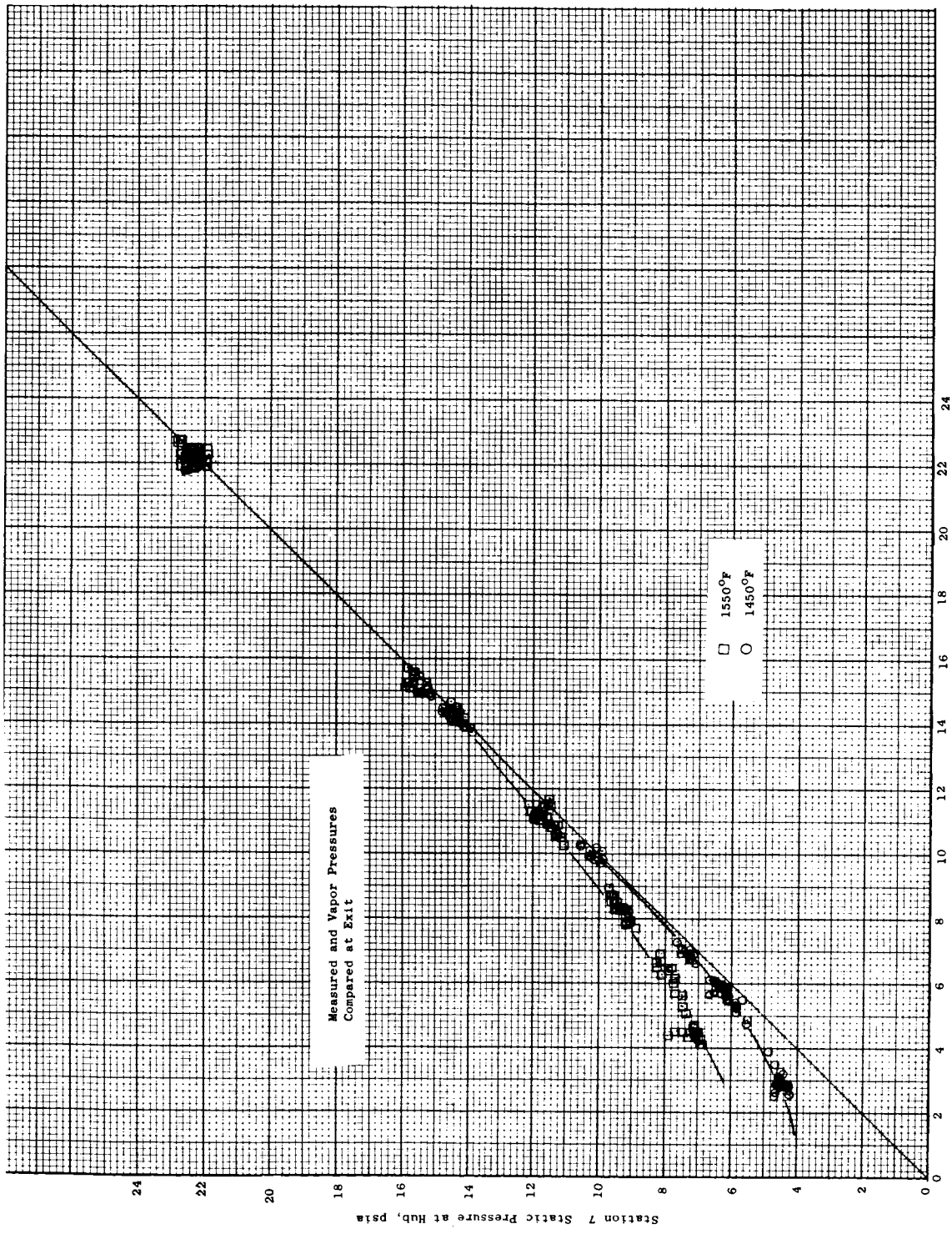


Fig. 16. Comparison of Measured Pressure with Vapor Pressure at Turbine Exit

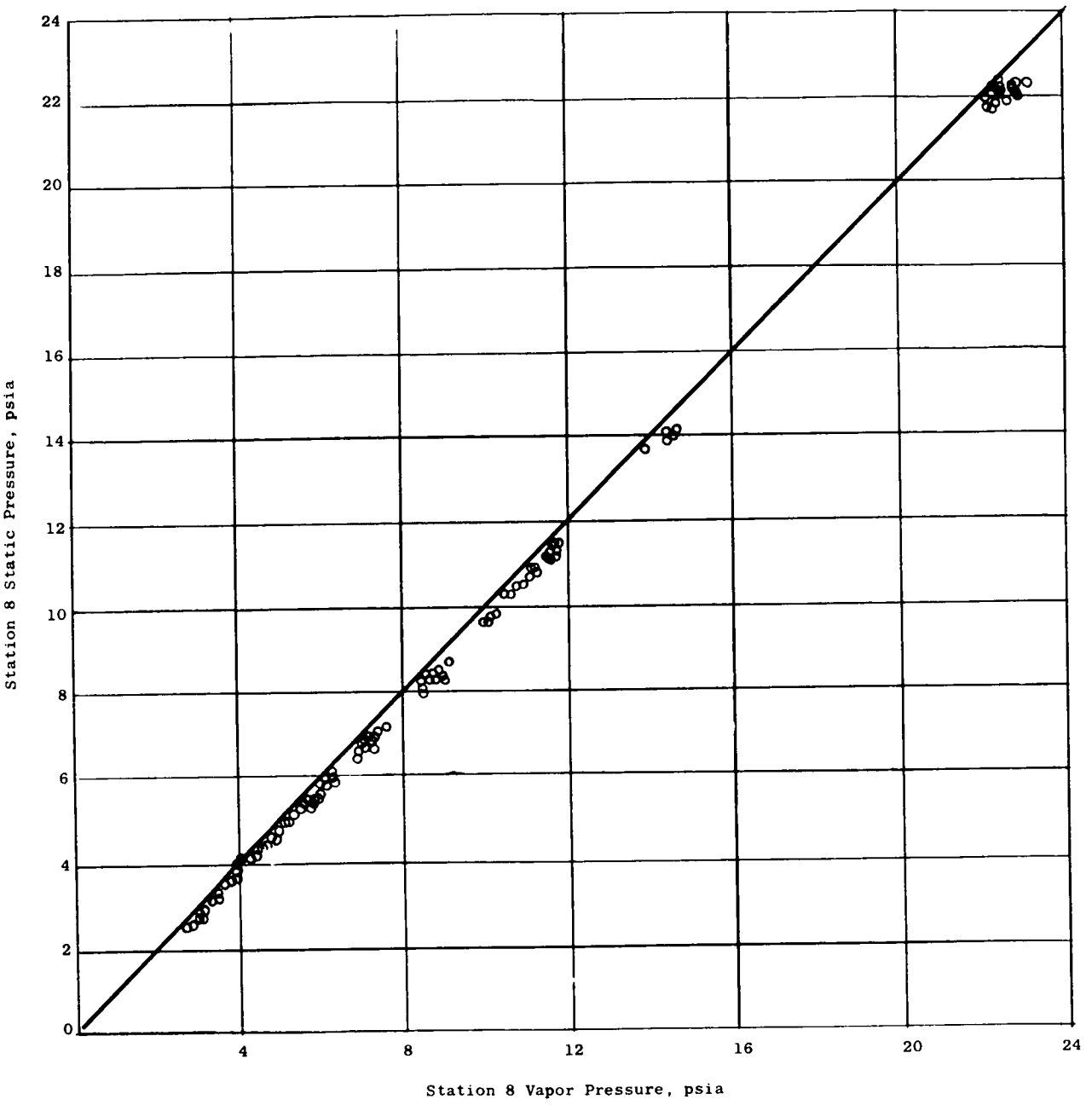


Fig. 17. Comparison of Measured Pressure with Vapor Pressure Downstream of the Turbine

same place. However, the amount of argon at this station is even greater than at the turbine exit station. Therefore, it may be concluded that the presence of the argon is not affecting the reading at the turbine exit station.

A second possible explanation of Figure 16 is that some degree of supersaturation exists at the turbine exit station. However, this possibility has not been fully evaluated. No positive conclusions concerning the flow conditions can be made at this time.

Shown in Figure 18 is a typical plot of interstage static pressures. The symbols denote test measurements and the lines show the predicted pressure levels. Although there are some deviations, the overall conclusion is that the efflux system gave very satisfactory pressure measurements.

B. VAPOR FLOW RATE MEASUREMENT

Originally, the turbine flow rate was determined by measuring the liquid flow rate out of the condenser with an electromagnetic flowmeter. The liquid flow rate and vapor flow rate through the turbine are equal only when the condenser liquid level is constant and there is no change in loop inventory. It was very difficult to maintain a constant liquid level in the condenser because the liquid surface was large (1600 sq.in.) compared to the flow area through the (1 in. diameter) flowmeter. A small change in condenser liquid level results in a large change in EMFM reading. The result was sizeable flow measurement errors. Consequently, the instrumentation in the annulus immediately upstream of the turbine inlet, which was used successfully to sense velocity transients during early performance testing, was utilized to measure steady state flow rate during performance testing. A calibration test in air was made of the inlet annulus instrumentation in the Flow Analysis Calibration Test (FACT) stand. The inlet annulus and the first stage nozzle diaphragm were used for this calibration test.

The objective of the calibration test was to experimentally calibrate the two-stage turbine inlet annulus instrumentation in air so that it could be used as the primary flow measurement device during turbine potassium vapor performance testing. Shown in Figure 19 is the test equipment, which

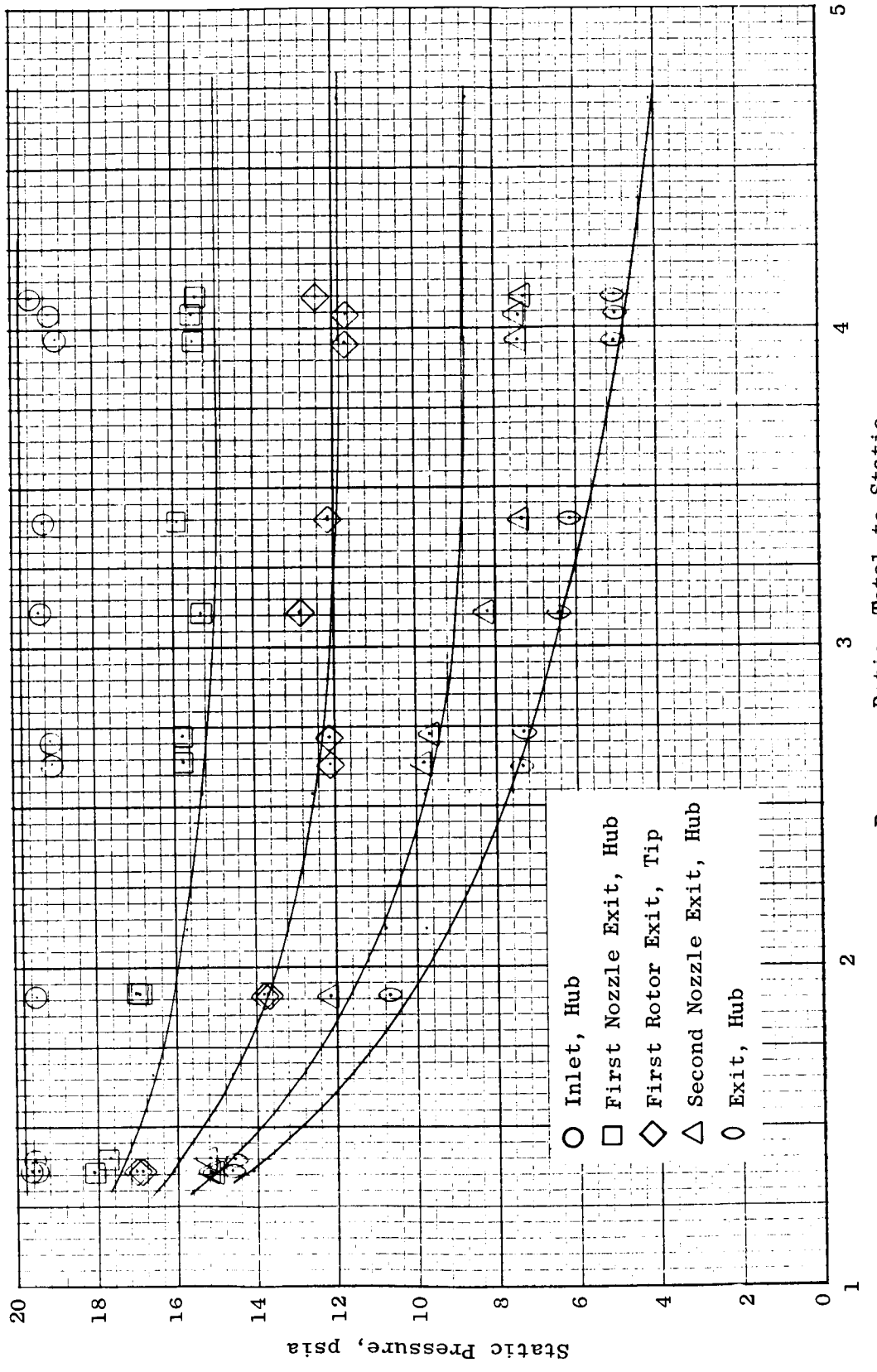


Fig. 18. Comparison of Measured and Calculated Pressure Profile. Turbine Inlet Temperature, 1450°F; Speed, 20,000 rpm.

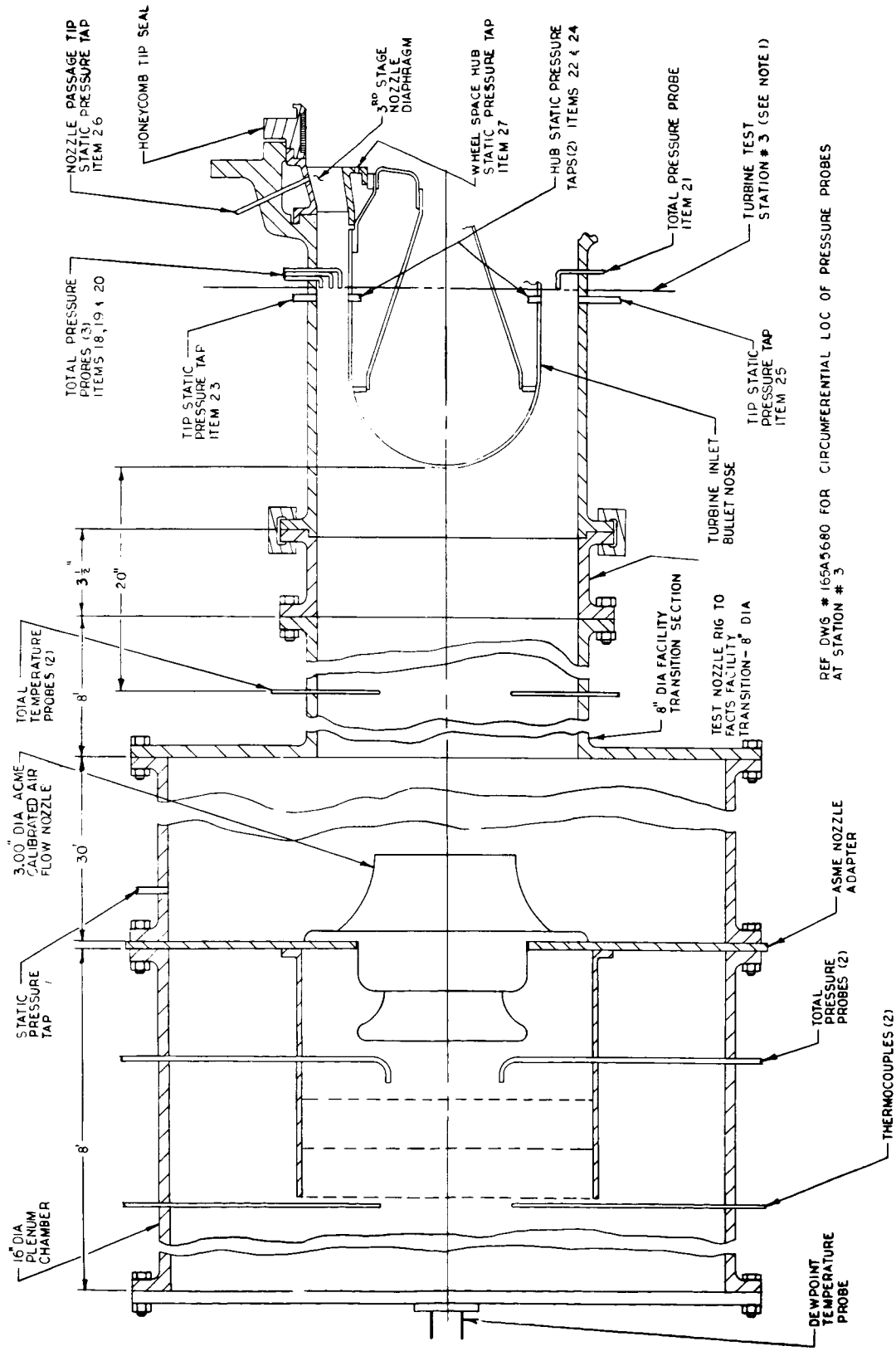


Fig. 19. Bullet Nose Annulus Air Calibration Test Rig Schematic

is comprised of the turbine inlet annulus, the first-stage nozzle diaphragm and the first-stage tip seal installed in the FACT stand, schematically presented. Upstream of the bullet nose, there is a calibrated ASME flow nozzle followed by a constant-area flow duct connected to the bullet nose annulus. The instrumentation stations are also shown in the figure.

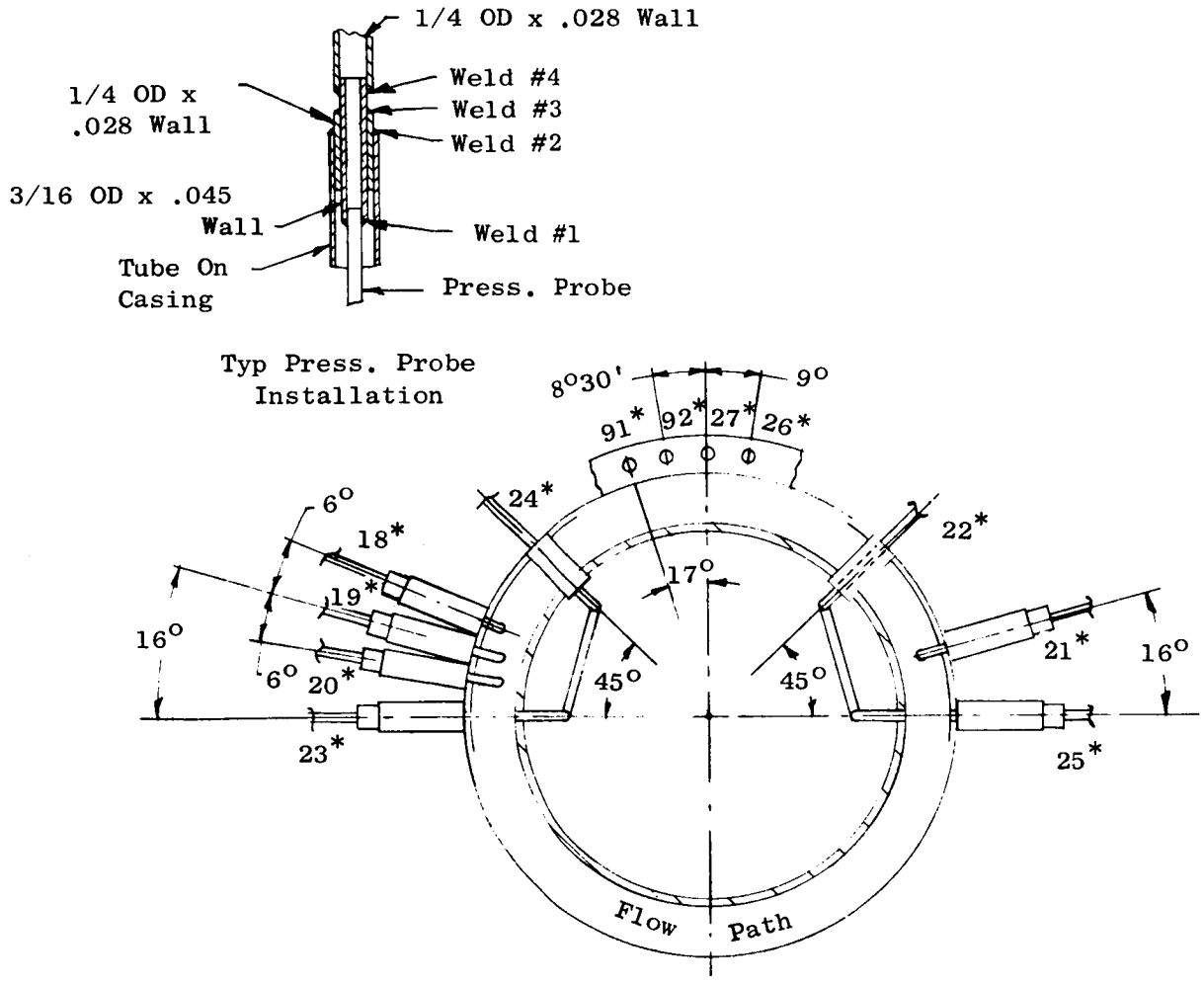
Shown in Figure 20 are the locations of the inlet annulus instrumentation (Station Number 3). This instrumentation consists of four total pressure probes and four static pressure taps. Three of the total pressure probes are located at the mid-point of three equal annulus area sections with an additional total pressure probe located 109 degrees away at the mid-point of the annular flow area. The static pressure taps include two pairs of hub and tip taps located 180 degrees apart. During the calibration testing, each total pressure was recorded along with three total to static differential pressure combinations. These pressure differential measurements were measured using differential pressure transducers connected between the desired taps.

In the constant area duct, preceding the inlet annulus and the first-stage nozzle diaphragm assembly, there were two total temperature thermocouples located approximately 20 inches upstream of the bullet nose as shown in Figure 19. Two static pressure taps are located in the pipe wall at the ASME nozzle exit which, along with two total pressure and two total temperature probes located upstream of the ASME nozzle, enable the flow to be determined.

In Figure 21, the inlet annulus flow coefficients are presented as a function of Reynolds number. These flow coefficients represent the ratio of the experimentally determined effective flow area in air to the actual inlet annulus area. The data presented is the average of six data scans at each nominal condition.

Using methods of compressible flow analysis, the following equation can be derived for the mass flow through the inlet annulus. (Reference 4).

$$W = C_f A_3 \sqrt{2g \frac{(P_{t3}-P_{s3})}{v_{t3}}} \sqrt{\frac{\gamma}{\gamma-1} \left[\frac{(P_{s3}/P_{t3})^{\frac{2}{\gamma}} - (P_{s3}/P_{t3})^{\frac{\gamma+1}{\gamma}}}{1 - (P_{s3}/P_{t3})} \right]} \quad (1)$$



All Nos. Marked * Refer to Item Nos. of Potassium Turbine Test Plan Rev #1 Dated 4-20-64

REF SK56131-475G1

Turbine Test Sta. #3

Fig. 20. First Stage Nozzle Diaphragm Inlet Instrumentation

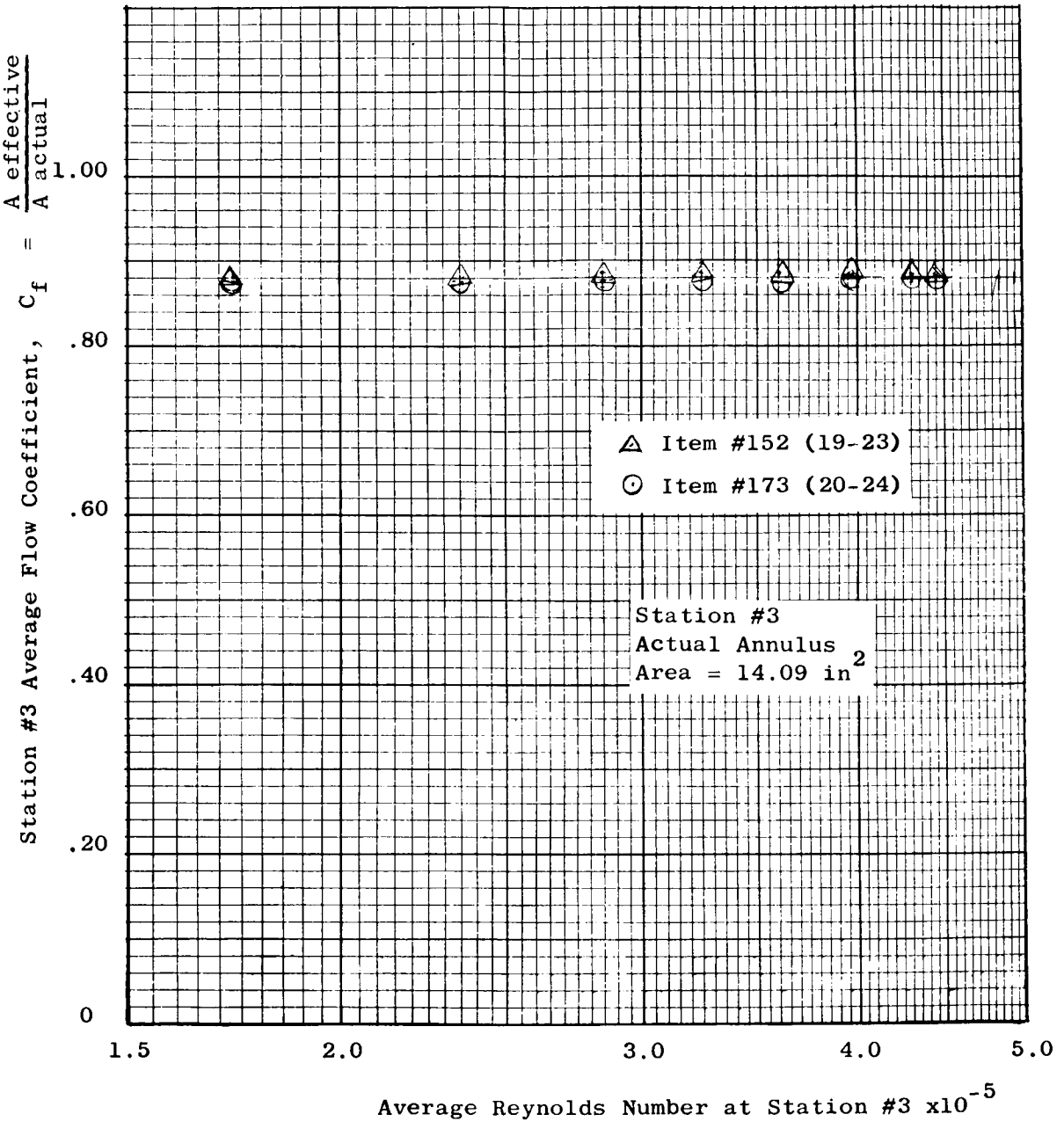


Fig. 21. Calibration Curve for Bullet Nose Annulus Flow Measurement

The experimental flow coefficient, C_f, was obtained by solving for this quantity in Equation (1). The Reynolds number was calculated as follows:

$$(Re)_3 = \frac{V_3}{v_{t3}} \frac{D_h}{\mu_{t3}} = \frac{D_h}{\mu_{t3}} \sqrt{\frac{2g\,(P_{t3}-P_{s3})}{v_{t3}}} \sqrt{\frac{\gamma}{\gamma-1}\left[\frac{1-(P_{s3}/P_{t3})^{\frac{\gamma-1}{\gamma}}}{1-(P_{s3}/P_{t3})}\right]} \quad (2)$$

and as Equation (2) indicated, it is based upon total conditions at station number 3. Potassium properties were taken from Reference 1.

Shown in Figure 22 are typical plots of turbine flow rate calculated from test data using the method described above. The symbols denote test points and the lines designate calculated performance. The good agreement of test data with calculated flow rate indicates that the inlet annulus flow measurement system using efflux pressure measurements is reliable, consistent, and accurate. For comparison the flow rates measured simultaneously with the electromagnetic flowmeter are shown in Figure 23. The flowmeter measures the liquid potassium flow rate out of the condenser, and the large variation is attributed to the fact that the condenser liquid level was not held constant. The conclusion is that the inlet annulus differential pressure measurements obtained with the efflux system yield flow rates which have less scatter than those from the electromagnetic flowmeter and are at levels which are in good agreement with the predicted flow rates.

As an indication of the type of data obtained from the performance test, the variation of turbine efficiency with pressure ratio is shown in Figure 24 for one rotative speed. Efficiency is the ratio of actual to ideal enthalpy change, therefore, the numerator is the measured power divided by the measured flow rate and the denominator is the ideal enthalpy change for the measured pressure ratio. The data were repeatable and in excellent agreement with performance predicted prior to the test.

VI. CONCLUDING REMARKS

The pressure measuring system described in this paper has been developed and successfully used in over 125 hours of potassium vapor testing. The performance of the efflux system compared favorably with that of the limp

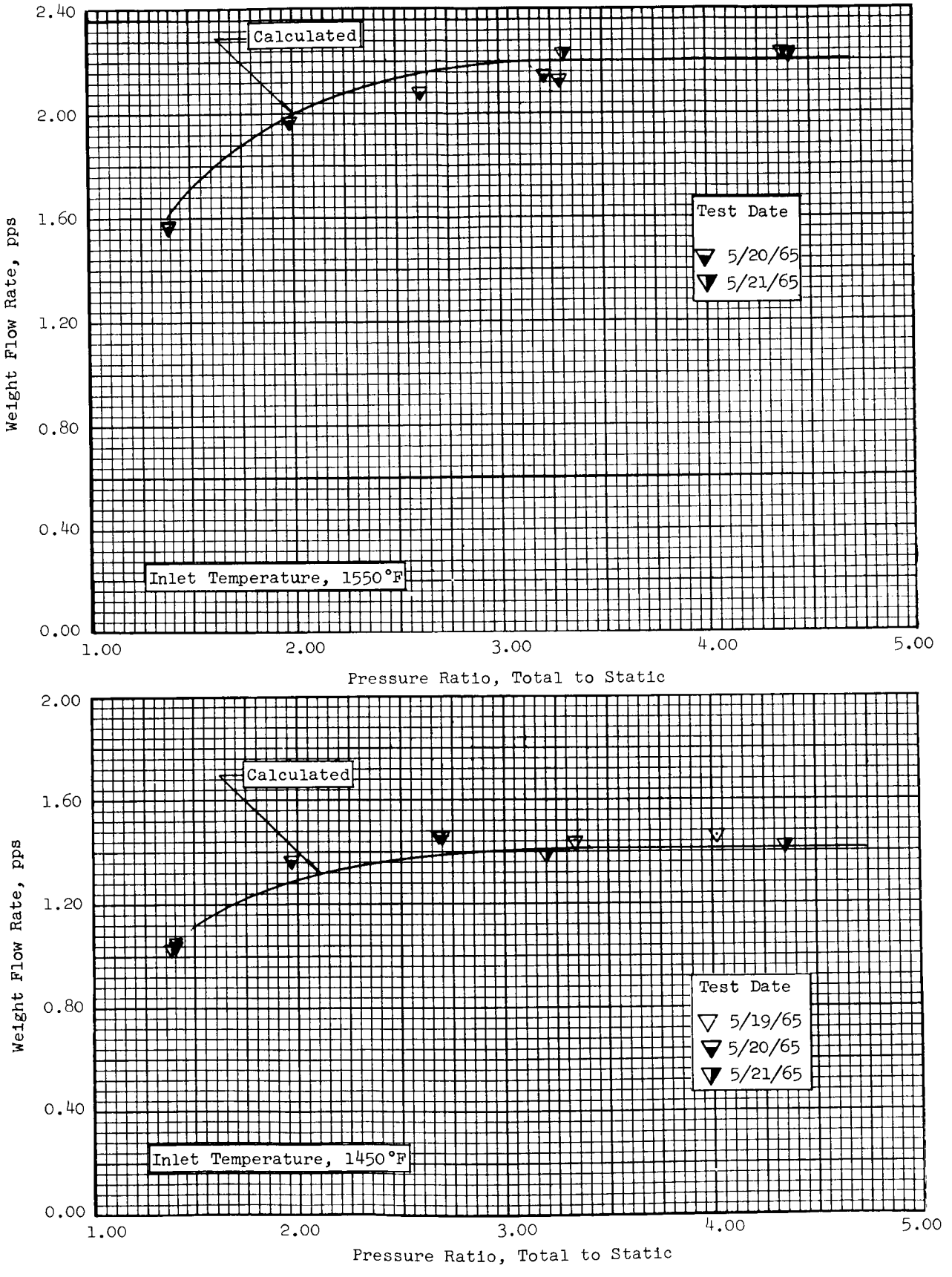


Fig. 22. Comparison of Measured and Calculated Weight Flow Rate. Speed, 19,300 rpm.

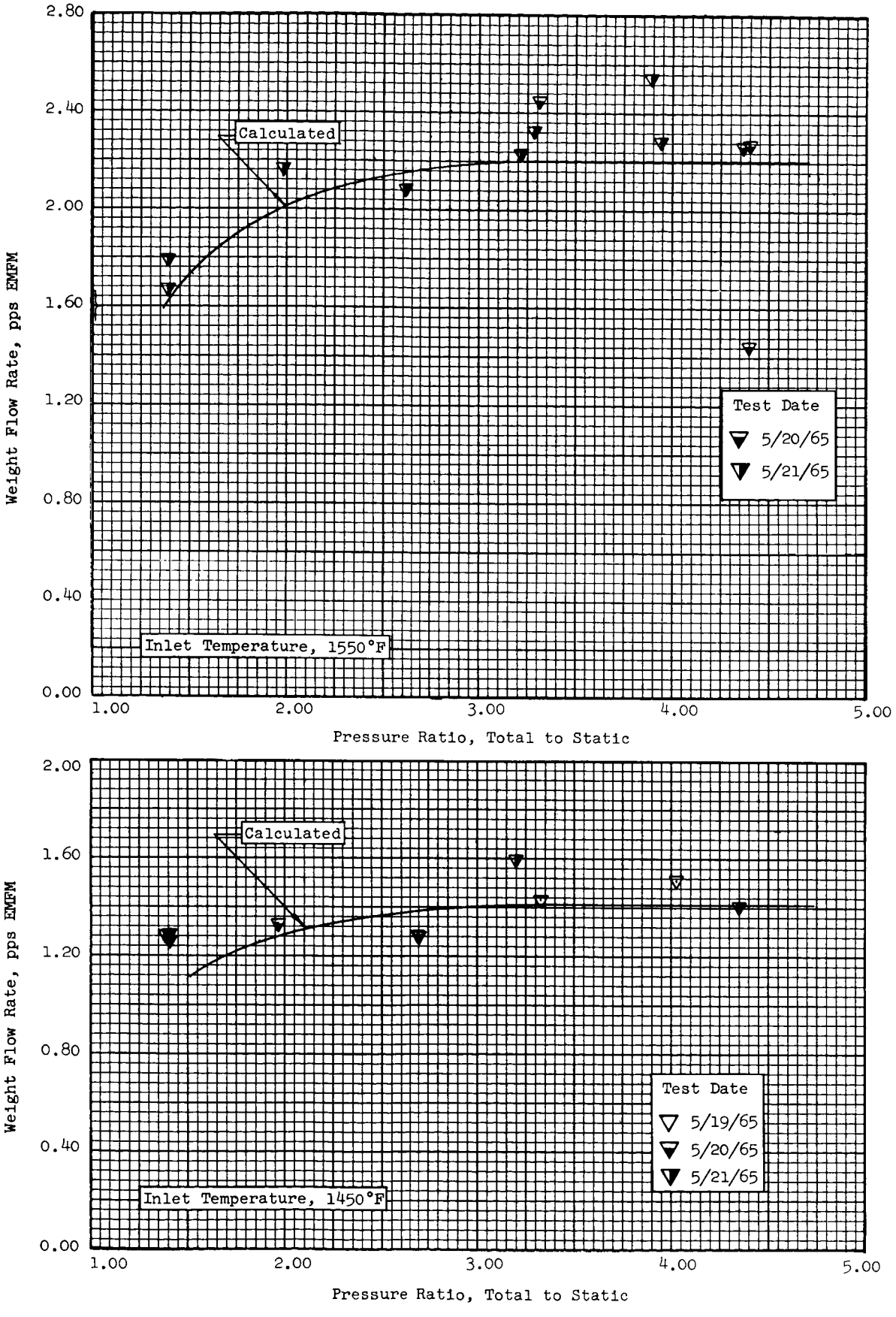


Fig. 23. Comparison of Measured and Calculated Weight Flow Rate. Speed, 19,300 rpm.

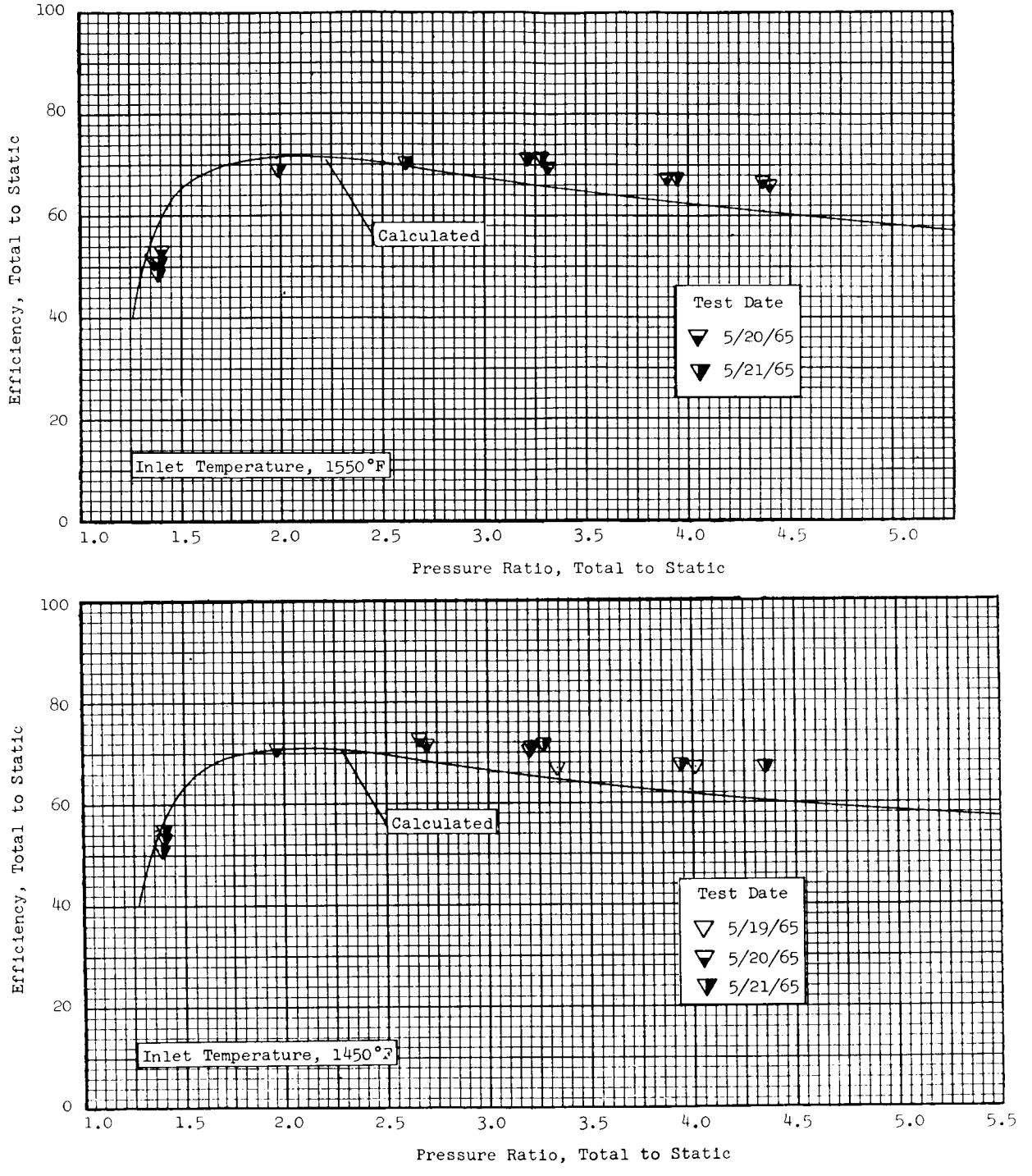


Fig. 24. Comparison of Measured and Calculated Efficiency, Total to Static. Speed, 19,300 rpm.

diaphragm pressure transducer. The figures presented are typical of the good results obtained in measuring turbine pressures, flow rates and efficiency. The efflux pressure measuring system was instrumental in obtaining good performance data to plot a map of turbine operating characteristics. It is expected that this type of system will find application in the development testing of alkali metal vapor systems and components.

LIST OF REFERENCES

1. J.P. Stone, C.T. Ewing, J.R. Spann, E.W. Steinkuller, D.D. Williams, and R.R. Miller, "High Temperature Properties of Sodium, Potassium, and Cesium", NRL Report 6128, August, 1964.

2. Two-Stage Potassium Test Turbine, Quarterly Progress Report No. 6, November 8, 1962, Contract No. NAS 5-1143, Space Power and Propulsion Section, RSD, General Electric Company, Cincinnati 15, Ohio.

3. R.J. Rossbach, "Critical Flow of Potassium Vapor Through Instrumented Converging-Diverging Nozzle", ASME 65-GTP-22.

4. Two-Stage Potassium Test Turbine, Quarterly Progress Report No. 15, February 8, 1965, Contract No. NAS 5-1143, Space Power and Propulsion Section, RSD, General Electric Company, Cincinnati 15, Ohio.

NOMENCLATURE

A_3	geometric flow area at station 3	$in.^2$
C_f	flow coefficient	
D_h	hydraulic diameter	in.
g	gravity constant	386 $in./sec.^2$
P_{s3}	static pressure at station 3	$lb./in.^2$
P_{t3}	total pressure at station 3	$lb./in.^2$
Re	Reynolds number	
V_3	velocity at station 3	in./sec.
v_{t3}	specific volume at station 3 total conditions	$in.^3/lb.$
W	weight flow rate	lb./sec.
γ	ratio of specific heats	
μ_{t3}	absolute viscosity at station 3 total conditions	$lb. - sec./in.^2$

ACKNOWLEDGEMENT

The authors would like to thank the National Aeronautics and Space Administration for permission to publish this paper. All of the work discussed herein was carried out under NASA Contract Number NAS 5-1143.

N66 31678

PRESSURE TRANSDUCER FOR LIQUID METAL APPLICATIONS*

Anthony J. Cassano and Richard E. Engdahl
Consolidated Controls Corporation
Bethel, Connecticut

(Paper presented by Anthony J. Cassano)

ABSTRACT

Development of a pressure transducer for use in liquid metal flow loops poses many design problems demanding the best from available materials. The program to be discussed involves the development of a pressure transducer providing accurate measurements in the liquid, vapor, and two-phase streams of a potassium loop operating at temperatures up to 1800°F. In addition to potassium, the transducer may also find use in loops containing sodium, lithium, cesium or rubidium. The transducer employs a thermionic diode sensor to convert the motion of a pressure-actuated refractory alloy capsule into a suitable electrical output.

INTRODUCTION

A great deal of present work on power generation and energy conversion involves closed cycle power systems using liquid metals as working and heat transfer media at elevated temperatures. Since small pressure

*Work supported by the National Aeronautics and Space Administration under Contract NAS 3-4170.

changes could indicate the onset of instability, there exists a need for instrumentation that can follow and record both average and perturbed pressure conditions in the liquid, vapor and two-phase streams. Envisioned use of these power systems for space applications imposes the additional requirements of light weight and long-term unattended operation.

The program to be discussed involves the development of a pressure transducer capable of providing accurate measurements in a potassium loop operating at temperatures up to 1800°F. The design approach uses the displacement of a diaphragm member by the liquid metal pressure. The displacement is then monitored by a thermionic diode sensor whose output indicates the pressure. The main problem areas include the high-temperature diaphragm deflection characteristics, diaphragm compatibility with liquid metals, and the accuracy and sensitivity of the thermionic diode sensor. The transducer will be developed for use as either ground or flight hardware for measuring absolute and differential pressures. The absolute pressure instrument will be developed for a full scale range of 80 psia and the differential instrument for ± 5 psid.

PRESSURE DEFLECTION SYSTEM

The typical pressure transducer depends upon the precision of a highly stressed spring member for its accuracy. In the present case, the spring member is a multi-convolution flat plate diaphragm which is displaced by liquid metal pressure. The maximum useful stress level is limited by the corrosion and creep characteristics of the diaphragm material in direct contact with the liquid metal; in this case potassium at 1800°F.

Corrosion by a liquid metal often takes place preferentially along grain boundaries. This attack is difficult to prevent completely, but its influence can be minimized by design. Selection of a diaphragm thickness that is large compared with the material grain size will lengthen the life of the diaphragm. Thus, material thicknesses of 0.02 to 0.06 inch are preferred over the conventional diaphragm thickness of 0.005 to 0.01 inch. Normally, to limit the attack by the alkali metals, unalloyed refractories (e.g., columbium or tantalum) must contain a low oxygen content. However, if the refractories are "gettered" by the addition of an element capable of forming a thermodynamically stable oxide (e.g., Zr, Ti, Y, Hf), the resistance to attack is

considerably improved. In fact, materials containing such gettering elements are capable of tolerating oxygen contents approaching the stoichiometry of the gettering metal without adverse corrosion effects. If the oxygen content of the alloy exceeds the stoichiometric limit of the getter element, the alloy tends to act like ungettered material.

The alloys selected for investigation as possible diaphragm materials were:

C-129Y	(Cb-10W-10Hf-0.1Y)
FS-85	(Cb-28Ta-10W-1Zr)
T-222	(Ta-10W-2.5Hf)
W-25Re	

The test configuration used for evaluation of the above alloys consisted of a double convolution bellows arrangement made up of four flat plate diaphragms. The configuration is shown in Figure 1. The diaphragms were about 1 inch in diameter and 0.02 inch thick. The inner diameter was about 0.2 inch. The ring plate diaphragm design was used for the W-25Re alloy while the machined diaphragm design was used for the C-129Y, FS-85 and T-222 alloys. In view of the known harmful effects of oxygen in refractory metals exposed to liquid alkali metals, the test configurations were assembled by electron-beam welding techniques to avoid oxygen pick-up. The test program

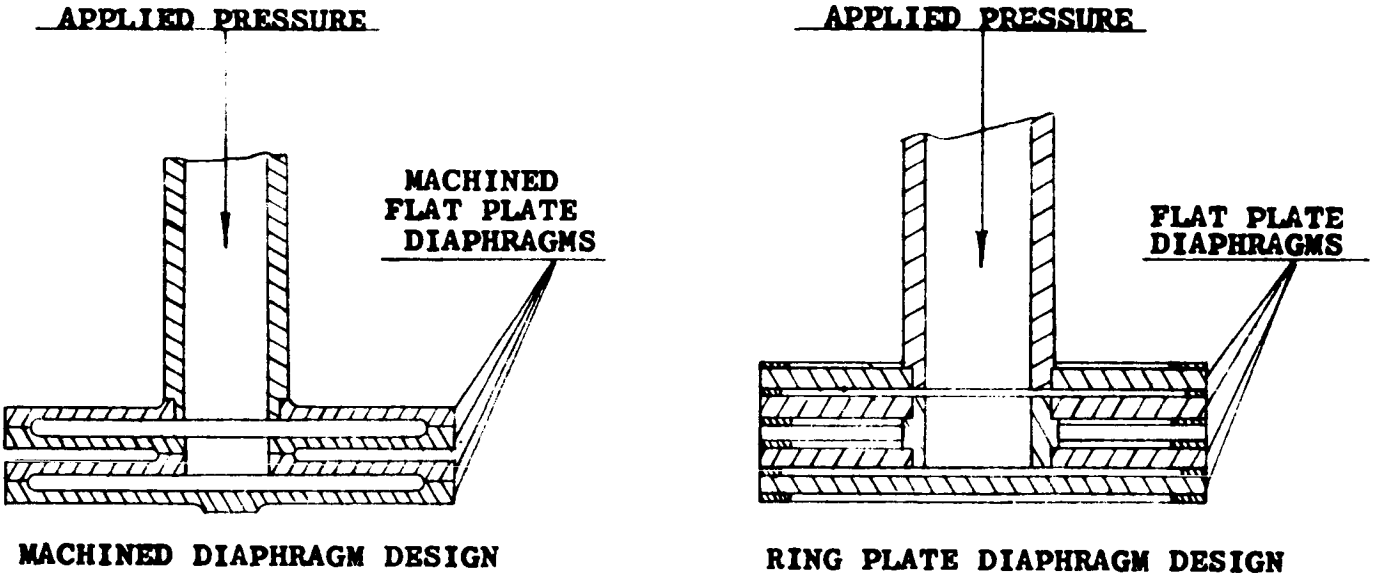


Fig. 1. Test Pressure Capsule Configurations

included (1) pressure cycling the test configurations at temperatures to 1800°F to determine linearity, reproducibility, and creep parameters, and (2) evaluating the compatibility of the test configurations with potassium at 1800°F and about 80 psia.

The pressure tests were performed in a Vacuum Test Facility (10^{-8} torr or better) with high purity argon used for pressure cycling.[1] The measured oxygen and water vapor content of the argon was held to maximum values of 0.5 and 1.2 parts per million respectively. The diaphragm deflection was measured to an accuracy of better than ± 20 microinches by combining a binocular microscope with a glass plate camera and using a shadowgraph instrument to read the resulting photos.[2,3] Analysis of the data with limited pressure and temperature cycling yielded the following results:[4]

1. Hysteresis effects at temperatures up to 1800°F were negligible for full scale deflections up to about 0.001 inch.
2. The increase in full scale deflection with temperature generally followed the predicted change based on literature values of Young's modulus.

3. Zero shift data generally showed that the W-25Re capsule was the most stable.
4. There is a definite need for extended pressure cycling to obtain stable pressure-deflection characteristics.

Potassium compatibility was investigated by introducing a charge of liquid potassium into the test configurations, sealing them and installing them in a vacuum chamber whose temperature was raised to 1800°F. This established a potassium vapor pressure inside the test devices of about 80 psia. A total of 500 hours at 1800°F was accumulated without sign of failure.[3,5] Metallographic examinations, presently underway, will determine the extent, if any, of liquid potassium attack.

THERMIONIC DIODE SENSOR

The use of a high vacuum thermionic diode as a pressure sensing element is based on device operation in the space charge limited mode, wherein the current flowing between the emitter and collector is distance dependent. If one of the electrodes (such as the collector) is moved as a function of pressure, the current is also a function of pressure. Now, if all other terms influencing the diode

current can be controlled, an accurate high temperature pressure transducer can be constructed. A complete treatment of the thermionic diode transduction approach has been published (Reference 6) and serves as a starting point for the experimental work needed to verify the analysis.

The current-spacing relation is a non-linear one with the current varying as the inverse square of the spacing. To achieve linearity, a system has been used which measures the difference between the currents flowing through a pressure-actuated collector (the diaphragm member described previously) and a fixed reference collector. The power supply for the system is programmed such that the voltage applied to the collectors maintains the sum of the two currents at a constant level determined by the voltage and distance corresponding to zero pressure. Reference to Figure 2 will perhaps clarify the above statements. Under zero pressure conditions, the emitter-active collector distance and the emitter-reference collector distance are equal, resulting in $i_a = i_r$ and $(i_a - i_r) = 0$. Depending upon the choice of the dc voltage, the current sum $(i_a + i_r)$ will have a definite

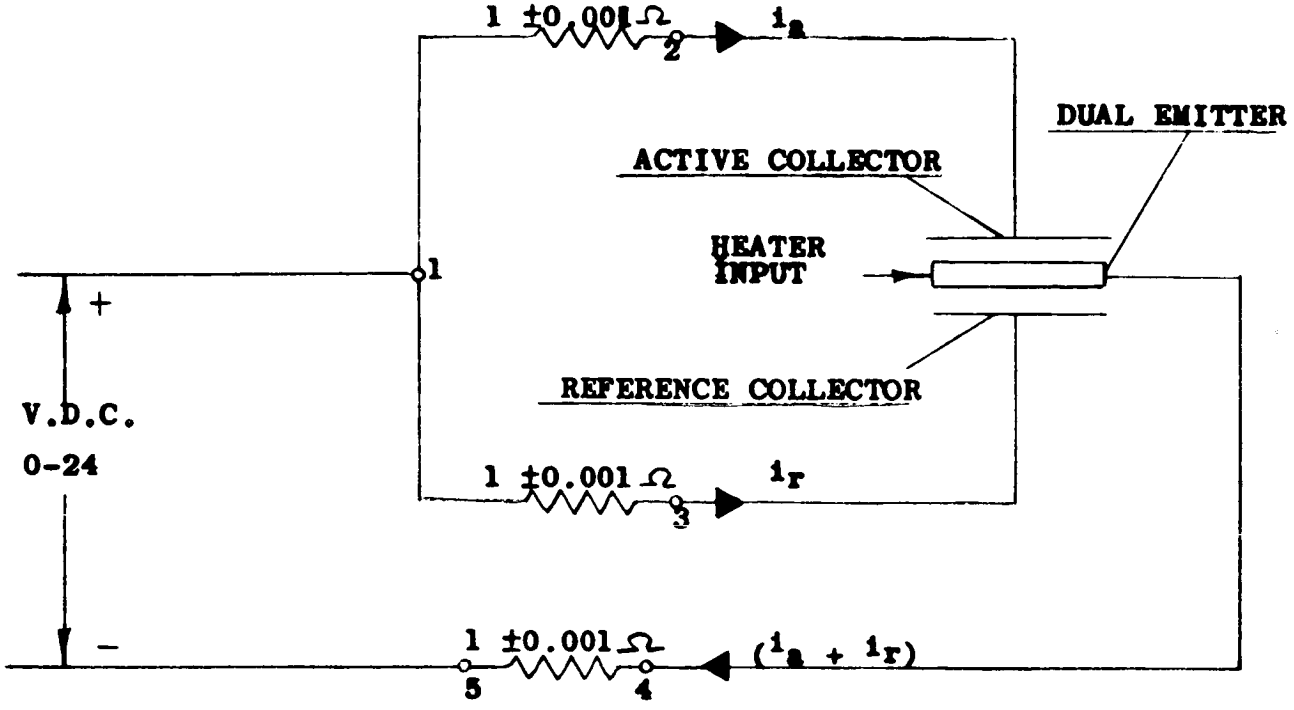


Fig. 2. Thermionic Diode Sensor Test Circuitry

value. Under pressure, the active collector will approach the emitter, causing i_a to rise while i_r remains constant. The dc voltage is then lowered to bring the sum $(i_a + i_r)$ back to its original value and the difference $(i_a - i_r)$ is taken as indicative of the pressure (active collector travel).

Figure 2 shows the test circuitry employing precision resistors and a digital voltmeter which was used to measure the various test parameters. The numbered positions in Figure 2 indicate the voltmeter connections. The parameters read using the various combinations of these connections are:

Voltmeter Connections	Reading
1-2	i_a
1-3	i_r
4-5	$(i_a + i_r)$
3-2	$(i_a - i_r)$
1-5	V

Typical test results are shown in Figure 3. The difference current $(i_a - i_r)$ is plotted as a function of active collector travel up to 0.001 inch. The initial spacing in

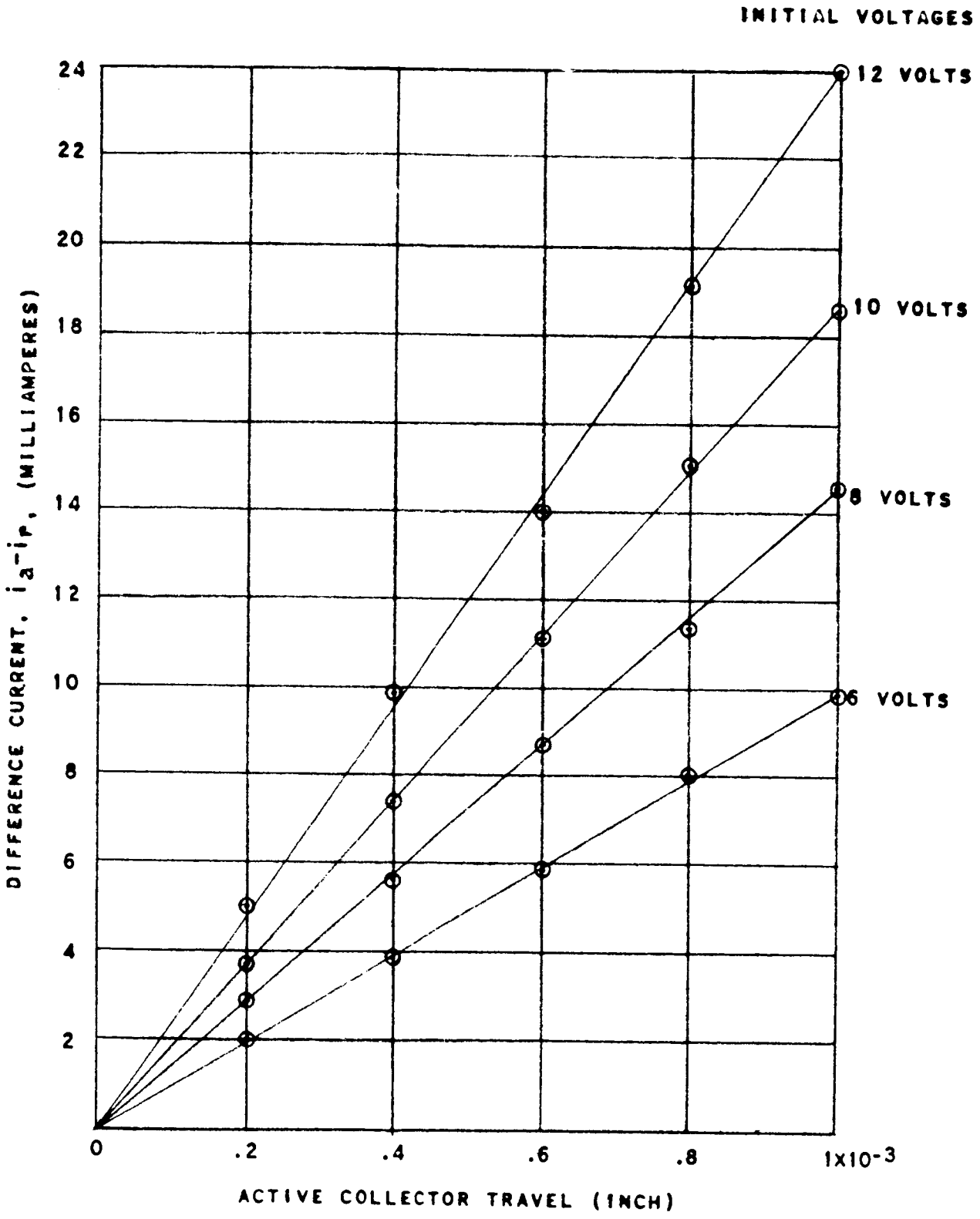


Fig. 3. Thermionic Diode Sensor Calibration

this test was 0.006 inch. Linearity was attained within a maximum deviation of ± 1.5 percent of full scale. These results definitely indicate the suitability of the thermionic diode sensor for use in the transducer.

THERMIONIC DIODE PRESSURE TRANSDUCER

A preliminary design for a complete absolute pressure transducer incorporating a double convolution pressure capsule and a thermionic diode sensor is shown in Figure 4.

The encapsulated heater assembly consists of a molybdenum body into which a cavity is machined. An electrical heater, or filament, is cast into the cavity and dual impregnated tungsten emitters are mounted on opposite faces of the molybdenum body.[5]

The unit is initially assembled without the protective cover assembly. The encapsulated heater assembly is mounted on posts which are part of the ceramic (Lucalox) base, thereby establishing a fixed emitter-reference collector distance. The emitter-ceramic assembly is then mounted in the housing using the adjusting ring for alignment purposes. After bake-out and emitter activation, the

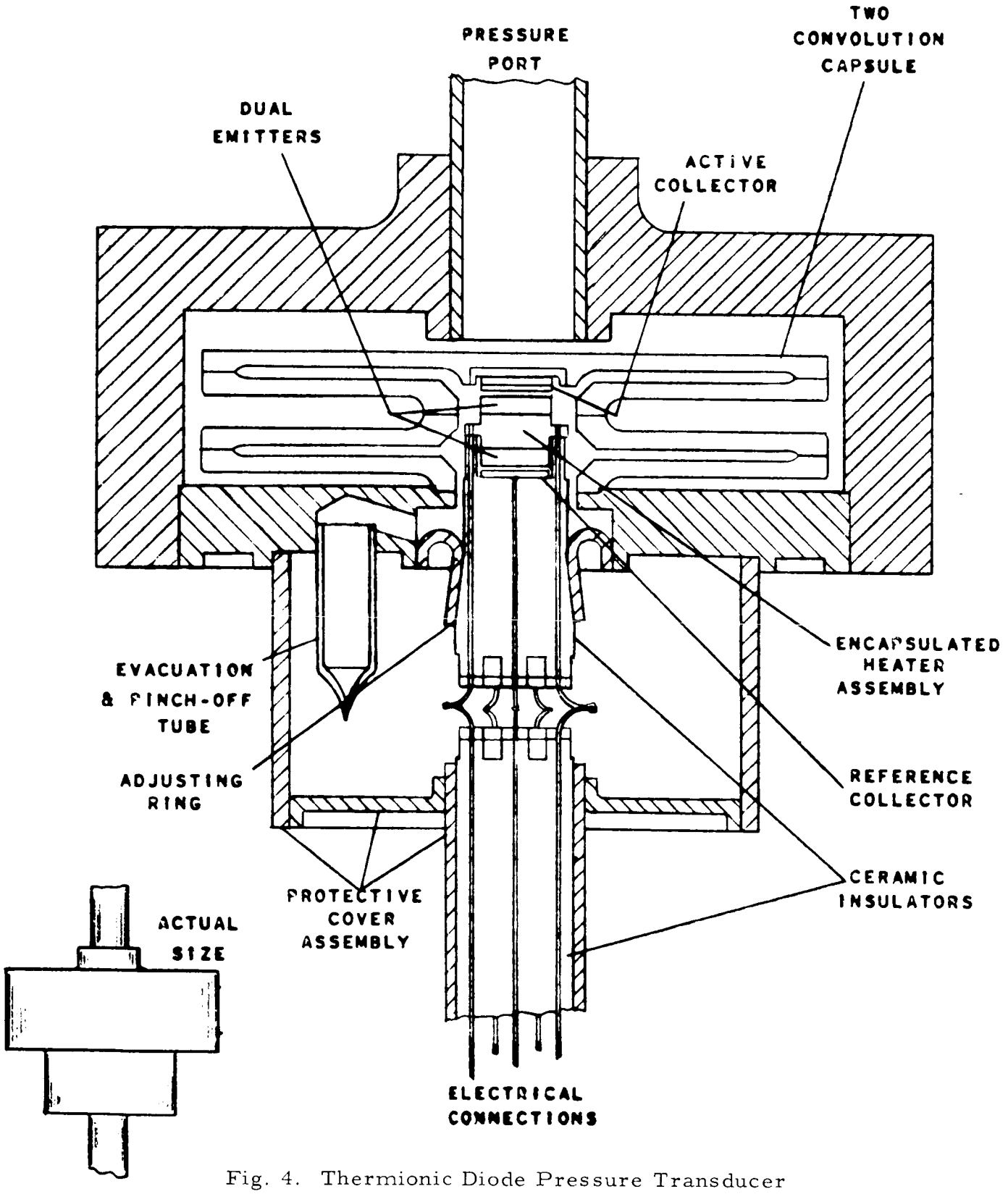


Fig. 4. Thermionic Diode Pressure Transducer

pinch-off tube is closed to maintain vacuum conditions in the thermionic section of the transducer and the adjusting ring can be used for alignment of emitter-active collector distance. To maintain this alignment and distance during operation, the protective cover assembly is provided. The electrical connections are brought out through a second ceramic assembly.

The seals employed in the transducer are of considerable importance. They must not only provide a vacuum-tight connection to assure proper operation of the thermionic diode sensor but must also provide a back-up liquid metal seal in the event of rupture of the pressure capsule.

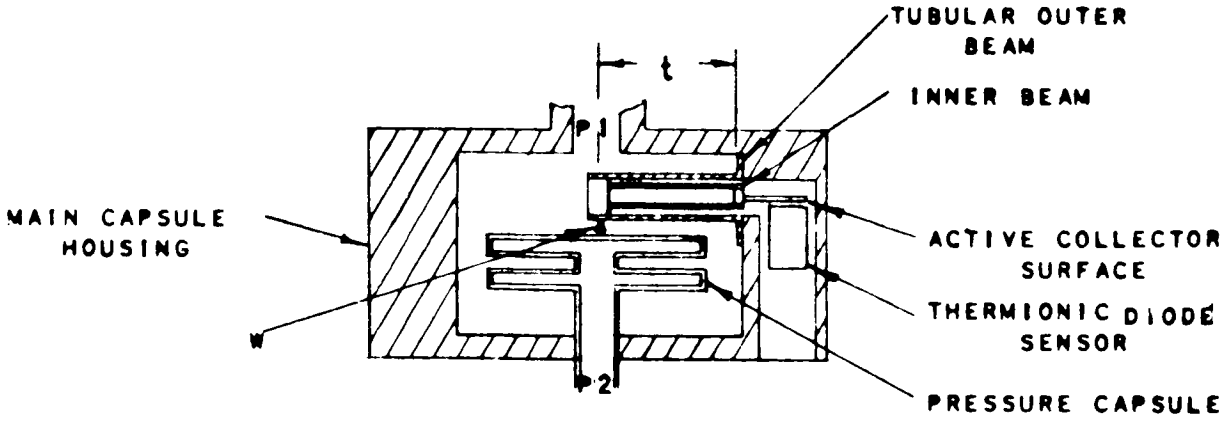
The main problem areas are the fabrication of the encapsulated heater assembly and development of the metal-ceramic technology necessary to obtain the required seal integrity. Work in these areas is proceeding on schedule with the preparation of test units designed to evaluate and improve the fabrication techniques to be used for the final transducer instrument. The present results of these efforts may be briefly summarized as follows.

1. The first two test units are currently in work. The first unit concentrates on the heater assembly mounted on its ceramic base. The thermionic diode sensor is installed in a fixture which allows controlled movement of a simulated active collector. This test provides experience in construction of the encapsulated heater and checking of the response characteristics of the thermionic sensor. The second experiment uses one of the test pressure capsules. An active collector is mounted inside the capsule along with the thermionic diode sensor. This test provides experience in fabrication of the complete transducer.
2. The encapsulated heater assembly uses a bare W-3Re spiral heater cast into the molybdenum emitter housing with an alumina/beryllia mixture. The heater power leads are rhenium wire connected to the heater by a welded joint which is embedded in the casting. The superior ductility of rhenium, when compared to tungsten or molybdenum, is needed to allow bending of the heater power leads during assembly of the transducer.
3. The metal-ceramic joining technique presently being used to fabricate the initial thermionic diode pressure

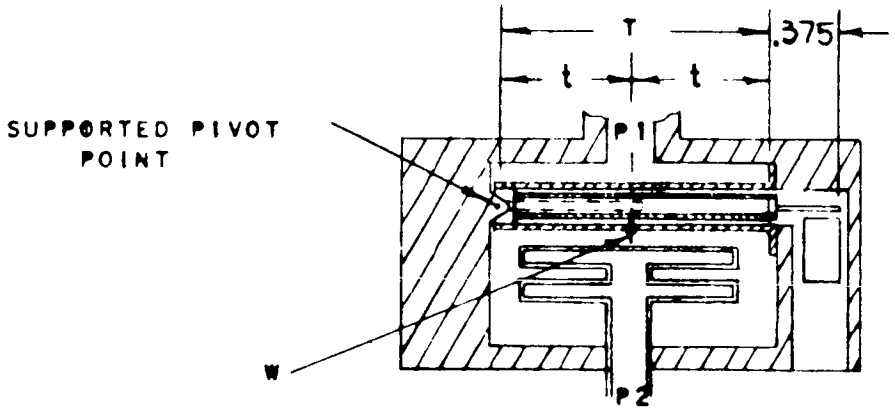
transducer models employs a tungsten/yttria metallizing compound and a nickel/niobium/titanium braze material. The integrity of the seal fabricated by this technique has been established by life testing. A sample Nb-1Zr/Lucalox seal was run at 1800°F for 2400 hours; the first 1000 hours of which were at 500 psia internal pressurization followed by 100 hour periods at 600, 700, 800 and 900 psia, and a final 1000 hours at 1000 psia. Work is presently underway to introduce the seal into the potassium compatibility test program.

DIFFERENTIAL PRESSURE TRANSDUCER

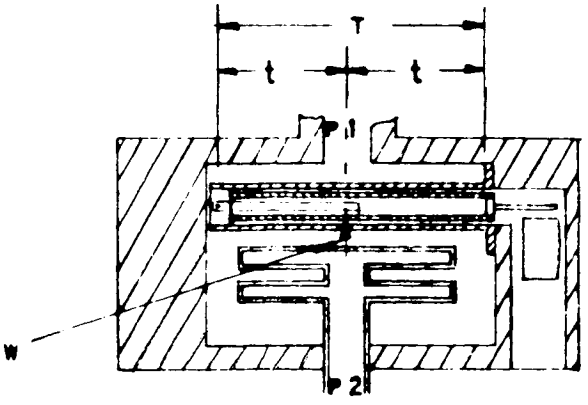
Three possible mechanical configurations for the differential pressure transducer (±5 psid) are show schematically in Figure 5. Each configuration uses the deflection of a composite beam assembly consisting of (1) an outer tubular beam member and (2) an internal beam member whose termination acts as the active collector surface for the thermionic diode sensor. The outer beam member will be exposed to the liquid potassium environment. A wall thickness of 0.025 inch has been assumed to be sufficient for liquid metal containment. The internal beam member will be sealed from



CASE I - CANTILEVER, END LOAD



CASE II - END COUPLE, SUPPORTED PIVOT



CASE III - END COUPLE AND END LOAD

Fig. 5. Differential Pressure Transducer Configurations

the liquid potassium and connected to the vacuum environment of the thermionic diode sensor.

The envisioned differential pressure transducer is of the same basic design as the absolute pressure transducer of Figure 4. For the differential pressure application, the thermionic diode sensor will be removed from the interior of the pressure capsule, isolated from the pressurized volumes, and probably embedded in the capsule housing. The pressures P_1 and P_2, whose differential ($P_1 - P_2$) is to be monitored, are applied to the external and internal surfaces, respectively, of the pressure capsule. The main capsule housing inner diameter is assumed to be about 1.5 inches and the active collector surface extends 0.375 inch beyond the fixed support of the outer beam member.

For Case I (cantilever, end load), the displacement of the pressure capsule is transmitted directly to the cantilevered end of the outer beam member, establishing an end slope θ_1 relative to the horizontal position. The deflection of the active collector surface from equilibrium therefore becomes $(t + 0.375)\ \theta_1$ inch less

the deflection of the outer beam end. For Case II (end couple, one end fixed, one end supported), the pressure capsule displacement is transmitted by a yoke arrangement as a couple acting on a supported pivot point at one end of the outer beam member. If the end slope at the supported pivot point is θ_2, the active collector deflection from equilibrium becomes $(T + 0.375)\ \theta_2$ inch. Case III (cantilever, combination end load and end couple) involves the removal of the supported pivot point of Case II, allowing free movement of the outer beam member subject to the superposition of two actions; i.e., the pressure capsule deflection transmitted by the yoke arrangement as (1) an end load and (2) an end couple.

The applicable relations needed to calculate the end slope and deflection parameters may be found in Reference 7. If we assume that the force exerted by the pressure capsule on the beam is one pound and the Young's modulus of the tubular outer beam material is about 30×10^6 psi, the results shown in Figure 6 are obtained.

The data show that Cases II and III hold promise of providing an active collector deflection of 0.001 inch for

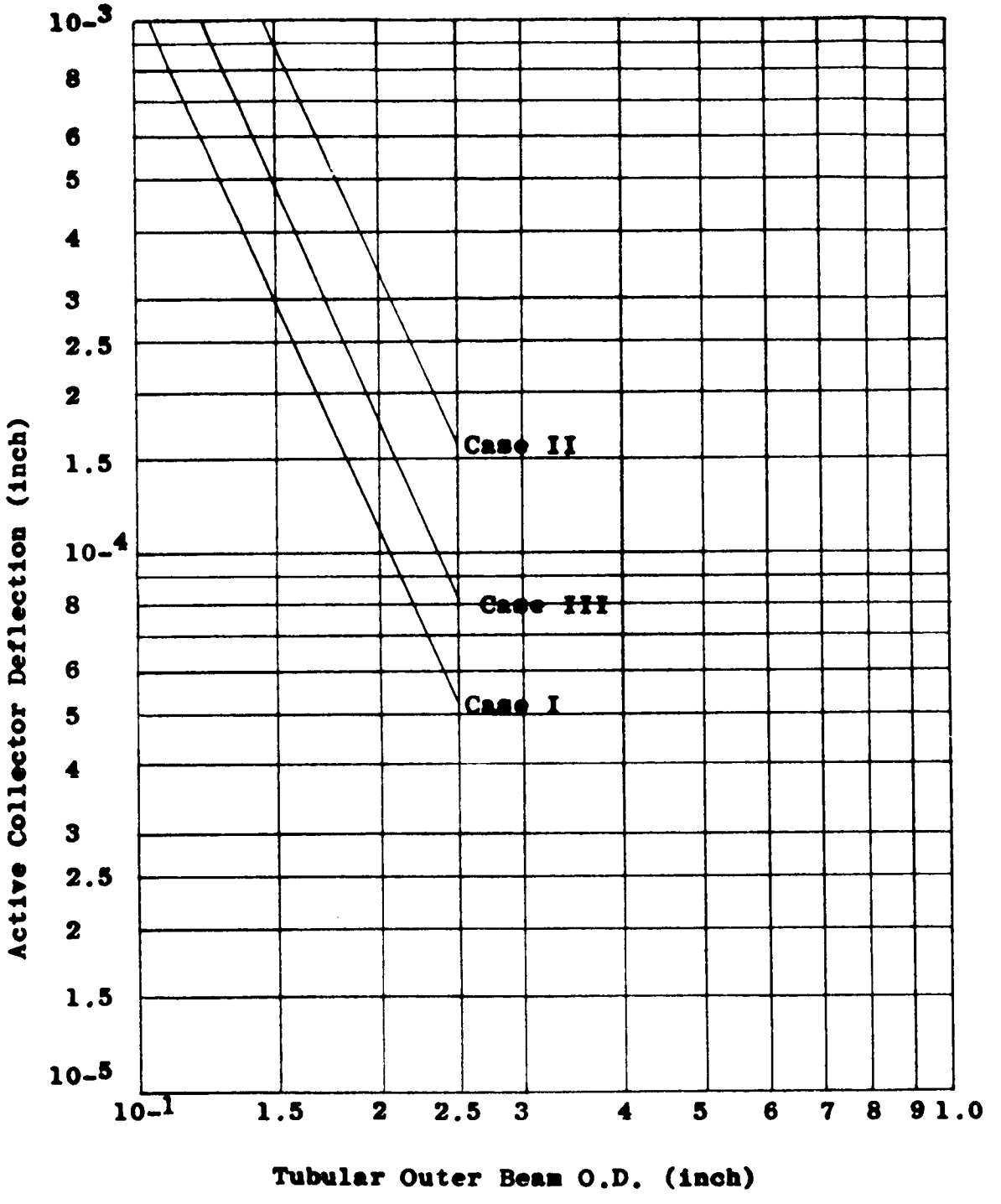


Fig. 6. Differential Pressure Transducer Deflection Characteristics

reasonably sized tubular beams. The value of 0.001 inch full scale deflection has been found to result in a feasible output for the thermionic diode sensor (see Figure 3). The difficulties inherent in Case II, which requires that the supported pivot point be inside the main capsule housing, make it mandatory to concentrate on Case III, for which the fabrication requirements would be far less stringent. Case III has the further advantage of providing a purely vertical active collector travel, since calculations show that the superposition of the end load and the end couple effects result in an end slope $\theta_3 = 0$.

CONCLUSIONS

The progress achieved thus far in the program to develop a pressure transducer for use in a liquid potassium loop at 1800°F indicates that the use of a multi-convolution pressure element and a thermionic diode sensor will result in an instrument capable of reliable and accurate operation. Since the vapor pressure of mercury, sodium, lithium, cesium and rubidium is of the same magnitude as that of potassium, there is no apparent reason why the transducer could not be used in loops containing these other liquid metals. If

potassium compatibility testing, now underway, is successful, there should be no compatibility problem associated with the use of the other liquid metals.

REFERENCES

1. R.E.Engdahl,ed.: First Quarterly Report, Pressure Measuring Systems for Closed Cycle Liquid Metal Facilities. NASA CR-54140, July 2, 1964.

2. R.E.Engdahl,ed.: Second Quarterly Report, Pressure Measuring Systems for Closed Cycle Liquid Metal Facilities. NASA CR-54193, September 28, 1964.

3. A.J.Cassano: Third Quarterly Report, Pressure Measuring Systems for Closed Cycle Liquid Metal Facilities. NASA CR-54276, December 28, 1964.

4. A.J.Cassano: Fourth Quarterly Report, Pressure Measuring Systems for Closed Cycle Liquid Metal Facilities. NASA CR-54371, April 5, 1965.

5. A.J.Cassano: Fifth Quarterly Report, Pressure Measuring Systems for Closed Cycle Liquid Metal Facilities. NASA CR-54439, June 28, 1965.

6. A.J.Cassano: Analysis of Two High-Temperature Liquid Metal Pressure Measuring Systems. IEEE Transactions on Aerospace, Vol.AS-3, No. 2, June 1965, p. 466.

7. R.J.Roark: Formulas for Stress and Strain. Third ed., McGraw-Hill Book Co.,Inc., 1954, p. 100.

SESSION 2

QUALITY AND VOID FRACTION MEASUREMENTS

Tuesday, September 28, 1965

CHAIRMAN: M. Gutstein
NASA

N66 31679

FORCED CONVECTION BOILING SODIUM STUDIES AT LOW PRESSURE

J. B. Heineman
Argonne National Laboratory

Because of the recent interest in the vaporization behavior of liquid metal coolants in fast reactors, especially with respect to reactor safety, reactor control, and Rankine cycle design, the Engineering Research Section initiated a modest program designed to provide fundamental experimental information concerning the two-phase flow of forced convection boiling sodium up to approximately atmospheric pressure. The program has been further expanded to include boiling heat transfer studies to a temperature of 2100°F. The initial effort embodies conventional loop materials for construction, whereas the more ambitious effort has required the use of Nb1%Zr alloy contained in a high vacuum environment. The latter installation is nearing completion and should eventually be capable of supplying very high heat fluxes in the entire quality range at pressures up to eight atmospheres.

The initial experiment was designed to obtain information concerning the vapor volume fraction, two-phase frictional losses, and boiling stability of flowing sodium at low pressure. Figure 1 is a schematic diagram of the apparatus and instrumentation. The loop is constructed of 1/2-inch tubing, type 316 stainless steel. The d.c. electromagnetic pump provides a maximum flow of 4 gpm and the boiler section may operate with a maximum heat input of 10 KW.

This loop has logged approximately 4200 hours of operation at temperatures above 1000° F, approximately 1000 hours at boiling temperatures between 1300 and 1650° F; enough operating experience and data have been accumulated to show quantitative results and some interesting qualitative observations.

A summary of the range of variables covered in this experiment is as follows:

Table I

Pressure psia	2 - 17
Temperature, ° F	1300 - 1650
Inlet Velocity, fps	1 - 5
Boiler Power Density, KW/liter	0 - 200

PRECEDING PAGE BLANK NOT FILMED.

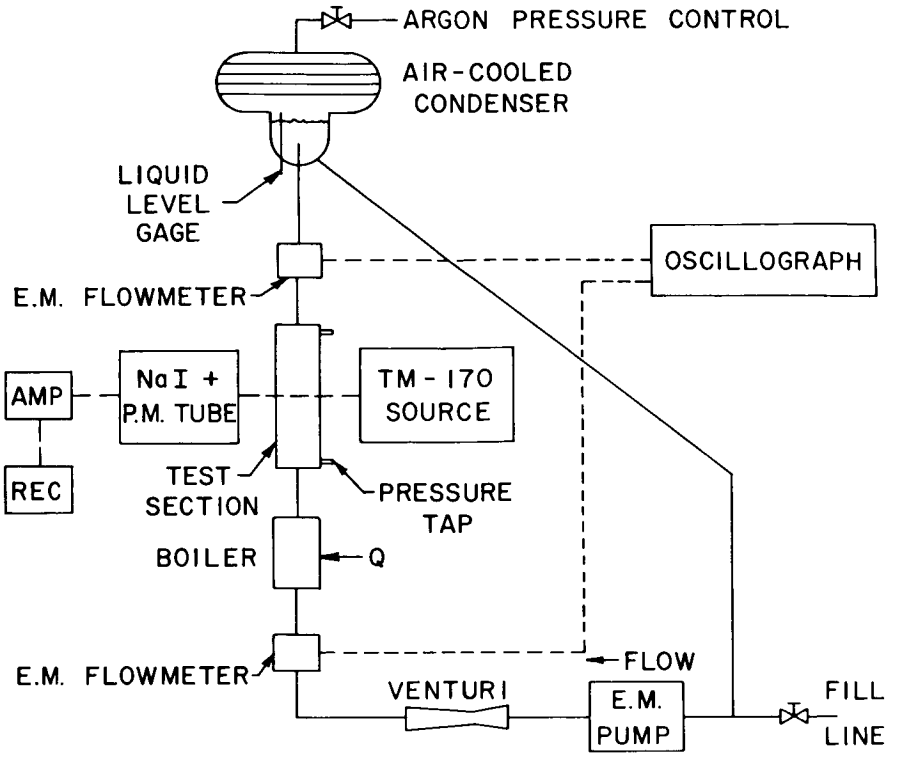


Fig. 1. Schematic of Apparatus

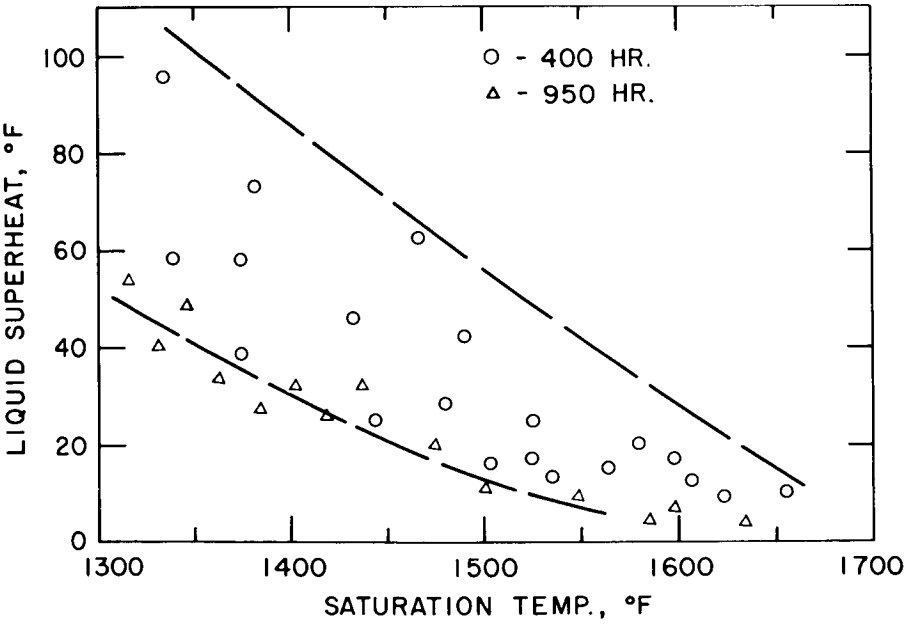


Fig. 2. Liquid Superheat Measurements

Liquid Superheat, ^{o} F	10 - 100
Quality	0.0005 - 0.01
Vapor Volume Fraction	0 - 0.87
Slip Ratio	5 - 100
Frictional Pressure Loss, in H_2O	0 - 40
Boiling Operation, hr	1000

The range of liquid superheats obtained prior to the initiation of boiling is rather low compared to those obtained by other experimenters. Further, there appears to be a decrease in superheat requirements with time. Figure 2 represents typical superheat measurements at two different points in time. Within the range of variables tested, there was no discernible flow rate effect. The phenomenon of liquid superheat is related to the more general problem of loop stability. There is certainly some relationship among the many parameters represented here which determines the type and degree of stability obtained in the system. Without attempting to define this relationship, it is stated here that, for the purposes of this experiment, a stable condition was achieved whenever the pressure fluctuations were small compared to the absolute value, the boiler inlet flow was steady, and the time-averaged void fraction at a point was constant for a time sufficient to collect data. These requirements can be quantitatively defined for the particular geometry studied. In general, stability was achieved in the pressure range greater than 7 psia, so the void fraction data presented here was obtained entirely in the range 7 to 17 psia.

The void fraction data has been completely analyzed and it appears that the electromagnetic flowmeter method is quite adequate for the measurement of this quantity for vertical upflow of two-phase liquid metals. It became obvious during the course of this experiment that the flowmeter method was yielding values that were consistently low in comparison to the gamma-attenuation technique, especially for fractions greater than 30 per cent. It was recognized that this discrepancy was probably due to the change in two-phase electrical conductivity with void fraction. Some correction factors have been calculated by Mr. Roger Carlson of Reactor Engineering and the results are shown as follows:

$$\alpha_i = 1 - K_1 E_o / K_o E_1 \tag{1}$$

$$\alpha_i = A\alpha \left[\frac{1 + f(\alpha)(\rho_f t/\rho_w h) + 1/S_c}{1 + \rho_f t/\rho_w h + 1/S_c} \right] \tag{2}$$

Maxwell: $f(\alpha) = (2 + \alpha)/(1 - \alpha)2$ (3)

Petrick: $f(\alpha) = \exp(3.8\alpha)$ (4)

where α is void fraction; E_o and E_1 are flowmeter outputs in the all-liquid and two-phase regions, respectively; K_o and K_1 are calibration constants; A, t, h, and S_c are geometric factors for a rectangular duct; ρ is electrical resistivity; and subscripts i, f, and w refer to the "ideal output", liquid, and duct wall, respectively.

The first equation shows the simple relationship, valid for low quality, derived on the basis that the flowmeter output is a function of liquid velocity only. The second equation is derived theoretically for the same quantity, including a factor $f(\alpha)$, which accounts for the change in two-phase electrical conductivity. The third equation is a theoretical expression, due to Maxwell, defining $f(\alpha)$. The fourth is an expression, derived empirically, due to M. Petrick. The important quantities here are the electrical resistivity ratios and $f(\alpha)$. It can be seen that if the liquid resistivity is much smaller than that of the wall, then $f(\alpha)$ is not a very important correction; however, as this ratio approaches one, the correction is more important.

Figure 3 shows a typical set of void fraction data, and it can be seen that no decision can be made concerning the correct curve. As it happens, a sodium - S.S. system has a low resistivity ratio, so that the $f(\alpha)$ correction is minimized. Data from a low temperature NaK - argon system were plotted in the same manner and this data falls on the Maxwell line. It is intended that this measurement device be used on the high temperature Nb-1% Zr system, in which the resistivity ratio is quite close to one at operating temperature, so it is quite important to decide which factor is correct.

It should be mentioned that, for higher quality systems, a quality factor is introduced into the original equation. One further point - the flowmeter-oscillograph system is fast enough to follow the variations in liquid velocity in the vicinity of the flowmeter; both slug flow and annular flow regimes were

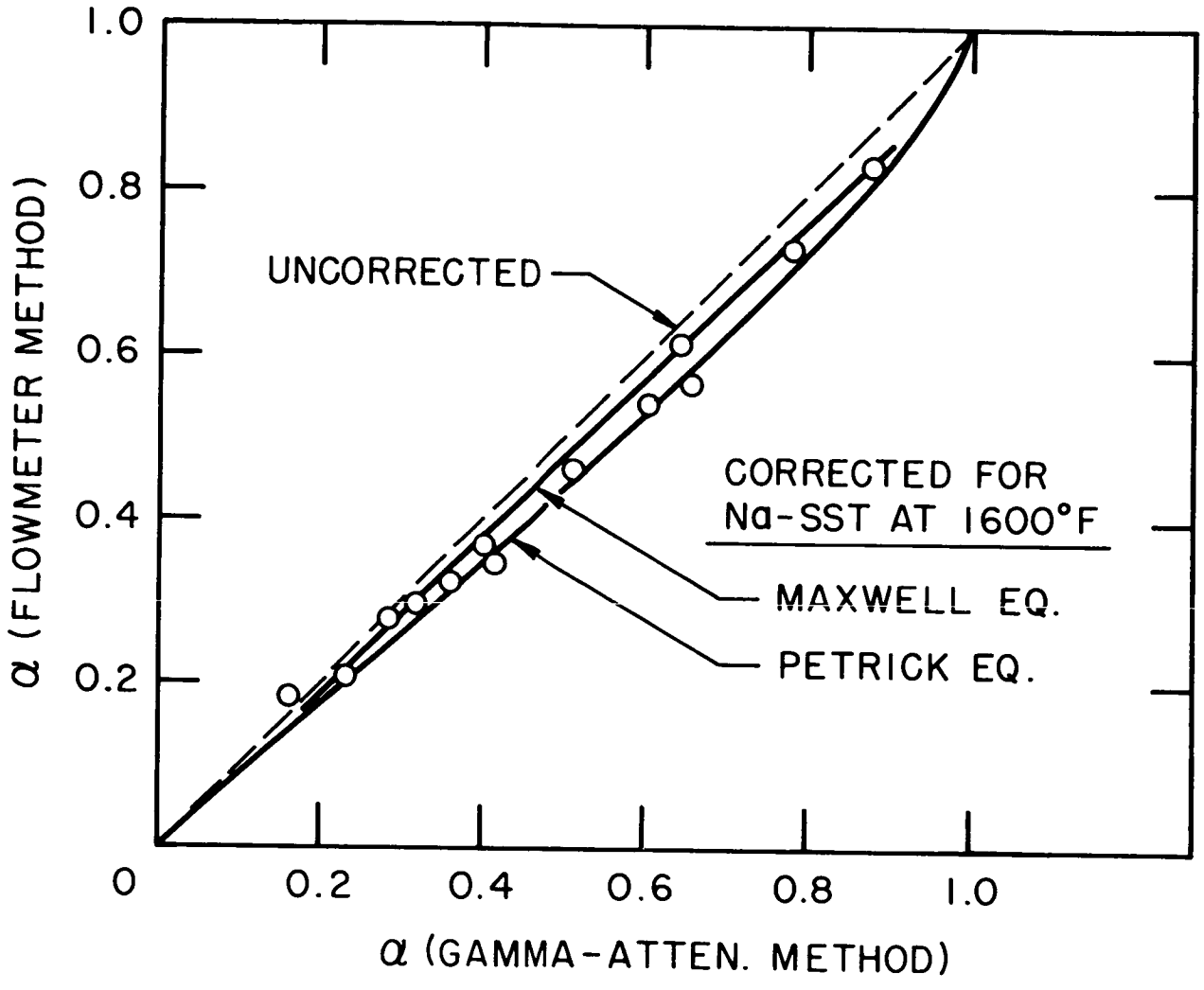


Fig. 3. Void Fraction Results

encountered here, according to the instantaneous flowmeter output. The gamma-attenuation system is also a fast response device, and the maximum readings corresponded quite well with the maximum readings from the flowmeter.

It should be emphasized that, in the foregoing analysis, data taken at less than 7 psia, i.e., at high density ratio, was not included; in general, stability was not achieved to the degree that meaningful data could be accumulated in this region - also, the more specific stability problems have not been detailed; stability studies will continue before terminating the experiment.

The pressure drop and slip ratio results have not been compared in detail to other correlations. The qualities here are very low so a definite dependence of two-phase friction factor is probably not clear. The slip ratios are definitely high compared to any of the lower temperature correlations. This may be a non-equilibrium effect, i.e., if the qualities are not as high as calculated from the equilibrium case, then the actual slip ratios are, of course, lower than appear here. As soon as the stability studies are complete, a topical report will be issued covering all of the above experiments in detail.

N66 31680

X-RAY MEASUREMENT OF VOID DYNAMICS IN BOILING LIQUID METALS

L. B. Wentz, L. G. Neal and R. W. Wright
TRW Systems, Redondo Beach, California

(Paper presented by L. B. Wentz)

I. INTRODUCTION

High superheats have been observed with boiling liquid metals. Therefore, it appears desireable that systems for investigating the void behavior of boiling liquid metals should be capable of response times of the order of one millisecond. This paper shows that such a time response is readily attainable by the use of x-ray attenuation for vapor-void measurements in liquid metal systems. Considerations of measurement interpretation, resolution, and accuracy are discussed. An experiment with a boiling potassium loop is described that demonstrates the techniques and in which voiding times of a few milliseconds were observed.

A survey of void measuring techniques by Gouse (1) shows that probes (2), radiation attenuation measurements using radioactive sources or x-rays (3, 4), and measurements of electromagnetic properties (4) have been used to determine the steady state void fraction in boiling liquid metals. The radiation attenuation methods seem to be the best for following void fraction changes. In particular, x-ray attenuation appears to be best suited for following the timewise variation in void fraction of boiling liquid metals because of the ready availability of sources of sufficient intensity to make accurate measurements on a short time scale. Measurements in the millisecond time scale would require prohibitively large radioactive sources. Probes may change the boiling characteristics of the system. Measurements of changes in electrical conductivity and magnetic permeability give a poor measure of void fraction (5).

The use of electromagnetic flowmeters for void measurements presupposes steady state flow.

II. DETERMINATION OF VOID FRACTION FROM X-RAY BEAM ATTENUATION MEASUREMENTS

General

X-rays (and gamma rays if not too energetic) are attenuated as they pass through matter in such a way that the decrease in the x-ray intensity with distance is proportional to the intensity:

$$\frac{dI}{dz} = \lambda I \qquad (1)^*$$

Where I is the x-ray beam intensity, z is the space coordinate in the beam direction, and λ is the attenuation coefficient which is a function of the material properties and the x-ray energy. For a uniform beam of monoenergetic x-rays which have passed through an attenuating material of thickness t, equation (1) may be integrated to give:

$$I = I_o \, e^{-\lambda t} \qquad (2)$$

Where I_o is the incident beam intensity and I is the transmitted beam intensity. When a broad x-ray beam passes through a material, the transmitted beam intensity is the sum of the transmitted intensities of the individual rays in the beam. The attenuation of each ray depends exponentially on the amount of material it traverses. Because of this the attenuation of the entire beam in a non-uniform material is not just a function of the void fraction, but it is also a function of the void distribution.

Consider an x-ray beam of rectangular cross section and width 2a, height 2b. Let a coordinate system with horizontal

*The special situations where this attenuation rate does not hold are not of interest here.

axis x, vertical axis y, and beam axis z have its origin at the center of the beam. The void fraction, α, in the portion of a channel which is traversed by the beam is given by:

$$1 - \alpha = \frac{1}{V} \int_{-a}^{a} \int_{-b}^{b} t(x,y)\ dxdy \qquad (3)$$

where V is the volume of the liquid-void mixture intercepted by the beam and t(x,y) is the total path in the liquid of a ray through (x,y). The attenuation due to the void is assumed to be negligible. Let S be the signal measured by a detection system which receives the transmitted beam and produces a signal k times the total number of x-ray photons intercepted per unit time. Then the signal in the absence of the liquid phase is:

$$S_o = 4abkI_o^* \qquad (4)$$

For a general liquid-void mixture:

$$S = k \int_{-a}^{a} \int_{-b}^{b} I(x,y)\ dxdy \qquad (5)$$

Substituting from (2) and (4), (5) becomes:

$$S = \frac{S_o}{4ab} \int_{-a}^{a} \int_{-b}^{b} e^{-\lambda t(x,y)}\ dxdy \qquad (6)$$

As a result of the non-linear parametric relationship between void fraction and measured signal, given by equations (3) and (6), measurement interpretation is not generally straight forward.

In cases where the liquid path length t is independent of x and y, such as in a homogeneous void distribution in a rectangular channel, the void fraction can be solved for exactly in terms of the measured signal. For example, if

*The attenuation due to the channel structure is taken into account in I_o.

$$t(x,y) = \ell \tag{7}$$

then equation (6) reduces to:

$$S = S_o\, e^{-\lambda \ell} \tag{8}$$

and for a channel of thickness T, equation (3) becomes:

$$1 - \alpha = \frac{\ell}{T} \tag{9}$$

this then gives:

$$\alpha = \frac{1}{\lambda T} \ln \frac{S}{S_o} + 1 \tag{10}$$

With the tube full of liquid (indicated by the subscript f)

$$\alpha = 0 \text{ and } \ln \frac{S_f}{S_o} = -\lambda T \tag{11}$$

Elimination of λT gives the result that

$$\alpha = \frac{\ln S/S_f}{\ln S_o/S_f} \tag{12}$$

LINEAR APPROXIMATION

For the general case where the void distribution is unknown, the void fraction cannot be determined exactly from the measured signal. However, under conditions for which the exponential attenuation is nearly linear, equations (3) and (6) can be solved to give a good approximation for void fraction in terms of measured signal. When the changes in void fraction about a reference measurement result in small enough beam attenuation changes, the exponential attenuation may be approximated by the first two terms of its power series representation. In many cases, experimental parameters can be adjusted such that the error in using this linear approximation does not increase the overall experimental error significantly. In this approximation, equation (2) becomes

$$I \approx I_o\,(1-\lambda t) \tag{13}$$

with a relative error approximately equal to $\frac{1/2\ \lambda^2 t^2}{1 - \lambda t}$.

Thus, when changes in λt are in the range of ± 0.2 from a reference value of λt, the relative error due to the linear approximation is less than 3% (see Figure 1).

When the linear approximation is valid, equation (6) becomes:

$$S \approx \frac{S_o}{4ab} \int_{-a}^{a} \int_{-b}^{b} \left[1 - \lambda t(x,y)\right] dxdy \qquad (14)$$

RECTANGULAR CHANNEL

For a rectangular channel of thickness T, equation (3) may be substituted into equation (14) to obtain the following relationship between void fraction and measured signal:

$$\alpha \approx \frac{1}{\lambda T} \left(\frac{S}{S_o} + \lambda T - 1 \right) \qquad (15)$$

As an illustration of the desirability of operating parameters such that the linear approximation is accurate, consider the extreme cases of void fraction distribution shown in Figure 2. The three test sections are viewed from above. They have 50% void ($\alpha = 1/2$) distributed in three different ways as shown. The void distribution is independent of position along the test section (independent of y). The void fractions are to be measured using a uniform x-ray beam of intensity I_o. Equations (3) and (6) give the following:

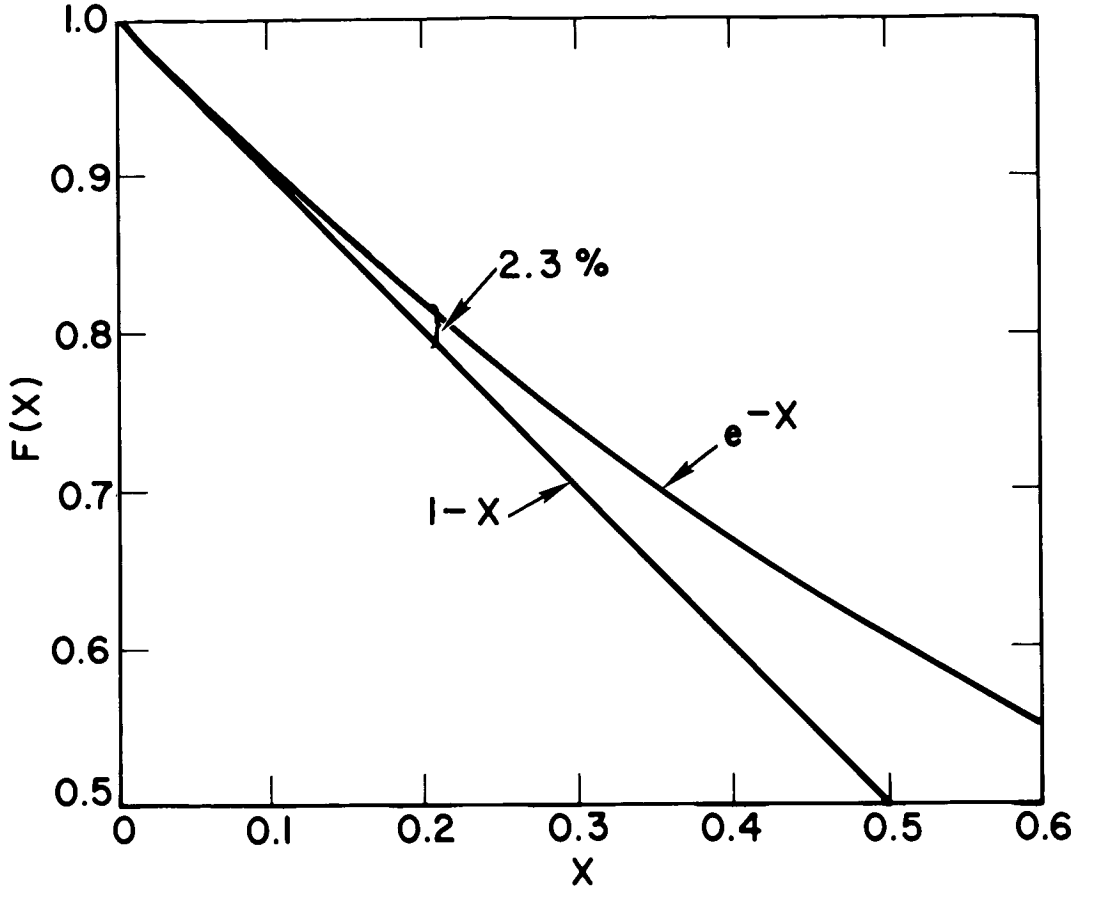


Fig. 1. Comparison of an Exponential Function with Its Linear Approximation

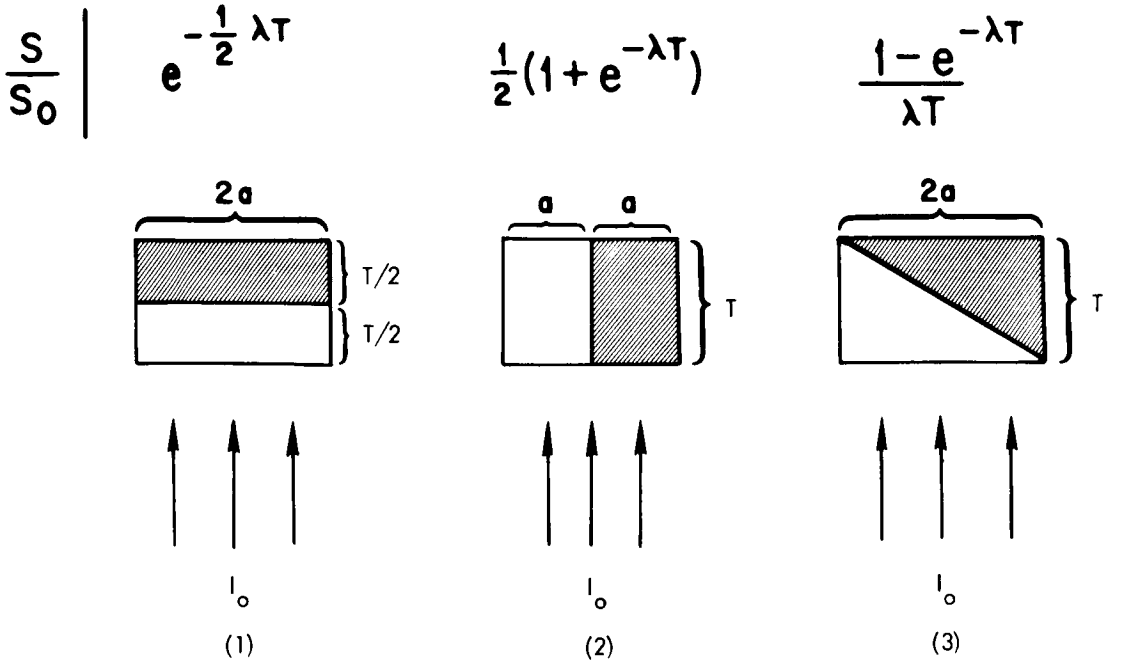


Fig. 2. Three Example Void Distributions with the Corresponding Expressions for the Attenuated X-Ray Signal

CASE No.	LIQUID PATH	TRANSMITTED INTENSITY OF RAY AT x	MEASURED SIGNAL ACROSS CHANNEL WIDTH
1.	$t(x,y) = \frac{T}{2}$	$I(x,y) = I_o e^{-\lambda T/2}$	$S = S_o e^{-\lambda T/2}$
2.	$t(x,y) = \begin{cases} 0 & -a<x<0 \\ T & 0<x<a \end{cases}$	$I(x,y) = \begin{cases} I_o \\ I_o e^{-\lambda T} \end{cases}$	$S = S_o \frac{1 + e^{-\lambda T}}{2}$
3.	$t(x,y) = \frac{T}{2a}(x+a)$	$I(x,y) = I_o e^{-T/2a(x+a)}$	$S = S_o \frac{1 - e^{-\lambda T}}{\lambda T}$

The measured signal is clearly different in each case. However, when λT is small enough that the linear approximation is permissible, the measured signal in all three cases is approximately:

$$S \approx S_o \left(1 - \frac{\lambda T}{2}\right).$$

Equation (15) for the void fraction then reduces to $\alpha = 1/2$.

TUBULAR CHANNEL

Similar considerations hold for cylindrical geometry. However, beam attenuation by the structural materials must be uniform over the beam area. Also, for beam widths greater than the mean bubble size, the linear approximation must be applicable at every chordal position in the beam. A uniform x-ray beam may be corrected for the cylindrical geometry by inserting a convex cylindrical attenuator made of tube

material into the beam so that the same path length in the tube material exists for every portion of the beam. When the tube walls are very thick, the additional beam intensity loss due to such a beam corrector may prove prohibitive. Scanning the tube with a narrow beam and referring measurements to a reference scan is one means of obtaining useful data without a beam corrector, but, the gain in transmitted beam intensity depends on the corrector and the beam size.

For a tubular test section of inside diameter 2a and length 2b, the void fraction is given by:

$$1 - \alpha = \frac{1}{2\pi a^2 b} \int_{-a}^{a} \int_{-b}^{b} t(x,y)\, dxdy \qquad (16)$$

Using the linear approximation, (14), for the measured signal with a rectangular collimator, (16) becomes

$$\alpha = \frac{2\frac{S}{S_o} - 2 + \lambda\pi a}{\lambda\pi a} \qquad (17)$$

Using the tube full of liquid as a reference, $\alpha = 0$ and $S = S_f$, equation (17) becomes

$$\alpha = \frac{S - S_f}{S_o - S_f} \qquad (18)$$

Using a reference measurement which is close to the average measured void fraction will improve the accuracy of the linear approximation. When the void fraction is to be

followed over the full range from 0 to 1, a reference calibration should be used for a void fraction of 1/2.

There are some measurement conditions for which the linear approximation is unnecessary. This occurs, as mentioned above, with a homogeneous void distribution. This is also true when the beam cross section is small enough that the void fraction doesn't vary appreciably across the beam width. This latter requirement appears to be fulfilled when the beam cross section is of the order of the mean bubble size.

When the change from one known void fraction distribution to another known distribution is all that is to be noted and intermediate distributions are of no concern, interpretation can be made directly on the basis of reference measurements at the initial and final void fraction distributions. The measurements reported in Section V are in this category since the transitions observed were between full and empty test sections.

DETERMINATION OF VOID FRACTION DISTRIBUTIONS

When measurements of local void fraction distributions are desired the channel must be scanned with a beam size which is smaller than the channel dimensions. If a strong enough source is available, the beam size can be made smaller than the average void bubble size. In this case, as mentioned above, the error due to void orientation becomes negligible. Void fraction can then be determined directly in terms of the measured signal without need of operating under the restrictions of the linear approximation. Scanning a channel with two x-ray beams at right angles makes it possible to reconstruct the three dimensional void distribution.

When a circular channel is scanned with one beam, the interpretation of the chordal void fraction measurements in terms of the actual local void fraction becomes a problem. If it is assumed that the spatial distribution of void fraction

is a function of distance from the tube center only, then the radial void fraction distribution, $\alpha_r(r)$, may be determined from measurements of the chordal distribution of void fraction, $\alpha_c(x)$, by the relationship:

$$\alpha_c(x) = \frac{1}{\ell} \int_{-\ell/2}^{\ell/2} \alpha_r(r)\, dz$$

where

r is the radial position coordinate
z is the position variable along a chord
$\ell(x)$ is the chord length

If α_r is approximated by the first few terms of an even polynomial in r, then α_r may be evaluated by integration.

$$\text{i.e. } \alpha_r = a_o + a_2 r^2 + a_4 r^4 + a_6 r^6$$

the coefficients a_i are found by evaluating the integral at a sufficient number of chords where the void fraction has been measured. The first few terms of the polynomial are sufficient since the measurements have limited accuracy. Where sufficient measurements are available, a least squares routine may be used to evaluate the coefficients. This method of finding the radial void fraction distribution from chordal measurements in circular tubes and annuli is similar to that used by Haywood, et al.[6], by Petrick[7], and by Schwarz[8].

III. MEASUREMENT ACCURACY AND SPACE AND TIME RESOLUTION

The accuracy with which a given signal change can be measured depends upon the magnitude of the signal change because of the constant value of electrical noise. Thus, maximum signal measurement accuracy is obtained by using the largest signal change feasible for a given void fraction change. However, the linear approximation requires that the signal change be no greater than about 20%. Therefore, a compromise is necessary in the choice of x-ray energy so that the total error is minimized.

A possible contributor to measurement error is the statistical uncertainty in the number of photons counted in a given time interval. The statistical uncertainty of a measurement of random events is equal to the square root of the average number of events in that measurement. Therefore, if a measurement is to be made in one millisecond with an accuracy of 1%, the required counting rate is 10^7 per second. Since void fractions are evaluated from intensity differences of the order of 10%, 1% accuracy in measured void fraction in one millisecond would require 0.1% accuracy in measured intensity or a counting rate of about 10^9 per second. Detection efficiencies less than one increase the number of quanta per second required from the source. Source strengths for making measurements at over 10^9 detected quanta per second are available in standard x-ray diffraction equipment. Measurements of the same accuracy using a radioactive source would require source strengths of the order of 10^4 curies. Radioactive sources with gamma ray energies which are compatable with the requirements for linearity and for sufficient signal change for the desired void change are useful for void measurements with steady state or slowly varying conditions in materials with high atomic numbers.

The counting rate of the detector is proportional to both the area and the intensity of the x-ray beam. Good spatial resolution requires small beam area and therefore high x-ray beam intensity.

Good time resolution requires that a sufficient number of x-ray photons be detected for the desired statistical accuracy in a time which is small compared to the time scale of void changes in the system. Time resolution can also be limited by detector and recording equipment frequency response.

The geometrical arrangement of source, test section, collimators, and detector has important effects on the overall measurement accuracy. The solid angle subtended by the detector as viewed from the two-phase liquid must generally be kept small, and the beam must be well collimated and shielded in order to avoid significant detection of scattered x-ray photons.

X-ray tube voltage ripple, fluctuation in amplification equipment gain, and thermal changes in test section attenuation and position are additional sources of error. The effects of x-ray tube voltage ripple can be removed by subtraction techniques if necessary. Signal integration over many cycles can be used if it doesn't seriously limit the time resolution. The effects of drifts in amplifier gains and in test section properties can be limited by frequent measurement of calibration strips.

IV. EFFECTS OF LIQUID METAL PROPERTIES ON X-RAY VOID MEASUREMENTS

The linearity conditions for λt can be realized for a given channel by an appropriate choice of x-ray or gamma ray energy. The variation of attenuation coefficients with photon energy for some liquid metals is shown in Figure 3 for the energy range between 10 and 1000 kev.[9] The dominant

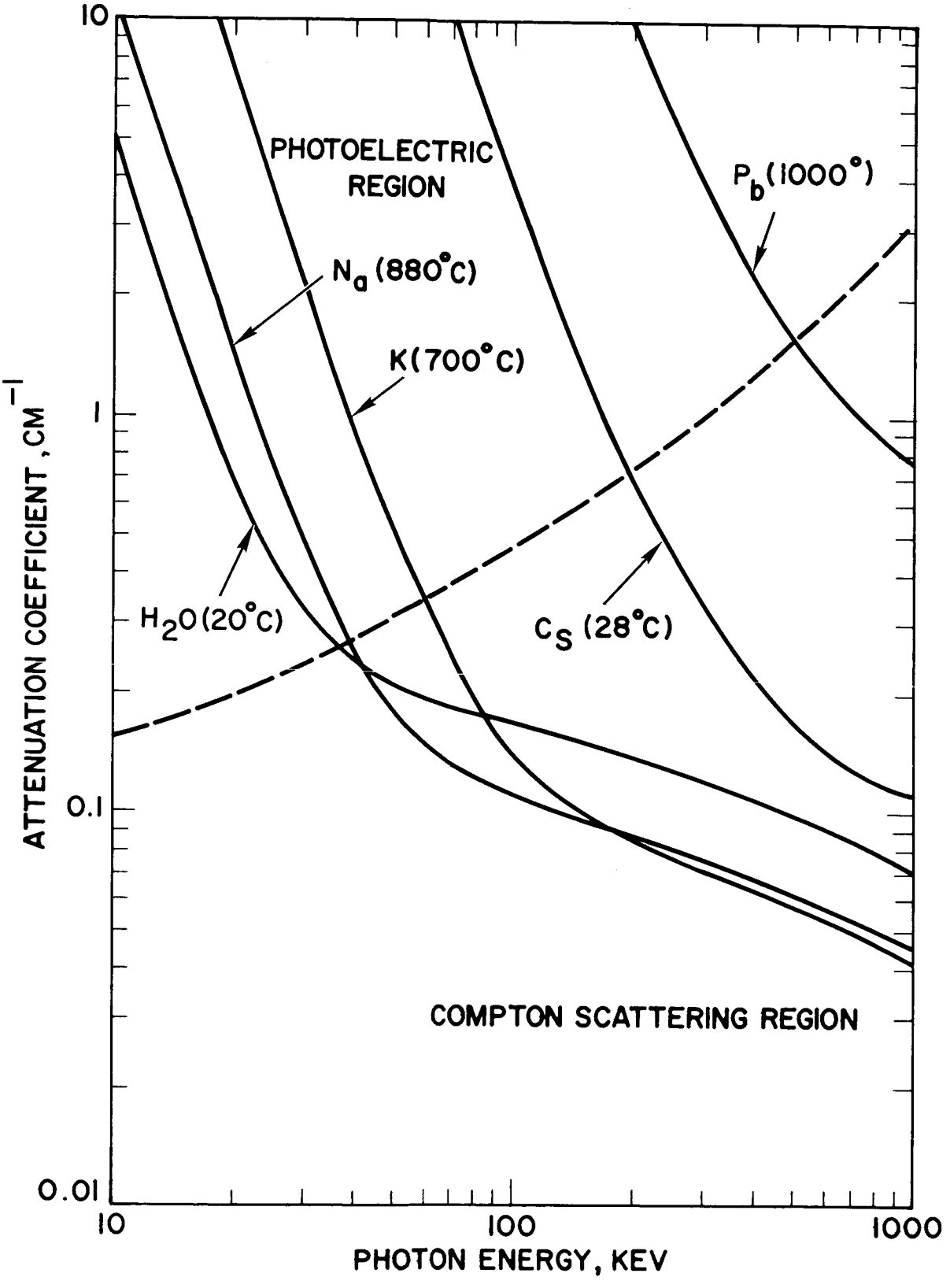


Fig. 3. Attenuation Coefficients versus Photon Energy for Several Liquid Metals at Elevated Temperatures and Water

attenuation process in the range above the dashed line is photoelectric absorption. In this range (but above the k edge energy) the attenuation is proportional to the fifth power of atomic number and varies with photon energy to the -7/2 power. In the region below the dashed line, the dominant attenuation process is Compton scattering which is directly proportional to atomic number and varies only slowly with energy. Electron-positron pair production is an additional attenuation mechanism above its threshold of 1.02 Mev. Because of the change of attenuation with energy, the x-ray beam used should be mono energetic enough that the transmitted energy spectrum does not vary significantly with the amount of absorber traversed. The mono energetic requirement is more restrictive in the photoelectric region than in the Compton scattering region.

It can be seen from Figure 3 that for measuring void fractions over the full range from 0 to 1 in an 0.8 cm thick channel, the optimum x-ray or gamma ray energies are 40 kev for sodium or water, 70 kev for potassium and 400 kev for cesium. Measurements cannot be made in the linear range when the above channel contains metals such as lead, mercury, or thallium since the attenuation coefficients for these metals are above about 0.4 cm^{-1}.

As can be seen from Figure 3, the attenuation characteristics of water are not much different from those of some of the liquid metals (e.g. sodium). For this reason many of the techniques for x-ray measurements in water are applicable to liquid metal systems.

Techniques for the measurement of voids in water have become well developed.[1] The system used in our laboratory utilizing the Molybdenum k_α x-rays of 17.5 kev has measured steam void fraction with an estimated standard error of 2% and detected relative void fraction changes of less than 2×10^{-3}[5, 10]. Due to the need for stronger test sections

for use with liquid metals at high temperatures, somewhat higher x-ray source intensities are needed for similar accuracies in liquid metal measurements. Otherwise, reference to Figure 3 shows that water and sodium have equivalent attenuation for 40 kev x-rays, and water and potassium are equivalent for 90 kev x-rays. Potassium, sodium, and lithium attenuate x-rays less than water in the Compton scattering region.

Using x-rays or gamma rays for measurement of void fractions in liquid metals with high atomic number requires sources with increasingly higher intensity and energy capabilities.

V. AN EXPERIMENTAL MEASUREMENT OF VOIDING RATES IN LIQUID POTASSIUM

A simple experiment was designed to demonstrate the x-ray measurement of void growth in boiling potassium. The apparatus, shown schematically in Figure 4, was charged with potassium so that the liquid level was in the two chambers above the U-tube. The space in the chambers above the potassium level was filled with nitrogen at one atmosphere pressure or less. Electrical heating tapes were used to maintain the liquid potassium at 200° C. The 1/4 in. o.d. stainless steel test section was heated by a two kilowatt induction heater. Wall thicknesses of .016 in. and .028 in. were used.

Tube wall temperatures, system pressure, and void fraction were monitored. The temperature measurements were made with 10 mil platinum-platinum 13% rhodium thermocouples. The system pressure was measured relative to atmospheric with a mercury manometer.

The bremsstrahlung beam (continuous spectrum) from an x-ray tube with a tungsten target was used for the void

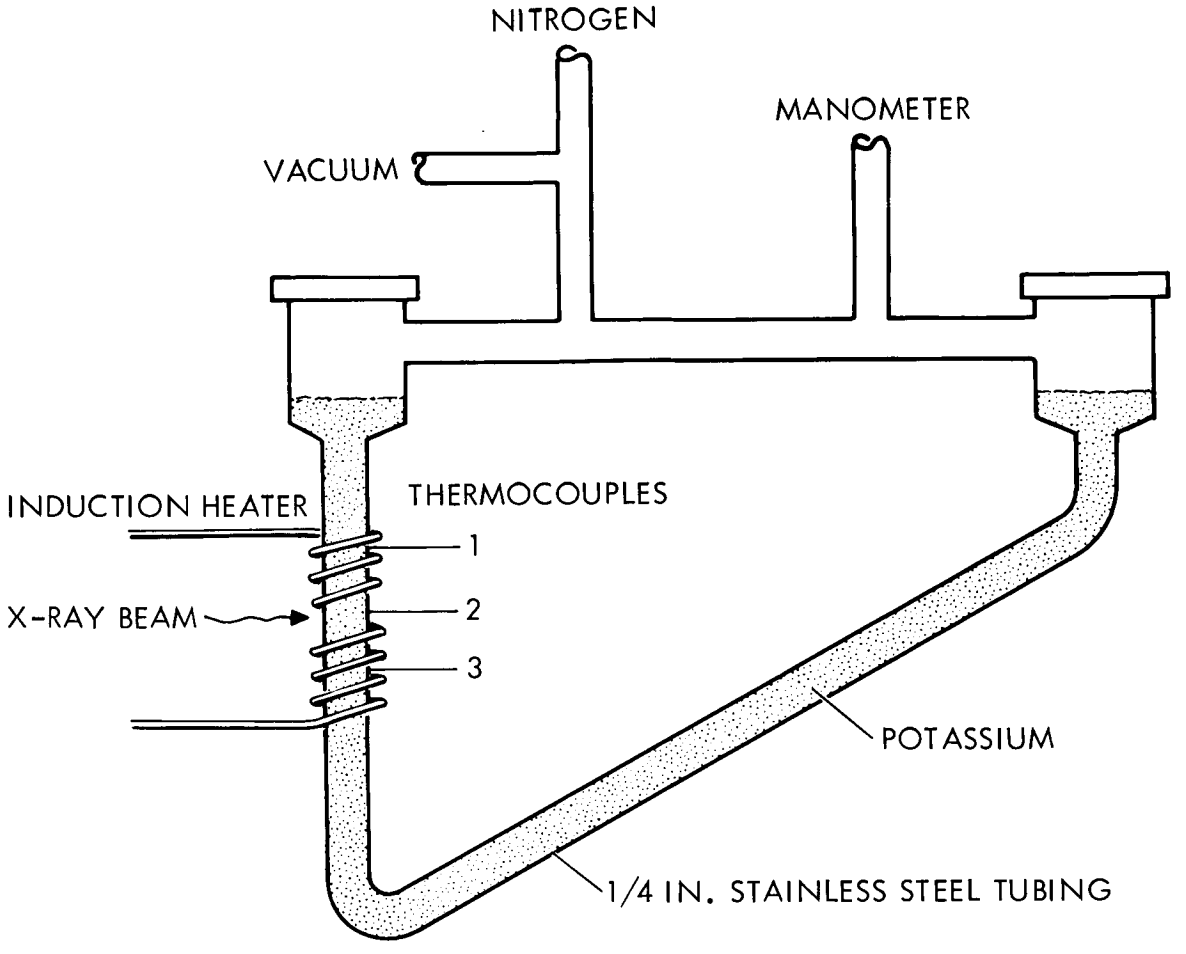


Fig. 4. Sketch of Experimental Apparatus for Demonstrating Transient Void Measurements in Liquid Potassium

measurements. The beam was collimated to a 0.1" x 0.2" rectangular cross section and then passed through the test section. The high voltage power supply for the x-ray tube was full wave rectified and filtered, but it had a ripple voltage of 8% peak to peak under the operating conditions of 40 kv and 10 ma electron beam current. Attenuation of the beam by filters and the tube walls resulted in a beam with a calculated maximum intensity at 37 kev and a full width at half maximum of 5 kev. A sodium iodide crystal viewed by a photo-multiplier was used to detect the transmitted x-ray beam. Individual counts were not resolved, but the photomultiplier tube output current was used as the detected signal.

Potassium near its boiling point has an attenuation coefficient of about 1.2 cm^{-1} at this energy. So the attenuation of a test section diameter of liquid potassium was $e^{.55} = 1.75$. This is beyond the range of linear attenuation, so that accurate measurement of intermediate values of void fraction between 0 and 1 were not possible with this system. In this experiment, however, we were only interested in full-empty voiding rates, so non-linear effects were unimportant. No tube wall thickness attenuation correctors were used.

The photomultiplier output was recorded simultaneously on a chart recorder at 10 mm/sec that had a 15 ms time constant and on an oscillograph at 50 in/sec that had a 1/2 ms time constant. The slower speed record was used to monitor general system behavior while the higher speed record provided rates and characteristics of the voiding.

About 10^8 x-ray quanta per second were detected. This would allow measurement of x-ray intensity in one millisecond to an accuracy of 0.3% at the quantum fluctuation limit, with a corresponding limit on void fraction accuracy under 1%. Such an accuracy was not attained in this demonstration experiment, however, because the emphasis was on voiding

rates and the errors from lack of compensation for tubular geometry, non- linear effects, calibration uncertainties, and thermal drifts were not reduced to the quantum fluctuation limit.

The experiments were started by turning on the induction heater. The test section wall temperature would then rise approximately linearly until nucleation occurred. At this time, the test section wall temperatures would drop suddenly by 30° C to 100° C, indicating the loss of superheat, and the test section would void. Subsequent void and temperature behavior would depend on the power level and pressure.

Figure 5 shows a recorder trace from a run at 1/2 atmosphere pressure and a heat flux of approximately 42,000 BTU/hr. $ft.^2$ The void fraction trace shows a linear drift during the heating period which indicates a decrease in the density of the potassium and the stainless steel wall that is consistent with the increase in temperature. Nucleation is evident from theabrupt change in x-ray transmission and the simultaneous temperature drop. The oscillograph recording of the x-ray signal showed that the beam area was voided in 4.5 milliseconds. Thus, potassium was expelled with a velocity of 100 cm/sec. After an interval of about 3 seconds at nearly constant temperature, the wall temperature began to climb rapidly. This is interpreted to be the result of complete drying of the test section wall. This run resulted in melting of a portion of the test section at a location between thermocouples 1 and 2.

At a higher pressure of one atmosphere and a heat flux of 50,000 BTU/hr. $ft.^2$ the initial voiding was followed by void collapse, as shown in Figure 6. This growth and collapse continued at a frequency of about 7.5 per sec until the experiment was stopped. The rate of void growth for the subsequent voiding was about the same, on the average, as for the initial bubble, a 4.5 millisecond risetime.

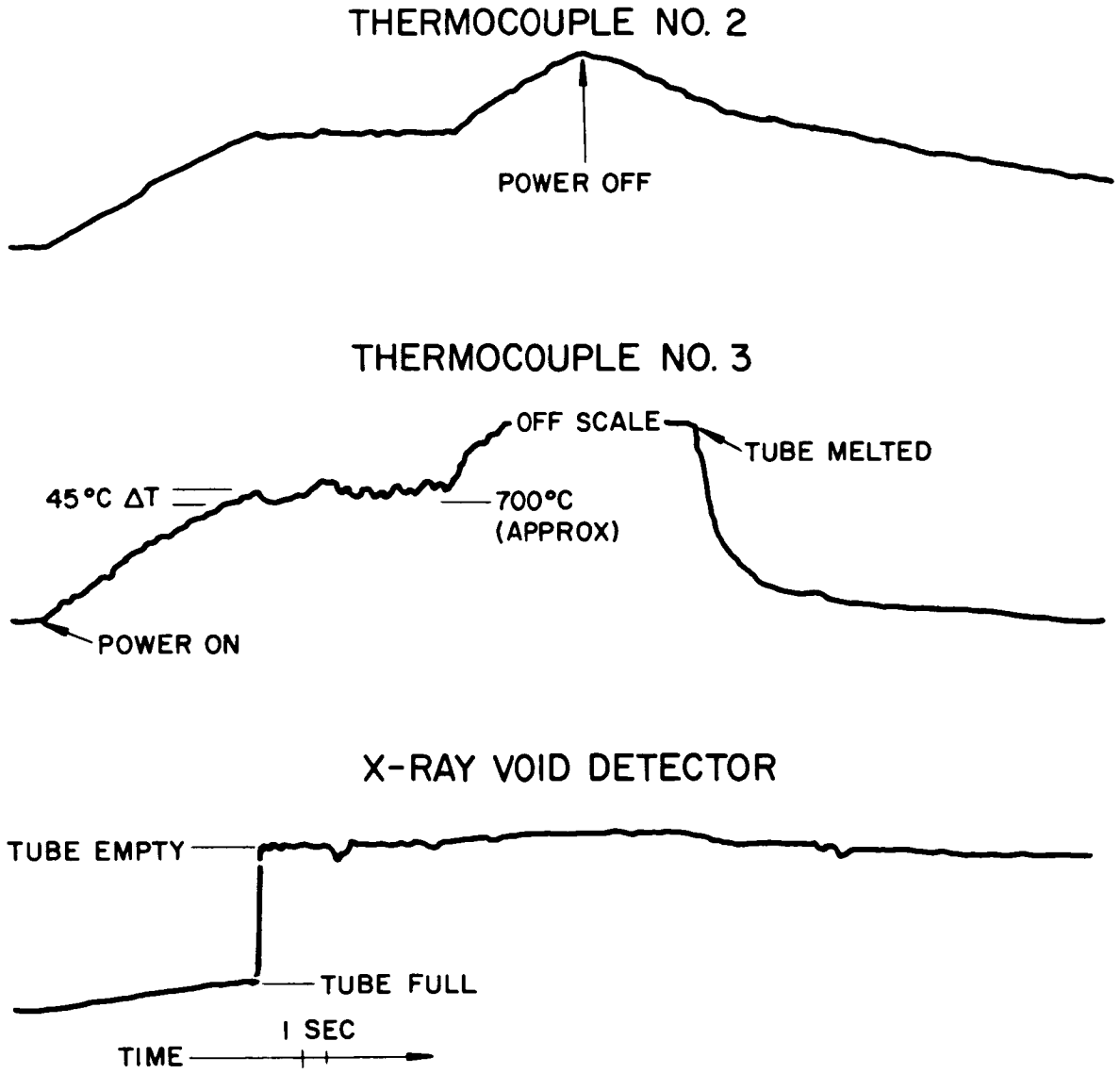


Fig. 5. Record of X-Ray Void Measurement and Two Thermocouple Traces during Boiling Expulsion of Potassium at 0.5 Atmospheric Pressure

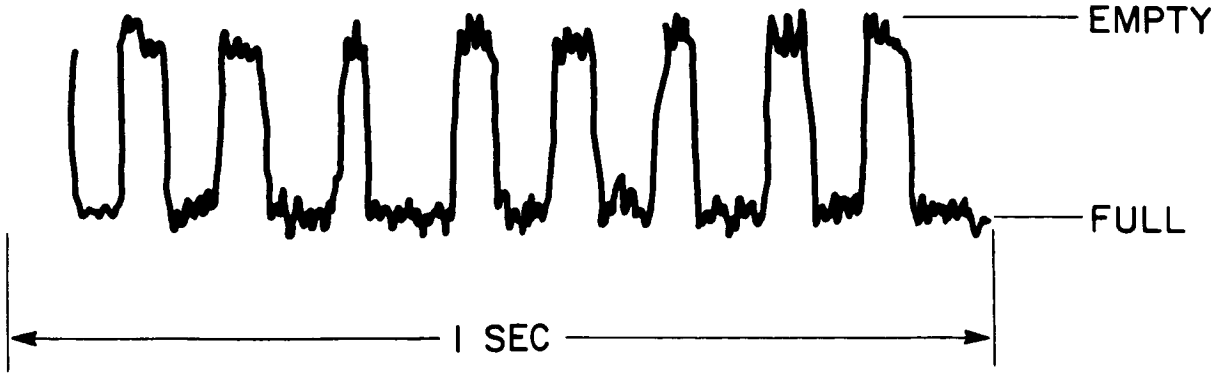


Fig. 6. Record of Periodic Voiding of Liquid Potassium at Atmospheric Pressure

However, the rise time varied with a standard deviation of 1 millisecond about the mean value of 4.5 millisecond.

VI. CONCLUSIONS

X-ray void fraction measurement techniques similar to those used in water are useful for void fraction measurements in liquid metal systems. Such measurements can be used to follow the rapid changes of void fraction which occur with boiling in liquid metals. Our experiment has shown that these changes occur in milliseconds.

Sodium and potassium have about the same x-ray attenuation coefficients as water over a wide range of energies, so the differences between them are mainly in boiling behavior. Potassium is somewhat more opaque to x-rays in the photoelectric region than water and sodium, but it becomes very similar to them above 100 kev. In liquid metals with high atomic number, such as mercury and cesium, prohibitively high energies may be required to stay within the linearity bounds stated above for measuring more than just small fluctuations about a reference void fraction.

Electronic system drifts must be considered in any given experimental situation when linearity and quantum noise limitations are low enough to permit high accuracy. With good equipment and frequent calibration, measurements in one millisecond with 3% uncertainty are possible. Space and time resolution are limited by the x-ray intensity available.

REFERENCES

1. S. W. Gouse: "Void Fraction Measurement," Massachusetts Institute of Technology, Report No. DSR 8734-2 (April, 1964).

2. L. G. Neal and S. G. Bankoff: "A High Resolution Resistivity Probe for Determination of Local Void Properties in Gas-Liquid Flow," A.I.Ch.E. Journal, 9, 490 (1963).

3. B. R. Adyanthaya: "Mercury Void Fraction Measurements Using a Collimated Gamma-Ray Beam," M. S. Thesis, University of Michigan, (June, 1961).

4. J. B. Heineman, J. F. Marchaterre and S. Mehta: "Electromagnetic Flowmeters for Void Fraction Measurement in Two-Phase Flow," Rev. of Sci. Instr., 34, No. 4, 399 (1963).

5. R. W. Wright: "Investigation of Methods of Void Measurement," Appendix A, 1959 Annual Summary Report, RWD-RL-167, Ramo-Wooldridge Division of Thompson Ramo Wooldridge Inc. (February 1960).

6. R. W. Haywood, G. A. Knights, M. A. Middleton and J. R. S. Thom: "Experimental Study of the Flow Conditions and Pressure Drop of Steam-Water Mixtures at High Pressures in Heated and Unheated Tubes," Inst. of Mech. Engrs. London, England (March, 1961).

7. K. Schwarz: "Investigations of the Distribution of Specific Gravity, The Water and Steam Velocities and the Frictional Pressure Drop in Vertical and Horizontal Boiler Tubes," V.D.I. Forschungs B.20, No. 445, 1 (1954).

8. Michael Petrick: "A Study of Vapor Carryover and Associated Problems," ANL-6581 (July 1962).

9. G. W. Grodstein: "X-ray Attenuation Coefficients from 10 kev to 100 Mev," National Bureau of Standards Circular 583 (April 30, 1957).

10. W. P. Ball, D. B. Langmuir and R. W. Wright: "X-ray Measurement of time Varying Steam Void Fraction in a Thin Water Channel," Trans. of ANS, 1, No. 2 (December, 1958).

N66 31681

INSTRUMENTATION FOR TWO PHASE METALLIC FLOWS

by

Richard E. Balzhiser

and

Lowell R. Smith *

Liquid Metals Laboratory
Department of Chemical and Metallurgical Engineering
University of Michigan

(Paper presented by R. E. Balzhiser)

ABSTRACT

Instrumentation for measuring pressure drop and void fractions in two phase metallic flows is discussed. A Taylor differential pressure gage was used to measure pressure drop over a 36-inch length of horizontal .495-inch tubing. Void fractions were determined at the center of this section using radiation attenuation techniques.

A thulium 170 source is used to provide a 0.084 Mev gamma ray for measurement purposes. A thallium activated NaI crystal is used for detection of the essentially monoenergetic beam. Problems in alignment at loop temperatures are cited as well as the importance of temperature control of the scintillator. The range of applicability for such measurements and results obtained will be discussed.

INTRODUCTION

In recent years metallic fluids have received consideration as possible heat transfer media in space electrical power generation cycles which involve boiling and condensing of the carrier fluid. The rigorous designs required in such applications necessitate the ability to make

* Pan American Petroleum Company, Tulsa, Oklahoma

PRECEDING PAGE BLANK NOT FILMED.

highly accurate predictions of two-phase flow phenomena. Although a voluminous literature exists on the subject of two-phase fluid flow, little has been reported on flow of metallic systems. The two-phase pressure drop along a tube in general is the summation of losses due to friction, acceleration effects, and hydrostatic head. Two-phase values usually are greater than those experienced in single-phase flows with comparable fluid throughputs. Frictional losses are always present and occur for any orientation of the flow channel and for adiabatic or heated conditions. Acceleration losses occur in forced-circulation boiling flows, where the continuous phase change causes the mixture density to vary along the tube. Such losses also occur in adiabatic flow at low pressure levels. Hydrostatic head terms are present only for vertical or inclined flow systems.

Knowledge of the mean two-phase mixture density is necessary in prediction of acceleration losses and hydrostatic head. In vapor-liquid flow, the mean velocities of the two phases, based on the cross sectional area of each, generally are not equal. Because of this "slip", the true fraction of the pipe cross section occupied by either phase differs from that calculated on the basis of the volumes of gas and liquid entering the tube. As a result, the mean mixture density cannot be calculated on the basis of quality (vapor mass fraction) alone, but requires a knowledge of the void fraction (fraction of the channel cross section occupied by vapor). Void fraction, then, is an important parameter in predicting the hydraulics of many two-phase flow systems, since without it the accelerative and hydrostatic contributions to the pressure drop cannot be evaluated.

Two phase flow studies were conducted in a specially instrumented test section incorporated within a forced circulation heat transfer loop. The loop was designed for use with molten alkali metals as the circulating fluids. A flow diagram of the system is shown in Figure 1. Liquid potassium flowed from the electromagnetic pump through the throttle valve, the magnetic flowmeter, and then entered the preheater where vapor was generated. The resulting two-phase mixture passed through the heat transfer section and the horizontal pressure drop test section. Flow continued through the condenser and into the hot well from which liquid was returned to the pump via the sub-cooler. The circuit was equipped with a liquid metal supply tank as well as valves and auxiliary lines for bleeding, pressurizing, venting, levelling, and draining.

In this study, potassium two-phase pressure drop and void fraction data were obtained from the test loop. Two-phase mixtures were generated in the preheater section, and the pressure drops were measured over a horizontal three-foot length of 0.495-inch ID tube. Mixture qualities within this test section were obtained by heat balance. Void fractions were measured at the middle of the pressure drop section using single-shot gamma-ray attenuation.

INSTRUMENTATION

Two-Phase Pressure Drop Measurement

Pressure drop data were measured over a horizontal 36-inch length of 0.495-inch ID Haynes-25 alloy seamless tubing with 0.065-inch wall.

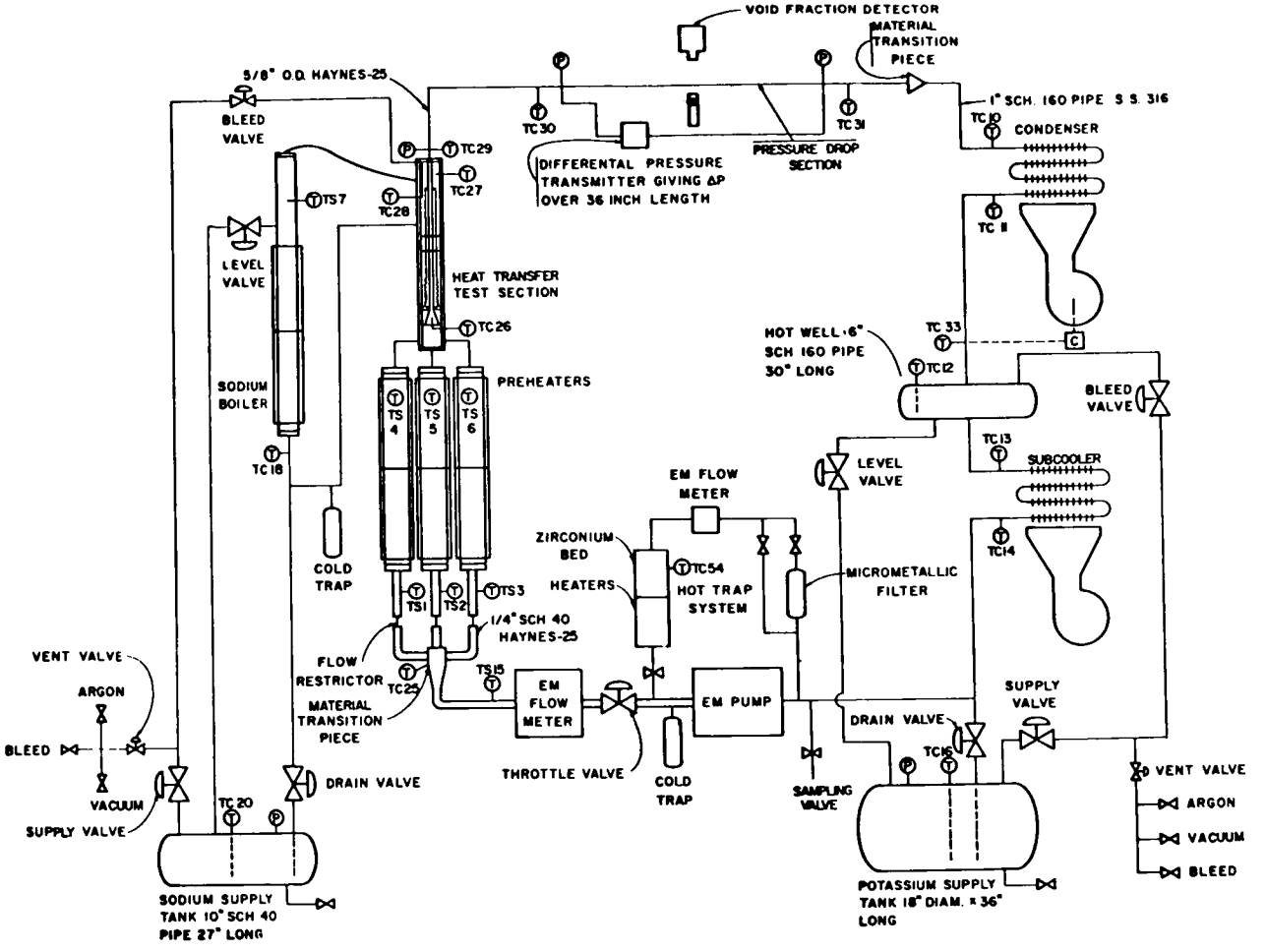


Fig. 1. Flow Schematic-Boiling Liquid Metal System

Fluid entered this section from a 10-inch horizontal calming section. The 4-inch long differential pressure taps were 1/4-inch schedule 40 Haynes-25 pipe nipples welded vertically to the bottom of the tube. Tap openings into the test section were about 3/16-inch diameter.

Pressure drop was measured with a Taylor Transaire Volumetric D-P Transmitter connected to a stainless steel pressure transmitting diaphragm assembly. The pressure transmitting fluid internal to the assembly was sodium-potassium eutectic alloy. The zero point of the transmitter exhibited a slight drift which was periodically checked and corrected. Data were recorded using Taylor Transcope Recorder. Values were accurate to one per cent of full scale, which was set at 100 or 300 inches of water.

Fluid temperatures were measured 10 inches upstream and 13 inches downstream of the inlet and outlet pressure taps, respectively. These well type thermocouples (TC 30 and TC 31) were located away from the ends of the test section to minimize their effect on flow patterns. These calming distances appear adequate in view of Richardson's observation (1) that sudden areal expansions caused no void fraction changes for air-water flow (α ranging from 0.30 to 0.80). Temperatures at the pressure taps were estimated from the thermocouple readings using the experimental pressure gradient and assuming thermodynamic equilibrium existed. Accuracy of the estimated pressure tap temperatures was shown to be better than 0.3 per cent for values above 1000°F (2).

Except at the point of void fraction measurement, the test section was covered with four inches of insulation to minimize heat losses.

Void Fraction Measurement

The theoretical basis of the gamma-ray attenuation technique for measuring void fractions has been reviewed elsewhere (1, 2). Although the mean two-phase fluid density in the region traversed by the radiation beam is sought, this value is not directly obtained in practice due to lack of appropriate absorption coefficients. The usual procedure is to obtain the void fraction by interpolation between detector signals read for single phase liquid and vapor flows. For the probable flow regimes encountered, it can be shown from Beer's Law that (1, 2)

$$\alpha = \frac{\ell n\ (N/N_\ell)}{\ell n\ (N_g/N_\ell)} \qquad (1)$$

Correct application of Equation (1) requires that all the count rates be observed at the same flow temperature. However, single values of N_g and N_ℓ at one temperature may be adjusted for use at all two-phase flow temperatures encountered (2, 3).

Source: Thulium-170 which decays by beta particle emission to Yb-170 yields two soft rays--a 0.053 Mev K X-ray and a 0.084 Mev unconverted gamma ray (2). Equation (1) assumes the radiation is monoenergetic, but since the low energy photons were almost completely absorbed by the pipe wall the detector saw primarily the 0.084 Mev radiation.

Myers (4) discussed in detail the reasons for choosing Tm-170 as the gamma-ray source. It was necessary to obtain an isotope with a sufficiently long half-life to insure essentially constant source strength during any one experimental run. The 127-day half-life of

Tm-170 meets this requirement, although it is short when considering experimental operations over several months. In long range use, however, corrections can be made for the decay. In addition to half-life considerations, the photon energy and approximation to monoenergeticity were examined. The density ratio of the potassium vapor-liquid system is in about the same range as for the air-water system. This fact suggested choosing a low energy gamma emitter which would allow detection of small changes in mixture density. However, if a photon too low in energy were chosen, the constant attenuation due to the channel wall would lower the emergent intensity below detection level and also damp out sensitivity. Myers' predictions (4) showed that for photon energies lower than about 60 Kev the tube wall attenuation would require using an unreasonably large source. On the other hand, for energies greater than 100 Kev the sensitivity in the potassium would suffer. These considerations, together with others discussed by Myers (4), led to the choice of Tm-170, which has a photon in the desirable energy range. For safety reasons, a beta decay source was preferred over an alpha decay type.

A nominal 10-curie Tm-170 source was purchased from Atomic Energy of Canada Limited (Ottawa). Preliminary calculations indicated that this strength was higher than necessary and could even lead to scaler overloading. Since experimental difficulties and delays were anticipated, it seemed wise to obtain the highest possible activity per unit cost. Excess strength was handled through collimation and shielding.

The source supplied by Atomic Energy of Canada had a strength of 9.8 curies when obtained. At the time of the potassium void fraction runs, the source strength was about 4.7 curies. The source is composed of metallic thulium and is encapsulated in stainless steel.

Detection Equipment: The schematic diagram of Figure 2 indicates the counting equipment which was employed. Scintillation detection was chosen over Geiger-Muller or proportional detection because of negligible dead time correction and high intrinsic counting efficiency.

The detector unit is an "Integral Line Assembly" produced by the Harshaw Chemical Company. It consists of a 1 1/2-inch diameter by 1-inch thick, thallium activated, sodium iodide crystal coupled optically to a 2-inch photomultiplier tube. The assembly includes an external magnetic shield to minimize the effects of the various electric and magnetic fields present near the potassium test loop. The assembly obtained has a pulse height resolution of 8.3 per cent at 661 Kev photon energy. The Harshaw literature (5) furnishes dimensions of these assemblies.

Physically, the detection of gamma radiation by the scheme in Figure 2 is as follows. When a photon impinges on the NaI(Tl) crystal, the interaction in the crystal yields a flash of light. This light flash is picked up by the photomultiplier tube which converts it to a low level current pulse. This pulse must be amplified before it can traverse a cable and furnish a signal to the scaler. The preamplifier

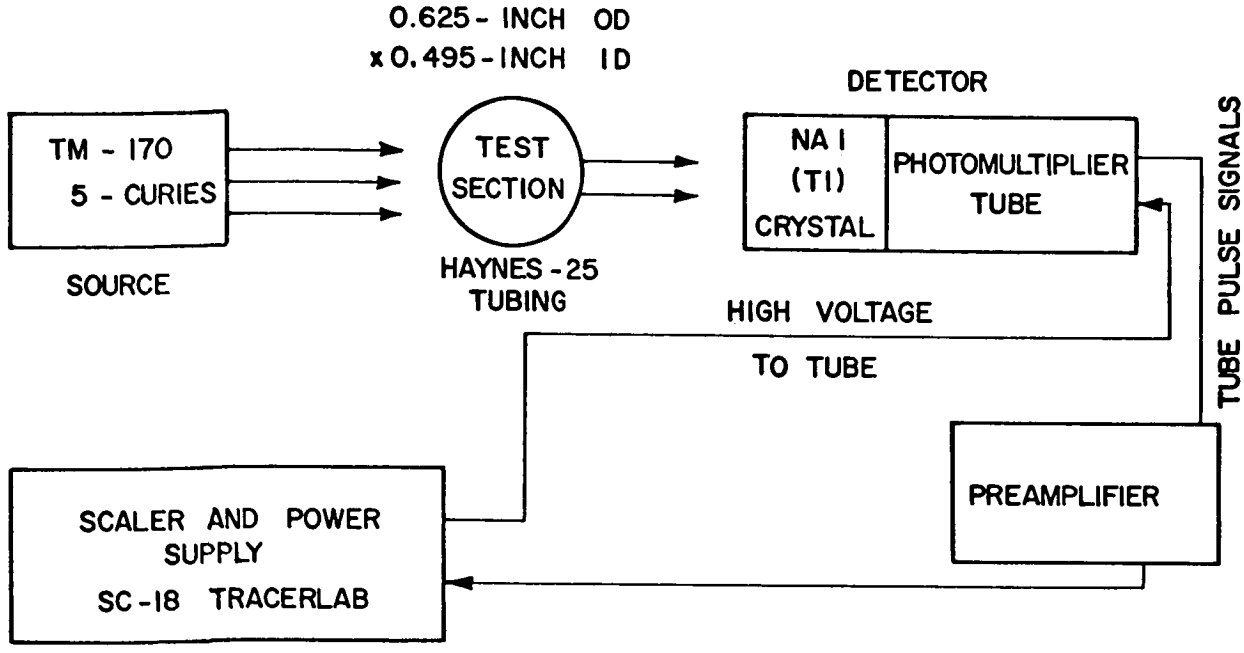


Fig. 2. Schematic Diagram of Void Fraction Measuring System

provides the necessary amplification which has a high degree of linearity. The scaler, a Tracerlab SC-18 Superscaler, has a discriminator which may be set to accept voltage pulses from the preamplifier only when the signal is above a minimum value. The discrimination is necessary to eliminate effects due to amplifier and phototube noise. In the potassium experiments, the discriminator was set at 0.25 volt. For every current pulse accepted by the discriminator, a count is registered by the scaler. Obviously, some photon interactions in the NaI(Tl) crystal are so weak that the amplified pulse is rejected by the discriminator. Thus, not every gamma photon striking the crystal produces a count.

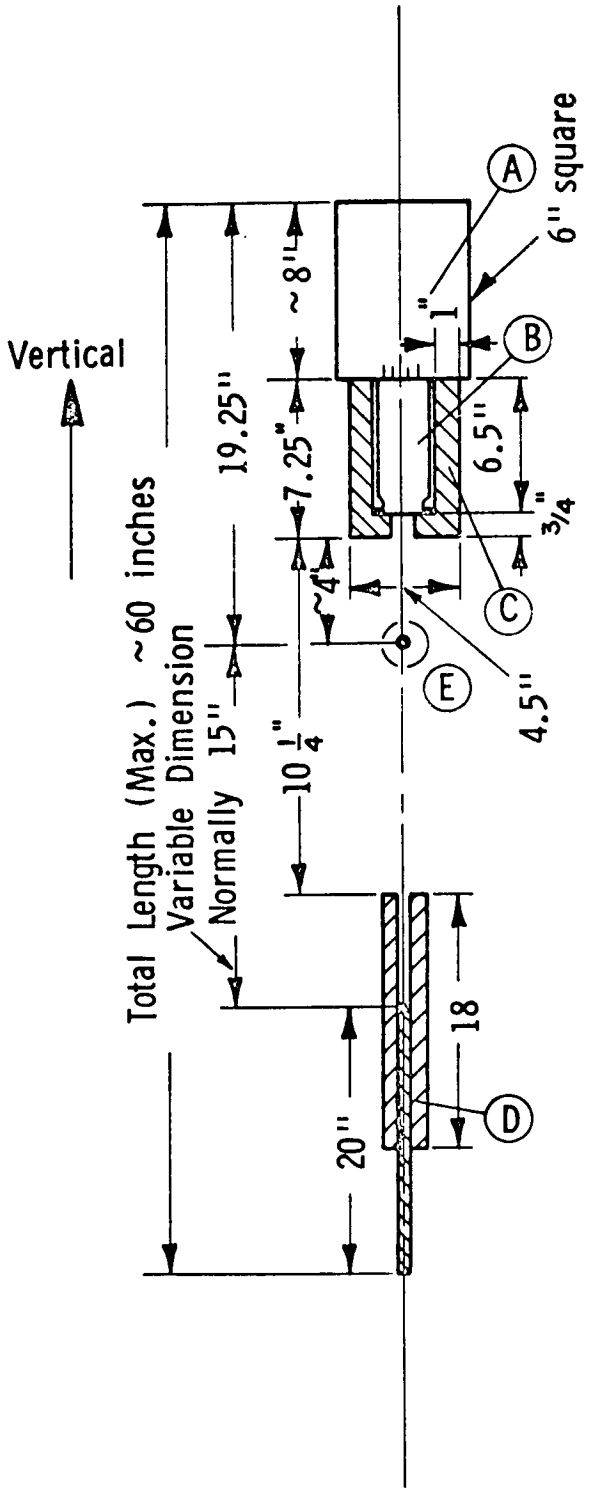
Before concluding this discussion of the detection equipment, mention should be made of its efficiency. The resolving time of the photomultiplier tube is about 0.25 microsecond (5). Inorganic scintillation crystals such as NaI(Tl), due to their high density, have a high stopping power and consequently a greater counting efficiency for gamma rays than do gaseous detectors. The alkali halides--particularly NaI(Tl)--have the added advantage of high light output, transparency, and suitable refractive index. The high atomic number of inorganic scintillators aids in photon conversion.

The theoretical absorption coefficients of NaI(Tl) for gamma rays having energies ranging over three orders of magnitude are available (5). Using these coefficients, the theoretical efficiencies of crystals of

various thicknesses can be obtained as a function of gamma energy. These theoretical or "intrinsic" efficiencies depend on source-to-crystal distance. They do not account for absorption by the crystal container or for the fact that only a fraction of the total interactions in the crystal are counted. (This latter factor depends on the scaler's discriminator setting.) Price (6) presents intrinsic efficiencies for 1 1/2-inch diameter by 1-inch thick NaI(Tl) crystals. For the source-to-detector distances suggested in Figure 3 and for the low energy radiation employed, the theoretical detection efficiency approaches unity. Although actual detection efficiencies cannot be this high, one can confidently assume that they were greater than 0.50 and perhaps as high as 0.80.

Shields and Collimator: In the interest of personnel protection it was necessary to shield the Tm-170 source. The shielding employed was such that the narrow working beam approximately 1/32-inch in diameter impinged unhindered on the flow channel but radiation in all other directions was substantially reduced. The detector was also shielded in order to minimize the effect of background radiation on the count rate.

The source has an end output of 4.5 mr/hr at 1 meter per curie. This strength includes Bremsstrahlung radiation. Figure 3 shows the shields for both source and detector and indicates the method of varying the source-to-detector distance by adjusting the location of source inside the shield by means of the positioning rod.



Key

A Preamplifier

B Harshaw Integral Line Scintillation Crystal & Photo-multiplier Tube, Type 6S4/E

C Steel Shield for Phototube, ~23 lbs.

D Source Shielding & Positioning Components ~21 lbs. Rod threaded to take source.

E Haynes 25 Tube 0.495-in. ID with 0.0625-in. wall

Fig. 3. Layout of Void Fraction Measuring Apparatus

The source shield was designed assuming that all the radiation is of 0.084 Mev energy, which was believed to allow considerable safety factor. Moreover, the design was based on a 10-curie strength. Even though these design precautions were taken, it was found that the steel tube did not stop the gamma rays as effectively as planned, and a 1/2-inch thickness of lead sheet was fastened around the steel tube during the experiments. Even before the lead was added, however, the dose rate in the loop control room was well within the acceptable safe limit.

Flow Rate Determination

Flow rate was controlled by varying the applied voltage to the pump or by regulating the throttle valve. Mass velocities varying up to 5.3×10^5 lb./(hr.)(sq. ft.) were achieved in the test section. Flow rates were measured with a MSAR Style FM-2 magnetic flowmeter.

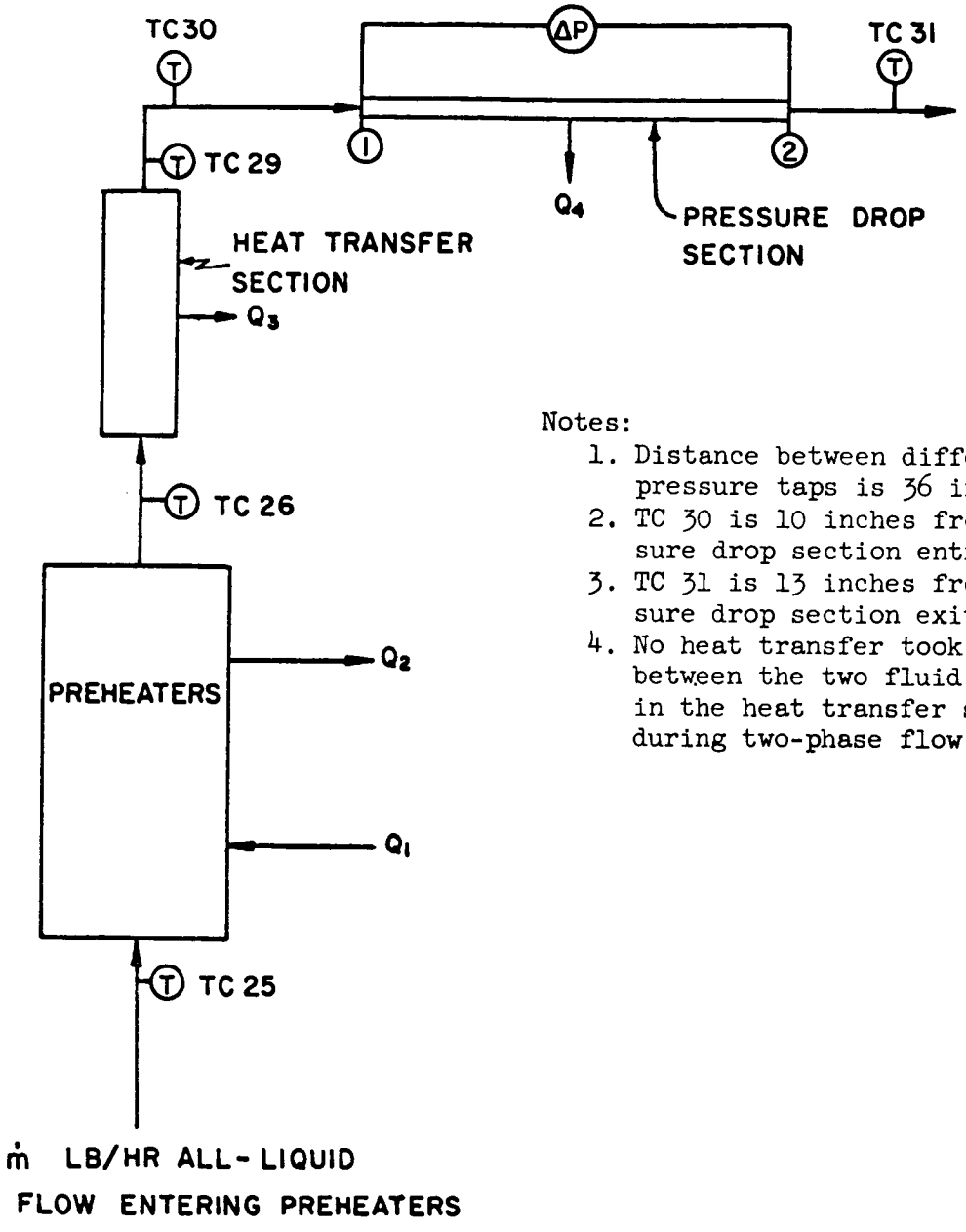
Theoretically derived calibration curves for pure potassium and sodium were furnished by the manufacturer. Prior to initiating the two phase studies the meter was calibrated by filling a known volume in the loop while maintaining a constant millivolt signal on the flowmeter. At 325°F the average of eight determinations indicated the curve provided by MSAR was within 1.7% of the measured values. Considering the accuracy with which temperature and millivolt signals could be read within the flowmeter, it was concluded that flowrates were known with an accuracy of $\pm$ 3% at low flow rates and $\pm$ 1% at high flows.

Quality Determinations

Qualities are measured by applying the energy balance to that portion of the loop shown in Figure 4. Q_1 represents the power supplied to the preheaters and is read directly from a wattmeter. Q_2, Q_3 and Q_4 represent heat losses from the preheaters, heat transfer test section, pressure drop test section and connecting piping. These values are determined by operating the loop in single phase flow at the temperature levels of interest. Heat losses can be determined by measuring the temperature changes on TC 25, 26, 29, 30 and 31 in combination with the flowrate and heat capacity data. These losses were plotted with respect to the fluid temperature.

Equilibrium was assumed to exist between liquid and vapor which in view of the mixing that occurs at the inlet to the heat transfer test section and again at the right angle bend above the test section should be a reasonably good assumption. Qualities within the pressure drop section were calculated by using the conditions at TC 30 and 31 as a base point from which to calculate changes over the test section. The pressure gradient measured in the test section was assumed to be constant over the length of pipe between TC 30 and 31.

The values obtained had an estimated accuracy of $\pm$ 5% at qualities above .04. At lower qualities the uncertainty increased rapidly.



Notes:

1. Distance between differential pressure taps is 36 inches.
2. TC 30 is 10 inches from pressure drop section entrance.
3. TC 31 is 13 inches from pressure drop section exit.
4. No heat transfer took place between the two fluid circuits in the heat transfer section during two-phase flow runs.

Fig. 4. Diagram of Open System Used in Quality Calculations

EXPERIMENTAL RESULTS

Two-Phase Pressure Drop Results

A typical section of the Taylor Transcope Recorder chart showing pressure drop and flowmeter traces is given in Figure 5. The section shown is for a flowmeter output of about 4 millivolts (490 lb./hr.) and 18.5 KW preheater power. These values produced an average quality in the test section of 0.0586. The pressure drop here was recorded in the 0-300 inches of water range, with the transmitter zero at 30 per cent of full scale. The mean pressure drop shown corresponds to 2.38 psi.

For most of the data reported, the pressure drop fluctuated regularly about a mean value. This mean value is reported as the value of the pressure drop. The pressure drop fluctuations were accompanied by oscillations in the flow rate, also recorded on the Taylor chart during most of the experimental operation. The data reported in this study were obtained for steadiest possible flow conditions--i.e., at conditions of zero or minimum flow rate fluctuations. A total of 226 pressure drop values were obtained. Table I indicates the ranges of the pertinent parameters achieved during the studies.

The differential pressure fluctuations were greatest at high preheater power levels and low pumping rates. Superheating of the liquid in the preheater is believed to be the explanation for this trend. At low flow rates the liquid moved into the preheater with little disturbance and the high power level caused it to superheat as it "crawled"

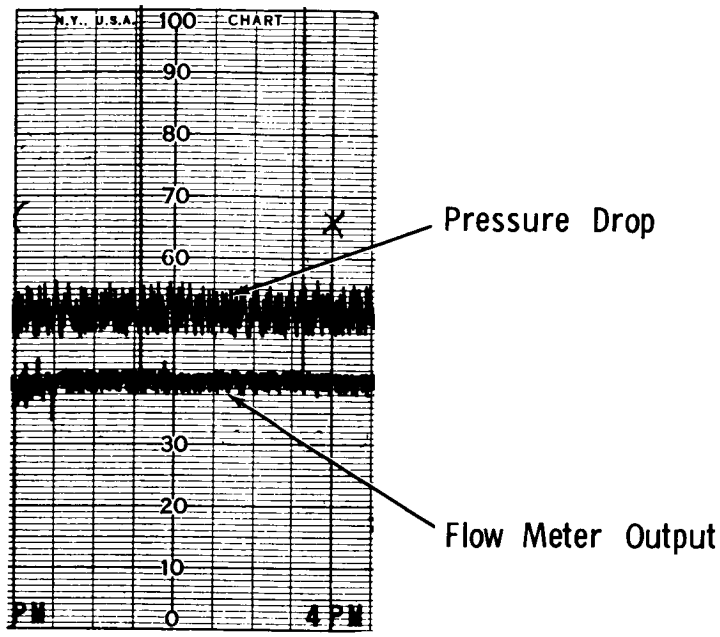


Fig. 5. Typical Section of Taylor Transcope Recorder Chart, Showing Pressure Drop and Flowmeter Traces

TABLE 1.

Range and Uncertainty of Experimental Quantities - Two-Phase Flow of Potassium

Two-Phase Pressure Drop Data

	Range	Uncertainty
Number of Data Points	226	
Pressure Drop, lbf./sq. in.	0.054 to 3.10	0.05 (maximum)
Total Mass Flow Rate, lbm./hr.	108 to 752	3.% (maximum)
Inlet Pressure, lbf./sq. in. abs.	0.54 to 15.8	0.03 (max at 1000°F)
Inlet Temperature, °F	923 to 1428	4 (max. at 1000°F)
Inlet Quality	0.0004 to 0.3788	Depends on quality level (1) 0.003 at x = 0.05
Average Quality	0.0065 to 0.3784	Depends on quality level (1) 0.003 at x = 0.05
Quality Change across Section	-0.0051 to +0.0312	Depends on quality level (1) 0.003 at x = 0.05

upward. More or less periodically a sudden nucleation occurred, producing a large volume of vapor which pushed a liquid slug up through the heat transfer section and through the pressure drop section. This surge is evidenced by a fluctuation in the pressure drop and flow meter traces, the latter being due to the sudden generation of vapor in the preheater.

After completion of two-phase runs, three all-liquid pressure drop values were obtained. These runs provided a check of the instrumentation and permitted a comparison of the two-phase data with the Lockhart-Martinelli correlation (7). The fact that only three points were taken over a narrow flow rate range is due to the test section's inclination of 3 degrees. At lower all-liquid flow rates the tube does not flow full.

In addition to quality and total flow rate, it was found that average test section pressure is of primary influence on two-phase pressure drop. The absolute pressure gauge at the outlet of the heat transfer section did not function satisfactorily throughout the two-phase flow runs. In the early runs the pressures indicated by the gauge compared favorably with equilibrium pressures corresponding to readings from TC29. Soon, however, the calibration changed and was not re-established. Both the zero and span of the pneumatic transmitter behaved erratically. Pressure levels in the pressure drop section were therefore taken as equilibrium vapor pressures at the test section temperature.

Figure 6 shows the scatter obtained when the Lockhart-Martinelli correlation (7) was attempted. Similarly poor results were obtained using the Bankoff (8) and Bertuzzi, Tek and Poettmann correlations (9). A two phase friction factor was defined using the vapor density which produced the best correlation of pressure drop with respect to quality, pressure and flow rate of the various procedures tried. Diameter was not varied and thus the adequacy of the resulting correlation, $f = 0.0138\ x^{1.54}$, could not be assessed. Figure 7 compares the best fit for the potassium data with the predictions of Lockhart-Martinelli (7) and Bertuzzi, Tek and Poettmann (9).

A few experiments on two-phase flows of metallic systems have been reported (10), but either the flow characteristics involved, the system geometries, or the method of data presentation precluded comparison with the results of this study. The only metallic pressure gradient and liquid fraction data for which a valid comparison could be made are the horizontal isothermal mercury-nitrogen results of Koestel (11). The pressure gradient data are compared with the potassium correlation in Figure 8 which shows very favorable agreement between the two fluid systems. This agreement, as compared with disagreement between the potassium and nonmetallic systems, suggests that some fundamental difference exists in pressure drop behavior between metallic and nonmetallic two-phase fluids.

Void Fractions

Figure 9 shows the void fraction results using the Martinelli

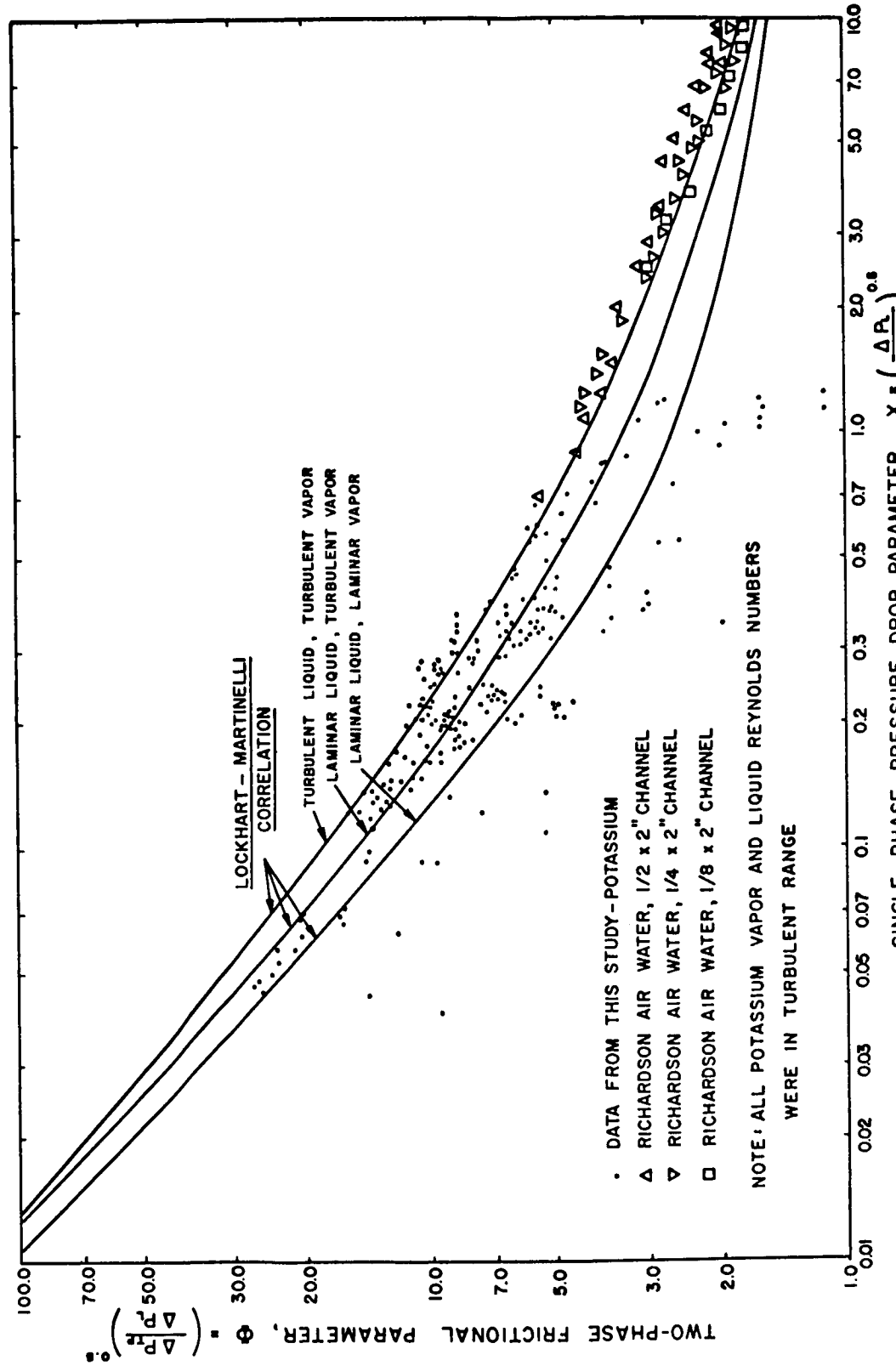


Fig. 6. Martinelli Type Plot of Potassium Two-Phase Frictional Pressure Drop Data

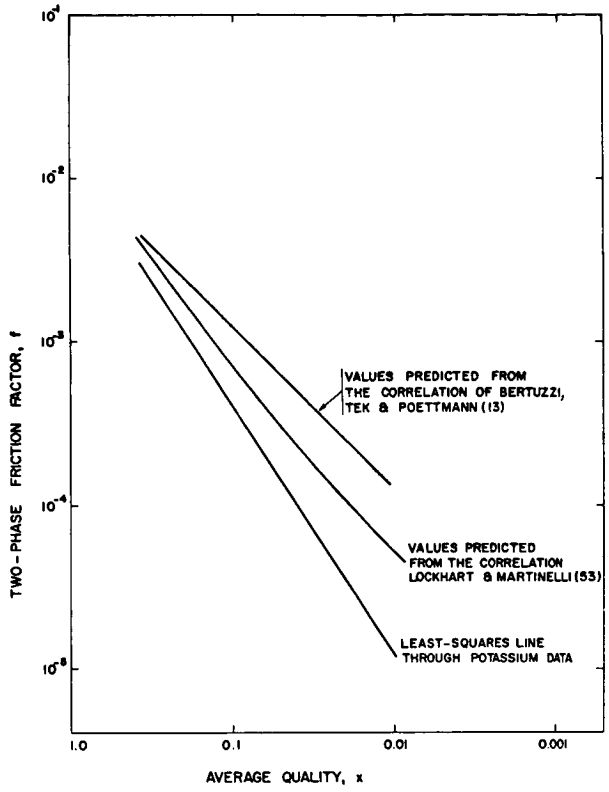


Figure 7

Comparison of Potassium Results with Values Predicted by Correlations of Lockhart and Martinelli (7) and Bertuzzi, Tek, and Poettmann (9)

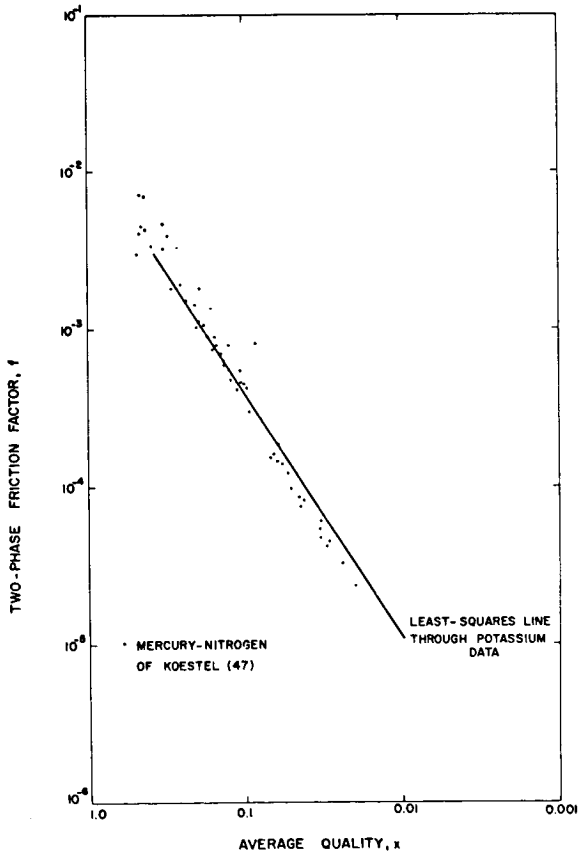


Figure 8

Comparison of Potassium Two-Phase Pressure Gradient Correlation with Mercury-Nitrogen Data of Koestel (11)

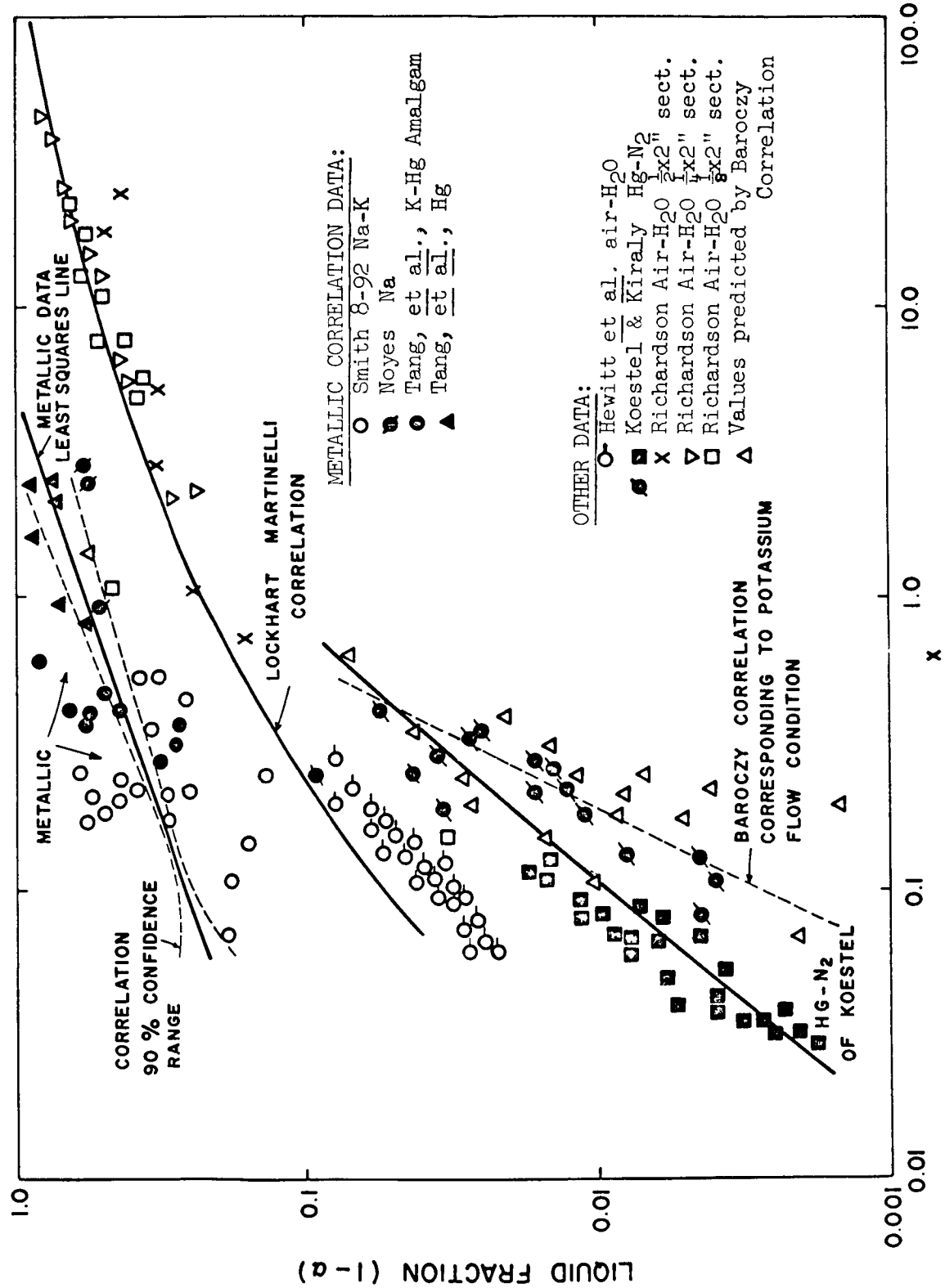


Fig. 9. Metallic Liquid Fraction Correlation Compared with Other Data and Correlations

parameter, $X = \frac{(\Delta P/\Delta L)_\ell}{(\Delta P/\Delta L)_g}$, to correlate the data. Seventeen points were obtained over the parameter ranges cited in Table II. As suggested in the figure the data scattered appreciably. However, as shown it appeared to concur with the mercury and potassium-mercury data of Tang, Smith and Ross (12) and the sodium data of Noyes (13) in yielding much lower void fractions (higher liquid fractions) than nonmetallic fluids. Only Koestel's mercury-nitrogen data (11) deviated from this behavior for metallic flows. However these studies were conducted in glass tubing where wetting definitely did not occur which might explain the discrepancies.

The slips corresponding to these void fractions were much higher than those ordinarily experienced with nonmetallic flows. No explanation other than the possible effect of wetting is offered at this time.

EFFECTIVENESS OF INSTRUMENTATION

The results cited definitely suggest that two phase metallic flows may exhibit behavior substantially different from nonmetallic fluids. Difficulties in instrumenting test sections definitely handicaps the investigator in his efforts to predict quantitatively the behavior in such systems. An analysis of the results to data suggests that conventional methods used to predict flow regimes for two phase mixtures (such as those proposed by Baker (14) and Ros (15)) are not applicable in metallic flows. However the extreme conditions under which two phase alkali metal flows are obtained makes it

TABLE 2.

Void Fraction Data

	Range	Uncertainty
Number of Data Points	17	
Total Mass Flow Rate, lbm./hr.	131 to 749	3.% (maximum)
Average Temperature, °F	879 to 1320	4 (max. at 1000°F)
Average Quality	0.0172 to 0.1647	Depends on quality level 0.003 at x = 0.05
Void Fraction	0.153 to 0.860	Variable - See Fig. 7 0.056 Average Standard Deviation

extremely difficult to study the flow patterns. Direct observation is virtually impossible and it appears necessary to utilize either gamma ray attenuation or a probing technique.

The single shot technique used here cannot distinguish between stratified or annular flows. If the beam could be rotated about the tube such distinction could likely be made. The large slip ratios suggested by these studies resulting from the large liquid fractions strongly suggests stratified flows inspite of the Baker and Ros predictions. The fluctuating flow rates and pressure drops would also be more likely for wavy, slug or plug flows than for a uniform annular flow.

Studies of this type would certainly b e nefit from a vapor generator in which instabilities were less pronounced. Subsequent operation and the insertion of nucleating devices in the preheaters have helped eliminate this difficulty.

Techniques for measuring flow rate proved quite adequate and the errors of from 1% - 3% in flow rate were tolerable. Quality determinations, although within 5% at qualities above .04, were subject to large errors at the low end of the range studied. Apparatus which incorporates a second stream, monitored separately, which is converted to vapor upstream of the test section could perhaps improve this limitation.

The radiation attenuation techniques used for void fraction measurements become useless at qualities above .15 - .2 as shown in Figure 10.

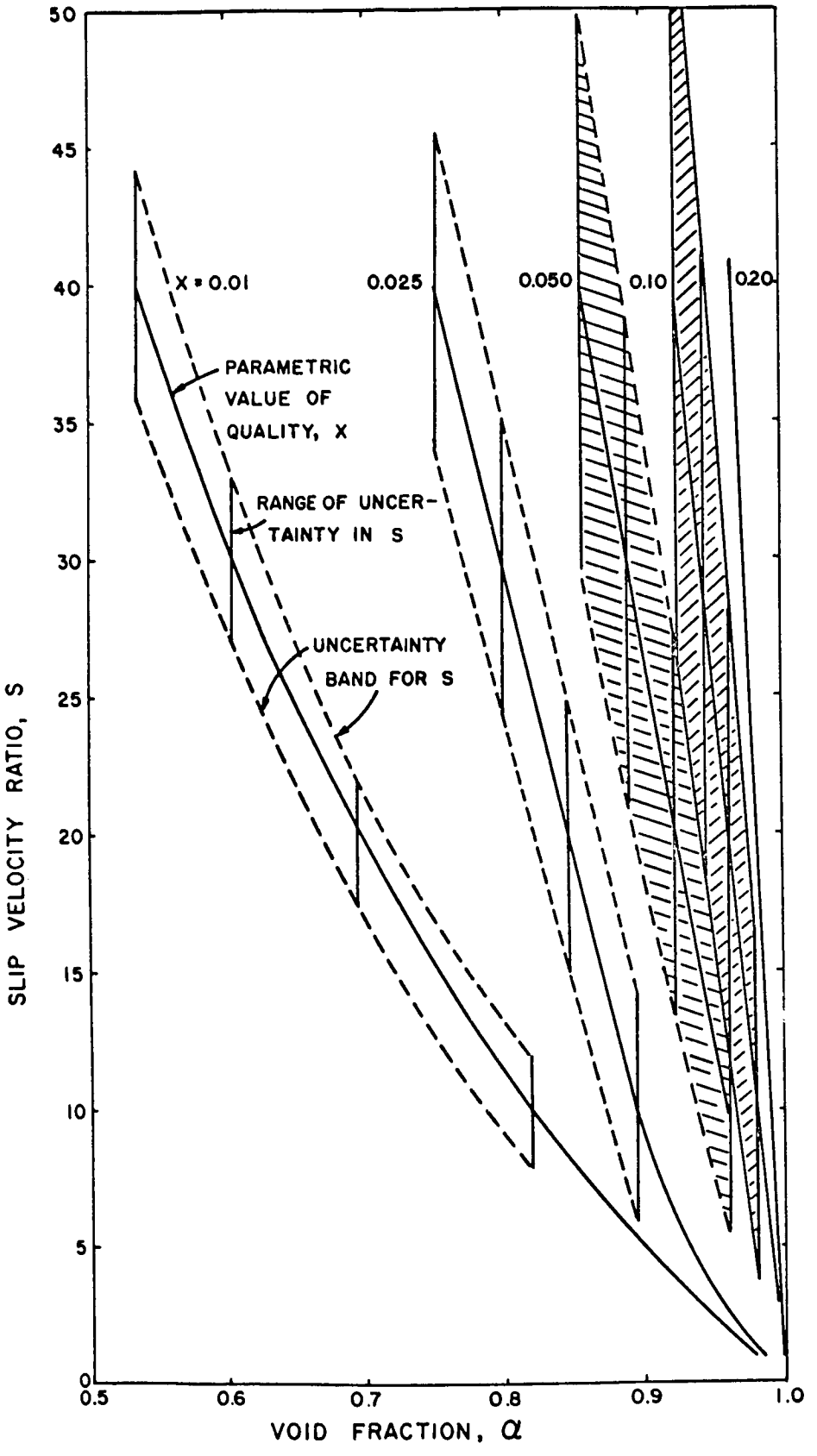


Fig. 10. Slip Velocity Ratio as a Function of Void Fraction and Quality for 8-92 Na-K at 1200°F, Showing Uncertainty in Slip Ratio

The substantial scatter found in these studies could likely be reduced by better temperature control of the scintillation detector and refinements to the collimator. Both of these changes have been incorporated into the studies now being conducted. Extreme care in alignment is important and difficulties arising from thermal expansion of the system must be considered.

The assumption of themodynamic equilibrium between vapor and liquid phases requires further study. Evidence exists that such a condition is not always achieved. The failure of the absolute pressure gage to operate satisfactorily in these studies necessitated such an assumption. Where possible such an assumption should be avoided.

ACKNOWLEDGMENTS

This study was made possible by financial support from the United States Air Force, Aeronautical Systems Division, Contracts AF 33(616)-8277 and AF 33(657)-11548.

REFERENCES

1. Richardson, B. L. "Some Problems in Horizontal Two-Phase, Two Component Flow." Argonne National Laboratories, Report ANL-5949 (December 1958).

2. Smith, Lowell R., "A Study of Pressure Drops and Void Fractions in Horizontal Two-Phase Flows of Potassium (8 per cent Sodium)." Ph.D. Thesis, The University of Michigan (April 1964).

3. Egen, R. A., Dingee, D. A. and Chastain, J. W., "Vapor Formation and Behavior in Boiling Heat Transfer." Battelle Memorial Institute, Report BMI - 1163 (February 4, 1957).

4. Myers, W. A. "A Method for Determining the Void Fraction of Two-Phase Potassium." Final Report for Course CME-690, The University of Michigan, Department of Chemical and Metallurgical Engineering, Ann Arbor (May 1963).

5. "Harshaw Scintillation Phosphors." Harshaw Chemical Company, Cleveland, Ohio, pp. 43 (1962).

6. Price, W. J. Nuclear Radiation Detection. McGraw-Hill, New York, 1958.

7. Lockhart, R. W. and Martinelli, R. C. "Proposed Correlation of Data for Isothermal Two-Phase, Two-Component Flow in Pipes." Chem. Eng. Prog. Vol. 45, 39 (1949).

8. Bankoff, S. G. "A Variable Density Single Fluid Model for Two-Phase Flow with Particular Reference to Steam-Water Flow." J. Heat Trans. Vol. 82, 265 (1960).

9. Bertuzzi, A. E., Tek, M. R. and Poettmann, F. H. "Simultaneous Flow of Liquid and Gas Through Horizontal Pipe." J. Pet. Tech. Vol. 8, (January 17, 1956).

10. Third Annual High-Temperature Liquid Metal Heat Transfer Technology Conference, Oak Ridge National Laboratory, Oak Ridge, Tennessee, September 4-6, 1963. Proceedings to be published.

11. Koestel, A. Thompson-Ramo Woolrige, Inc., Cleveland, Ohio. Tabulated data which had been previously published in TRW Report ER-4104 (June 1960).

12. Tang, Y. S., Smith, C. R. and Ross, P. T. "Potassium-Mercury Amalgam Boiling Heat Transfer, Two-Phase Flow, and Properties Investigation." Allison Division, General Motors Corp., Indianapolis, Indiana, Eng. Dept. Report No. 3549 (September 16, 1963).

13. Noyes, R. C. "Summary of Recent Results of Sodium Boiling Studies." Presented at Third Annual High-Temperature Liquid Metal Heat Transfer Technology Conference, Oak Ridge National Laboratory, September 4-6, 1963. Proceedings to be published.

14. Baker, O. "Simultaneous Flow of Oil and Gas." Oil and Gas J. Vol. 52, No. 14, 185 (1954).

15. Ros, N. C. J. "Simultaneous Flow of Gas and Liquid as Encountered in Well Tubing." Trans. Soc. Pet. Eng. of AIME. Vol. 222, 1037 (1961).

N66 31682

AN ACCURATE ONE-SHOT GAMMA ATTENUATION TECHNIQUE FOR MEASURING VOID FRACTIONS

J. K. Ferrell

John W. McGee

(Paper presented by J. K. Ferrell)

North Carolina State University

Department of Chemical Engineering

Raleigh, N. C.

PRECEDING PAGE BLANK NOT FILMED.

INTRODUCTION

The accurate determination of the local volumetric vapor fraction, commonly termed the void fraction, of vapor-liquid mixtures is essential to an understanding of the fluid mechanics of two-phase flow. Many methods have been developed for measuring the void fractions of a flowing, two-phase mixture. The most commonly used method employs the attenuation of low energy gamma radiation.

Two techniques employing gamma-ray attenuation are frequently used. One technique is to traverse the flow channel with a thinly collimated gamma beam. With the other technique, the one-shot method, the gamma rays are collimated so that the entire cross section of the flow channel is "viewed" by the gamma beam at one time. The one-shot method is simple and fast, but the void fractions determined may be a function of the void distribution. Large errors in the measured void fraction, especially in large flow channels, may occur where non-uniform distribution of voids are encountered. The more complicated traverse technique, which is not in error because of void distribution, is generally used to obtain more accurate void fraction measurements. However, for small flow channels, one-half inch in diameter and smaller, the accuracy attained using the traverse method is usually no better than that of the one-shot method due to the experimental difficulty of traversing a small area and interpreting the data obtained.

The objective of the investigation reported upon here was to improve the accuracy of the one-shot technique for measuring local void volume fractions of two-phase fluids in small flow channels by eliminating the dependence of the measurements on the void distribution in the flow channel.

CRITERION FOR THE DESIGN OF A ONE-SHOT COLLIMATOR

The gamma-ray attenuation of a two-phase mixture has been considered by Petrick* for two limiting cases. In the first case the liquid and vapor phases are assumed to exist in layers parallel to the gamma beam. The

*Petrick, M., "Two-Phase Air-Water Flow Phenomena", ANL-5787 (1958).

resulting equation for the void volume fraction, α, is:

$$\alpha = \frac{I_x - I_f}{I_g - I_f} \tag{1}$$

where: I_x = intensity of the gamma radiation after passing through a flow channel containing a fluid of unknown void volume fraction.

I_f = intensity of the gamma radiation after passing through the identical flow channel containing the same fluid as a liquid at the same temperature and pressure.

I_g = intensity of the gamma radiation after passing through the identical flow channel containing the same fluid as a vapor at the same temperature and pressure.

In the second case the gamma beam is assumed to be perpendicular to individual layers of vapor and liquid. The resulting equation for the void volume fraction becomes

$$\alpha = \frac{\ln \frac{I_x}{I_f}}{\ln \frac{I_g}{I_f}} \tag{2}$$

The attenuation relationship which is followed by an actual two-phase mixture is probably a combination of these two limiting cases. However, experimental results from models of two-phase fluids indicate that the second case is usually followed more closely.

To facilitate the development of the criterion for designing a one-shot collimator that will give accurate void fraction measurements independent of the void distribution in the flow channel, a hypothetical setup of the gamma source, flow channel, and gamma radiation detector will be considered. A sketch of the setup is presented in Figure 1. Let the source be fixed at a convenient distance from the flow channel. Let the gamma rays be collimated before entering the flow channel by a rectangular lead collimator of sufficient width to "view" the entire cross section of the flow channel and of a convenient length for a one-shot collimator. Let the collimator and source be fixed so that they are centered on the flow channel. On the opposite side of the flow channel let a gamma radiation detector of sufficient size (larger

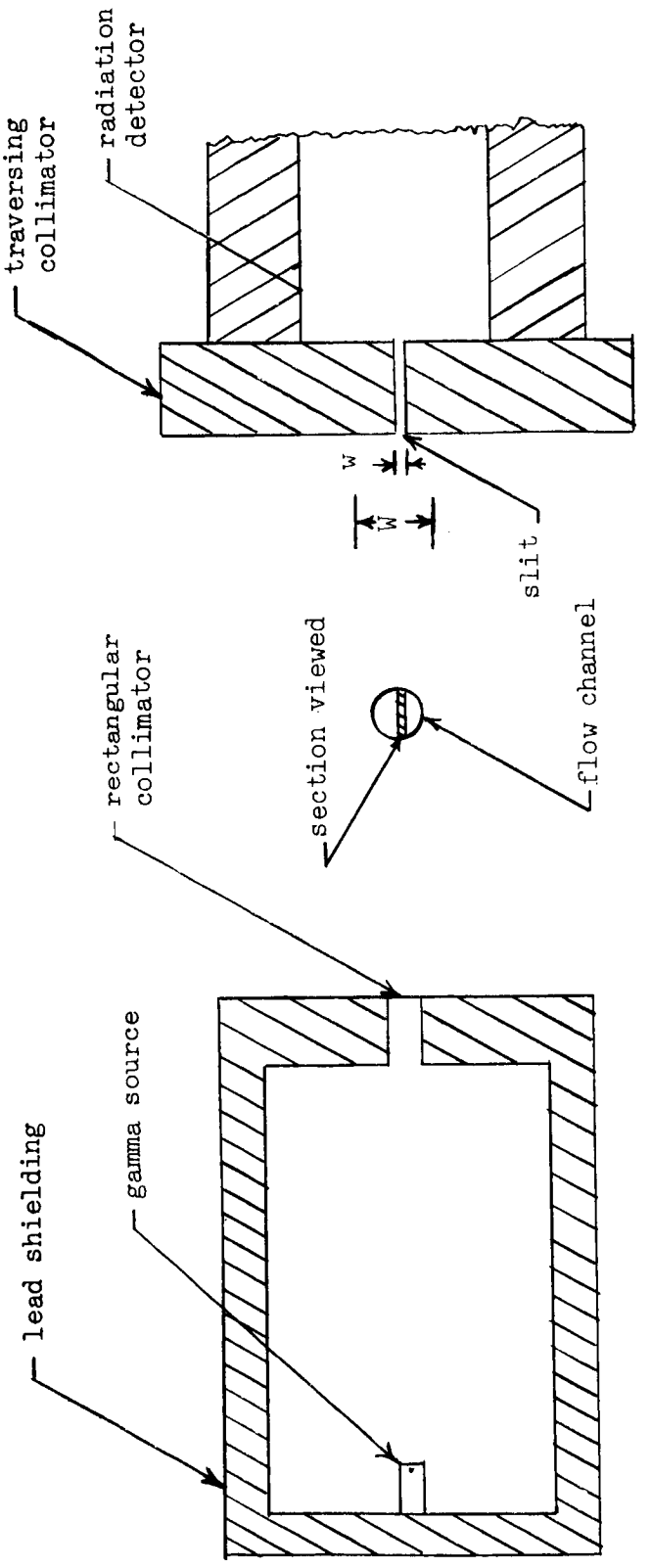


Fig. 1. Sketch of the Hypothetical Gamma Source, Flow Channel, and Radiation Detector Setup

than is needed to view the entire cross section of the channel) be centered on the flow channel in line with the source and be fixed there. Just in front of the detector let a lead collimator with a slit of length, h, and width, w, be installed such that a traverse of the flow channel can be made by moving only the collimator. The length, h, should be approximately equal to the length of the collimator on the source side. The width, w, should be several times smaller than the width of the collimator on the source side.

Let a traverse be made so that the total volume of the flow channel viewed is divided into n segments as the slit collimator traverses the width of the flow channel in increments of length, w. Let the intensity of the gamma rays passing through the slit collimator be measured in terms of a count rate. For later convenience, let the count rates be divided by h, the length of the slit collimator. Then in traversing the flow channel one obtains the following data:

$I_x^{(k)}$ = count rate per unit length of collimator obtained for the kth segment of the volume of the flow channel containing a fluid of unknown void fraction.

$I_f^{(k)}$ = count rate per unit length of collimator obtained for the kth segment containing the same fluid in the liquid state at the same temperature and pressure.

$I_g^{(k)}$ = count rate per unit length of collimator obtained for the kth segment containing the same fluid in the vapor state at the same temperature and pressure.

A_k = cross-sectional area of the flow channel contained in the kth segment.

A_t = total cross-sectional area of the flow channel.

The void volume fraction of the fluid in the kth segment, α_k, is:

$$\alpha_k = \frac{I_x^{(k)} h - I_f^{(k)} h}{I_g^{(k)} h - I_f^{(k)} h} \tag{3}$$

provided that equation (1) is applicable. Let

$$X_k = I_x^{(k)} - I_f^{(k)}$$

and

$$D_k = I_g^{(k)} - I_f^{(k)} \tag{4}$$

Then

$$\alpha_k = \frac{X_k}{D_k} \tag{5}$$

and the volume of voids in the kth segment, V_k, is:

$$V_k = \alpha_k h A_k = \frac{h X_k A_k}{D_k} \tag{6}$$

The total volume void fraction determined by the traverse, α_T, is the total volume of voids viewed divided by the total volume of the flow channel viewed or

$$\alpha_T = \frac{\sum_{k=1}^{n} V_k}{A_t h} = \sum_{k=1}^{n} \frac{X_k A_k}{D_k A_t} \tag{7}$$

The void fraction determined using equation (7) should be independent of the void distribution in the flow channel. The problem now is to determine the shape of a one-shot collimator that will give a volume void fraction, α_S, equal to α_T for any void distribution in the flow channel. The width, W, of the one-shot collimator is determined by the width or diameter of the test section since the entire cross section of the flow channel has to be viewed by the gamma ray beam at one time. To determine the shape of the one-shot collimator with which to replace the slit collimator one needs to determine the length of the collimator at several points along its width, W. The hypothetical traverse considered previously divided by the volume of the flow channel viewed into n segments and at the same time divided the width, W, into n increments of equal width, w. Therefore, the one-shot collimator can be assumed to be made up of n sections each of width, w, and some unknown length.

Let L_k be the length of kth section of the one-shot collimator. Assume that the number of gamma photons passing through a unit length of the kth

section of the one-shot collimator is proportional to the number of gamma photons passing through a unit length of the slit collimator when it is in position to view the kth segment of the flow channel. Assume further that the proportionality is constant for each section. Let I_x, I_f, and I_g be the count rates obtained with the one-shot collimator for a flow channel containing fluid of unknown void fraction, fluid in the liquid state and fluid in the vapor state, respectively. Then

$$I_x = b \sum_{k=1}^{n} I_x^{(k)} L_k$$

$$I_f = b \sum_{k=1}^{n} I_f^{(k)} L_k \qquad (8)$$

$$I_g = b \sum_{k=1}^{n} I_g^{(k)} L_k$$

Using equations (1) and (8), the void fraction determined by the one-shot technique is:

$$\alpha_S = \frac{\sum_{k=1}^{n} I_x^{(k)} L_k - \sum_{k=1}^{n} I_f^{(k)} L_k}{\sum_{k=1}^{n} I_g^{(k)} L_k - \sum_{k=1}^{n} I_f^{(k)} L_k} \qquad (9)$$

Expanding the right side one obtains

$$\alpha_S = \frac{(I_x^{(1)} L_1 + I_x^{(2)} L_2 + \ldots + I_x^{(n)} L_n - I_f^{(1)} L_1 - \ldots - I_f^{(n)} L_n)}{(I_g^{(1)} L_1 + I_g^{(2)} L_2 + \ldots + I_g^{(n)} L_n - I_f^{(1)} L_1 - \ldots - I_f^{(n)} L_n)}$$

Using equations (4), this relation can be written as

$$\alpha_S = \frac{L_1 X_1 + L_2 X_2 + \ldots + L_n X_n}{L_1 D_1 + L_2 D_2 + \ldots + L_n D_n} \qquad (10)$$

Expanding equation (7), one obtains

$$a_T = \frac{X_1 A_1}{D_1 A_t} + \frac{X_2 A_2}{D_2 A_t} + \cdots \frac{X_n A_n}{D_n A_t}$$

This expression can be written as

$$a_T = \frac{\frac{X_1 A_1}{D_1} + \frac{X_2 A_2}{D_2} + \cdots + \frac{X_n A_n}{D_n}}{A_t} \qquad (11)$$

If a_S is to be equal to a_T, then it is necessary that the numerator of the right hand side of equation (10) be proportional to the numerator of the right hand side of equation (11), i.e.,

$$L_1 X_1 + L_2 X_2 + \cdots + L_n X_n = c\left(\frac{X_1 A_1}{D_1} + \frac{X_2 A_2}{D_2} + \cdots + \frac{X_n A_n}{D_n}\right) = 0$$

This equation can be written as

$$X_1\left(L_1 - \frac{c A_1}{D_1}\right) + X_2\left(L_2 - \frac{c A_2}{D_2}\right) + \cdots + X_n\left(L_n - \frac{c A_n}{D_n}\right) = 0 \qquad (12)$$

Since the X_k can have any value, the coefficients of the X_k must be equal to zero. Therefore,

$$L_1 = \frac{c A_1}{D_1}$$

$$L_2 = \frac{c A_2}{D_2} \qquad (13)$$

$$L_n = \frac{c A_n}{D_n}$$

Let L_j be the length of the one-shot collimator at the center section of the collimator. Then the length, L_k, of the collimator at any other segment can be determined relative to the arbitrary length L_j. The final relationship

from which the shape of the one-shot collimator can be determined is:

$$\frac{L_k}{L_j} = \frac{A_k}{D_k}\frac{D_j}{A_j}$$

or

$$\frac{L_k}{L_j} = \frac{A_k}{I_g^{(k)} - I_f^{(k)}} \frac{I_g^{(j)} - I_f^{(j)}}{A_j} \qquad (14)$$

where K = 1, 2, ... , n.

Using equation (14) it should be possible to design a one-shot collimator which can be used to determine volume void fractions that are independend of the void distribution in the flow channel whenever the assumptions made in the derivation are valid. Even though equation (2) usually gives a more accurate answer for void fractions, all void fractions in the previous analysis were calculated using equation (1) because the resulting equations are much easier to solve. However, even if equation (2) were the theoretically correct equation to use, equation (1) would be a good approximation to it if the fraction attenuation, $(I_g - I_f)/I_g$, is not very large. This may be seen by writing equation (2) with finite series instead of the logarithms.

$$\alpha = \frac{\frac{I_x - I_f}{I_f} - \frac{(I_x - I_f)^2}{2I_f^2} + \frac{(I_x - I_f)^3}{3I_f^3}}{\frac{I_g - I_f}{I_f} - \frac{(I_g - I_f)^2}{2I_f^2} + \frac{(I_g - I_f)^3}{3I_f^3}}$$

If all terms except the first one of the series are neglected, equation (1) is obtained.

The assumption of a constant proportionality between the number of gamma photons passing through a unit length of the kth section of the one-shot collimator and the number of gamma photons passing through a unit length of the slit collimator when it is in position to view the kth segment of the flow channel is not exactly valid. In the one-shot collimator the gamma-rays can enter the detector at almost any angle, whereas those passing through the

collimator have to be almost parallel to the slit walls which are separated by a very small width. It seems reasonable to believe that this effect would be greater at the center of the one-shot collimator than at its edge. Thus, the proportionality constant might be greater near the center of the collimator than at the edge.

The shape of the one-shot collimator should be independent of the source strength since the quantity $(I_g^{(j)} - I_f^{(j)}/(I_g^{(k)} - I_f^{(k)})$ is not a function of source strength. However, the shape of the collimator will be a function to some extent of the energy level of the gamma radiation and of the particular fluid used in the flow channel. In addition, as shown in Figures 4 and 5, the shape of the collimator is strongly influenced by the channel wall thickness.

DESIGN OF A SPECIFIC ONE-SHOT COLLIMATOR

The procedure for designing a one-shot collimator is first to determine the width of the collimator so that the entire cross-sectional area of the flow channel is viewed by the gamma beam. Divide this width into an appropriate number of small increments of equal width. The number and size of the increments needed to define the shape of the collimator will depend upon the size and shape of the flow channel. Choose one of the increments, preferably the increment in the center of the collimator, and let its length be L_j at the midpoint of the increment. Using equation (14), calculate the value of L_k (in terms of L_j) at the center of each of the other increments. Finally, assign a definite length to L_j so that the one-shot collimator views the desired volume of the flow channel. Although somewhat arbitrary, the cross-sectional area of the collimator is determined to a degree by the count rate desired and by the fact that one is interested in determining local values of the void volume fraction.

In order to use equation (14)one needs attenuation data for the flow channel when it is full of liquid and when it is full of vapor for each of the small increments. This data can be calculated from a knowledge of the geometry of the source-flow channel setup and the appropriate attenuation coefficients. The data may also be obtained experimentally by using a traverse which approximates the hypothetical traverse used in the derivation of equation (14).

A one-shot collimator was designed for determining the void fraction of a steam-water mixture in a 0.5 inch O.D. x 0.035 inch wall stainless steel test section. The setup included a 12 millicurie thulium - 170 gamma source (effectively a point source) located 8.38 inches from the center line of the tube and 12.12 inches from the first component of the radiation detector, a 2 inch O. D. x 1 inch thick thallium activated sodium iodide crystal. The crystal is shielded from stray radiation by a 1 inch thick lead shield into which a 1.250 inch thick lead collimator can be inserted.

The width of the collimator was made 0.620 inches. This width was divided into 12 increments of width 0.05 inches, six on either side of the center of the collimator, plus two increments of 0.01 inches at each of the two edges. Because of symmetry, the shape of the collimator was defined by determining the shape for one quadrant of it. The attenuation data was obtained by traversing the tube when empty and when filled with lucite using two collimators having slits of 1/16 inch x 1/2 inch and 1/32 inch x 1/2 inch. Lucite was chosen since its attenuation characteristics are approximately the same as those of water for the gamma radiation used. The traverse was made using a setup in which the source and detector are aligned and mounted on a carriage which is pivoted on the detector side. The carriage was moved in increments by a set-screw arrangement. Because of the scatter in the experimental data near the tube wall, three points were calculated to verify the shape of the curves presented in Figure 2.

Table 1 contains the pertinent data used in the design of the one-shot collimator. The shape of the collimator calculated and the shape of the collimator actually built are shown in Figure 3. Figures 4 and 5 show the calculated and built shapes of two additional collimators; a 0.625 inch O.D. by 0.083 inch wall, and a 0.625 inch O. D. by 0.020 inch wall, stainless steel tube.

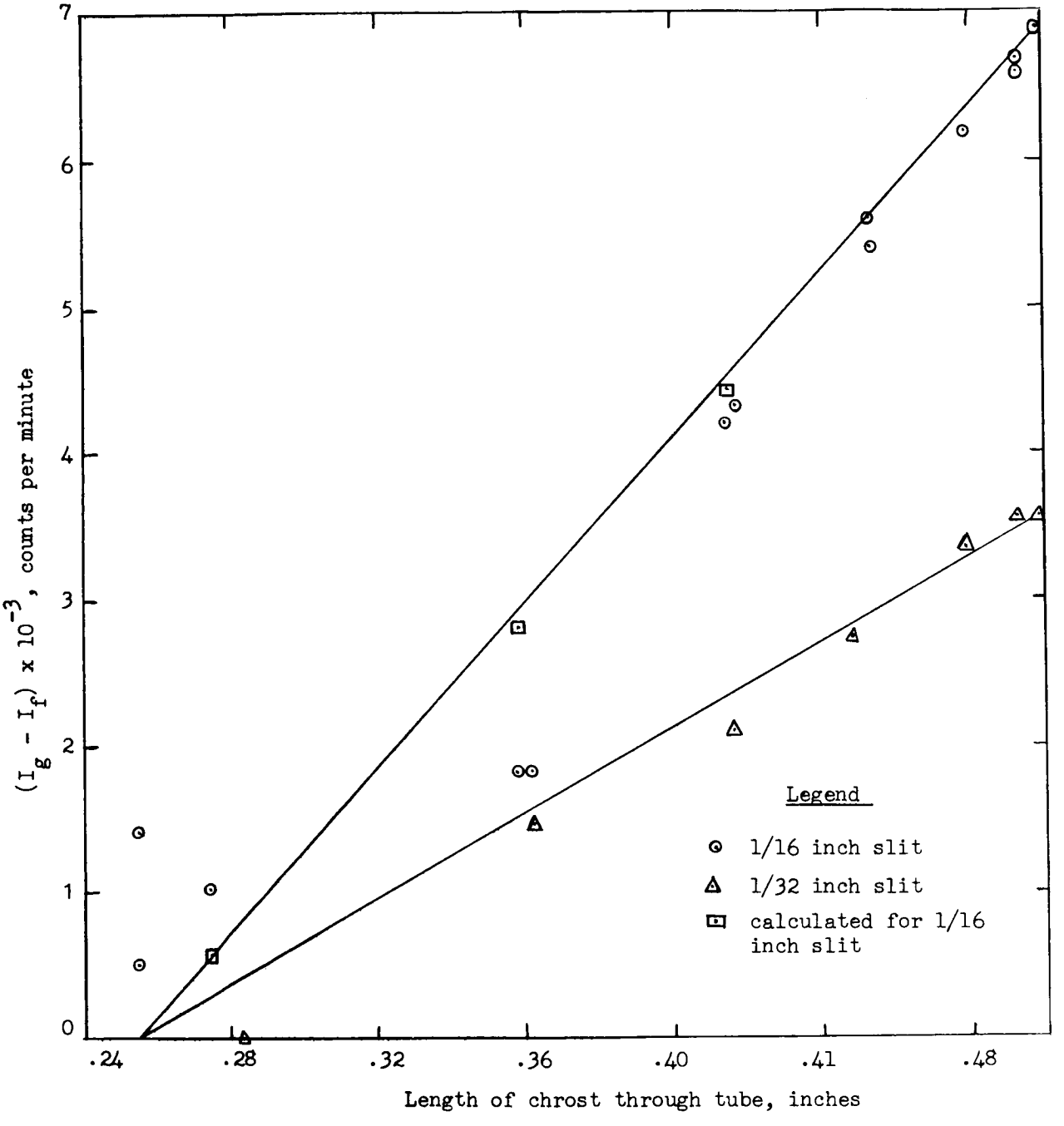


Fig. 2. Attenuation Data Obtained from Traverse of 0.5 inch O.D. x 0.035 inch Wall Stainless Steel Tube When Empty and When Filled with Lucite

Table I. Data Used in Designing a One-Shot Collimator for a 0.5 Inch O.D. x 0.035 Inch Tube Wall

Section of Collimator	Distance from Center of Collimator	Cross-Sectional Area of tube viewed, A_k	Length of Chord through tube	$\frac{A_k}{A_1}$	$\frac{I_g^{(1)} - I_f^{(1)}}{I_g^{(k)} - I_f^{(k)}}$	$\frac{L_k}{L_1}$	$\frac{L_k}{2}$
	Inches	Square Inches	Inches		(From Figure 2)	(Using Eq.14)	(L_1=0.5) Inches
	.000						
1	.025	.014718	.4968	1.0000	1.000	1.000	.250
	.050						
2	.075	.014323	.4870	.9732	1.043	1.013	.253
	.100						
3	.125	.013501	.4674	.9173	1.139	1.045	.261
	.150						
4	.175	.012168	.4352	.8267	1.348	1.114	.278
	.200						
5	.225	.010106	.3900	.6866	1.802	1.237	.309
	.250						
6	.275	.006628	.3220	.4503	3.656	1.646	.412
	.300						
7	.305	.000492	.2659	.1670*	23.417	3.911	.978
	.310						

*Approximated by $(A_7/A_1) \times 5$ since the increment for this section of the collimator is 1/5 of the increment used in the other sections.

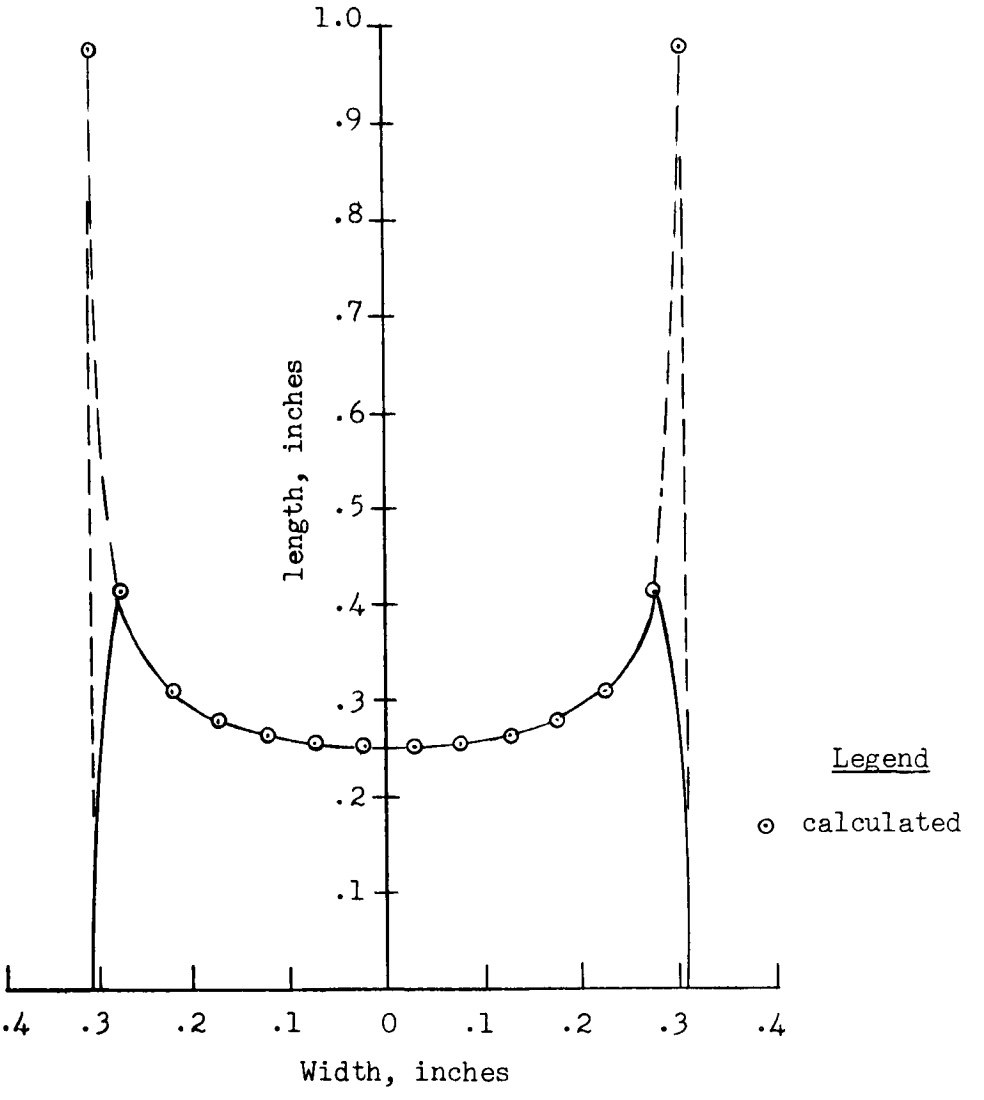


Fig. 3. Shape of Upper Half of One-Shot Collimator Designed for 0.5 inch O.D. x 0.035 inch Wall Stainless Steel Wall

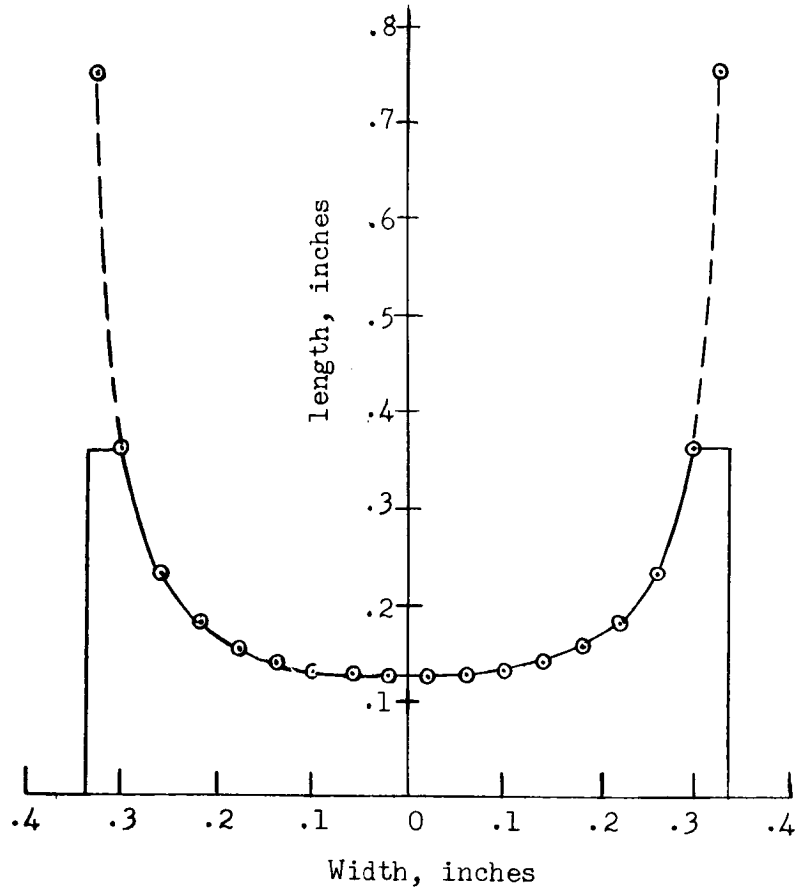


Fig. 4. Shape of Upper Half of One-Shot Collimator Designed for 0.625 inch O.D. x 0.083 inch Wall Stainless Steel Tube

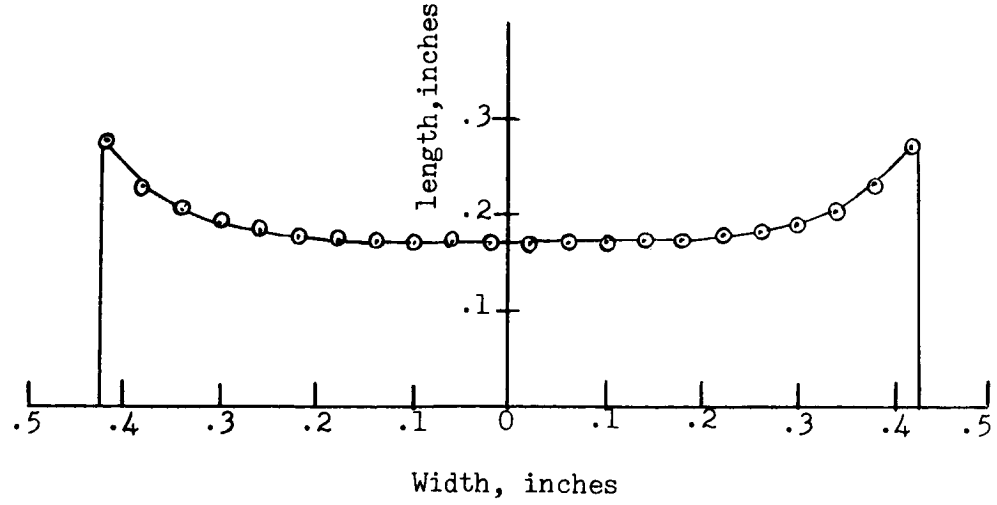


Fig. 5. Shape of Upper Half of One-Shot Collimator Designed for 0.625 inch O.D. x 0.020 inch Wall Stainless Steel Tube

EVALUATION OF THE ONE-SHOT COLLIMATORS

The one-shot collimators were tested by measuring the void fractions of a number of Lucite models inside the stainless steel tubes. These models were carefully machined and were of a variety of void fractions and void distributions. The physical measurements of these models are presented in Table 2. The maximum error in the actual void fractions, α_a, which are based on the physical measurements, is approximately $\pm$ 0.005.

The electronic equipment consisted of a Harshaw, Type HS-4, Integral Line Scintillation Detector, a Nuclear Chicago, Model DS-5, preamplifier, a Nuclear Chicago, Model 1810, radiation analyzer, and a Nuclear Chicago, Model 192 A, scaler. The detector was shielded from stray radiation and from magnetic fields and was maintained at a constant temperature. Integral counts were taken; therefore, the upper discriminator of the radiation analyzer was not used. A Sorensen, Model 3000 S, constant voltage regulator supplied power to the scaler and radiation analyzer. The variation in count rates obtained with this equipment can be predicted accurately from the statistical nature of the radiation emission. The performance of the equipment is, therefore, considered excellent.

The procedure was to take four one-minute counts for each model and use an average value. The empty tube and full tube were counted about every 30 minutes. The void fractions determined from the count rate data, α_c, were calculated using equation (2). Equation (2) gave slightly more accurate results on the average than did equation (1). The full-tube models were used to calculate I_f. The count rates measured were in the neighborhood of 400,000 counts per minute. The average attenuation, $(I_g - I_f)/I_g$, varied between 0.1233 and 0.1900.

The results of the evaluations are presented in Tables 4, 5, and 6, and in Figures 7, 8, and 9. For comparison the results of a test of a circular one-shot collimator using the same equipment and some of the same models are presented in Table 3 and Figure 6. The average magnitude of the error using this circular collimator is 0.0320, approximately four times the error obtained with the specially designed collimators. The large error was due to the strong dependence of the measured void fractions upon void distribution.

Table II. Physical Measurements of Lucite Models

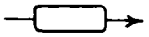
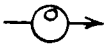
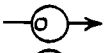
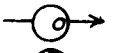
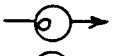
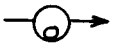
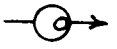
Model	O. D. in.	I. D. in.	Model	O. D. in.	I. D. in.
101	.427	.000	124a		.305 x .304
102	.426	.055	124b		.305 x .304
103	.427	.086	125a		.404 x .149
104	.426	.104	125b		.404 x .149
105	.426	.120	126		.425 with .096 hole
106	.426	.137	127a		.426 with .083 hole
107	.425	.173	127b		.426 with .083 hole
108	.426	.209	127c		.426 with .083 hole
109	.426	.250	127d		.426 with .083 hole
110	.426	.300	128a		.426 with .173 hole
111	.427	.348	128b		.426 with .173 hole
112	.426	.385	128c		.426 with .173 hole
113	.426	.390	128d		.426 with .173 hole
114	.424	.000	201	.463	.000
115	.419	.000	202	.464	.076
116	.414	.000	203	.464	.113
117	.409	.000	204	.464	.144
118	.400	.000	205	.463	.211
119	.385	.000	206	.463	.317
120	.360	.000	207	.464	.404
121	.320	.000	208	.454	.000
122	.260	.000	209	.438	.000
123	.150	.000	210	.400	.000
			211	.290	.000

Table III. Gamma Attenuation Measurements of Lucite Models Using Circular Collimator

Model	α_a	α_c	Error
103	.046	.054	.008
106	.113	.137	.024
107	.178	.209	.031
108	.248	.295	.047
109	.351	.402	.051
110	.501	.575	.074
111	.666	.724	.058
118	.127	.112	-.015
120	.293	.250	-.043
121	.441	.386	-.055
124a	.356	.315	-.041
124b	.356	.317	-.039
125a	.582	.611	.029
125b	.582	.530	-.052
126	.367	.412	.045

Table IV. Gamma Attenuation Measurements of Lucite Models Using Collimator for 0.500 inch I. D. x 0.035 inch Wall Tube

Model	α_a	α_c	α_c	α_c	α_c	Average α_c	Average error
102	.025	.038	.027			.033	.008
103	.046	.037	.052	.045	.054	.047	.001
104	.069	.072	.078			.075	.006
105	.088	.084	.093			.089	.001
106	.113	.120	.130	.110	.112	.118	.005
107	.178	.168	.168	.178	.182	.174	-.004
108	.248	.244	.255	.244	.257	.250	.002
109	.351	.362	.348			.355	.004
110	.501	.506	.518			.512	.011
111	.666	.683	.687			.685	.019
112	.818	.841	.826			.834	.016
113	.840	.858	.851			.855	.015
114	.022	.032	.020			.026	.004
115	.041	.031	.030	.037		.033	-.008
116	.066	.069	.062			.066	.000
117	.088	.087	.084			.086	-.002
118	.127	.113	.109	.125	.118	.116	-.011
119	.192	.181	.191			.186	-.006
120	.293	.277	.283			.280	-.013
121	.441	.424	.435			.430	-.011
122	.631	.626	.629			.628	-.003
123	.877	.876	.874			.875	-.002
124a	.356	.350	.331			.341	-.015
124b	.356	.355	.349			.352	-.004
125a	.582	.592	.592			.592	.010
125b	.582	.604	.603			.604	.022
126	.367	.374	.384			.379	.012
127a	.046	.049	.046			.048	.002
127d	.046	.044	.047			.046	.000
128a	.174	.187	.170			.179	.005
128b	.174	.168	.178			.173	-.001
128c	.174	.181	.162			.172	-.002
128d	.174	.170	.167			.168	-.006

Table V. Gamma Attenuation Measurements of Lucite Models Using Collimator for 0.625 inch O. D. x 0.083 inch Wall

Model	α_A	α_c	α_a	α_c	α_c	Average α_c	Average error
202	.030	.015	.024			.020	-.010
203	.062	.063	.052			.057	-.005
204	.098	.083	.098			.091	-.007
205	.213	.190	.190	.191	.187	.190	-.023
206	.471	.446	.433	.440	.453	.443	-.028
207	.762	.758	.743	.762	.752	.754	-.008
208	.041	.046	.040			.042	.001
209	.109	.093	.108			.101	-.008
210	.258	.267	.264	.260	.270	.265	.007
211	.585	.628	.608	.601	.609	.612	.027

Table VI. Gamma Attenuation Measurements of Lucite Models Using Collimator for 0.625 inch O. D. x 0.020 inch wall

Model	α_A	α_c	α_c	α_c	α_c	Average α_c	Average error
201	.383	.375	.369			.372	-.011
202	.399	.395	.386			.390	-.009
203	.419	.402	.414			.408	-.011
204	.442	.438	.450			.444	.002
205	.513	.501	.490			.495	-.018
206	.672	.663	.657			.660	-.012
207	.853	.848	.845			.847	-.006
208	.407	.400	.396			.398	-.009
209	.448	.439	.440			.440	-.008
210	.541	.541	.525			.533	-.008
211	.743	.744	.733			.739	-.004

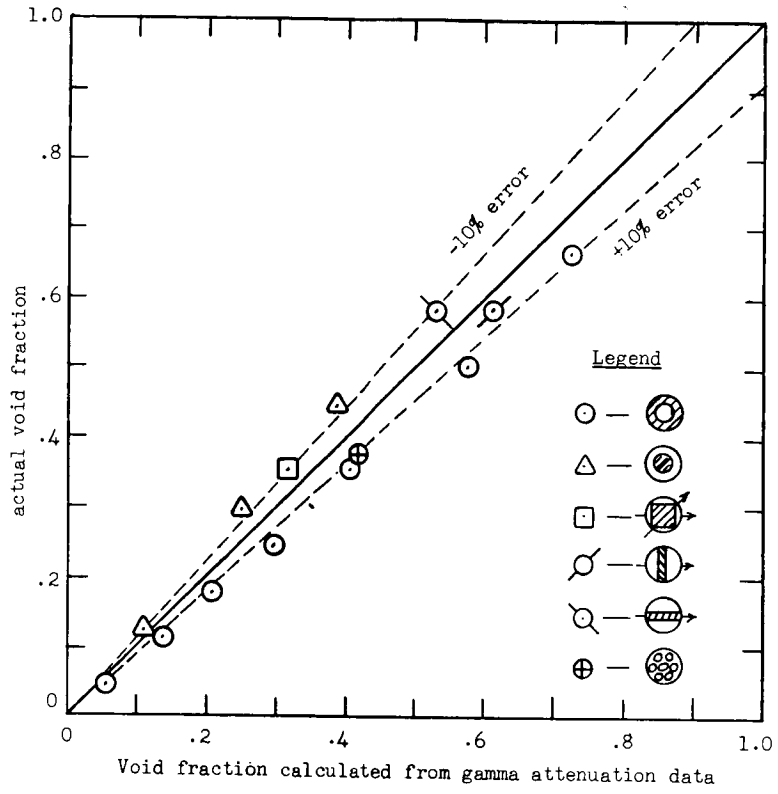


Fig. 6. Void Volume Fraction Calibration Using Circular Collimator

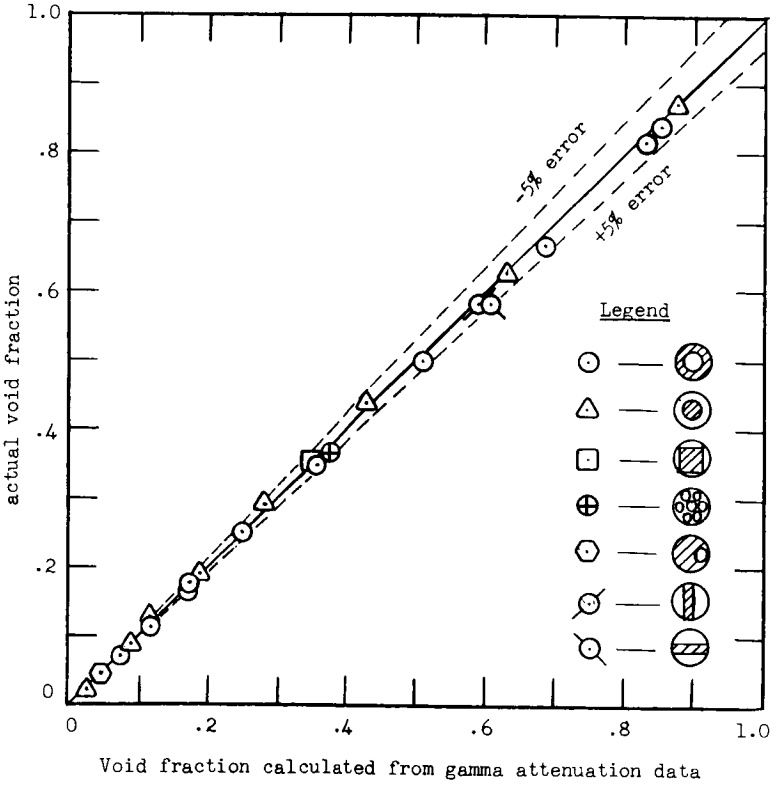


Fig. 7. Void Volume Fraction Calibration Using Collimator for 0.500 inch O.D. x 0.035 inch Wall Stainless Steel Tube

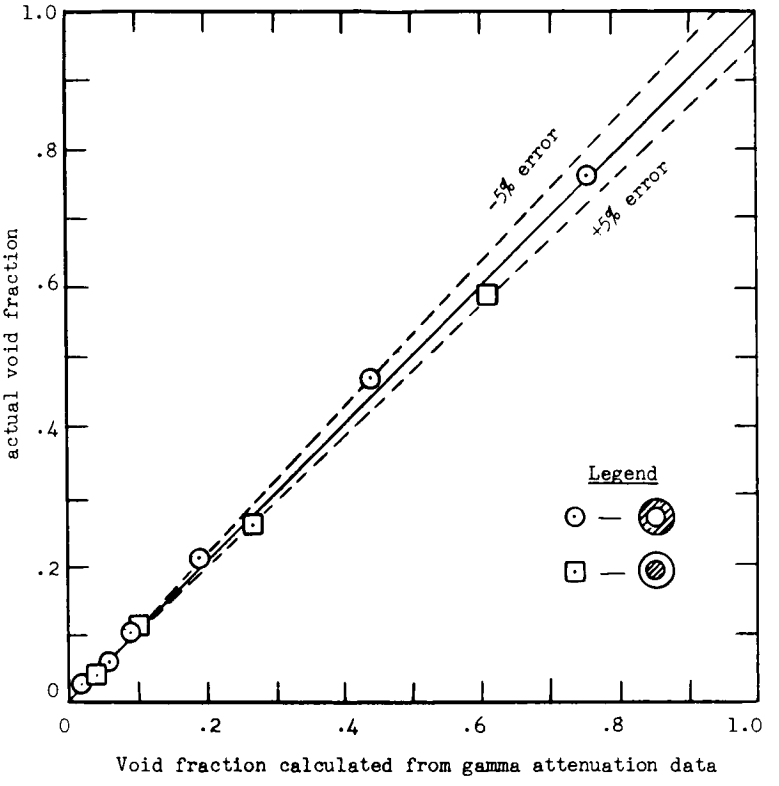


Fig. 8. Void Volume Fraction Calibration Using Collimator for 0.625 inch O.D. x 0.083 inch Wall Stainless Steel Tube

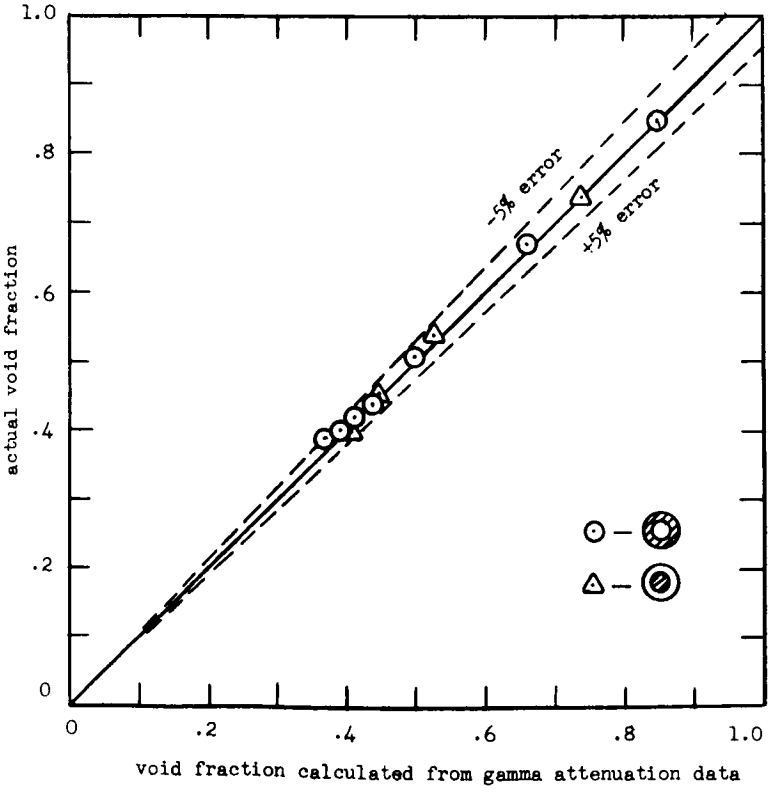


Fig. 9. Void Volume Fraction Calibration Using Collimator for 0.625 inch O.D. x 0.020 inch Wall Stainless Steel Tube

The average magnitude of the error for all of the specially designed collimators, the sum of the magnitudes of $(\alpha_c - \alpha_a)$ divided by the number of runs, was 0.008. Every void fraction determined using the specially designed collimators had less than $\pm$ 5% error for void fractions greater than about 35%. The per cent error naturally increases as the void fraction decreases due to the error introduced by the variations in count rate caused by the random distribution in time of the disintegrations of the radioactive material. This error is almost constant over the entire range of void fractions. For this particular setup errors in the calculated void fraction due to the statistical nature of the source was less than $\pm$ 0.0125, 97% of the time.

The void fractions calculated for the collimator shown in Figure 3 were almost independent of the void distribution. However, there was a tendency for the void fraction measurements to be slightly high for voids concentrated in the center of the tube and slightly low for voids concentrated on the wall of the tube. This tendency was largely eliminated for the collimator shown in Figure 5 by making the collimator more nearly as calculated near the wall.

The collimator shown in Figure 4 was designed using the attenuation coefficients of iron, water, and air for an energy of 0.08 MEV. A later experiment showed that these assumed attenuation coefficients were in error. The experimentally determined attenuation coefficients were found to decrease as the thickness of stell increased. These effective attenuation coefficients were used in the design of the collimator shown in Figure 5.

CONCLUSIONS

It can be concluded that the shape of the collimator used in the one-shot technique greatly affect the dependence of the void fraction measurements on the void distribution in the flow channel, and that the criterion for designing a one-shot collimator developed here will provide accurate void fractions measurements independent of the voil distribution.

Cautions should be used in extending this method to situations where the average attenuation is greater than about 20% or to larger diameter flow channels.

N66 31683

DEVELOPMENT OF ALKALI METAL QUALITY METER*

by

Peter Tauson and R. L. Ammon
Westinghouse Electric Corporation
Astronuclear Laboratory
P. O. Box 10864
Pittsburgh, Pennsylvania 15236

(Paper presented by P. Tauson)

* This information was developed under Contract No. AF 33(615)-2495 sponsored by the

Air Force Aero Propulsion Laboratory
Research and Technology Division
Air Force Systems Command
United States Air Force

PRECEDING PAGE BLANK NOT FILMED.

DEVELOPMENT OF ALKALI METAL QUALITY METER

by

Peter Tauson and R. L. Ammon
Westinghouse Research Corporation
Astronuclear Laboratory

ABSTRACT

The measurement of the quality of alkali metal vapor involves two major goals:

1. Collection of a representative sample, and
2. Measurement of the sample quality.

The first is a study in itself because of the tendency of alkali metal liquids to adhere to the walls. The second is the analysis of the quality of vapor of a collected sample. This paper will deal primarily with the second goal.

The method used is to measure the amount of energy required to dry the sample and compare it with the amount of energy required to superheat the sample to a preset amount of superheat ΔT.

Fundamentally, two equations are involved

$$H_1 = W(1 - x)\lambda, \text{ and} \tag{1}$$

$$H_2 = W C_p \Delta T. \tag{2}$$

Solving for quality x:

$$x = 1 - \frac{C_p}{\lambda}\left(\frac{H_1}{H_2}\ \Delta T\right) . \tag{3}$$

The actual form is somewhat more complex due to thermal and flow characteristics: however, an instrument can be constructed to provide the measurements of quality. This technique is now being developed by Westinghouse Astronuclear Laboratory under Air Force sponsorship (Contract No. AF 33(615)-2495).

ALKALI METAL QUALITY METER

INTRODUCTION

The majority of space power plants which are under development to generate electrical power by means of turbo-generators utilize alkali metal vapors, particularly potassium, as a working fluid.

The available materials and the available heat sources are generally inadequate to achieve the very high temperature required for superheat. Therefore, the use of saturated vapor presently appears to be the most economical approach.

The saturated-vapor approach is complicated, however, by the fact that the actual quality of vapor entering the turbine and the changes in quality of vapor as it progresses through the turbine are not known. Since the condensed liquid can be a source blade erosion, it is desirable to approach 100% saturation without exceeding this point and incurring condensation. Therefore, to evaluate the turbine performance and the relation between the vapor quality and the erosion of the blades, it is necessary to measure the quality of the vapor as it enters the first stage and at various other points in the turbine.

The determination of vapor quality by methods which employ a decrease in energy (such as a throttling calorimeter or ice bath calorimeter) are not practical approaches, particularly for low quality vapor such as is present in the later stages of a turbine. This led to investigation of measuring quality by the method described below.

CALORIMETER APPLICATION

Fundamentally the calorimeter is a device which will analyze the vapor sample for its liquid content, thus defining the mass ratio of vapor to liquid or the vapor quality. While in a general application, such as sampling the fluid in a conduit, the accuracy of sampling will depend on sampling techniques, the calorimeter can be used for direct measurements of any desired flow filament to determine the quality at that filament. Repeating the process for a number of such devices to pick up samples at different filaments will determine the quality distribution in a radial or axial direction. An analysis

of the quality along a turbine blade or an analysis of quality at various stages of a turbine can be accomplished with a single probe calorimeter.

A number of other applications, such as determination of effectiveness of separators, the characteristics of vapor leaving the boiler, the changes in vapor quality along some axial paths, the determination of quality distribution radially to define acceptable sampling techniques, etc., can be determined with a single probe calorimeter.

CALORIMETER CONCEPT

Assume that a sample of fluid, representing the flow, can be heated sufficiently to evaporate it and slightly superheat the resultant vapor. (This initial superheat serves to assure complete evaporation of all of the liquid in the sample.) Barring any unaccounted heat losses, the heat balance equation will appear as follows:

$$H_1 = w\left((1 - x)\,\lambda + C_{p_1}\,\Delta T_1 \right) , \qquad (1)$$

where

H_1 = heat input,

w = mass flow rate,

x = quality,

λ = latent heat,

C_{p_1} = specific heat in the superheat range of ΔT_1, and

ΔT_1 = temperature rise of vapor leaving the first heating cycle.

A schematic of such an arrangement appears in Figure 1. Equation (1) demands, for its solution, accurate measurement of heat input, the temperature rise, the mass flow value, and the temperature of the entering fluid. We can assume at this point that the values of C_p and one value of λ are accurately known.

The measurement of the flow rate (w) in a closed loop system is very difficult. It would be desirable, therefore, to eliminate this measurement. To that end, a second cycle

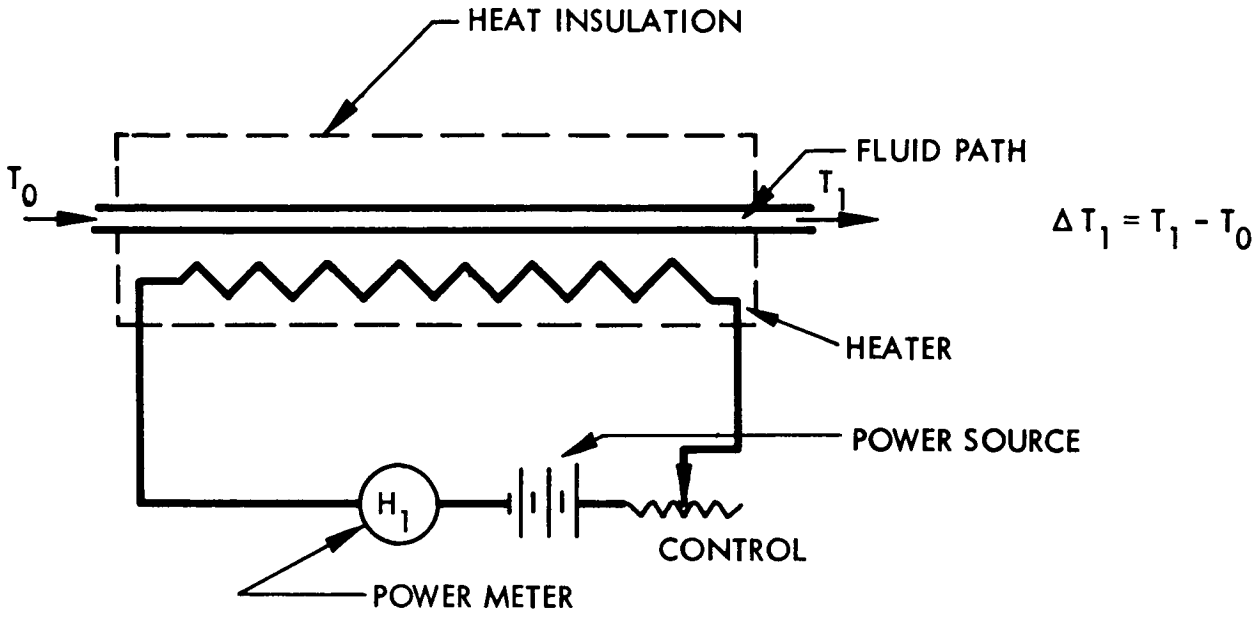


Fig. 1. First Stage of Additive Heat Calorimeter (Basic Concept)

of heating is added to the original arrangement, bringing the temperature to a still higher level. The heat balance equation for this step (again barring heat losses) is

$$H_2 = W \times C_{p_2} \Delta T_2 , \tag{2}$$

where

H_2 = heat input into second cycle,
w = mass flow rate (same as Equation 1),
C_{p_2} = specific heat in superheat range of ΔT_2, and
ΔT_2 = additional temperature rise.

Schematically, the arrangement is now a bit more complex (Figure 2). The value of quality can now be solved from the equations above in terms of measurable values of temperature increments and heat input as shown in Equation 3.

$$x = 1 - \frac{C_{p_2} \Delta T_2}{\lambda} \left[\frac{H_1}{H_2} - \frac{C_{p_1} \Delta T_1}{C_{p_2} \Delta T_2} \right] \tag{3}$$

Equation (3) is the fundamental equation of the additive calorimeter. The remaining problem is to isolate and define the heat losses.

CALORIMETER DESIGN

The approach taken by Westinghouse is to reduce these losses to an amount so small as to be able to neglect them if possible. Several avenues have been considered to accomplish this end.

The first and most obvious is to lag the entire instrument with sufficient amount of insulating materials to reduce the losses to a negligible amount. This solution results in a very clumsy and heavy unit, which has a large, characteristic thermal lag before it reaches equilibrium. This method was used on an initial bread board model, however, and served adequately to check the feasibility of the additive heat approach.

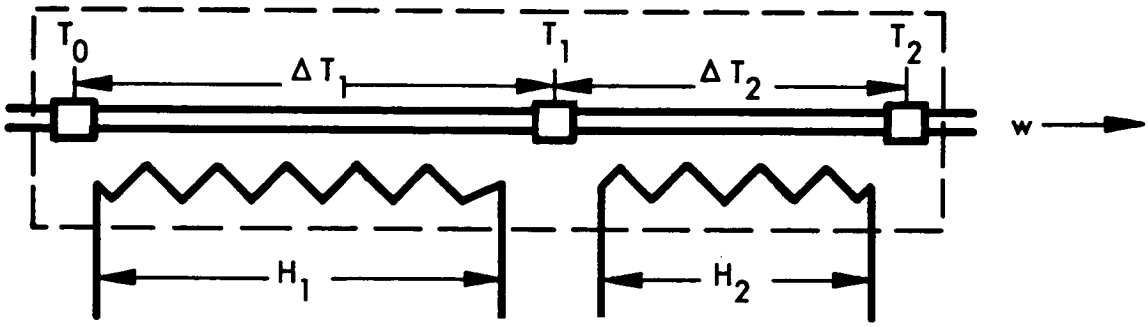


Fig. 2. Both Stages of Additive Heat Calorimeter

A second method would be to enclose the calorimeter and provide a vacuum insulation. This method appeared much more satisfactory from the standpoint of response time, but still had a considerable heat loss by radiation to the environment. It required an appreciable number of heat reflectors to reduce the heat losses to an acceptable level.

A third method is to jacket the calorimeter with a vapor jacket to conserve the heat. This could be accomplished by returning the vapor processed in calorimeter through a jacket enveloping the calorimeter before returning it to the system.

And a fourth technique utilizes guard heaters designed and controlled to maintain the outer skin temperature at the level which would preclude the heat flow in either direction.

The method actually adopted is a combination of the vapor jacket and the vacuum enclosure around the jacket, with provision for a supplemental guard heater. (The heat loss calculations performed for the calorimeter, as designed, do not indicate the necessity for the guard heater.) The actual design of the test calorimeter is shown on Figure 3.

The alkali metal enters the calorimeter through sample tubing leading to the coil. Just ahead of the coil a thermocouple is installed to record the initial temperature of the vapor. A heating unit mounted inside of the coil increases the energy of the vapor, evaporating the remaining liquid and slightly superheating the vapor. A second thermocouple records the superheat temperature (T_1). In actual installation the thermocouples are interconnected to measure the temperature difference (ΔT_1) between entering temperature and leaving temperature of the vapor. This temperature difference then becomes the signal used to control the heat input to heater (H_1).

Upon leaving the "drier" coil, the vapor enters the "superheater" coil where the temperature of the vapor is raised an additional increment (ΔT_2). A thermocouple (T_2) at the exit is interconnected with the intermediate thermocouple (T_1) to measure the temperature difference (ΔT_2). This difference is used to control the heat input into the second heating unit (H_2) located inside the super-heater coil.

To prevent any excessive, direct heater radiation from influencing the thermocouple reading, the units, each comprised of coil and heater, are enclosed in a reflecting "can" (refer to Figure 3). This assembly, in turn, is enclosed in a cylinder which has an adapter

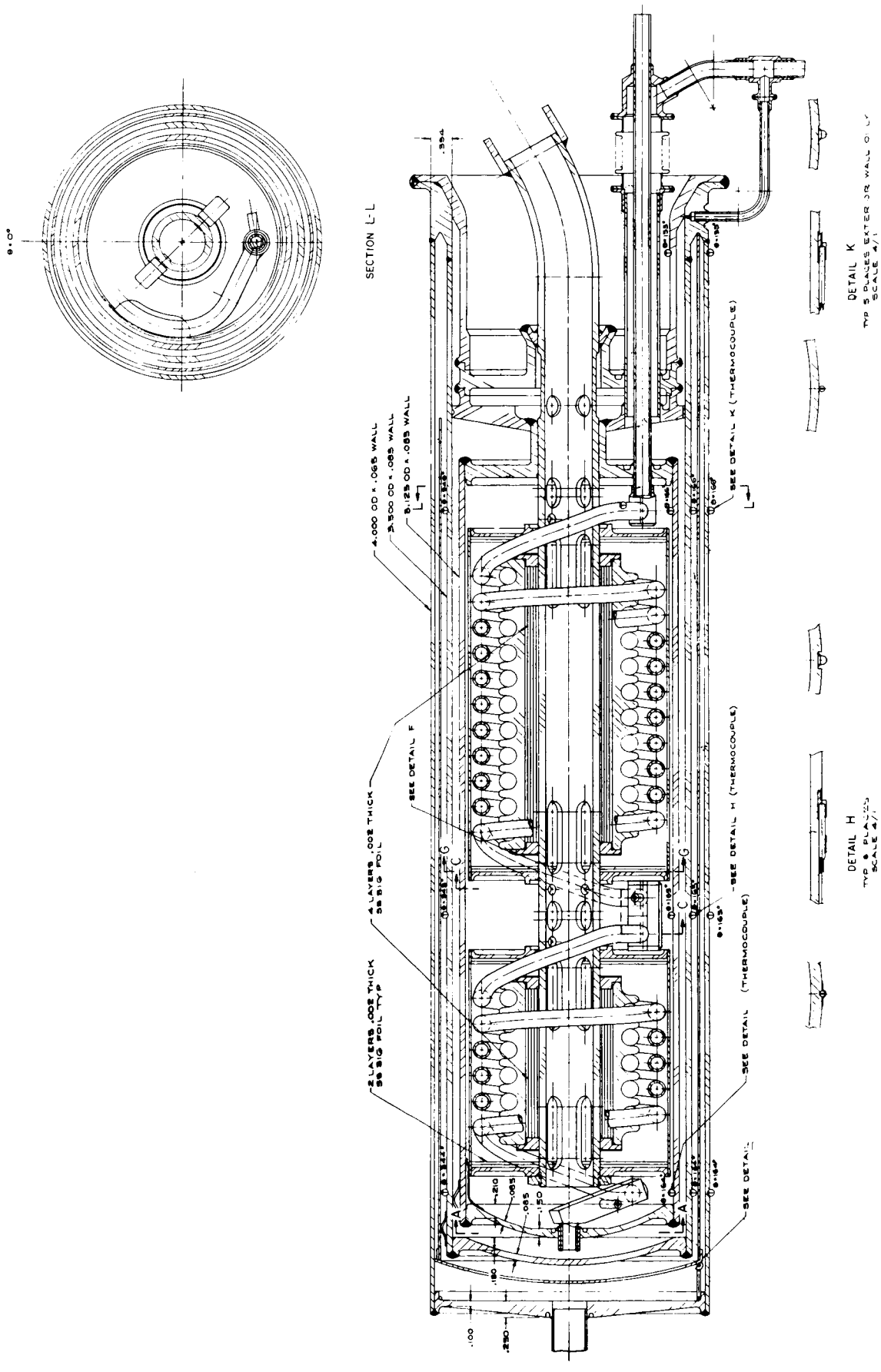


Fig. 3. Section through the Test Calorimeter

at the "top" to accept the exit vapor from the superheater coil. The entire unit is then enclosed in a vacuum bottle with built-in reflectors to minimize the heat loss from vapor return.

The annular passage between the cylinder enclosing the coil cans and the vacuum bottles serves as a return passage for the vapor. The return passage terminates in a smaller annular passage surrounding the sample tube before it is returned to the system.

The interior of the calorimeter is evacuated to eliminate heat transfer by convection from one heater to the other. Figure 4 shows the calorimeter components before assembly.

MATERIAL SELECTION

The first calorimeters for steam and low temperature (1600°F) potassium evaluation are constructed of 316 stainless steel. The selection of 316 stainless steel was based on compatibility requirements of possible potassium test systems. The lower temperature (1600°F) potassium evaluation of the calorimeter concept is to be carried out in one of several potassium systems located at ORNL. These systems are constructed of 316 stainless steel and, in order not to compromise the objectives of the systems, the calorimeters are constructed of the same material. The high temperature potassium calorimeter will be constructed of a suitable refractory metal alloy. Since the high temperature potassium calorimeter evaluation will require a refractory metal loop operating in an ultra high vacuum, the design of the calorimeter will be modified accordingly.

CONSTRUCTION

Due to the nature of the application, the calorimeter is an all welded structure with the exception of the vacuum feed throughs for heater power leads and thermocouples.

The utilization of the return vapor as a guard heater for the calorimeter dictated the design of the unit. A series of concentric tubes as shown in Figure 4 serve as the outer vacuum jacket, return vapor chamber, and radiation shielding. These sub assemblies were designed to permit disassembly of the calorimeter for repair or modification.

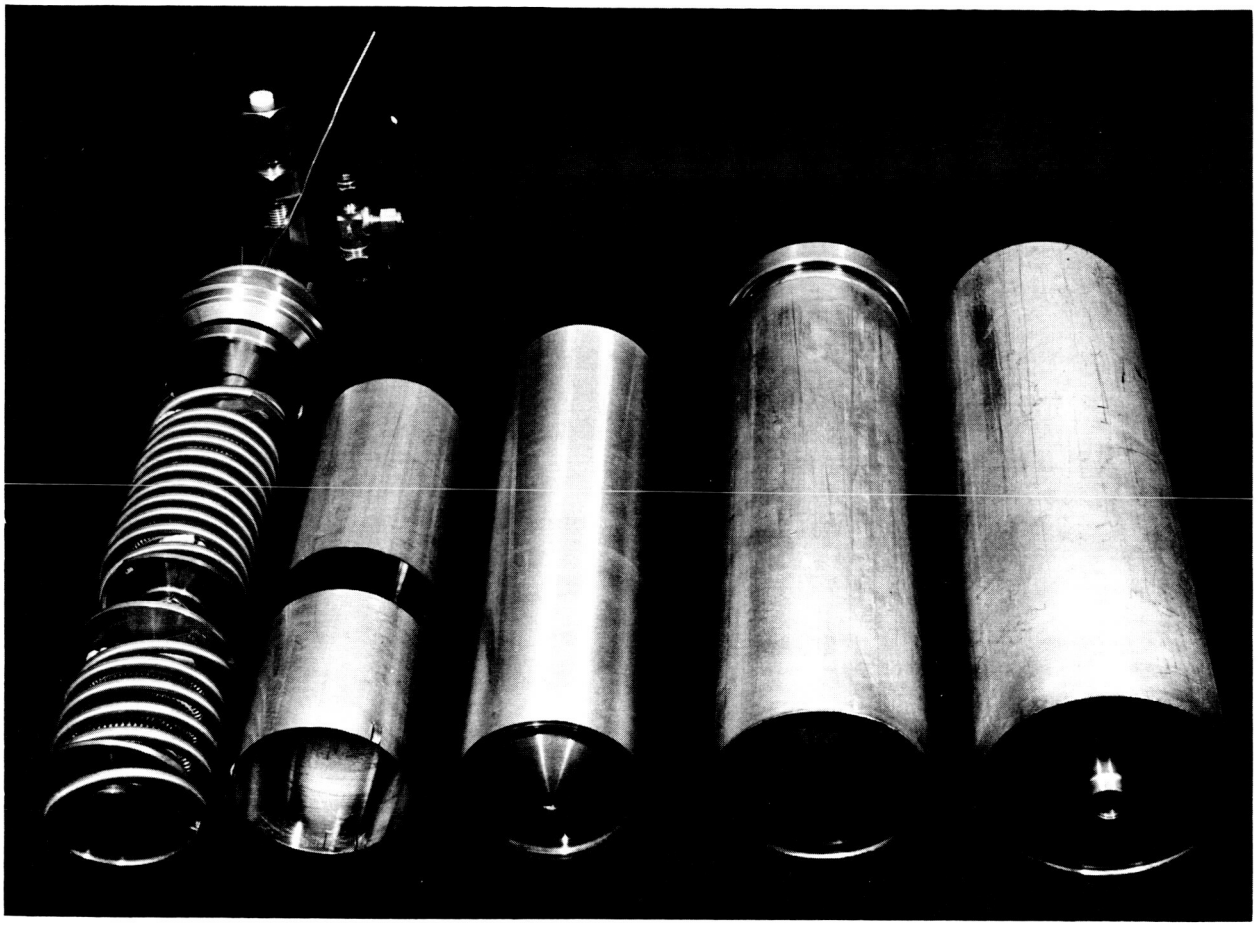


Fig. 4. Calorimeter Subassemblies

The working portion of the calorimeter which consists of coils containing the vapor surrounding the heater elements are contained within radiation shields in the evacuated central portion of the calorimeter. The evacuation of this volume is necessary to reduce heat losses and to prevent misdirection of the heat by reduction of convection currents. The drier and assemblies are contained within radiation shields to thermally isolate these units from each other. The heaters consist of nichrome V helical wore wound around on a fixed core. The pitch of the heater coincided with the pitch of the vapor coil.

Temperatures are measured at the strategic locations by means of stainless steel clad thermocouples located in thermowells located at the entrance to the drier coil, between the drier and superheater coil, and at the exit of the superheat coil. The thermocouples along with the power leads for the heaters emerge from the calorimeter through the central tube which is sealed by means of a conax fitting. The central portion of the calorimeter and the end vacuum chamber are also evacuated by means of a separate line.

CALORIMETER TEST PROGRAM

The calorimeter test program will be conducted in three stages:

1. The initial test series, now in progress, utilizes steam as the working fluid. This test will serve as a preliminary check of calorimeter operation and a check of potential accuracy of the system.

 A test to determine the effects of miniaturization will follow the initial shakedown test. A half-scale version of the calorimeter will be used for this test.

2. The next test series will be run with potassium vapor at about 1500°F. This test is scheduled to be run at Oak Ridge National Laboratory and will serve to check the operation of the basic model and the miniaturization model of the calorimeter with potassium vapor.

3. The third series of tests planned involve a calorimeter designed to operate at temperatures up to 2000°F. This unit will be made from a refractory alloy suitable for high temperature operations. Final plans for this series have not yet been defined.

MATERIAL SELECTION

The first calorimeters for steam and low temperature (1500°F) potassium evaluation are constructed of 316 stainless steel. The selection of 316 stainless steel was based on compatibility requirements of possible potassium test systems. The lower temperature (1500°F) potassium evaluation of the calorimeter concept is to be carried out in one of several potassium systems located at ORNL. These systems are constructed of 316 stainless steel and in order not to compromise the objectives of the systems, the calorimeters are constructed of the same material. The high temperature potassium calorimeter will be constructed of a suitable refractory metal alloy. Since the high temperature potassium calorimeter evaluation will require a refractory metal loop operating in an ultra high vacuum, the design of the calorimeter will be modified accordingly.

CONSTRUCTION

Due to the nature of the application, the calorimeter is an all welded structure with the exception of the vacuum feed throughs for heater power leads and thermocouples.

The utilization of the return vapor as a guard heater for the calorimeter dictated the design of the unit. A series of concentric tubes as shown in Figure 3 serve as the outer vacuum jacket, return vapor chamber, and radiation shielding. These sub assemblies were designed to permit disassembly for repair or modification.

The working portion of the calorimeter which consists of coils containing the vapor surrounding the heater elements are contained within radiation shields in the evacuated central portion of the calorimeter. The evacuation of this volume is necessary to reduce heat losses and to prevent misdirection of the heat by reduction of convection currents. The drier and assemblies are contained within radiation shields to thermally isolate these units from each other. The heaters consist of nichrome V helical wire wound around on a fixed core. The pitch of the heater coincided with the pitch of the vapor coil.

Temperatures are measured at the strategic locations by means of stainless steel clad thermocouples located in thermowells located at the entrance to the direr coil, between the drier and superheater coil, and at the exit of the superheat coil. The thermocouples along with the power leads for the heaters emerge from the calorimeter through the central tube

which is sealed by means of a conax fitting. The central portion of the calorimeter and the end vacuum chamber are also evacuated by means of a separate line.

CALORIMETER ACCURACY

The accuracy of the calorimeter depends on accuracy of measurement and the accuracy of values of thermodynamic parameters C_p and λ.

Possible it is best to treat these separately when regarding the general calorimeter Equation (3) (repeated below):

$$x = 1 - \frac{C_{p_2}\Delta T_2}{\lambda}\left[\frac{H_1}{H_2} - \frac{C_{p_1}\Delta T_1}{C_{p_2}\Delta T_2}\right] . \qquad (3)$$

As was mentioned above, the ΔT_1 is a small amount of superheat, possibly not exceeding $10^{\circ}F$ and, ΔT_2 is a larger amount, in the neighborhood of $100^{\circ}F$. A comparison of $\frac{H_1}{H_2}$ with the values of $\frac{C_{p_1}\Delta T_1}{C_{p_2}\Delta T_2}$ shows that variations in the latter values do not significantly effect the values in the brackets. For initial superheat of $10^{\circ}F$ and final superheat of $110^{\circ}F$ the value of $\frac{C_{p_1}\Delta T_1}{C_{p_2}\Delta T_2}$ remains in the neighborhood of 0.11, while the value of $\frac{H_1}{H_2}$ is approximately 4.0 for quality of 90%. Furthermore, since it is dependent on $\left(\frac{C_{p_1}}{C_{p_2}}\right)$ — a ratio of specific heats — that error resulting from values of specific heat being in error by as much as $\pm$ 10% will effect both the numerator and denominator equally, thus cancelling out. This leads to the justification of substituting C_1 for $\frac{C_{p_1}\Delta T_1}{C_{p_2}\Delta T_2}$ in the calorimeter basic equation.

The equation can now be rewritten as shown below:

$$x = 1 - \frac{C_{p_2} T_2}{\lambda} \left[\frac{H_1}{H_2} - C_1 \right] . \qquad (4)$$

In estimating errors in quality, the two sources of error are (1) errors on measurements, and (2) errors in values of thermodynamic parameters.

1. Errors in Measurements

For the calorimeter designed to operate between 80% and 100% quality, the estimated error in T_2 of $2^{\circ}F$ (or 2%) and the estimated error in power ratio of 3%, the calorimeter error in reading moisture will be 6%. Since moisture is 20%, for 80% quality, the error in quality is $\frac{0.06 \times 0.20}{0.80} = 0.015$ or 1-1/2%

At 95% quality, the error will be reduced to $\frac{0.06 \times 0.05}{.95} = .0032$ or 0.3% of the quality actually read.

2. Error in Thermodynamic Parameter

It is estimated that the error in specific heat values can be as high as 10%, and the error in latent heat is probably 2%. This will result in an error in measuring moisture of approximately 12%, resulting in possible error in quality at 80% of

$$\text{Error} = \frac{0.12 \times 0.20}{0.80} = 0.03 \text{ or } 3\%.$$

In order to meet a desired accuracy of 2% for the range of quality between 80% and 95% and a desired accuracy of 1/2% between 95% quality and 100% quality, it is imperative to improve the accuracy of the values of thermodynamic parameters. It might be possible to accomplish these improvements by accurate measurements of C_p through a controlled laboratory test using instrumentation similar to the calorimeter and an accurate measurement of the fluid flow.

STEAM TEST FACILITIES

The initial tests of the calorimeters will be conducted using steam. A layout of the test facilities is shown in Figure 5. Two methods of checking the vapor quality of the steam passing through the test section will be used. A throttline calorimeter which is suitable for measuring vapor qualities in the range 95 to 100% will provide one technique. A second method

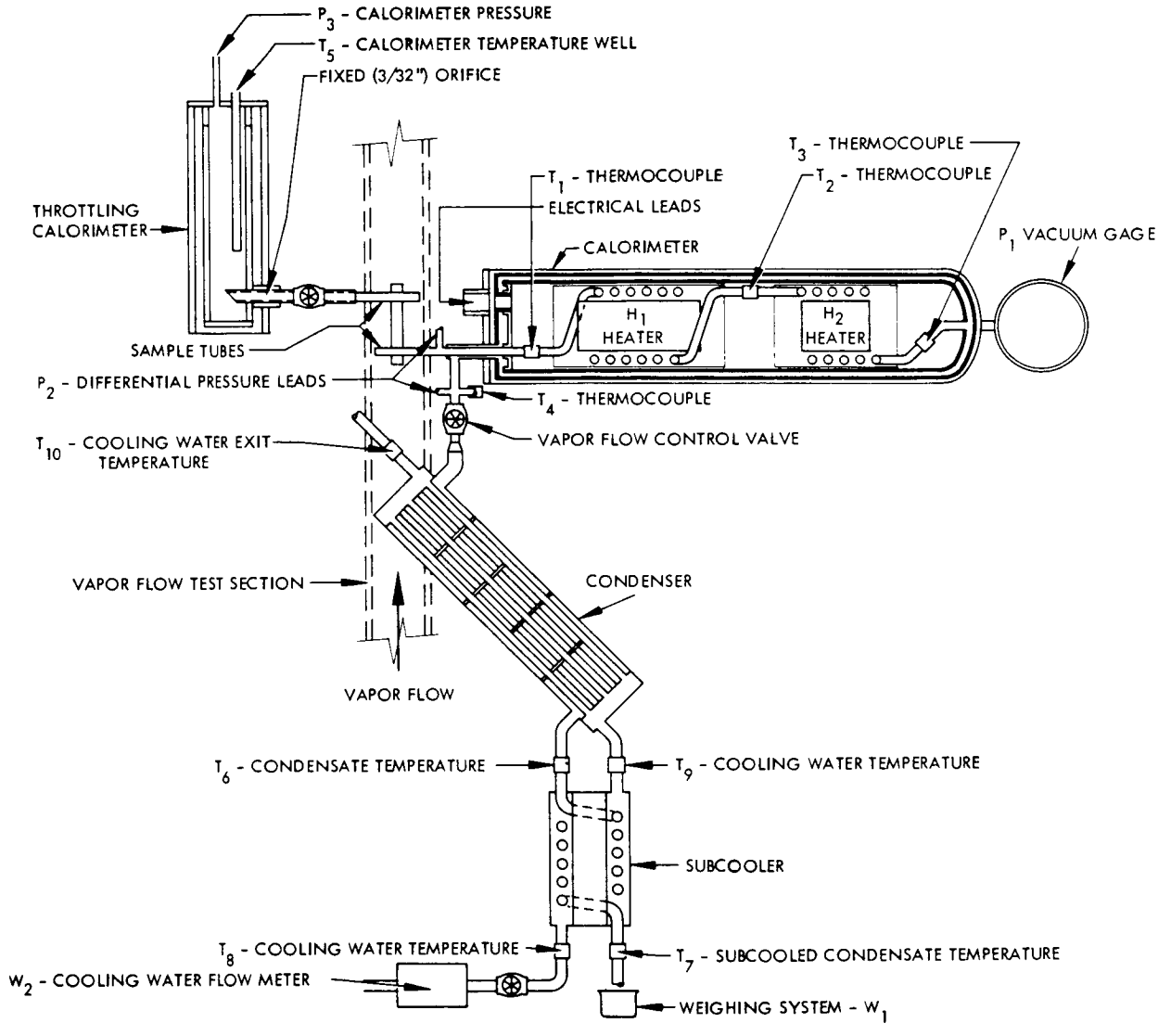


Fig. 5. Layout of Steam Test Set-up

involves the accurate measurement of the mass and heat content of a sample extracted from the main steam supply. A condenser and subcooler are shown in Figure 5 along with appropriate temperature and cooling water flow measuring devices for determing the heat content of the condensate. The mass of the condensate is determined by simply collecting and weighing the output of the subcooler. This arrangement can also be used in conjunction with the operation of the calorimeter. Knowing the mass flow through the calorimeter during calorimeter operation permits determination of heat losses through the use of the appropriate equations.

Steam is supplied to the vapor flow test section from two steam sources of different qualities. The 90 and 99 per cent quality steam can be mixed to provide steam in the test section at all intermediate qualities. For qualities below 90 per cent, water is injected into the steam line by means of a pressurized system. With this technique qualities as low as 80 per cent can be achieved which is the lower limit of the range of interest.

ACKNOWLEDGEMENT

The detail design of the calorimeter and its adaptation to the ORNL loop was worked out in close coordination with Mr. A. Fraas and the personnel under his supervision.

SESSION 3

BEARING FILM MEASUREMENTS

Tuesday, September 28, 1965

CHAIRMAN: J. Couch
NASA

N66 31684

LIQUID-METAL LUBRICATED BEARING INSTRUMENTATION

D. R. Grieser, Battelle Memorial Institute
J. L. Morris, Air Force Aero Propulsion Laboratory (WPAFB)

(Paper presented by D. R. Grieser)

Current interest in high-speed turbine, power systems using liquid metals as the working fluid, has led to intensive research on high-speed bearings. Component capabilities and system design requirements have resulted in the choice of liquid-metal lubricated, fluid film bearings, for load support of the high-speed rotating elements in the power unit. Research studies of these types of bearings have revealed difficulties in achieving satisfactory stability and dynamic load capacity because of the low viscosity of elevated temperature liquid metals and errors in turbulent flow analysis. The difficulties of measuring the fluid film behavior in the bearings during operation has forced the experimenter to "black box" studies of performance. The consequent lack of internal measurements has made the interpretation of performance data much more difficult.

The present work was initiated in an effort to develop instrumentation to permit measurement of the thickness, pressure, and continuity of the lubricant film. Techniques were selected that can directly measure the film with a minimum perturbation of the film and the bearing behavior. Miniaturized transducers are required to facilitate the measurement of film thickness and pressure profiles within a single bearing. The capability for being hermetically sealed is necessary to resist attack by the liquid-metal environment. A capability for operating at elevated temperatures without cooling is desired so that the normal thermal environment of the bearing is not altered.

Two techniques were selected as having the potential for most closely meeting the desired characteristics. An eddy-current/inductance technique was chosen for the measurement of film thickness and detection of film continuity. A technique based on the Villari effect was chosen for the measurement of film pressure.

The development of these techniques into prototype measuring instruments is currently in progress. Bench simulation studies have been performed on preliminary transducer models in order to assess the potentiality of the techniques for the projected bearing measurements and to obtain an empirical estimate of measurement sensitivity and temperature effects. Analytical studies have also been performed to assist in the design of prototype transducer systems for which more rigorous, bearing simulations are now being prepared. Although the past study covered the application of these techniques to the liquid metal, film bearings

PRECEDING PAGE BLANK NOT FILMED.

in general, the future effort will be concentrated on application to a bearing system of current interest. The prototype film-thickness instrumentation is being developed for a 1-inch size, K-94 sleeve/TZM journal bearing, potassium lubricated at a nominal operating temperature of 600 F.

Film-Thickness Measurement

The film-thickness measurement technique is based on the use of electromagnetic induction. The specific phenomenon of sensing film thickness is dependent upon the electrical and magnetic properties of the journal surface.

Nonmagnetic, Nonconducting Journal Surface. An electric current is induced in the electrically conducting liquid-potassium film by a coil buried in the bearing sleeve. The magnetic field produced by this induced current is sensed by the coil and appears primarily as a resistive loading. The loading is a function of the film thickness; therefore the thickness can be determined by measuring the alternating-current resistance of the coil. An inductive change occurs but this is a secondary effect amounting, in a typical example, to a signal about one-tenth that of the resistance change. The materials of interest falling into this category are the metal oxides such as Al_2O_3, MgO, and BeO.

Nonmagnetic, Electrically Conducting Journal Surface. As with the nonconducting journal, a current is induced in the potassium film by the coil buried in the bearing sleeve. However, in this case, current is also induced in the conducting journal. The film thickness can be determined only if the journal conductivity differs from that of the potassium because otherwise a thickness change could not produce an electrical change. The closer the match in conductivity, the smaller the change in a-c resistance of the coil with changes in film thickness; therefore the lower the intrinsic sensitivity. The inductive change is relatively small, since the field lines extending through the potassium film are always in a conducting medium in this case. An inductive change about 2 percent as large as the resistance change was noted. The materials of interest falling into this category are the refractory metals such as tungsten and molybdenum and alloys such as TZM, Inconel, many hard facing alloys, and binderless cermets.

Ferromagnetic, Electrically Conducting Journal Surface. As with the nonmagnetic, electrically conducting journal surface, current is induced in both the potassium film and the journal, resulting in a distinctive a-c resistance component in the coil performance. The ferromagnetic character of the journal surface, however, produces differing results depending on the frequency of measurement. For high frequencies such as are used for a nonmagnetic conductive journal, the results are similar to those for a nonconductive journal, because the magnetic properties of the journal make it appear to have a very high resistance similar, in effect, to an insulator. For lower frequencies, a resistive loading and also an inductive coupling occur which are functions of the proximity of the journal surface to the coil. Thus, for lower frequencies, there will be a large change in inductive reactance as well as a change in a-c resistance of the coil. The materials of interest falling into this category are nickel, iron, and cobalt bonded cermets, and ferritic stainless steels.

In practice, a small electromagnetic coil is buried in the stationary sleeve of the bearing. For protection from the potassium vapor and liquid, the coil and electrical leads must be hermetically sealed. If the sleeve is a nonconductor, the coil is potted into a blind hole so that the coil is located within a few thousandths of an inch of the potassium film but is separated from it by a thin diaphragm of the sleeve material. The electrical leads into the back of the transducer hole are to be ceramic shielded, metal sheathed, and hermetically sealed to the bearing sleeve and to the bearing container vessel.

If the bearing sleeve is an electrical conductor, it may be necessary for the transducer coil to be potted into a nonconductive insert which is bonded into a hole reaching through the bearing sleeve, so that only a nonconductive diaphragm separates the coil from the potassium film. This will be mandatory if both the journal and the sleeve are conductors, because the transducer sensitivity will be markedly reduced by the shielding effect of an additional conductor between the coil and the potassium film.

The external instrumentation consists of a power supply for excitation of the transducer coil and output signal conversion for display and recording. The specific frequency of excitation should be chosen to optimize the transducer performance for the particular bearing materials, individual transducer characteristics, and film-thickness range to be measured. The present laboratory

investigations indicate that the most useful operating frequencies are between 6 and 15 megacycles for a nonmagnetic conductive journal and in the kilocycle range for a strongly magnetic journal.

Conversion of the transducer output signal will include linearization and automatic temperature compensation to assist on-site analysis of bearing performance. The output signal will also be converted to a level appropriate for display on a simple indicating meter or for recording on an oscilloscope or chart recorder, depending upon the desired form and dynamic response for the display.

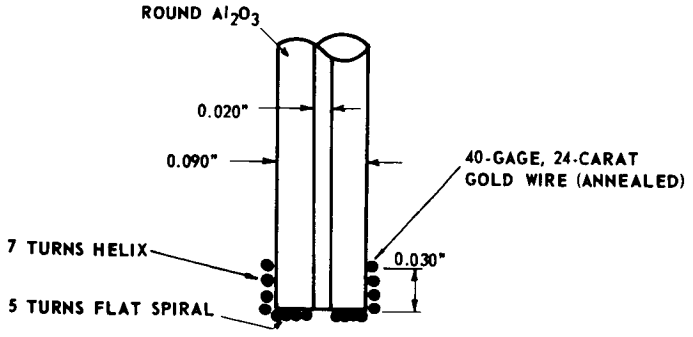
Experimental Study

Design restrictions were placed upon the transducer in order to satisfy projected application to future bearing development needs. A maximum probe diameter of 0.1 inch has been chosen to permit multiple-unit instrumentation of bearings as small as 0.25 inch diameter. The capability for operating temperatures up to 1200 F and a dynamic response of up to 2000 cycles per second is being sought as well as an ultimate accuracy for the film-thickness measurement system of ±10 microinches over a range of 50 to 5000 microinches.

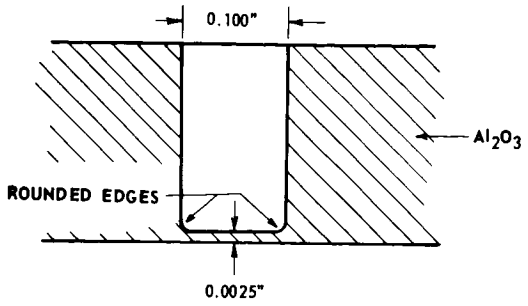
The experimental studies performed to date have been used as preliminary evaluations of coil designs. The data have been used to determine the effect of film-to-coil spacing, coil temperature, and journal materials. Film-simulation data have been used to support analytical studies, to reveal problem areas, and to assist in predicting practical performance goals.

Several dozen coils of differing geometries were fabricated and from among them the design illustrated in Figure 1 was found to have the highest sensitivity. Essentially it consists of two open wound coils of 3-mil, bare, gold wire--one a spiral and the other a helix. One test coil was wound on an alumina tube and potted with high-temperature elements into a 0.100 inch blind hole ultrasonically drilled into an alumina block. The unit was then cycled in a furnace to a 1200 F maximum temperature for determining the thermal performance. Both the "Q"* of the coil and the d-c resistance were measured as a function of temperature. These data are shown plotted in Figure 2. Examination of these data showed that the inductance of the circuit was essentially constant over the entire temperature

*Ratio of the inductive reactance to the total a-c resistance.



1a. Prototype "Cupcake" Design



1b. Mounting Hole in Bearing Sleeve

Fig. 1. Prototype Design for Thickness-Transducer Coil

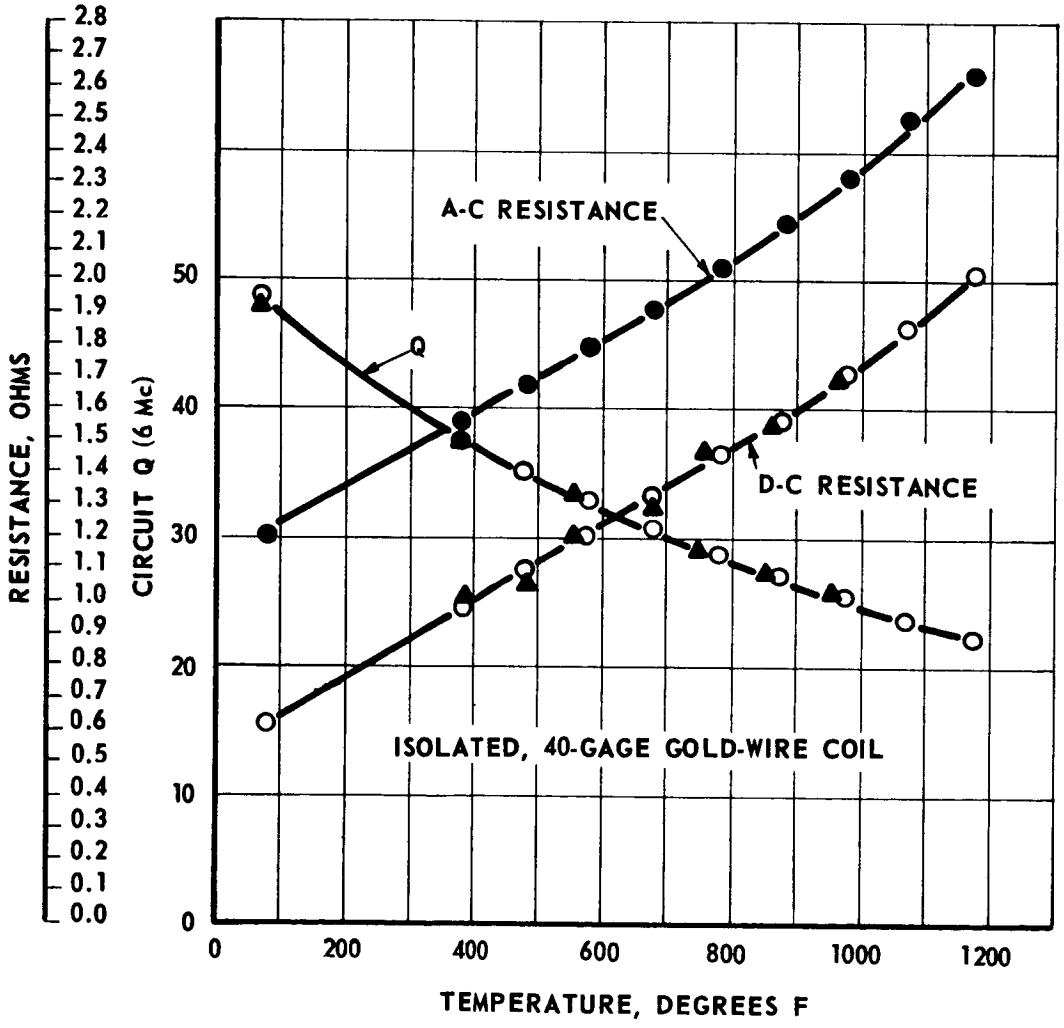


Fig. 2. AC and DC Resistance and Q of Transducer Circuit versus Temperature

range, with a change of less than ±0.5 percent. The total a-c and the d-c resistance increased as a parabolic function of temperature. A statistical analysis of the data indicating a high degree of stability. From these experiments, it has been concluded that the effect of temperature on the total a-c resistance can be compensated for by using the d-c resistance of the coil as a temperature monitor.

A second series of experiments was performed to determine the effect of the separation distance between the coil and the film. These data are shown in Figure 3. Examination of these data showed that although the magnitude of the Q reading was greater at larger coil-to-foil spacing, the Q-versus-film-thickness shape remained nearly the same. It has been concluded from this that differences in transducer characteristics because of differences in coil-to-foil spacing which may result during fabrication can be compensated for with relative ease.

The third series of experiments was conducted with foils of lead to simulate at room temperature the electrical behavior of a potassium film at 400 F. A Lucite, a tin, and a steel block were used to represent three different types of journal surfaces. Three sets of Q readings were obtained as a function of foil thickness--one set with each simulated journal material. These data are presented in Figure 4. Except for the dotted portion of the curve obtained with lucite, the data indicate that the Q decreases with increasing electrical resistance of the film-journal combination. Independent measurements showed that the inductive reactance was nearly constant with film thickness at the relatively high excitation frequency of 6 megacycles used for these experiments. These curves therefore show that the total a-c resistance can be used as a measure of the film thickness. The relatively gentle slope of the lead foil-on-tin case indicates the relatively low sensitivity that can be anticipated when attempting to measure a potassium film on a TZM journal. Interesting is the similarity in behavior between the magnetic journal case and the nonconductive journal case. At the high excitation frequency used for these experiments, the effective penetration of the magnetic flux into the steel is so shallow as to make the journal appear to be a nonconductor. As expected, the dotted portion of the nonconductive journal curve illustrates that in this case coupling of the flux lines is lost as the film thickness approaches very small values.

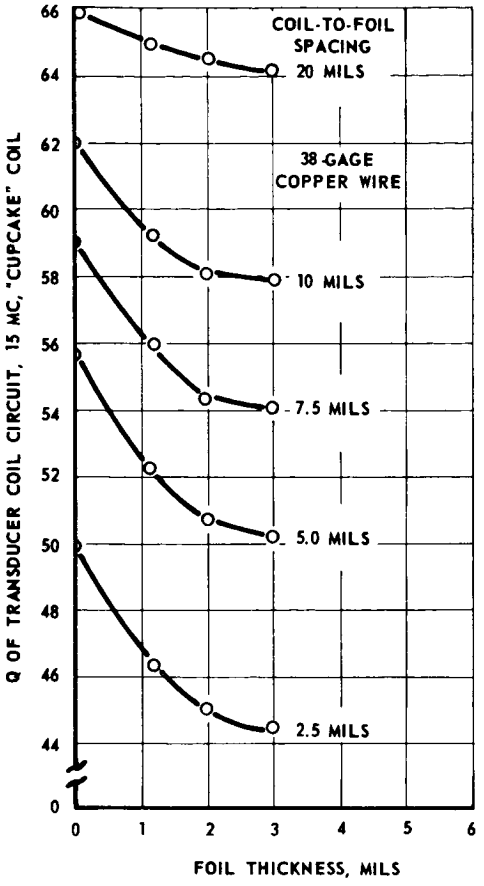


Fig. 3

Effects of Foil Thickness and Coil-to-Foil Spacing on Q at 15 MC

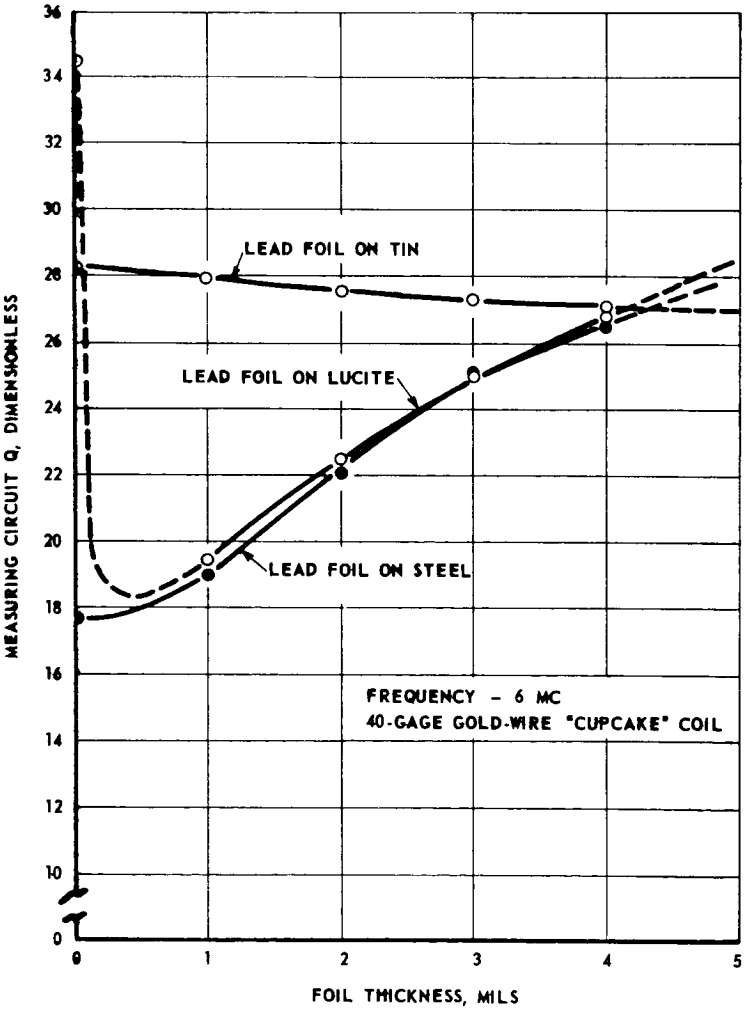


Fig. 4

Results for Three Material Combinations

An additional study was made of the magnetic journal case in which excitation frequencies in the kilocycle per second range were used. These showed that the significantly greater change in output as a function of film thickness could be obtained by operation at lower frequencies. Past experience with the low frequency gaging to a magnetic shaft however was disappointing since slight permeability variations around the journal surface were detrimental to the measurement of journal position. As a consequence, it may be more practical to operate at high frequencies when attempting to gage to a magnetic journal, even though sacrificing sensitivity, in order to minimize the effect of permeability variation.

Application of Current Interest

The development of a journal bearing for a turbine power unit, operating on potassium, is currently in progress at other laboratories. The present and future effort in the development of a film-thickness measurement system is being concentrated upon eventual application to this bearing development. Consequently, the current materials and operational parameters have been used to establish specific goals for the instrumentation development. The bearing to be instrumented is a simple, 1-inch diameter journal type with a K-94* sleeve (static member) and a TZM** journal (rotary member). The working fluid is potassium at operating temperatures in the 550-650 F range. Automatic linearization and temperature compensation of the output signal within ±10 percent is a design goal for the measurement system. With the additional aid of in situ calibrations, a minimum precision of ±20 microinches is sought over a film-thickness range of 50 to 3000 microinches with an absolute accuracy of ±30 microinches. A dynamic response in excess of 2000 cycles per second is expected. The materials and design will be chosen to permit heatup excursions to 1200 F without damage to the transducer.

A conceptual design for the prototype transducer is shown in Figure 5. The main features illustrated are: (1) the mounting of the transducer coil in an alumina insert to reduce the coupling of the electromagnetic field to the conductive bearing sleeve, and (2) the use of a three-wire (two lead wires and the sheath) connection to the transducer to help minimize the effects on the output signal of

*12 Co, 2 TaCb, bal. WC (kennametal)

**0.5Ti, 0.08 Zr, bal. Mo.

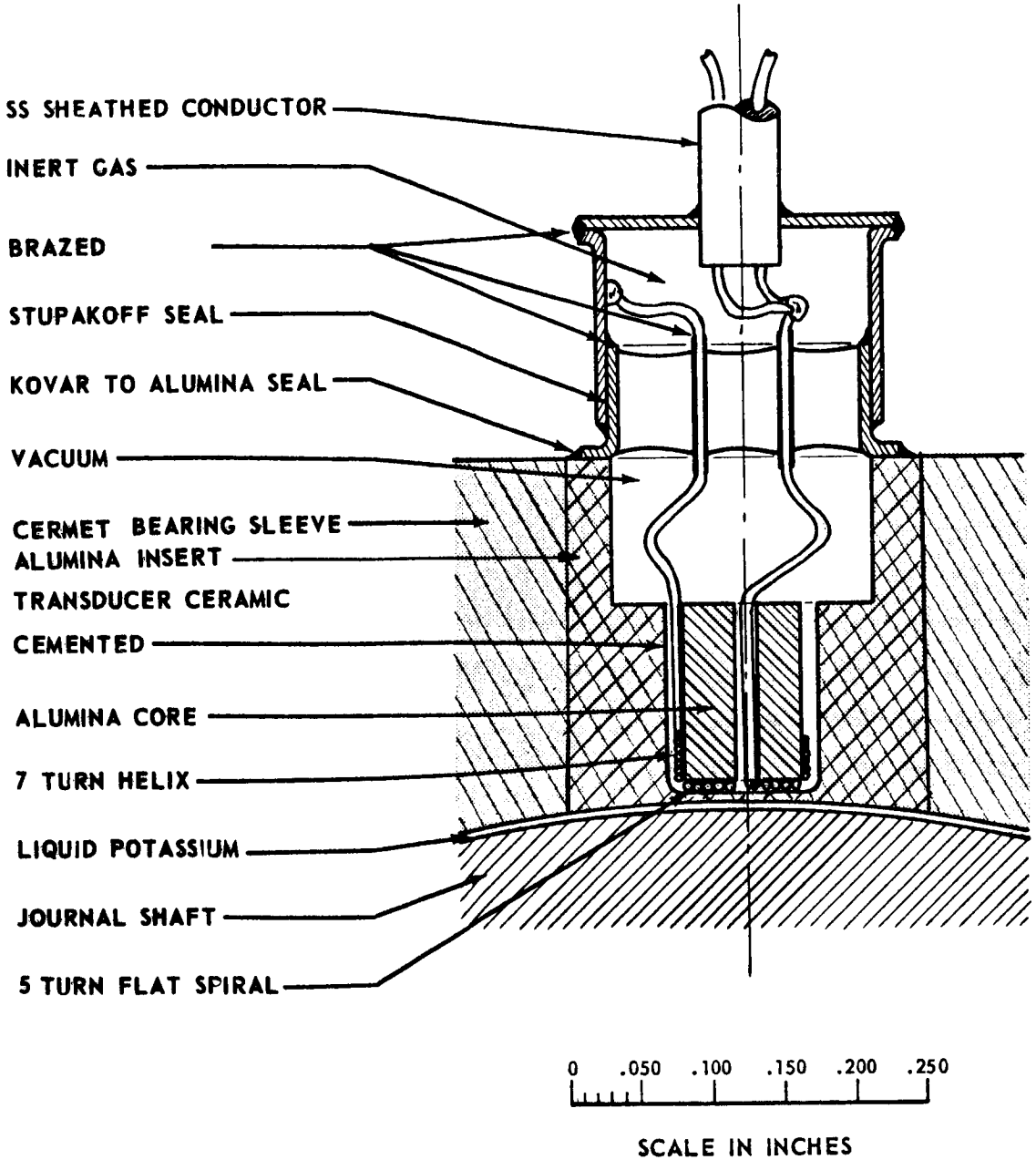


Fig. 5. Prototype Film Thickness Transducer Design

lead-wire resistance change with temperature. A more direct means of attachment and hermetic sealing of the sheathed output cable is now being developed in which a metal tube will be pressure-bonded to the bearing sleeve simultaneously with the alumina insert. This tube will then be sealed to the protective sheath on the output cable after potting the coil into the insert and attachment of the lead wires.

Currently, a unit is being constructed for determining the static and dynamic performance of prototype film-thickness measurement units with potassium. The facility includes a drive unit capable of output spindle speeds up to 24,000 rpm and a pumped-loop, potassium cleanup-and-filter system. A simulated journal bearing will be used in the evaluation in order to permit a greater degree of control and reliability than would be possible with an actual journal bearing. The bearing journal will consist of a ground and lapped sleeve of TZM attached to the high-speed spindle. The transducer coils will be mounted in blocks of K-94 using the design, materials, and processes to be employed in the eventual application. The K-94 blocks will simulate partial segments of a full journal bearing and will be rigidly attached to side arms which will extend through bellows seals in the side of the potassium enclosure surrounding the end of the drive spindle. The side arm extensions will be fastened to a system of flexible pivots which will maintain alignment of the K-94 nosepieces with the TZM journal while permitting precisely controlled movements of the nosepieces toward and away from the journal as a means of establishing known and controlled film thicknesses of potassium between the simulated bearing sleeve and journal. Figure 6 is a cutaway drawing of this bearing simulation assembly. The performance of the instrument system will be studied as a function of film thickness, temperature, journal speed, and presence and absence of a full potassium film between the sleeve and journal.

Film Continuity

During the study of coil-to-foil spacing, it was found that the coil inductance changed by 2.2 percent for a spacing change of from 2.5 to 5 mils whereas the coil inductance changed less than 0.5 percent during the film-thickness studies with the simulated conductive journals. Based on these measurements made during the bench studies, it has been concluded that the film-thickness transducer can be used to detect the presence of discontinuities in the potassium film caused

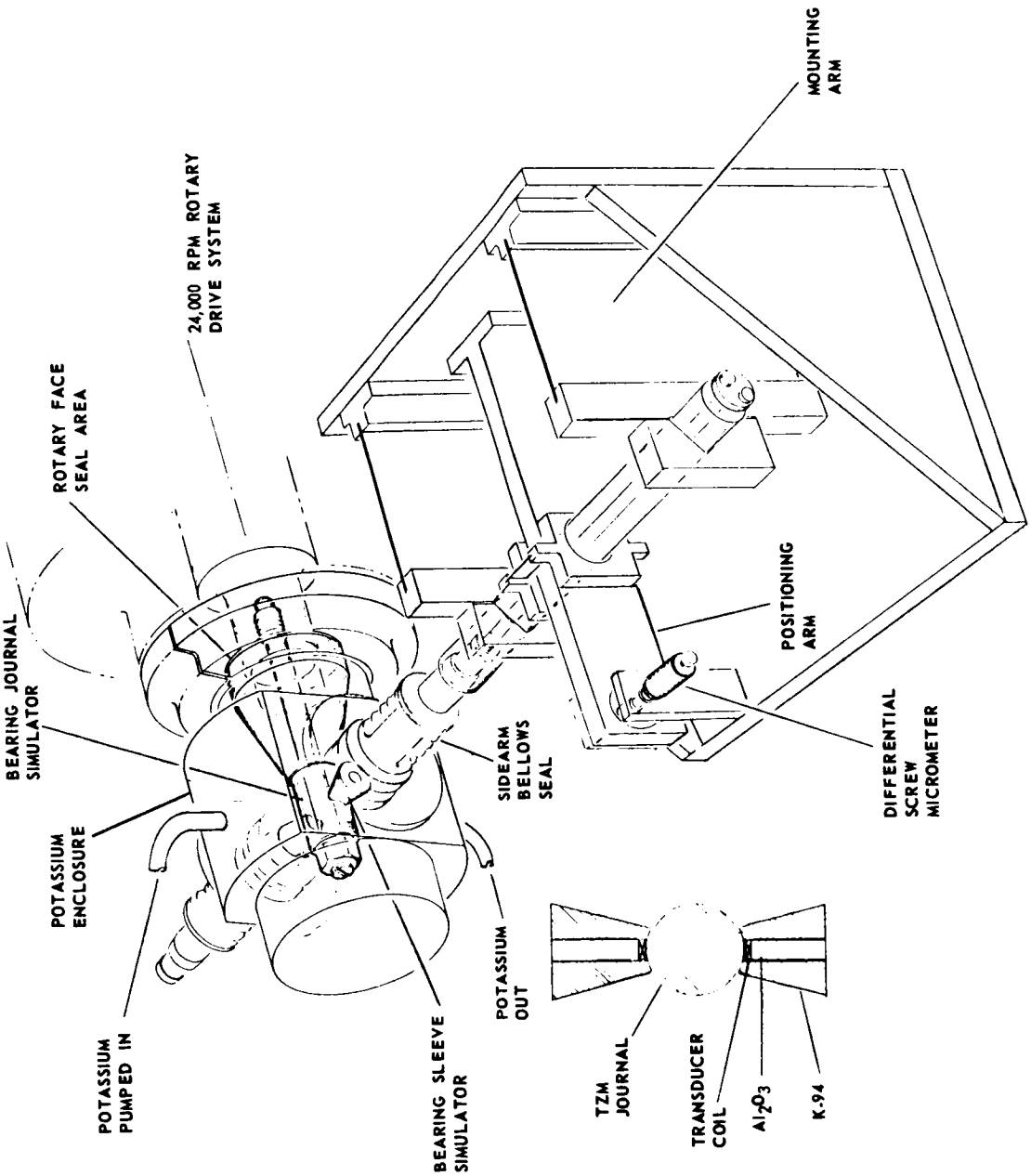


Fig. 6. Potassium Journal Bearing Simulator for Film Thickness Transducer Evaluation

by cavitation or inadvertent cover-gas entrainment. The technique will be analogous to the conventional use of inductance/eddy-current techniques for the detection of bonding flaws in clad metal surfaces.

Experimental evaluations will be made during the performance studies of the film-thickness technique by measuring the transducer characteristics with and without potassium between the sleeve and journal. From this can be determined the maximum response to film discontinuities. In the course of dynamic film-thickness evaluations, it will be possible to induce cavitation by orienting the sleeve segment with relation to the journal to obtain a divergent film gap. For a particular temperature, minimum gap size, and gap divergence, hydrodynamic analysis will permit the estimation of the critical rotation speed above which cavitation can occur. The effectiveness of the transducer for detecting film discontinuity in a journal bearing film can then be evaluated by comparing experimental measurement of critical speed with calculated values.

Film Pressure

The film-pressure instrumentation is being developed for future laboratory studies of liquid-metal lubricated bearing behavior rather than for a specific current application. A capability for mounting on 0.2-inch centers is being sought in order to facilitate the measurement of pressure profile within a single bearing. Pressures in the range of 0-200 psia are to be measured with a sensitivity of ±2 psi and an absolute accuracy of ±4 psia at temperatures up to 1000 F. It has additionally been specified that the pressure transducer be flush mounted with the bearing surface to minimize perturbation of the lubricant film hydrodynamics and consequent falsification of the pressure measurement that can occur most severely in thin films at high shear rates.

The pressure-detecting device consists of two major parts; a diaphragm that converts film pressures into translational forces and a high modulus force-detector unit. The detector is arranged so that deflection of the diaphragm by film pressure causes strain in a core piece upon which a coil of wire is wound. The core piece is fabricated from a material which exhibits a change in permeability with strain (Villari effect). Measurements of the electrical properties of the coil then provide the indication of pressure.

The conceptual design resulting from the development studies is illustrated in enlarged cross section in Figure 7. In this design the diaphragm deflects upward as a result of film pressure and compresses the coil core, the other end of which is restrained from moving by virtue of the coil housing sleeve held in place by the flange and clamping sleeve. Both the coil core and coil housing sleeve are ferromagnetic materials. The design therefore provides a path for magnetic flux lines to pass axially through the core and return via the coil housing sleeve and small air gap between housing sleeve and lower end of the core. This air gap permits the lower end of the core to move freely. Under compression, the magnetic properties of the core change, causing corresponding changes in the impedance of the coil wound upon it. The change consists mainly of a decrease in inductive reactance of the coil, which is measured by external instruments.

The coil housing sleeve is made of the same material as the core but is designed with sufficient area so that essentially all of the strain with diaphragm deflection occurs in the core piece. In early experimental models of the device, the housing sleeve was simply restrained at the top surface rather than at the lower flange as in the prototype design. The design of Figure 7 provides a compensation for thermal expansion, since as the core expands so does the housing sleeve, thus tending to maintain a given starting position with respect to the diaphragm. Since the lower flange does not rest directly against the diaphragm, the compensation for expansion cannot balance exactly unless an appropriate thickness of bearing-sleeve material is substituted for part of the core. The method proposed for doing this uses a "nosepiece" of bearing material of proper thickness located between the diaphragm and core, as shown in Figure 7.

The diaphragm behavior was studied mathematically in order to determine a desirable mechanical design and to estimate the forces and translations that could be expected with the specified film pressures. The force detector was investigated largely with an experimental approach to try to achieve high sensitivity for small forces and displacements. The combined diaphragm and force detector have not yet been examined experimentally in an assembled form.

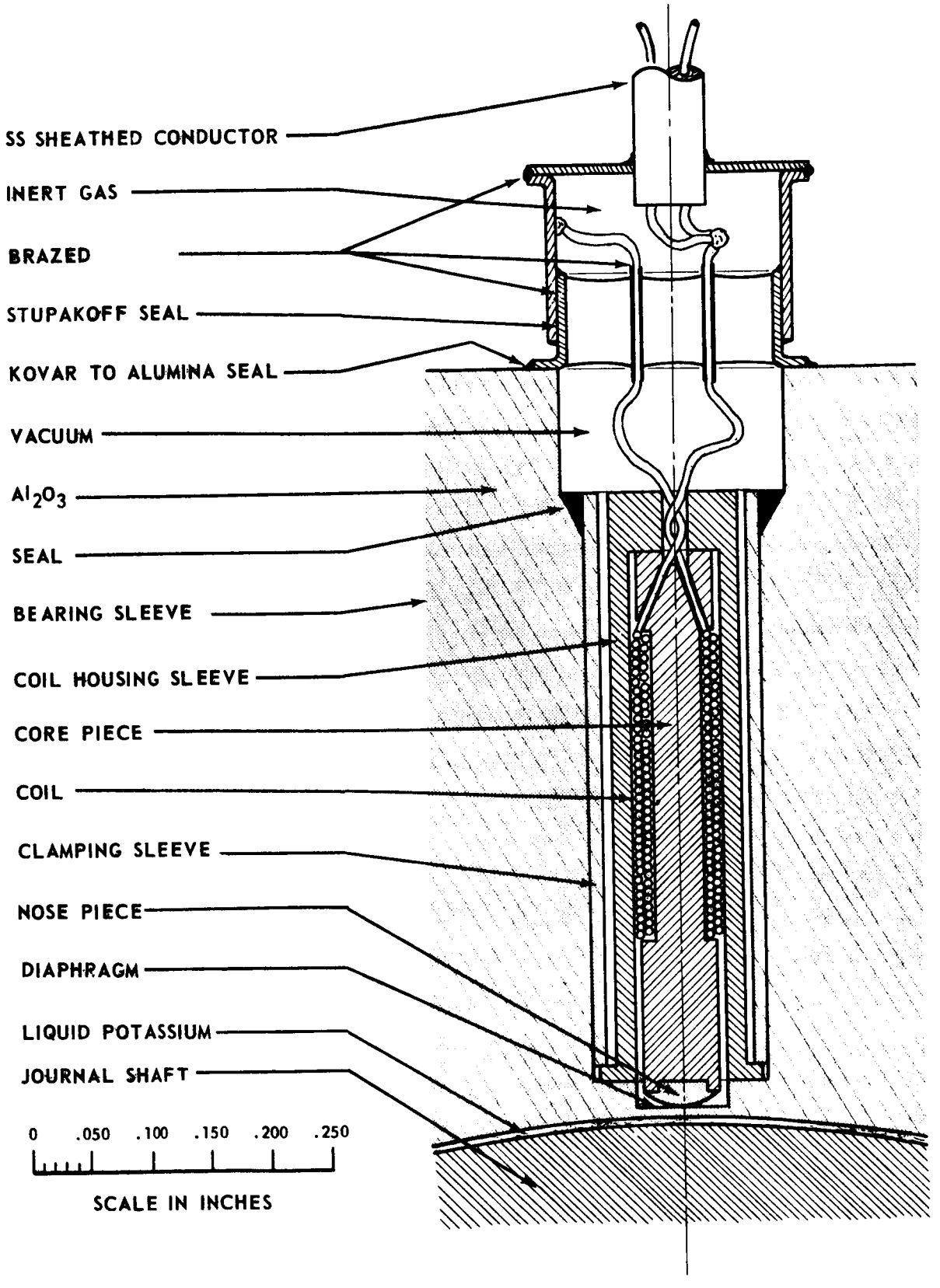


Fig. 7. Prototype Pressure-Transducer Design

Experimental Study

Preliminary laboratory experiments have been performed to aid in the selection of a transducer design and core materials, and to permit an assessment of capabilities and problem areas. An example of the kinds of data obtained is illustrated in Figure 8. In this series of evaluations, an experimental, miniature, force transducer, enclosed in a furnace, was connected into an a-c bridge circuit and load response curves obtained at four temperature levels. From a study of these and other experiments, it was determined that Nivco alloy exhibited the most favorable behavior from the standpoint of strain sensitivity, yield strength, Young's modulus at elevated temperature, damping coefficient, machinability, impact strength, and resistance to oxidation. The operating temperature, however, must be limited to a maximum of 950 F in order to avoid a time-transient behavior. Mechanical conditioning can be used to improve stability and reduce hysteresis effects. The maximum temperature excursion should be limited to 1050 F to avoid breakdown of the ceramic insulation in the close-wound coil of the transducer.

Currently a more efficient force transducer design has been evolved in which the air gap in the magnetic flux path has been avoided. The current core design is that of a miniature, elongated, proving ring which is the Villari effect core and the wire is coiled around the two elongated sides. The core looks similar to the eye end of a darning needle with coils wound around the two long sides. This configuration is shown in Figure 9. Experimental studies will be performed on prototype pressure transducer units incorporating this modified force transducer core using a heated, pneumatic pressurization apparatus. Separate potassium compatibility experiments will be conducted to determine the efficiency of the hermetic sealing process. The pneumatic studies will be designed to determine the sensitivity, hysteresis, and thermal and dynamic behavior of the prototype units.

Acknowledgments

The authors wish to thank Messrs. A. F. Leatherman and J. Flora of the Battelle Systems Engineering Division for their extensive contribution to the conduct of this research. This program is presently being supported by the United States Air Force under contract AF 33(615)-2812.

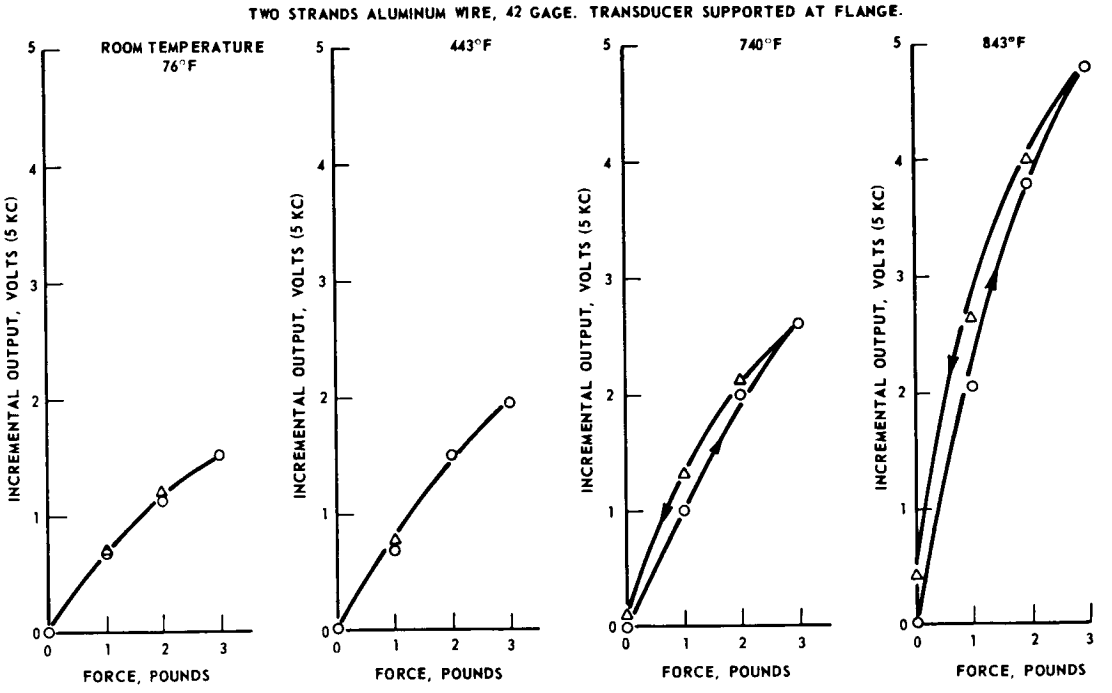


Fig. 8. Nivco Force Detector Unit Response at Four Temperatures

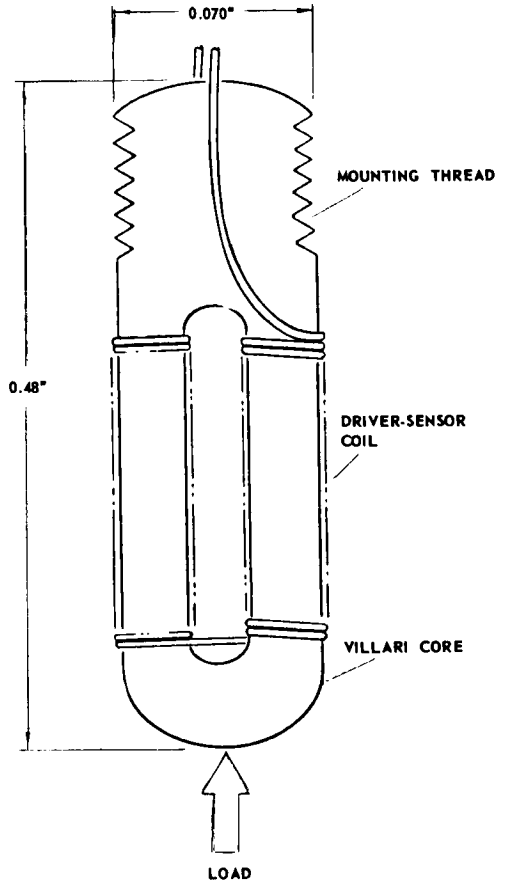


Fig. 9. Pressure-Transducer-Core Design without Air Gap

N66 31685

DEVELOPMENT OF PERFORMANCE-MEASURING INSTRUMENTATION FOR A LIQUID-METAL TURBINE-DRIVEN BEARING TEST RIG

by

L. W. Stillwell and R. Herman
AiResearch Manufacturing Company of Arizona
Phoenix, Arizona

(Paper presented by N. F. Pratt)

1.0 INTRODUCTION

During the preliminary planning phases for a potassium turbine with potassium-lubricated bearings, it became apparent that the development of liquid-metal journal and thrust bearings required special performance-measuring instrumentation. One problem that occurs in the design of bearings is that of journal bearing stability, a problem common to all high-speed rotating machinery. Information concerning the stability of the bearing can be obtained from accurate measurements of the journal whirl in the bearing. These measurements must be made reliably and accurately under all bearing operating conditions. Thus, instrumentation was to play a key role in the success of this program.

Because of the high cost and long time required to set up and test candidate bearings in potassium, preliminary stability tests were to be conducted in a special test rig consisting of rotors supported on test bearings lubricated by conventional fluids. The bearing performance-measuring instrumentation had to be capable of performance with both conventional fluids such as water and oil and also with 600°F potassium. Typical parameters to be measured were the following:

(a) Whirl of the journal in the bearings and, in turn, the liquid-metal film thickness existing between the journal and the bearing under various test conditions.

(b) Axial location of the shaft thrust pad with respect to the thrust bearing.

(c) Speed of the journal shaft.

The film-thickness variations in the journal bearings and shaft motions expected were 0.001 inch or less. These parameters had to be measured within an accuracy of ±0.000050 inch. A review of commercially available instrumentation confirmed the opinion that our requirements necessitated improvement in the presently available equipment.

A development program was initiated to provide the necessary instrumentation. Through this program a film-thickness measuring system based on eddy currents was designed and developed. Correspondence between film thickness in the journal bearings and motion of the journal was obtained from a knowledge of the journal and bearing dimensions. To measure the axial motion of the shaft, a specially designed linear variable differential transformer (LVDT) was obtained commercially. To monitor shaft speed, a special monopole pickup was designed and fabricated. This pickup is similar to commercially available pickups. All of these systems provided sufficient signal-to-noise ratios to permit satisfactory magnetic-tape recordings with the desired accuracies at a frequency response reasonably flat from 0 to at least 400 cps.

This report will discuss only the film-thickness measuring system.

2.0 FILM-THICKNESS TRANSDUCER

2.1 Theory of Operation

When a coil of wire carrying an alternating current is placed near a conducting material, eddy currents are induced in the conducting material. These eddy currents are generated so as to oppose the exciting current in the coil and cause a change in the magnetic field. The change in the magnetic field, which can be measured by a second coil in the field, is a function of the conductivity of the material near the coil, the distance between the material and the coil, and the shape and size of the material.

In using eddy-current-type transducers for film-thickness measurements, consideration must be given to the permeability and conductivity of the material being measured and the excitation frequency supplied to the coil. The standard depth of penetration of eddy currents is expressed by:

δ = standard depth of penetration in inches

μ_r = permeability of the material relative to air

f = exciting current frequency in cycles per second

σ = conductivity of the material in percent IACS (International Annealed Copper Standard)

At 600°F, the conductivity of potassium is 5.9 percent IACS and the permeability is 1.0. If an exciting frequency of 20 kc is considered, the standard depth of penetration is calculated to be 0.092 inch. It will be somewhat less than this value in this design due to the metal wall employed between the coils and the potassium to protect the coils from the potassium.

2.2 Transducer Design

In this system technique, the basic device employed to measure film thickness consisted of two coils mounted diametrically opposite each other on each side of the journal shaft. Two sets of coils located at 90 degrees to each other permitted detection of the change in film thickness due to motion of the axis of rotation of the shaft in any radial direction. Since each set of coils was connected in series opposition, as shown in Figure 1, motion of the shaft from the center null position produced a net output from the coils. An additional benefit from connecting the coils in opposition was that temperature compensation was also provided. Since the coils were used in pairs, the effects of distributed capacitance, coupling coefficients, variation in turns, ratios, and total inductance were minimized.

The coil cores were machined from lava stone and then fired at 2000°F to cure the stone. Critical dimensions were held to a tolerance of 0.0005 inch. The cores provided a form on which to wind the wire and functioned essentially as air cores. They were quite stable, both mechanically and electrically. Thermal gradients were minimized by providing small holes for the circulation of cooling gas. The cores were wound with a nickel-clad copper wire coated with a ceramic insulation (see Figure 2). To reduce electrical noise, metal shielding was placed around the coils

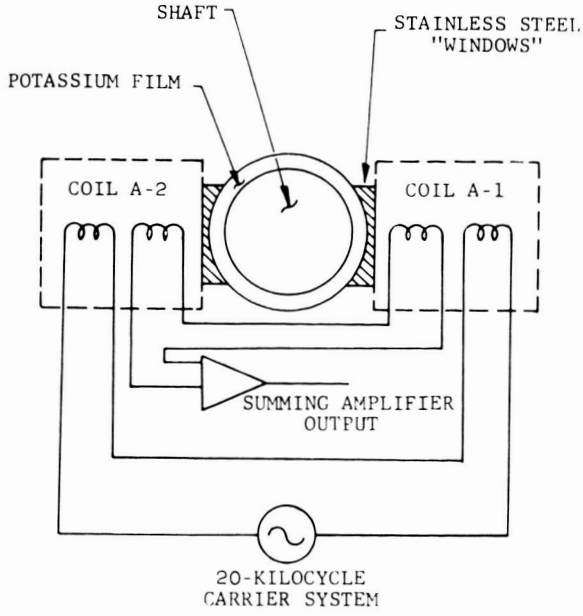


Fig. 1

Differential Output Film Thickness Measuring System

Summing Amplifier

output = $K[E_{(A-2)} - E_{(A-1)}]$

where $E_{(A-1)}$ = coil A-1 voltage

$E_{(A-2)}$ = coil A-2 voltage

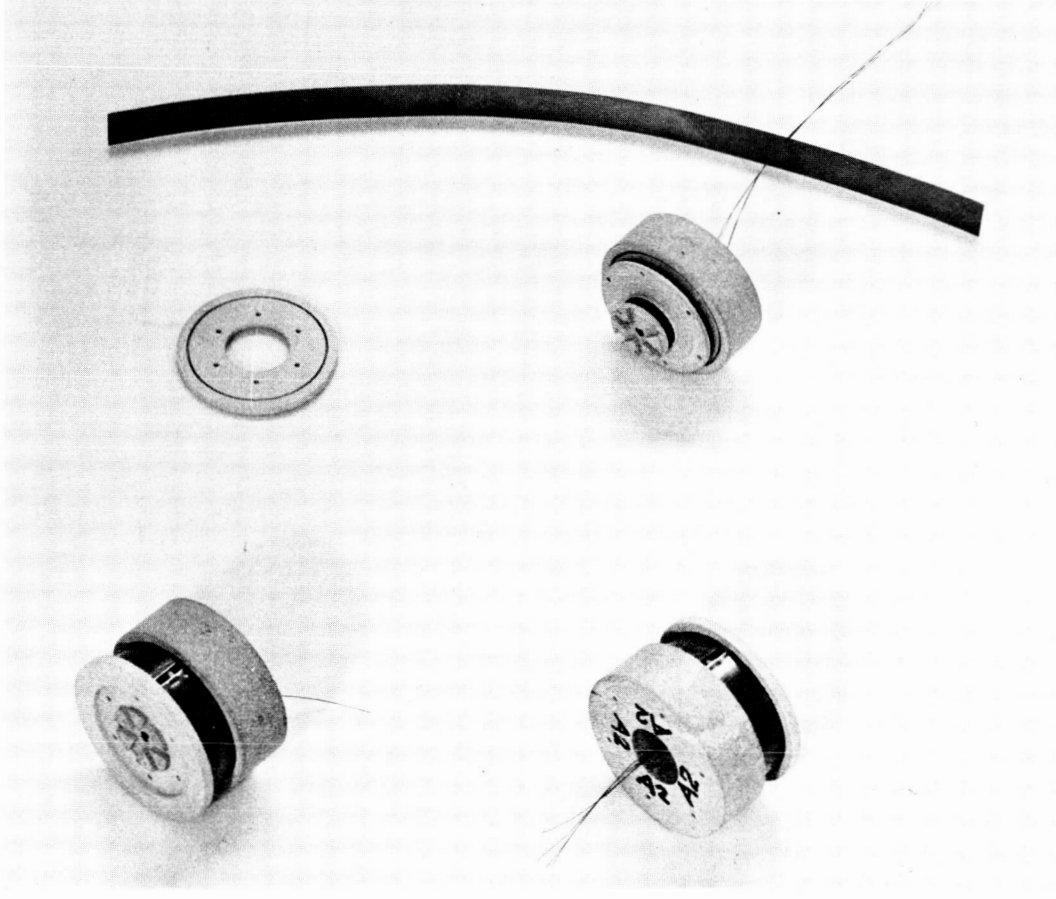


Fig. 2. Eddy-current Coil Assembly

Support for the coils in the turbine housing was provided by special instrumentation holders as shown in Figure 3. Four cavities were machined in the holder--one for each coil. Interconnecting passages were also machined in the holder to provide access for cooling-gas flow and wire connections. The inner portion of the holder at the bottom of each coil cavity has a stainless-steel "window" 0.010 inch thick to permit the electromagnetic field from the primary windings of the coils to induce eddy currents in the potassium layer between the housing and the turbine shaft. The bearing configuration precluded the possibility of placing the film-thickness transducers in the bearings. Therefore, they were mounted adjacent to the bearings, and the journal extended beyond the bearing. The clearance between the journal and the transducers was increased to 0.015 inch. This transducer location imposes several additional accuracy requirements on the turbine manufacture and assembly. The turbine shaft extension must run true with the turbine shaft in order for the measurements to have meaning. The actual shaft runout must be held to 0.00050 inch to permit measurements within the required accuracy. With the measurements of the film thickness at the transducer locations, and knowledge of the journal and bearing dimensions, the film thickness in the bearing and the motion of the shaft about the center line of the bearing can be determined.

A factor that influences the sensitivity and noise level of the eddy-current coil is the resistivity of the turbine shaft extension. The higher the resistivity, the more satisfactory the results. Unsuccessful attempts were made to fasten a ceramic sleeve to the shaft. As an alternate solution, the shaft was provided with a titanium alloy sleeve (6Al-4Va-90Ti) as shown in Figure 4. This material has a resistivity of 176 microhm-cm at 68°F. Subsequent tests indicated that this material was very satisfactory.

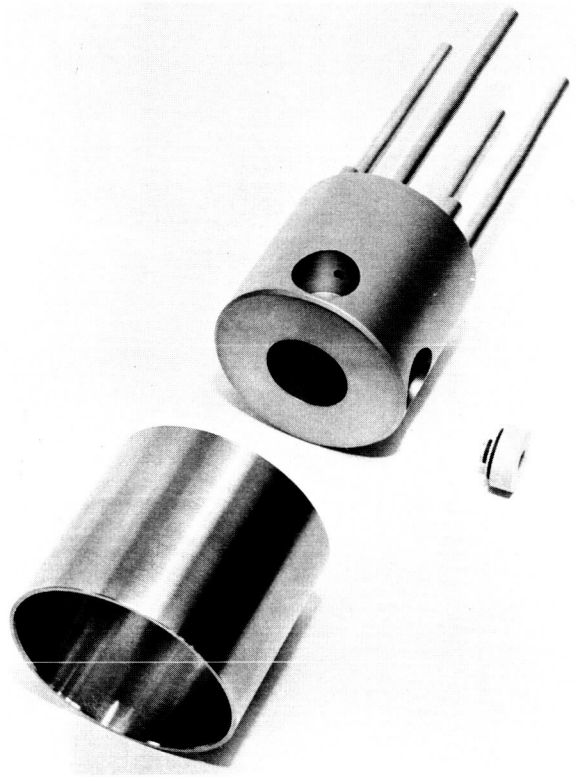


Fig. 3

Instrumentation Holder for Film Thickness Instrumentation

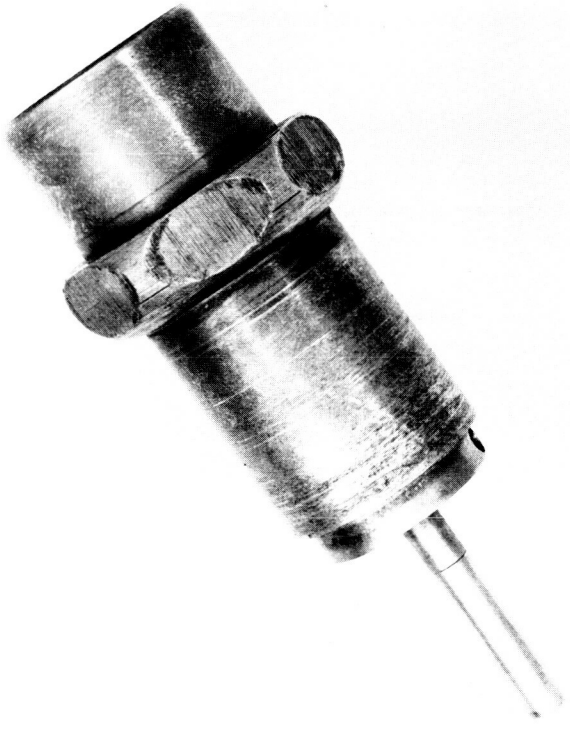


Fig. 4.

Turbine Shaft Sleeved Nut with LVDT Core

The instrumentation holders were welded into the turbine instrumentation housings and connectors provided for all the instrumentation wiring (see Figure 5). These parts were assembled in such a manner that the coils were completely sealed from the liquid potassium. After the instrumentation housings were completed, they were calibrated in the special calibration fixture discussed in Section 3.0. During final assembly of the turbine, the instrumentation housings were welded to the turbine housings and became an integral part of the turbine. A schematic of the turbine assembly and film-thickness transducers is shown in Figure 6.

2.3 Carrier System

The excitation of the primary coil windings was accomplished by using a Consolidated Electrodynamics Corporation Type 1-127 Carrier Amplifier. This system consisted of a 20-kilocycle oscillator, four amplifier channels, a regulated power supply, and controls for balancing, setting sensitivity, metering output, and calibrating. The frequency response of the system extended from 0 to 5,000 cps.

2.4 Operation of Instrumentation with Water

The operation of the instrumentation with water or oil is similar to the operation in potassium. However, since the water and oil are not good conductors of electricity the generation of eddy currents is accomplished by providing a good electrical conductor for the turbine shaft extension rather than a poor one as in the case of potassium. Thus, the presence of water or oil between the transducer and the conductive shaft does not affect the operation of the instrumentation.

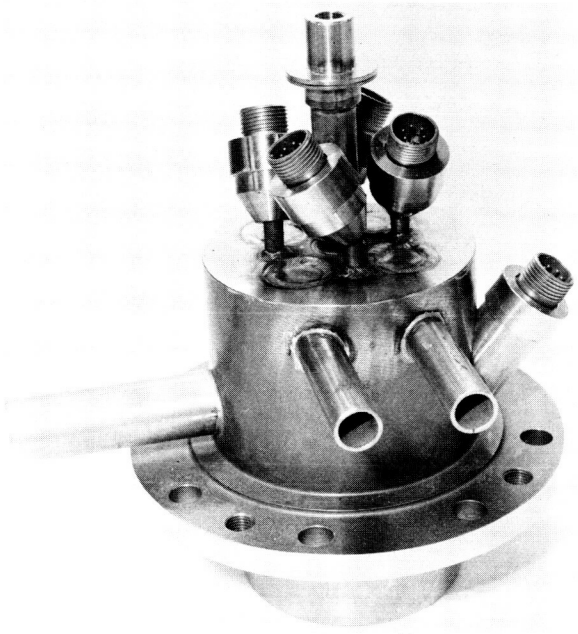


Fig. 5

Instrumentation Housing Assembly with Connectors and Instrumentation Holder

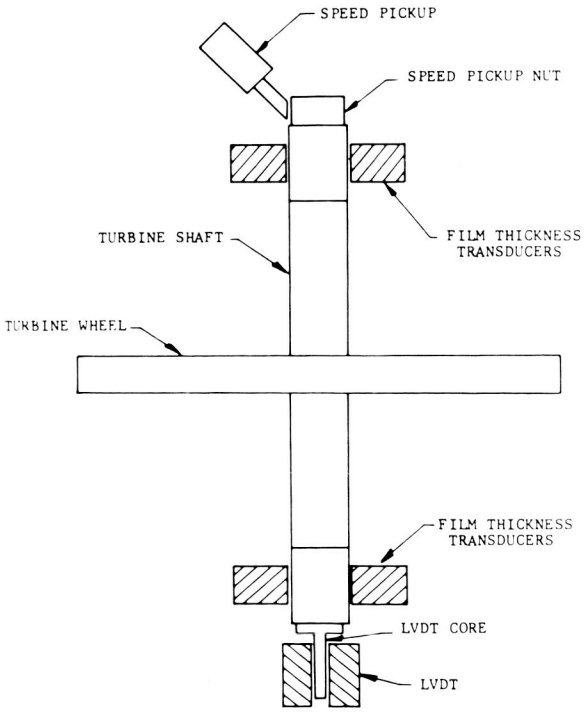


Fig. 6

Schematic of Turbine Wheel and Instrumentation

3.0 CALIBRATION OF TRANSDUCERS

Calibration of the film-thickness transducers was necessary in order to provide a correlation between signal output and film thickness. Both the resistivity of the potassium and the electrical parameters of the coils are functions of temperature. The effect of rotating the shaft in the potassium was not known, and therefore, it was also necessary to provide a calibration as a function of speed. Calibration of the transducers for operation in water or oil was also necessary, with the conductive shaft extension used to activate the transducers.

Radial motion of a simulated turbine shaft relative to the film-thickness transducers was obtained with a milling head cross-slide assembly. The shaft motions varied the potassium film thickness between the transducers and the shaft. A high-speed grinding head motor rotated the shaft in the liquid potassium. Heating of the calibration rig was obtained with electrical strip heaters.

The calibration rig, shown in Figure 7, provided the following modes of operation:

(a) Temperature variation from ambient to 600°F.

(b) Rotational speeds from 0 to 25,000 rpm when filled with potassium at 250°F.

(c) Motion of the simulated turbine shaft in three mutually perpendicular planes.

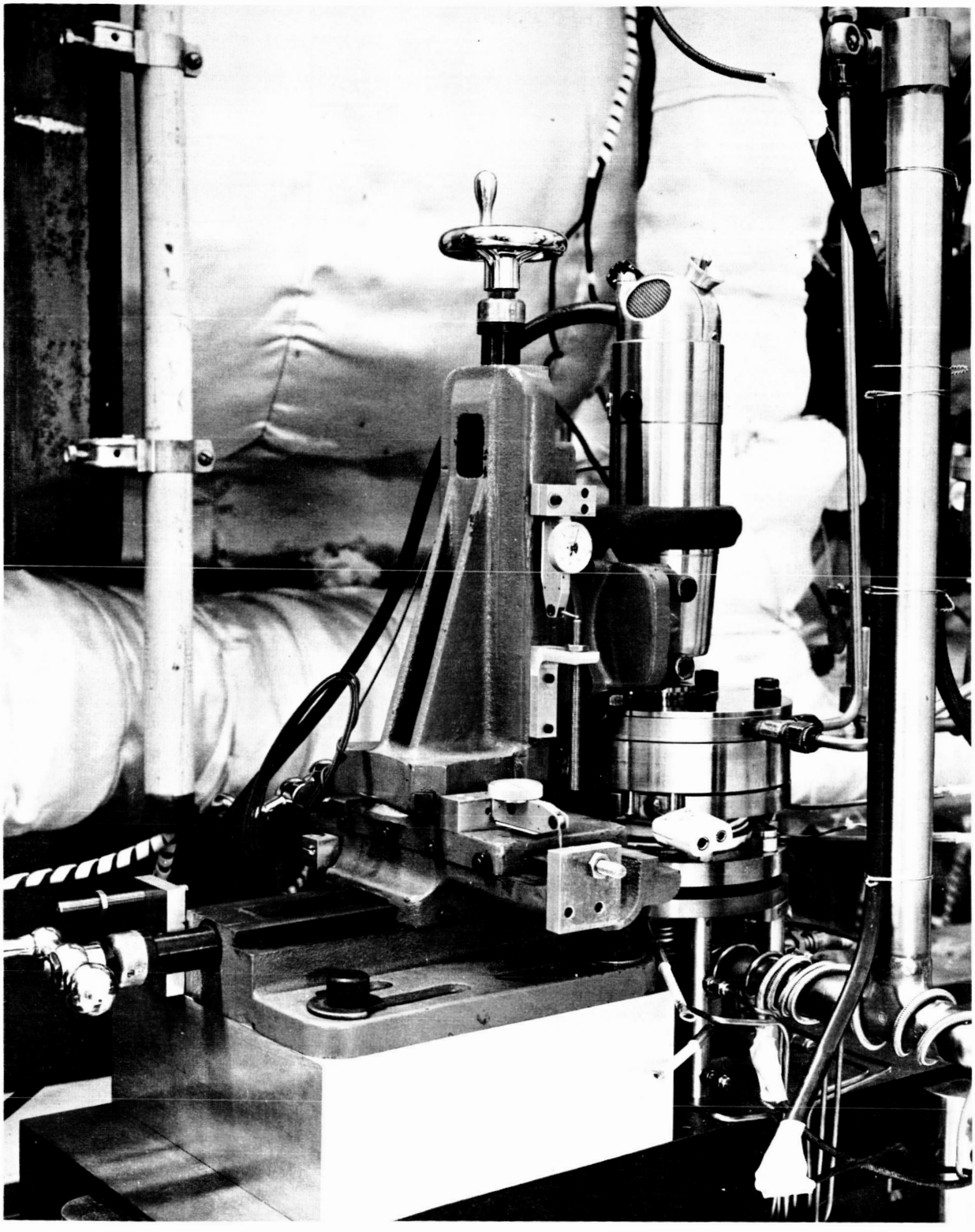


Fig. 7. Liquid-potassium Calibration Rig

(1) Horizontal motions of ±0.015 inch

(2) Vertical motion of ±0.050 inch

(3) 0.0001-inch dial indicators on the two horizontal planes and a 0.001-inch indicator on the vertical plane

Protection from contact with the ambient air must be provided for the liquid potassium to eliminate oxide formation. This was accomplished by using a rotating carbon-face seal and a stationary Teflon seal, as shown in Figure 8. Argon was used as a cover gas between the Teflon seal and the potassium. The argon was discharged through oil bubblers. A standpipe served as a reservoir for liquid potassium and replenished any potassium that might be discharged through the bubblers.

It was anticipated that there might be cavitation around the shaft during high-speed rotation. To study this problem, a plastic model of the instrumentation housing was constructed and the shaft was rotated with water in the cavity. Cavitation and vortexing in the water were eliminated during rotation by completely filling the cavity with water up to the carbon seal and placing discs in the large cavity above the instrumentation holder. This same technique was used when liquid potassium was used in this operation.

Because of some oozing of potassium past the Teflon seal during calibration, periodic cleaning of the upper surface of the seal was required and the possibility existed that there was cavitation during shaft rotation. If cavitation had occurred or any voids formed around the shaft, the sensitivity of the eddy-current system would have changed as the shaft was rotated. The data indicated that the sensitivity was constant up to the maximum speed. In all probability, the entire cavity was filled with potassium; cavitation was prevented by the discs in the cavity, and the pressure buildup in the cavity was contained by the Teflon seal.

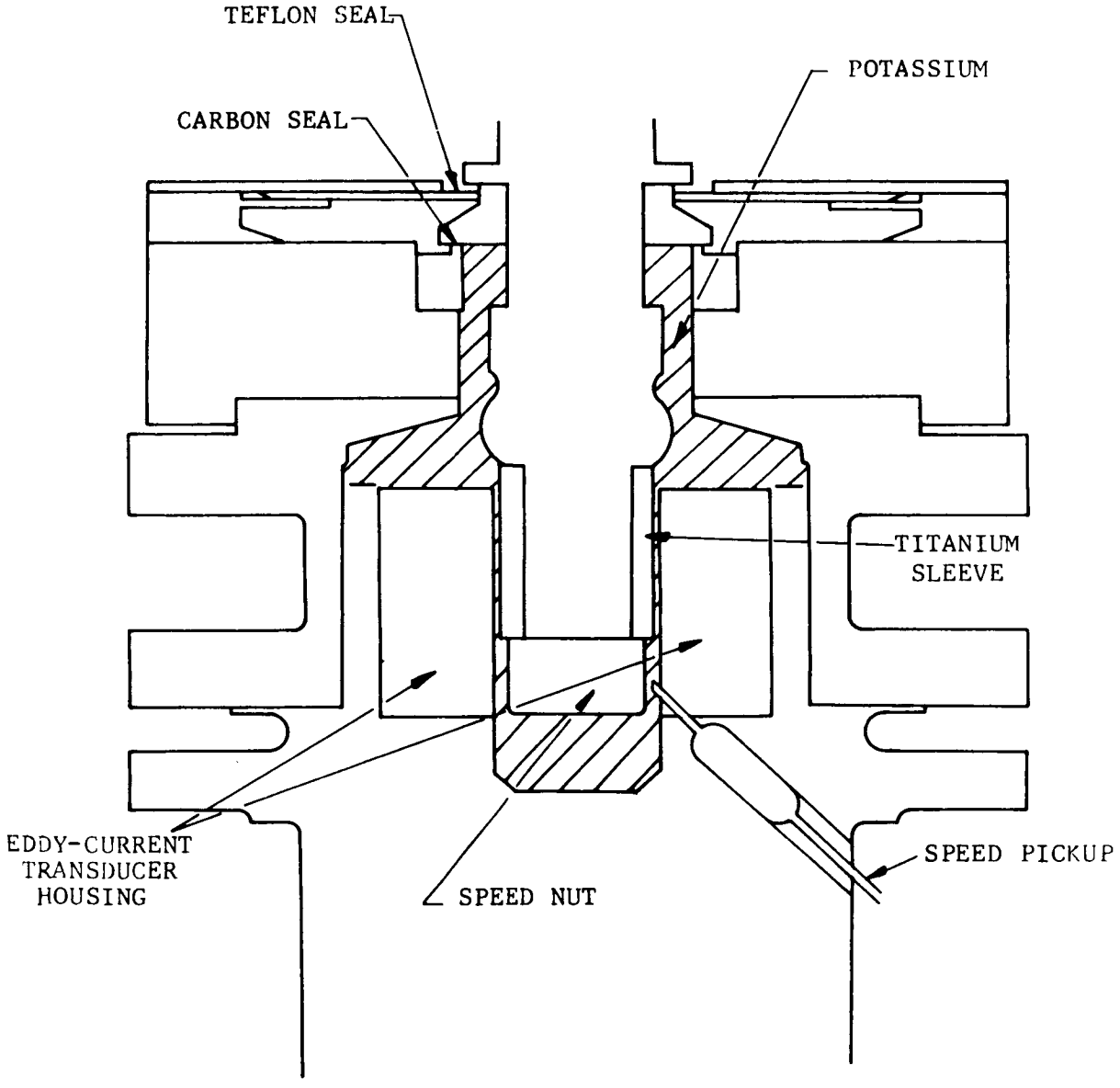


Fig. 8. Cross Section of Calibration Rig

Calibration of the eddy-current transducers was performed in two steps. First, a calibration with no shaft rotary motion was accomplished by stabilizing the calibration rig at a certain temperature and shifting the location of the simulated turbine shaft radially by known amounts from its center position up to a maximum displacement of 0.002 inch. The coil outputs for each position were recorded on a 14-channel Ampex FR600 tape recorder. An internal electrical calibration provided by the carrier system was also recorded. This electrical signal provided a calibration for the film-thickness transducers when the instrumentation housings were installed in the turbine. A calibration was then performed by recording the output from the transducers as the shaft was rotated at various speeds up to 25,000 rpm with the rig stabilized at 250°F. As the shaft was rotating it was also moved laterally in discrete steps up to a maximum displacement of 0.002 inch. This motion was performed in the horizontal plane in two mutually perpendicular directions.

Additional calibrations have recently been performed on a second set of instrumentation housings. For these calibrations, the calibration rig was modified to provide a more accurate indication of the simulated turbine shaft motion. Shaft motion was indicated with Hamilton Watch Company dial indicators LI4-002, which have an accuracy of ±0.000020 inch. A different type of potassium seal assembly was also used on the calibration rig. No rotary shaft motions were produced during these calibrations. The calibrations were performed at various temperatures up to a maximum of 650°F.

4.0 PERFORMANCE OF INSTRUMENTATION

4.1 Results with Calibration Rig

All the data obtained from the calibration rig was recorded on magnetic tape. This data was, in turn, reproduced on a CEC oscillograph. The data obtained from the static motions of the shaft was plotted as an output in arbitrary units versus film-thickness change in thousandths of an inch (see Figure 9). Several sets of curves were obtained for different operating temperatures.

From the plots of output versus thickness change, the slopes of the curves (sensitivity) were determined and the average slope for a given temperature calculated. These slopes were then plotted versus temperature. A "least squares" fit for a straight line was made for each set of data as shown in Figure 10.

The same techniques were used to reduce the data obtained for the electrical calibration signal from the carrier amplifier system.

The two sets of data--sensitivity in volts output per unit thickness change and the electrical calibration in volts- were then combined to give the system calibration in thousandths of an inch film-thickness change (see Figure 11). The calibration was used in the following manner. When the carrier amplifier calibrator switch was energized, the resulting output from the amplifier for a given temperature corresponded to a film-thickness difference between the shaft and one sensing coil and the shaft and the opposing sensing coil, as indicated by the graph. The

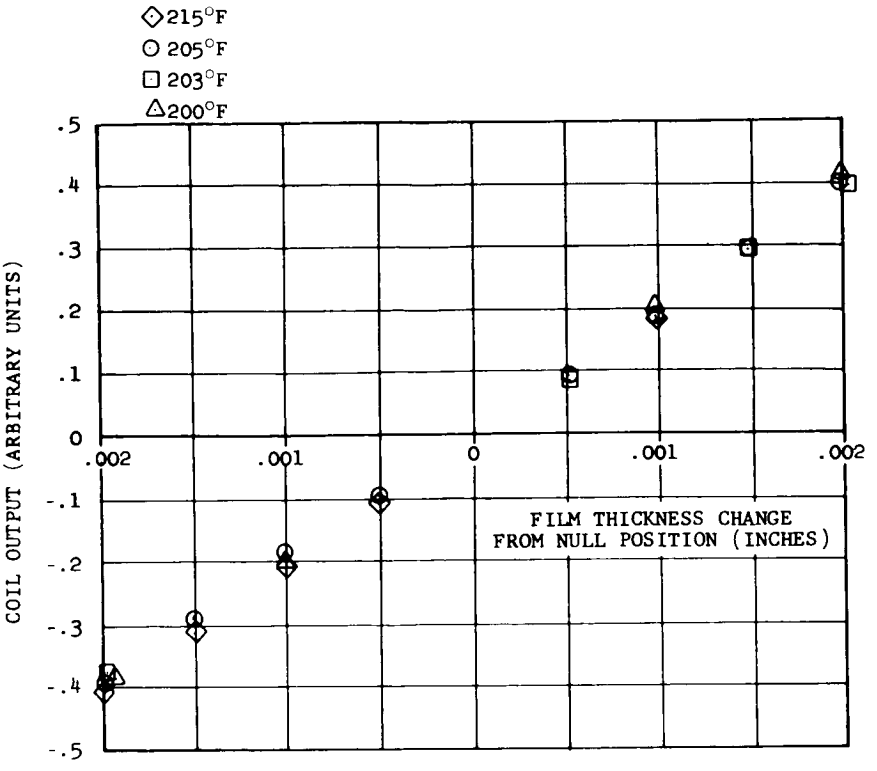


Fig. 9. Coil Output as a Function of Film Thickness Variation

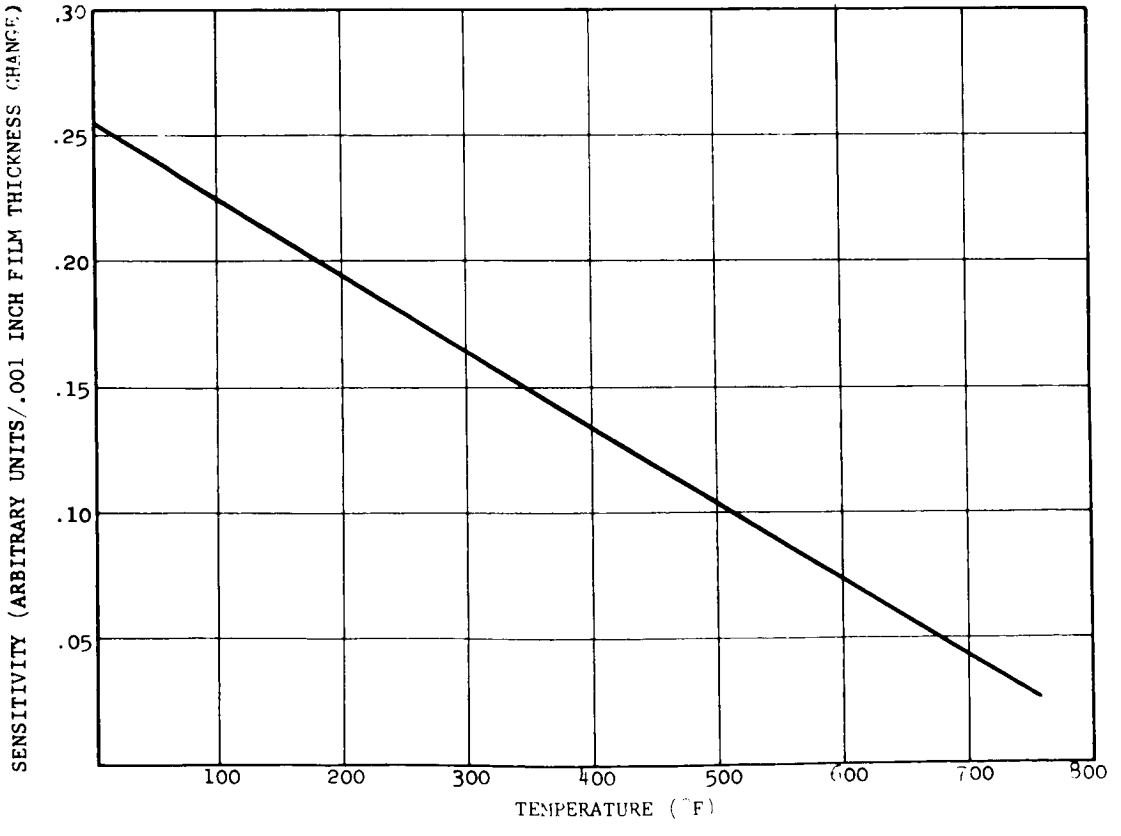


Fig. 10. Static Sensitivity as a Function of Temperature

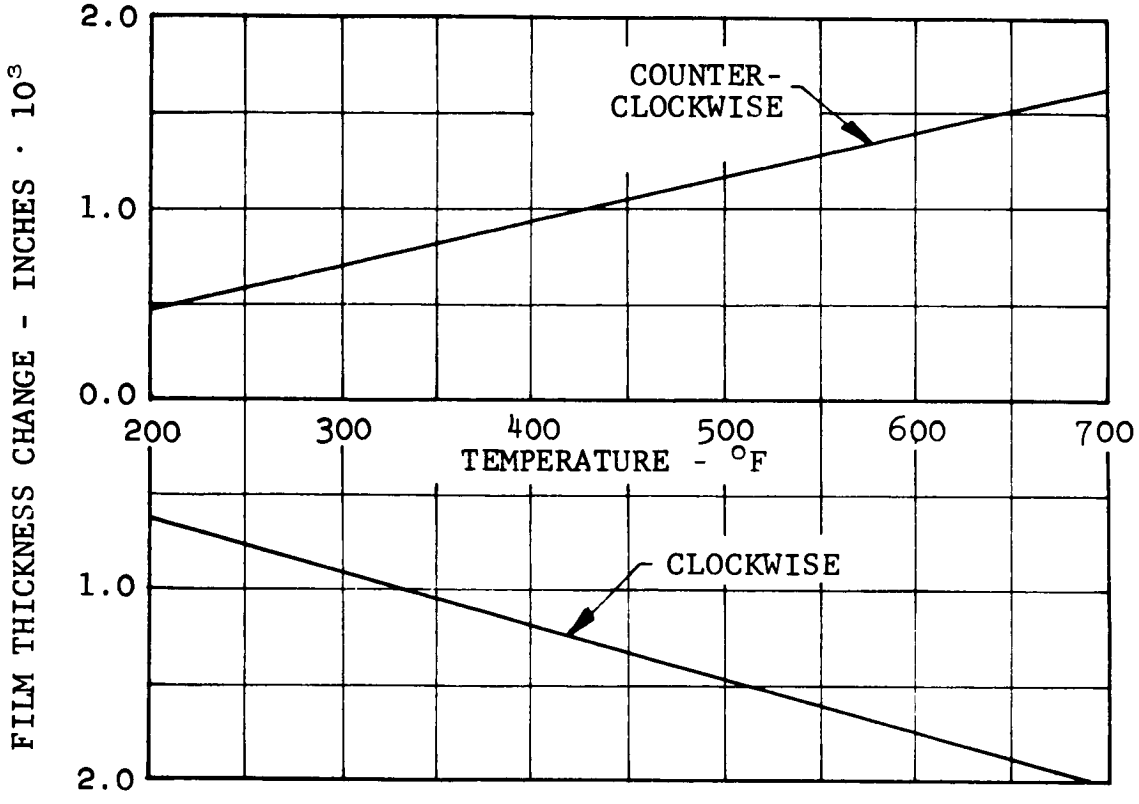


Fig. 11. Film Thickness Calibration for the CEC Carrier Amplifier

clockwise and counterclockwise rotations on the graph refer to the rotation of the calibrator switch. By combining the calibration signal with the film-thickness transducer signals obtained during a turbine run, the actual film thickness was determined during turbine operation.

The results obtained during rotation of the simulated turbine shaft were most encouraging. The temperature was held constant at 250°F for all the rotational runs. The eddy-current transducer outputs were recorded as a function of displacement and speed. Calculations were performed to obtain sensitivities as a function of rotational speed at a constant temperature (see Figure 12). It can be seen that, for all practical purposes, the sensitivity remained constant up to a maximum speed of 25,000 rpm. As was mentioned previously, any voids in the volume between the eddy-current transducers and the shaft would cause a decrease in sensitivity. Also, it was expected that if speed had an effect on the sensitivity, it would tend to lower the sensitivity as the speed was increased. Since there were no changes in sensitivity, it was believed that voids were absent and that rotational speeds up to the maximum tested had no effect on the sensitivity of the eddy-current transducers.

The Lissajous figures obtained during the dynamic calibration from the transducer outputs for a rotational speed of 17,000 rpm are shown in Figure 13. Radial motion of the shaft from its center position was ±0.001 inch in two mutually perpendicular directions in a horizontal plane.

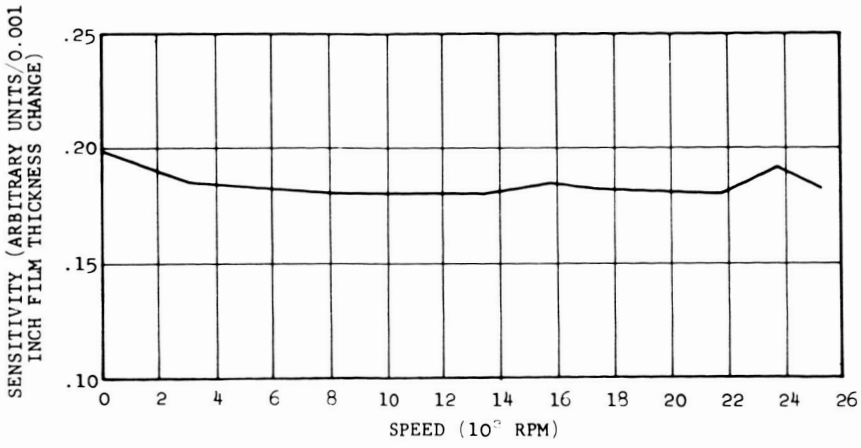


Fig. 12. Sensitivity as a Function of Rotational Speed

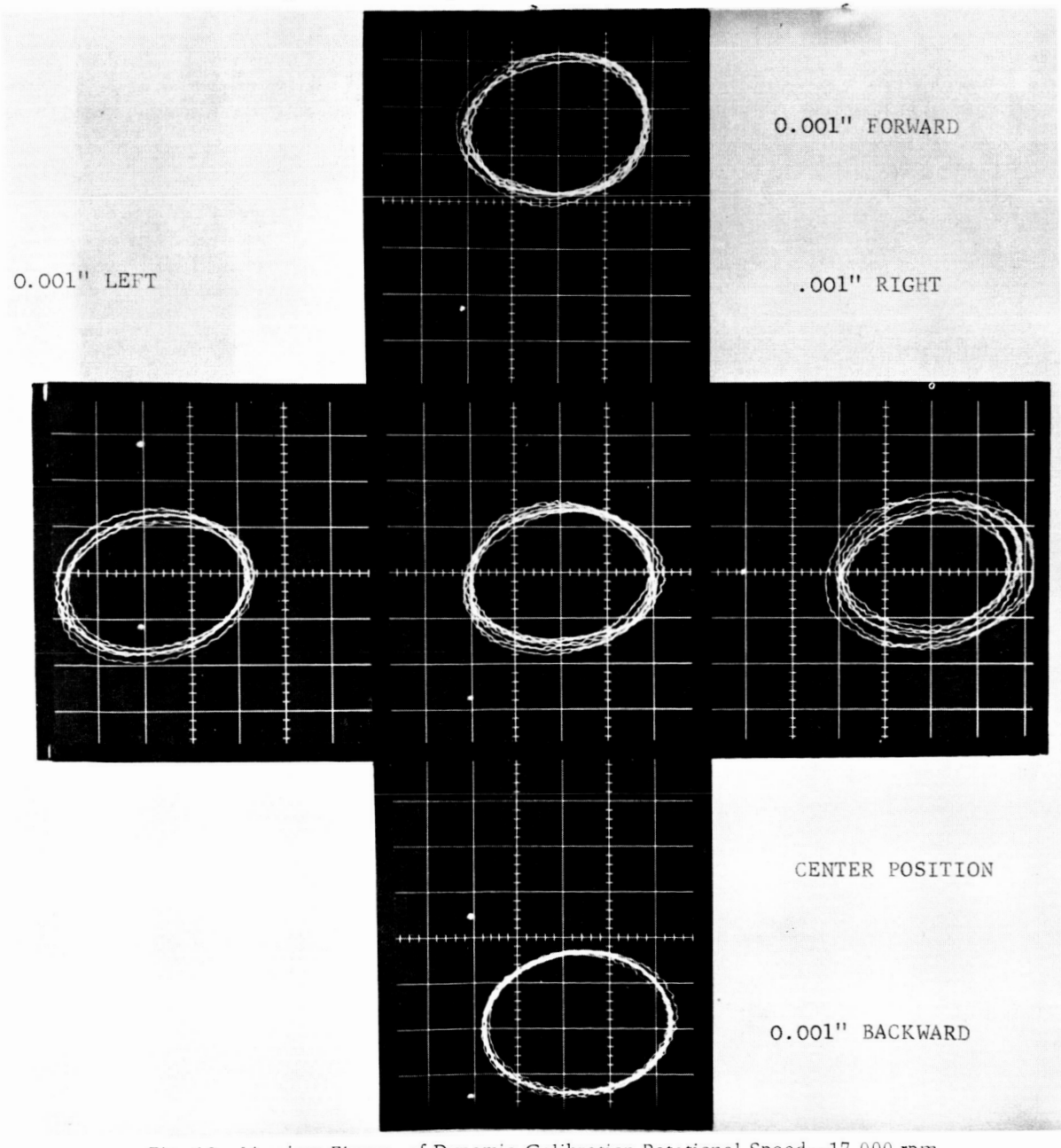


Fig. 13. Lissajous Figures of Dynamic Calibration Rotational Speed--17,000 rpm

4.2 Results in the Bearing Test Loop

To date the film-thickness instrumentation has been operated on three different occasions in the bearing test loop during the past 2 years. The first two times the potassium turbine was operated for about 30 hours in each case. Except for minor problems in the transducers such as an intermittent weld that was arced closed, no difficulties were experienced. There were no problems due to electrical drift or overheating, even though temperatures in excess of 700°F were experienced by the transducers.

The third turbine run was for an extended period of approximately 200 hours. During this period, the transducer temperature was held very constant, near 600°F. Again no major problems were experienced, and the transducers gave reliable results all during the turbine test. Teardown inspections of the turbine bearings and bearing mounts verified the data recorded during the test runs.

4.3 Bearing Configurations and Performance Data

A number of journal bearings, such as floating-ring, pivoted-pad, hybrid, and lobed types are being evaluated for stability characteristics. Each type has demonstrated stability characteristics under certain test conditions.

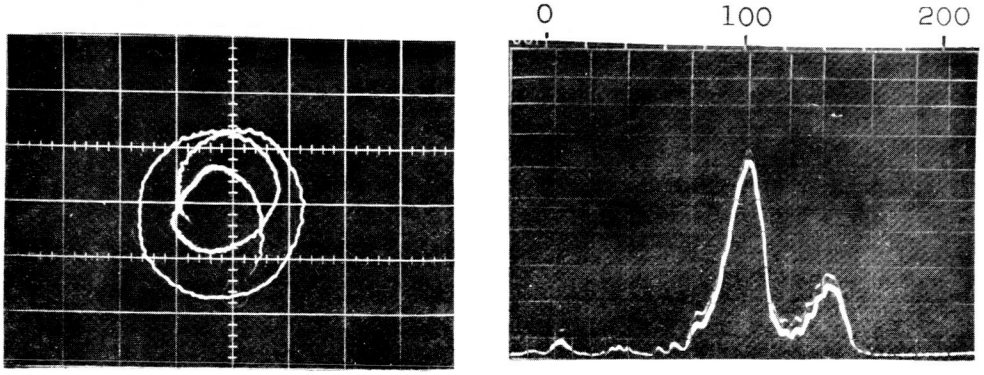
Figure 14 shows a floating-ring bearing that was tested with the use of light oil. Representative operation of this bearing, showing motion of the shaft and frequencies comprising this motion, is shown in Figure 15.

Figures 16 and 17 show a hybrid bearing and representative motions for a speed of 20,000 rpm at two supply pressures.

Figure 18 shows a three-pad pivoted-pad journal, with operating characteristics shown on Figure 19, with the shaft oriented vertically.



Fig. 14. Floating Ring Bearing



SHAFT MOTION

PANORAMIC FREQUENCY, CPS

SHAFT SPEED = 8,700 RPM
RING SPEED = 4,800 RPM
LUBRICANT = LIGHT OIL AT 200°F (1.45 CP)
SHAFT HORIZONTAL

Fig. 15. Floating Ring Bearing Stability

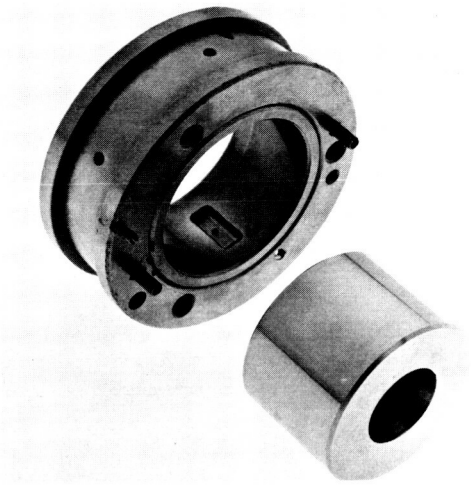


Fig. 16. Hybrid Bearing

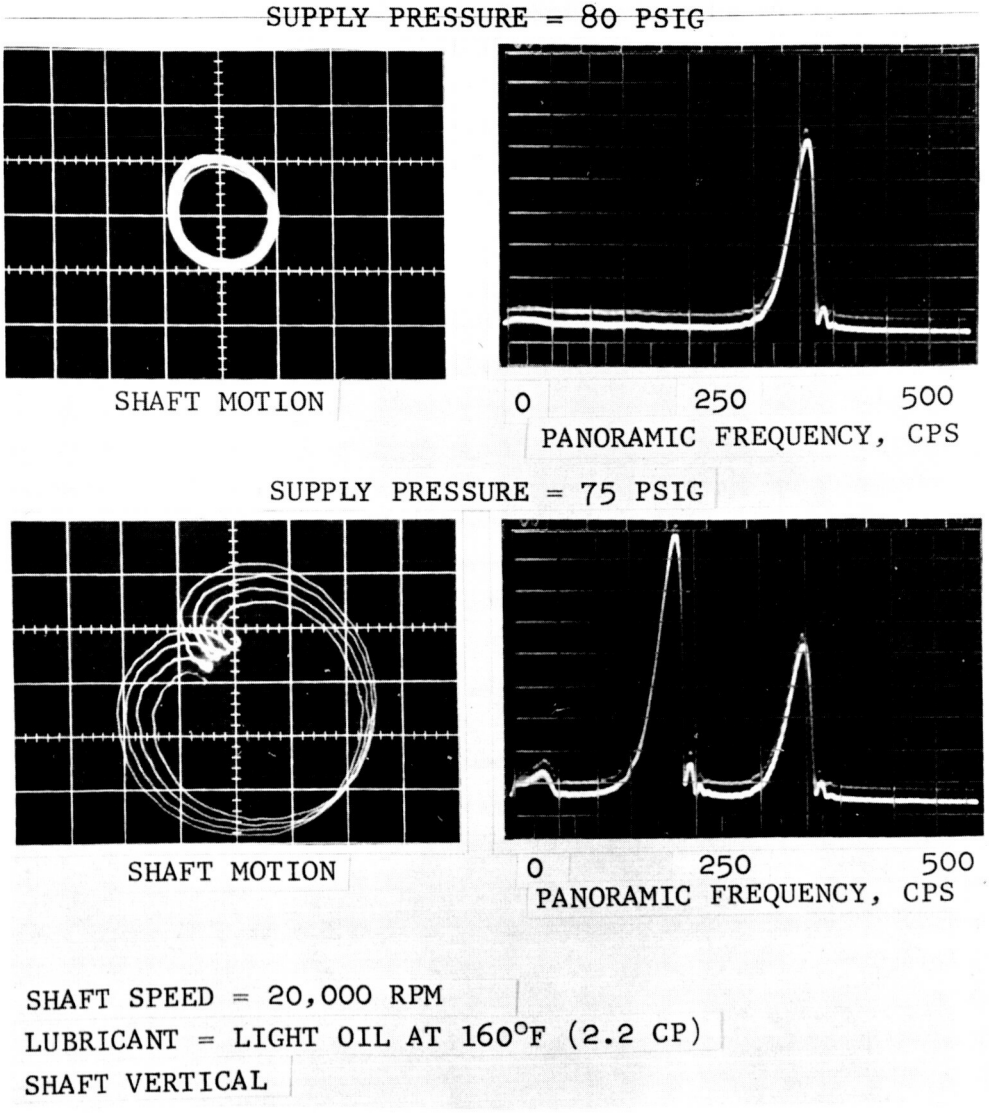


Fig. 17. Hybrid Bearing Stability Data

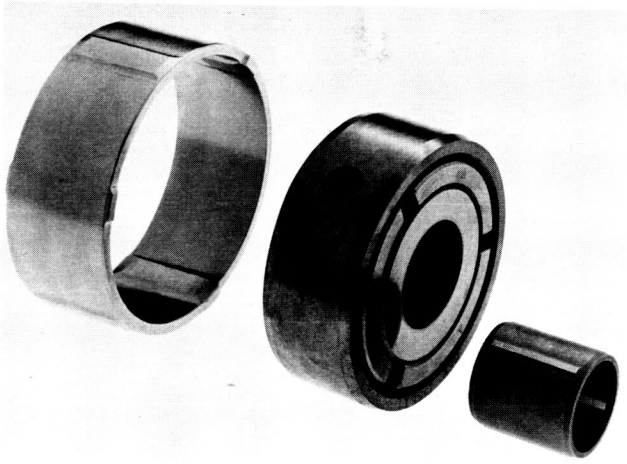
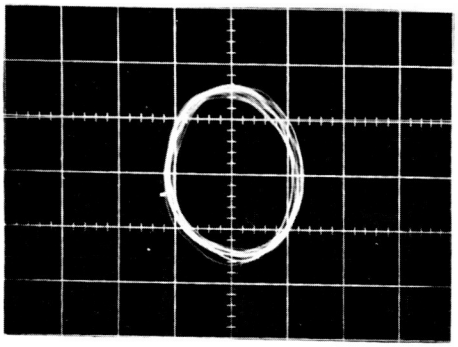
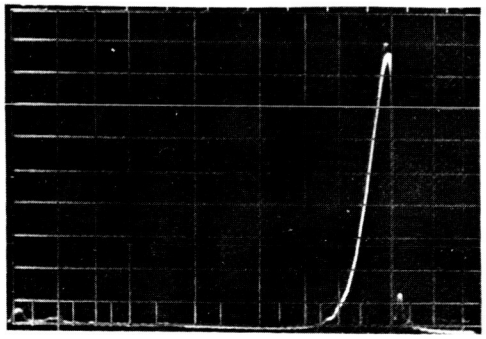


Fig. 18. Pivoted-pad Bearing

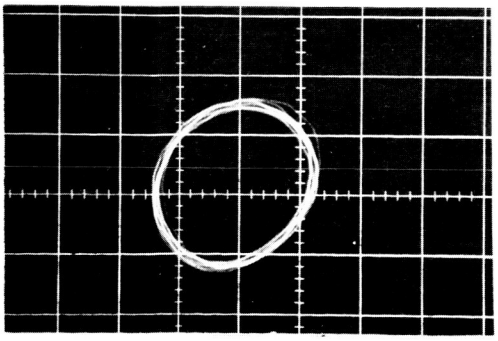


SHAFT MOTION



0 250 500
PANORAMIC FREQUENCY, CPS

SPEED = 26,000 RPM
LUBRICANT = WATER AT 140°F (0.46 CP)



SHAFT MOTION

SPEED = 24,000 RPM
LUBRICANT = POTASSIUM AT 600°F (0.25 CP)

Fig. 19. Pivoted-pad Bearing Stability Data

N66 31686

APPROACHES TO THE MEASUREMENT OF THE STEADY STATE AND DYNAMIC PERFORMANCE CHARACTERISTICS OF LIQUID-METAL LUBRICATED BEARINGS

by

E. B. Arwas *
F. K. Orcutt *
B. Sternlicht *

(Paper presented by E. B. Arwas)

ABSTRACT

This paper presents a discussion of the instrumentation necessary for fundamental investigations, as well as for bearing development and for monitoring of bearing performance in turbomachinery. It points out through examples, that considerable advances applicable to liquid metal lubrication can be accomplished with "easy to use" fluids that simulate some of the important properties of liquid metals and making use of instrumentation that is already developed. Indirect measurements which, in conjunction with accepted theoretical relations, provide meaningful interpretation of bearing performance are also discussed.

* Mechanical Technology Inc., 968 Albany-Shaker Road, Latham, New York

PRECEDING PAGE BLANK NOT FILMED.

1. INTRODUCTION

There is a rapid growth in the application of process fluids as lubricants. Freon, water, gasoline as well as other liquids and gases have all been successfully employed in a number of modern turbomachines. More recently liquid metals have been applied as lubricants in Rankine Cycle turbomachinery The use of process fluid lubrication has many inherent advantages including:

a) Longer life
b) Simplification and, hence, increased reliability
c) Operation at cryogenic and pyrogenic temperatures
d) Operation in radioactive environment
e) Elimination of many accessories
f) Elimination of contamination
g) Much reduced sealing problems

These trends have brought with them new demands on bearing and lubrication technology. New lubrication theory had to be developed and its validity checked in precise experiments. Examples of such new theoretical developments included analysis for compressible flow lubricants (gases) as well as for lubricant films where the Reynolds Number is large, resulting in turbulent flow, as with low kinematic viscosity fluids used in high speed bearings. The development of the process fluid lubricated bearings also required new developments in bearing materials and bearing instrumentation.

Specifically in the case of liquid metal lubrication, the bearing designer has been faced in the last several years with a number of problems simultaneously. Turbulent lubrication theory (required in view of the very low kinematic viscosities of liquid metals) was not adequately developed. Design data based on such theory and on accurate experimental work was equally absent. Bearing materials selection for the high operating temperatures of liquid metal systems raised problems of compatibility with the environment, erosion and corrosion. Adequate instrumentation was also not available, a principal deficiency being instrumentation for film thickness measurment. This was primarily due to the electrical conductivity of liquid metals, which ruled out the use of some well developed proximity gauges such as capacitance pickups. Measurement of bearing

performance was also complicated by the necessarily limited accessibility in liquid metal environment.

This paper presents a discussion of the instrumentation necessary for fundamental, lubrication investigations as well as for bearing development and for monitoring of bearing performance in turbomachinery. It points out through examples, that considerable advances applicable to liquid metal lubrication can be accomplished with "easy to use" fluids that simulate some of the important properties of liquid metals and making use of instrumentation that is already developed. Indirect measurements which, in conjunction with accepted theoretical relations, provide meaningful interpretation of bearing performance are also discussed.

2. BEARING PERFORMANCE MEASUREMENTS

While liquid metals can serve as bearing lubricants, their properties differ significantly from those of conventional lubricants, such as hydrocarbon oils. Table 1 below lists some of these properties for some liquid metals and other fluids.

TABLE 1

	* SAE 10 oil at 150°F	Liq. K at 800°F	Liq. Na at 800°F	Liq. Hg at 400°F	Water at 120°F	Silicone Fluid at 120°F
Absolute Viscosity (Cp)	12	0.18	0.25	1	0.56	0.41
Density (gms/Cm^3)	0.85	0.73	0.84	13	0.99	0.76
Kinematic Viscosity (Cs)	14	0.25	0.30	0.08	0.57	0.54
Surface Tension (dynes/Cm)	20	80	190	430	68	16
Gas Solubility (moles/mole)	10^{-3}	$<10^{-9}$	$<10^{-9}$	$\ll 10^{-9}$	10^{-5}	10^{-3}

* Commonly used turbomachinery oil.

In particular, liquid metals have very low values of kinematic viscosity. Because of this the fluid film Reynolds Number ($Re = \frac{\pi DNC}{\nu}$) reaches large values. In high speed turbomachinery, the fluid film of liquid metal bearings is turbulent. The classical, well demonstrated lubrication theory which is the basis of fluid film bearing design was based on the assumption of laminar flow in the bearing film.

New theory, based on turbulent flow in the film had to be derived for design of liquid metal lubricated bearings. Accurate measurement of both the steady state and dynamic characteristics of the bearings have to be repeated in the turbulent regime in order to check the validity of the new theory. Particular emphasis had to be placed on the dynamic characteristics (which are more difficult to measure than the steady state ones), in view of the high operating speeds of the turbomachinery for which liquid metal lubricated bearings are intended.

Table 2 below lists the principal performance characteristics of fluid film bearings. Measurement of these quantities is difficult, even in bearings lubricated with conventional oils or with air and using existing, well proven instrumentation.

TABLE 2

Bearing Performance Characteristics

STEADY-STATE OPERATION

Bearing Type	Performance Characteristics	Design Specifications
Self-Acting	Eccentricity Ratio Attitude Angle Friction Torque	Bearing Geometry (including tolerances) Load Speed Fluid Properties
Externally-Pressurized	Eccentricity Ratio Attitude Angle Friction Torque Lubricant Flow Rate	Bearing Geometry (including tolerances) Restrictor Characteristics Load Speed Fluid Properties Supply and Drain Pressures
	DYNAMIC OPERATION AND ROTOR-BEARING DYNAMICS	
Self-Acting	Fluid Film Stiffness Coefficients Fluid Film Damping Coefficients System Ctrical Speeds Response to Unbalanced Loads (synchronous whirl orbits) Threshold of Instability (Half-frequency whirl)	Bearing Geometry (including tolerances) Steady State Load Speed Fluid Properties Dynamic Loads (mechanical unbalance, time-varying electrical, aeordynamic & other loads) Rotor Mass & Stiffness Distributions

Table 2 (cont'd)

Externally-Pressurized	Fluid Film Stiffness Coefficients Fluid Film Damping Coefficients System Critical Speeds Response to Unbalanced Loads (synchronous whirl orbits) Threshold of Instability (fraction frequency whirl)	Bearing Geometry (including tolerances) Steady State Load Speed Fluid Properties Supply and Drain Pressures Dynamic Loads (mechanical unbalance, time-varying electrical, aerodynamic and other lods) Rotor Mass and Stiffness Distributions Restrictor Characteristics

An important case in point is the direct measurement of film thickness. Typical clearance ratios in bearings (radial clearance/bearing radius) are of the order of 10^{-3} inches/inches so that the measured film thicknesses in the loaded regions of a bearing are frequently smaller than 10^{-3} inches. In order to obtain meaninful data (for example for correlation with theory) the measurement errors should be at least an order of magnitude smaller than the quantity measured. Consequently, error limits on bearing film thickness instrumentation are generaly set at $\pm$ 50 microinches or less. Furthermore, the transducers have to be small enough to insert in a bearing without influencing its performance. Temperature effects should be negligible or it should at least be possible to compensate or to make accurate correction for them. Linearity is also a critically important attribute of the transducer and its associated circuitry, particularly when the measured film thickness is a variable quantity,e.g., with a dynamically loaded shaft.

A variety of measurement techniques have been tried for film thickness measurements (Ref. 1), but it is only in the last several years that two principal types of transducers (capacitive and inductive) and their associated amplification equipment have been developed that largely meet the stringent requirements mentioned above. These transducers which are discussed later in this paper are not useable in their present form with liquid metals, as they were developed for lubricant films which are not electrically conductive. Currently work is in progress (Ref. 2) to develop a similar transducer which can be used with an electrically conductive lubricant film. Even after such instruments are fully developed and proved out their use to measure liquid metal bearing film thicknesses will be a difficult undertaking in vew of the high operating temperatures of the bearings and the very limited accessibility of liquid metal systems.

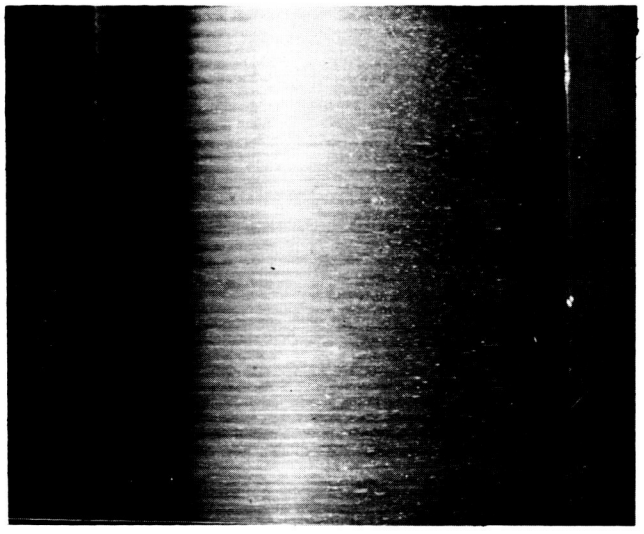
Bearing performance measurements are required for several quite distinct purposes including:

1. Verification of new lubrication theory
2. Measurement of the characteristics of specific bearing geometries
3. Measurement of the rotor-dynamic performance of rotor-bearing assemblies in test equipment and in prototype turbomachinery.
4. Monitoring of bearing and rotor-dynamic performance in turbomachinery.

Fundamental experimental investigations conducted for the purpose of checking the validity of new lubrication theory (in this case turbulent flow lubrication, Refs. 3 and 4) must be conducted with a high level of accuracy. Relatively simple test equipment and easy accessibility to the instrumentation are particularly important since frequent calibration is generally necessary for accuracy of measurement and to guard against instrument drift. It is therefore preferable to conduct such investigations in fluids other than liquid metals, which are easier to use, but whose physical properties (viscosity and density) closely resemble those of liquid metals. Such fluids include distilled water and the very light silicone fluids (0.65 centistoke silicone fluid). Relatively large bearings and bearing clearances are used to induce turbulence at low speeds and to improve measurement accuracies.

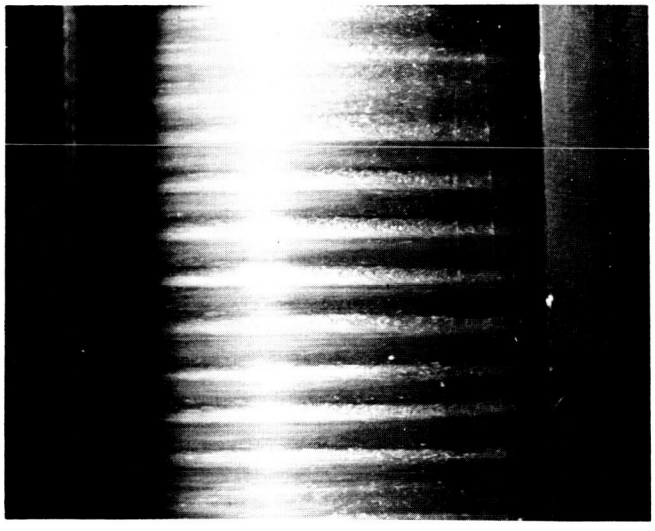
The existing, well proven capacitance and inductance type transducers can be used with the above mentioned "easy-to-use" fluids, to measure such quantities as film thickness, eccentricity ratio, attitude angle and shaft orbits in response to dynamic loads. Conventional flowmeters are used for measurements of lubricant flow and commercial, strain-gauge type torquemeters are used to measure friction. The transition in the fluid film from laminar to vortex flow to developed turbulence (shown in Fig. 1) can be observed and accurately measured as a function of the fluid film Reynolds Number and the bearing eccentricity (Refs. 5 and 6). The detailed shape and magnitude of the pressure profiles (Fig.2) can be measured with manometer banks or pressure gauges. Considerable progress has already been made in this area obtained thus far has closely substantiated the new turbulent lubrication theory (Ref. 7).

For operation in high-speed, high-temperature turbomachinery specific bearing configurations have to be chosen on the basis of such factors as: very high stability



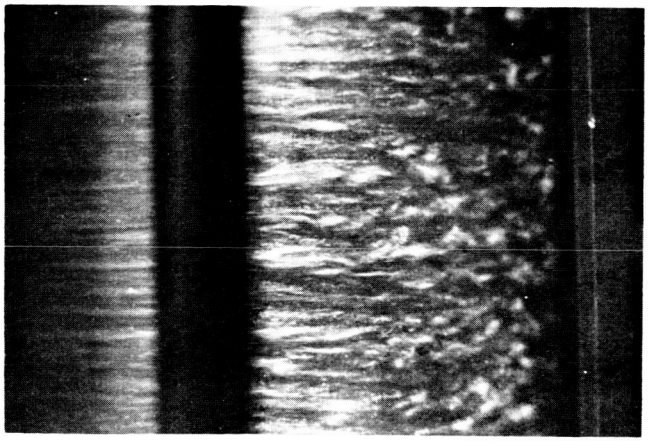
(a)

$\sqrt{1/2\ T} = 38,\ N_{Re} = 152$



(b)

$\sqrt{1/2\ T} = 105,\ N_{Re} = 419$



(c)

$N_{Re} = 1850$

Fig. 1. Flow Patterns between Rotating Eccentric Cylinders.
a. Laminar flow prevails for low N_{Re}
b. Onset of vortex flow occurs at about $\sqrt{1/2\ T} = 42.6$
c. Transition to fully developed turbulence occurs at about $N_{Re} = 1500$.

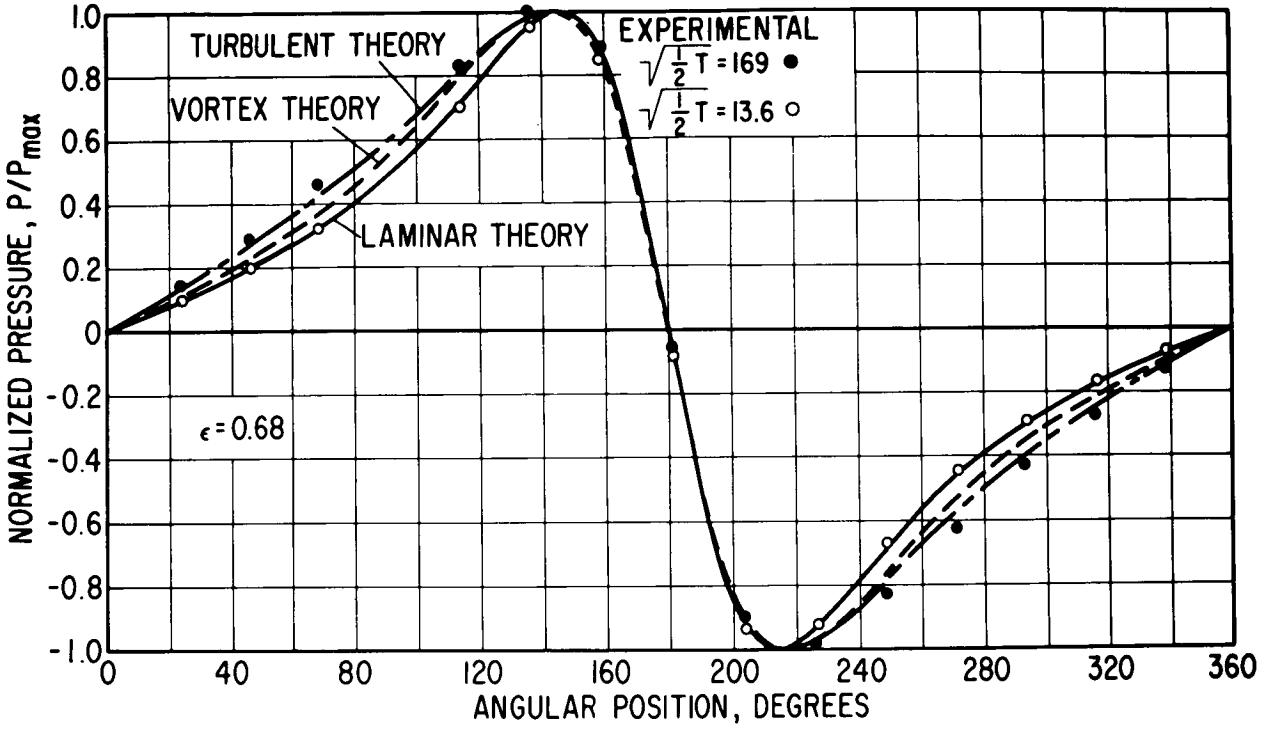


Fig. 2. Comparison of Measured and Theoretical Pressure Distributions for Vortex Flow between Eccentric Cylinders

thresholds, tolerance of thermal gradients and misalignment, low power loss and others. Typical bearing geometries that meet these objectives include the tilting pad and the floating ring bearings. Accurate measurement of their performance characteristics, as listed in Table 2, are required. For this purpose, it is desirable to initially conduct the measurements in "easy to use" fluid so that detailed performance maps can be obtained. In a second step, the bearings must be evaluated in a liquid metal environment in order to determine whether other, unpredicted effects on bearing performance occur.

As previously noted, particular emphasis has to be placed in these evaluations on the dynamic performance of the bearings. Here, the critical parameters are the stiffness and damping coefficients of the fluid film. The fluid film stiffness can be obtained directly by measuring the slopes of the load-deflection curves of the bearings obtained at different speeds and for different directions of the load vector. The fluid film damping can be measured from the decay of the oscillations following application of a known impact force (Log-decrement method). Alternately, these quantities can be derived from measurement of the orbital journal motions in the bearing under a rotating force vector. A detailed discussion of the relationship between the bearing dynamic characteristics and the rotor response to rotating loads such as mechanical unbalance is given in Ref. 8. As long as the purpose of the investigations is to determine bearing characteristics, it is advisable to use a fully rigid rotor in order to avoid any interaction between the rotor and bearing flexibilities. Measurements of this type have been accomplished and are described for example, in Refs. 9 and 10.

The later stage in bearing evaluations has to be conducted in liquid metals, in order to verify the general applicability of the design data. Here again relatively simple experimental apparatus, with a fully rigid shaft should be used. Film thickness instrumentation now under development for liquid metal environment (Ref. 2) can be used directly in the bearing, if available. However, other existing film thickness transducers can also be used, located outside the bearing seals in a cover gas atmosphere. With a fully rigid shaft and with such probes located on both sides of the bearing (to correct for any misalignment), extremely accurate data in the steady-state and dynamic characteristics of liquid metal lubricated bearings can be obtained.

A significant problem area that is apparent in high speed, liquid metal lubricated bearings is the high power loss of such bearings, resulting from the turbulence in the film. In order to limit such parasitic losses, as well as the associated loss induced by the need to pass large coolant flow to remove the heat generated, it is anticipated that the high speed, liquid metal turbomachinery will be designed with relatively small diameter shafts and will operate in the flexible rotor range, as is the current practice in conventionally lubricated turbomachinery such as aircraft jet engines, steam and gas turbines and others.

The experimental investigations called for here are measurement of the interactions between the bearings and the rotor. It is advisable to conduct these experiments on a test apparatus that simulates as closely as possible the mass and inertia distributions of the specific rotors of interest. Once again, it is advisable to conduct the experiments first with "easy to use" fluids that closely simulate the viscosity and density of the liquid metal of interest in order to obtain detailed performance maps rapidly and accurately. A more limited investigation in the liquid metal environment is then only necessary to check the validity of the performance maps.

The measurements in such tests are principally of rotor response to unbalanced loads (synchronous-whirl amplitudes), location of system critical speeds, and threshold of rotor-bearing instability (half or fractional-frequency whirl). Later in this paper, discussion is given of how these measurements can be made with existing instrumentation, both with "easy to use" fluids and with liquid metals.

Even after the bearing and rotor-dynamic characteristics have been experimentally evaluated in bearing test rigs and in dynamic simulator test rigs, some questions still remain regarding the rotor-dynamic performance of a specific turbomachine. The reasons for this are that the dynamic forces in such turbomachinery, principally those due to electrical or aerodynamic unbalances, are frequently improperly defined. In addition, thermal gradients and consequent distortions and misalignments are sometimes greater than anticipated in the thermal analysis of the turbomachine. Finally, high temperature creep can result in significant shifts of the mass center of the rotor causing large dynamic loads on the bearing. Here, it is extremely difficult to use conventional bearing film thickness instrumentation for reasons of space and accessibility. While this problem is greater with liquid

metals, it is also true of other turbomachinery systems. Even the most highly developed film thickness transducers are inherently sophisticated and delicate instruments. The probe dimensions range from a minimum of about 0.1 inch diameter to much larges sizes, as high as 1/4" and 1/2", and frequent calibration is necessary to guard against instrument drift. Except in very special cases (e.g., high speed, prototype gas bearing turbomachinery), it has not proved feasible to incorporate them in actual turbomachines. Here reliance has to be placed principally on indicrect methods, the principal measurement being those of temperatures and force. For example, it can be shown from theory (e.g., Ref. 11) that the temperature rise in bearings is very strongly a function of the bearing film thickness. Accurate calculation can be made to establish the bearing temperature vs film thickness relation and the temperature measurements then used to indirectly measure the operating film thickness. Force measurements can be made either by strain gauging the bearing support or, more conveniently, by use of accelerometers. In the factory test of a prototype, provisions can generally be made to supplement these measurements with film thickness gauges located in more readily accessible parts of the rotor or, if necessary on a rotor extension. These measurements can then be related to the film thickness in the bearing through the calculated rotor mode shape and deflection curves, as discussed later in the paper. On conclusion of the prototype testing these supplementary film thickness measurements would be removed and the continuous monitoring of the delivered turbomachinery conducted entirely by the thermocouple and accelerometer measurements, as is the present practice with conventionally lubricated machines.

The various necessary bearing and rotor-dynamic performance measurements conducted during the different stages of development have been briefly reviewed above. In the balance of this paper previous experience with such measurements as well as a preliminary discussion of some potentially useful new techniques for liquid metal environment are discussed.

3. EXPERIMENTAL MEASUREMENTS WITH "EASY TO USE" FLUIDS

Water, air and siliconse fluid have all been used as lubricants in experimental studies of process fluid lubrication in which the process fluid is a low-

viscosity liquid such as the alkali liquid metals. Water was used in an investigation of bearing stability (Ref. 12) and water and light turbine oil have been used in preliminary check out of apparatus for use with liquid metals (Refs. 13 and 14). Air has been used as the lubricant for a "scaled-up" 6 ft. diameter bearing which hot wire anemometry was used to study turbulent flow patterns in eccentric annuli (Ref. 15). Low viscosity silicone oil has been used both for fundamental studies of superlaminar flow in concentric annuli (Refs. 5 and 6) and for studies for bearing performance (Refs. 7, 9 and 10).

Eddy-current sensors have been used for shaft locus measurements in most of the work with water and silicone fluid. The transducer in this type of sensor is a coil of fine wire. A high-frequency current is passed through the coil and this induces eddy currents in a nearby conducting body. AC coupling, or loading of the coil by the conductive surface causes coil resistance to vary depending on the proximity of the surface to the coil.

Capacitance gauges are used extensively in gas-lubricated bearing work but they have seldom been used with liquid-lubricated bearings. There is a large difference in the dielectric constants of air and liquids which results in spurious effects if both are present in the gap between probe tip and shaft surface. It has proven to be extremely difficult to maintain a completely air, or liquid, free environment in the immediate vicinity of the bearings with the shaft running at high speeds.

Eddy current gauges may also be affected by a mixed-phase environment depending on the liquid. If the liquid is a conductor or a poor dielectric, eddy currents will be induced in the liquid thus loading the coil and changing the sensitivity with respect to proximity of the conducting surface. This effect has been a factor in the choice of which fluid is used to simulate liquid metals. Water is a poor dielectric and there has been difficulty with zero shift and variable sensitivity when eddy-current sensors are used with water-lubricated bearings (Ref. 12). Silicone fluid is an excellent dielectric and there is no noticeable effect of changing the environment from air to silicone fluid or some mixture of the two (Ref. 16)

(a) Fundamental Studies of Superlaminar Flow in Concentric and Eccentric Annuli

Silicone fluid with finely divided aluminum powder suspended in it has been

used in visual studies of superlaminar flow in concentric and eccentric annuli representing lubricant films in bearings. In Fig. 1 photographs of laminar flow, vortex flow and fully developed turbulence obtained by this method are shown. Experimental data on friction torque and pressure distribution have also been obtained for comparison with the vortex flow and turbulent flow lubrication theories (Refs. 5 and 6). Agreement between experiment and theory has been good as is illustrated by the pressure distribution results shown in Fig. 2. The experimental data have verified the turbulent lubrication theory on the fundamental level. Other experiments in which the steady-state and dynamic performance of actual bearings are measured were needed to evaluate the theory as a design analysis tool.

(b) Steady-State Performance of Bearings in Turbulent-Flow Regime

Early experimental work with low-viscosity fluids including data on a full cylindrical bearing using water (Ref. 17) and steady-state load capacity measurements of a 60-degree partial-arc bearing (Ref. 16) did not agree very well with the turbulent lubrication theory then available. Much better agreement with these experimental data was obtained subsequently with the more recent theory based on an eddy viscosity concept (Refs. 4a and 4b). This evidence of correlation between theory and experiment for steady-state load conditions encouraged further investigations in which both the steady-state and the dynamic properties were measured experimentally and compared with theoretical data. The measurements were made first for the basic bearing elements - a single partial-arc pad and a full cylindrical bearing (Ref. 7). Again the correlation between experiment and theory was good so that now similar results have been obtained for the composite bearings which were considered to be of greatest practical value for liquid-metal lubricated machinery - the tilting pad (Ref. 9) and the floating-ring (Ref. 10) journal bearings.

The improved correlation between theory and experiment is illustrated by the data for the tilting pad bearing which is much more complex, and therefore more difficult to analyze than the partial-arc bearing. Shaft position was measured by proximity sensors located at both ends of the test bearing housing, outside the seal and scavenging rings. Figure 3 shows a cross section of the test bearing housing with a tilting-pad

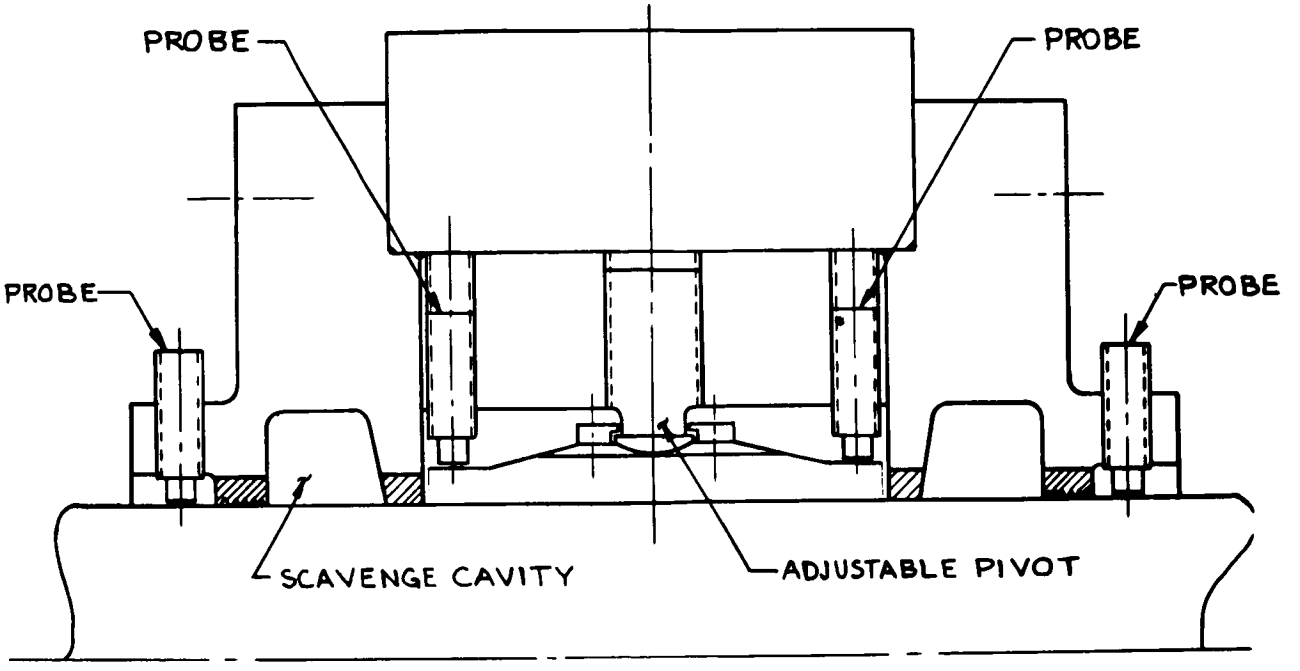


Fig. 3. Cross Section of Test Bearing Housing with Tilting-pad Bearing Installed

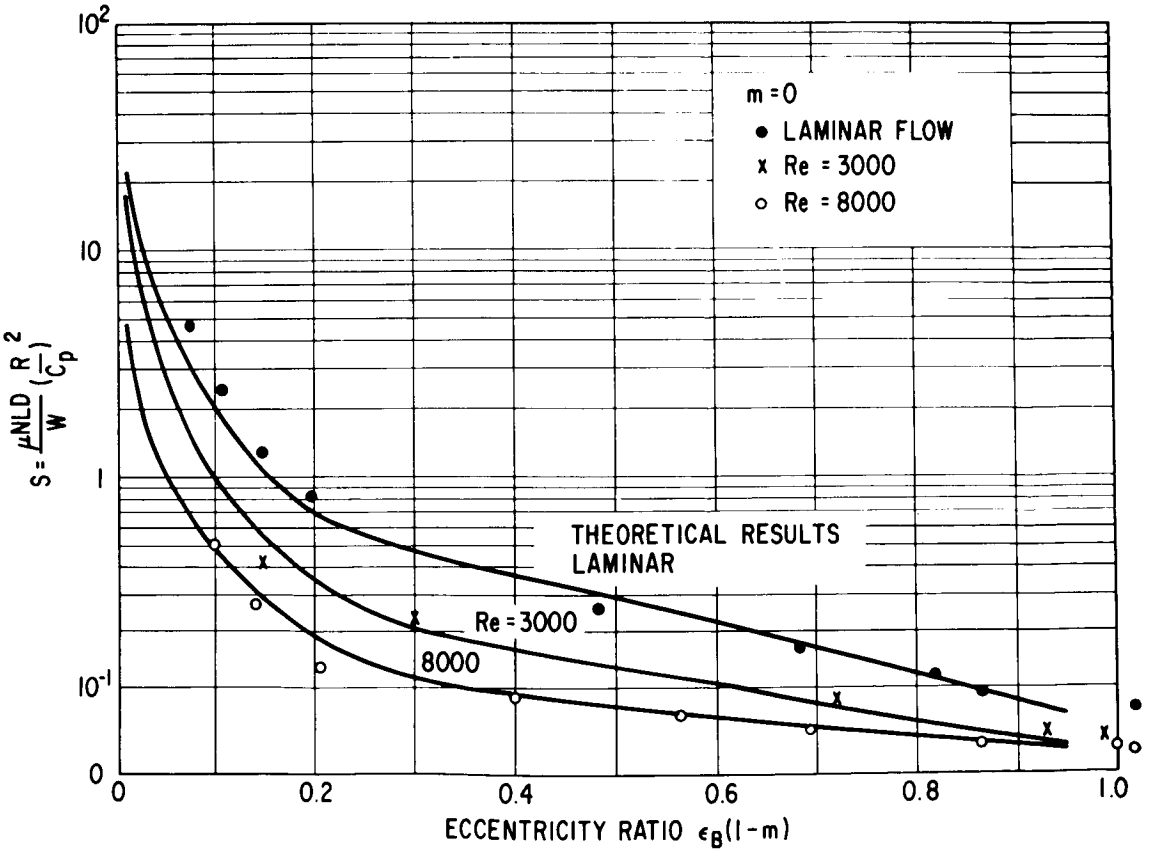


Fig. 4. Comparison of Measured and Calculated Steady-state Load Capacity for the Tilting-pad Bearing

bearing installed. There are two probes at each end of the housing, one to measure motion in the vertical plane and one in the horizontal plane. To compensate for the effects of shaft bending under large static load, the outputs of the probes at both ends were averaged by adding them using summing amplifiers. In addition to the probes outside the bearing cavity to measure shaft locus, other probes are located inside the housing, in a silicone fluid environment, to measure roll and pitch motions of one of the bearing pads. The steady-state load capacity data (Fig. 4) are presented as eccentricity ratio plotted against Sommerfeld Number for several values of Reynolds Number and for laminar flow.

The laminar flow lubrication theory has been thoroughly verified by a number of independent investigators. Good agreement between theory and measurement in the laminar flow regime established confidence in the apparatus and its instrumentation. Correlation at high Reynolds Numbers has consistently been comparable to the laminar flow correlation thus demonstrating that the turbulent lubrication theory is an effective design analysis tool for steady-state bearing operation. Equally satisfactory correlation between measured and calculated bearing friction torque and lubricant flow rates has been obtained (Refs. 9 and 10).

(c) Dynamic Performance of Bearings in Turbulent Flow Regime

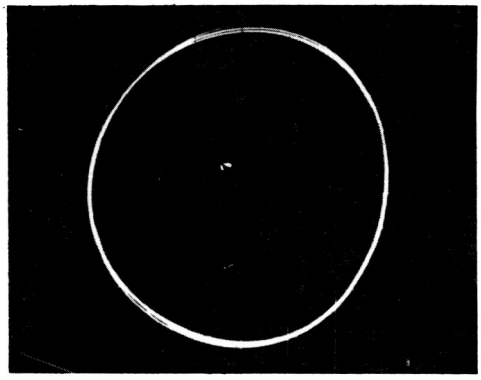
The theoretical dynamic stiffness and damping coefficients of the bearing are used to compute critical speeds, stability limits and response to dynamic load of bearing-rotor systems. Comparison between theoretical and measured bearing dynamic properties was made by comparing the calculated stability threshold and rotor response to unbalance load with experimental measurements. A stability analysis was performed for the partial-arc bearing to predict,for each of several different speeds, the load at which fractional-frequency whirl instability should first occur. Whirl should exist at this load and at lower loads according to the analysis. Experimental measurements were made by progressively reducing the load at constant speed until whirl was first observed. The theoretical and measured results showed good correlation as noted in Table 3.

TABLE 3

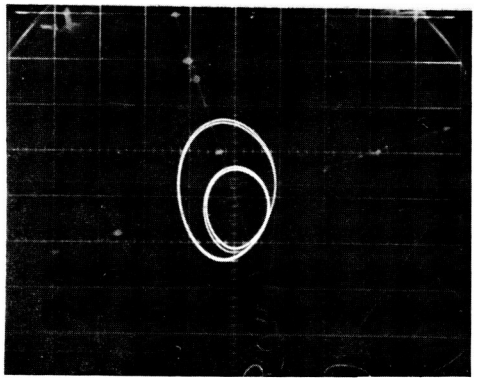
Reynolds Number	Shaft Speed rpm	Load at Onset of Fractional Frequency whirl - lbs.	
		Experiment	Theory
5820	3500	132	110
8314	5000	198	175
11304	8000	312	350

Deliberate known unbalance weights were added to the shaft to produce synchronous rotating loads of known amplitude and the resulting motion of the shaft center was measured. Figure 5 shows some examples of oscilloscope photographs of shaft motion in response to synchronous rotating load for several different types of bearings. Figure 5d shows measurements for both motion and force transmitted to the bearing by the shaft with the partial-arc bearing. The force measurement was obtained by clamping the bearing between piezoelectric load cells in the vertical and horizontal planes and placing their outputs on the oscilloscope with X-Y presentation. Agreement between measured and theoretical rotor response to dynamic load has been consistently good for the various bearing types investigated (partial-arc, tilting-pad and floating-ring), with comparable correlation for laminar and turbulent flow operating conditions (Refs. 7, 9 and 10). In Fig. 6 some measured and calculated response orbits are shown for the partial-arc bearing operating at constant speed (4000 rpm) with varying steady-state load.

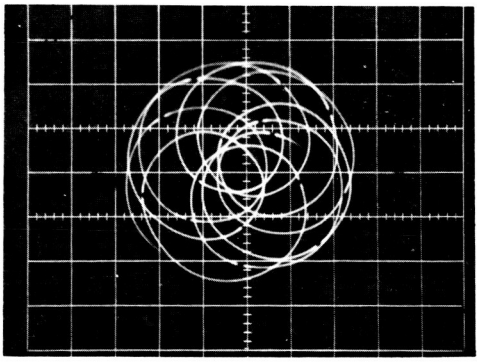
In performing rotordynamics analysis, the rotor is represented by a series of masses connected by springs representing rotor mass distribution and flexural stiffness (Ref. 8). The bearings are represented by spring and damping coefficients which must be computed for each speed from dimensionless bearing design data. In the table given in Fig. 7, the rotordynamics response program output for a flexible-rotor configuration operating in turbulent flow bearings at 10,500 rpm is presented (Ref. 18). As shown, the rotor was divided into 13 mass stations and the motion of the shaft axis in response to the specified



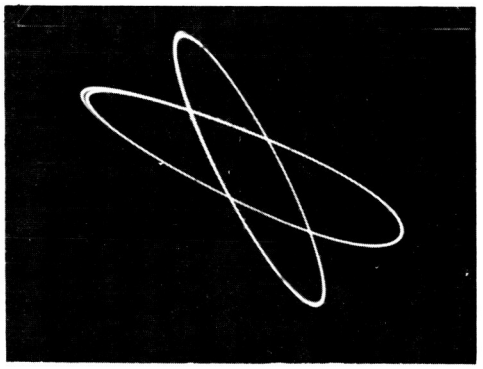
(a) Shaft Motion--Tilting Pad Bearing Showing Synchronous Response Orbit. 1 div = .2 mils.



(b) Shaft Motion--Partial-Arc Bearing Showing Fractional Frequency Whirl and Synchronous Response Orbits. 1 div = .55 mils.



(c) Shaft Motion--Floating-Ring Bearing Showing Fractional Frequency Instability of Both Films. 1 div = 1.18 mils.



(d) Shaft Motion and Dynamic Bearing Load-Partial-Arc Bearing. The force measurement is the trace with the more nearly vertical orientation. 1 div = .212 mils and 15.9 lb.

Fig. 5. Oscilloscope Photographs of Shaft Motion and Bearing Force Measurements

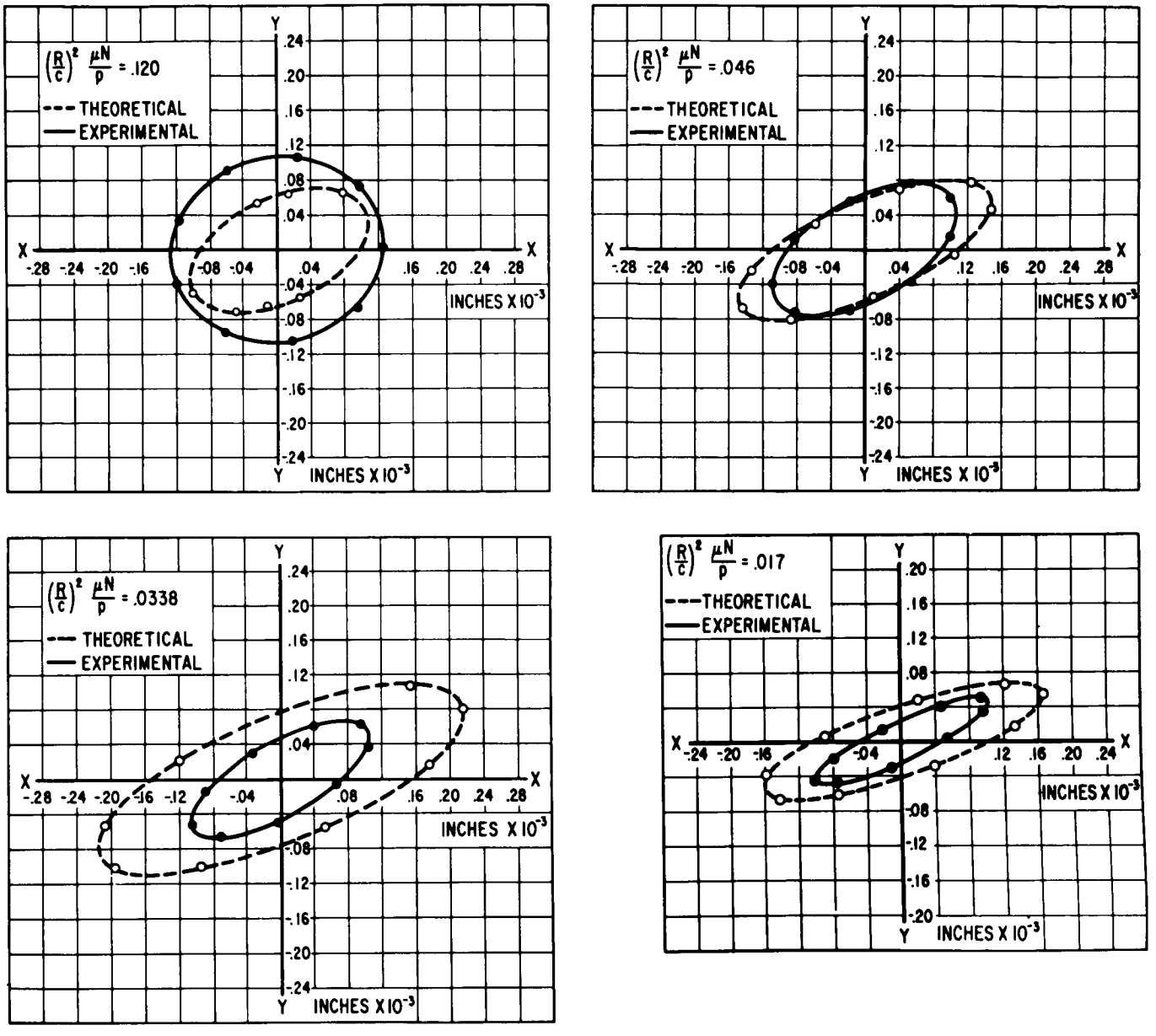
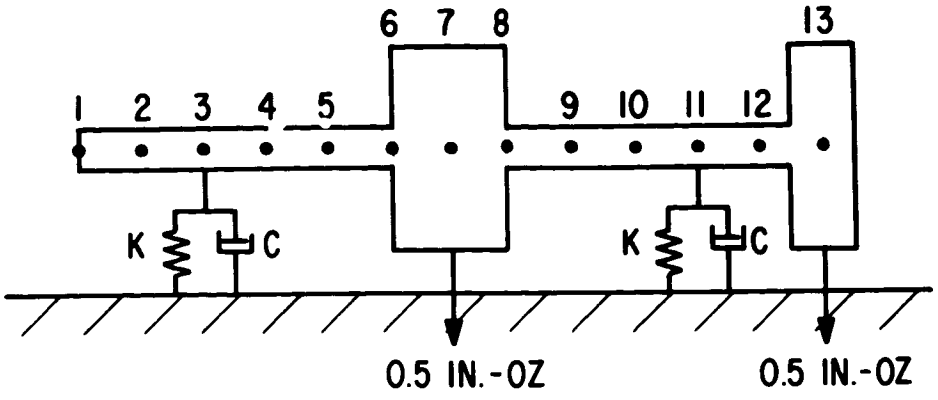


Fig. 6. Theoretical and Measured Response Orbits for Partial-arc Bearing C/R = 4×10^{-3} in./in., Arc Length = 100°, R_e = 5820



Rotor Speed = 10500.00 rpm

Trans. K	Trans. C	Rotat. K	Rotat. C
1.5000000E	1.7000000E+02	0.0000000E-01	0.0000000E-01
1.4500000E+05	1.7000000E+02	0.0000000E-01	0.0000000E-01

STATION	DEFLECTION (MILS)	PHASE ANGLE, DEG.
1	5.7421E-01	-5.9107E+01
2	3.5793E-01	-7.6544E+01
3	2.4155E-01	-1.2179E+02
4	3.9357E-01	-1.7647E+02
5	4.6658E-01	1.7639E+02
6	7.4351E-01	1.6048E+02
7	8.8909E-01	1.5464E+02
8	1.0398E+00	1.5040E+02
9	1.2645E+00	1.4088E+02
10	1.3212E+00	1.3740E+02
11	1.5951E+00	1.2323E+02
12	1.9601E+00	1.1219E+02
13	2.4353E+00	1.0375E+02

Force Transmitted to Bearing Housing

Brg. No.	Trans.Force (lbs)	Phase Angle
3	4.26999E+01	-1.5696E+02
11	2.80327E+02	8.7235E+01

Force Transmitted to Foundation

Brg. No.	Trans.Force (lbs)	Phase Angle	Pedestal Motion Ped.Def.(mils)	Phase Angle
3	4.29690E+01	-1.5696E+02	8.59379E-02	-1.5684E+02
11	2.82094E+02	8.7235E+01	5.64187E-01	8.7361E+01

Fig. 7. Rotor-bearing Representation and Program Output for Rotordynamics Analysis

unbalance load is computed for each mass station. In this case, the shaft motion is a circular orbit whose radius is given for each mass station along with the phase angle between the motion and the unbalance force vector. These results describe the mode and amplitude of vibration of the entire shaft. This is important because it means that the theoretical bearing dynamic properties and the rotordynamics analysis can be verified experimentally by measurements at any point along the shaft – it is not necessary to make the measurements directly at the bearings. The analysis also provides computation of the force transmitted by the shaft to each bearing housing and the motion of the pedestal or housing.

Experimental measurements of the response of flexible-rotor/bearing configurations, including the one described in Fig. 7, are being obtained and compared with the theoretical results. Measurements are made at mass stations 1, 4, 7, 10 and 13. The theoretical response and comparative experimental data for stations 4, 10 and 13 when there are equal and in-line unbalance weights at each of the two concentrated masses are given in Figs. 8, 9 and 10 to illustrate the correlation. These results have shown that with proper design it is entirely feasible to operate rotors through and well above their third system critical speed with low-viscosity, and hence low-damping lubricant. Moreover, the combined turbulent flow lubrication theory and rotordynamics analyses can be used to predict dynamic performance with good accuracy. Thus, the important features of the performance of each of the three rotor-bearing systems as determined by theoretical analysis have been verified by experimental measurement. These features include:

1. The location of the critical speeds
2. The comparative importance of the several critical speeds on the behavior of the system
3. The sensitivity of the system to the magnitude, phase angle and location of the unbalance weights.

From these data, the designer can evaluate the suitability of his proposed rotor-bearing system design. He knows whether there are any operating speeds which should be avoided and he is able to establish some meaningful specifications on allowable unbalance.

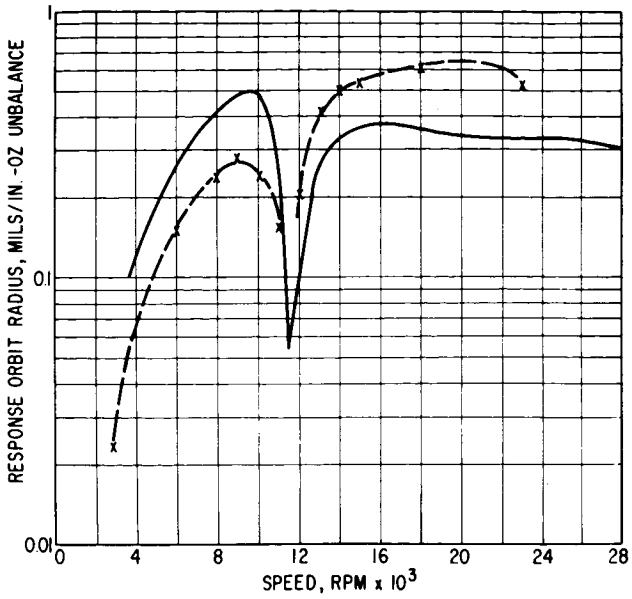


Fig. 8

Theoretical and Measured Rotor Response to Unbalance Load--Two Mass System, Unbalances in-line-Station 4

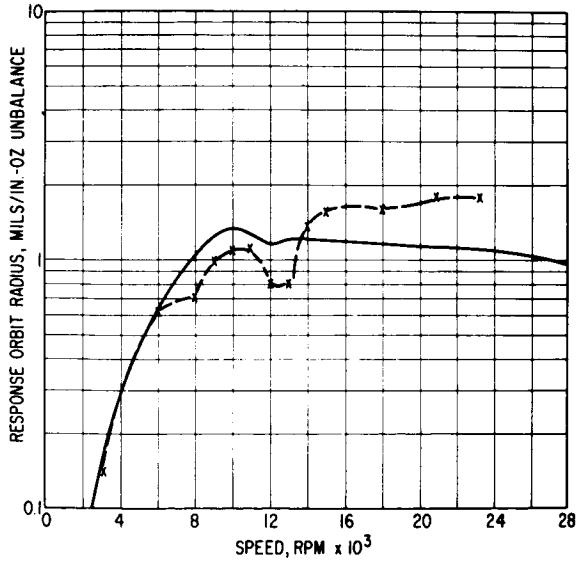


Fig. 9. Theoretical and Measured Rotor Response to Unbalance Load--Two Mass System, Unbalances in-line-Station 10

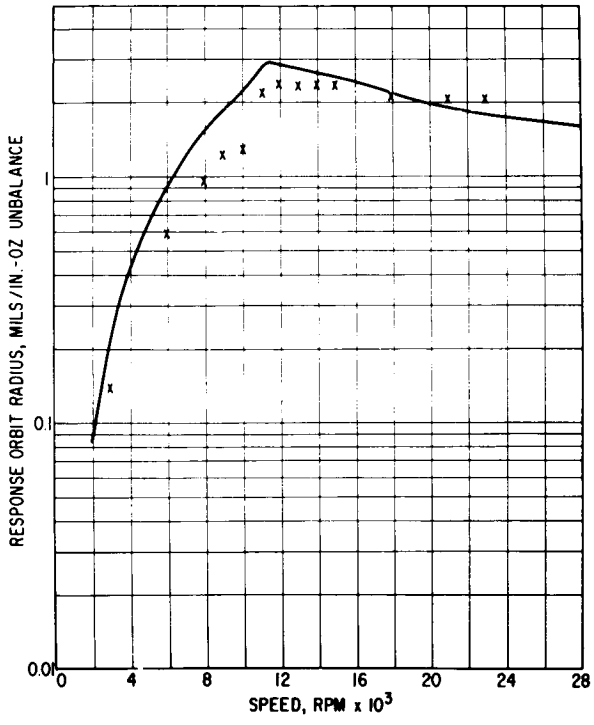


Fig. 10. Theoretical and Measured Rotor Response to Unbalance Load--Two Mass System, Unbalances in-line-Station 13

(d) Performance of Proximity-Measurement Instrumentation in Experiments with Silicone Fluid

In all of this work with silicone fluid lubricants, the eddy-current proximity sensors performed well with few really troublesome problems. There have been some difficulties with temperature induced zero drift, especially with the floating-ring bearings when probes were located inside the bearing housing to measure the eccentricity of the ring in the outer bearing. Heated lubricant flowing out from the ends of the bearing passed directly over the probes and the resulting zero drift was enough to prevent accurate steady-state ring eccentricity measurements (shaft eccentricity measurements combining inner and outer film eccentricities were not affected). In the flexible rotor experiments, two probes at each measurement position arranged for push-pull operation were used successfully to greatly reduce temperature drift.

There has been some difficulty with spurious effects in the form of high-frequency hash caused by variations in the magnetic permeability of the shaft. Demagnetization of the shafts helped but did not completely eliminate the problem. The solution has been to use variable electronic filters set to remove the high-frequency irregularities while passing the synchronous or fractional-frequency signal variations which are of interest. The orbit patterns shown in Fig. 5 were obtained with filtered sensor outputs. Another solution is to plate the shaft in the region of the probes with 3 to 5 mils of a non-permeable metal.

4. EXPERIMENTAL MEASUREMENTS WITH LIQUID METAL LUBRICATED BEARINGS

The key measurement tool for liquid-metal lubricated bearing experiments will continue to be proximity sensors. The requirements of the application would seem to mean that these proximity sensors should:

a. Tolerate and function in the high-temperature, liquid-metal environment
b. Be free from zero drift and changing sensitivity in spite of large temperature variation
c. Have high frequency response in order to follow dynamic motion of the shaft
d. Be mounted directly on or in the bearing without disturbing its performance or perturbing flow patterns in the lubricant film
e. Be small in relation to the bearing

This is an imposing list of requirements and it will require a substantial advance in the development of proximity sensors to meet all of them.

It is possible to perform worthwhile experimental work with liquid-metal lubricated bearings even if the "ideal" proximity sensor is not yet available. Some of the above requirements can be circumvented by incorporating special features into the test apparatus or by making use of theoretical analysis. In other instances, indirect methods can be used to establish the value of one variable from measurements of another. In this section some possible methods for obtaining needed data with instrumentation that does not meet all the above criteria are described. In most cases, these concepts are not presented as proven, practical methods of measurement. Rather they are presented to illustrate possible alternates or supplements to direct film thickness measurements. The purpose is to stimulate thinking and show that there are ways of making effective use of the instrumentation which is available in spite of its limitations. In considering these approaches, it should be recognized that there are requirements both for experimental research data obtained with special experimental apparatus and for methods of monitoring the performance of prototype machines. In development activity it is frequently necessary only to identify problem areas and the requirements for accuracy or broad capability are less stringent than would be the case for research studies. On the other hand, there is usually less latitute in adapting the machine design to the limitations of the instrumentation.

(a) Remote Location of Sensors

There are obvious advantages to locating the proximity sensors outside the bearing cavity, away from the liquid metal environment. This approach must of course take account of the fact that the relative location of sensor and bearing surface may change because of differential expansion or distortion; that is, the signal level corresponding to zero film thickness may become uncertain.

The steady-state eccentricity of the shaft in the bearing can be established in spite of zero-shift or a shift in relative location of the probe and bearing surface if provision can be made in the apparatus to reverse the load direction. If the load amplitude is kept constant but the direction is reversed, the eccentricity can be taken as half the resulting displace-

ment of the shaft center. Since this also identifies the bearing center locus, attitude angle measurements can also be obtained. In cases where load reversal is not feasible, it may be possible to obtain zero radial load by operating with the rotor in a vertical attitude or by just counterbalancing the shaft weight. The bearing center can then be located since, with zero load, the shaft and bearing centers should coincide.

Zero drift does not prevent accurate measurements of dynamic motion of the rotor so rotor response and instability can be measured by remote probes. If the rotor is rigid, the motion at the bearings can be determined from measurements at any two remote planes of measurement. With either rigid or flexible rotors, the motion at any measurement plane can be calculated by rotordynamics analysis and compared directly with the measurements as was done in the work on flexible rotors lubricated with silicone fluid.

Even with remote location, the sensors would still be in a high-temperature environment. Proximity sensors to operate at high temperatures are available now. For example, capacitance probes have been developed and used in gas-lubricated bearing experiments at temperatures up to 1400 F (Ref. 19).

A series of calibration curves at temperatures from room temperature to 1600 F are shown in Fig. 11, for the capacitance probe. Experimental eddy current and magnetic-reluctance sensors have been operated at 1200 F (Ref. 20) and eddy-current sensors for 1200 F operation are available commercially.

(b) Separate Method for Steady-State Film Thickness Measurement

The drawbacks and limitations of all of the non-contacting electrical proximity sensors are most troublesome when the requirement is for accurate, steady-state, highly localized measurements of film thickness. This type of measurement is needed to investigate distortion of the bearing or its supporting structure and thermal gradients in both the axial and the radial directions.

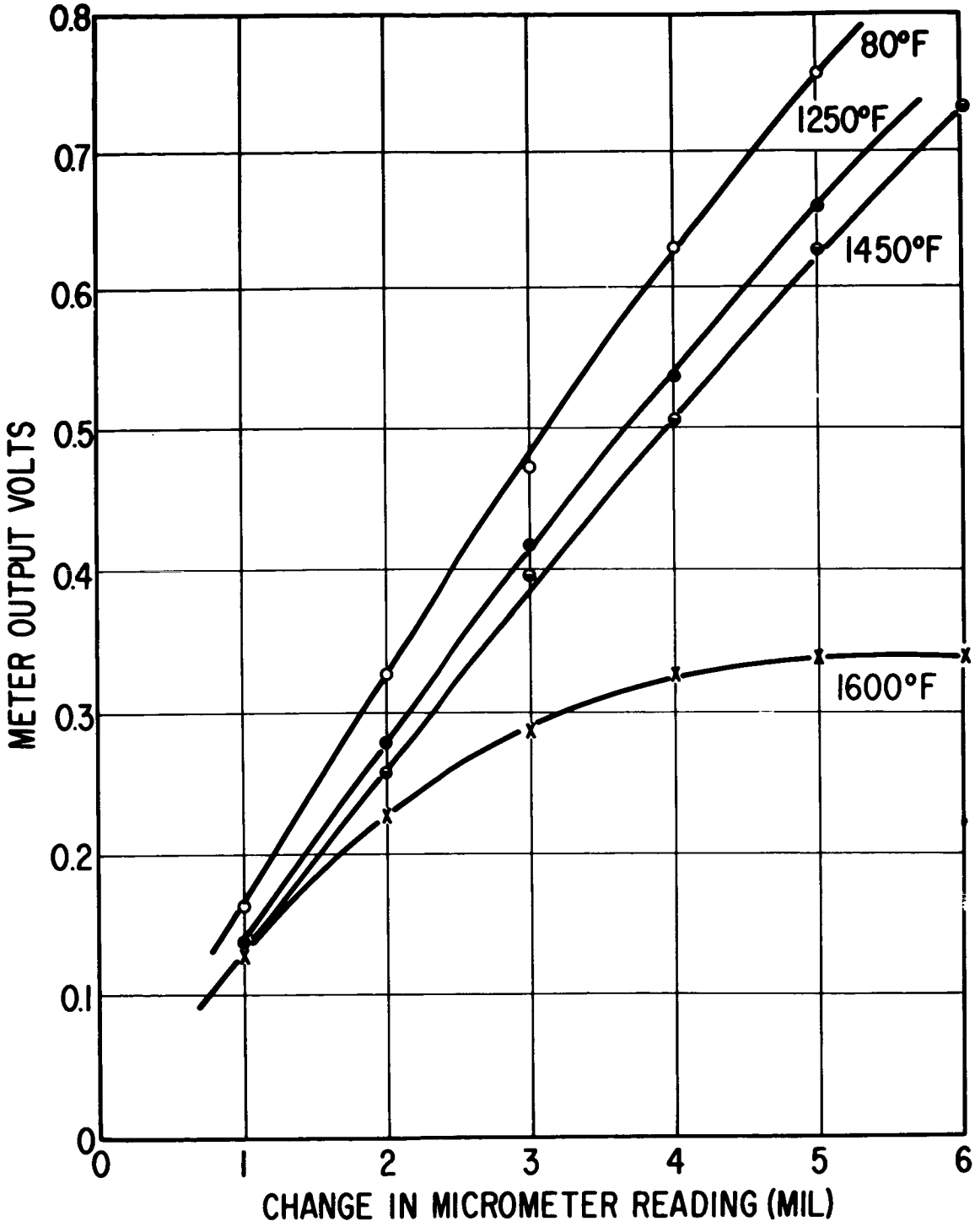


Fig. 11. Calibration Curves for High-temperature Capacitance Probes

If the dynamic shaft motions are measured separately, the frequency response requirements can be relaxed and the concepts for film thickness measurement can be broadened. One concept for direct steady-state film thickness measurement would be to put small holes or taps in the bearing surface and force liquid metal out of these holes into the bearing film (Fig. 12). The flow for a constant supply pressure, or the pressure difference required to obtain a specific flow, would depend on the restriction to flow at the entrance. This will depend in part on the film thickness since the minimum cross section for flow will be the annular region bounded by the hole diameter and the gap between bearing and shaft surfaces. The pressure in the film surrounding the hole will also influence the result. The hole itself can be used as a pressure tap to measure the pressure in the immediate vicinity by determining the supply pressure necessary to just stop flow in either direction. Calibration experiments will be needed but it should be possible to perform these outside the apparatus using a fluid other than a liquid metal. An analysis to establish calibration requirements will have to be performed.

The flow restriction concept for film thickness measurement has the advantages of an absolute zero reference (zero flow corresponds to zero film thickness), remote location of the transducer (for flow or pressure measurement) which permits close control of its environment, and very small area resolution. Also, the sensors can be introduced with minimum disturbance to the bearing mechanical and thermal characteristics. The requirement for considerable support or secondary equipment such as an auxiliary liquid-metal supply, and pressure and flow measurement equipment is an obvious drawback.

If the more limited objective of establishing the existence and relative magnitude of axial clearance variation without precise measurements of absolute film thickness is accepted, the use of variable flow restrictor sensors becomes somewhat more straightforward. Then, it is necessary only to compare pressures measured at various holes space over the bearing surface since misalignment will result in a non-symmetrical film pressure distribution.

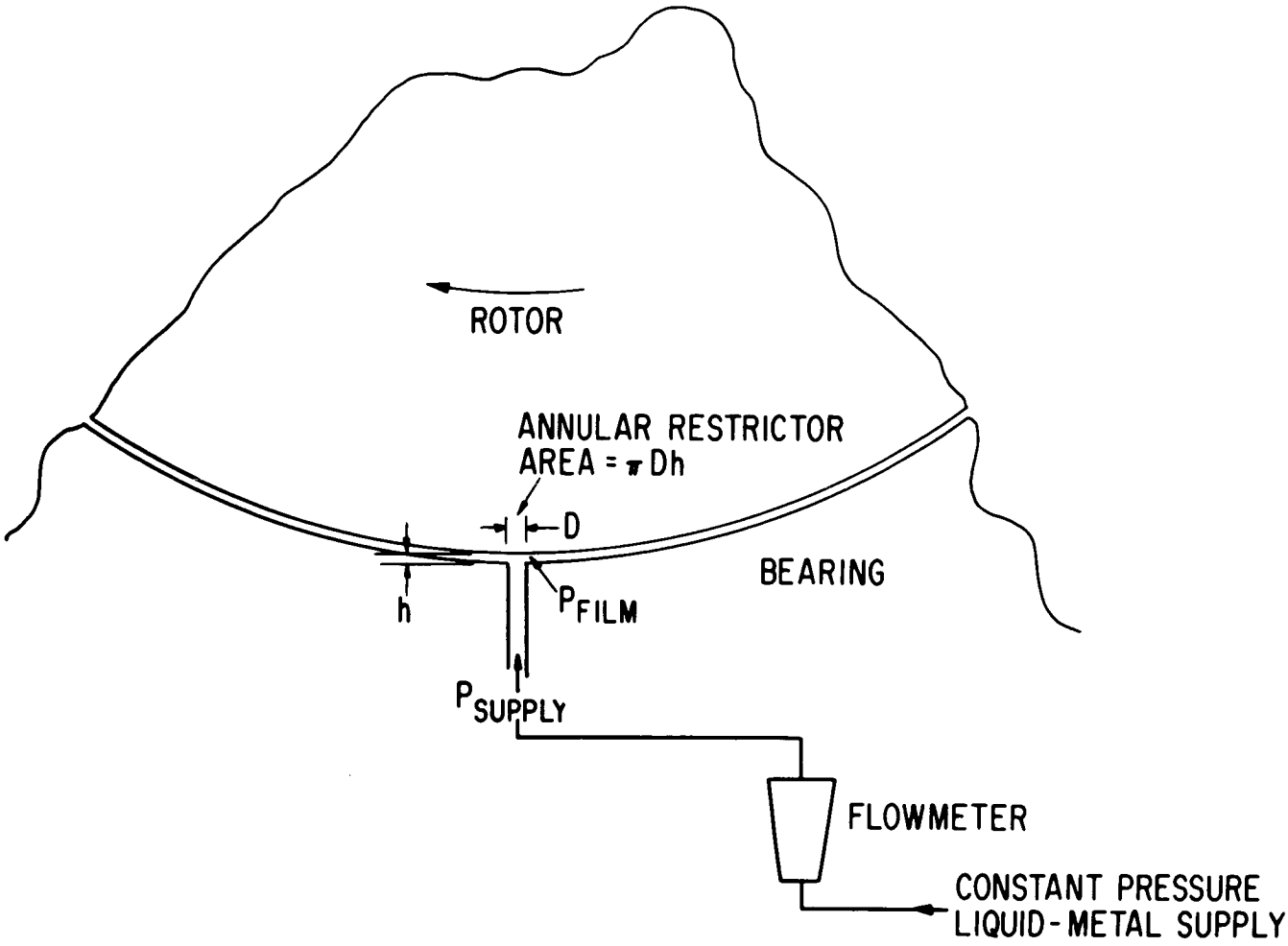


Fig. 12. Illustration of Variable Flow Restrictor Film Thickness Measurement Concept

If there are no high frequency response requirements, it is natural to consider mechanical riders or probes as possible methods of measurement. First thoughts along these lines are that it is still necessary to have an electrical transducer of some type to measure the mechanical deflection or position of the rider and therefore no advantage is gained. In addition, there are the problems of rider or probe wear and hydrodynamic effects at the shaft contact. It might be more fruitful to consider mechanical means of establishing a single film thickness reference point to be used in connection with remote, non-contacting transducers. Transducer zero drift or sensitivity change would not be a factor in this type of measurement since the object is only to identify a relatively sudden change in signal which occurs at a specific value of film thickness.

(c) Indirect Methods of Measurement

Variables such as film thickness or dynamic motion can sometimes be measured by indirect methods involving measurement of some other related operating variable. For example, the dynamic performance of a machine can be monitored by measuring force transmitted to the bearing supports. Shaft motion and transmitted force can be related by rotor dynamic analysis as shown by Fig. 13, in which the calculated force transmitted to one of the bearings and shaft motion at the bearing are plotted for identical operating conditions of the flexible-shaft apparatus using silicone fluid lubricant. Bearing instability can also be detected from force measurements. This was illustrated by the force measurements made with a partial-arc bearing using silicone fluid lubricant. High-temperature strain gauges which can function in a liquid metal environment are available for force measurements (Ref. 20). Sprayed ceramic coatings are used to insulate the foil strain gauges from the surface, to bond the gauge to the surface and to protect the gauge and its leads from the liquid metal. Good static and dynamic measurements can be obtained up to about 1200 F. Above that temperature there is difficulty with static measurements due to creep but dynamic measurements can be made up to at least 1500 F. Or, the Villani effect principle for pressure measurement (Ref. 2) can be used.

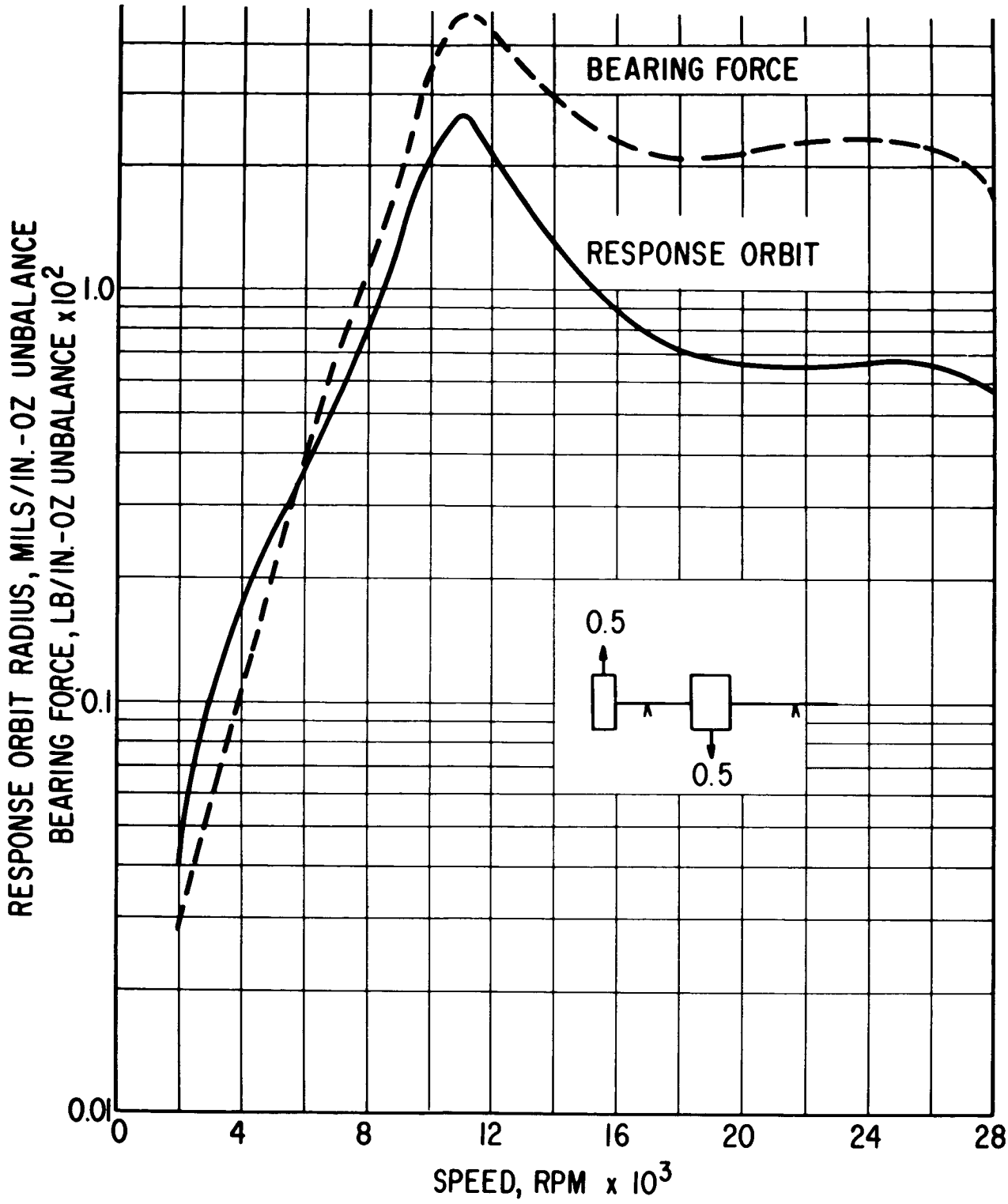


Fig. 13. Rotor Response and Bearing Force at the Bearing between the Concentrated Masses

The existence of bearing misalignment can be detected and an indication of its severity can be had by measuring the righting couple transmitted to the bearing mounting. In principle, the same thing can be done for axial clearance variation caused by axial thermal gradients since this will result in a non-symmetrical distribution of load capacity about the bearing centerline.

5. SUMMARY, CONCLUSIONS AND RECOMMENDATIONS

The experimental investigation of liquid metal lubricated bearings for high speed applications requires measurement of such quantities as: lubricant film thickness, friction torque, lubricant flow, lubricant pressure distribution, journal orbits under dynamic loads and rotor-bearing stability. Many of these measurements, particularly those involving the lubricant film thickness and its variation under dynamic loads cannot now be made in a liquid metal environment, as reliable, proven instrumentation for this purpose is not yet available. The principal difficulties are caused by the electrical conductivity of liquid metal films, the high temperatures of liquid metal bearings, the lack of accessibility inherent in liquid metal systems as well as the need for high measurement accuracy combined with the limited space available for transducers in the bearings. Currently, some work is in progress to develop inductive type film thickness transducers to overcome at least some of these problem areas. This effort should be pursued to facilitate the development of liquid metal bearing systems.

It should be noted, however, that bearing performance measurements are required for a variety of purposes, including: verification of new lubrication theory, experimental evaluation of promising bearing concepts, rotor-bearing dynamics experiments and monitoring of bearing performance in turbomachinery. Some of these can be accomplished now using existing instrumentation, for example by conducting the tests in fluids that simulate the lubrication properties of liquid metals as well as by the use of indirect measurement techniques. Thus, much progress has been made to date by using such lubricants as silicone fluid, water and air to verify turbulent lubrication theory (required because of the low viscosity of liquid metals), as well as to evaluate bearing concepts for use with low viscosity lubricants and to study the dynamics of flexible rotors supported in bearings lubricated with low viscosity fluids. Indirect measure-

ment techniques that can be used with liquid metal systems include: remote location of sensors, separate sensors for measurement of steady state and dynamic film characteristics, temperature and transmitted-force measurements to indicate film thickness, as well as others discussed in this paper. Such indirect measurements are also particularly important for the monitoring of actual turbomachinery bearings, where the inherently delicate, direct film thickness probes are impractical even with conventional lubricants. Such indirect methods of bearing performance measurements are therefore required for the development and operation of liquid metal bearing systems and they should be developed for these purposes.

ACKNOWLEDGEMENT

Some of the experimental observations, test results and data cited in this paper have been obtained in the course of theoretical and experimental investigations of turbulent-lubrication, liquid-metal bearings and rotor-bearing dynamics previously conducted at M.T.I. These investigations were sponsored by agencies of the U. S. Government, under the following contracts:

NAS-w-771 and NAS-w-1021 - Mr. J. P. Joyce, NASA Project Manager
AT(30-1)-3363 - Mr. N. Grossman, AEC Project Manager

REFERENCES

1. Sternlicht, B. and D.D. Fuller, "A New Method for the Determination of Attitude and Eccentricity in Journal Bearings," Lubrication Engineering, April 1957.

2. Guieser, D.R. et al, "Liquid-Metal-Lubricated Bearing Instrumentation," Part I: Prototype Sensor Performance with Simulated Film AFAPL TR-65-31, Part I, March 1965.

3. Constantinescu, V.N. "On Turbulent Lubrication," Proceedings of the Institute of Mechanical Engineers, Vol. 173, 1959.

4a. Ng. C.W. and C.H.T. Pan, "A Linearized Turbulent Lubrication Theory," ASME Paper No. 65 LuB-29.

4b. Elrod, H.G. Jr., C.W. Ng and C.H.T. Pan,"A Theory for Turbulent Fluid Films and Its Application to Bearings," A.E.C. Report NYO 3363-2. M.T.I. Report No. 65TR9, March 1965.

5. Vohr, J.H. "Analysis of Turbulent Lubrication, Vol. 2, An Experimental Study of Vortex Flow and Turbulence in Concentric and Eccentric Annuli," M.T.I. Report 64TR20 (Vol. 2 of Final Report on Contract NAS-w-771).

6. Vohr, J.H. "Experimental Study of Superlaminar Flow Between Non-Concentric Rotating Cylinders," M.T.I. Report 65TR43, Vol. 3 of the final Report on NASA Contract NAS-w-1021.

7. Orcutt, F.K. and E.B. Arwas, "Analysis of Turbulent Lubrication, Vol. 1, The Static and Dynamic Properties of Journal Bearings in Laminar and Turbulent Regimes," MTI Report 64TR19, Vol. 1 of Final Report on NASA Contract NAS-w-771, May 1964.

8. "Rotor-Bearing Dynamics Design Technology," - Part III. Design Handbook for Fluid Film Bearings, Mechanical Technology Inc. May 1965. Technical Report AFAPL TR-65-45, Part III.

9. Orcutt, F.K. "Steady-State and Dynamic Properties of the Tilting-Pad Journal Bearing in Laminar and Turbulent Regimes," MTI Report 65TR32-Vol. 1 of Final Report on Contract NAS-w-1021.

10. Orcutt, F.K. and C.W. Ng, "Steady-State and Dynamic Properties of the Floating-Ring Journal Bearing in Laminar and Turbulent Regimes, MTI Report 65TR33, Vol. 2 of Final Report on Contract NAS-w-1021.

11. Sternlicht, B. "An Indirect Method of Film Thickness Measurement in Fluid Film Bearings," ACTA IMEKO, 1961 - International Conference on Instrumentation, Budapest 1961.

12. McHugh, J.D. "Low Viscosity Bearing Stability Investigation," NASA-CR-54039, Final Report on Contract NAS 3-2111, April 1964.

13. Hall, J. and R. Spies, "Research in the Field of Liquid-Metal-Lubricated Bearings," RTD - TDR - 63 - 4289, Part II, December, 1964.

14. AiResearch Manufacturing Co., "Quarterly Progress Report for Period Ending December 31, 1964" Snap 50/SPUR Contract AF 33(616)-2289, APS-5152-R1.

15. Burton, R.A. and H.J. Carper, "Fundamental Investigation of Liquid-Metal Lubricated Journal Bearings," SwRI-1228-40, Quarterly Report No. 2 or Contract AT(11-1)-1228, October 1964.

16. Orcutt, F.K. "Investigation of a Partial Arc Pad Bearing in Super-laminar Flow Regime," ASME Paper 64-LubS-8, TRANS. ASME. Series D. Vol. 87, No. 1. pp. 145-152, March 1965.

17. Smith, M.I. and D.D. Fuller, "Journal Bearing Operation of Superlaminar Speeds," ASME Paper 55 Lub-26, 1955.

18. Orcutt, F.K. and E.B. Arwas, "An Investigation of Rotor-Bearing Dynamics with Flexible Rotors and Turbulent Flow Journal Bearings - Part I - Analysis, Design and Fabrication of the Test Apparatus," AEC Report NYO-3363-2, MTI Report 65TR12, March 1965.

19. Lewis, P. and J. Meacher, "Research on Gas Lubrication at High Temperatures and Low Flow Rates," TDR No. APL-TDR-65-56, March 1964, pp.69-79.

20. Weymouth, L.J. "Strain Gauge Application by Flame Spray Techniques," Inst. Soc. of Am. Preprint 16.5-1-64, presented at 19th Annual Conference, New York, October 1964.

SESSION 4

LIQUID LEVEL AND IMPURITY MEASUREMENTS

Wednesday, September 29, 1965

CHAIRMAN: P. A. Lottes
Argonne National Laboratory

N66 31687

LIQUID-METAL LEVEL DETECTOR AND INDICATOR

L. W. Stillwell
AiResearch Manufacturing Company of Arizona

Phoenix, Arizona
(Paper presented by N. F. Pratt)

I INTRODUCTION

This report describes the design, development, and operation of two types of liquid-metal position detectors. These instruments have been used on the liquid-metal loops utilized by AiResearch as part of the development program for space power systems. The two types of detectors are:

(a) A portable, manually operated detector used for checking shipping containers, locating freeze or oxide plugs in piping, etc., where a continuous readout is not required.

(b) A permanently mounted, automatic detector used to determine the level of liquid metal in the piping, tanks, etc., where a continuous readout of the liquid level is required.

The development of these instruments was prompted by the necessity of determining accurately the level of liquid metals such as potassium, sodium, NaK, and mercury through stainless-steel containers. Container wall thickness may be up to 0.2 inch and wall temperatures to 1600°F. Since all existing systems had basic disadvantages that prohibited their use in most cases, the eddy-current liquid-level detector was developed by AiResearch instrumentation engineers.

PRECEDING PAGE BLANK NOT FILMED.

II THEORY OF OPERATION

Eddy currents are generated in a conducting material when in the presence of an alternating flux field. The depth to which the circulating currents penetrate the material is dependent on both the exciting current frequency and the conductivity and permeability of the material, expressed mathematically as follows:

$$\delta = \frac{56}{\sqrt{\pi \mu_r f \sigma}}$$

where δ = standard depth of penetration, inches

μ_r = permeability of the material relative to air

f = frequency of the exciting current, cps

σ = conductivity of the material, percent IACS

With the assumption that a coil is used to produce an alternating flux field, the eddy currents circulating in the conductive material set up magnetic fields which tend to distort and weaken the magnetic fields produced by the exciting coil. This reduces the inductance of the coil; and if a secondary coil is wound near the exciting coil, the coupling between the two coils is greatly reduced.

The exciting frequency must be chosen such that the frequency is low enough to permit eddy currents to penetrate the stainless-steel wall and yet high enough to permit good coupling between the primary and the secondary windings.

III ELECTRICAL DESCRIPTION

Two electrically identical coils, each containing a bifilar-wound primary and secondary, make up the sensor of the automatic liquid level unit. The two coils, one a fixed reference coil for temperature compensation and the other a movable search coil to seek the conductive liquid metal, are connected in series opposing in the secondary circuit and series driven by a 5-kc oscillator in the primary circuit (Figure 1). When both coils are positioned on an empty stainless-steel container or tube, their outputs are exactly equal and the difference output from the secondary circuit is zero. However, when the seeking coil is positioned on a section of tube that contains a conductive liquid, the loss in coupling between its primary and secondary windings causes its induced secondary voltage to drop. The secondary voltages of the two coils are no longer equal, and a difference voltage appears across the secondary circuits. If the search coil is allowed to slowly change its position from an empty part of the tube to a full part, the secondary will be observed to increase from zero volts to approximately 250 microvolts for the following conditions (Figure 2):

(1) Primary drive voltage, 2 volts at 5 kc

(2) Coil diameter, 1 inch

(3) Coil-to-tube spacing, 0.7 inch

(4) Tube, 3/4-inch Sch. 40 stainless pipe partially filled with 600°F potassium

These conditions were chosen as standard, since they best represented the conditions with which the unit was designed to work.

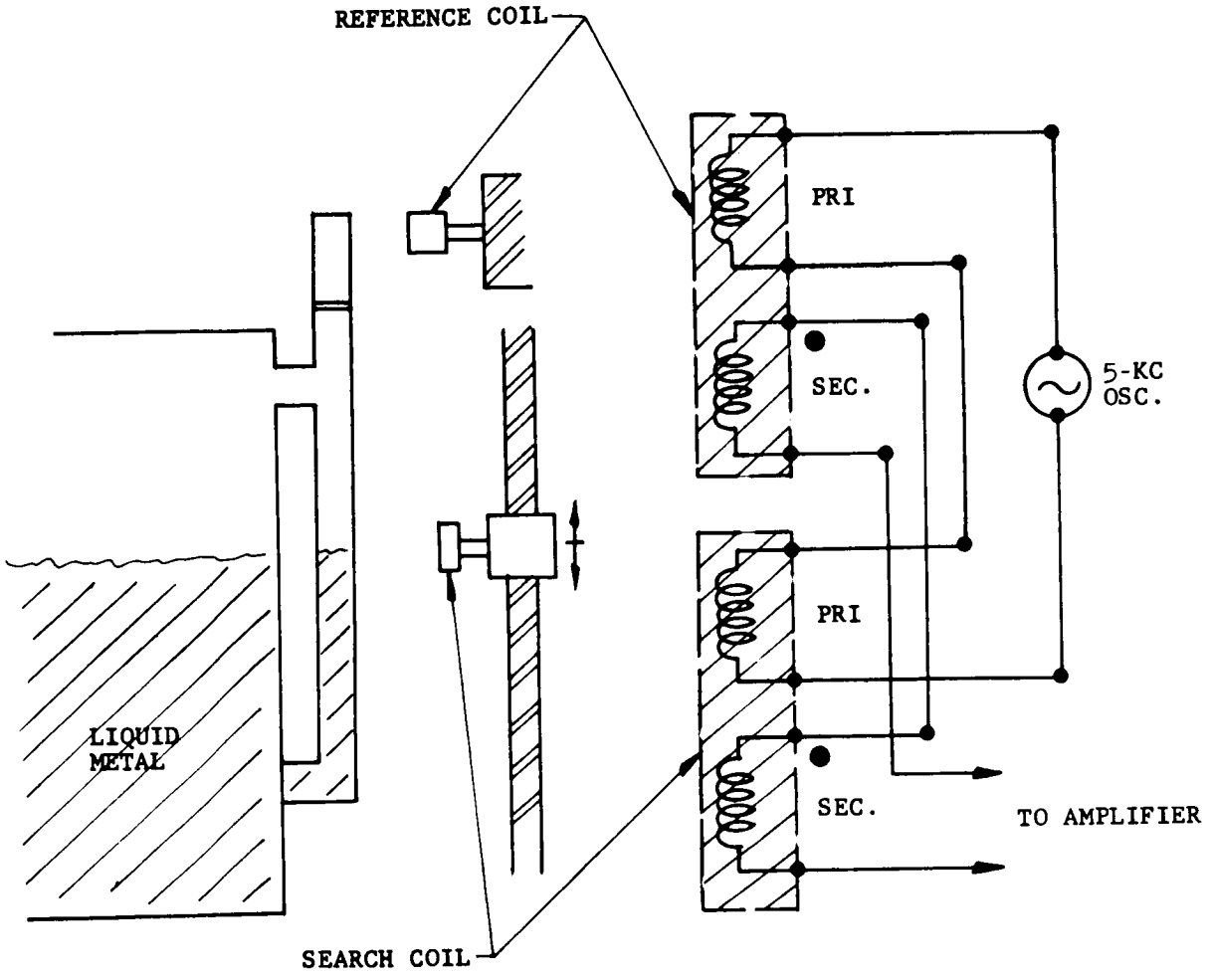


Fig. 1. Schematic of Liquid-Metal Level Detector

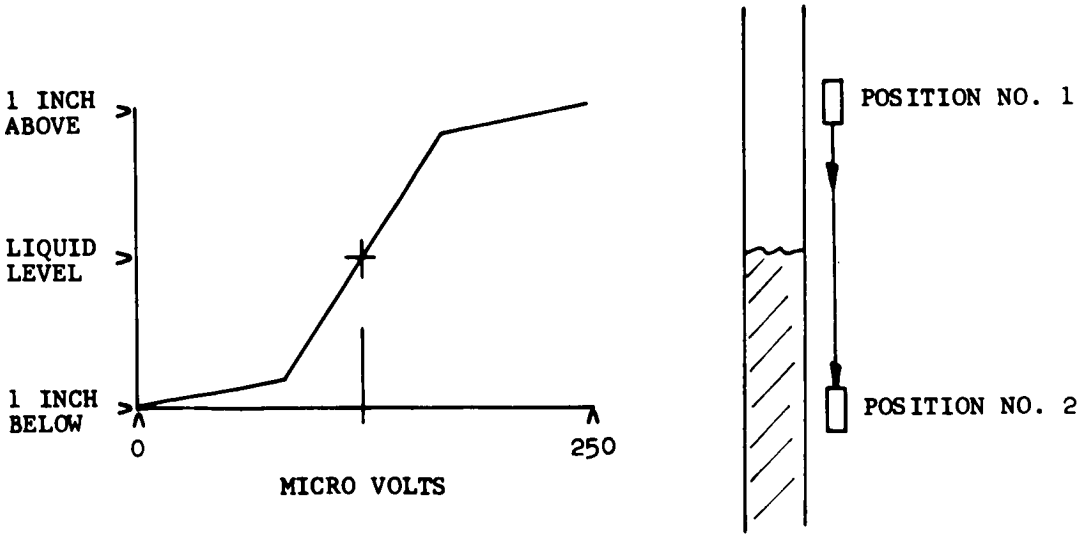


Fig. 2. Output from Search Coil as It Goes from One inch above Level to One inch under Level.

The circuitry following the reference and search coils, represented by the block diagram (Figure 3), may be briefly described as follows: Output from the two coils is fed to an RC balance network to compensate for any small electrical differences between the two coils. The balance network then drives a 5-kc bandpass filter to clean the signal of any unwanted induced voltages. An emitter follower acts as a buffer stage between the filter and the first amplifier section. A gain potentiometer separates the first stage of amplification from the second. The output of the amplifier consists of an emitter follower transformer coupled into a full-wave diode bridge. At this point, any error signal due to an unbalance condition between the two coils would appear as a d-c voltage always in one polarity (Figure 4). Because this voltage is to be used to provide an error signal to control a commercial servo system, its polarity must represent the direction the search coil must go to seek the level. This could be accomplished in two ways: First, the full-wave bridge could be made phase-sensitive to produce a negative or positive voltage, depending on the phase of the error signal. Second, the output from the bridge could be biased with a small fixed negative voltage (Figure 5). The latter was chosen since it allowed greater ease of balancing. A regulated power supply provides power for both the 5-kc oscillator and amplifier-detector circuit and it also provides a d-c excitation voltage for the probe position readout.

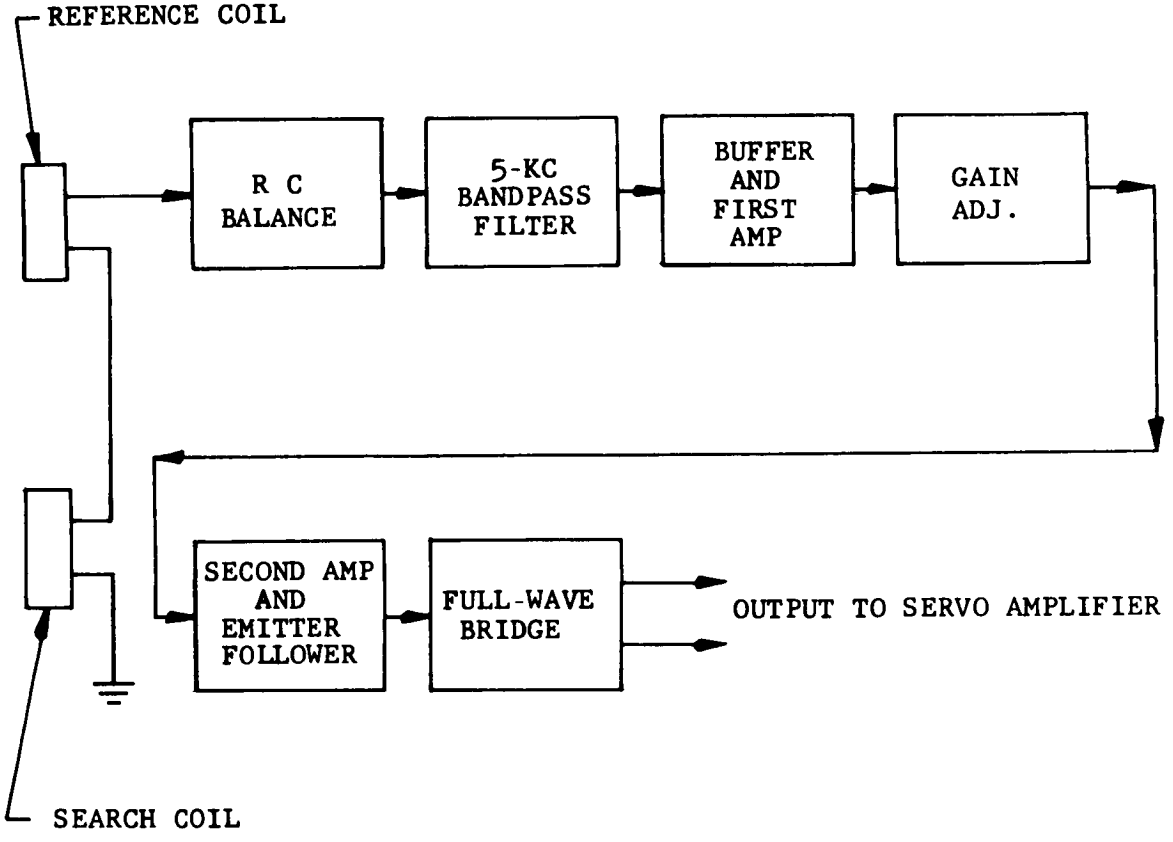


Fig. 3. Block Diagram Signal Conditioner

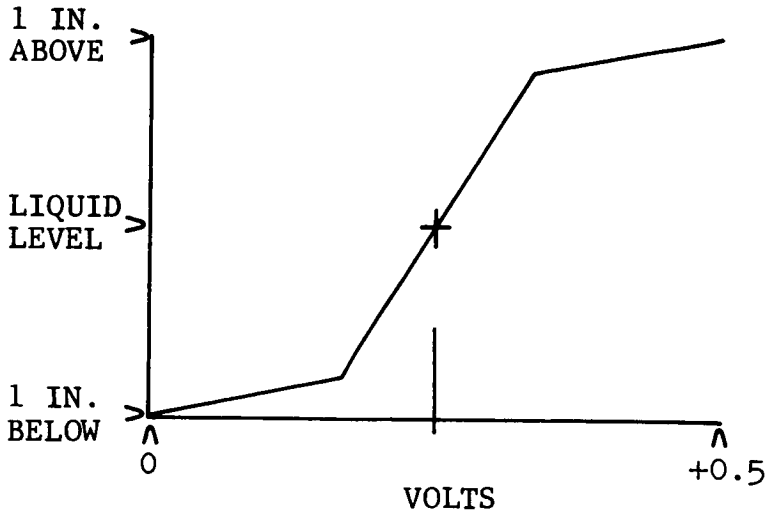


Fig. 4. Output from Full-wave Bridge (No Bias)

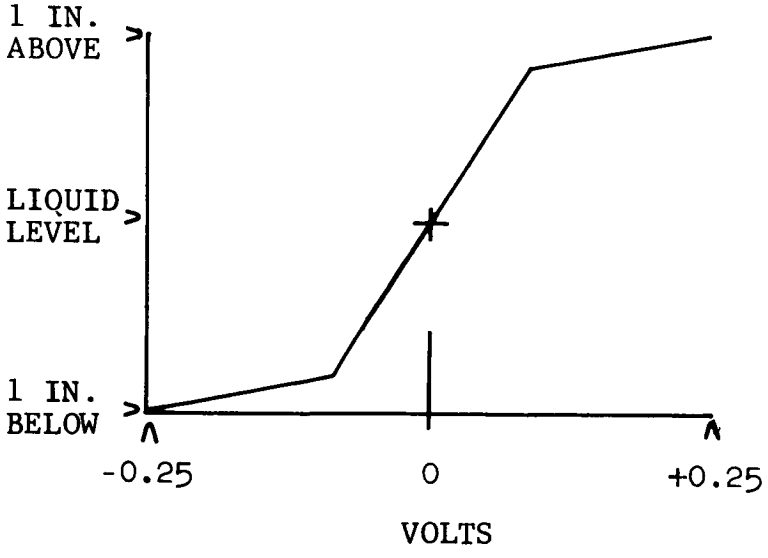


Fig. 5. Output from Full-wave Bridge (Bias Inserted)

IV MECHANICAL DESCRIPTION

In general, the mechanical system consists of a supporting frame and mounting brackets, a servo drive system, an air-cooling system, and a potentiometer coupled to the drive shaft (Figure 6).

The supporting frame may be of various sizes and shapes to best fit a particular situation. It is constructed of aluminum struts and has mounting brackets that attach it rigidly to the container or tube to be scanned. The frame also provides a fixed mounting for the reference coil.

The search coil is mounted on a carrier which is guided by a linear ball bearing riding on a hardened steel rod. The coil assembly is driven by a recirculating ball screw coupled through a gearbox to a commercial 10-watt servomotor. A 270-degree potentiometer is also coupled to the ball-screw through a small gearbox. This potentiometer, in a simple bridge circuit, provides a panel meter readout of the linear position of the search coil.

Experimental temperature results with the coil systems indicate that the coil temperature should not exceed 300°F and the ΔT between the two coils should not be greater than 25°F. Therefore, a small instrument blower mounted on the bottom of the frame assembly is used to purge the reference and search coil areas with ambient air. The size of this blower is varied, depending on the size of the unit and the temperatures involved.

Limit switches are positioned at extreme ends of the scanning range to prevent damage to the drive system.

A system of relays overrides the limit switches and provides an appropriate error signal to drive the scanning coil in the direction desired by the operator.

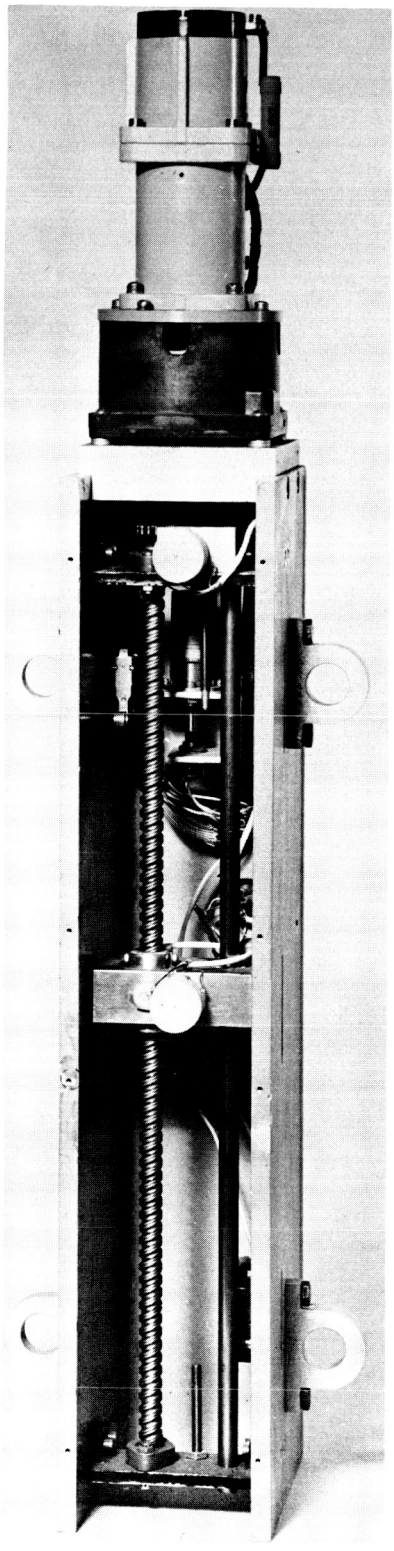


Fig. 6. Automatic Liquid Level Detector

V MOUNTING AND OPERATION

To date, the five systems installed at AiResearch have all been mounted on 3/4-inch Schedule 40 stainless-steel pipe welded into the container wall as a sight tube. The systems have ranged in size from 5 feet to 2 feet. Combined operating time now totals over 1,500 hours with one unit measuring 1600°F potassium.

VI MANUAL DETECTOR

The coils are similar to those of the automatic detector. Both coils are mounted in a ceramic holder with a brass shield between the two coils (see Figure 7). The primaries of the two coils are connected in series and powered by a primary excitation oscillator. The output of the secondary coils, connected in series opposing, is resistance- and capacitance-balanced, amplified, and then rectified. The rectified signal is indicated on a d-c microammeter.

The battery-powered electronic components are mounted in a portable case, as shown in Figure 8, with the reference and search coils mounted in a holder.

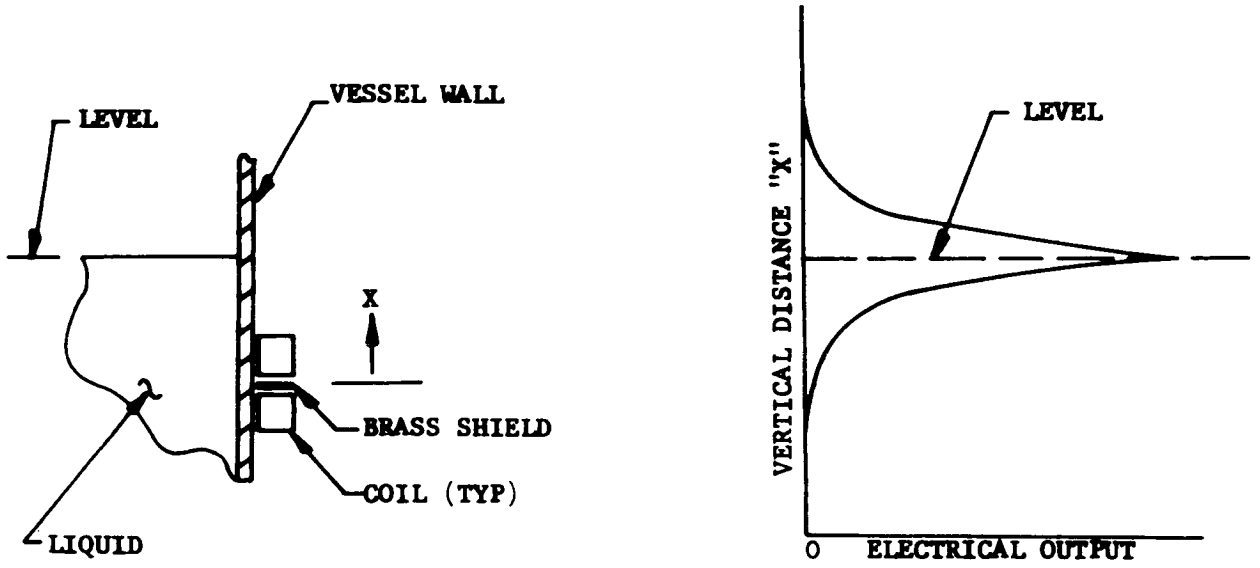


Fig. 7. Manual Liquid Level Detector

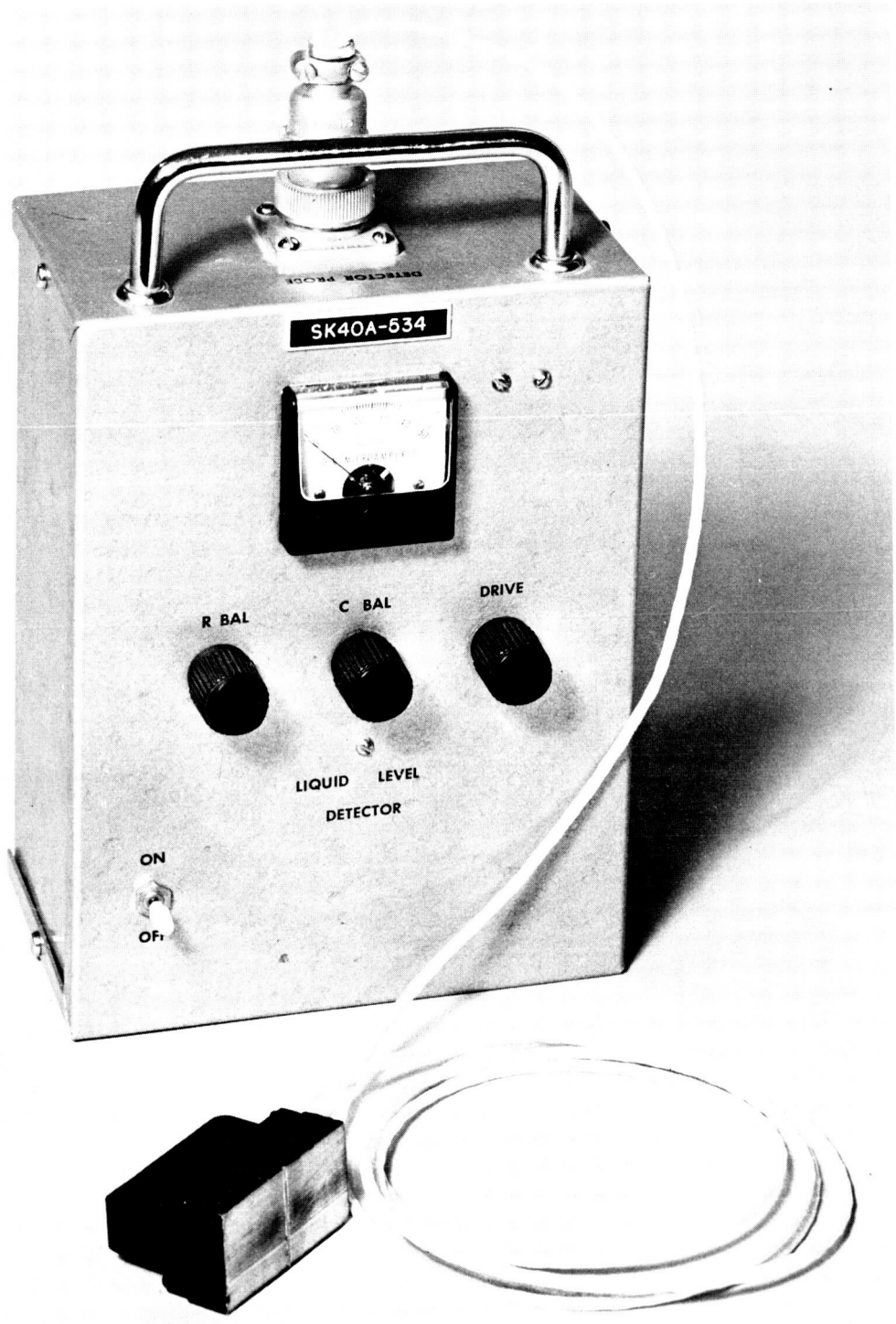


Fig. 8. Manual Liquid Level Detector

N66 31688

EXPERIENCES AND DEVELOPMENTS IN INSTRUMENTATION FOR LIQUID METAL EXPERIMENTS*

H. J. Metz and M. M. Yarosh
Oak Ridge National Laboratory
Oak Ridge, Tennessee

Introduction

Experiments in the use of liquid metals in power generation systems for reactor and for space application have increased in recent years. A very high degree of system reliability is mandatory because of the end use. This has made it imperative to obtain accurate information from experimental systems to ensure that a thorough understanding of system operation is achieved. For this understanding, data must be obtained through appropriate techniques and apparatus for measurement of the parameters to be described.

Large and complex potassium systems have been built at Oak Ridge National Laboratory during the past few years to meet program needs. One such system and its attendant instrumentation will be described in detail. A discussion of operating experience with some of the instrumentation will be followed by more detailed information on the instruments themselves.

Part 1

M. M. Yarosh

The Intermediate Potassium System[1, 2, 3, 4, 5, 6, 7, 8, 9]

The Intermediate Potassium System (IPS) was built as a part of the Medium Power Reactor Experiment Program. This system uses the Rankine cycle with potassium as the working fluid. Figure 1

*Research sponsored by the U. S. Atomic Energy Commission under contract with the Union Carbide Corporation.

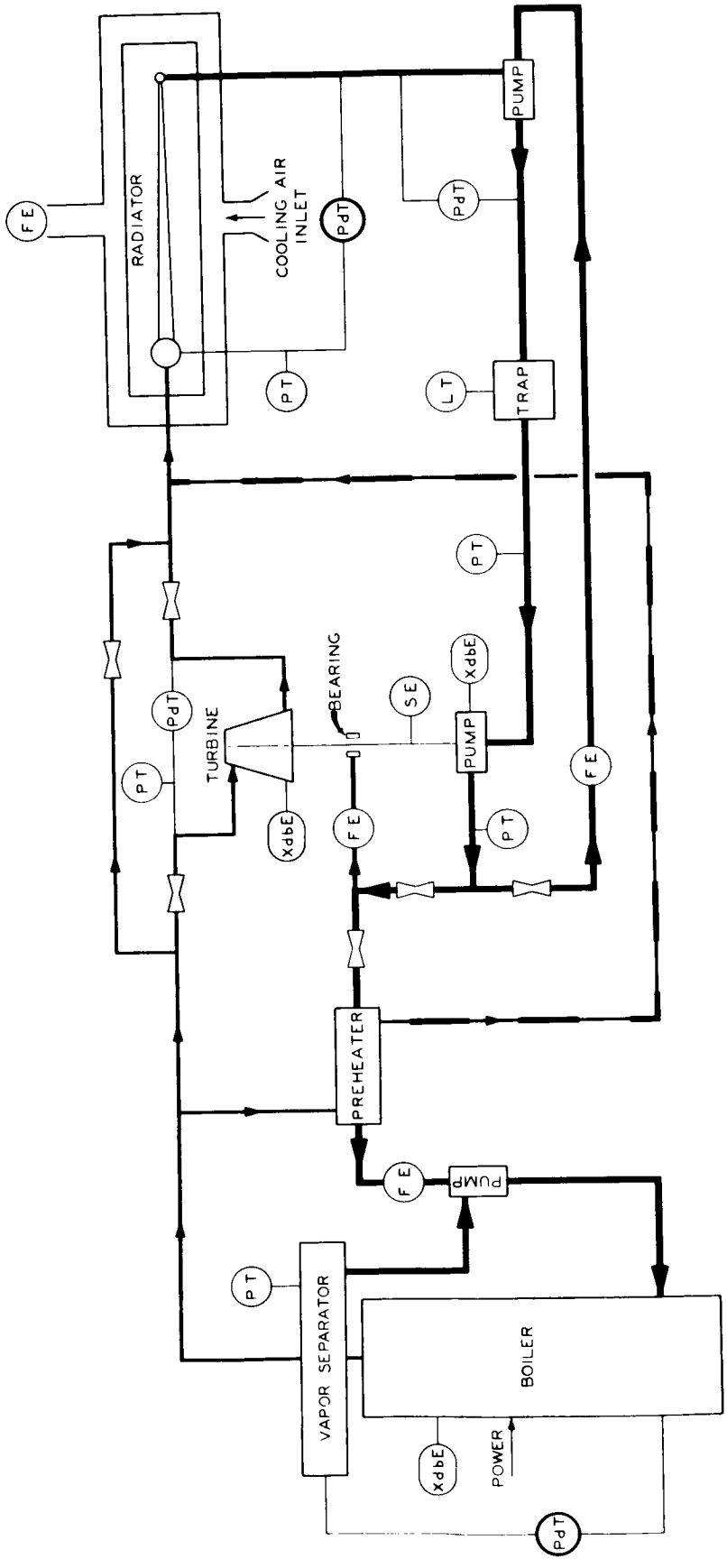


Fig. 1. Instrumentation Diagram Intermediate Potassium System

is a flow diagram for this system. Liquid potassium is delivered from a turbopump to supply the net feed for the boiler. The mixture of potassium liquid and vapor leaves the boiler and passes through a separator unit. The liquid is recirculated while the vapor is used to drive the turbopump unit, and in the final design, the potassium vapor will also drive a turbogenerator unit. In the present system, the vapor for power generation is bypassed through a throttling valve to the radiator. Heat is transferred from the radiator to an air-cooled shroud surrounding the radiator. A portion of the vapor is bled off to a liquid preheater, and the condensate from this unit is discharged to the radiator inlet. The system condensate is returned from the radiator to the suction side of the turbopump.

Figure 1 also shows the principal instrumentation exclusive of thermocouples on the test rig. For system design and for system control studies, there are a number of very important parameters which must be measured. These include system operating pressures, pressure drops, system flows and liquid level measurements, turbopump speed, and, finally, system temperatures.

Control of the system is dependent on the inventory distribution within the system and the affect of this inventory distribution on system pressures and component performance. For example, an increase in boiler power from a steady state operating condition results in additional vapor delivered to the turbopump and to the radiator. This, in turn, causes an increase in turbopump speed and in pump discharge-pressure and flow. The additional vapor to the radiator results in a change in liquid inventory at the liquid end of the radiator and a change in suction pressure to the radiator scavenging-pump. The change in radiator and scavenging-pump conditions is reflected in the scavenging-pump discharge-pressure to the turbopump suction.

It is important to establish the precise relationships between power changes, inventory distribution, and system pressures and

flows. To accomplish this, the instrumentation shown on the flow diagram was installed.

The inventory is monitored with a level recording system described later in this report. A modification of this instrument, a liquid-metal manometer, is used to determine pressure drop when a phase change exists between the pressure measuring points and permits a convenient measure of liquid level. For boiler pressure drop and radiator pressure drop measurements, a liquid-metal level-indicator manometer is used. We have found that the radiator manometer is a sensitive measure of liquid accumulation in the radiator liquid headers during system operation.

Instrument Location for Pressure Measurements

Pressure measurements are required in both liquid and vapor-filled portions of the system. The instrument piping and transmitter elevations are important considerations in making such measurements. For both absolute and differential pressure measurements, Foxboro pressure transmitters are used. These units have an advantage of permitting adjustment of the instrument range and zero but are limited to a maximum temperature of 400°F. As a result, standoffs must be used in both the liquid and vapor regions. This causes some major problems. Measurement of the absolute pressure in a vapor system at perhaps 1000°F with the use of a 400°F instrument leads to vapor condensation and refluxing of the liquid in the instrument lines. The hot vapor cannot be allowed direct contact with the instrument sensing element. Instrument lines must be correctly sized and properly sloped so that there will be vapor cooling and condensation without chugging and without introducing variable-head errors. The use of intermediate liquid seals results in high instrument inertia and delays the instrument response to system changes. Thus, a NaK-filled seal system reduces the speed of instrument response to system perturbations.

Figure 2 illustrates a typical installation of a liquid-metal manometer, PdT 62, and a Foxboro differential-pressure transmitter, PdT 63. Both are located on the radiator end of the system. The circled call outs are temperature measurement points on the piping. The manometer reflects the net effect of the liquid level in the radiator tubes and the pressure drop between the vapor header and the suction side of the liquid scavenging-pump. The temperature of the vapor line to the manometer must be carefully controlled to prevent vapor condensation. Liquid line temperatures are adjusted to permit a matching of temperatures at the junction of the instrument and process liquid line. Some condensation and evaporation may occur within the manometer, but careful temperature control will reduce this to a minimum.

To date, accurate measurements of very low pressures, below 2 psia, have proved unsatisfactory in these systems. Absolute pressures in the radiator portion of the system may be well below 1 psia, and an accurate reading of this value is important. When absolute pressure measuring devices are connected to low-pressure liquid points in the system, care must be taken to avoid a vertical rise in the standoff which may prevent measurement of the pressure. For example, a pressure of 0.1 psia is equivalent to about 4 in. of potassium.

Pressure measuring devices must be installed so that potassium may be drained from instrument lines in the system during a shut down. The technique of "boiling off" trapped potassium liquid is ineffective where instrument temperatures are limited to 400°F. Failure to remove potassium from the instrument and adjacent lines may result in oxide plugs near the instrument and may require removal of the entire instrument.

Temperature Measurement Using Infrared Photography

The radiator on the Intermediate Potassium system consists of 144 tubes arranged in six banks of twelve tubes on each side of a

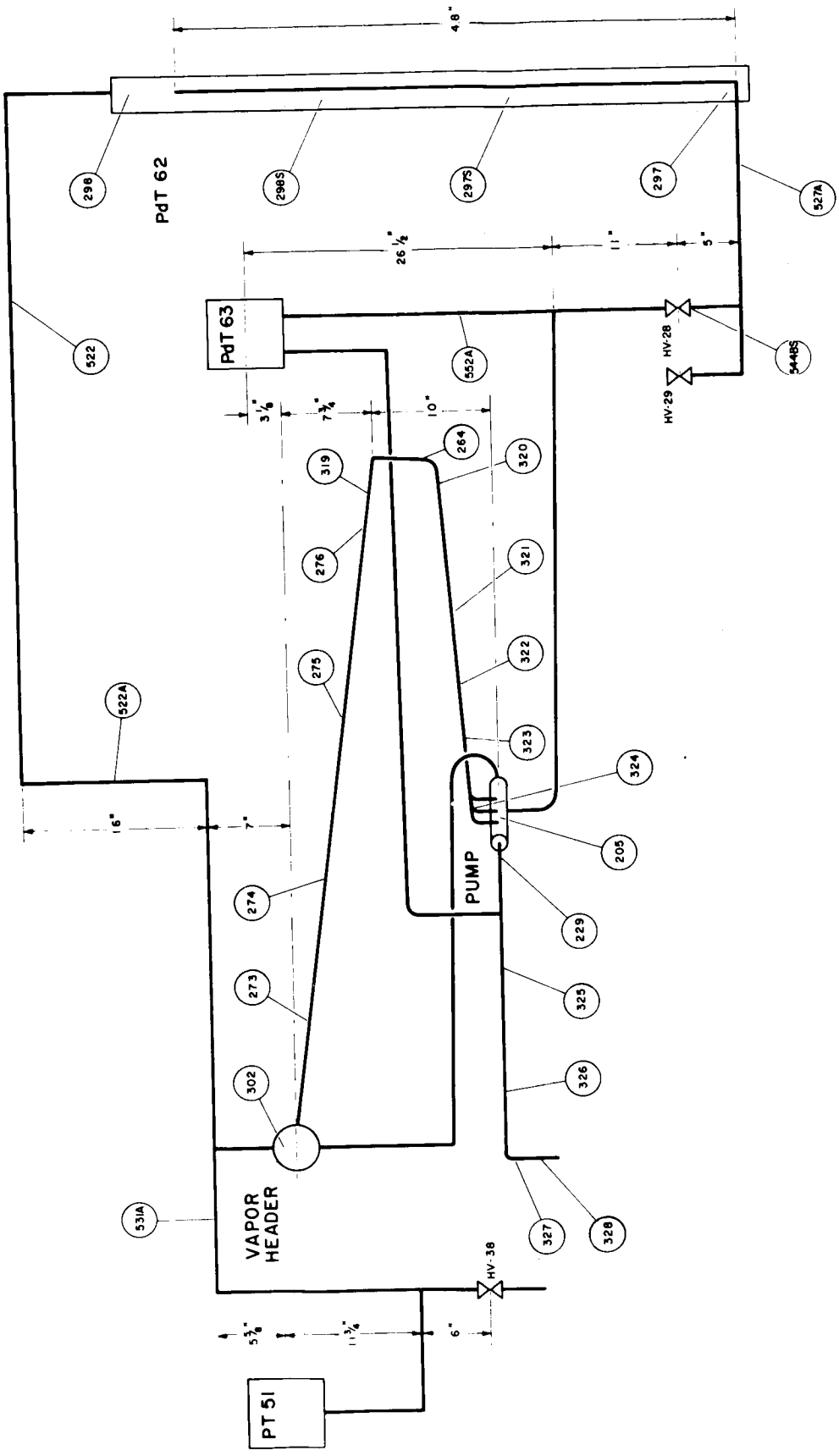


Fig. 2. Temperature and Pressure Instrumentation, IPS Radiator Circuit

central tapered header, as shown in Fig. 3. The radiator is enclosed within an air-cooled stainless-steel shroud, as shown in Fig. 7. Knowledge of the potassium flow distribution in these radiator tubes is important and can best be obtained from the temperature pattern on the tubes. The use of a large number of thermocouples, together with the readout equipment to obtain sufficient information to establish a radiator temperature pattern, would entail a substantial cost in equipment and installation. In an attempt to obtain temperature data more easily, viewing ports were installed in the heat sink so that the radiator could be observed during operation. Photographs were taken of the radiator, using 9000A° Polaroid infrared-sensitive film. Results to date indicate that substantial temperature differences existing within the radiator unit are easily seen, and that liquid collecting at the discharge end of the radiator is being detected by temperature measurement. Figure 4 shows a photograph taken during normal operation. There is no evidence of any substantial temperature change along or across the tubes. One would conclude that liquid has not accumulated in the tubes or headers. Figure 5 shows a similar view, but note now that the liquid headers are no longer visible, indicating that a substantial reduction in temperature has occurred along the tube. In this case a temperature drop of approximately 125°F has occurred across the indicated sharp film density change. Confirmation that this is indeed liquid inventory accumulating has been obtained from the liquid level indicators at other places in the system. Figure 6 is an example of system operation under very much off-design conditions which gave a highly nonuniform loading on the radiator tube banks.

We believe that with the use of reference thermocouples and careful control of film exposure times, a film density vs temperature gradient relationship can be established. This would permit improved quantitative results from the infrared technique.



Fig. 3. IPS Radiator

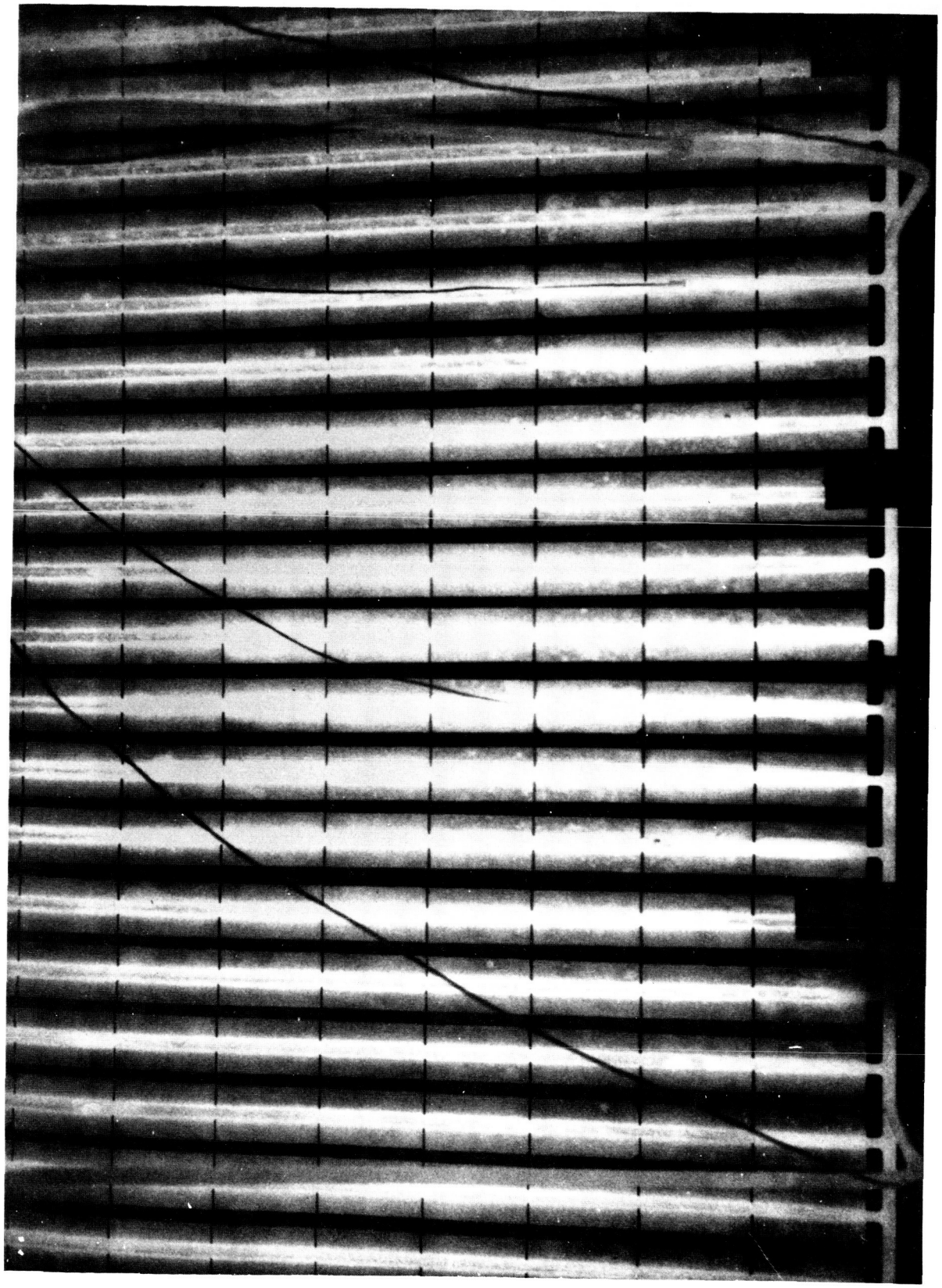


Fig. 4. Liquid Headers of Radiator Unit during Normal Operation

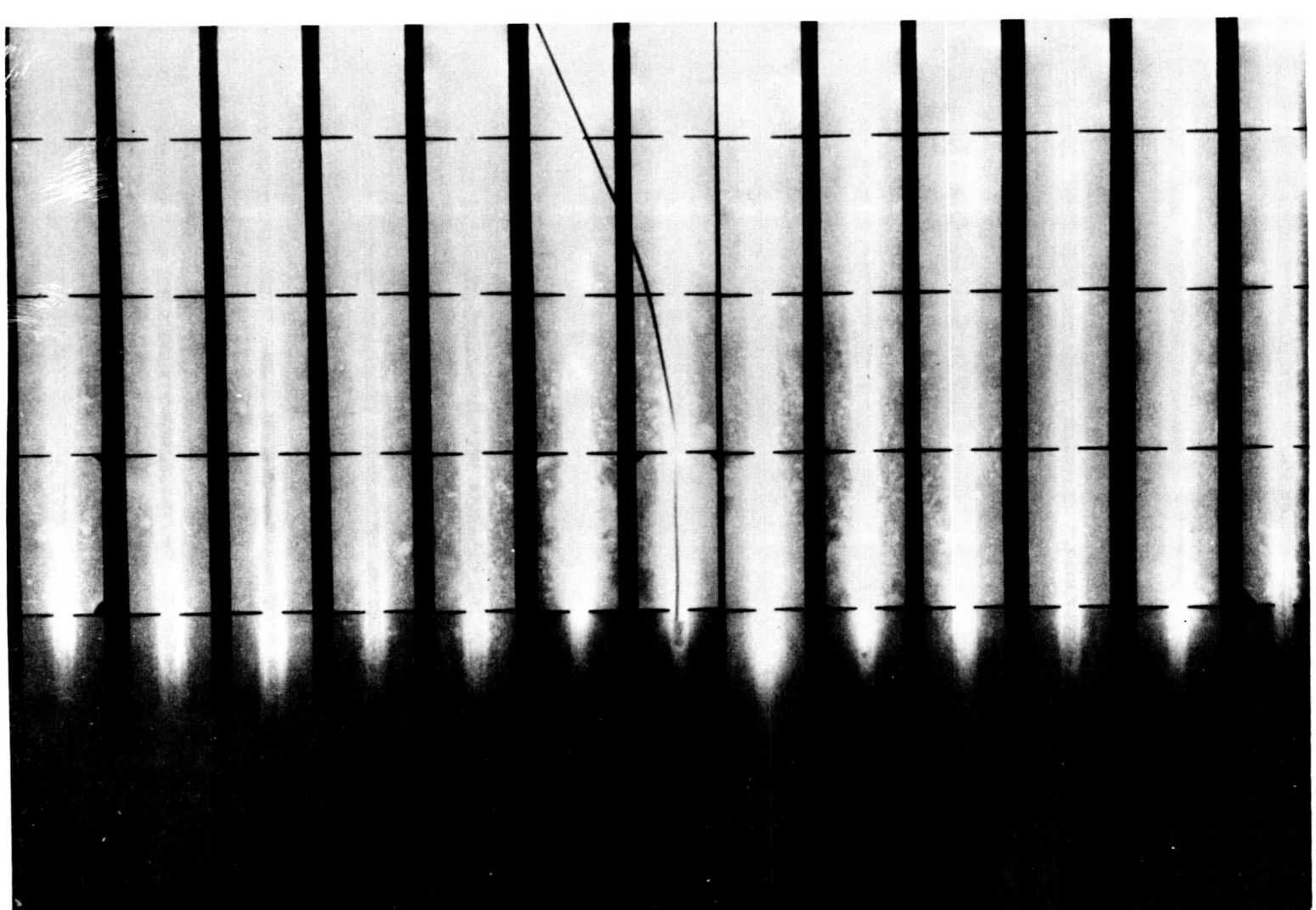


Fig. 5. IPS Radiator Showing Uniform Loading of Tubes



Fig. 6. Nonuniform Loading of IPS Radiator

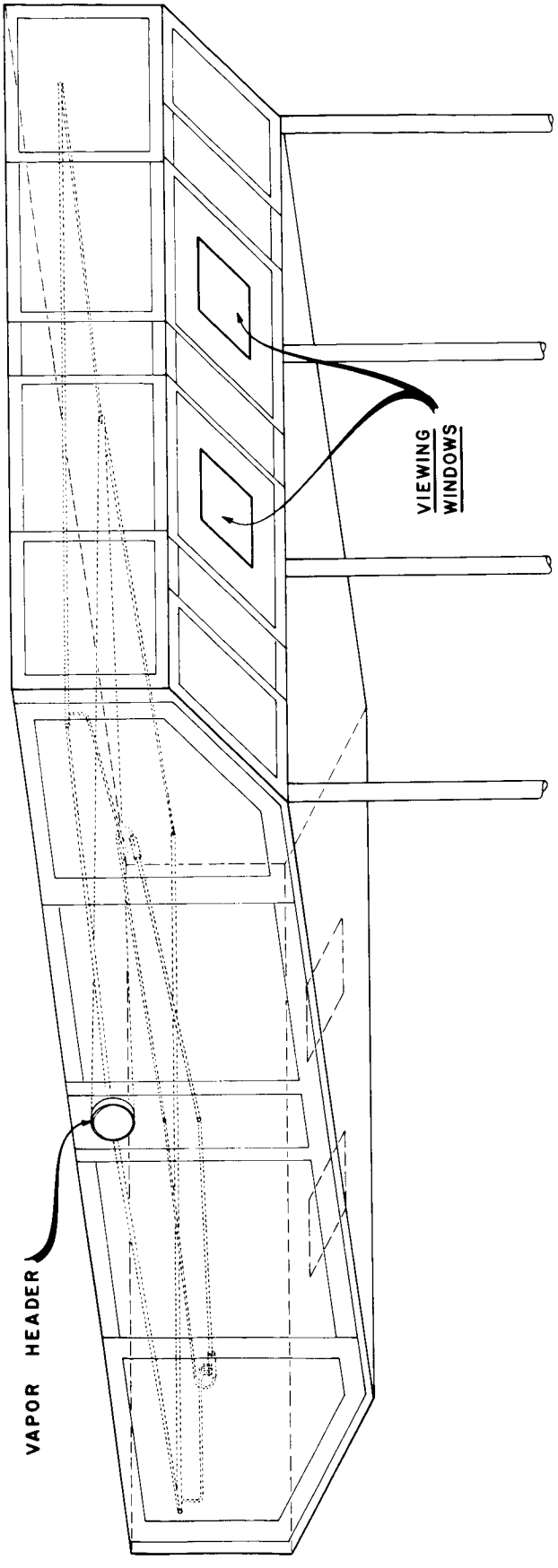


Fig. 7. Air-Cooled Shroud for Radiator

Part 2

H. J. Metz

Liquid Level

The level of liquid metal in vessels can be measured by five or more methods. Some are for single-point measurements, some are for continuous-level measurements, and some are for both. Some continuous level elements can compensate for temperature changes and others only with difficulty or not at all. The different possible level devices are compared below.

1. Resistance type - single point or continuous. Temperature compensated easily to give true level. Radiation resistant. No temperature limitations.[2, 3, 5, 6, 19, 21, 22, 24, 25, 26, 30, 31, 32, 33]

2. Inductive devices with or without floats - single point or continuous. Temperature compensation not inherent. Not easy to make radiation resistant. More temperature limited than the resistance type.[10, 11, 12, 13, 14, 16, 17, 18, 26, 29]

3. Differential pressure - continuous. Temperature compensation not easy. Radiation resistant only when seals are used to isolate device from system. Temperature limited depending on system pressures.[10, 11, 12, 13, 14, 18, 26]

4. Radiation adsorption - single point or continuous. Temperature compensation not easy. Almost useless in a reactor system. Probably not temperature limited.

5. Ultrasonic probe - single point only. The background of experience in high-temperature liquids is limited.[14, 15]

6. Others, not shown, are included to avoid the error of incomplete classification.[26]

Resistance-type level elements were put in the Intermediate Potassium System because we needed continuous level measurement and because the resistance elements are economical, small, accurate, and dependable compared to other available equipment.

All IPS level elements are made from lengths of stainless-steel tube which has been swaged over two magnesium-oxide-insulated stainless-steel wires. The ratio of resistance of the wire to the tube is designed to be about 100 to 1. One end of this tube is welded closed, and the assembly is inserted into the vessel from the bottom, as shown in Fig. 8. One internal wire is for current, and the other is for potential. The other current and potential wires connect to the end of the tube outside the vessel.

Accuracies of ±1% of full scale can be achieved on "I" tubes by calibration. Level element outputs can be calculated with an accuracy of ±5% of full scale if careful resistance measurements are made. The tube wall resistance is best obtained by measuring the resistance of a 10 to 20 ft length of swaged material from which the level element is to be made. The ohms per inch can then be used in the calculations.

A 48 inch, resistance-type liquid-metal manometer unit was tested. Figure 9 is a diagram of the experiment. The first excitation and readout system was direct current, as shown in Fig. 10, Type C. We knew that thermoelectric emf must be compensated for in a direct current system, and, as shown in Fig. 11, the problem was severe. Earlier tests had shown that the level element material generated no thermal emf between the wires and the tube wall. The emf was generated by a stainless-steel vs potassium thermocouple. Next, the excitation was changed to alternating current similar to Type A in Fig. 10. The results are shown in Fig. 12. (The approximate output was 22.3 mv ac at 10% and 3.6 mv at 90%.) There was no trouble from thermal emf. Finally, the measuring system of B, Fig. 10, was tested. The results are shown on Fig. 13.

Figure 14 shows the results from a test of a 3/16 in. OD level element in a different test facility which had a length of 12 inches in the vessel and a length of 6 inches outside the vessel. The increased

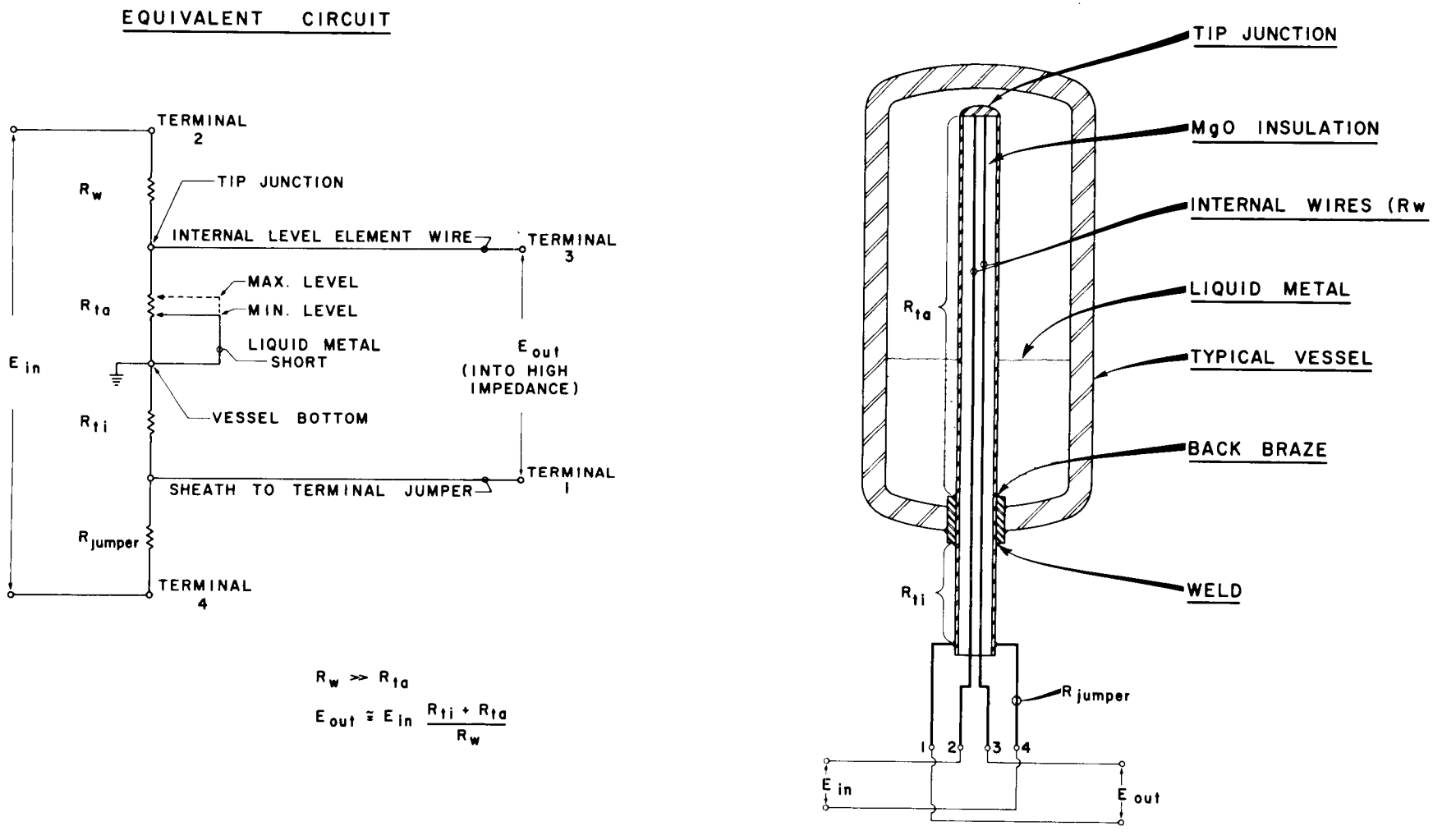


Fig. 8. "I-Tube" Liquid-Metal Level Element

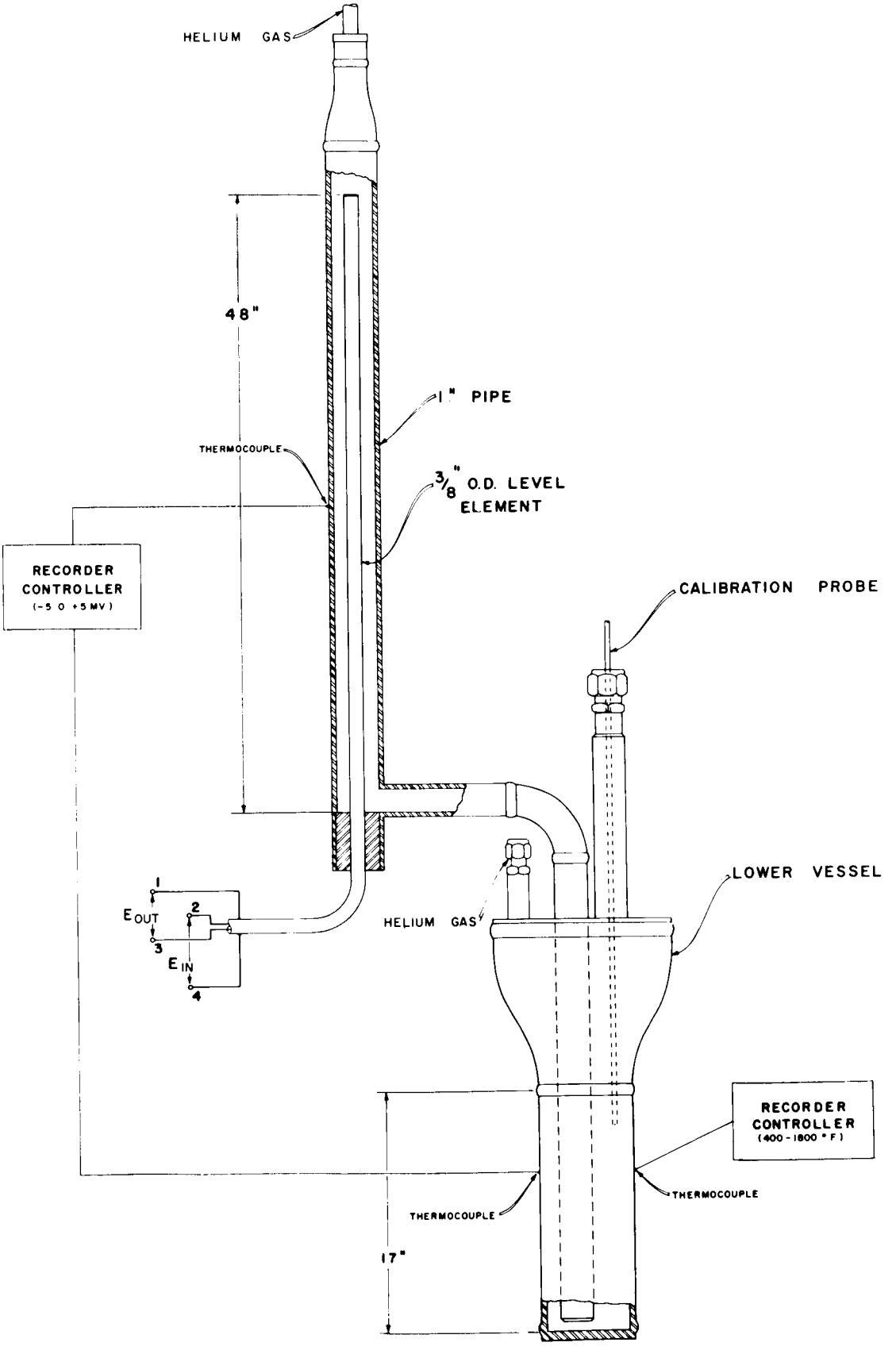


Fig. 9. Δp Manometer Level Element Test Facility

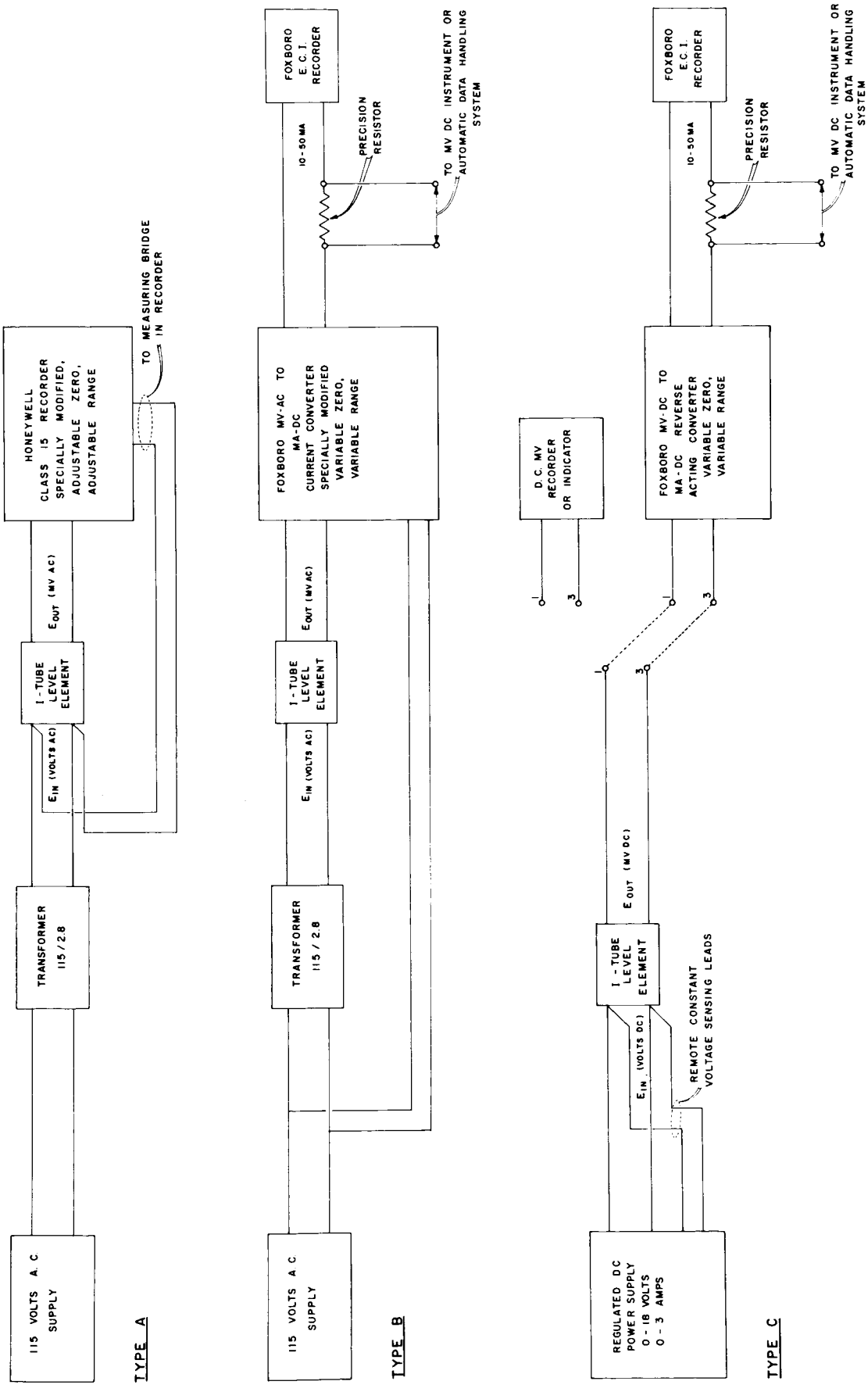


Fig. 10. Instrumentation Schematic Diagrams for "I-Tube" Liquid-Metal Level Elements

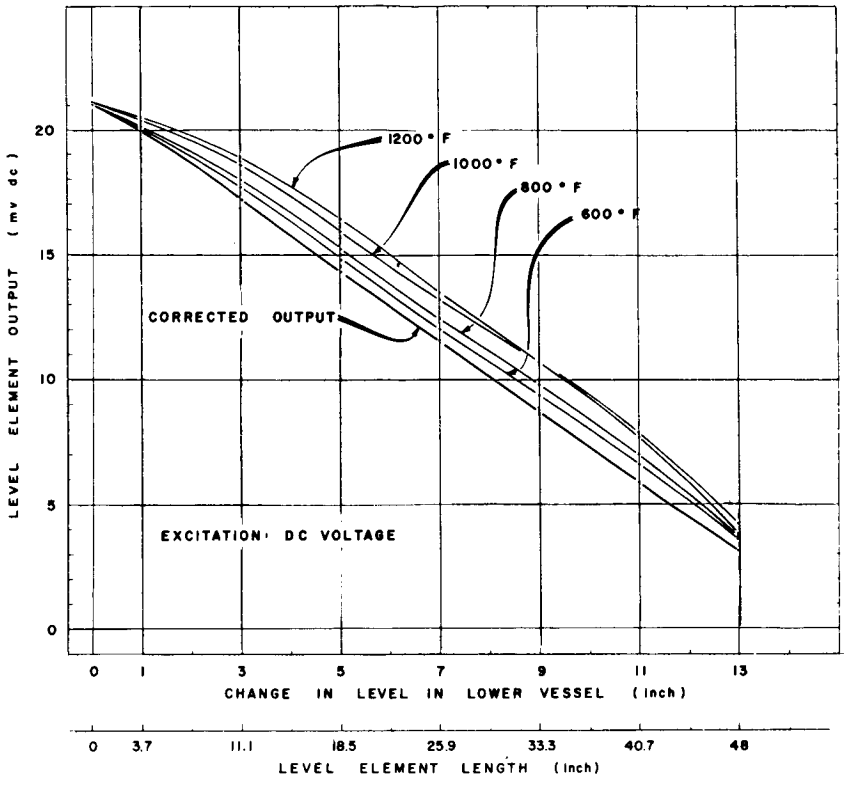


Fig. 11. Level Element Output for dc Excitation

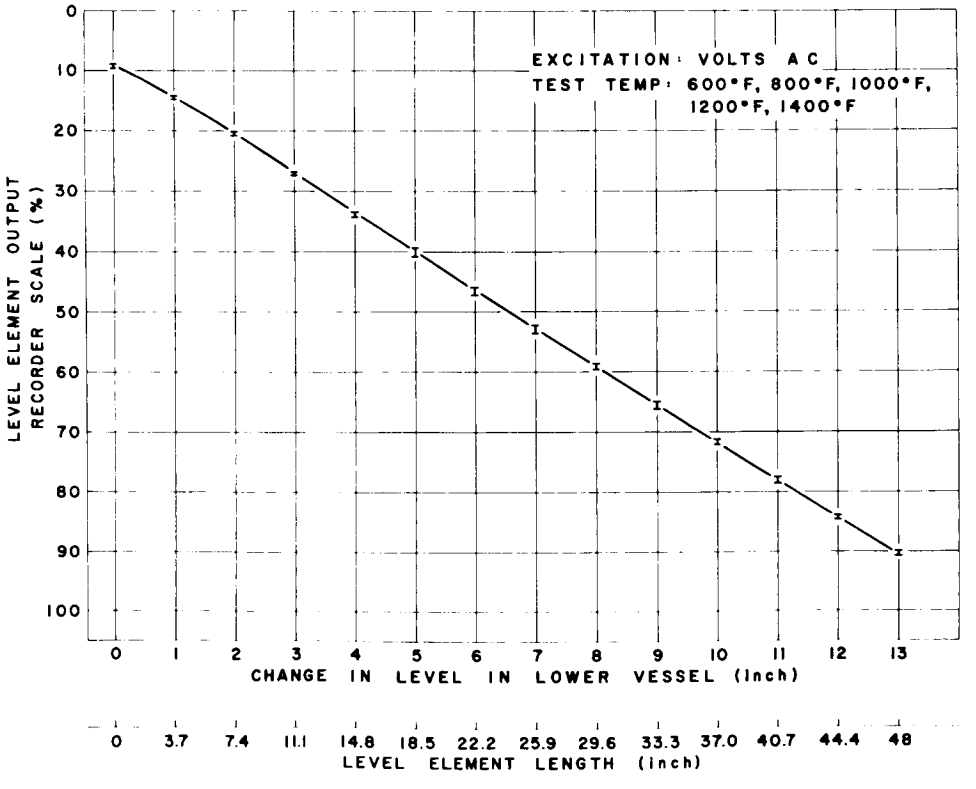


Fig. 12. Level Element Output for ac Excitation

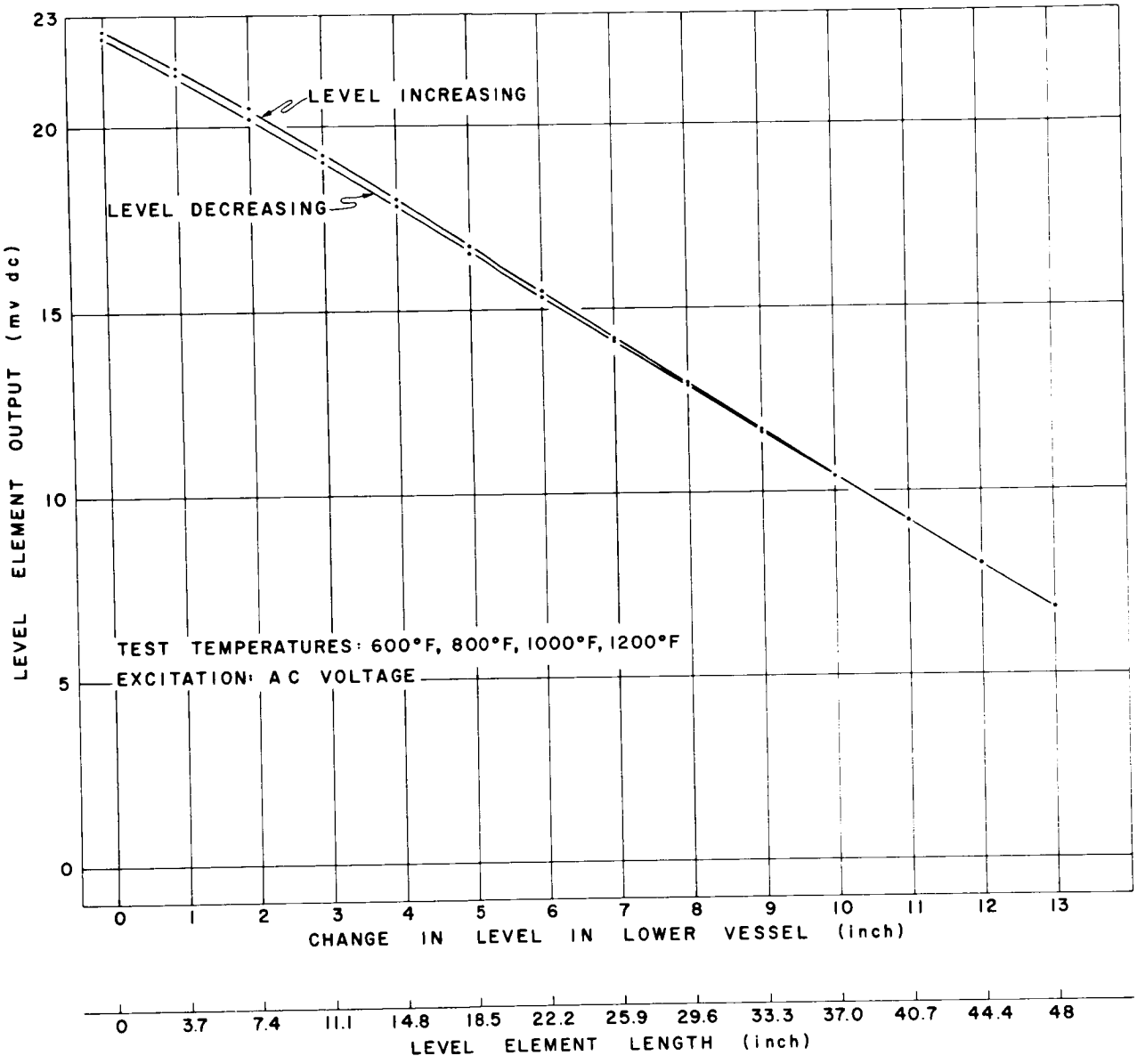


Fig. 13. Level Element Output for the ac to dc Converter

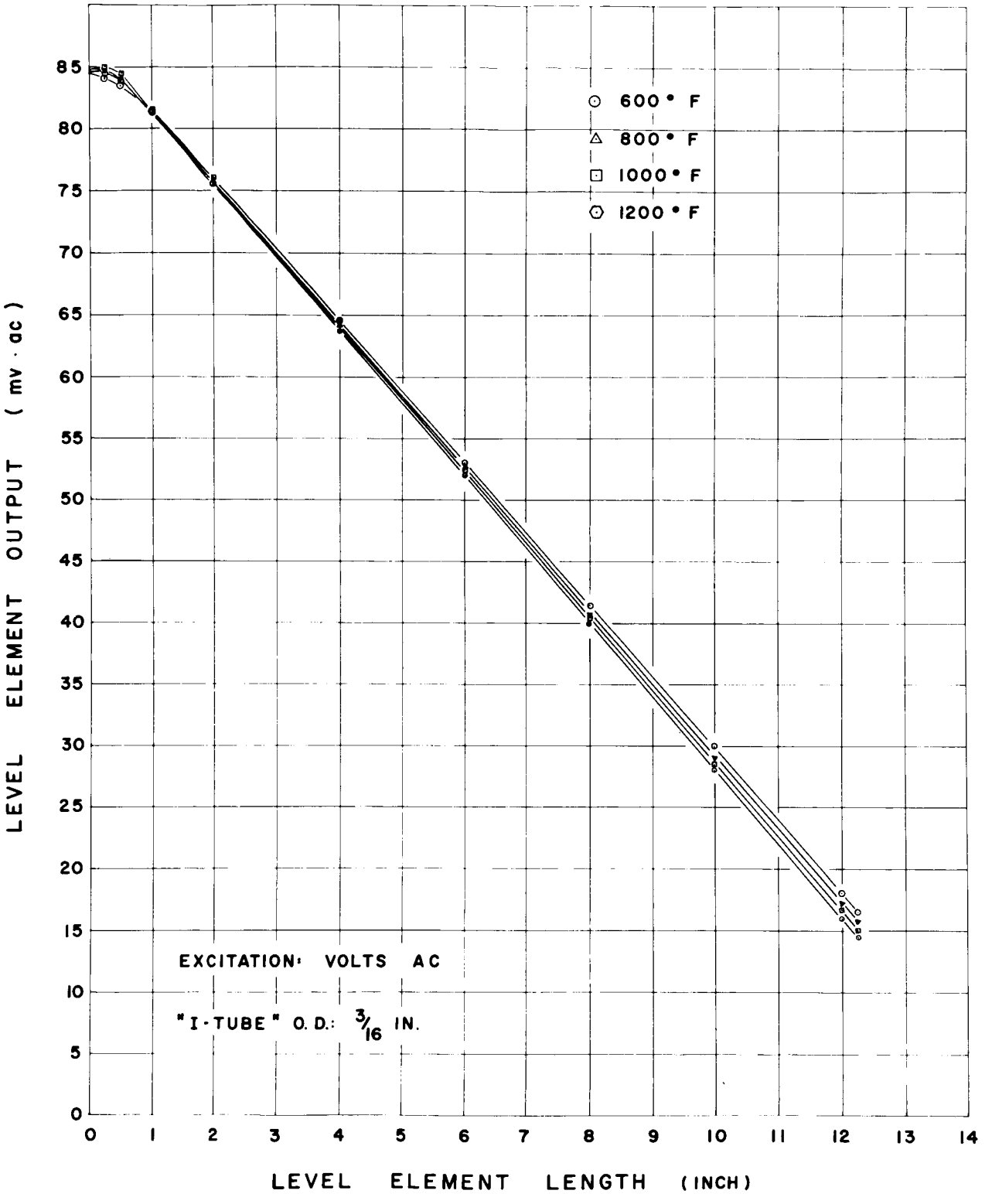


Fig. 14. Level Element Output for 3/16 in. Element

error with temperature was caused by the lower ratio of inside to outside length of the "I" tube in this test as compared to the "I" tube in the manometer test (2 to 1 compared to 8 to 1).

A variety of devices based on electromagnetic induction have been used to measure liquid level in high temperature systems. In a molten salt system, we are successfully using a float fastened to magnetically susceptible material. This is surrounded by a high-temperature linear-differential-transformer which is outside the fluid containment wall. Units of this type are in excellent condition after two years at a coil temperature of 1000 to 1250°F. The accumulated errors were about 1/4 in. in a 5 in. span. The transformer was made from machined lava forms on which were wound bare, pure nickel wires to make up the primary and the secondary coils. The transformer was canned in Inconel to protect it from atmospheric corrosion and from physical damage. The Armco iron core was canned in INOR-8 to protect it from corrosive molten salt.

When induction coils are moved along the side of a vessel that contains a conductive fluid such as liquid metal, the level can be detected. Such a coil can be moved by hand or by a servo-follower mechanism. A hand-movable type has been built at ORNL.

A continuous, inductive-type, liquid-metal level-detector is being developed, and a pilot model is being tested. The interesting feature of this detector is its ability to detect level through nonmagnetic material up to 1/2 in. thick plus thermal insulation 1/4 to 1/2 in. thick. The transducer consists of three superimposed, rectangular coils, each about 2 inches wide, and of a length determined by the desired range of the instrument. The middle coil is excited by an alternating current of appropriate frequency, and the two outer coils are connected to a detector circuit which has an output proportional to the level. The instrument will be tested on a liquid-metal level test experiment, and, based on the results of these tests, circuits will be developed for compensating for liquid-metal resistivity changes and detector output changes caused by temperature changes of the metal container.

An ultrasonic, single point, level probe has been used to detect the level of molten salt (Fig. 15). It is suitable for use in liquid metal systems. This probe was developed, with ORNL assistance, by Aeroprojects, Inc. under contract to the AEC. The instrument is basically an acoustic impedance device and consists of an electronic power oscillator, a magnetostrictive transducer, a standing wave ratio detector, a transmission rod, one or more force-insensitive feed-throughs, and a sensing plate. Energy is supplied to the transmission rod through the magnetostrictive transducer at a frequency that causes the rod to resonate. The force-insensitive feed-throughs allow the excitation rod to penetrate containment vessels without prohibitive loss of ultrasonic energy and without compromising the integrity of the containment envelope.

The presence or absence of fluid at the sensing plate is determined by detecting the decrease in the standing wave ratio present on the resonant transmission rod. A prototype of this instrument was tested for six months in the Molten Salt Level test rig and was found to be a dependable instrument, provided the excitation frequency remained constant. The instrument was successfully tested with the heated section at temperatures from 1000 to 1500°F. The tests will continue until any long term changes have been found and analyzed. To date, the only change found has been a shift in the frequency of maximum level sensitivity caused by a change in the resonant frequency of the rod.

Pressure

Differential pressure in the Intermediate Potassium System is measured by two methods.

1. All-welded, 400°F maximum, process-type, differential-pressure-transmitters.

2. Liquid metal manometers in which one or both sides of the manometer are connected to vapor-filled lines or vessels.[5]

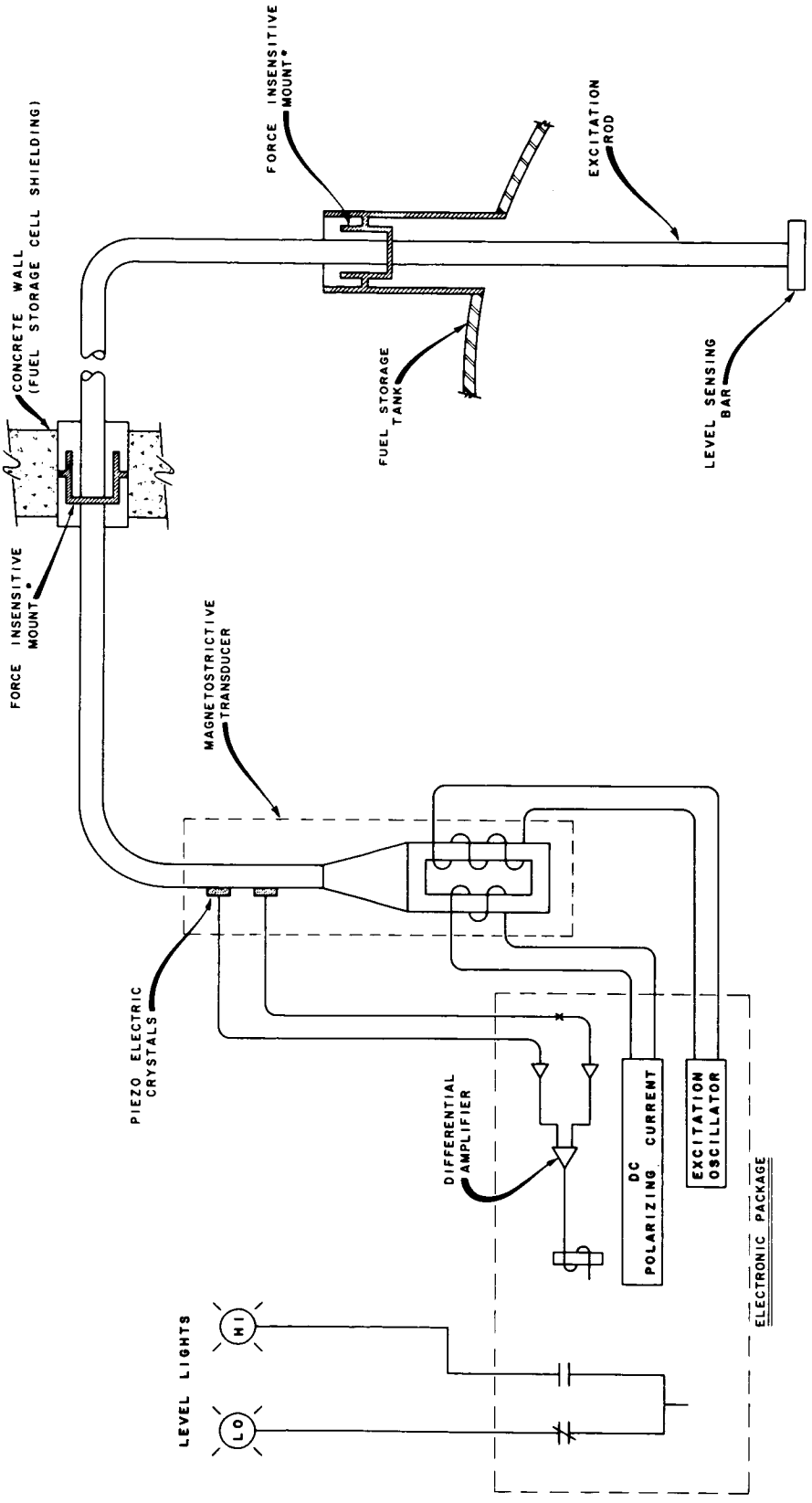


Fig. 15. MSRE Fuel Storage Tank Ultrasonic Level Indicator System

Differential pressure transmitters are needed which have the following characteristics.

1. Operate without error at system temperatures which may be 1500°F on one side and 400°F on the other side.

2. No liquid-filled seals which can cause change in fluid-head errors when the temperature changes; which limit the temperature at low absolute pressures; and which cause the instrument to respond slowly.

3. The part of the device exposed to the process fluid should be small, plain, and should drain completely dry when the system is drained. There should be no small clearances or small holes or pockets that can accumulate impurities and solid particles.

4. There should be a built-in method to heat the device and to hold the temperature at each process side or connection at the desired value automatically.

5. The span and zero should be adjustable at least as much as in equivalent industrial instruments.

6. Accuracy and stability should be equal to equivalent industrial instruments.

7. There should be built-in methods to check zero and to check span without making a connection into process lines or into the process sides of the instrument.

8. The design should be applicable at temperatures up to 2200°F when the instrument is made from appropriate materials.

9. The instrument should not be affected by electromagnetic interference nor should it be damaged by radiation. The presence or absence of gravity should have no effect.

Manometers - Differential Pressure

Several differential pressures anticipated in the IPS were too low to be measured accurately with differential pressure transmitters currently available for liquid metal use. A 48 inch liquid-metal

manometer was tested and found to be satisfactory. The elevations of lines, vessels, and manometers and the temperatures of the liquid metal in any nonhorizontal lines and in the manometer leg had to be known so that the true differential pressure could be calculated.

Gage Pressure Transmitters

The IPS gage-pressure transmitters are the filled-system-seal-type which use NaK for pressure transmission from the seal to the bourdon tube.[27] The Oak Ridge National Laboratory has used this type of pressure transmitter with good results. These transmitters may be permanently damaged if the temperature of the seal unit is more than 800°F when the process side of the seal is evacuated. Damage is caused by a permanent distortion of the seal diaphragm by the NaK vapor pressure. Transmitters must not be exposed to conditions under which the NaK vapor pressure causes more than about 1/3 psi differential pressure across the seal diaphragm.

We recommend that the seal unit always be installed above the bourdon tube. When the process is going from below-atmospheric pressure to above-atmospheric pressure or from full-vacuum to some higher below-atmospheric pressure, the head of fluid in the seal capillary may behave in the same way as the mercury in a barometer, if the seal is below the tube. Further gas bubbles may be evolved from the liquid in the bourdon tube, or gas pockets that are present may expand. When any of these things happen, there is a flow of NaK back and forth in the capillary tube between the seal and the bourdon tube. It may take hours for a transmitter system to reach equilibrium, and the pressure at the bourdon tube will be transmitted, not the pressure at the process side of the seal diaphragm.

We have wrapped metal-sheathed heating elements around the seals to keep them at desired temperatures. This may have caused unequal heating of different parts of the seals. Now we put the seals in aluminum-bronze castings which have cartridge heaters imbedded

in them. This assures even heating of the seal and allows accurate seal temperature measurement. This is important when process pressures reach a full vacuum. Seals can be installed directly above vapor or liquid lines because the seals can operate at the process temperature.

Bourdon tube pressure gages are in use to measure liquid metal pressure in some of our other systems. The bourdon tube and socket are all-welded, stainless-steel, with a welding connection from the socket to the process system. The gages and tubes to the process equipment are installed in a constant temperature oven which keeps the liquid metal in the gages and tubes from freezing. The gages can operate up to about 250°F. The gages and tubes serve as cold traps when there is much oxide in the liquid metal. The gages must be calibrated at operating temperature.

Microphones

A qualitative and useful instrument that we have employed on our liquid metal systems is a microphone. Microphones have been placed on the boiler, on system pumps, and on the turbopump unit. On the boiler we find them quite useful in determining whether stable boiling exists. On the turbopump they indicate when cavitation occurs in the turbopump. Wide turbine speed oscillations can be heard. These microphones must operate at ambient temperatures to 200°F in the presence of severe 60 cycle and RF noise. Commercial dynamic, crystal, or ceramic microphones were tried and found to be unsatisfactory. Crystal or ceramic microphones could not stand the temperature cycling, and dynamic microphones had low outputs and picked up excessive electrical noise. Carbon microphones appeared to offer a solution to both the noise and the temperature problems.

For our applications, commercial carbon microphone packaging left much to be desired. They were large, and in most cases, they

were not suited to operation at 200°F. A microphone package capable of operation at 200°F was obtained by packaging small carbon microphone buttons from World War II throat microphones, as shown in Fig. 16. A standoff from the vessel was used to keep the microphone below 200°F. The upper temperature limit of the microphone has not been determined. The block diagram of an entire system is also shown on Fig. 16. Because of the low current drain of the carbon button, small, noise-free, mercury-batteries were used to supply power.

RPM

Measurement of the speed of totally-enclosed, potassium-vapor-driven turbines and direct-connected potassium pumps is difficult. Ambient noise, both acoustical and electrical, space limitations, and high temperatures contribute to the problem. For some small ORNL built turbopumps, a series of magnetic type detectors were built, as shown in Fig. 17.[3,5,6,19] The test of a prototype circular-magnetic-path speed pickup has shown that good results can be obtained. This is shown in Fig. 18. The last two designs will be field tested. The speed of the IPS turbopump is being measured with an Electro Products Model 721434A speed transducer which has a design life of 1000 hours at 800°F. The transducer is air cooled to hold it at about 700°F. It is deteriorating at this temperature.

It has not been possible to use vibration or noise to infer turbine speed. The presence of electric heaters and different kinds of electromagnetic liquid-metal pumps has made large signals necessary in order to get a tolerable signal-to-noise ratio. When signal levels were low, high-common-mode-rejection amplifiers and high-pass and low-pass filters were successfully used.

Because the signal-to-noise ratio of magnetic speed pickups was poor, an experiment was performed to find out if pulses of radiation from a source imbedded in a rotating part could be used to measure speed. The experiment indicated that this method is feasible.

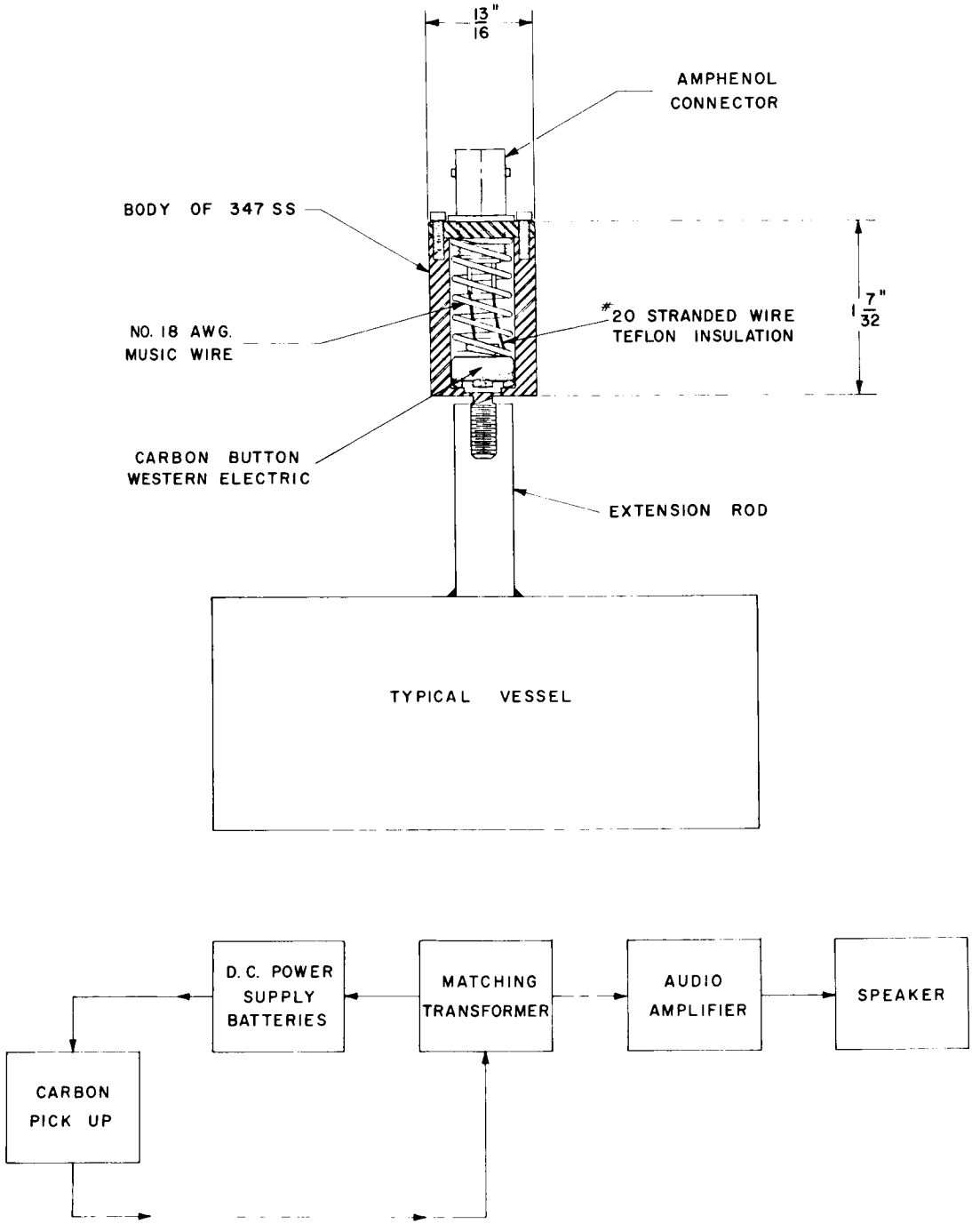


Fig. 16. Microphone System

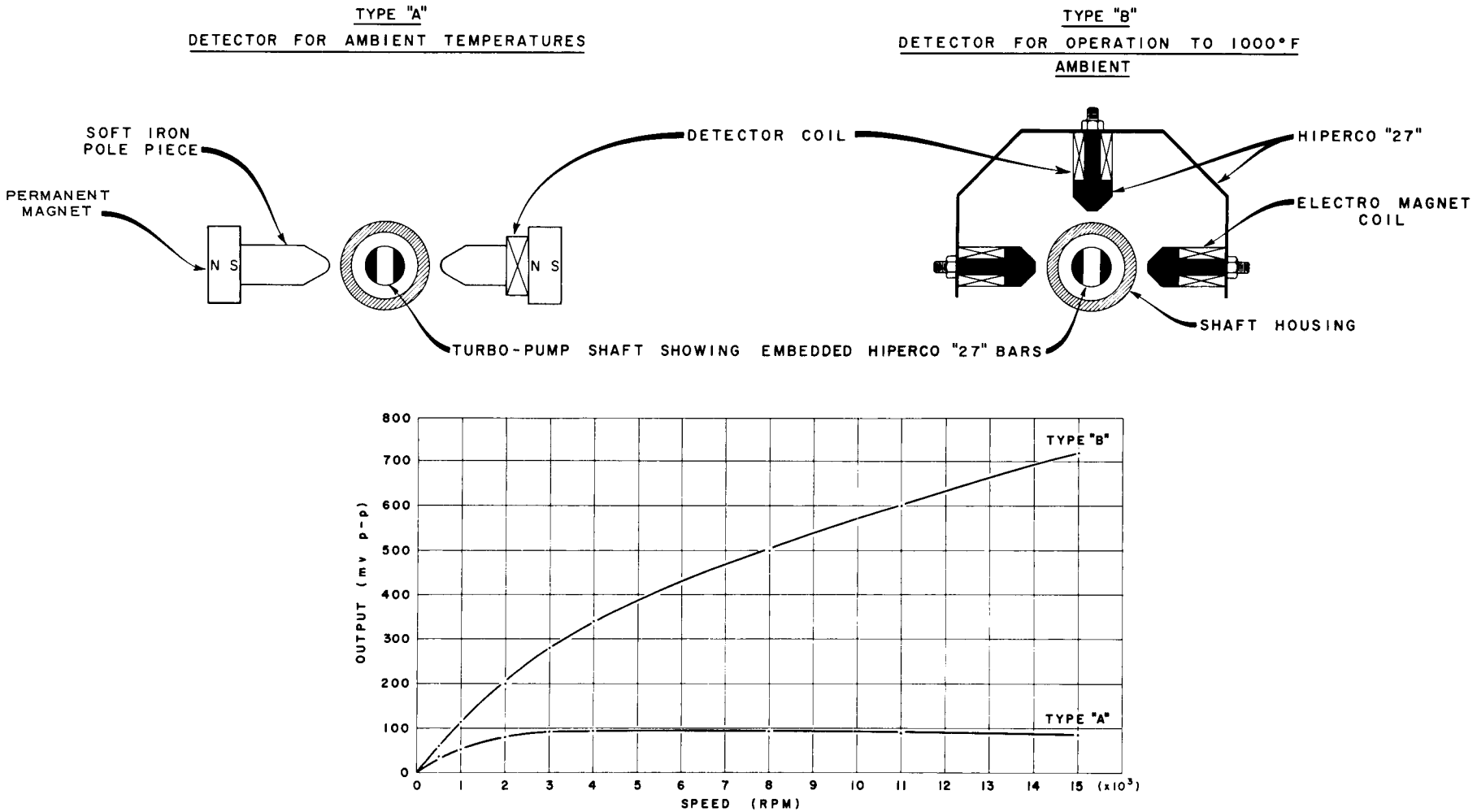


Fig. 17. Speed Detector for a Totally Enclosed Turbine

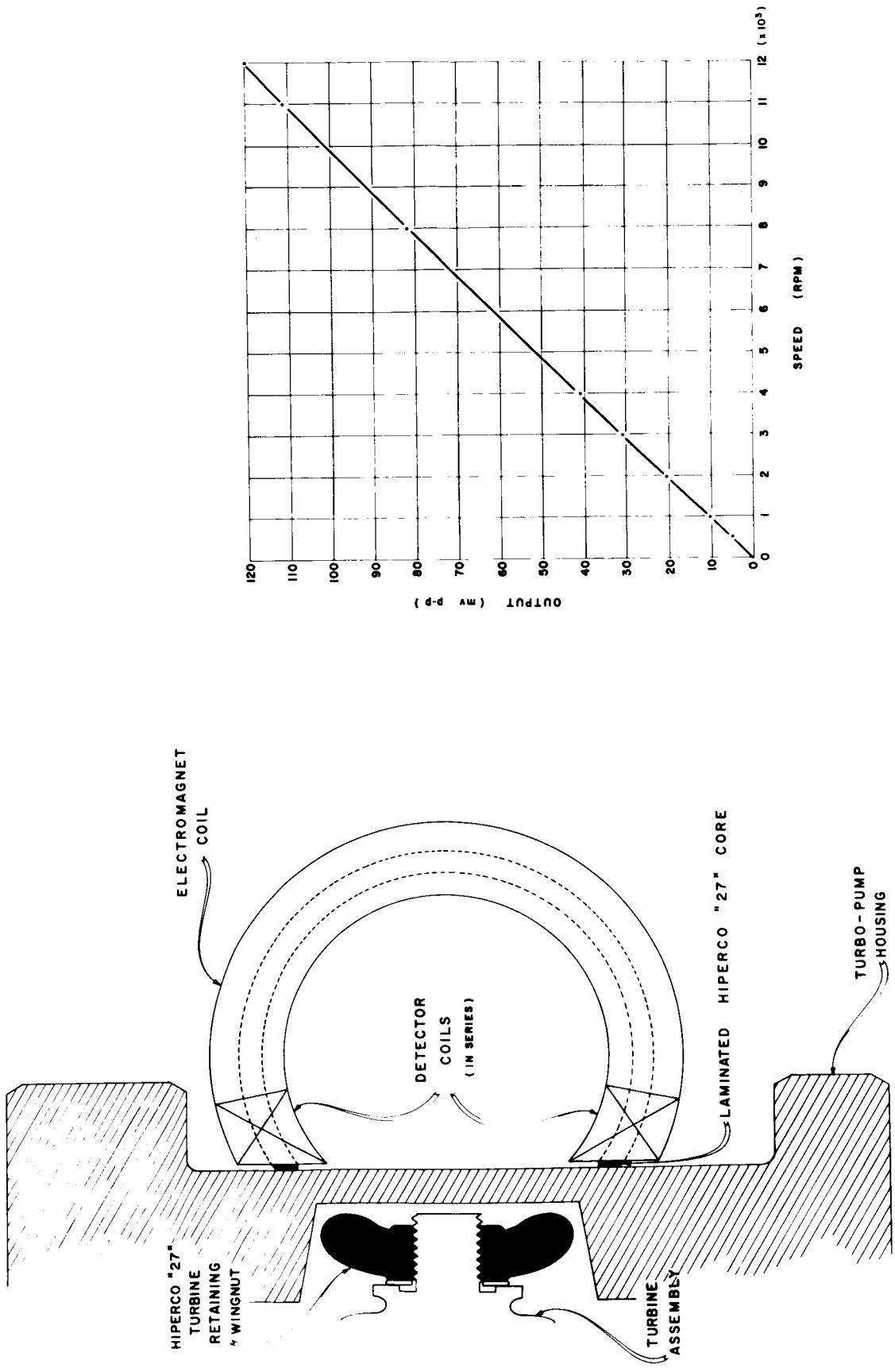


Fig. 18. Detector for a Ford Aeroneutronic Turbopump

Oxygen Analysis in Liquid Metal

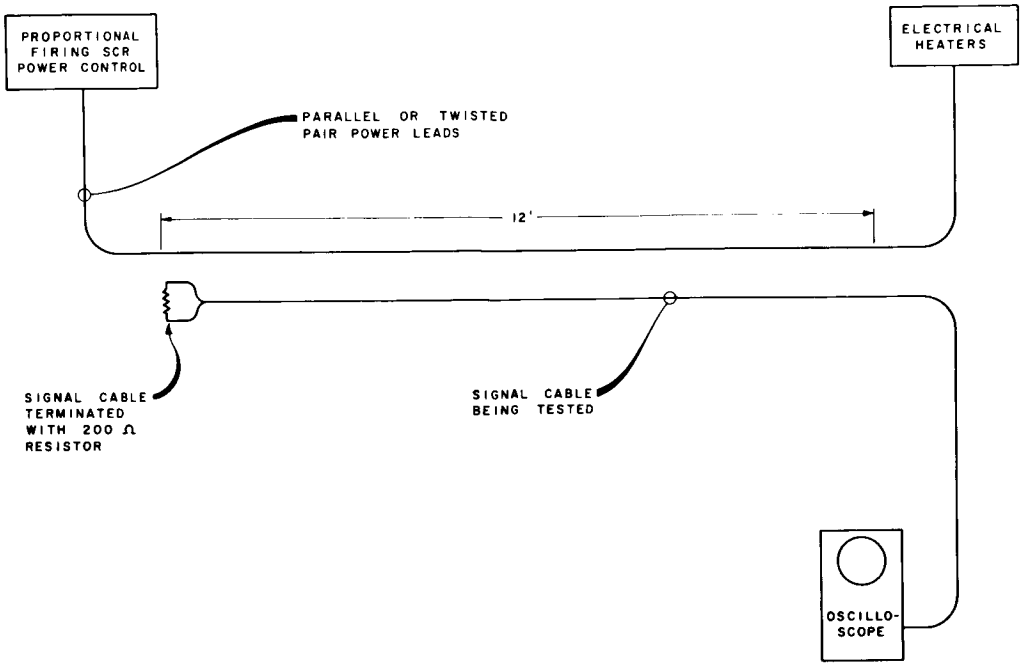
The MPRE program is obtaining some United Nuclear Corporation oxygen meters which will be tested and used. At this time, these devices, as well as a Blake meter, are being tested at Los Alamos.

EMI Noise[19]

The IPS was the first large Reactor Division experiment that was designed to have relatively little electromagnetic interference generated by a solid-state power-control system and as little noise as possible picked up by instrument signal leads. Preceding experiments taught us that electromagnetic interference was a wicked enemy of magnetic speed measurement, of high-speed scanning by monitoring systems, of the recording of accurate data with high-speed recording systems, and of the recording of accurate data by an area-wide data system.

Power wiring and cables were put in wireways separate from signal wires. Pairs of power wires at the experiment were twisted to reduce electromagnetic radiation. All thermocouple compensating extension wires were twisted pairs which were enclosed in two separate film-type electrostatic shields. The two thermocouple wires were of different diameters so that the resistances per foot of each wire were about equal. This made it more difficult for common-mode noise to become normal-mode, erroneous signals. All instrument signal leads other than thermocouples are shielded, twisted pairs.

Figure 19 shows a diagram of an experiment that was done to find out how much noise was picked up by different kinds of wire; Fig. 19 also shows a table of the results from this experiment.



CABLE TYPE	EMF MEASUREMENTS (VOLT p-p) COMMON MODE				EMF MEASUREMENTS (mv p-p) NORMAL MODE			
	POWER LEVEL (kw)				POWER LEVEL (kw)			
	12.8		50		12.8		50	
	POWER LEADS		POWER LEADS		POWER LEADS		POWER LEADS	
	PARALLEL	TWISTED	PARALLEL	TWISTED	PARALLEL	TWISTED	PARALLEL	TWISTED
1. CHROMEL/ALUMEL, NO. 17 AWG STRANDED, POLYVINYL, UNSHIELDED.	80	78	118	110	400	400	600	500
2. SAME AS NO. 1 WITH ALUMINUM-BACKED MYLAR SHIELD. SHIELD GROUNDED.	26	23	38	33	80	80	100	122
3. CHROMEL (NO. 20 AWG)/ALUMEL (NO. 24 AWG) EQUAL RESISTANCE WIRES, POLYVINYL, TWISTED AND DOUBLE SHIELDED. SHIELDS NOT GROUNDED.	68	31	100	168	3	3	5	4
4. SAME AS NO. 3 WITH BOTH SHIELDS GROUNDED.	0.18	0.13	0.16	0.19	2.8	2.7	4.6	3.6
5. COPPER, NO. 18 AWG, TWISTED AND UNSHIELDED.	38	70	112	96	400	350	600	500
6. COPPER, NO. 18 AWG, TWISTED AND SHIELDED. SHIELD GROUNDED. (MICROPHONE CABLE)	0.4	0.31	0.38	0.31	4	1.2	4	2.2
7. COPPER, NO. 22 AWG, TWISTED AND SHIELDED. SHIELD GROUNDED. (SPECIAL LOW LEVEL SIGNAL CABLE S10-362-)	0.25	0.17	0.21	0.18	1.4	1.5	2.3	2.6
8. COPPER, NO. 18 AWG, TWISTED AND SHIELDED. SHIELD GROUNDED (RG-108).	0.36	0.31	0.32	0.31	2.4	3	3	4.4

Fig. 19. Noise Picked Up by Wires

REFERENCES

1. SPP Semiann. Progr. Rept. Dec. 31, 1962, ORNL 3420.
2. SPP Semiann. Progr. Rept. June 30, 1963, ORNL 3489.
3. SPS Semiann. Progr. Rept. Dec. 31, 1963, ORNL 3571.
4. MPRE Quart. Progr. Rept. Sept. 30, 1963, ORNL 3534.
5. MPRE Quart. Progr. Rept. Mar. 31, 1964, ORNL 3641.
6. SPP Semiann. Progr. Rept. June 30, 1964, ORNL 3683.
7. MPRE Quart. Progr. Rept. Sept. 30, 1964, ORNL 3748.
8. MPRE Quart. Progr. Rept. Dec. 31, 1964, ORNL 3774.
9. MPRE Quart. Progr. Rept. Mar. 31, 1965, ORNL 3818.
10. MSRE Semiann. Progr. Rept. Jan. 1963, ORNL 3419.
11. MSRE Semiann. Progr. Rept. July 1963, ORNL 3529.
12. MSRE Semiann. Progr. Rept. Jan. 1964, ORNL 3626.
13. MSRE Semiann. Progr. Rept. July 1964, ORNL 3708.
14. MSRE Semiann. Progr. Rept. Feb. 1965, ORNL 3812.
15. MSRE Semiann. Progr. Rept., ORNL 3872 (not issued).
16. Instrumentation and Controls Div. Ann. Progr. Rept. Sept. 1, 1962, ORNL 3378.
17. Instrumentation and Controls Div. Ann. Progr. Rept. Sept. 1, 1963, ORNL 3578.
18. Instrumentation and Controls Div. Ann. Progr. Rept. Sept. 1, 1964, ORNL 3782.
19. Instrumentation and Controls Div. Ann. Progr. Rept. Sept. 1, 1965, ORNL 3875.
20. W. R. Miller, High Temperature Pressure Transmitter Evaluation, ORNL 2483 (May 16, 1958).

21. R. G. Affel, G. H. Burger, and R. E. Pidgeon, Level Transducers for Liquid Metals, ORNL 2792 (April 12, 1960).

22. Salvadore J. Fanciullo, Development of Liquid Metal Level Probes, PWAC 423, N64-19283 (April 27, 1964).

23. R. G. Affel, G. H. Burger, and C. L. Pearce, Calibration and Testing of 2- and 3-1/2-inch Magnetic Flowmeters for High Temperature, ORNL 2793 (March 21, 1960).

24. H. Robinson and C. R. Droms, Liquid Metal Level Instrument, General Electric Co., R52GL85 (March 18, 1952).

25. C. R. Droms, Second Report on Liquid Metal Level Instrument, General Electric Co., R55GL1 (Dec. 21, 1954).

26. C. B. Jackson, Editor, Liquid-Metals Handbook, Sodium-NaK Supplement, TID 5277 (June 1, 1955).

27. Taylor Instrument Companies Bulletin 98432 (P).

28. Taylor Instrument Companies Specification Sheet 98432-S1.

29. M. W. Saba, Private Communication, Airesearch Mfg. Co., PSMWS-362-0723 (June 23, 1964).

30. N. H. Briggs, R. F. Hyland, and G. W. Greene, "I" Tube Liquid-Metal Level Elements (to be published).

31. C. R. Droms, Supplement to Report No. R55GL1 - Second Report on Liquid Metal Level Equipment Tests on Primary Detector, General Electric Co., Cat. No. 24B619G1 (Feb. 1, 1955).

32. R. F. Hyland, "I" Tube Liquid Metal Level Elements, Part I, Oak Ridge Recorder, Vol. 10, No. 9 (May 1965).

33. R. F. Hyland, "I" Tube Liquid Metal Level Elements, Part II, Oak Ridge Recorder, Vol. 10, No. 10 (June 1965).

N66 31689

IMPURITY AND LIQUID LEVEL MEASUREMENTS FOR THE FARET LOOP*

by

A. G. Hosler**

and

F. A. Smith
Argonne National Laboratory
Argonne, Illinois

(Paper presented by A. G. Hosler)

*This work performed under the auspices of the USAEC

**From the USAEC Chicago Operations Office

Impurity and Liquid Level Measurements for the FARET Loop

Introduction

The FARET Fuel Assembly Flow Test Loop will test full-length, nineteen element, FARET fuel assemblies. It is a 304 stainless steel isothermal loop with sodium temperatures up to 1200°F and bulk sodium flow rates of up to 800 gpm. The current sodium impurity levels have been measured and are reported in this paper. These will serve as initial conditions for future determinations of changes in the impurities of the loop sodium. Sodium impurities will be measured by plugging valves, spectrochemical analyses, amalgamation with mercury, a Blake meter, and possibly the United Nuclear Corporation oxide meter.

The test loop will also include a self-seeking level probe. The use of a probe of this type for sodium service is believed to be unique. The probe has been designed and constructed by the Electronics Division at ANL for use by the Reactor Engineering Division on the FARET loop.

Level Instrument

Figure 1 shows the installation of the instrument on the sodium storage tank used with the FARET loop. The electronic circuit uses vacuum tubes throughout. An all solid-state circuit could be used to achieve a considerably more compact system.

The level instrument uses a coil operating in a thimble as one arm of a bridge circuit. The impedance of the coil is determined, in part, by the electrical resistance of the material surrounding the thimble. The coil acts as the primary of a transformer, and the thimble and material surrounding the thimble acts as the secondary. The coil induces eddy currents in the thimble and in any electrical conducting material

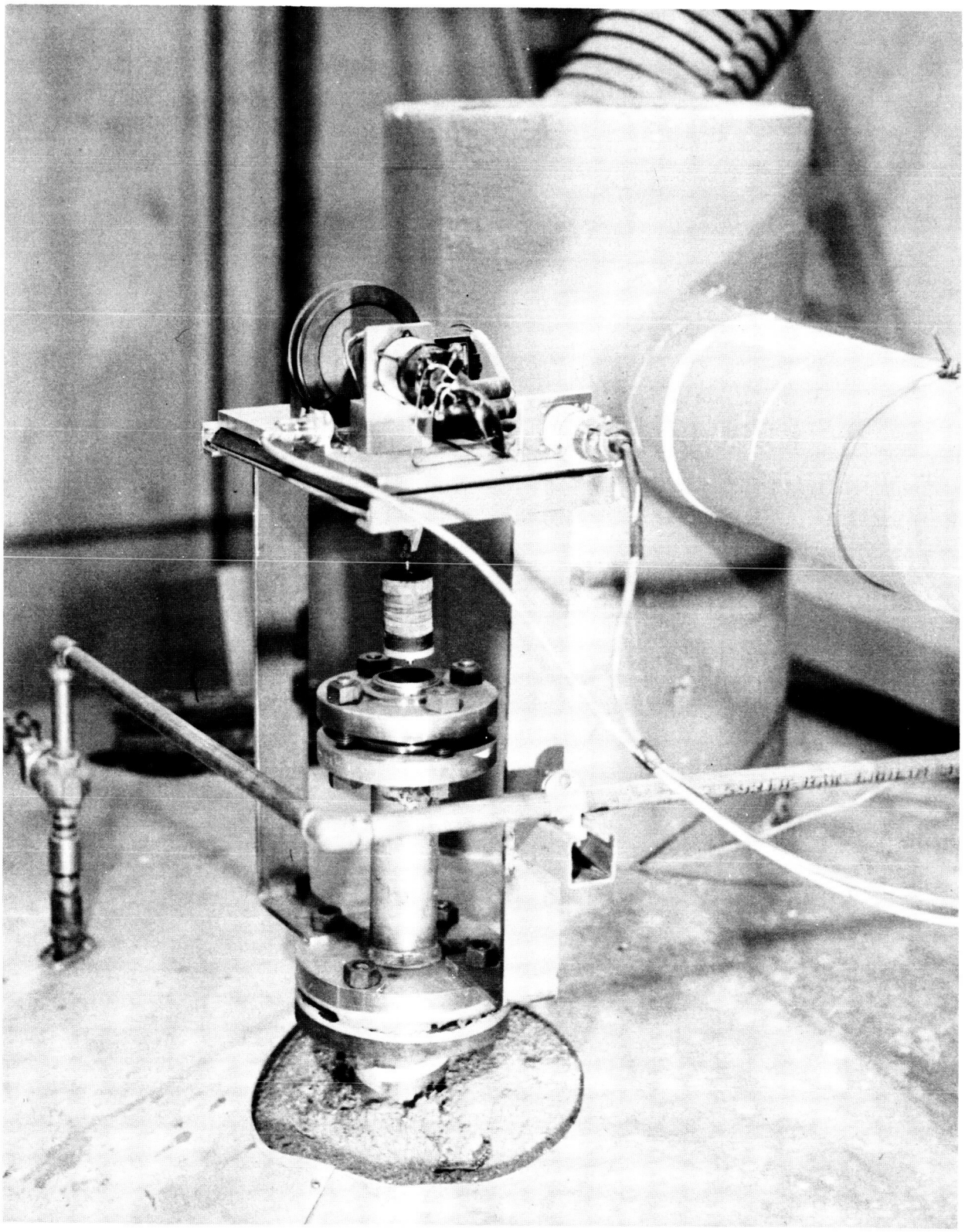


Fig. 1. Level Probe Installation

surrounding the thimble. The magnitude of the currents increases as the material's electrical resistance decreases. Also, the eddy currents are induced in a direction such that their resulting flux is opposite to that of the coil. It follows that the eddy currents reduce the flux linking the coil turns. Because the inductance of the coil depends upon the magnitude of the magnetic flux linking its turns, the inductance of the coil will decrease as the resistance of the material surrounding the thimble increases.

The bridge circuit is adjusted so that it is balanced with the probe positioned at the sodium-cover gas interface. After the bridge is balanced, a change in the sodium level will cause the bridge to become unbalanced. The signal resulting from the unbalance is used to effect the driving of the probe in a direction to reobtain balance.

Figures 2 and 3 are block and schematic diagrams of the electronic circuit used with the level detector. A 100 kc crystal-controlled tuned-grid tuned-plate oscillator is used to supply a signal to the voltage amplifier. The output of the amplifier is applied to a Maxwell bridge. The 100 ohm potentiometer is used to obtain balance with respect to the magnitude of the signal, and the 25 ohm potentiometer is used to correct for phase shift. A signal proportional to the unbalance of the bridge circuit is used as the input signal to a second voltage amplifier, the output of which is applied to a transformer having a center-tapped secondary.

The signal across the primary of the transformer is proportional to the unbalance of the bridge and is 0^{o} or 180^{o} out of phase with the oscillator signal, the phase displacement being dependent upon the position of the probe relative to the sodium surface, i.e., whether the probe is above or below the sodium level. To obtain a d-c signal

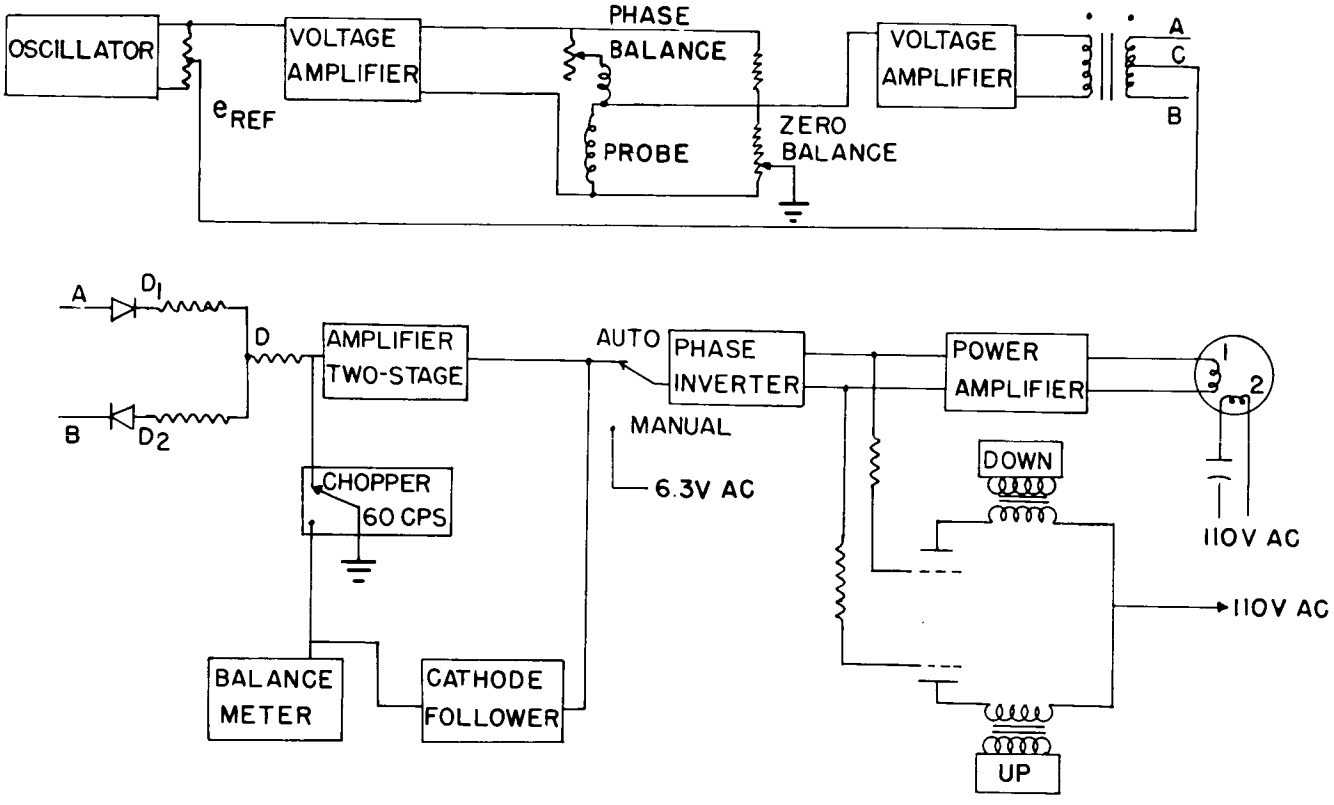


Fig. 2. Self Seeking Liquid Metal Level Probe

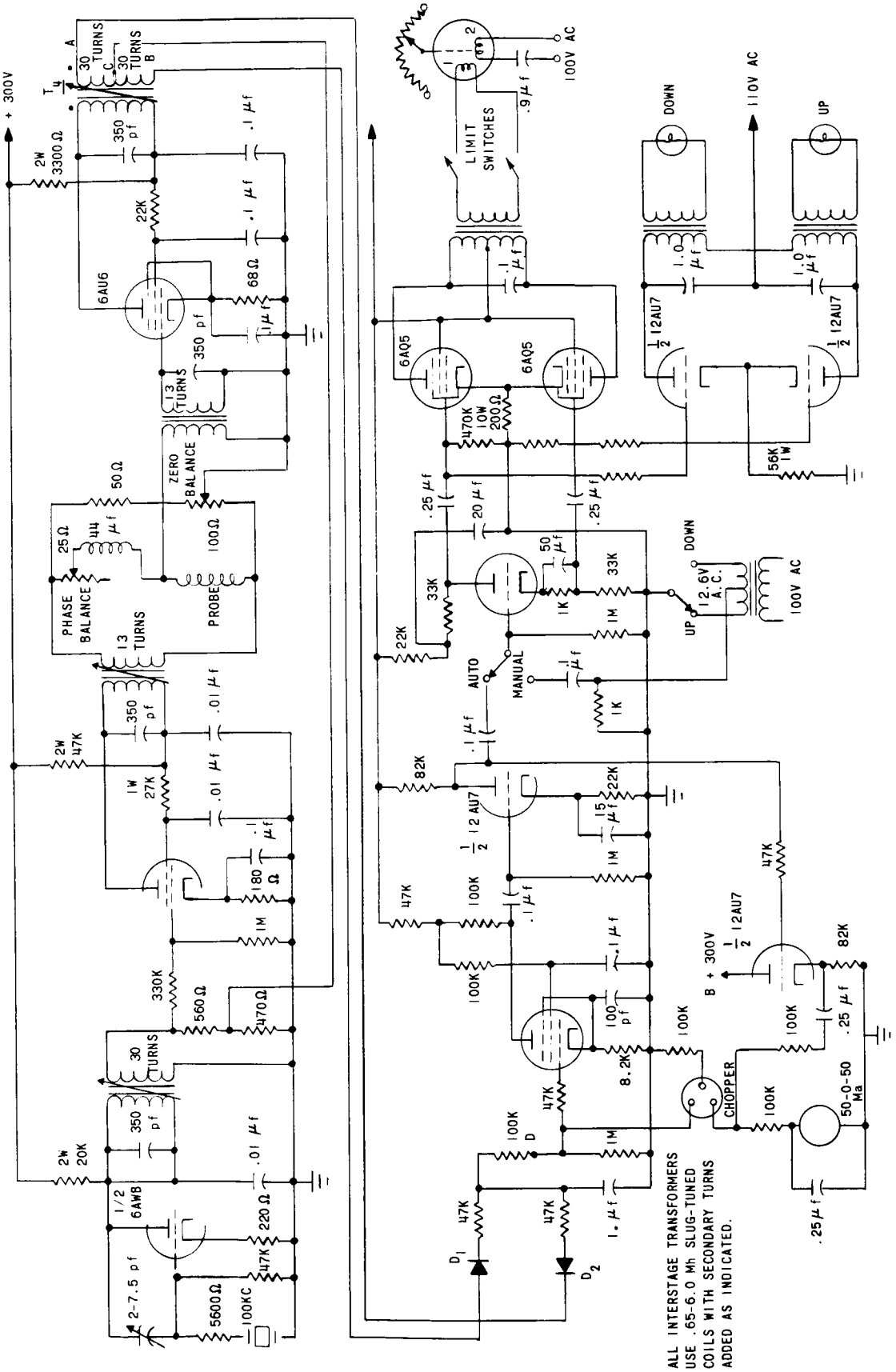


Fig. 3. Self Seeking Liquid Metal Level Probe

whose sign will be dependent upon the probe position relative to the sodium level, the center tapped transformer and R-C circuit are used. With the transformer wound as indicated and with the reference and error signal in phase, a positive signal equal to $e_{ref} + e_{CA}$ will be passed by D_2, during the positive portion of the cycle and a negative signal equal to $e_{ref} + e_{CB}$ (e_{ref} will now be negative with respect to ground) will be passed by D_2 during the negative portion of the cycle. With e_{ref} greater than e_{CA} or e_{CB}, ($e_{CA} = e_{CB}$), the peak positive instantaneous voltage applied to the R-C circuit will be greater than the peak negative instantaneous voltage by a factor of 2 e_{ref}; therefore, the grid of the voltage amplifier in the next stage will be positive. When the reference and error signal are 180^{o} out of phase, the amplifier signal will be negative.

The signal at point D is chopped by a chopper. The chopper provides a d-c signal of 60 pulses per second. The chopped signal is applied to a two-stage voltage amplifier that is followed by a phase inverter and a push-pull power amplifier. The output from the power amplifier is applied to one winding of a two-phase motor. The second winding is supplied by the 110 VAC line supply. Because the chopper is also powered by the line supply, winding No. 1 will be either 0^{o} or 180^{o} out of phase with the line supply. The phase shift will depend upon whether the chopper is grounding a positive or negative signal. The capacitor in the circuit of winding No. 2 provides for a 90^{o} phase shift of the line supply; thus, the phase shift between windings Nos. 1 and 2 will always be 90^{o}, but the led or lag of a given winding relative to the other and, thus, the direction the motor will run will depend upon the sign of the chopped signal.

Manual operation of the motor is obtained by substituting the input signal of the phase inverter with a signal from a center-tapped transformer whose primary is excited by the line supply. The direction of motor run depends upon which half of the transformer secondary is used.

The balancing of the bridge requires a meter to indicate the unbalance of the circuit. The signal for the meter circuit is obtained from the input to the phase inverter. A cathode follower is used to isolate the meter and meter amplifier circuits and provide impedance matching. The chopper is used to ground the signal at the bottom of the pulse. If the signal were not grounded, the *a*verage value of the signal across the meter and, therefore, the meter reading would not vary with the degree of unbalance of the bridge.

The purpose of the circuit connected to the input of the power amplifier is to provide pilot light indication of the direction of probe movement. The signs of the signals applied to the two grids are 180^{o} out of phase because of the action of the phase inverter. The two plates of the 12AU7 are supplied with a-c line power. The tube section that conducts current is the section whose a-c grid signal is in phase with the a-c plate supply.

Operation of the instrument requires setting of the zero adjustment. The correct zero is obtained by moving the probe across the sodium-cover gas interface using the manual control and noting the distance of meter pointer movement from the maximum positive to maximum negative positions. Movement will occur only when the probe is close to the interface. The zero adjustment is set so the maximum displacement from the center zero point is the same on both positive and negative sides of the zero point.

Although the probe has been used in the sodium storage tank as shown in Figure 1, there was no means at that time of changing the sodium level in the tank to test the ability of the probe to follow the sodium level. The only testing involved the manual displacement of the probe and then allowing the probe to automatically return to the sodium-cover gas

interface. The instrument was found to have a dead band of one-half inch. When the FARET loop becomes operational, the instrument will be given a more thorough testing.

At the present time various means of suspending the probe in the thimble and connecting the coil to the bridge are being studied. Both tapes and wire have been tried. The tapes have the problem that, because each tape winds on top of itself, it forms shorting turns on the tape drum. The tape leads act as a varying resistance in the bridge arm, thus upsetting the bridge balance. Wires have been wound on the drum in groves to form non-shorting turns, but the wire then forms a varying inductor. Because the tapes do a better job of supporting the coil than the wires, the approach has been to use tapes and correct for the varying resistance by placing a potentiometer in the bridge circuit. The potentiometer is mechanically connected to the drum using the proper gear ratio so as to maintain a constant arm resistance. Also, the stainless steel tapes have been replaced with solid gold tapes to decrease the tape resistance.

The sensitivity of the probe has been increased by decreasing the frequency of the oscillator. The increase in coil sensitivity results from the inverse relationship between the coil excitation frequency and magnetic flux penetration. The disadvantage of going lower in frequency is that crystal size and cost go up greatly. At significantly lower frequencies oscillators other than crystal controlled are necessary. Although the bridge balance may be upset by shifts in frequency, the system is not highly critical and a well design non-crystal-controlled oscillator could be used.

The self-seeking liquid level probe has the following advantages over other types of level instruments:

1. Requires a minimum of headroom over the tank
2. Linear response with level
3. Automatic over entire range, no range switching, no manual manipulation
4. Operates in a thimble, complete removal is simple and not exposed to sodium vapors
5. Easy to fabricate
6. Gives continuous indication

Disadvantages are:

1. May require temperature compensation
2. Sensitive to sodium impurities
3. Exceedingly slow speed of response

Sodium Impurity Measurement

The sodium to be used in the FARET loop has seen service in the test facility used to test pumps of the type proposed for use in EBR-2. The facility consisted of three loops connected to a common sodium supply line and dumptank. The loops were used to test a mechanical pump and one a-c and one d-c electromagnetic pump. The loops were constructed of twelve-inch Type 304 stainless steel. Loop operation was approximately 14,000 hours for the mechanical pump, 9000 hours for the a-c electromagnetic pump, and 170 hours for the d-c electromagnetic pump. Operating temperature was usually from 700°-900°F.

Prior to the operation of the EBR-2 pump test facility each loop was cleaned by filling with sodium at 300°F, running at 500°F, and draining to a dumptank at 500°F, where it was allowed to cool at 300°F. After cooling the process was repeated two times.

No hot traps or cold traps were used with the pump test facility loops. The reason for no trapping was to allow for any buildup of oxide that might occur to allow testing for possible plugging of the bearing sodium

supply orifice. It was also considered desirable to test the pumps under more adverse conditions of sodium quality than would be expected in a power plant.

Following the completion of the testing in early 1959, the sodium was drained to the dumptank and the facility dismantled with the exception of the dumptank which was left standing. The sodium has been maintained in the tank at about 250°F. It is expected that the sodium will be transferred to the FARET loop in December 1965.

Prior to its transfer to the loop, several plugging meter runs, two chemical analyses, and one mass spectrometer analysis have been made on the sodium.

Figure 4 shows the plugging valve used with the loop. The valve differs from other valves in that it is designed so that the bellows seal all parts having relative motion from the sodium vapor. The valve was also fabricated with relaxed tolerances which has eliminated binding at the high temperatures.

The plugging temperatures obtained with the sodium were at essentially the sodium solidus temperature. Results from chemical analysis have indicated an oxide content of 19-49 ppm.

The results of the spectrochemical analysis and typical concentrations for new sodium are given below:

	FARET loop, ppm	New Na, ppm
Cr	100	-
Fe	150	2
Ni	75	2

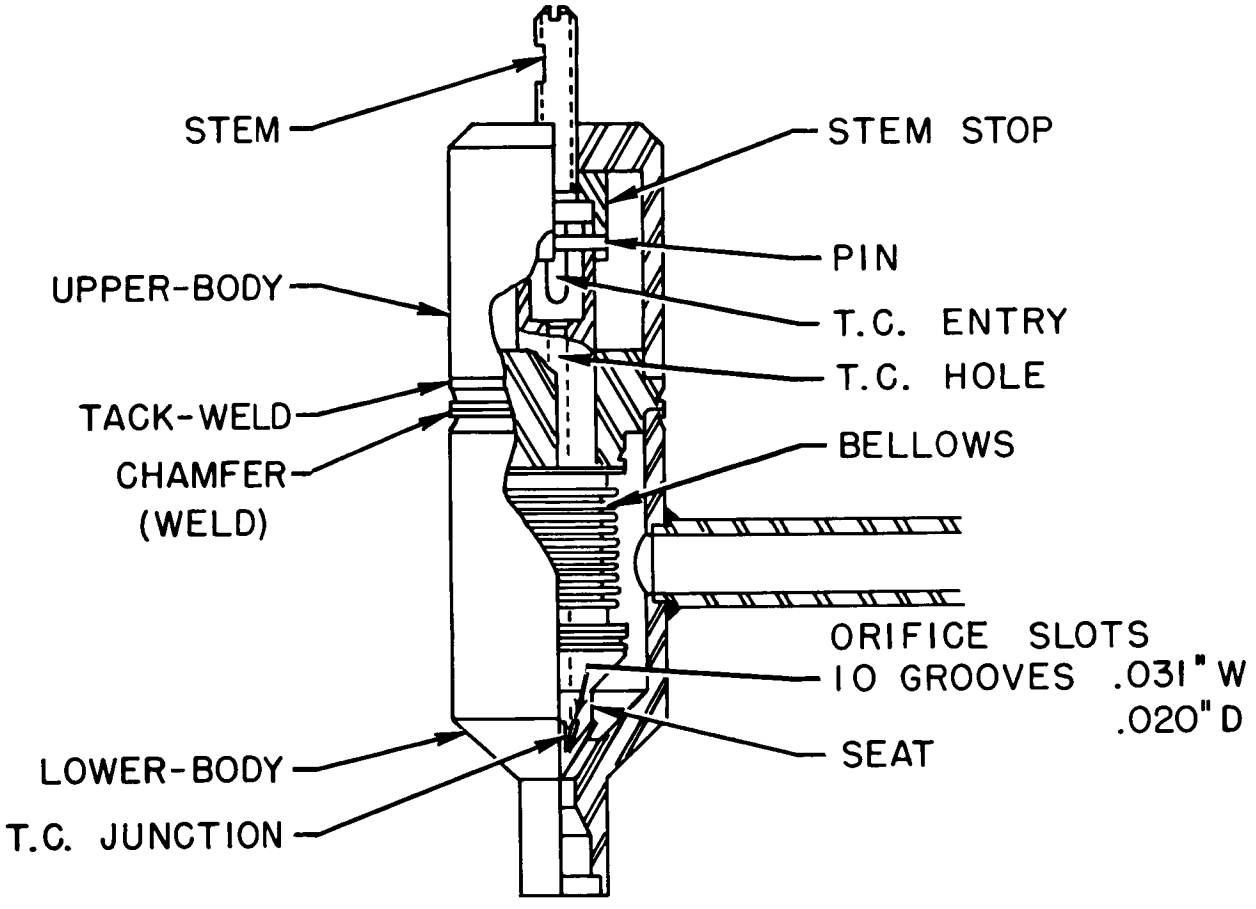


Fig. 4. Improved Plugging Valve--1200°F

With the above concentrations a rough estimate has been made of the corrosion rate of the Type 304 stainless steel under the EBR-2 pump test facility operating conditions. The corrosion rates obtained were:

Element	mg/dm^2-mo
Fe	15
Ni	8
Cr	10

In Reference 2 corrosion rates of -22.2 to -36.3 mg/dm^2-mo are given for Type 316 stainless steel at 1200°F and a sodium velocity of 6.6 ft/sec.

References

1. Armstrong, R. H., et al, "FARET Fuel Assembly Flow Test Loop," American Nuclear Society Eleventh Annual Meeting, Gatlinburg, Tennessee, June 21-24, 1965.

2. GEAP-4313, "Sodium Mass Transfer: VIII Corrosion of Stainless Steel in Isothermal Regions of a Flowing Sodium System," February 1964.

N66 31690

The Liquid Metal Oxygen Meter*

by

B. Minushkin, United Nuclear Corporation

(Paper presented by Kurt Goldmann)

The Liquid Metal Oxygen Meter is an on-line instrument for continuously measuring the effective oxygen content in liquid metals. It is installed directly in an operating system and provides continuous indication of changes in oxygen activity without necessity for sampling and chemical analysis. It is specific for oxygen, and is useful at low oxygen levels in the range from 1 ppm to 100 ppm. It is extremely sensitive to small changes in oxygen concentration, particularly at low levels. Its response to changes in oxygen content is rapid, it is relatively insensitive to changes in liquid metal temperature, and it is independent of liquid metal velocity over reasonably large ranges.

DESCRIPTION

The instrument consists of two components, a Sensor and an Indicator as shown in Fig. 1. The Sensor is installed

*This paper also bears the number UNC-SPLM-61.

Development work performed under Contract AT(30-1)-2877 for the United States Atomic Energy Commission.

PRECEDING PAGE BLANK NOT FILMED.

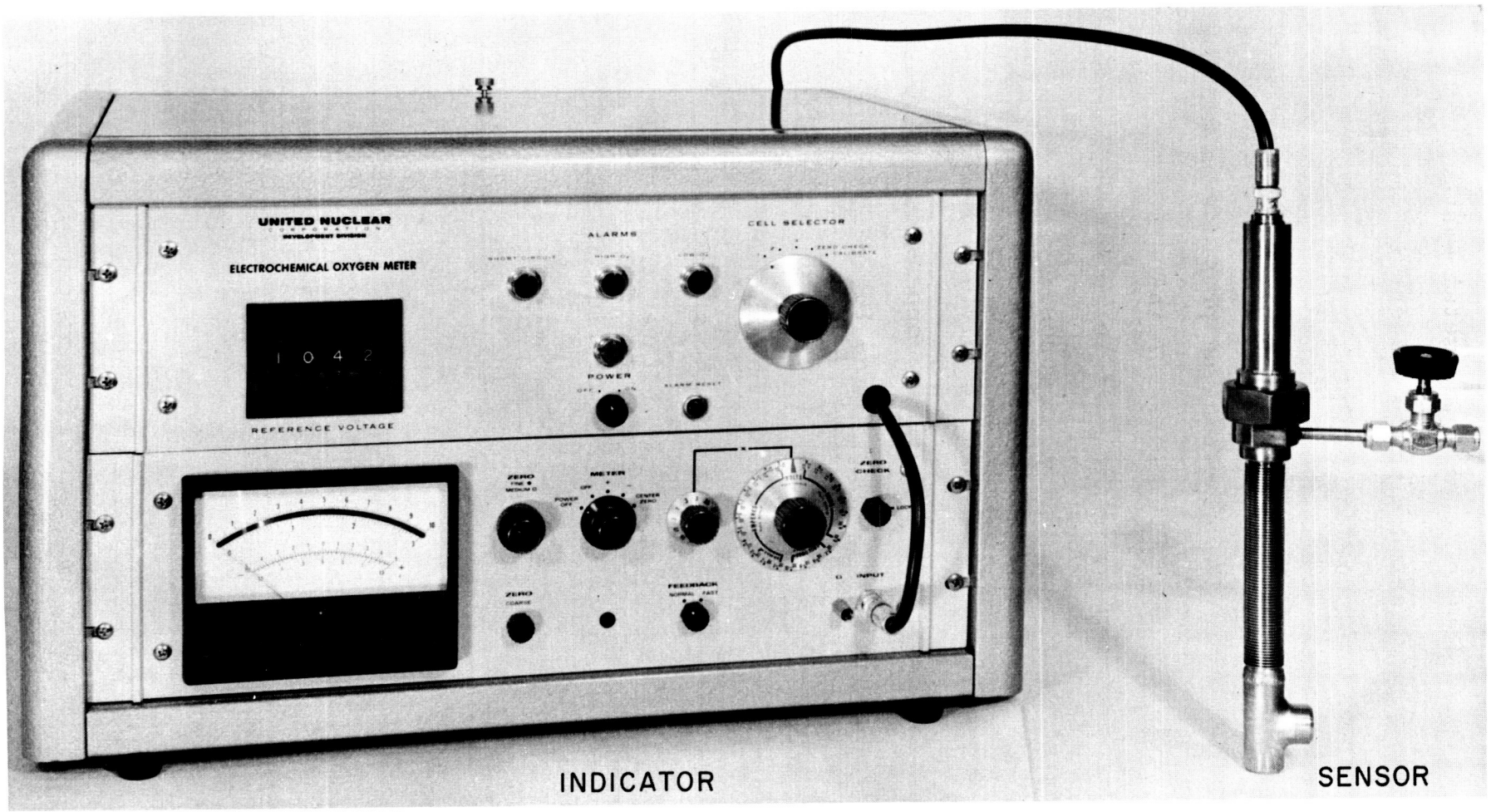


Fig. 1. Liquid Metal Oxygen Meter Sensor and Indicator

in a main or bypass line of the liquid metal system. The Indicator may be located either adjacent to the Sensor or in the system control center.

The Sensor consists of an electrode assembly and a housing as shown in Fig. 2. The housing provides an all-stainless steel containment envelope for the electrode assembly. Its principal parts are a $\frac{1}{2}$ in. standard pipe tee, a finned cooling section, and a Conoseal union.

The key elements in the electrode assembly are a solid electrolyte, thoria-yttria tube, and a copper-copper oxide reference electrode located inside the bottom of the tube. The electrode assembly is inserted into the housing and coupled by means of the Conoseal union. Liquid metal is allowed to freeze in the annular space between the electrolyte tube and the finned tube. The liquid metal in the annulus provides a primary seal and protects the electrolyte tube from thermal and mechanical shock. The electrode assembly is easily installed and replaceable in the field.

The lower end of the electrode assembly, which contains the reference electrode, projects into the liquid metal flowing through the tee. The electrode assembly in

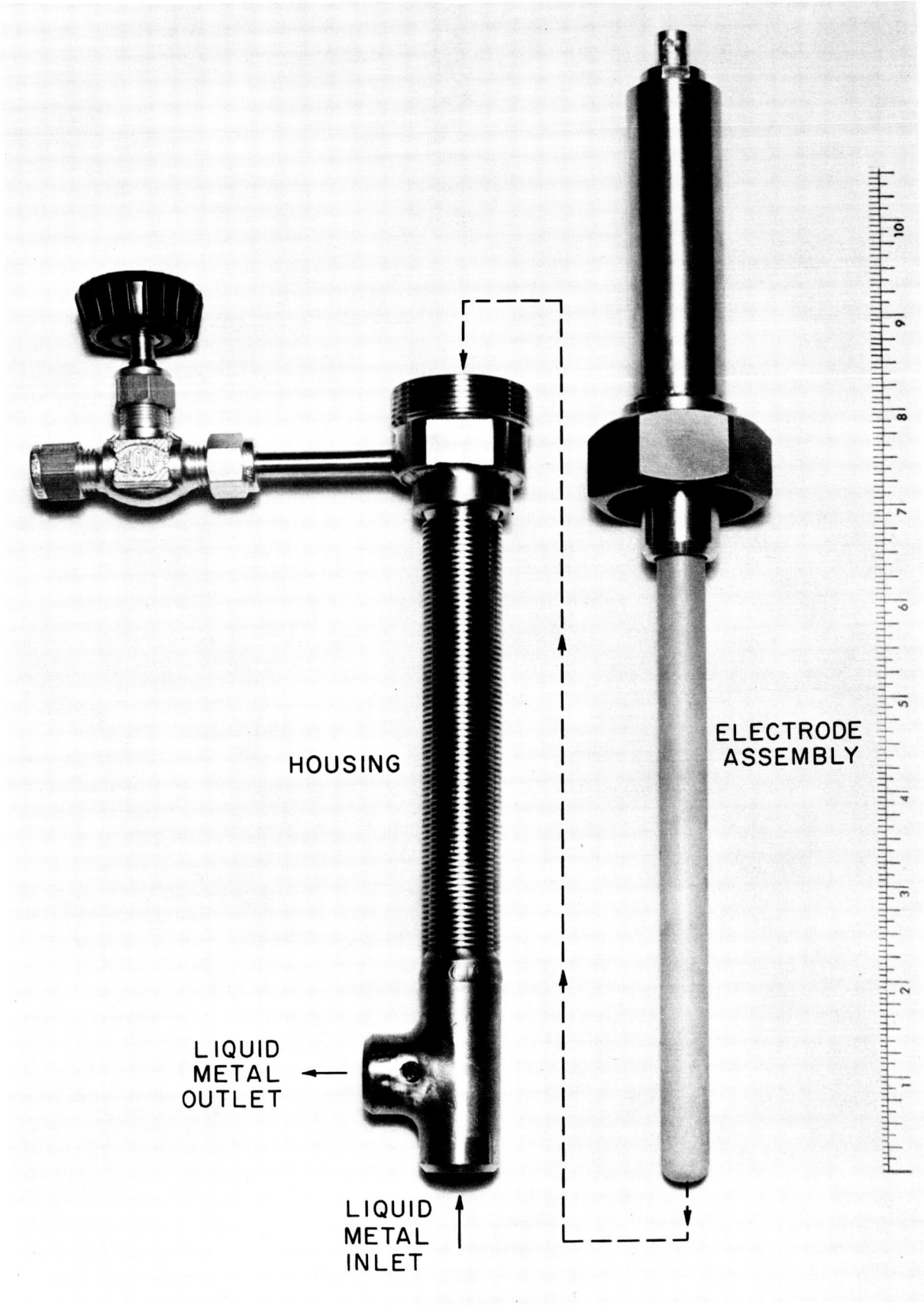


Fig. 2. Liquid Metal Oxygen Meter--Sensor

contact with flowing liquid metal forms a galvanic cell which develops a voltage that is a direct measure of the activity (or effective concentration) of oxygen in the liquid metal.

The Indicator measures the voltage developed by the Sensor. It is a specially designed differential voltmeter with a very high input impedance. The input circuitry is guarded and special precautions are taken with insulators, electrical connections, and cables to eliminate error-causing leakage currents. The cell current is limited to avoid polarization and oxygen migration from the reference electrode into the liquid metal. The Indicator is provided with a recorder output and alarms to indicate malfunctions and high or low limit oxygen contents.

As of this date, 30 meters utilizing this design have been built and 21 of these have been operated in forced circulation loops at United Nuclear and at three field test sites. A total of approximately 24,000 hours of Sensor operation have been accumulated. The meters are easily installed and operated by personnel with only a minimum of training and experience. Electrode replacement can be accomplished within 15 to 30 minutes in a properly designed installation.

PERFORMANCE CHARACTERISTICS

Reproducibility of Performance

The response of the meter to changes in the oxygen content of liquid metals is reproducible. A plot of the logarithm of oxygen concentration vs cell emf yields a straight line as shown for a particular cell in sodium in Fig. 3. In addition, varying the sodium flow rate from 0.4 to 0.8 gpm has no apparent effect upon the response of the meter to changes in oxygen content. A least squares fit of the data for this particular Sensor yields a negative slope of 36.3 $volt^{-1}$.

Data for 20 Sensors have been similarly evaluated, and the slopes of the log C vs E lines are summarized in Table 1. The average slope is 36.5 $volt^{-1}$ with a standard deviation of 2.7, which compares favorably with a theoretical value of 39.5 $volt^{-1}$.

Absolute voltages are within 20% of theoretical values, but can vary from Sensor to Sensor due to variable material properties of the electrolyte. A Sensor must, therefore, be calibrated if it is to be used for measuring absolute values of oxygen concentrations. Calibration is not necessary if the meter is to be used only for

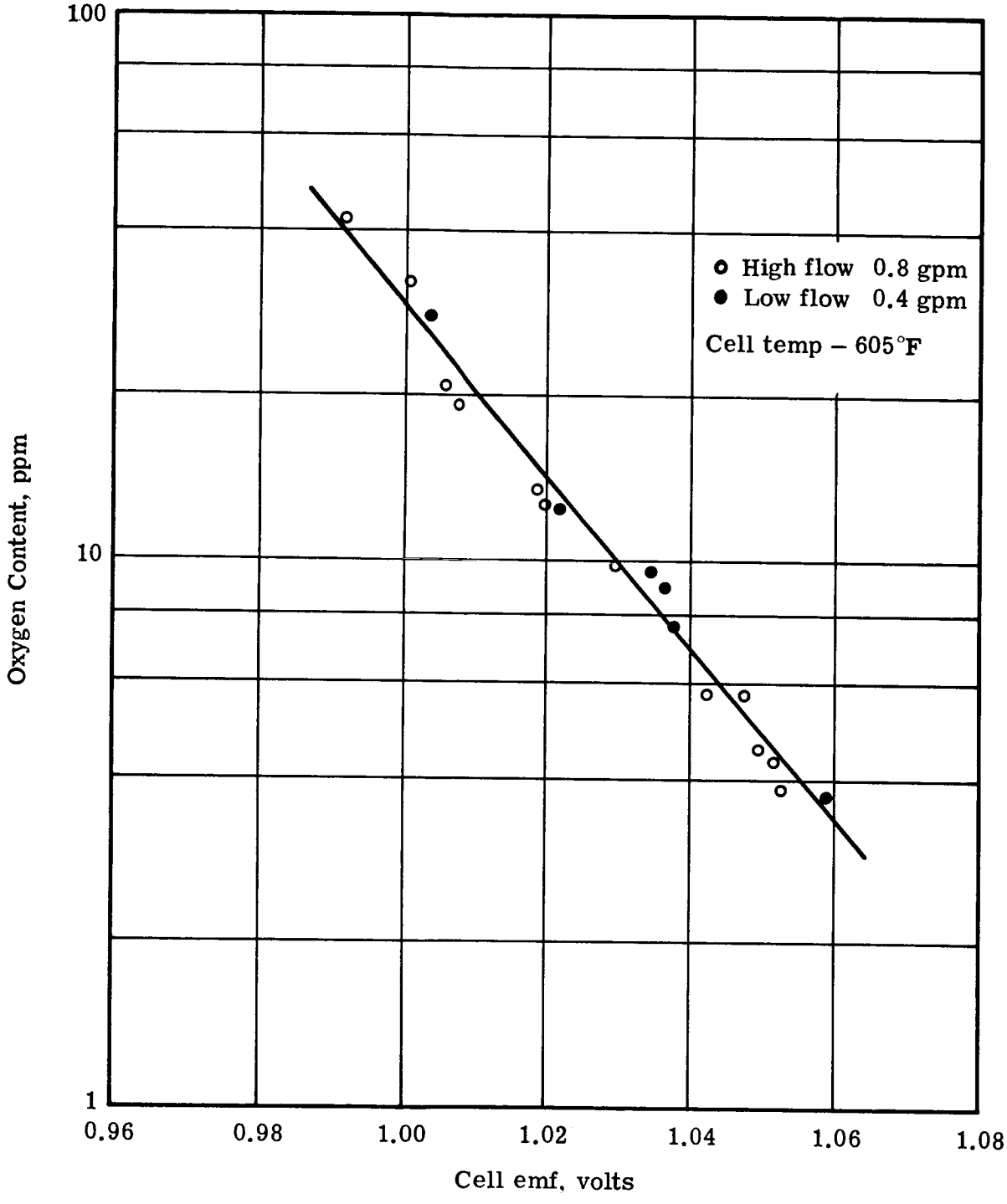


Fig. 3. Effect of Sodium Flow Velocity on Cell Calibration

TABLE 1 — SLOPE OF THE LINE OF LOGARITHM OF CONCENTRATION VS VOLTAGE

Cell	Least Squares Slope, volt^{-1}	Number of Points	Correlation Coefficient
1	-37.7	4	-0.98
2	-34.3	3	-0.99
3	-35.2	5	-0.96
4	-36.8	6	-0.92
5	-32.8	6	-0.86
6	-41.8	6	-0.94
7	-35.7	7	-0.98
8	-35.4	7	-0.99
9	-35.8	7	-0.96
10	-35.1	7	-0.97
11	-41.4	4	-0.99
12	-43.6	5	-0.99
13	-36.3	18	-0.99
14	-32.9	18	-0.99
15	-33.1	18	-0.99
16	-33.0	18	-0.98
17	-38.2	17	-0.97
18	-40.6	17	-0.96
19	-37.6	12	-0.98
20	-33.1	12	-0.92
Avg.	-36.5		
Std. Dev.	2.7		

measuring relative changes in oxygen concentration.

Response to Changes in Cold Trap Temperature

Fig. 4 displays measurements of cold trap temperature and oxygen content over a period of 69 days. Voltage readings on the meter have been converted to ppm of oxygen concentration and are shown as a solid line. Shown as a dashed line in Fig. 4 is the oxygen concentration as inferred from cold trap temperatures. Meter reponses clearly follow the changes in the cold trap temperature. At the 20 ppm level, differences amount to about 4 ppm or 20%, a remarkably small discrepancy at this low oxygen content.

For these tests, the cold trap was loaded with a large excess of oxygen so that it may be assumed that the sodium in the system was saturated with oxygen at the cold trap temperature. The oxygen solubility relationship which was used is shown in Fig. 5. It was obtained by drawing the most representative straight line through published data on a plot of log of oxygen content vs. the reciprocal of absolute temperature.

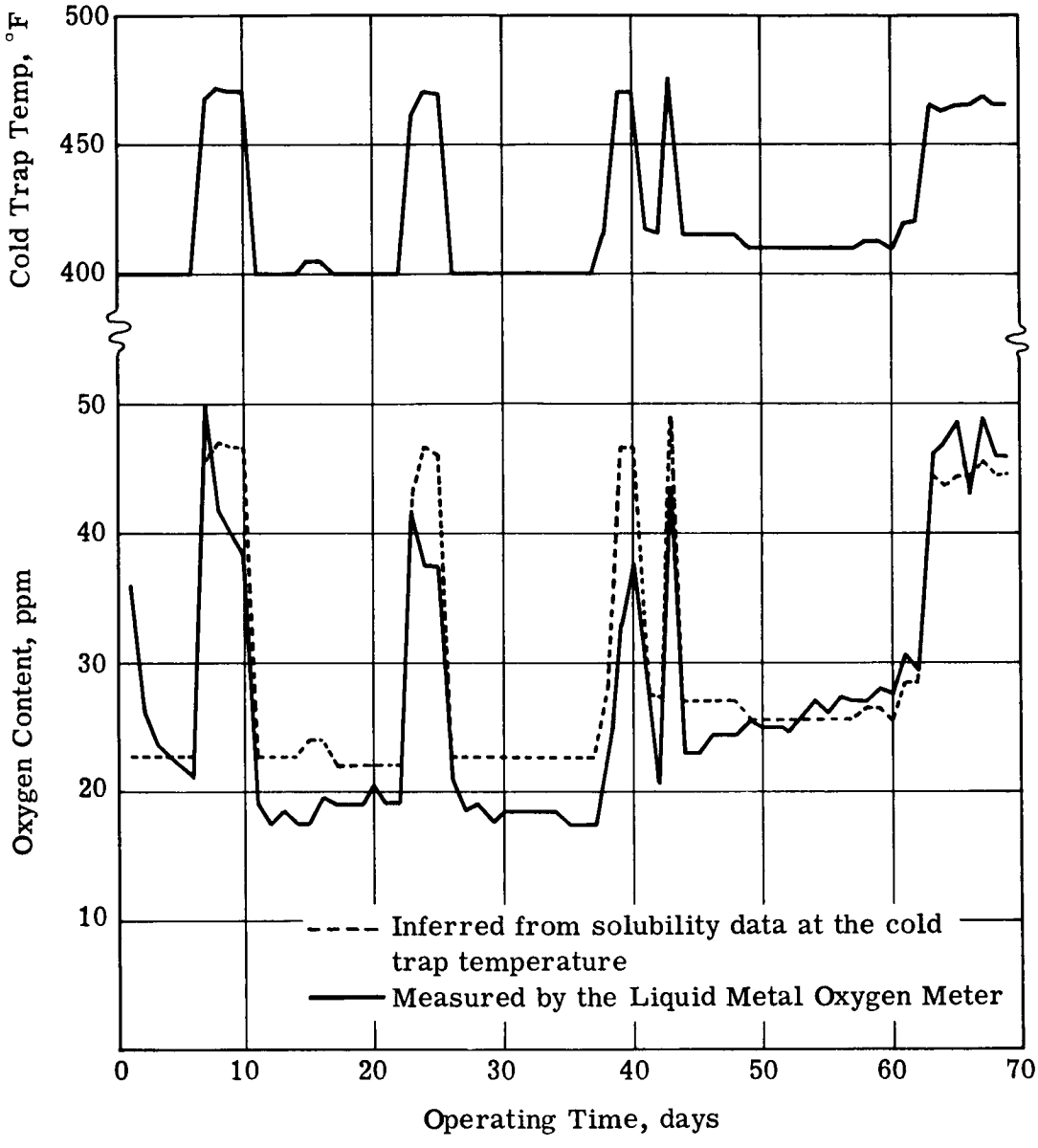


Fig. 4. Response to Changes in Cold Trap Temperature

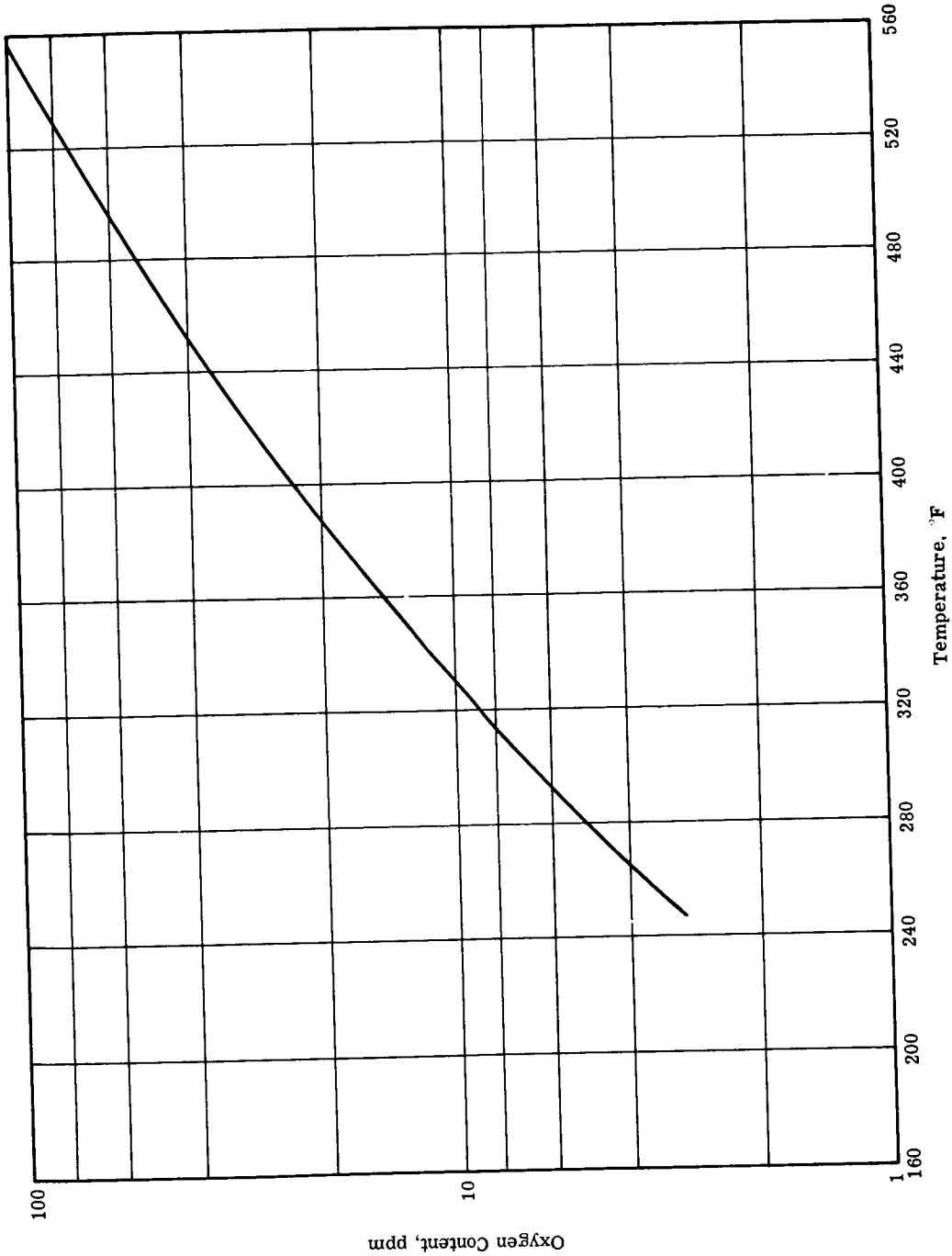


Fig. 5. Solubility of Oxygen in Sodium

Temperature Coefficients

Temperature coefficients for the oxygen meter were measured by observing voltage vs cell temperature at constant cold trap temperature. The data for seven meters are summarized in Table 2. In the range from 580 to 655°F, the temperature coefficient is 0.52 mv/°F. It is constant within this range and reproducible for all of the meters. The data were obtained at oxygen contents from approximately 4 to 18 ppm. No apparent effect was observed of oxygen concentration within this range. A temperature variation of 10°F (causing a voltage change of ~5 mv) corresponds to an equivalent oxygen concentration change of approximately 18% - a readily acceptable error in the ppm range. Furthermore, temperatures can easily be controlled to within 10°F, and the coefficient appears sufficiently reproducible to apply a correction.

Response to Additions of Oxygen

The response of the meter to direct additions of Na_2O to the system is shown in Fig. 6. At time zero, the oxygen was added by a tea bag method to the sodium downstream of the meter, and the sodium containing dissolved

TABLE 2 — CELL TEMPERATURE COEFFICIENT FOR SEVEN CELLS

Temperature Range, °F	Temperature Coefficient ΔE/ΔT, mv/°F
580 to 633	0.55
590 to 630	0.48
604 to 640	0.51
602 to 655	0.50
604 to 656	0.52
598 to 650	0.54
602 to 655	0.51
Avg	0.52

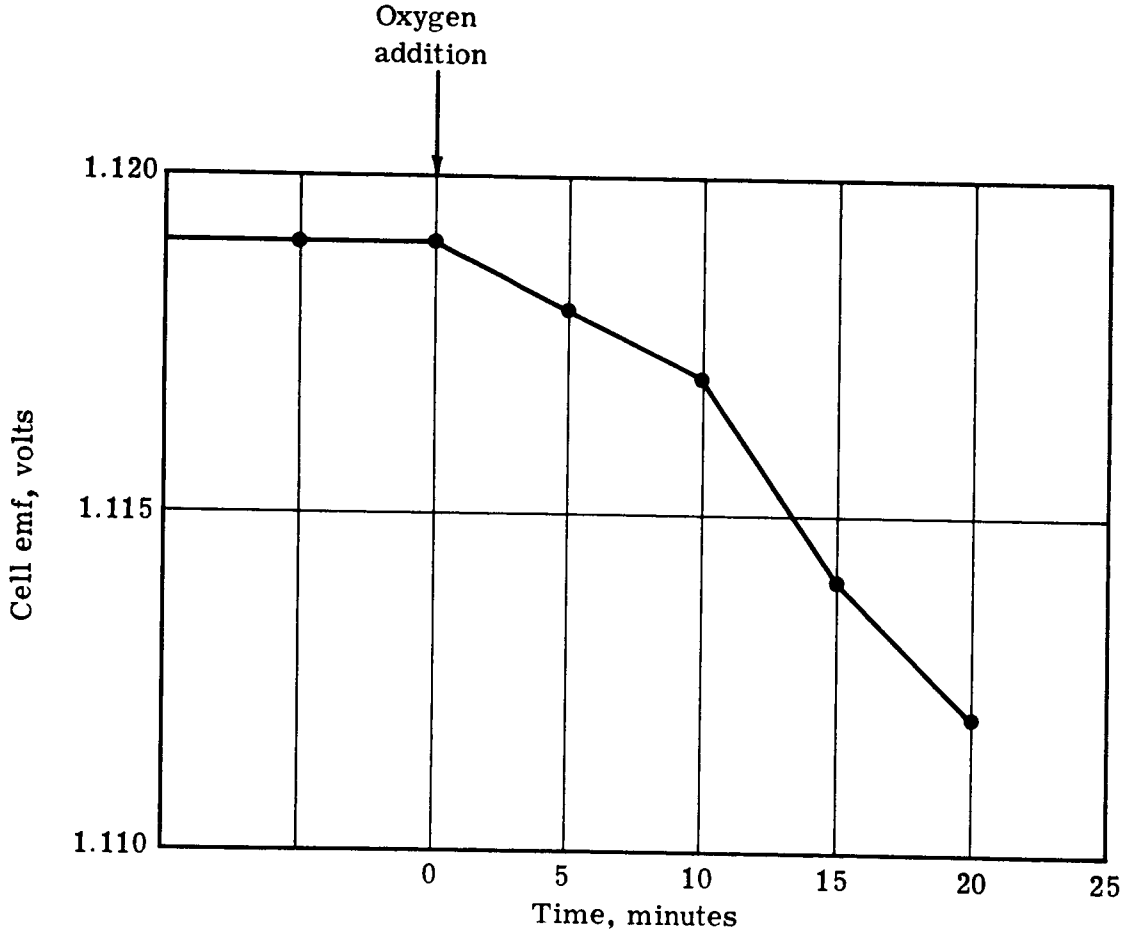


Fig. 6. Meter Response to Addition of Oxygen

oxide had to complete one circuit before it could be seen by the meter. The circuit time was approximately 4 minutes and the initial response to the oxide addition was observed within 5 minutes. Subsequent decreases in cell voltage readings reflect the further solution of the added oxide rather than any apparent sluggishness in meter response.

The total meter voltage change during this addition indicated an increase of 26 ppm oxygen compared with an estimated addition of 32 ppm based on the weight of oxide and an estimate of the sodium inventory in the loop. The agreement is excellent in view of the experimental difficulties.

Effects of Other Impurities

The Liquid Metal Oxygen Meter measures the thermodynamic activity of dissolved oxygen in liquid metals. In an idealized system in which no other impurities are present, activity is also proportional to total oxygen content.

In real systems, other impurities are present. They generally do not affect meter output unless they form compounds with oxygen. As an example, if water is

injected into excess sodium at low temperature, NaOH forms and dissolves in the sodium. The meter will generate a voltage representative of the oxygen activity for the NaOH. If the sodium is then heated above ~630°F, the NaOH dissociates, hydrogen is released to the cover gas and Na_2O forms and dissolves in the sodium. The meter will respond by showing a higher oxygen activity after these changes have taken place, although the total amount of oxygen did not change. Similarly, other oxygen bearing soluble compounds, such as carbonates or ferrates, will generate voltages which are indicative of their oxygen activities. Oxides which are practically insoluble, such as ZrO_2, will not affect meter readings.

Thus, the meter measures oxygen activity which is the effective oxidizing potential of the liquid metal. Since oxygen activity, rather than total oxygen, effectively determines corrosion rates, it is expected that the Liquid Metal Oxygen Meter will prove particularly useful for corrosion studies and for monitoring oxygen activity in liquid metal systems in which low corrosion rates must be maintained.

N66 31691

An Inert Gas Purity Tester*

by

J. McKee, United Nuclear Corporation

(Paper presented by Kurt Goldmann)

INTRODUCTION

United Nuclear Corporation has developed an instrument for measuring inert gas purity which has proven useful in glove box operations typically encountered in handling alkali metals. The sensor is a hot wire filament. It is consumed by oxidizing impurities in the gas, and its life is a measure of the total concentration of such impurities.

DESCRIPTION

The instrument (Fig. 1) consists of two components, a Filament Changer and a Control Unit. The Filament Changer (Fig. 2) is used inside the glove box. It supports a titanium filament and supplies electrical heating current to it. At the end of the test, a handle is manually turned to release the burned out filament and replace it

*This paper also bears the number UNC-SPLM-63.

PRECEDING PAGE BLANK NOT FILMED.

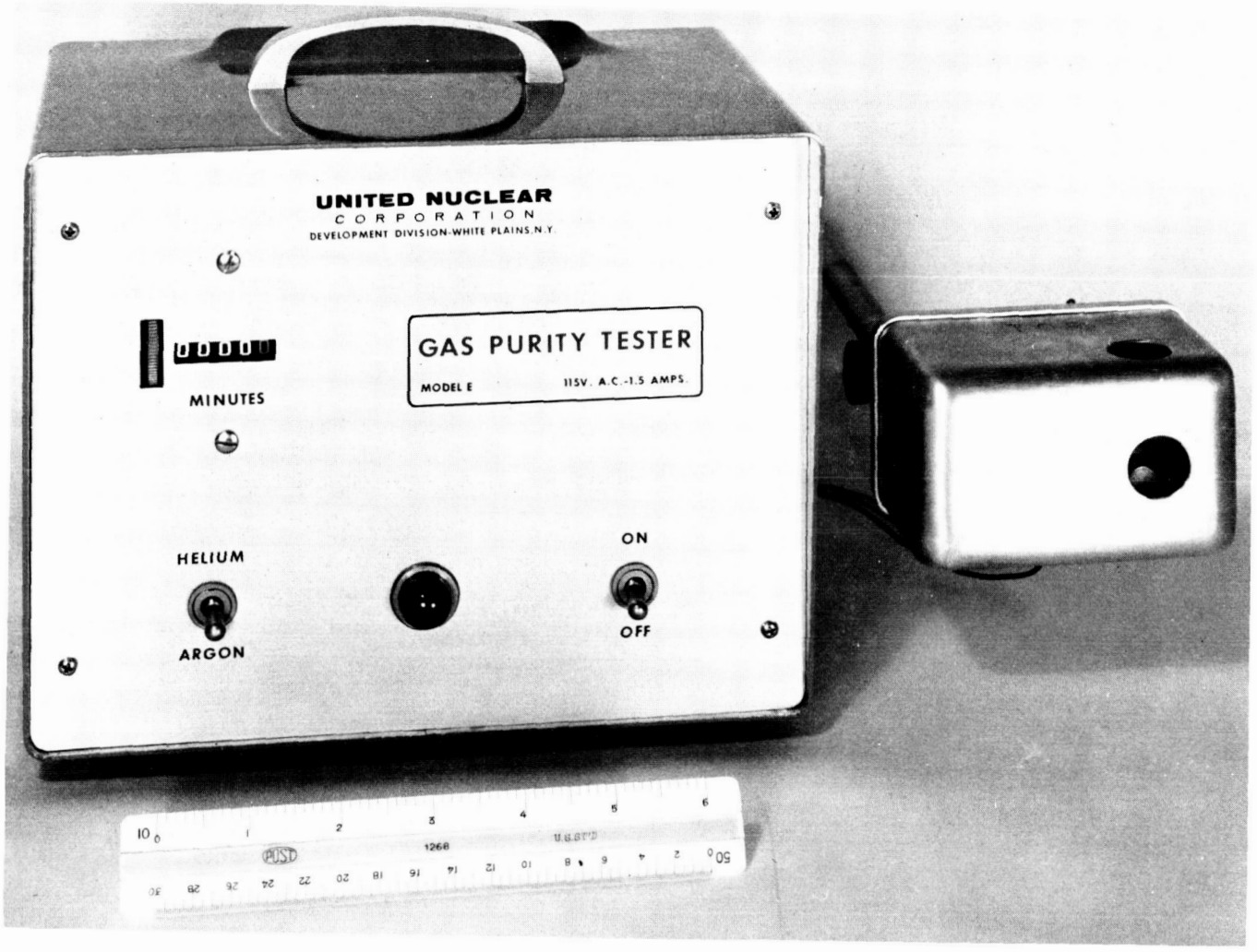


Fig. 1. Control Unit and Filament Changer with Cover On

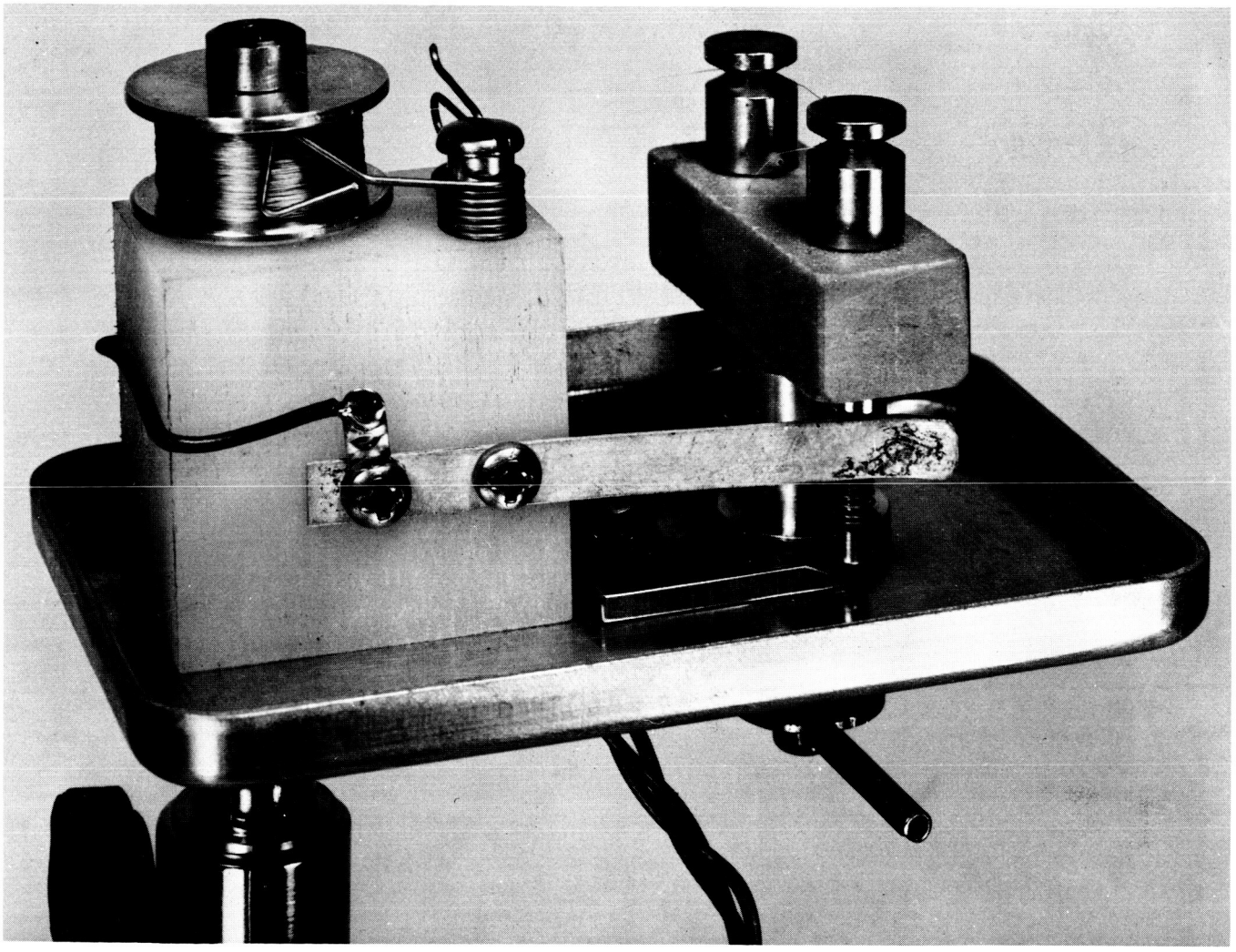


Fig. 2. Filament Changer

with a new one. A small replaceable spool provides wire for 2000 tests. The cover shields the filament from drafts and dust and catches the burned out filaments. It does not affect the filament life and may be omitted if desired. The glove box wall must contain two current feed-through terminals to which the Filament Changer can be connected. A third wire is provided to ground the Filament Changer base plate if desired.

The Control Unit (Fig. 3) is used outside the glove box. It supplies essentially constant 60 cps current to the filament. The timer is manually set to zero before the test and provides digital readout of filament life in minutes. A selector switch adjusts the filament current for testing either helium or argon. When the filament burns out, the pilot light goes out, the timer stops and an alarm is energized.

CALIBRATION PROCEDURE

For the calibrating tests, invarient gas purity was achieved by maintaining a steady flow of gas from large reservoirs through a small glass chamber 1 inch in diameter by 6 inches long. Four 1-inch long filaments were strung side by side on metal supports in this tube in



Fig. 3. Control Unit

such a way that they could be tested sequentially. Gas flows on the order of 600 cc/min through this tube were fast enough to effectively swamp out impurity sources from outgassing without affecting the filament temperature. The gas flow past the hot wire due to thermal convection was apparently considerably faster than the 2 cm/sec net flow along the tube. The total oxygen absorbed by the 1-inch long filament at burnout is about 0.1 mg, which represents negligible gettering of the gas stream.

By mixing controlled flows from two cylinders of different and known purity, the oxygen content of the gas in the test chamber could be held at any desired level between about ten and several thousand ppm. Care was taken to minimize the manifold surface area. After hot vacuum outgassing and several hours of equilibration at constant flows, the life of the four filaments in the test chamber could be held reproducible within $\pm$3%. The two flowmeter readings could not be held more constant than this.

Because helium is a much better coolant than argon, nearly twice as much current is required to obtain the same filament temperature. It was found possible to adjust the current settings so that essentially the same

curve of filament life versus oxygen content was obtained for both helium and argon. This curve is shown in Fig.4. The absolute accuracy of this curve at the high purity end of the range has not, as yet, been established.

The water content of gas from a high pressure cylinder cannot be held constant at high levels, hence water had to be added to the gas stream just ahead of the test chamber. Maintenance of reproducible water content in the test chamber proved to be quite difficult due to sensitive sorption effects. The work was carried far enough to indicate that titanium seems about equally reactive with oxygen and water vapor under the test conditions. When impurity concentrations are expressed in ppm by volume, as is traditional with gases, a given oxygen concentration is equivalent to twice as much water because it contains twice as much oxygen by weight. Since the filament test does not distinguish between water and oxygen, the calibration curve is plotted as a function of equivalent oxygen content.

Nitrogen additions were found to have little effect on the filament life. Although titanium is known to react with nitrogen, at the initial test temperature the filament is apparently so much more reactive with oxygen that

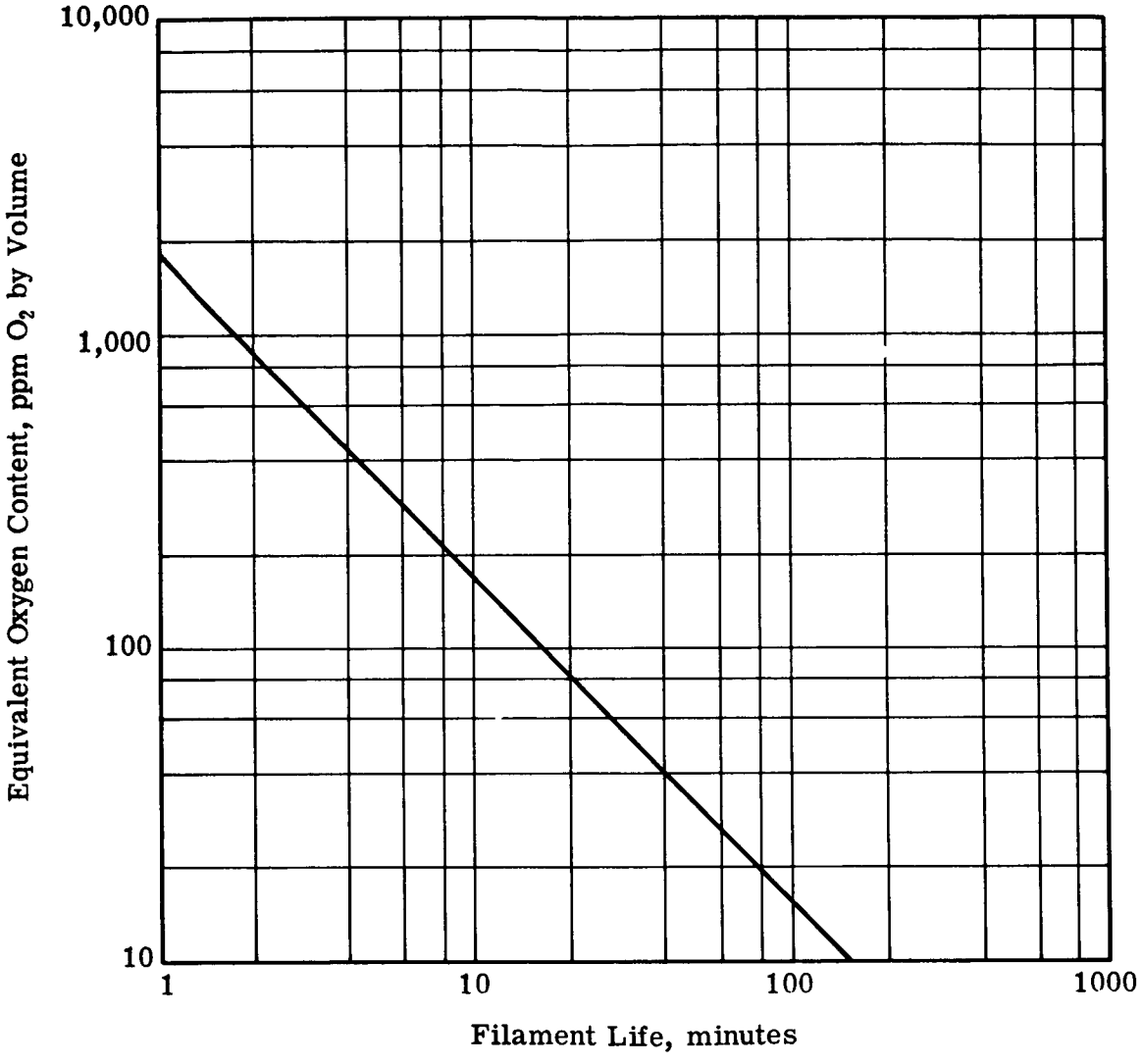


Fig. 4. Gas Purity Tester Calibration Chart--
Equivalent Oxygen Content in Argon or Helium

nitrogen effects are masked. The instrument can, in fact, be used to measure oxidizing impurities in nitrogen, although tungsten wire is much better than titanium for this purpose.

REPRODUCIBILITY

Several types of filament current control were tried. At constant voltage, the filament cools off as its resistance rises and hence would have indefinite life. At constant power, the filament temperature stays more nearly constant, but test time goes up and reproducibility is unimproved or slightly worse. At constant current, the filament temperature rises with the resistance, which goes from about 10 to 20 ohms at burnout. This shortens the test time and gives the best reproducibility. It also avoids any errors due to variable contact resistances. Constant current is approximated simply by putting a large ballast resistor in series with the filament across the 115 volt input. Although the current decreases slightly during the test, the decrease itself is quite consistent and hence does not affect the overall reproducibility. The resultant circuit is simple, rugged and highly reliable.

The current settings are adjusted to produce an initial filament temperature of about 1900°F, as read by an optical pyrometer under non-black body conditions. At lower settings, the test time goes up rapidly and at higher settings reproducibility is impaired for reasons which are not yet understood.

The filament life is less sensitive to variations in control unit input voltage than might be expected. A rise in input voltage of 5% produces about a 3% decrease in a seven minute filament life. This source of error can be eliminated by plugging the control unit into a small constant voltage transformer.

Filament properties such as diameter, composition and surface oxide also affect its electrical resistance and thereby its life. It is estimated that deviations of ±20% from the calibration curve occur in practice due to various factors affecting reproducibility.

EXPERIENCE

The instrument has been used in a variety of glove boxes at United Nuclear laboratories and outside production facilities. It has found application principally in checking the gas atmosphere in a box prior to a critical

operation. The meter has also been applied to monitoring the atmosphere continuously in high purity chambers. In connection with the latter use, it has been found that gas purity in a chamber changes with time, even if extreme precautions are taken to minimize contamination.

With excellent glove box practice, it is possible to achieve a filament life of several hours. In such cases, the instrument can be used as an alarm by keeping the filament hot. The occurrence of leaks in gloves or windows is very quickly detected. In many boxes, the filament life is less than 30 minutes, and trends in atmosphere purity are readily followed by burning a series of filaments.

Use of the sensing element directly in the glove box atmosphere eliminates significant cost, inconvenience and errors associated with sampling systems. The simplicity of the instrument permits routine use by glove box operators with a minimum of maintenance.

N66 31692

INSTRUMENTATION FOR EVALUATING CAVITATION DAMAGE RESISTANCE AND HIGH FREQUENCY FATIGUE OF REFRACTORY ALLOYS IN HIGH TEMPERATURE LIQUID ALKALI METALS

By

H. S. Preiser* and A. Thiruvengadam**

(Paper presented by H. S. Preiser)

INTRODUCTION

Magnetostriction devices for laboratory studies of cavitation damage phenomena have been used by many investigators in the past (References 1-4). In recent years many improvements have been made on these devices such as simplification of circuits, reduction of power consumption, increase in efficiency and ease of operation. Mason (Reference 5) introduced the idea of an exponential horn coupled to a transducer which performed the function of a velocity transformer. This idea was utilized at California Institute of Technology (Reference 6) to attain substantial linear vibratory motion at relatively high amplitudes (2×10^{-3} inches) from a modest power input of 200 watts. Further magnification of amplitude from the same power source is possible by stepped cylindrical horns in lieu of the exponential types (Reference 7). Extensive work has been accomplished for obtaining rapid, reproducible and reliable cavitation damage data by magnetostriction testing (Reference 8).

* Principal Research Scientist and Director, Materials Division, HYDRONAUTICS, Incorporated, Laurel, Maryland.

** Senior Research Scientist and Assistant Director, Materials Division, HYDRONAUTICS, Incorporated, Laurel, Maryland.

PRECEDING PAGE BLANK NOT FILMED.

The compact size and versatility of the magnetostriction device has permitted its ready adaptation to a controlled environment test chamber for conducting cavitation damage studies in high temperature liquid alkali metals. The overall test facility is shown in Figure 1.

The details of design and operation of this integrated test facility, which incorporates a closed loop for storage, purification, transfer and disposal of sodium, has been described adequately in the literature (References 1-4). This cavitation damage facility is capable of maintaining a test retort of liquid sodium at temperatures up to 1500°F for an eight hour period with an oxide purity of about 35 ppm.

THE DESIGN AND FUNCTION OF THE COMPONENTS OF THE MAGNETOSTRICTION APPARATUS

Description

Basically the system consists of a nickel transducer element which contracts in length under the influence of a magnetic field. This is known as the magnetostrictive effect. The magnetic coil surrounding the stack is powered by an oscillating current source which causes the stack to vibrate longitudinally. The amplitude of vibration of the nickel transducer is limited by its magnetostrictive characteristics and is usually quite small, even at resonance. In order to further amplify this vibratory motion to useful output levels it is necessary to couple mechanically a velocity transformer to the working end of the transducer. In the work reported, an

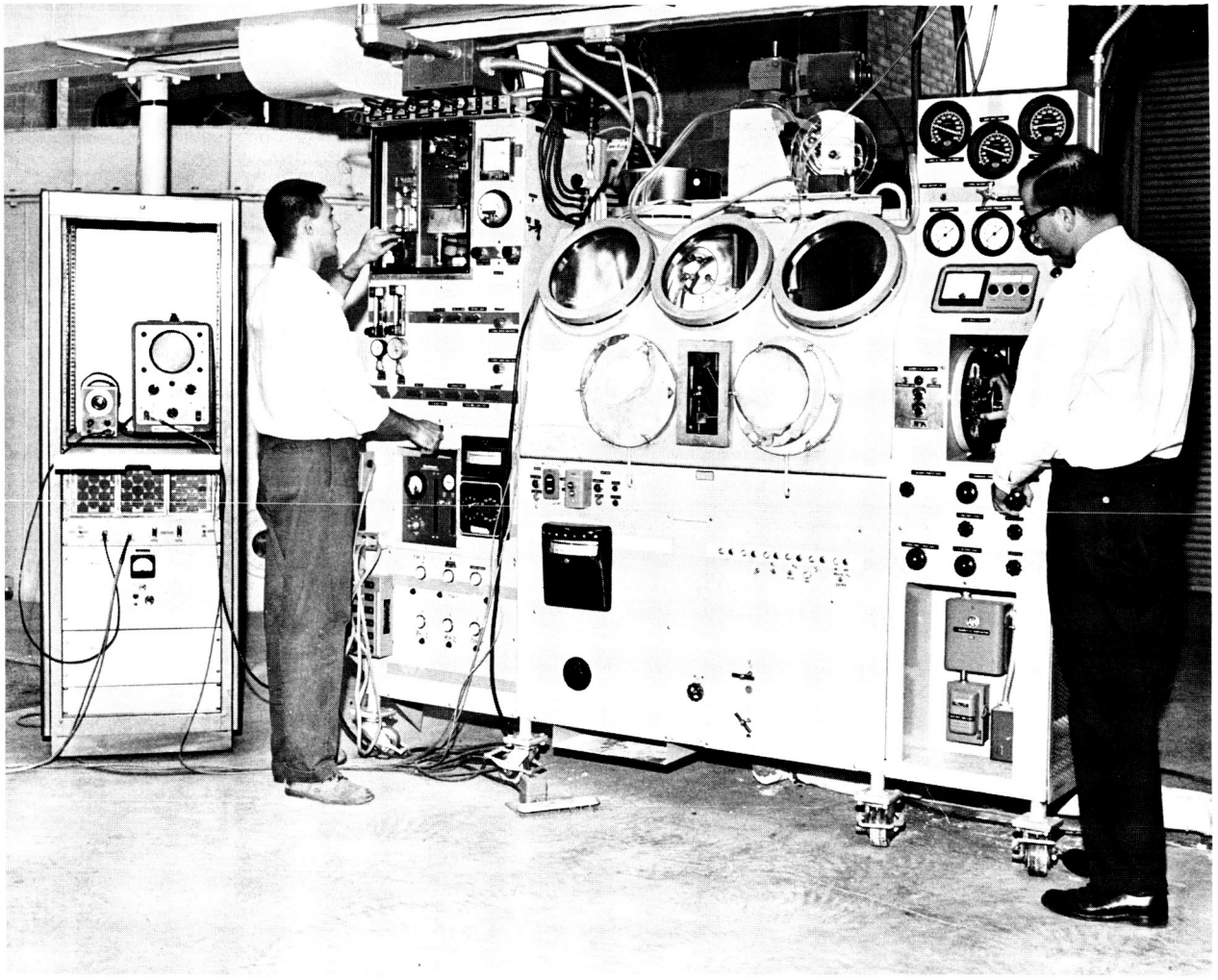


Fig. 1. Outside View of "Dry-Box" Facility for Testing Cavitation Damage in Liquid Metals

exponential horn or a double cylinder stepped horn is used. Careful impedance matching of the electromechanical coupling of the transducer and transformer elements is essential for efficient operation. The technique of design is described in detail in the literature (References 7, 9, and 10).

Equipment Details

The particular apparatus used in these investigations are as follows (Figure 2):

Transducer - A commercial transducer was used which consisted of a pure laminated nickel stack made up of annealed U shaped sheets of pure nickel about 0.005 inch thick. Each lamination was coated with an epoxy resin and potted together to form a rigid rectangular assembly, having a cross-section of 1-3/4" × 2" and a length of 6 inches. A pair of insulated exciting coils, wound in a series aiding direction is fitted over each leg of the slotted transducer. The resonant frequency of the transducer is 14 kcs. The power requirements are about 200 watts to produce an amplitude at the transducer of about 0.0005 inch. The impedance of the transducer uncoupled is about 16 ohms. DC biasing is furnished by means of a permanent magnet positioned in the open end of the slot.

Velocity Transformer - A threaded stub is firmly attached to the transducer by means of soldering so that an interchangeable velocity transformer can be adapted. The amplification factor for an exponential horn varies directly as the ratio of the larger and smaller diameters. For the double cylindrical horn greater amplifications can be realized, because the amplification factor varies as the ratio of the square of the larger and smaller diameters.

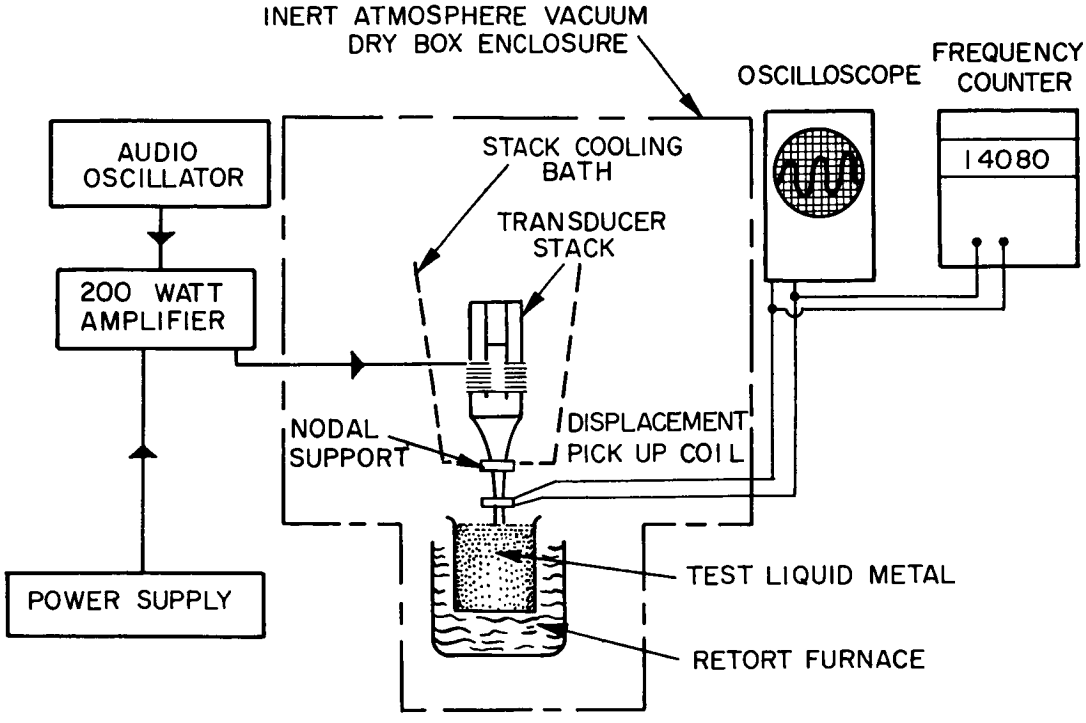


Fig. 2. Block Diagram of the Magnetostriction Apparatus Used for Cavitation Damage Test and for High Frequency Fatigue Tests

Cooling - The heat generated because of the internal friction of the transducer must be dispelled in order not to alter the operating conditions of the equipment. Successful cooling has been obtained by submerging the unit in a kerosene bath containing a cooling water coil.

Amplifier - Any standard linear amplifier (push-pull type) can be used for powering the transducer exciting coils.

Audio Oscillator - The amplifier is driven by a standard audio oscillator capable of stable frequency control over a range of 20 kcs. A wide range gain control for regulating the input signal is required. The oscillating input to the amplifier imparts an oscillating current to the exciting coils causing the transducer to be driven in a vibratory mode of the same frequency. Tuning of the oscillator to the resonant frequency of the system will produce maximum amplitude.

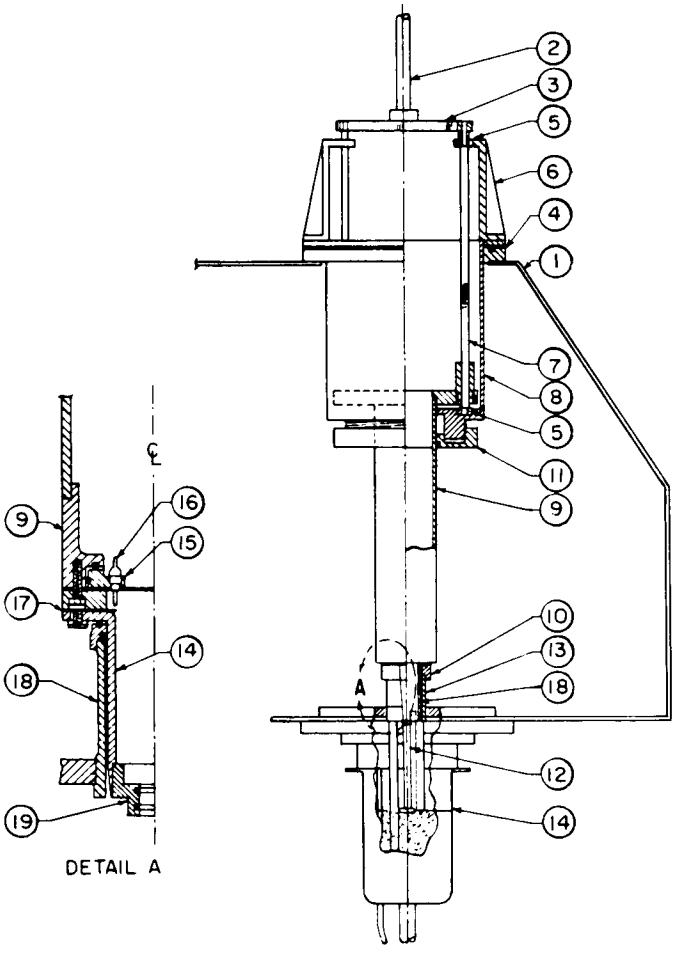
Pick-Up Coil - Some means of measuring the amplitude of vibration is required. Any means is satisfactory in generating an electrical signal as a function of physical displacement. Piezoelectric transducers, reluctance and capacitance pick-ups have been used by others with success. The method employed in these investigations is to provide a simple coil of fine wire (similar to a voice coil of a loudspeaker) at an anti-nodal point on the velocity transformer. The residual magnetic field existing in the velocity transformer is sufficient to generate a voltage signal in the coil which

varies with the amplitude. Sometimes when paramagnetic materials are used, the signal output of the coil can be increased by means of a fixed ring magnet mounted in close proximity to the coil. The voltage output of the coil is fed to any standard oscilloscope. The amplitude of the sine wave generated (voltage) is a function of the physical amplitude of the specimen. This signal voltage can be calibrated against the measured physical displacement by means of observations of a fixed point on the specimen through a filar microscope.

Elevating Mechanism and Tubular Housing - The transducer and horn assembly is mounted into a vacuum tight tubular housing, Figure 3. The support flange is so arranged that it electrically isolates the horn from the housing. The tubular housing is positioned vertically in the dry box by means of an external geared motor drive.

CALIBRATION OF MAGNETOSTRICTION ASSEMBLY

A detailed study of the characteristics of the magnetostriction transducer system was made, to determine the frequency at which the best quality factor (or efficiency) (Q, defined as the ratio of usable energy stored to the total input energy) is obtained for cavitation damage and high frequency fatigue studies in liquid sodium. This is especially important for the fatigue experiments since the transducer must be operated at or near the optimum Q because of the increased damping of metals at higher temperatures.



1. REFRACTORY METALS DRY BOX
2. DRIVE SHAFT
3. SPUR GEARS
4. SEAL - ELEVATING HOUSING
5. RADIAL BEARING
6. BEARING SUPPORT
7. BALL BEARING JACK SCREW
8. ELEVATING MECHANISM HOUSING
9. TRANSDUCER HOUSING
10. SEAL - TRANSDUCER HOUSING
11. COMPRESSION CAP
12. MAGNETOSTRICTION HORN
13. MALE TELESCOPIC SEAL (HOUSING)
14. RETORT ASSEMBLY
15. NODAL FLANGE (INSULATED)
16. CERAMIC THRU - SEAL
17. MICARTA INSULATION
18. FEMALE TELESCOPIC SEAL (RETORT)
19. VOICE PICK-UP COIL SUPPORT

Fig. 3. Elevating Mechanism and Tubular Housing for New Facility

The procedure undertaken was as follows: The resonant frequency of the transducer-velocity transformer combination can be varied by changing the length of the extension rods attached to the free end of the velocity transformer. The relationship between the amplitude (pick-up coil voltage) and the frequency is experimentally determined for various resonant frequencies as shown in Figure 4 for approximately constant power input. From these data the quality factor for each resonant frequency was determined by the following formula:

$$Q = \frac{1}{\alpha} = \frac{0.55\ f_n}{\Delta f} \qquad [1]$$

where

Q is the quality factor,

α is the logarithmic decrement,

Δf is the band width at half the maximum amplitude, and

f_n is the resonant frequency.

The value of Q for various resonant frequencies has been plotted as a function of f_n in Figure 5. The design of the high frequency fatigue specimens was also based on an operating frequency of 14.0 kcs to obtain a near optimum quality factor.

The operation of the magnetostriction oscillator at temperatures up to 1500°F (using a 316 stainless steel velocity transformer) has been proven to be feasible. In this connection,

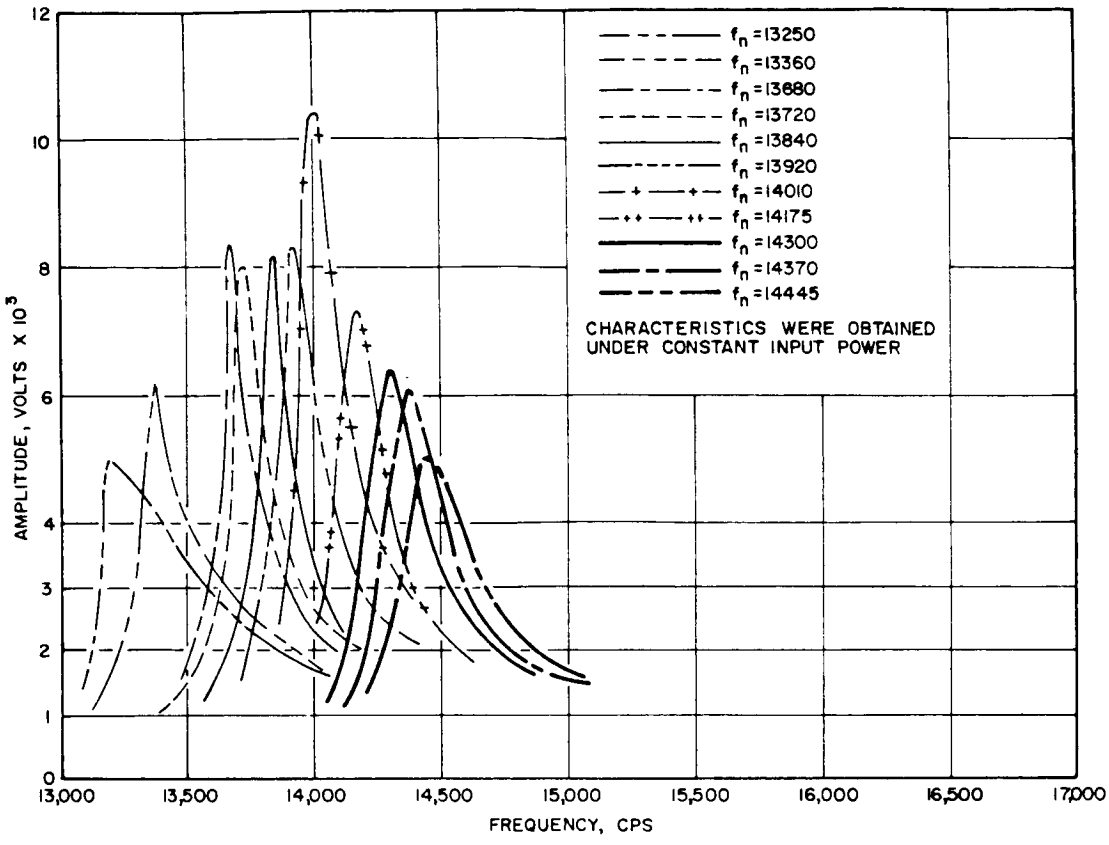


Fig. 4. Characteristics of the Transducer

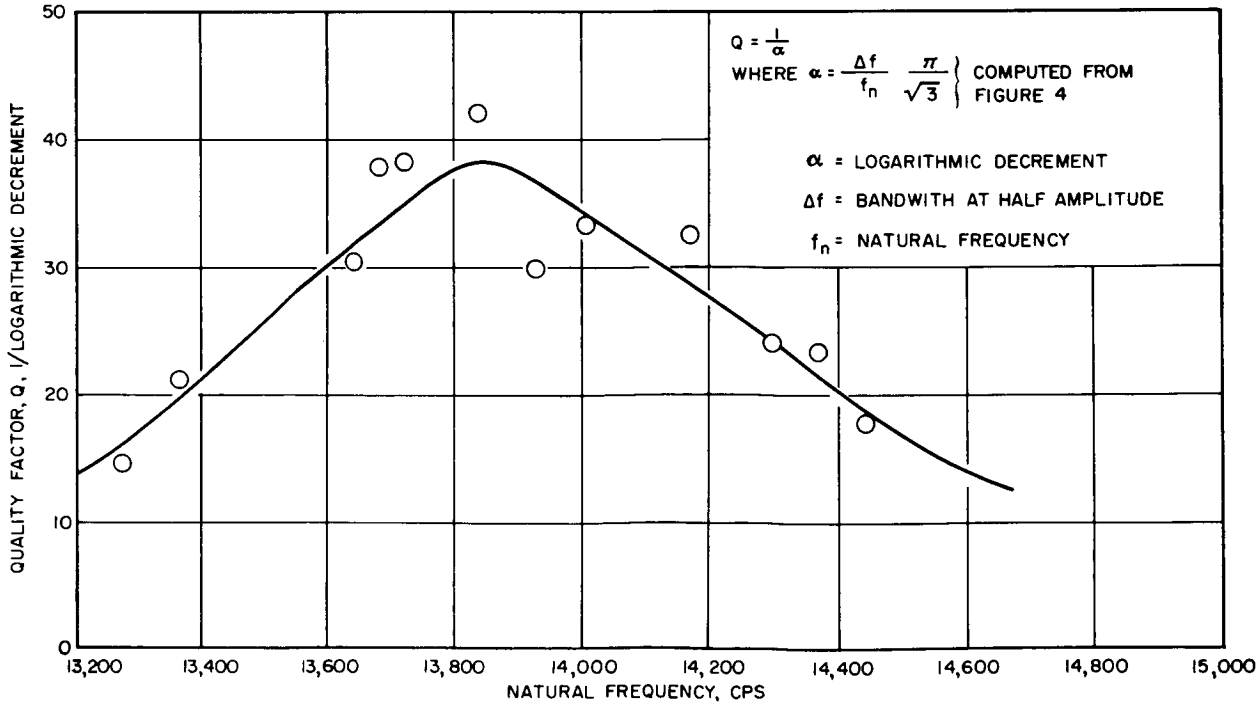


Fig. 5. The Effect of Natural Frequency on the Quality Factor

minor difficulty was experienced early in the program with loss of the oscilloscope display voltage which monitored the amplitude of the transducer. This trouble was diagnosed as loss of magnetic strength in the pick-up coil — permanent magnet system. The above condition was corrected by installing a more powerful magnet with a higher curie point.

STANDARDIZATION OF TEST PROCEDURES FOR CAVITATION DAMAGE

A detailed study of the effect of test parameters in evaluating the cavitation damage resistance of materials has been made (Reference 8). Some of the salient findings will be briefly touched upon here. The reproducibility of results with a simple flat faced test specimen is as good as the other more complex specimen shapes. The dimensions of the container of the liquid have relatively insignificant effect on the test results if one avoids extremes. The same conclusion holds good for the depth of immersion of the specimen in the test liquid. The rate of volume loss varies as the square of specimen diameter in the steady state zone.

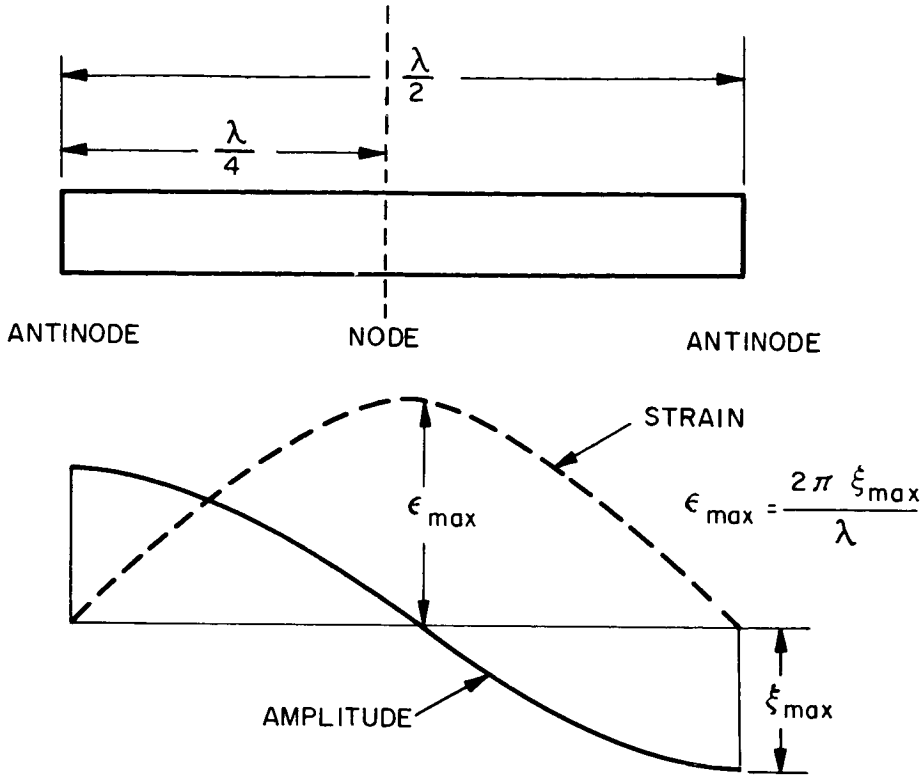
These results have led to the logical standardization of test procedures (Reference 8). A simple flat faced specimen of suitable dimensions may be used to obtain the relationship between the damage rate and the test duration until the steady state zone is reached. In the steady state, it would be meaningful to plot the relationship between the amplitude of oscillation and the rate of damage for each material.

HIGH FREQUENCY FATIGUE TESTING AT HIGH TEMPERATURES

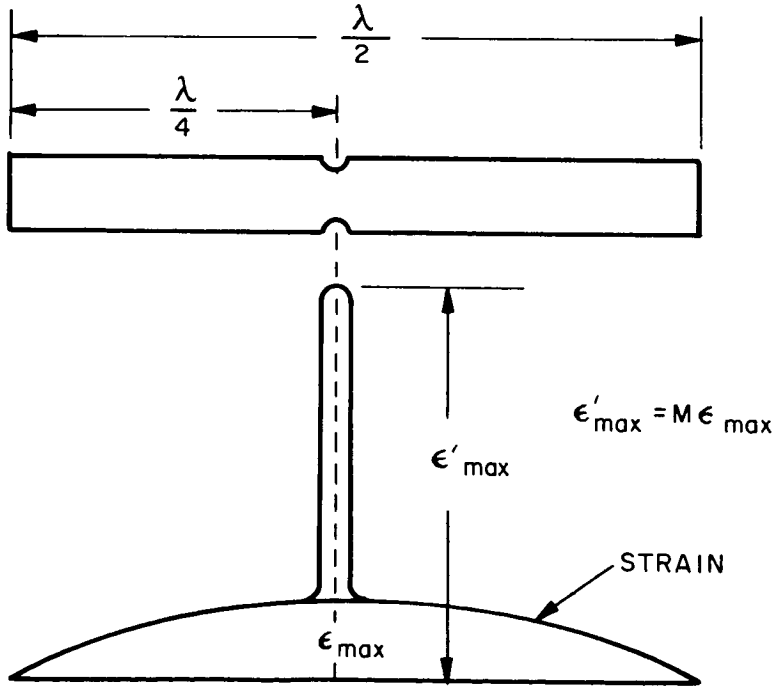
The versatility of the magnetostriction apparatus is best demonstrated by its use in conducting high frequency fatigue tests. This method has been the subject of investigations recently by Mason (Reference 5), Neppiras (Reference 7), Fox (Reference 11) and Thiruvengadam (Reference 12). All these experiments were confined to room temperatures. However, we have extended this approach to high temperatures in liquid metal environments up to 1500°F (Reference 13).

The basic principle of the design of the high frequency fatigue specimens is as follows: When a longitudinal vibration of a half wave length of a metallic rod is produced by means of an oscillator, the maximum strain is produced at the node while the maximum velocity and displacement are produced at the antinodes at either end of the rod (Figure 6). If a notch is produced at the node, then the strain is further amplified at the node. It is necessary to amplify the strains by means of a notch because of the power limitations of the driving oscillator. There are two other unwanted side effects due to this notch, namely: (i) the fatigue notch sensitivity and (ii) the change in resonant frequency. These two effects will be discussed subsequently.

The main idea is to attach a half wave length of the metallic rod to the free end of the velocity transformer and to vibrate it at the best frequency selected from considerations of the quality factor. The half wave length can be experimentally



a - UNNOTCHED HALF-WAVE LENGTH SPECIMEN



b— NOTCHED HALF-WAVE LENGTH SPECIMEN

Fig. 6. Basic Principle of High Frequency Fatigue Specimen Design

determined by adjusting the rod length to resonate at the best frequency. An accurate determination of this length and frequency will give the value of velocity of sound for each of the metals tested by the relationship

$$\lambda f_n = c \qquad [2]$$

where

λ is the wave length,

f_n is the resonant frequency, and

c is the velocity of sound.

The modulus of elasticity also can be calculated after determining the density of the metals by the conventional water displacement method, by

$$E = \rho c^2 \qquad [3]$$

where

E is the modulus of elasticity, and

ρ is the density of the metal.

Table 1 gives the physical properties thus determined for each of the two metals tested at two temperatures.

Notch Sensitivity

As pointed out earlier, a notch was provided at the node to induce the required strains. It is known that fatigue is sensitive to notches depending upon the geometry of the notches. This effect is characterized by a factor η known as notch sensitivity

$$\eta = \frac{K_f - 1}{K_t - 1} \qquad [4]$$

where

$$K_f = \frac{\text{un-notched fatigue strength}}{\text{notched fatigue strength}} \text{ , and}$$

K_t = the theoretical stress concentration factor.

Experimental information on η as a function of notch radius at elevated temperatures is not readily available for these metals. The notch radius for room temperature studies was selected so that η would be as close to unity as possible, Reference 12. The same notch radius was adopted for high temperature studies also since no experimental data were readily available for these metals. Next, the theoretical stress concentration factors for round bars may be found from Reference 14. The dimensions of the notch selected are shown in Figure 7.

The stresses are calculated as follows: The maximum strain at the node for a uniform rod in sinusoidal vibration is given by

NOTES:

1. GROOVE (DETAIL "A") IS TO BE SMOOTH, FREE FROM CHATTER TOOL MARKS, GROOVES OR OTHER DISCONTINUITIES. THE DIMENSIONS OF THE GROOVE MUST BE IDENTICAL FOR ALL SPECIMENS IN A LOT ± .001 AS MEASURED WITH AN OPTICAL COMPARATOR.
2. FINISH IN GROOVE 63 OR BETTER
3. DIMENSION "A" EQUALS HALF WAVE LENGTH OF SOUND

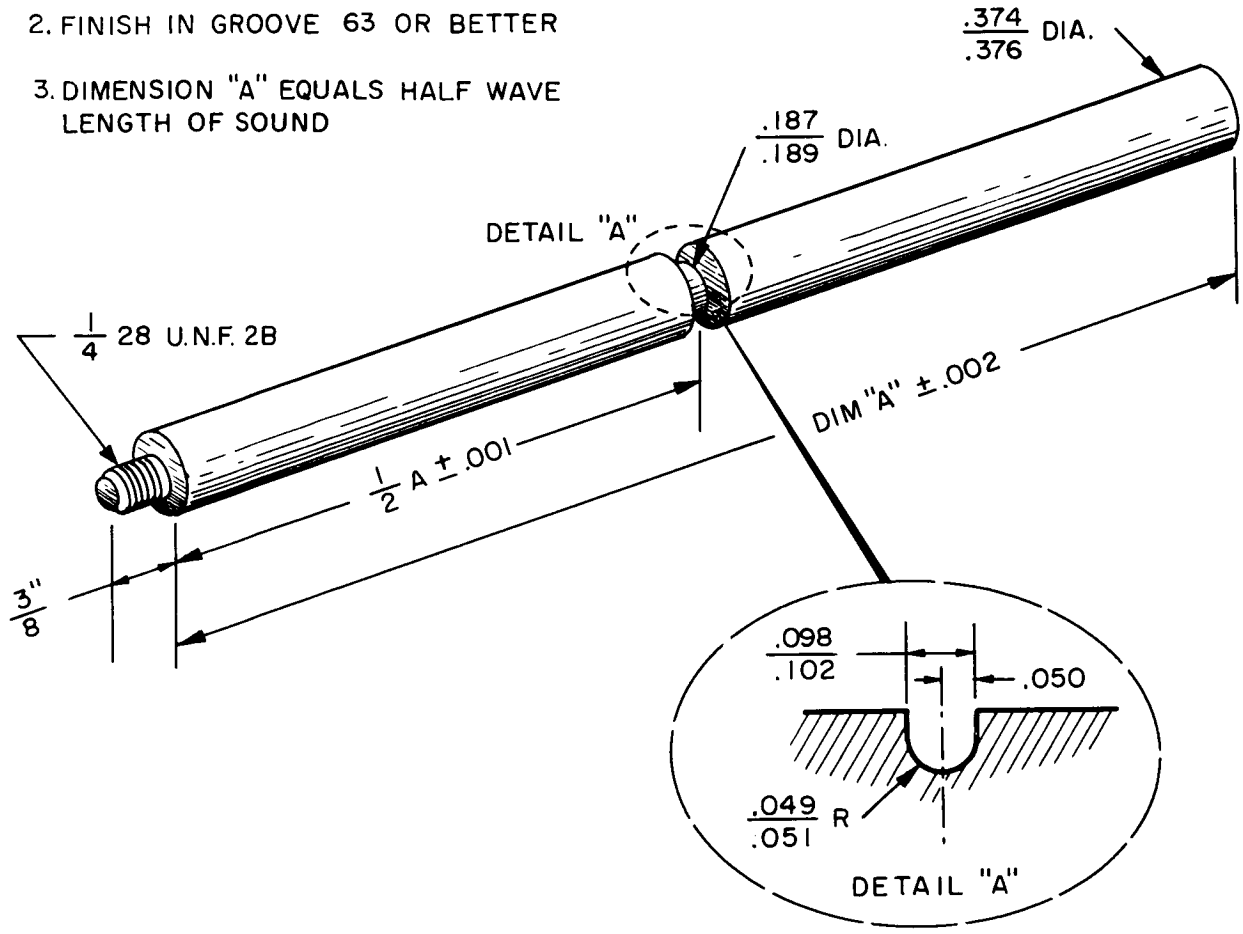


Fig. 7. High Frequency Fatigue Specimen

$$\epsilon_{max} = \frac{2\pi \xi_{max}}{\lambda} \qquad [5]$$

where ξ_{max} is the maximum amplitude. The stress amplitude σ_a is given by

$$\sigma_a = \epsilon_{max} \cdot E \qquad [6]$$

For the present design, the theoretical stress concentration factor from Reference 14 is 1.65 and the area ratio is 4. Hence the magnification factor, M is 4 times 1.65 and the stress amplitude is given by

$$\sigma_a = 6.6 \frac{2\pi}{\lambda} \xi_{max} \cdot E \qquad [7]$$

Effect of Notch on Resonant Frequency

Another effect of the notch is to lower the resonant frequency slightly. This can be rectified by reducing the length of the fatigue specimen after a few trial and error experiments. This modified length can also be predicted by an approximate theory following Neppiras (Reference 15). However, the change in wave length due to the notch remains within 10 percent as shown in Table 1 and this can be taken into account in the calculation of stresses.

TABLE 1

Test Parameters of High Frequency Fatigue Specimens

Metal	Temp. °F	Wave Length Inches	Modulus of Elasticity-psi × 10^6	Specimen Length-Inches	Resonant Frequency cps
316 Stainless Steel	1000	12.2	21.8	5.500	14140
	1500	11.3	18.5	5.125	14080
TZM	1000	15.0	42.0	7.000	13990
	1500	14.5	39.0	6.750	14080

TYPICAL TEST RESULTS

Cavitation Damage Tests

Making use of this facility, five metals have been tested for their cavitation damage resistance in liquid sodium up to 1500°F. A typical set of results are shown in Figure 8 from tests conducted at 400°F. It is interesting to note that the curves in Figure 8 cross each other indicating the interaction of testing time (Reference 13). The relationship between the reciprocal of the rate of volume of loss and the estimated strain energies for four metals at 1000°F is shown in Figure 9. These results generally confirm the earlier findings that the energy absorption characteristics of metals during fracture represent their cavitation damage resistance. However, much more detailed and intensive investigations are necessary for confirming these relatively limited results because of the lack of actual test results on the mechanical properties of these metals at these high temperatures and at these high strain rates.

High Frequency Fatigue Tests

To understand the relationship between the cavitation damage resistance and the environmental fatigue behavior of metals, high frequency fatigue tests on 316 stainless steel and on TZM alloy were conducted in liquid sodium at two temperatures (1000°F and 1500°F) using the magnetostriction apparatus described earlier. Typical test results are shown in Figure 10 and 11 for 316 stainless at 1000°F and at 1500°F at two oxide

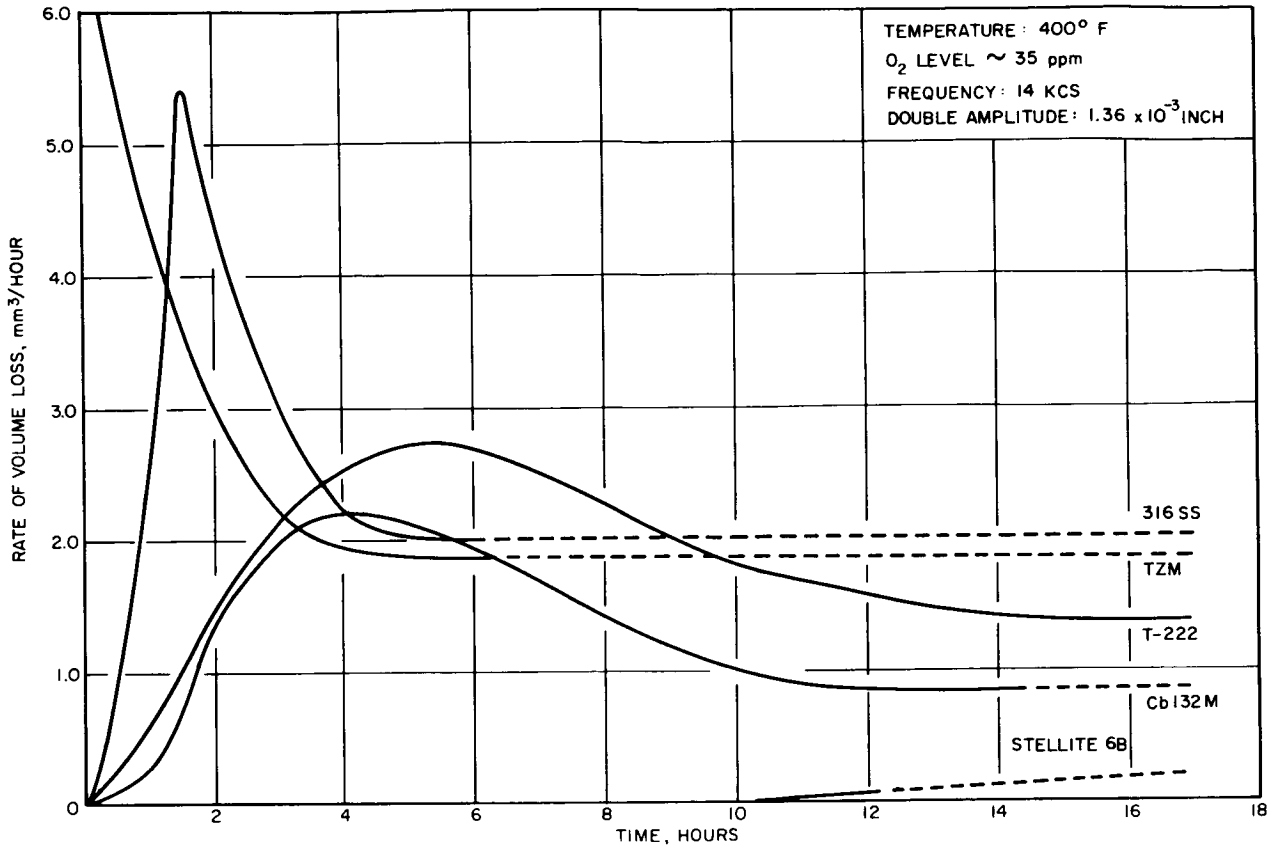


Fig. 8. Relative Cavitation Damage Resistance of Five Metals Tested in 400°F Sodium

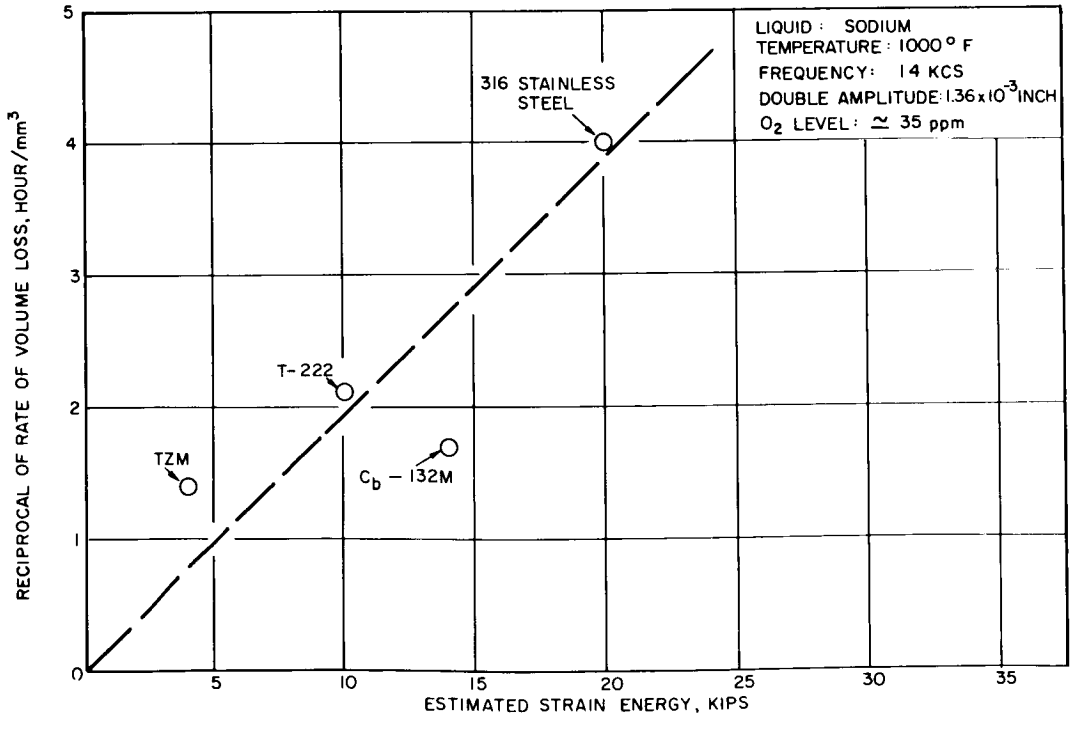


Fig. 9. Relationship between Cavitation Damage Resistance and Estimated Strain Energy at 1000°F

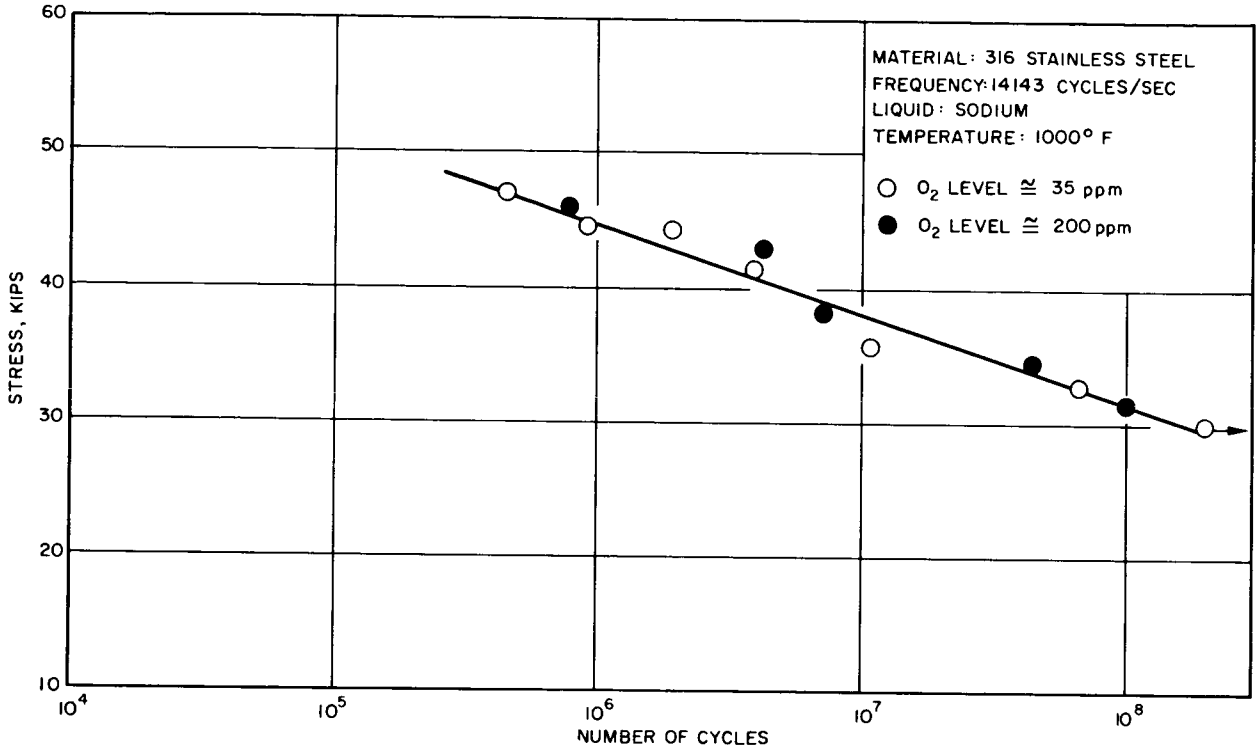


Fig. 10. High Frequency Fatigue Curve for 316 Stainless Steel in 1000° Liquid Sodium at Two Oxide Levels

levels in liquid sodium (Reference 13). In Figure 11 the results of Danek and Achter (Reference 16) at low frequency (4-5 cps) on 316 stainless steel at 1500°F in 3×10^{-5} torr vacuum with mechanical drive and resonant magnetic drive are shown along with the data obtained from the present high frequency fatigue data in 1500°F sodium at 14,000 cps.

CONCLUDING REMARKS

The magnetostriction apparatus installed in a controlled environment chamber described in this paper has been highly useful in evaluating the cavitation damage resistance and the fatigue behavior of high temperature alloys in liquid sodium. It is believed that this approach can also be extended to other liquid metals.

ACKNOWLEDGMENTS

These investigations were supported by the National Aeronautics and Space Administration under Contract NAS 3-4172. In particular, we would like to acknowledge the many useful comments offered by Mr. James P. Couch of NASA Lewis Research Center during the development of the subject instrumentation.

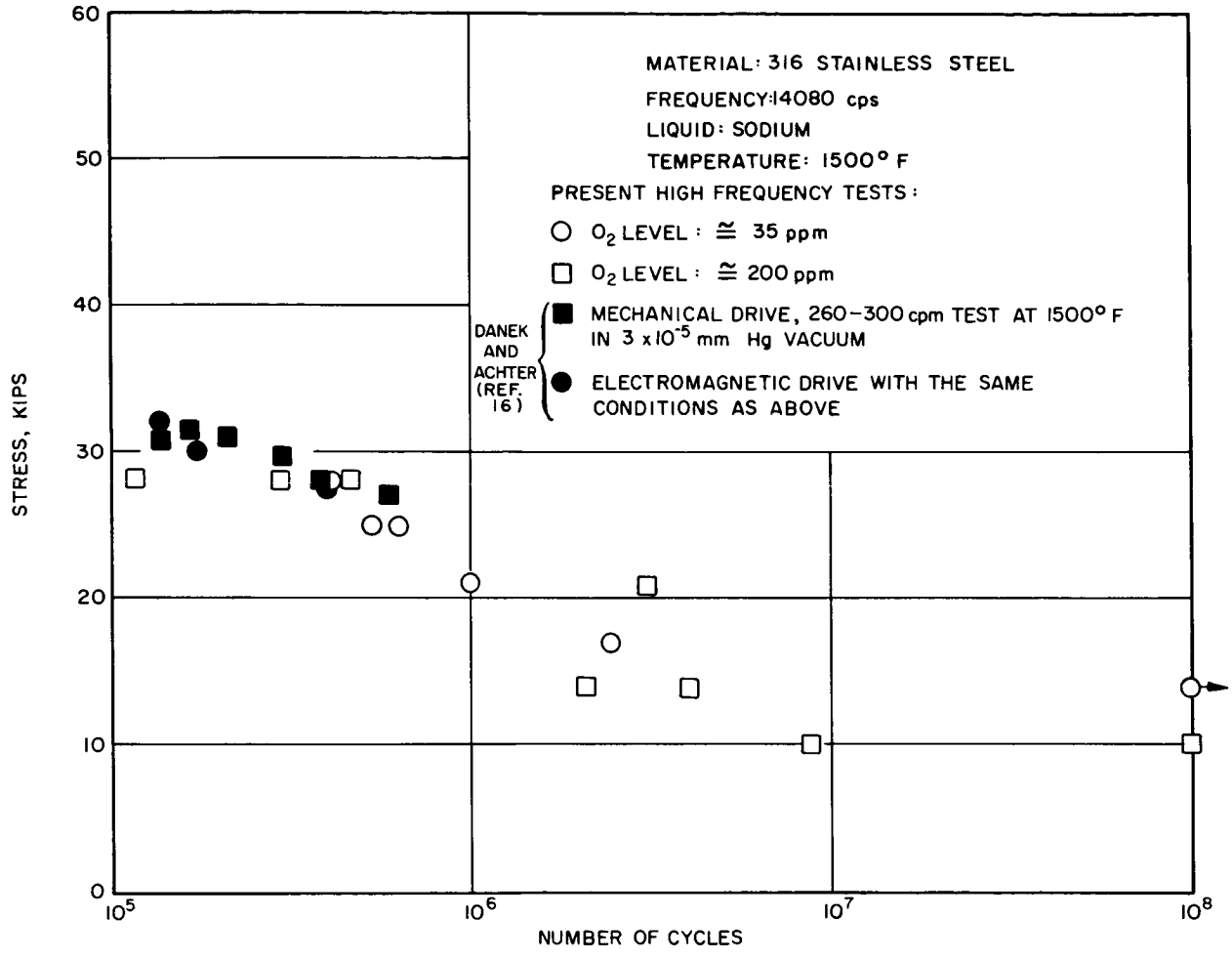


Fig. 11. Comparison of High Frequency Fatigue in 1500°F Sodium and Low Frequency Fatigue in 1500°F Vacuum

REFERENCES

1. "Handbook of Cavitation Damage," HYDRONAUTICS, Incorporated Technical Report 233-8, March 1965.

2. Preiser, H. S., Thiruvengadam, A., and Couchman, C., III, "Cavitation Damage in Liquid Sodium," HYDRONAUTICS, Incorporated, NASA CR-54072, April 1964.

3. Preiser, H. S., Thiruvengadam, A., and Couchman, C, III, "Cavitation Damage Research Facilities for High Temperatures Liquid Alkali Metal Studies," ASME Symposium on Cavitation Research Facilities and Techniques, Philadelphia, Pa., May 1964.

4. Couchman, C., III, Preiser, H. S., and Thiruvengadam, A., "Cavitation Damage in Liquid Metals," Technical Progress Report 467-1, NASA CR-54332, HYDRONAUTICS, Incorporated, March 1965.

5. Mason, W. P., "Internal Friction and Fatigue in Metals at Large Strain Amplitudes," Jour. Acoustic Soc. Am., Vol. 28, No. 6, pp. 1207-1218, 1956.

6. Plesset, M. S., "On Cathodic Protection in Cavitation Damage," Trans. A.S.M.E., Vol. 82, Series D, No. 4, Jour. Basic Engr., pp. 808-817, December 1960.

7. Neppiras, E. A., "Very High Energy Ultrasonics," British Jour. of Applied Physics, Vol. 11, pp. 143-150, April 1960.

8. Thiruvengadam, A., and Preiser, H. S., "On Testing Materials for Cavitation Damage Resistance," HYDRONAUTICS, Incorporated Technical Report 233-3, December 1963.

9. Wise, B. A., "Design of Nickel Magnetostriction Transducers," Platinum Metals and Applied Physics Section, Development and Research Division, The International Nickel Company, Inc.

10. Hueter, T. F., Bolt, R. H., "Sonics," John Wiley and Sons, Inc., New York, London, Third Printing, June 1962.

11. Fox, A., "A Comparison of Ultrasonic and Conventional Axial Fatigue Tests on Aluminum Alloy Rod," Materials Research and Standards, pp. 60-63, February 1965.

12. Thiruvengadam, A., "High Frequency Fatigue of Metals and Their Cavitation Damage Resistance," HYDRONAUTICS, Incorporated Technical Report 233-6, December 1964.

13. Thiruvengadam, A., Preiser, H. S., and Rudy, S. L., "Cavitation Damage in Liquid Metals," HYDRONAUTICS, Incorporated Technical Report 467-3, NASA CR-54459, June 1965.

14. Lyman, T, ed. Gerlach, C. H., Assoc. ed. Metals Handbook, 1954 Supplement. The Am. Soc. for Metals, p. 98, 1954.

15. Neppiras, E. A., "Techniques and Equipment for Fatigue Testing at Very High Frequencies," Proc. ASTM, Vol. 59, pp. 691-709, 1959.

16. Danek, G. J., Jr., and Achter, M. R., "A High Temperature Vacuum and Controlled Environment Fatigue Tester," ASTM Bulletin No. 234, pp. 48-52, December 1958.

SESSION 5

HEAT TRANSFER

Wednesday, September 29, 1965

CHAIRMAN: R. M. Scroggins
USAEC

N66 31693

A METHOD FOR THE DETERMINATION OF LOCAL HEAT FLUXES IN LIQUID METAL HEAT EXCHANGERS

by

Ralph P. Stein

Argonne National Laboratory

Argonne, Illinois

Abstract

A new method is presented for the determination of local heat fluxes and fully developed local overall heat transfer coefficients in liquid metal or laminar flow double-pipe heat exchangers. The method uses measurements of outer wall temperature distributions and inlet and outlet fluid temperatures. Possible application to liquid cooled or heated condensers or boilers is discussed.

Work performed under the auspices of the U. S. Atomic Energy Commission

PRECEDING PAGE BLANK NOT FILMED.

1. INTRODUCTION

One of the more difficult quantities to determine from experiments with liquid metal or laminar flow heat exchangers is the local heat flux at locations along the axial length of the exchanger. With heat transfer between turbulent non-metallic fluids local heat fluxes can usually be inferred with sufficient accuracy from inlet and outlet temperature measurements and a simple one dimensional analysis based on the assumptions that local heat transfer coefficients depend on Reynolds and Prandtl numbers only and are independent of axial position. With liquid metals and laminar flow, however, these assumptions are not usually valid;[5,6] heat transfer coefficients depend on the operating conditions of the heat exchanger in a complicated manner; a significant fraction of the total heat exchange occurs in regions where heat transfer coefficients are not independent of axial position. As a result, more direct methods are occasionally attempted - for example, by measuring two or more temperatures within the heat transfer wall at the same axial location. The difficulties associated with such measurements are well-known. It is to be expected that these difficulties will be magnified at the high liquid metal temperatures of interest today.

The purpose of this paper is to describe, and show the basis of, a method of inferring both local overall heat transfer coefficients and heat fluxes from the relatively simple and accurate measurements of temperature distributions along the outer wall of double pipe heat exchangers, as well as of inlet and outlet temperatures. Although the method is limited to regions of the exchanger along which local overall heat transfer coefficients are independent of axial position - i.e., along regions of "fully developed" heat transfer* - the method tests whether a fully developed region exists, and identifies the location and extent of this region.

The method, and its basis, can be briefly summarized as follows. When applied to double pipe heat exchangers, analyses derived from application of basic physical principles rather than from the use of heat transfer coefficients,

*In this paper, a region of fully developed heat transfer in a heat exchanger is one over which the local overall heat transfer coefficient is independent of axial position by definition.

lead to mathematical expressions for the fluid temperature distribution which involve infinite series of exponential functions of the heat exchanger axial position multipled by an "eigenvalue." As a result, when the logarithm of a suitably expressed outer wall temperature difference is plotted vs axial position, the graph becomes linear over fully developed regions - if such a region exists. The slope of the linear portion of the graph is proportional to the least non-zero, or first, eigenvalue. The first eigenvalue is found to be proportional to the fully developed local overall heat transfer coefficient. With outlet "bulk" temperatures measured and the first eigenvalue determined from the slope of the outer wall temperature graph, the local heat flux at the exchanger outlet is easily computed. The flux distribution along the length of the exchanger is then easily calculated from a simple expression applicable over the fully developed region as located by the linear portion of the outer wall temperature graph.

The method has been tested successfully with a mercury to mercury co-current flow double pipe heat exchanger.[2] Application to the counter-current flow case has not been tested yet; and, as will be seen, there are complications associated with this case that makes such tests necessary before the feasibility of the method as applied to counter-current flow can be ascertained with certainty.

An outline of the development of the method is given below as applied to both co-current and counter-current flow double pipe heat exchangers, as well as to an idealized version of a liquid metal cooled or heated condenser or boiler.

2. GENERAL CONSIDERATIONS

A double pipe heat exchanger is shown schematically in Figure 1, which also identifies some of the nomenclature to be used. As indicated, subscript "1" is used to identify quantities associated with the tube side of the exchanger, while subscript "2" refers to the annular space.

The type of analysis mentioned previously determines fluid temperature distributions as functions of both radial and axial position. Discussions of these analyses will not be given here; instead reference is made to publications that are either available in the existing heat transfer literature, or will be so shortly. For consistency with the most pertinent of these publications,[2,5,6,7,8] the same nomenclature will be used except for the axial position variable. In previous publications, a dimensionless axial position variable was defined relative to the

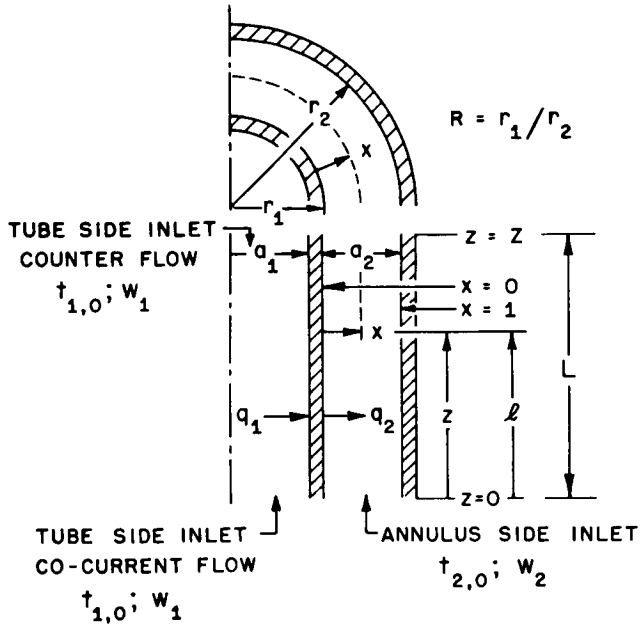


Fig. 1. Double-Pipe Heat Exchanger

tube side properties of the exchanger. Since in this paper interest is focused on temperature distributions in the annular space only, it is more convenient to define the axial position variable relative to the properties of the annulus side of the exchanger. Thus, the dimensionless axial position variable z is defined by

$$z = (4/Pe_2)(\ell/D_2) \tag{1}$$

where Pe is the Peclet number, D is the hydraulic equivalent diameter, and ℓ is distance measured from the inlet end of the annular space. A dimensionless overall heat exchanger length Z is also defined by the above with $\ell = L$.

The usual local overall heat transfer coefficient, U_2, is defined by

$$U_2 = q_2/(\bar{t}_1-\bar{t}_2) \tag{2}$$

where q_2 denotes heat flux density into the annular space from its inner surface, t denotes fluid temperature, and the over-scores refer to "bulk" (heat content or "mixing-cup" mean) values.

For convenience and for consistency with other publications, equation (1) is rewritten in dimensionless form as

$$Nu_2^o = F_2/(\bar{\xi}_1-\bar{\xi}_2) \tag{3}$$

where Nu_2^o is an overall Nusselt number based on annulus side properties and is given by

$$Nu_2^o = U_2D_2/k_2 \quad ; \tag{4}$$

F_2 is a dimensionless heat flux defined by

$$F_2 = q_2D_2/k_2(t_{2,0}-t_{1,0}) \tag{5}$$

With x denoting radial position as indicated in the figure, $\xi_i(x,z)$ represents a dimensionless fluid temperature distribution and is defined by

$$\xi_i = (t_i-t_{1,0})/(t_{2,0}-t_{1,0}) \tag{6}$$

so that

$$\bar{\xi}_i = (\bar{t}_i - t_{1,0})/(t_{2,0} - t_{1,0}) \tag{6a}$$

Note that, according to the figure and equation (6), $\xi_2(x,0) = 1$ for both co-current and counter-current flow; while $\xi_1(x,0) = 0$ for co-current flow and $\xi_1(x,Z) = 0$ for counter-current flow. Also $\xi_2(1,z)$ represents a dimensionless outer wall temperature distribution.

A simple heat balance over a differential element of axial length gives the relation

$$F_2 = \frac{1+R}{R} \frac{d\bar{\xi}_2}{dz} \tag{7}$$

where R is the ratio of the inner to the outer radius of the annular space.

The bulk temperature difference $\bar{\xi}_1 - \bar{\xi}_2$ can be expressed as a simple linear function of $\bar{\xi}_2(z)$ with the assistance of a heat balance over a finite portion of axial position. For co-current flow, the expression

$$\bar{\xi}_1 - \bar{\xi}_2 = H - (1+H)\, \bar{\xi}_2(z) \tag{8a}$$

results; while for counter-current flow

$$\bar{\xi}_1 - \bar{\xi}_2 = (H-1)\, \bar{\xi}_2(z) - H\bar{\xi}_2(Z) \quad ; \tag{8b}$$

where H is the heat capacity mass flow rate ratio defined by

$$H = \frac{C_2 W_2}{C_1 W_1} \tag{9}$$

If the overall Nusselt number Nu_2^o were known over a portion of heat exchanger length which includes either end of the exchanger, then equations (3), (7) and (8) can be combined and integrated to give a simple expression relating the flux distribution $F_2(z)$ to the inlet or outlet bulk temperature difference. This expression would, of course, be valid only over that portion of the exchanger length for which the overall Nusselt number were known. The method proposed in

this paper determines the fully developed - i.e., z independent - value of Nu_2^o from measurements of the temperature distribution along the outer wall of the annular space. The relationship between these measurements and the fully developed value of Nu_2^o will now be discussed and applications of equations (3), (7) and (8) illustrated.

3. CO-CURRENT FLOW

An analytical solution for the annulus side fluid temperature distribution in a co-current flow heat exchanger[2,5,6,7] can be written as

$$\xi_2(x,z) = H/(1+H) + \sum_{n=1}^{\infty} G_n(x)\exp.(-\alpha_n^2 z) \tag{10}$$

The annulus side bulk temperature can then be expressed as

$$\overline{\xi}_2(z) = H/(1+H) + \sum_{n=1}^{\infty} \overline{G}_n\exp.(-\alpha_n^2 z) \tag{11}$$

where $\overline{G}_n$ is the appropriate average value of the function $G_n(x)$. In the above, the α_n^2 are positive real numbers (eigenvalues) such that $\alpha_n^2 < \alpha_{n+1}^2$, and the functions $G_n(x)$ are independent of z.

By applying equation (11) to equations (3), (7) and (8a), it is easily shown that when z is sufficiently large so that all but the first term of the infinite series can be neglected, then

$$Nu_2^o = [(1+R)/R][\alpha_1^2/(1+H)] \tag{12}$$

- i.e., the heat transfer is fully developed since Nu_2^o is independent of z.

When equation (12) is valid, equation (10), as applied at the radial position x corresponding to the outer wall of the annular space - i.e., x = 1 - can be written as

$$\xi_2(1,z) \overset{\sim}{\sim} H/(1+H) + G_1(1)\exp.(-\alpha_1^2 z) \tag{13}$$

Thus, it is to be expected that a graph of log $[\xi_2(1,z) - H/(1+H)]$ vs z will become

linear for sufficiently large z. As applied to experimental data, the linear portion of such a graph - if one exists - identifies a region over which Nu_2^o is independent of axial portion - i.e., a region of fully developed heat transfer. The slope of the linear portion of this graph will be equal to $-\alpha_1^2$, from which Nu_2^o may be computed by equation (12).

With Nu_2^o known and with measured values of the fluid outlet temperatures, equation (3) can be applied to compute $F_2(Z)$, the local heat flux at the exchanger outlet.

With Nu_2^o independent of z over a known portion of the outlet end of the exchanger, equations (3), (7), (8a), and (12) can be combined and integrated to give

$$F_2(z)/F_2(Z) = \exp.[\alpha_1^2(Z-z)] \tag{14}$$

from which the local heat flux distribution can be computed over the fully developed heat transfer region. (Equation (14) can also be obtained by application of equation (11), truncated at n = 1, to equations (7) and (8a).)

4. COUNTER-CURRENT FLOW

An analytical solution for the annulus side fluid temperature distribution in a counter-current flow heat exchanger[3,4,7,8]* can be written as

$$\xi_2(x,z) = H\bar{\xi}_2(Z)/(H-1) + \sum_{n=1}^{\infty} \left\{ U_n(x,Z)\exp.(-\alpha_n^2 z) - V_n(x,Z)\exp[-\gamma_n^2(Z-z)] \right\} \tag{15}$$

*The nomenclature used in references (3) and (4) is not the same as used here. Also, these references as well as reference (7) express temperature distributions in somewhat more compact form involving both positive and negative eigenvalues. Simple redefinition of appropriate terms will give the equivalent of equation (15).

The annular side bulk temperature can then be expressed as

$$\bar{\xi}_2(z) = H\bar{\xi}_2(Z)/(H-1) + \sum_{n=1}^{\infty} \left\{ \bar{U}_n(Z)\exp.(-\alpha_n^2 z) - \bar{V}_n(Z)\exp.[-\gamma_n^2(Z-z)] \right\} \tag{16}$$

where $\bar{U}_n(Z)$ and $\bar{V}_n(Z)$ are the appropriate "x" average values of the functions $U_n(x,Z)$ and $V_n(x,Z)$. In the above the α_n^2 and γ_n^2 are positive real numbers (eigenvalues) such that $\alpha_n^2 < \alpha_{n+1}^2$ and $\gamma_n^2 < \gamma_{n+1}^2$. The functions $U_n(x,Z)$ and $V_n(x,Z)$ are independent of z and become independent of Z for sufficiently large values of Z. The relative magnitudes of the γ_n^2 and α_n^2, and the behavior of the functions $U_n(x,Z)$ and $V_n(z,Z)$ as Z becomes large, depend on whether the heat capacity mass flow rate ratio H is greater or less than unity. Because of this, it is preferable to separate these two cases.

Case of H > 1

For this case, as Z becomes large, $U_n(x,Z)$ approaches zero, while $V_n(x,Z)$ approaches a finite non-zero value; also $\gamma_1^2 < \alpha_1^2$.[8] Thus, for sufficiently large values of Z and small values of z, it is to be expected that equation (16) can be approximated by

$$\bar{\xi}_2(z) \approx H\bar{\xi}_2(Z)/(H-1) - \bar{V}_1(Z)\exp.[-\gamma_1^2(Z-z)] \tag{17}$$

Note that small values of z and large values of Z correspond to regions near the inlet to the annulus side of a "long" heat exchanger.

Application of equations (3), (7), and (8b) shows that when equation (17) is valid

$$Nu_2^o = [(1+R)/R][\gamma_1^2/(H-1)] \tag{18}$$

- i.e., the heat transfer is fully developed. Under these conditions, equation (15) as applied to the outer wall of the annular space - i.e., at x = 1 - can be written as

$$H\bar{\xi}_2(Z)/(H-1) - \xi_2(1,z) \overset{\sim}{\sim} V_1(1,Z)\exp[-\gamma_1^2(Z-z)] \tag{19}$$

Thus, it is to be expected that for $H > 1$ and sufficiently large Z a graph of $\log[H\bar{\xi}_2(Z)/(H-1) - \xi_2(1,z)]$ vs z will become linear in regions close to and including the inlet to the annulus side of the exchanger. As applied to experimental data, the linear portion of such a graph, if one exists, identifies a region over which the heat transfer is fully developed. The slope of the linear portion of this graph will be equal to γ_1^2 from which Nu_2^o can be computed by equation (18).

With Nu_2^o known and with measured values of fluid inlet and outlet temperatures, equation (3) can be applied to compute $F_2(0)$, the local heat flux at the inlet to the annulus side of the exchanger. With Nu_2^o independent of z over a known portion of the annulus inlet end of the exchanger, equations (3), (7), (8b), and (18) can be combined and integrated to give

$$F_2(z)/F_2(0) = \exp.(\gamma_1^2 z) \tag{20}$$

from which the local heat flux distribution can be computed over the fully developed region.

Case of $H < 1$

For this case, as Z becomes large, $U_{n_2}(x,Z)$ approaches a finite non-zero value, while $V_n(x,Z)$ approaches zero; also, $\alpha_1^2 < \gamma_1^2$.[8] Thus, for sufficiently large values of both Z and z, it is to be expected that equation (16) can be approximated by

$$\bar{\xi}_2(z) = - H\bar{\xi}_2(Z)/(1-H) + U_1(x,Z)\exp.(-\alpha_1^2 z) \tag{21}$$

Note that large values of both z and Z correspond to regions near the outlet of the annulus side of a "long" heat exchanger.

As before, when equation (21) is valid, the heat transfer is fully developed, but now

$$Nu_2^o = [(1+R)/R][\alpha_1^2/(1-H)] \tag{22}$$

and

$$\xi_2(1,z) + H\bar{\xi}_2(Z)/(1-H) \overset{\sim}{\nu} U_1(1,Z)\exp.(-\alpha_1^2 z) \tag{23}$$

Thus, it is to be expected that for $H < 1$ and sufficiently large Z, a graph of $\log [\xi_2(1,z) + H\bar{\xi}_2(Z)/(1-H)]$ vs z will become linear in regions close to and including the outlet of the annulus side of the exchanger. As applied to experimental data, the linear portion of such a graph, if one exists, identifies a region over which fully developed heat transfer exists. The slope of the linear portion of this graph will be equal to $-\alpha_1^2$ from which Nu_2^o can be computed by equation (22). As before $F_2(Z)$ is computed from equation (3) and equations (3), (7), (8b), and (22) when combined and integrated give

$$F_2(z)/F_2(Z) = \exp[\alpha_1^2(Z-z)] \tag{24}$$

from which the local heat flux distribution can be computed over the fully developed region.

Feasibility

The feasibility of the procedure as applied to actual counter-current flow data depends on the rapidity with which the functions $U_1(x,Z)$, when $H > 1$, and $V_1(x,Z)$, when $H < 1$, approach zero as Z becomes large. If these functions do not approach zero at a rate sufficiently rapid to justify equations (17) and (21) in ranges of practical interest, then the outer wall temperature graphs will not become linear at the appropriate ends of the exchanger. Under some conditions, linearity might be obtained along the central regions of the exchanger. In such cases, equation (18) or (22) will still be valid and will allow a determination of the fully developed local overall heat transfer coefficient as well as the location and extent of the fully developed region. It will not be possible, however, to obtain the magnitude of the local heat flux, although the relative flux distribution over the fully developed region can still be computed from expressions similar to equations (20) and (24). The results of computations, now in progress, and of experiments, planned for the near future, are needed before more definitive statements of feasibility are possible.[1]

The case of H = 1 is a special one - at least in a mathematical sense. Analytical solutions appear to have a form similar to equation (15) but include a term linear in z. As to be expected, for H = 1 the heat flux distribution is uniform over at least the central regions of the exchanger - but further work is required before the behavior at the ends of the exchanger are understood.

5. AN IDEALIZED CONDENSER OR BOILER

When the tube side fluid is a vapor-liquid mixture with either condensation or evaporation taking place as a result of heat exchange with a liquid metal flowing through the annular space, then $\bar{\xi}_1$ will be equivalent to a dimensionless saturation temperature. If pressure changes along the tube are sufficiently small, $\bar{\xi}_1$ may be considered to be independent of axial position and assigned a value of zero.

If it is now assumed that condensing or boiling heat transfer coefficients are either independent of axial postion or very large compared to tube conductance and/or annulus heat transfer coefficients, then an analytical solution for the annulus side fluid temperature distribution is easily obtained[7] and can be written as

$$\xi_2(x,z) = \sum_{n=1}^{\infty} G_n(x)\exp.(-\alpha_n^2 z) \tag{25}$$

As in the previous cases, it is easily shown that when z is sufficiently large so that all but the first term in the infinite series of equation (25) can be neglected, then

$$Nu_2^o = (1+R)\alpha_1^2/R \tag{26}$$

- i.e., the heat transfer is fully developed. Also, equations (12), (13), and (14) of the co-current flow case with H = 0 apply, so that the same procedures based on outer wall temperature distribution measurement can be used.

The idealizations upon which the validity of equation (25) depend may in some - if not most - cases be satisfactory approximations only beyond some unknown axial distance from the actual inlet. In such cases the procedures still apply, since the linearity and interpretation of the slope of the outer wall temperature graph, as well as equation (14), do not require that the actual location defining $z = 0$ be known.

6. CONCLUDING REMARKS

In addition to the determination of the existence, extent, and location of the fully developed region, the outer wall temperature graph can also be used to determine the relative local heat flux distribution directly. Equations (14), (20), and (24), when plotted as the logarithm of the local heat flux ratio vs z, will have the same slope as the outer wall temperature graph in the fully developed region. As a result, a line drawn parallel to the linear portion of the outer wall temperature graph and intersecting the logarithm of unity at the appropriate value of z, will give the relative local heat flux as a function of z along the fully developed region. Graphical constructions of this kind are illustrated in figures 2 and 3. In these figures, the appropriate outer wall temperature difference is denoted by θ. For the co-current flow heat exchanger, and idealized condenser or boiler

$$\theta = \xi_2(1,z) - H/(1+H) \tag{27}$$

(For the condenser or boiler, $H = 0$).
For the counter flow heat exchanger,

$$\theta = H\bar{\xi}_2(Z)/(H-1) - \xi_2(1,z) \tag{28}$$

when $H > 1$; and

$$\theta = H\bar{\xi}_2(Z)/(1-H) + \xi_2(1,z) \tag{29}$$

when $H < 1$.

Figure 4 illustrates a possible outer wall temperature difference graph for counter flow with $H < 1$, but with Z not sufficiently large.

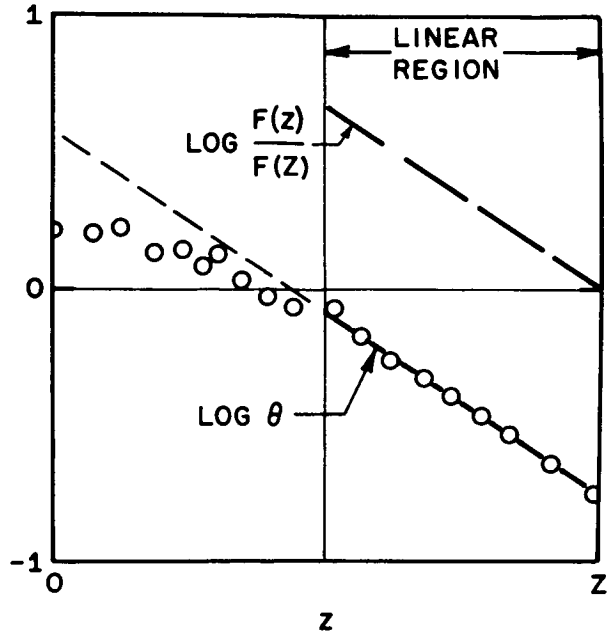


Fig. 2. Possible Outer Wall Temperature Difference Graph for Co-Current Flow or Counter Flow with H < 1

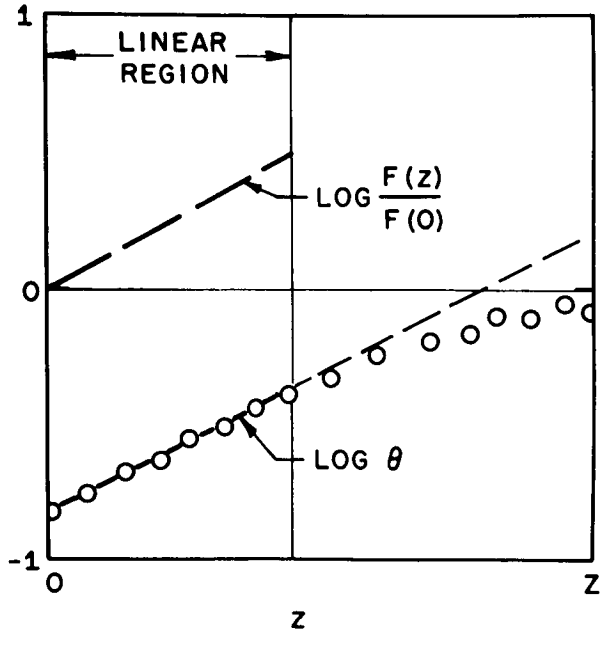


Fig. 3. Possible Outer Wall Temperature Difference Graph for Counter Flow with H > 1

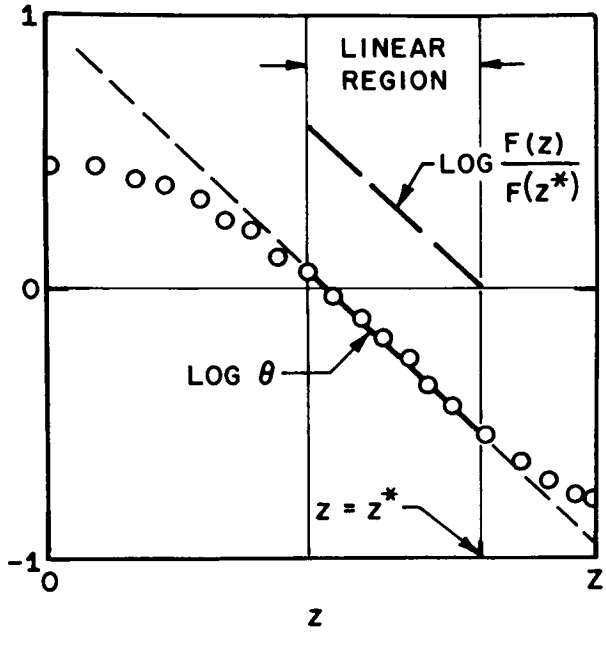


Fig. 4. Possible Outer Wall Temperature Difference Graph for Counter Flow with H < 1 and Z not Sufficiently Large

Nomenclature

a	width of annulus, or tube radius, ft
C	heat capacity, Btu/(lbm)(^{o}F)
D	equivalent hydraulic diameter, ft ($D = 2a$)
F	dimensionless local wall heat flux, eq. (5)
H	heat capacity mass flow rate ratio, eq. (9)
k	fluid thermal conductivity, Btu/(hr)(ft)(^{o}F)
ℓ	axial position, ft
L	heat exchanger length, ft
Nu^{o}	Nusselt number based on local overall heat transfer coefficient, eq. (4)
Pe	Peclet number, $D\bar{u}/\alpha$
q	local wall heat flux, Btu/(hr)(ft^2)
R	annulus radius ratio (inner radius divided by outer radius)
t	fluid temperature, ^{o}F
$\bar{u}$	average fluid velocity, ft/hr
U	overall heat transfer coefficient, eq. (2), Btu/(hr)(ft^2)(^{o}F)
W	mass flow rate, lbm/hr
x	relative radial position
z	dimensionless axial position, eq. (1)
Z	dimensionless exchanger length, eq. (1) with $\ell = L$.
α	thermal diffusivity, ft^2/hr
α_n, γ_n	eigenvalues
θ	dimensionless outer wall temperature difference, eqs. (27), (28), and (29)
ξ	dimensionless fluid or wall temperature, eq. (6)

Subscripts

1	tube side
2	annulus side
o	inlet

An over-score denotes a bulk average value.

Acknowledgement

The research, upon which the material in this paper is based, is performed under the auspices of the United States Atomic Energy Commission, Division of Reactor Development, Engineering Development Branch.

References

(1) Brown, R. W. Jr., Ph.D. Thesis Research, Notre Dame, in progress at Argonne National Laboratory (Sept. 1965).

(2) Merriam, R. L., "An Investigation of Liquid Metal Heat Transfer in a Co-Current Flow Double Pipe Heat Exchanger," ANL-7056 (In Press). M.S. Thesis, Marquette University, June 1965.

(3) Nunge, R. J. and W. N. Gill, "Analysis of Heat or Mass Transfer in Some Counter Current Flows," Int. J. Heat Mass Transfer, 8, 873 (1965).

(4) Nunge, R. J., W. N. Gill, and R. P. Stein, "On Local Heat Transfer Effects in Counterflow Parallel Plate Heat Exchangers," Research Results Ms. 65-263, Ind. Eng. Chem., 57, No. 9 (Sept. 1965).

(5) Stein, R. P., "Heat Transfer Coefficients in Liquid Metal Co-Current Flow Double Pipe Heat Exchangers," in Proceedings of 1963 High Temperature Liquid-Metal Heat Transfer Technology Meeting, Vol. 1, p. 194, ORNL-3605 (1964).

(6) Stein, R. P., "The Graetz Problem in Co-Current Flow, Double-Pipe Heat Exchangers," ANL-6889 (1964).

(7) Stein, R. P., "Liquid Metal Heat Transfer," in Advances in Heat Transfer, Vol. III, (T. F. Irvine and J. P. Hartnett, Eds.) Academic Press, New York (In Press).

(8) Stein, R. P., "Mathematical and Practical Aspects of Heat Transfer in Double-Pipe Heat Exchangers," in preparation for Third International Heat Transfer Conference, Aug. 1966.

N66 31694

EXISTENCE OF NON-EQUILIBRIUM, INVERSE TEMPERATURE PROFILE IN BOILING TWO-PHASE FLOW*

John C. Chen
Brookhaven National Laboratory
Upton, New York

(Paper presented by O. E. Dwyer)

*This work was performed under the auspices of the U.S. Atomic Energy Commission.

The results of recent experiments with boiling two-phase flow of potassium indicate the existence of an inverse temperature profile in the two-phase fluid. This note presents some of the results and a theoretical explanation for this phenomenon.

Experiment

Wall and fluid temperatures were measured for vertical, axial flow of potassium vapor and liquid through a boiling section. As shown in Figure 1, twelve thermocouples were used to measure temperatures at various radial positions in the boiler wall, and three immersion thermocouples located at the axis of the pipe were used to measure the fluid temperature. The test section was installed in a pumped loop which supplied potassium vapor-liquid mixtures at controlled temperatures, pressures, flow rates, and qualities.

Figure 2 shows temperature data collected for three sample boiling runs. Temperatures measured in the wall and in the fluid are plotted against the log of the radial position. Runs B-12b and B-9b represent the "normal" situation where the i.d. wall temperature is higher than the fluid temperature. Run B-11b represents the unexpected situation where the wall temperature is lower than the fluid center line temperature. This inverse temperature profile actually was found for a majority of the runs in this particular series of tests. The ranges of variables covered in the test were:

Mass velocity 3 to 10 x 10^5 lb/hr-ft^2

Potassium temperature - 1510° to 1650°F

Boiling pressure - 28 to 42 psia

Vapor quality - 0.7 to 17.0%

Boiling heat flux - 10,200 to 81,700 Btu/hr-ft^2

The measured difference between i.d. wall temperature and fluid core temperature, $(T_w - T_o)$, ranged from +4.2° to -9°F.

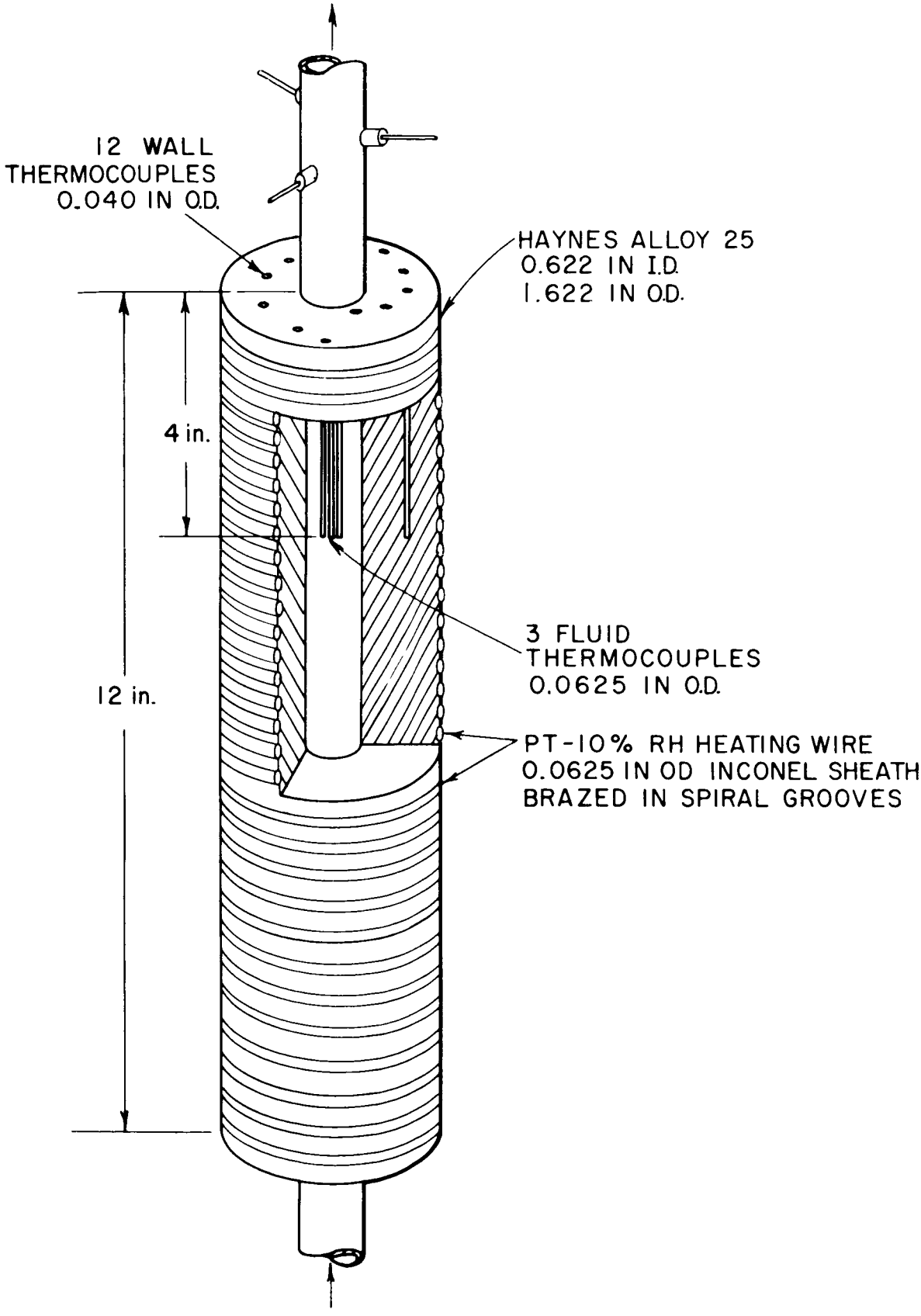


Fig. 1. Test Section I

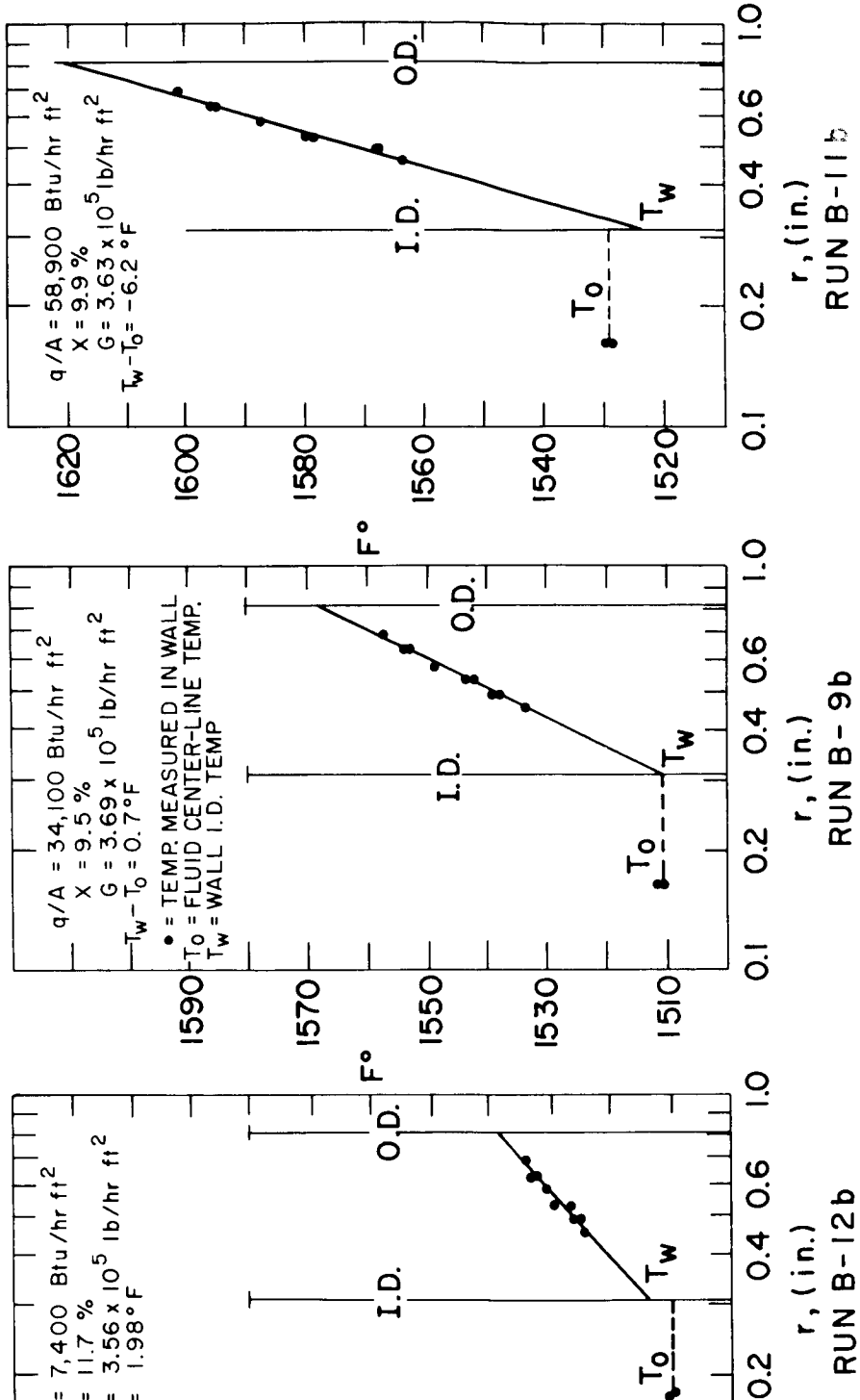


Fig. 2. Temperature Profiles in Test Section

The runs with negative temperature differences were first thought to be in error, but repeated checks of the experimental method and equipment served only to verify the phenomenon. Heat fluxes calculated from the slope of the temperature gradient in the wall were in agreement with input power measurements. Repeated thermocouple calibrations made no apparent difference. With the large number of thermocouples used in determining the wall temperatures, the degree of uncertainty in the extrapolated i.d. wall temperature was much smaller than the negative temperature differences obtained. Most important, runs with single phase flow gave positive temperature differences of up to $30^{o}F$, as expected. The measured single phase Nusselt numbers agreed with the recent data of Baker and Sesonske[1] and with the theoretical predictions of Dwyer.[2]

It was finally concluded that the observed negative temperature differences represent a true phenomenon.

Theory

All the runs with negative temperature differences were in the quality range of 9 to 17%. At the test pressures, two-phase flow of this quality would be of the annular type where the vapor flows in a central core (with varying amounts of entrainment) and the liquid flows in an annular film on the pipe wall. Figure 3a shows the postulated radial temperature profile for cases where a negative temperature difference exists. With net heat input there must be a temperature drop through the liquid film to a vapor-liquid interface temperature which would be close to, or equal to, the saturation temperature, T_s. It is often assumed that the vapor temperature in the core stays approximately constant at the saturation temperature throughout the vapor cross section, as shown by the dotted line in Figure 3a. However, since the measured core temperature, T_o is higher than

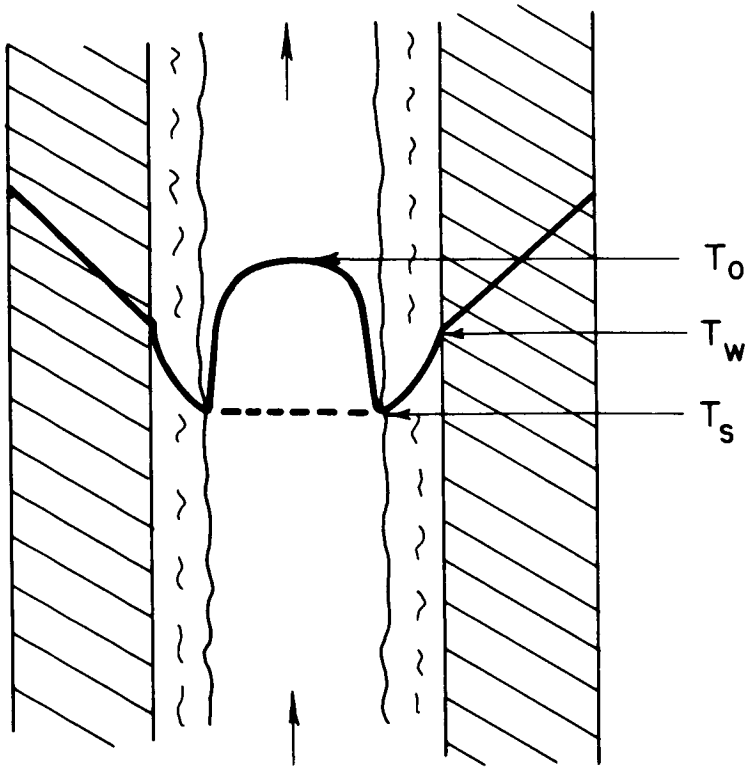


Fig. 3a

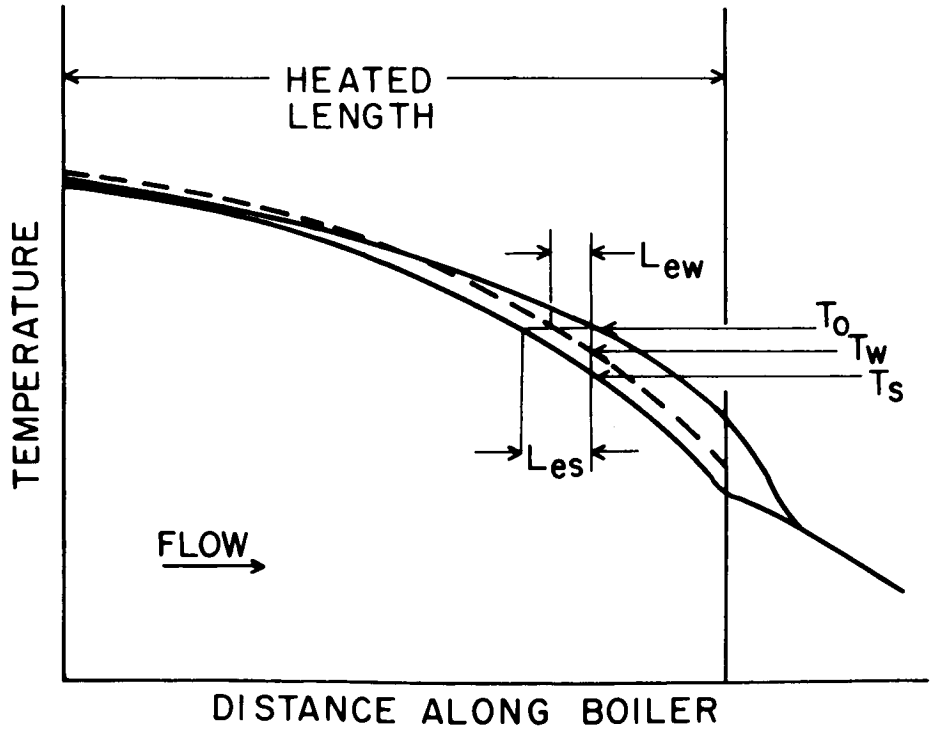


Fig. 3b

Temperature Profiles in Boiling Two-Phase Flow

the i.d. wall temperature, the profile must then necessarily invert and rise from the value T_s at the interface to the value T_o at the center line of the vapor core. This implies that the vapor core exists in a superheated state relative to the local pressure. The question is then, what is the mechanism causing the vapor core to be at this higher-temperature, non-equilibrium state.

The answer can be found in an examination of the axial temperature profile along the boiler, as shown in Figure 3b. Associated with the pressure drop through the boiler there is a corresponding decrease in saturation temperature from inlet to outlet. With net vapor generation, both the quality and the differential drop increase toward the exit end of the boiler so that the axial profile of the saturation temperature is concave downward as shown in the figure. In accordance with the second law of thermodynamics, the inside wall temperature must be greater than the saturation temperature at any axial position, as shown by the dotted curve in Figure 3b. If the two-phase fluid enters the boiler at equilibrium then the vapor temperature at the boiler entrance would be equal to the saturation temperature. As the vapor flows through the boiler it sees a cooler liquid annulus and must necessarily give up sensible heat, cooling as it flows through the boiler. Where there is high slip and high vapor velocity, it is conceivable that the vapor reaches the measurement point from an upstream higher temperature point before it can reach equilibrium with the local temperature. The vapor temperature profile for this case would then rise from the saturation temperature in the vicinity of the liquid interface through a boundary layer to some superheat value represented by T_o in the central core. This would account for the observed inverse temperature profile for boiling two-phase

flow by associating heat transfer from the wall to the liquid annulus with non-equilibrium cooling of the vapor core. The heat transferred to the liquid is converted into latent heat by bubble nucleation and growth and/or by evaporation at the liquid-vapor interface.

Factors which could be expected to enhance this non-equilibrium effect are high pressure drop through the boiler, a steep vapor temperature-pressure curve, high slip, high vapor velocity, and high liquid thermal conductivity. Factors which would tend to diminish this non-equilibrium effect are liquid entrainment in the vapor core, increased turbulent mixing, destruction of the annular flow pattern, and increased vapor thermal conductivity. The existence and degree of the non-equilibrium, inverse temperature profile are then governed by a balance of these various factors. The properties of alkali metals uniquely satisfy the conditions which enhance this non-equilibrium effect. Thus, comparing potassium to water at 1 atm pressure, the vapor pressure curve of potassium is four times steeper than that of water, slip ratios in two-phase flow have been measured to be orders of magnitude higher for potassium than for water,[3] vapor velocities at the same total flow rate and at the same quality are much greater for potassium, and the liquid thermal conductivity of potassium is 45 times that of water. It is likely due to these factors that the inverse temperature profile phenomenon has not been reported in earlier experiments with two-phase boiling flow of water. Heretofore, other experimenters with boiling liquid metals have not attempted to measure the fluid core temperature and so were not able to observe this effect.

The superheat difference between T_o and T_w or T_s represents some equilibrium distance as illustrated in Figure 3b. This equilibrium distance has been calculated for the data and is

plotted in Figure 4 as a function of acceleration pressure drop in the boiling test section. There appears to be a trend for increasing equilibrium distance with increasing pressure drop, as would be expected. For an average equilibrium distance of approximately 5 in. the vapor residence time was calculated to be of the order of 1 to 2 milliseconds. This short time supports the assumption that the vapor can travel from an upstream point to the measurement point before it reaches equilibrium with the local temperature.

Verifying Experiment

A second series of experiments, using a different test section, was carried out to test this hypothesis of an inverse temperature profile. The second test section was similar to the first but was constructed from Ni, had a smaller inside diameter (0.300 in.) and a thicker wall (1.35 in.), and was radiantly heated. Twelve thermocouples were located in the wall in the same manner as shown in Figure 1. Two in-fluid thermocouples were located at the same axial plane but at different radial positions, as indicated in Figure 5. One was placed at the centerline to measure core temperature, T_o, and the second was placed against the i.d. to measure temperature of the fluid film near the wall, T_f. In this manner, it was possible to measure two points on the temperature profile and thus obtain a direct indication of whether or not temperature inversion occurs in the two-phase stream. The ranges of variables covered in the second series of experiments were:

Mass velocity	4 to 8 x 10^5 lb/hr-ft^2
Potassium temperature	1370^o to 1515^oF
Boiling pressure	12.2 to 24.9 psia
Vapor quality	1.9 to 9.4%
Boiling heat flux	5000 to 91,500 Btu/hr-ft^2

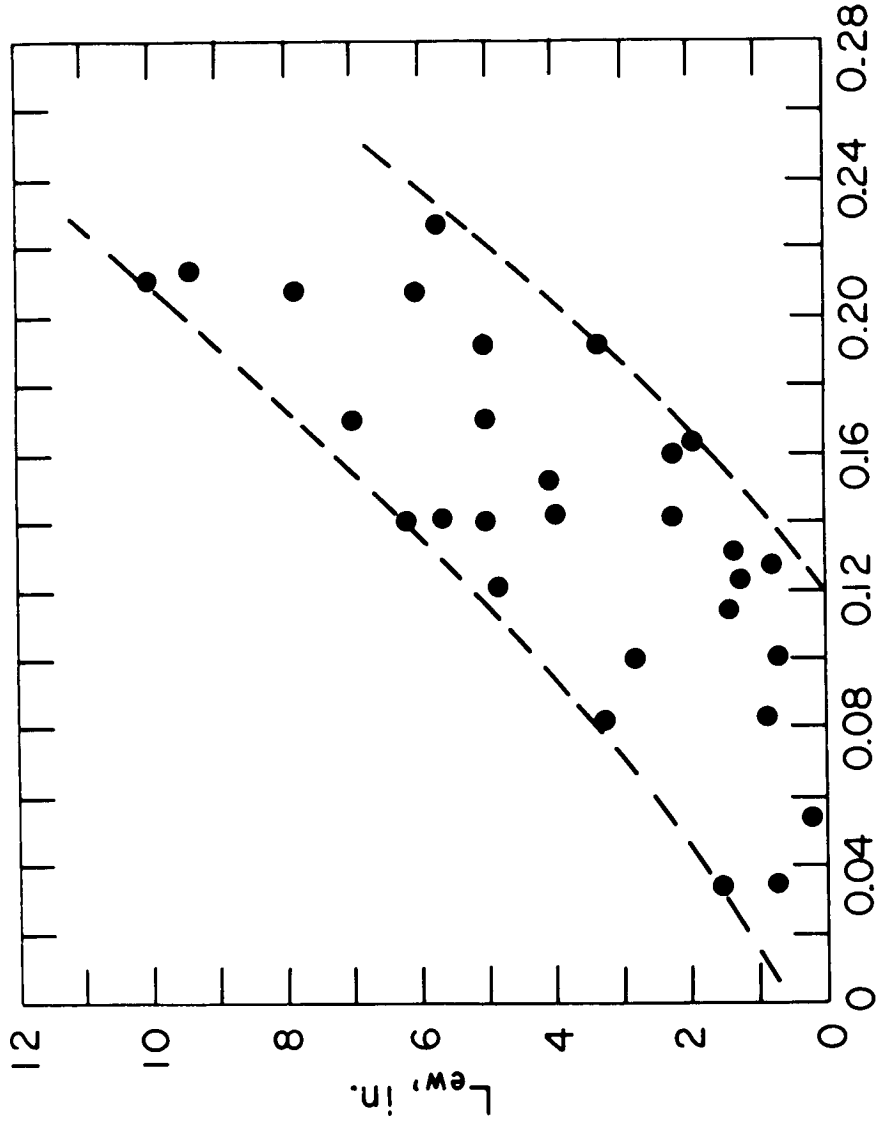


Fig. 4. Equilibrium Distances

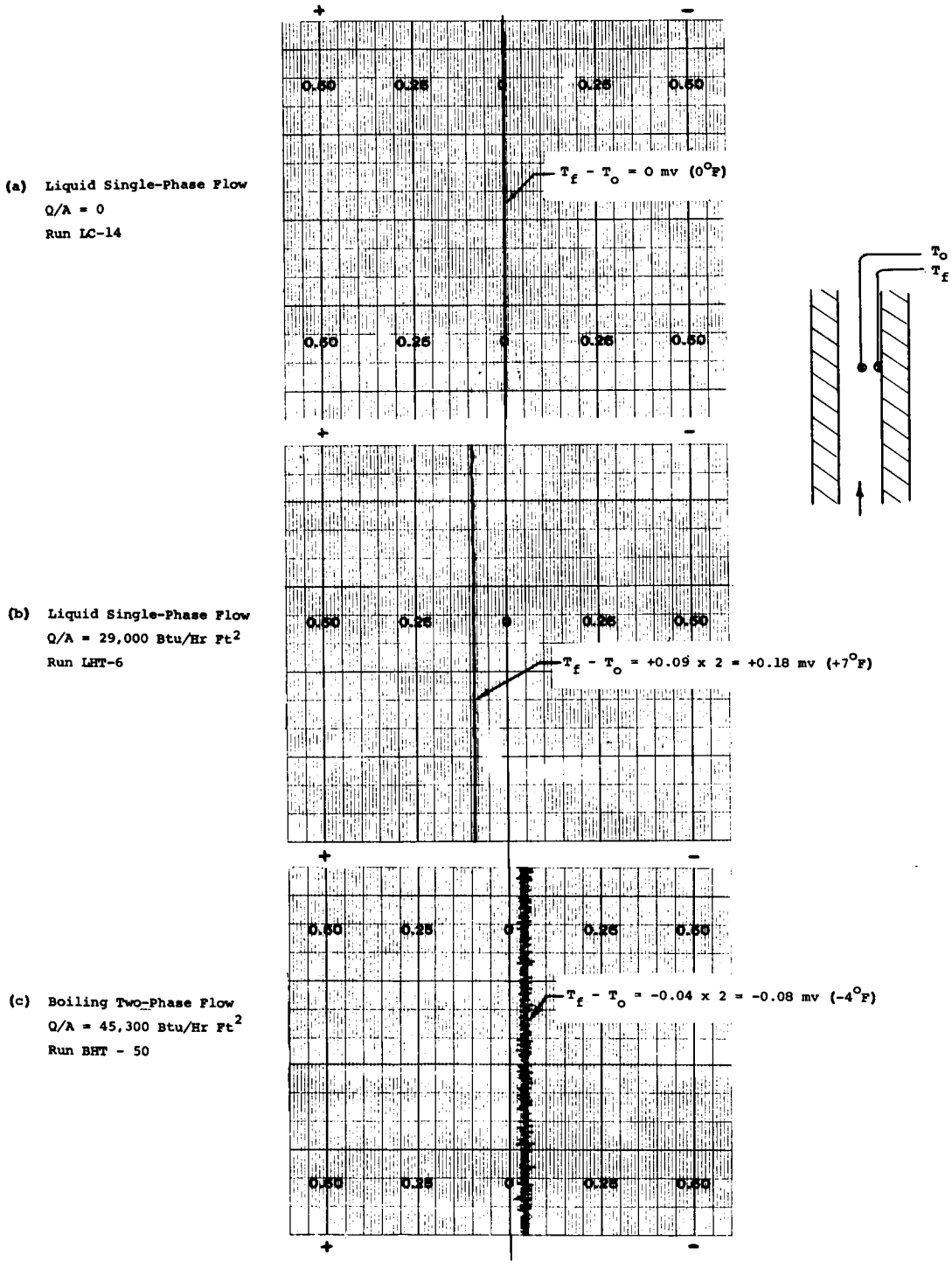


Fig. 5. Instrument Traces of Temperature Difference

A number of runs were also made with single-phase (liquid) flow, under both adiabatic and net heat input conditions, for comparison to the two-phase runs.

Results of this second series indeed verified the existence of an inverse temperature profile with two-phase flow. This is illustrated in Figure 5 which shows sample recorder traces of the temperature difference $T_f - T_o$. For single-phase, adiabatic flow the difference is zero as it should be. For single-phase flow with heat input, $T_f - T_o$ is positive, indicating a normal temperature profile. For boiling two-phase flow, $T_f - T_o$ is seen to oscillate about a mean value which is definitely negative, indicating an inverse temperature profile. Figure 6 gives further examples of experimental results, showing the types of temperature profiles measured in the wall and in the fluid for both single-phase and two-phase heat transfer. The inversion of fluid temperature profile in the case of two-phase flow is indicated by the dotted curves. All the two-phase runs in this second series of tests showed this inverse profile.

Summary

Experimental results indicate the presence of an inverse temperature profile in boiling liquid-metal, two-phase flow. This phenomena can be caused by a non-equilibrium condition in the vapor core which is accentuated by high pressure drop, a steep vapor temperature-pressure curve, and high velocity-high slip flow. Such an inverse profile is sufficiently different from the normally assumed picture heretofore that it can have an important bearing on the understanding and general theory of convective boiling. Further efforts to check and document this phenomenon are under way.

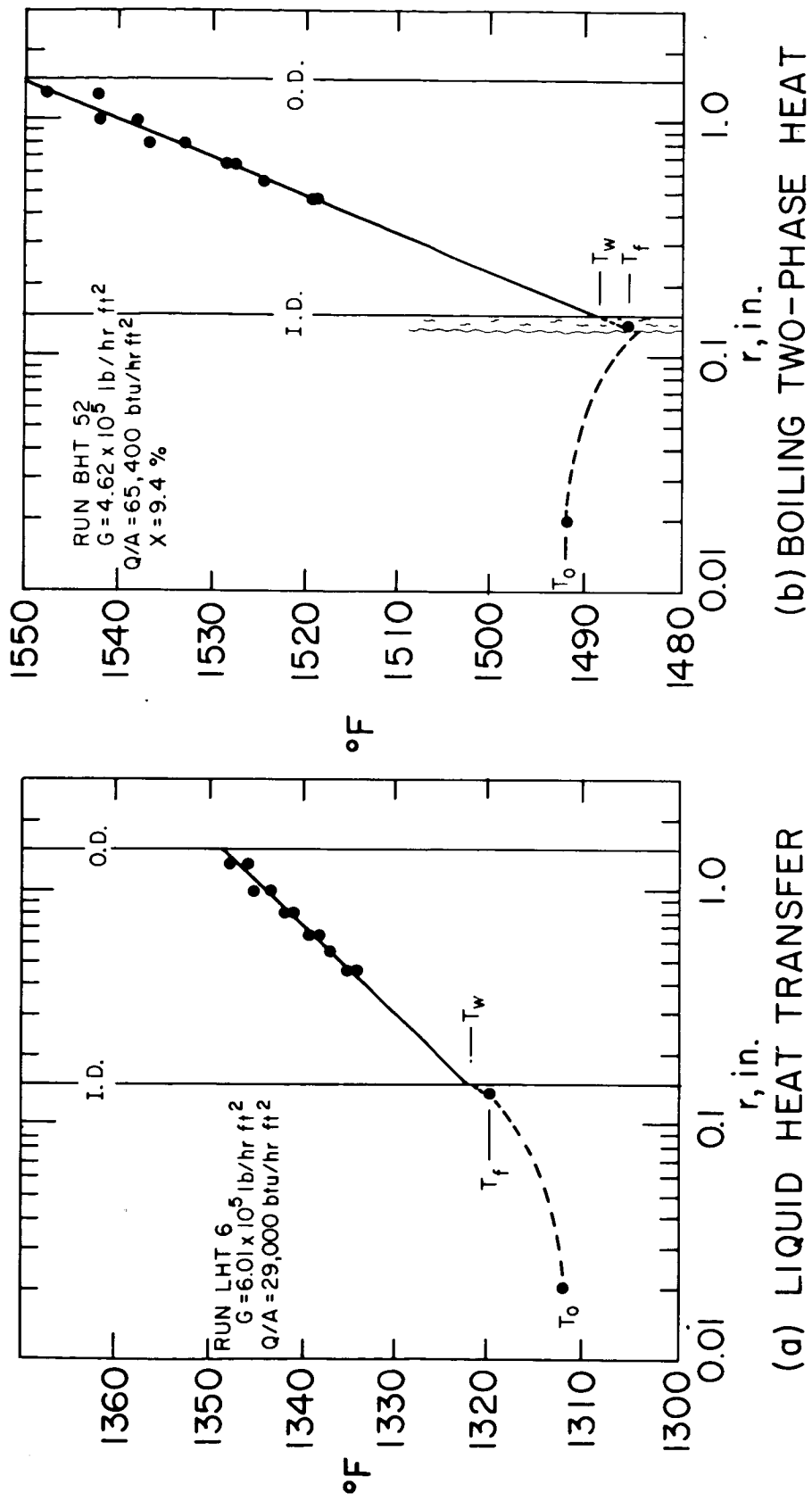


Fig. 6. Boiling Temperature Profiles Measured in Test Section II

Acknowledgments

The invaluable help of Mr. S. Kalish and Mr. P. Hlavac, heat transfer engineers, during operation of the test facility is gratefully acknowledged, as is the general guidance and many helpful suggestions given by Dr. O. E. Dwyer.

References

1. Baker, R. A., and Sesonske, A., Nuclear Science and Engineering 13, No. 3 (1962).
2. Dwyer, O. E., AIChE Journal 9, 261 (1963).
3. Smith, L. R., (with Prof. R. E. Balzhiser), "A Study of Pressure Drops and Void Fractions in Horizontal Two-Phase Flows of Potassium," Ph.D. Dissertation at the University of Michigan (1964).

EXPERIMENTAL STUDIES OF BOILING OF SODIUM AND CONDENSING OF POTASSIUM

James P. Lewis

National Aeronautics & Space Administration

Lewis Research Center

Cleveland, Ohio 44135

This paper was presented orally at the conference by the author but was not available for publication.

N66 31695

SUPERHEAT WITH BOILING ALKALI METALS*

J. A. Edwards§ and H. W. Hoffman
Oak Ridge National Laboratory
Oak Ridge, Tennessee

(Paper presented by H. W. Hoffman)

ABSTRACT

The results of experiments in a natural-circulation loop to establish the magnitude of the superheat associated with alkali-metal boiling are reported. For potassium boiling on an as-received (commercially smooth) surface, the superheat measured ranged from 500°F at a saturation temperature of 1500°F down to 230°F at T_{sat} = 1770°F. Wall-temperature oscillations, which occur in the presence of these large superheats because of the unusual thermal properties of the liquid metals, were of the order of 170 to 300°F at a frequency of 1.5 cycles/min. Because of maximum surface temperature limitations, sodium could not be boiled on this surface.

Significant reductions in the magnitude of the superheat and, hence, in the amplitude of the wall temperature oscillations were effected by modifying the boiler surface. Thus, on a surface containing eight 0.006-in. diameter × 0.040-in.-deep cylindrical holes, the superheat with potassium was reduced about fortyfold below the value obtained on the as-received surface. A porous surface, formed by sintering of stainless steel particles on the inside tube surface, was less effective than the surface with discrete holes but still showed appreciable reductions in the superheat. Similar results were obtained with sodium.

Over the limited range of these experiments, the superheat data for both potassium and sodium correlate reasonably with predictions based on a model involving a spherical vapor bubble in thermal equilibrium within a liquid pool of uniform temperature.

*Research sponsored by the U. S. Atomic Energy Commission under contract with the Union Carbide Corporation.

§ORINS Summer Research Participant; Professor of Engineering Mechanics, North Carolina State University, Raleigh, North Carolina.

PRECEDING PAGE BLANK NOT FILMED.

INTRODUCTION

Experiments with potassium boiling under pool, natural-circulation, or forced-convection conditions have indicated that large superheats are associated with the boiling process in alkali liquid metals. An initial calculation by Krakoviak,[1] reported at the preceding conference on liquid-metal technology, suggested that for potassium the superheat for bubble initiation should lie in the range 125 to 375°F and for sodium, between 250 and 775°F. Since the first presentation by Krakoviak in 1963, we have quantitatively measured the superheat in experiments with pool and natural-circulation systems and have demonstrated agreement with predictions. At the same time, we have refined and extended our analyses as our understanding of the mechanisms of bubble formation and growth in a liquid-metal environment and of the role of the surface in boiling has developed. While some of these studies have been reported previously,[2-4] a brief review of the theory and a description of the experimental apparatus is appropriate.

SUPERHEAT PREDICTION

A force balance on a spherical bubble in thermal equilibrium within a liquid of uniform temperature yields:

$$P_v - P_\ell = \frac{2\sigma}{r} , \qquad (1)$$

where P_v is the pressure within the bubble; P_ℓ, the liquid pressure outside the bubble; σ, the surface tension at the interface; and r, the bubble radius. Thermal equilibrium requires that the vapor temperature equal the temperature of the surrounding liquid ($T_v = T_\ell$). The vapor temperature also corresponds to a saturation temperature associated with the pressure in the bubble ($T_v = T_{sat,P_v}$). Hence, since the pressure in the bubble exceeds the liquid pressure (by a $2\sigma/r$ at equilibrium), the liquid must be superheated — i.e., T_ℓ must exceed the saturation temperature, $T_{sat,P_\ell} \equiv T^*_{sat}$, associated with P_ℓ.

The magnitude of this superheat can be estimated directly from Eq. (1), following the above reasoning, using experimentally determined vapor pressures and assumed values for T_ℓ and r. Alternatively, the superheat can be expressed

explicitly as a temperature difference by combining Eq. (1) with the integrated Clausius-Clapeyron equation;* thus

$$\Delta T_{sat} = T_v - T^*_{sat} = \frac{R_v T_v T^*_{sat}}{h_{fg}} \ell n \left(1 + \frac{2\sigma}{r P^*_{sat}}\right) , \qquad (2)$$

where T_v is the vapor temperature at the pressure, P_v; T^*_{sat}, the liquid saturation temperature at the pressure, $P_\ell \equiv P^*_{sat}$; R_v, the gas constant; and h_{fg}, the latent heat of vaporization at the temperature, $T_v = T_\ell$. In this derivation, we assume that the perfect gas approximation (relating T and P along the saturation line) is valid and that the liquid specific volume may be neglected in comparison with the vapor volume.‡ For small values of the superheat and of the pressure ratio $(2\sigma/r)/P^*_{sat}$, Eq. (2) may be written in the approximate form:

$$\Delta T_{sat} = \frac{2 R_v (T^*_{sat})^2 \sigma}{h_{fg} r P^*_{sat}} . \qquad (3)$$

In applying Eqs. (2) and (3), T_v (and hence T_ℓ) is taken to be the measured wall temperature and r, the effective radius of the surface cavities (nucleation sites). Thus, Eq. (1) describes the maximum superheat (sin β = 1)§ and, hence, possibly overpredicts the superheat. Measurement of the contact angle with the alkali liquid metals is needed before compensation for this factor can be included in the analysis. On the other hand, temperature gradients in the liquid near the heater surfce and adjacent to the bubble interface lead to an average liquid temperature which is less than the measured wall temperature and, hence, to experimental values for the superheat which are greater than those predicted for cavities of a given radius. Data obtained in this study with a cavity of known size demonstrate this effect.

*The Clausius-Clapeyron relation applies correctly only along the saturation line where $P_v = P_\ell$; a rigorous thermodynamic formulation pointed out by R. N. Lyon requires that $(\partial P_v/\partial T)_{P_\ell} = \Delta S/V_v$ but complicates the computation of the superheat.

‡Since $V_v/V_\ell \sim 1300$ at the atmospheric boiling temperature (1394°F), there is ample justification for the latter assumption. Further, as seen in the footnote above, only V_v enters in the rigorous thermodynamic presentation.

§For bubbles nucleating at a surface cavity, $\Delta P = (2\sigma/r) \sin \beta$, where β is the angle of contact between the bubble and the surface measured with respect to a normal to the surface.

If Eq. (1) when coupled with reliable data on the vapor pressure is accepted as correctly predicting the superheat, the errors introduced by the assumptions necessary to the development of Eqs. (2) and (3) can be assessed. The results of a comparison of superheats caclulated using these three equations are given in Table 1 for three cavity sizes at two saturation temperatures.

Table 1. Comparison of Calculated Superheats for Potassium

Method of Calculation	Superheat, ΔT_{sat}						
	T_{sat} (°R) →	1860			2260		
	r (in.) →	10^{-3}	10^{-4}	10^{-5}	10^{-3}	10^{-4}	10^{-5}
Eq. (1)[a,b]		9.5[c]	80	390	2.2	21.6	179
Eq. (2)		9.5	80	385	2.2	21.3	178
Eq. (3)		13.2	132	1320	2.4	24.1	241

[a]Vapor pressure: $\log p = 6.12758 - 8128.77/T - 0.53299 \log T$, where p is the absolute pressure (atm) and T, the absolute temperature (°R). [C. T. Ewing et al., "High Temperature Properties of Sodium and Potassium, Twelfth Prog. Rep. Period 1 July to 30 Sept. 1963," U. S. Naval Research Laboratory Report NRL-6094, June 1964.]

[b]Surface tension: $\sigma = 0.0091 - 0.00246 \times 10^{-3} T$, where σ is the surface tension (lb_f/ft) and T, the absolute temperature (°R); for T > 2200°R, σ is assumed constant at 0.00370 lb_f/ft). [J. W. Cooke, "Thermophysical Properties: Alkali Liquid Metals," p. 114, Studies in Heat Transfer and Fluid Mechanics, Prog. Rep. Oct. 1, 1963 – June 30, 1964, H. W. Hoffman and J. J. Keyes, Jr., editors, USAEC Report ORNL-TM-1148, Oak Ridge National Laboratory, August 1965.]

[c]Superheats shown according to Eq. (1) were obtained by interpolation between machine-calculated values; accuracy of estimate ~2%.

We note first that in the temperature range examined Eq. (2) predicts superheats which agree substantially with the values calculated from Eq. (1), while Eq. (3) seriously overestimates the superheat. At lower saturation temperatures, Eq. (2) also generates higher values; e.g., at T_{sat} = 1460°R, Eq. (2) predicts superheats about 5% greater than those calculated by Eq. (1). Further, the discrepancy between the superheats calculated according to Eqs. (2) or (3) and

Eq. (1) decreases with increasing saturation temperature and increases with decreasing cavity radius.

Equation (2) has been found by several investigators to be valid for water even at extremely high superheats. In particular, Griffith and Wallis,[5] studying nucleation from cavities of various shapes, obtained favorable agreement between experimental and predicted values. Since the surface tensions for the alkali metals differ from that for water by at most a factor of 2, it is reasonable to anticipate that Eq. (2) will also satisfactorily predict the superheat necessary for boiling with this class of fluids.

Based on the above arguments, Eq. (2) has been selected [in preference to Eq. (1)] as being adequate for the prediction of the superheat and is used subsequently for comparison with the experimental data obtained in this study. Thus, a primary objective of our experiments is the verification of Eq. (2) with respect to the alkali liquid metals. Associated with the high superheat required for bubble nucleation are surface-temperature oscillations of large amplitude. These oscillations, which arise because the high thermal conductivities and diffusivities of the alkali liquid metals effect a rapid release of the energy stored in the superheat once a bubble forms, can cause significant damage to the physical system. Hence, an attendant purpose of this investigation is the characterizing of various surface treatments as to their effectiveness in reducing the superheat.

EXPERIMENTAL APPARATUS

The small, natural-circulation loop used in this study of boiling with the alkali liquid metals is illustrated schematically in Fig. 1. This loop, of 20-in. × 20-in. overall dimensions, was constructed of 1/2-in., schedule 40, type 347 stainless steel pipe and contained three test surfaces (A, B, and C in Fig. 1) having the characteristics listed in Table 2. By properly orienting the loop and controlling the heaters, the boiling performance of each of these surfaces could be examined in turn. Outside tube-surface temperatures were measured with 0.010-in. Chromel-Alumel couples; the loop pressure was determined using a Bourdon tube gage (0 to 30 psia range) maintained of the calibration temperature.

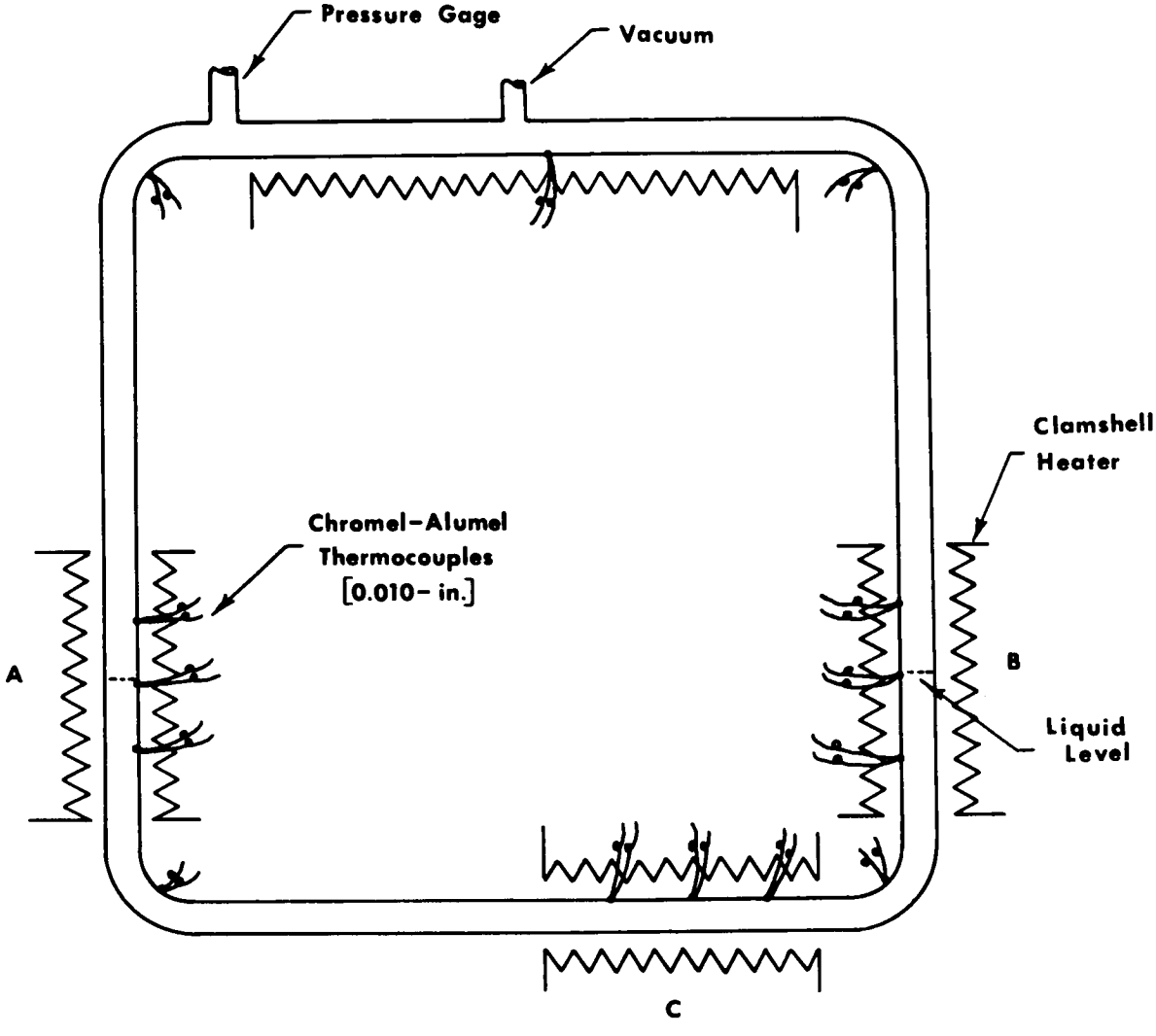


Fig. 1. Natural-Circulation Superheat Loop

Table 2. Boiling Surface Characteristics

Region	Surface Treatment
A	Porous surface coating of sintered stainless steel particles; average pore size: 44 μ (min = 12.7 μ; max = 111.8 μ)
B	Two axial, diametrically opposed rows of four 0.006-in.-diam, ~0.040-in.-deep holes arranged on 2-in. centers; rows offset axially by 1 in. with respect to each other
C	As received

TEMPERATURE PATTERNS

Boiling of both potassium and sodium on the three test surfaces was studied at heat fluxes between 16,000 and 37,000 Btu/hr·ft^2. Outside-surface temperature patterns at several saturation temperatures are shown in Figs. 2 and 3; these traces are random selections from the continuous recordings of the wall temperatures. While these data were obtained with potassium, the behavior exhibited is also representative of that observed with sodium.

The salient features deduced from these temperature profiles may be summarized as follows:

1. Boiling of potassium on an as-received (commercially smooth) surface is accompanied by wall-temperature variations of extremely large amplitude (of the order of 170 to 300°F) which recur cyclically at a frequency of ~1.5 cycles/min. Because of maximum-allowable-temperature limitations, we were unable to achieve boiling with sodium on this surface.

2. On all surfaces, the magnitude of the temperature fluctuations decreases with increasing saturation temperature, while the frequency of the oscillations increases.

3. In general, the surface with discrete holes (surface B) is more effective than the sintered surface (surface A) in reducing the amplitude of the temperature oscillations. The sintered surface is also more erratic in

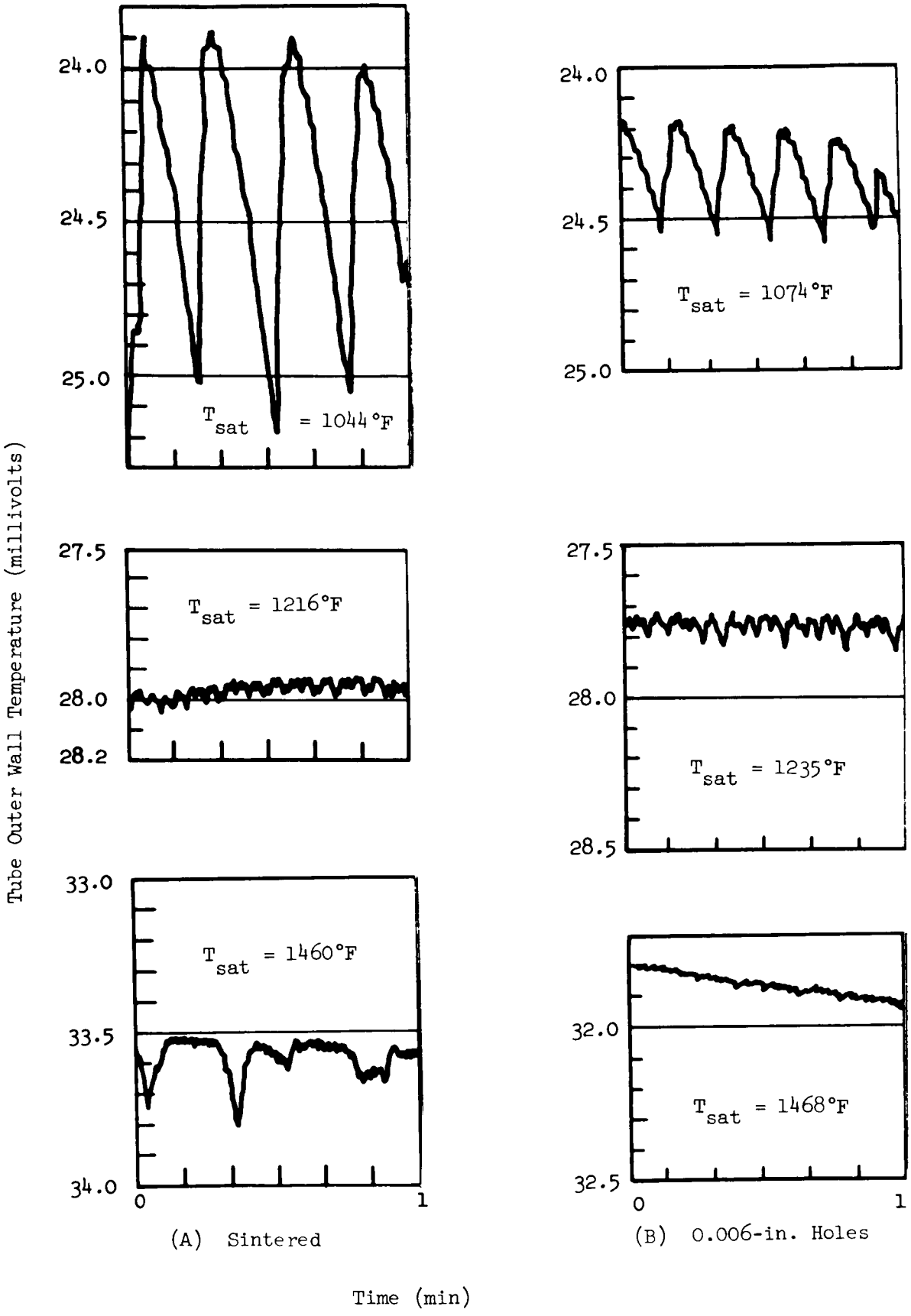
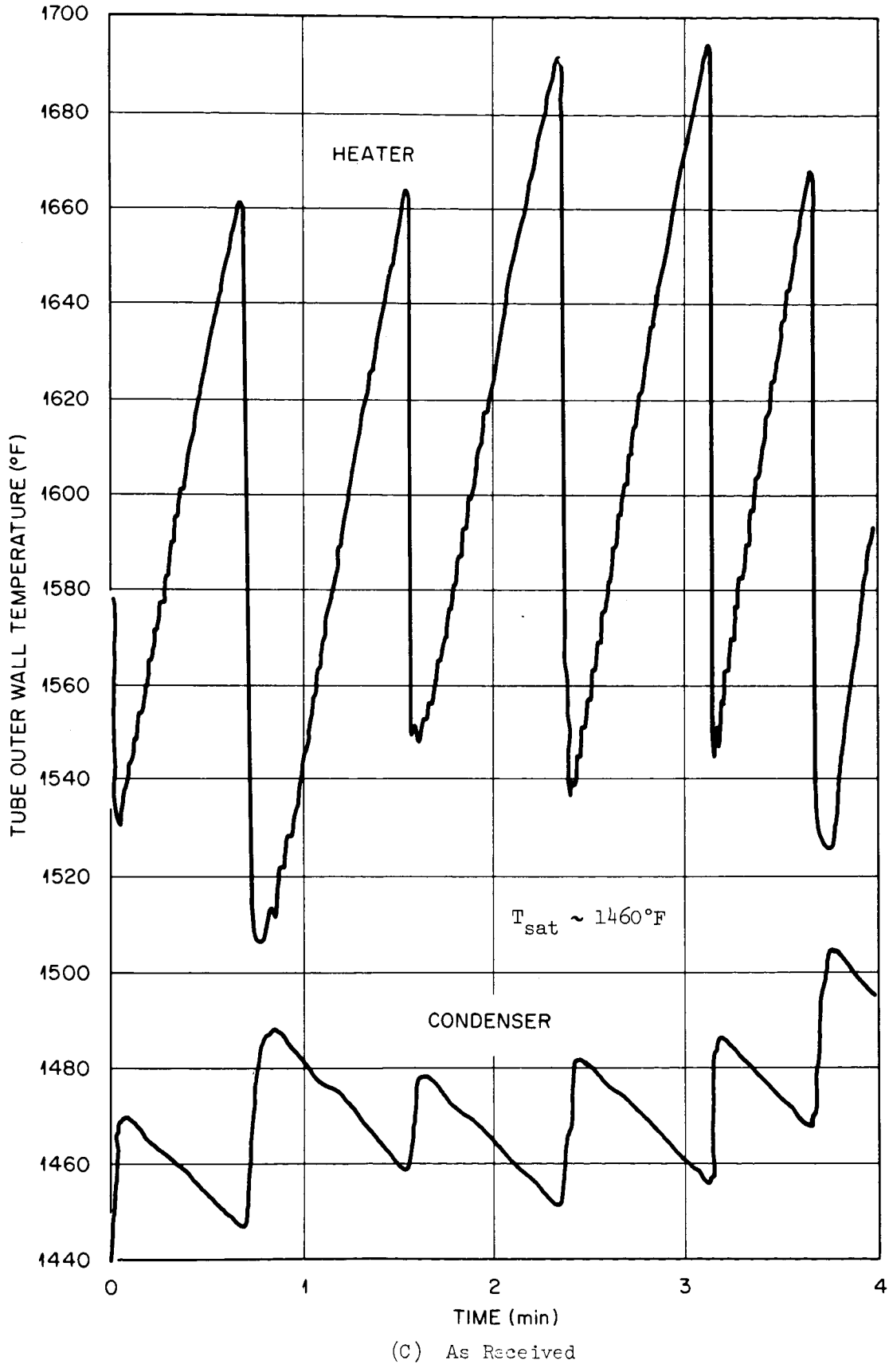


Fig. 2. Outside Tube Wall Temperatures for Potassium Boiling on Treated Surfaces



(C) As Received

Fig. 3. Outside Tube Wall Temperatures for Potassium Boiling on an As-Received Surface

performance. A comparison of these two surfaces in these aspects with boiling potassium is made in Fig. 4; the same general trends were noted with sodium.

SUPERHEAT RESULTS

The results obtained for the superheat with sodium and potassium on the various surfaces in the natural-circulation loop are summarized in Figs. 5 through 9 in relation to the saturation temperature. The superheat has been taken to be the difference in wall temperatures – corrected for the temperature drop through the wall – between the maxima in the heated region and the minima in the condenser region (see Fig. 3). The solid curves shown in these figures are the superheats predicted by Eq. (2) as a function of the saturation temperature and the cavity radius. Since these data were obtained under "steady-state" conditions, the superheats determined may be assumed to represent boiling from activated sites. Thus, presumably, the initial activation of a cavity requires a larger superheat. However, the possibility that these sites are quenched at the end of each cycle and, hence, that the data give maximum superheats must be admitted until more detailed experiments are performed.

As-Received Surface. Results for potassium boiling on the as-received surface are shown in Fig. 5; superheats as high as 500°F (at T_{sat} = 1560°F) were observed. For saturation temperatures above 1400°F, the data lie slightly above the curve for an apparent cavity radius of 10^{-5} in. Since water at atmospheric pressure boils readily on commercial finish surfaces at a superheat of ~30°F and with some care at superheats as high as 90°F, we can deduce from Eq. (2) that nucleation sites of the order of 10^{-4} in. to 3×10^{-5} in. exist. On very smooth surfaces, even higher superheats can be achieved with water. Thus, Kenrich et al.[6] measured a superheat of 306°F for atmospheric water boiling on the inside surface of a glass capillary; according to Eq. (2), this superheat corresponds to a bubble radius of 0.6×10^{-6} in. In view of the extremely good wetting characteristics of the alkali liquid metals, the indication of effective cavity sizes equivalent to those for water boiling on smooth surfaces is not unreasonable.

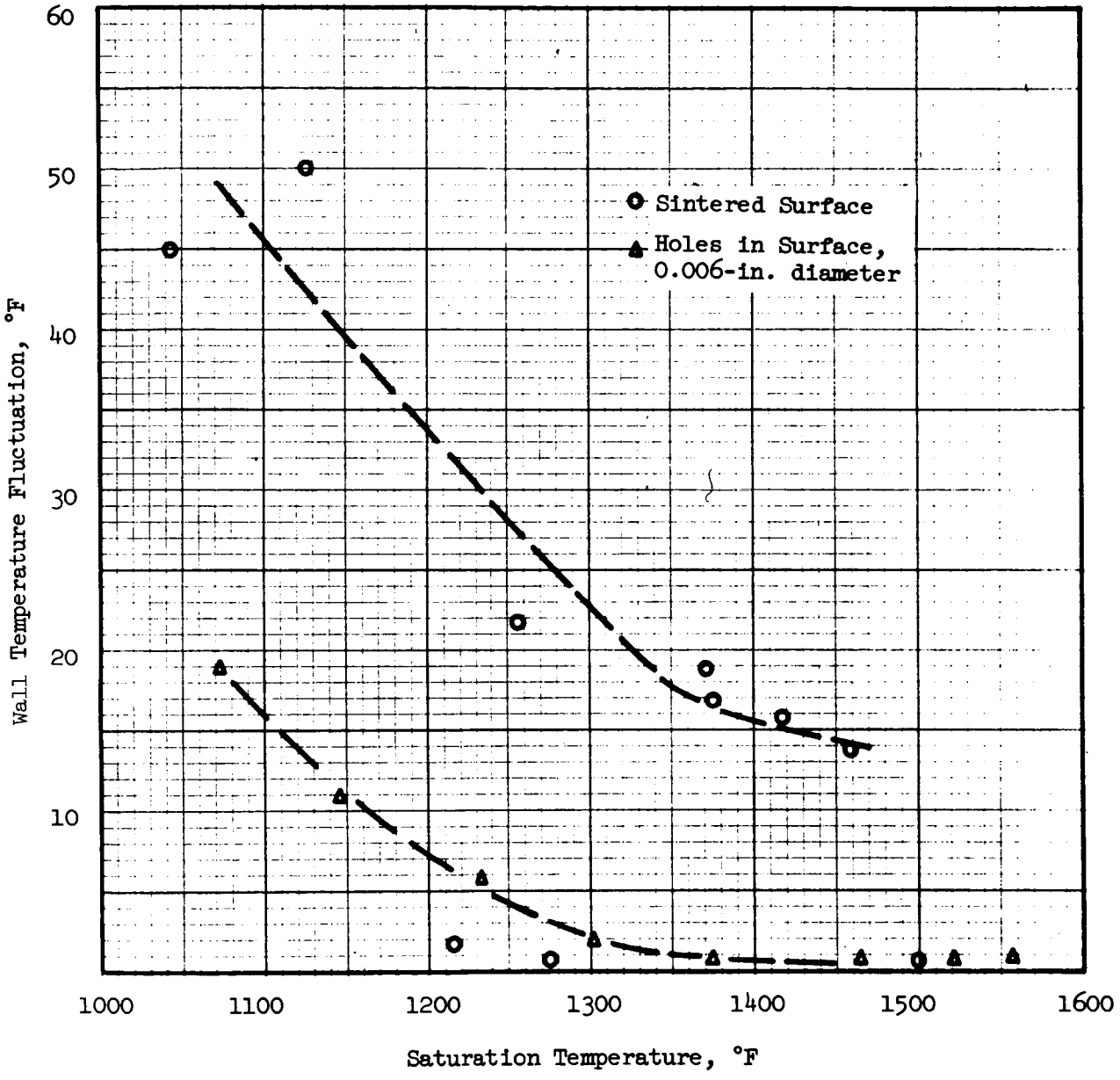


Fig. 4. Boiler Wall Temperature Fluctuations with Potassium

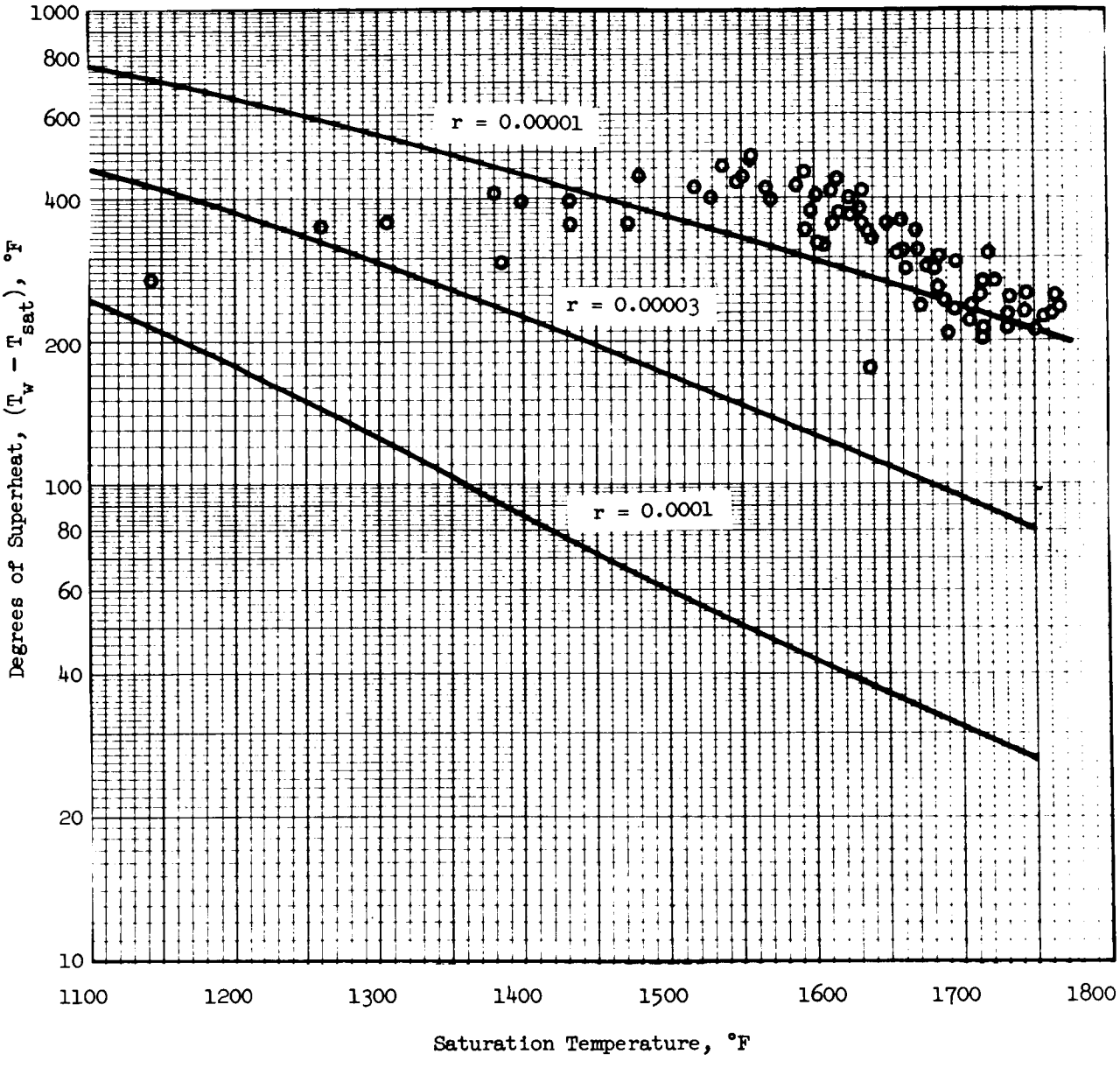


Fig. 5. Liquid Superheat with Potassium, As-Received Surface

For saturation temperatures below 1400°F, the data for potassium boiling on the as-received surface show a progressive decrease in the superheat with decreasing saturation temperature. This behavior was not observed in earlier data with a slightly altered as-received surface[4] and will be re-examined in later experiments.

Sodium could not be boiled on this surface, since the superheat required for boiling could not be attained without exceeding the maximum allowable temperature in the test section. Liquid temperatures ranging up to 1850°F were reached without evidence of boiling. For this maximum condition, the saturation temperature was 900°F (measured system pressure was 0.78 psia); hence, the superheat required to initiate boiling was greater than 950°F in this circumstance.

Surface with Holes. Figures 6 and 7 show, respectively, the results with potassium and sodium boiling on the surface containing 0.006-in.-diam holes. The superheats observed are reduced significantly below those found for boiling on the as-received surface; e.g., with potassium, the superheat measured at 1400°F on this surface was ~10°F as opposed to a value of ~400°F on the as-received surface. With sodium at its atmospheric boiling temperature (1618.8°F), the measured superheat was about 65°F. The cause for the large scatter in the potassium data is unresolved.

Over the saturation temperature range of 900 to 1300°F, the potassium data correlate reasonably with superheats predicted by Eq. (2) for cavities of 2×10^{-3} in. This result agrees well with the actual cavity radius of 3×10^{-3} in. In contrast, Eq. (2) indicates a cavity size slightly smaller than 10^{-3} in. (in the range $1200 < T_{sat} < 1400$) for sodium boiling on this same surface. However, this discrepancy may derive from an uncertainty in the value for the surface tension of sodium.

The data for both potassium and sodium indicate that a minimum superheat is reached at a saturation temperature about 150°F below the normal boiling point. For potassium, this minimum value is between 7 and 12°F; and for sodium, between 60 and 80°F. The data with sodium preclude our earlier supposition that the minimum observed with potassium derived from sensitivity limitations

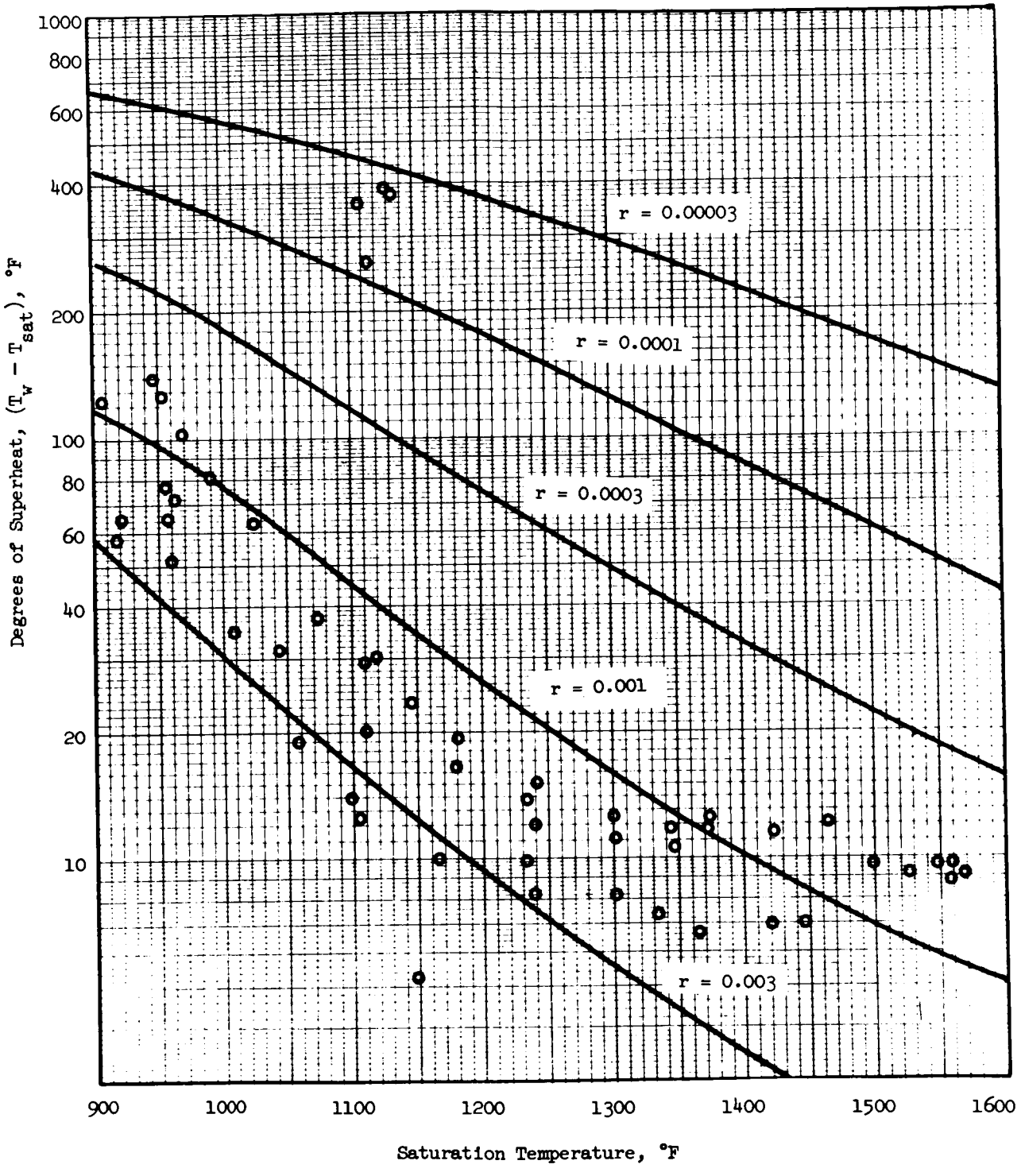


Fig. 6. Liquid Superheat with Potassium, 0.006-in.-diam Holes in Surface

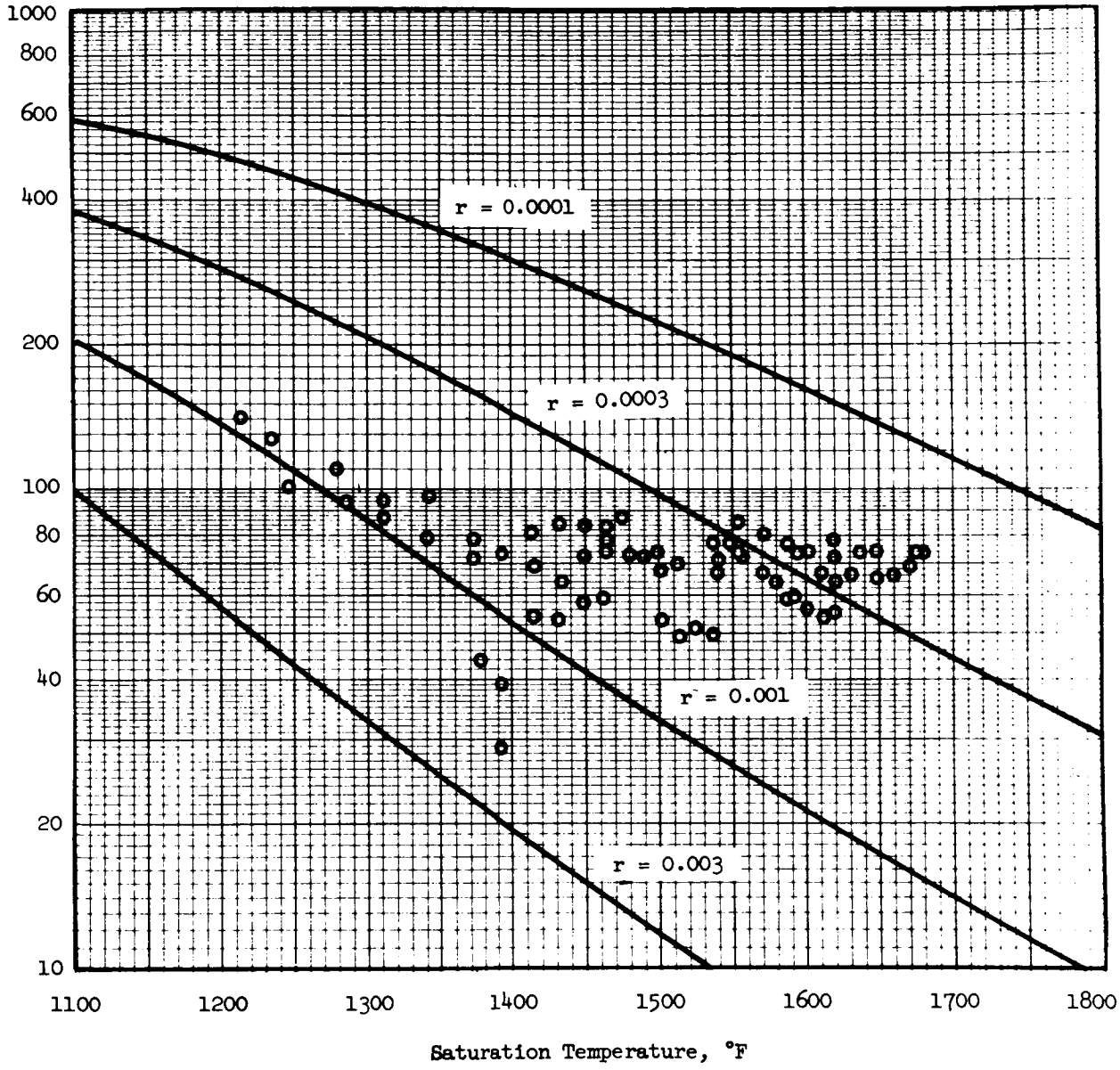


Fig. 7. Liquid Superheat with Sodium, 0.006-in.-diam Holes in Surface

in the measurement instrumentation. A possible explanation for this behavior, involving the time-dependent variation in the liquid temperature, is in a too early stage for presentation now.

Sintered Surface. Superheats measured for potassium and sodium boiling at various saturation temperatures on a surface treated to create a porous coating are displayed in Figs. 8 and 9, respectively. The reduction in the superheat, while not as great as observed with the surface having discrete, small-diameter holes, is still substantial. For example, the superheat for potassium at 1400°F was about 18 ± 5°F and for sodium at 1620°F, 50°F.

The scatter in the potassium data (Fig. 8), most noticeable in the temperature span 1300 to 1450°F, has been discussed in detail previously[2,4] and shown to relate to changes in the boiling mode on this surface. For the "stable mode" in which the wall temperature fluctuations are similar in character to those observed on the surface with holes (see Fig. 2), the superheats correlate with values predicted by Eq. (2) for a cavity radius of $\sim 5 \times 10^{-4}$. The average pore radius for this sintered surface was determined to be between 1×10^{-4} in. and 6×10^{-4} in. Again, the sodium data suggest cavity sizes somewhat smaller than those indicated by the potassium results; over the temperature range 930 to 1300°F, the apparent cavity size is $\sim 2 \times 10^{-4}$ in. The uncertainty in the sodium surface tension may account for most of this discrepancy.

Minimum superheats (~12°F for potassium, 50°F for sodium) do not differ significantly from the values observed on the surface with holes. This suggest further that this phenomenon is dependent on liquid, rather than surface, conditions.

DISCUSSION

These experiments have shown that extremely large superheats exist for boiling with the alkali liquid metals on normal, as-received surfaces. For potassium, these superheats range from ~500°F at a saturation temperature of

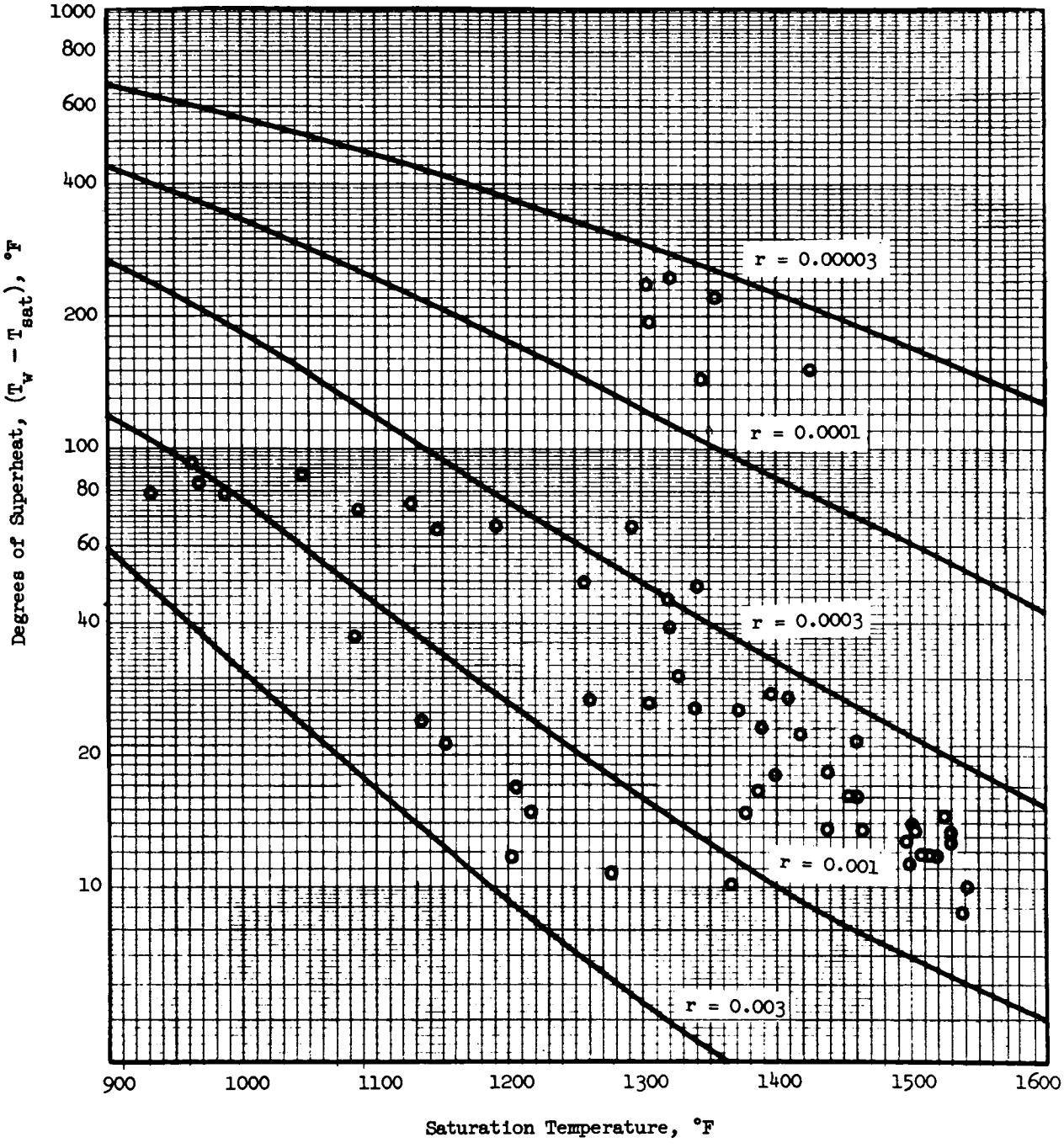


Fig. 8. Liquid Superheat with Potassium, Sintered Surface

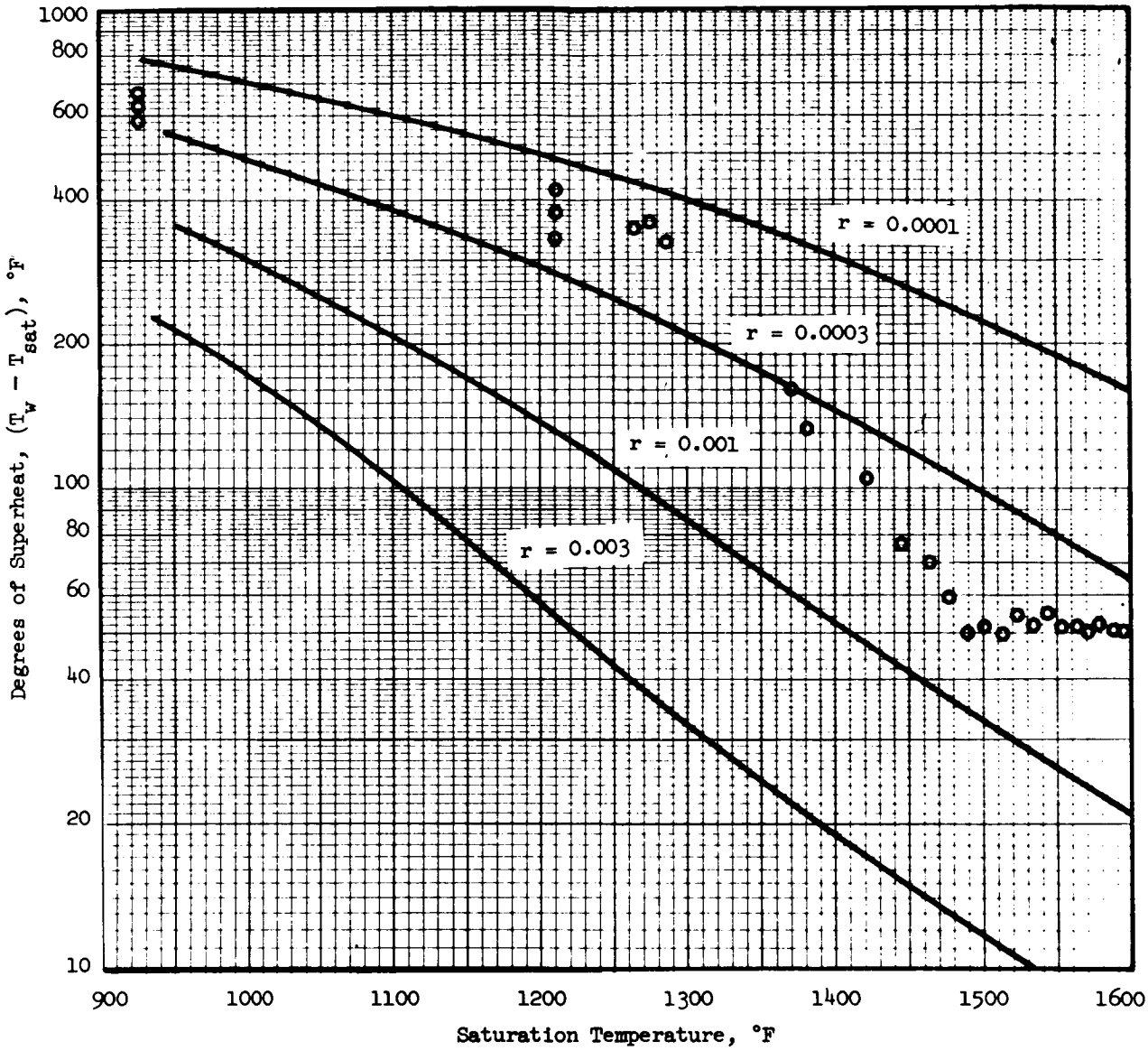


Fig. 9. Liquid Superheat with Sodium, Sintered Surface

1500°F down to about 230°F at T_{sat} = 1770°F. Along with the high superheats, wall-temperature oscillations of large magnitude occur; these oscillations are a source (through thermal fatigue) of potential damage to the boiler walls. Hence, in considering boiling alkali metals as coolants for nuclear power systems, means must be found for reducing the superheat. The data suggest two methods:

1. The operating temperature can be increased. Thus, for potassium on the as-received surface, the superheat can be reduced from about 500°F at T_{sat} = 1400°F to ~200°F at 1800°F. On the surface with holes, the wall-temperature fluctuations, which were of ~65°F amplitude and ~1.2 cycle/min frequency at T_{sat} = 820°F, decreased to ~1°F amplitude and ~50 cycle/min frequency as the saturation temperature increased to 1260°F. However, with increasing saturation temperature, the operating pressure also increases — from 1 atm at 1400°F to slightly more than 5.5 atm at 1800°F.

2. The surface can be modified. Thus, the presence of discrete 0.006-in.-diam holes resulted in a nearly fortyfold decrease in the superheat with potassium at 1400°F. The sintered metal surface, while not as effective as the one with holes, also reduced the superheat required for boiling significantly. However, with this latter surface, the performance was more erratic and fluctuated between several modes.

The studies described constitute a beginning in our understanding of superheat phenomena in the alkali liquid metals. While we have obtained a quantitative measure of the superheat for boiling with potassium and sodium on several surfaces, we have not defined an optimum surface treatment or established the effects of heat flux and cavity shape. A second-generation natural-circulation loop has been constructed that incorporates a number of instrumentation and design improvements as well as cylindrical and re-entrant cavities and a wider heat flux capability. With this system, we hope to increase the precision and accuracy of our measurements and thus resolve some of the uncertainty in the data trends.

The theory thus far developed [Eq. (2)] appears adequate for predicting the superheat for nucleation from cavities of known radius at moderate heat

fluxes; testing of Eq. (2) at higher fluxes and under controlled conditions with cavities of other than cylindrical shapes and different L/d ratios remains. Problems relating to bubble growth rates, the effect of inert gases on bubble nucleation, and the influence of temperature gradients in the liquid are also being considered in our attempt to understand and quantitatively describe the boiling process with the alkali liquid metals.

ACKNOWLEDGMENTS

The authors acknowledge the prior efforts of A. I. Krakoviak, the laboratory assistance of B. J. Sutton, and the conscientious typing of Dolores Eden.

REFERENCES

1. A. I. Krakoviak, "Superheat Requirements with Boiling Liquid Metals," pp. 310–333, Proceedings of 1963 High-Temperature Liquid-Metal Heat Transfer Technology Meeting, Vol. I, USAEC Report ORNL-3605, Oak Ridge National Laboratory, November 1964.

2. H. W. Hoffman and A. I. Krakoviak, "Convective Boiling with Liquid Potassium," pp. 19–37, Proceedings of the 1964 Heat Transfer and Fluid Mechanics Institute, W. H. Gredt and S. Levy, editors, Stanford University Press, Stanford, California, 1964.

3. A. I. Krakoviak, "Boiling Potassium Heat Transfer: Superheat Phenomena," pp. 21–26, Studies in Heat Transfer and Fluid Mechanics, Progress Report for Period January 1 – September 30, 1963, H. W. Hoffman and J. J. Keyes, Jr., editors, USAEC Report ORNL-TM-915, Oak Ridge National Laboratory, October 1964.

4. A. I. Krakoviak, "Boiling Potassium Heat Transfer: Superheat Phenomena," pp. 15–28, Studies in Heat Transfer and Fluid Mechanics, Progress Report for Period October 1, 1963 – June 30, 1964, H. W. Hoffman and J. J. Keyes, Jr., editors, USAEC Report ORNL-TM-1148, Oak Ridge National Laboratory, August 1965.

5. P. Griffith and J. D. Wallis, "The Role of Surface Conditions in Nucleate Boiling," Chemical Engineering Symposium Series, Vol. 56, pp. 49–63, 1960.

6. F. B. Kenrick, C. S. Gilbert, and K. L. Wismer, "The Superheating of Liquids," Journal of Physical Chemistry, 28: 1297–1307 (1924).

N66 31696

PRESSURE DROP WITH FORCED-CONVECTION BOILING OF POTASSIUM*

R. P. Wichner and H. W. Hoffman
Oak Ridge National Laboratory
Oak Ridge, Tennessee

(Paper presented by R. P. Wichner)

ABSTRACT

The results are given for the pressure drop with boiling potassium in forced-convection flow through a vertical, circular tube. The data, which comprise a single series of measurements (Series D), were obtained in a 6-ft long × 0.270-in.-ID tube having pressure taps at 1-ft spacings over the final 4 ft of the channel. The pressure-measurement system and its deficiencies are discussed; the primary difficulty appears to be "aging" of the diaphragms in the pressure transmitters over long exposure times at high temperatures. The pressure distribution along the boiler was estimated using both homogeneous and Lockhart-Martinelli descriptions of the flow; the calculated exit pressures compared favorably with the measured values.

*Research sponsored by the U. S. Atomic Energy Commission under contract with the Union Carbide Corporation.

INTRODUCTION

The pressure drop associated with forced-convection boiling is of significant concern in the design of power systems utilizing this mode of cooling and has been the subject of intensive study. Most attention has focused on water in a variety of geometries at high system pressures. More recently, interests have broadened to include lower pressure systems (including subatmospheric) and other coolants (such as the alkali liquid metals).

While we have been accumulating pressure-drop data in the course of our heat-transfer studies with boiling potassium in upward forced flow through vertical circular tubes, we have described our results only briefly at these conferences.[1] The discussion which follows considers some of the difficulties we have encountered in making these measurements and gives a preliminary analysis of the data.

EXPERIMENTAL APPARATUS

The test channels utilized in our initial studies with boiling potassium provided only limited information on the pressure drop. Thus, both the "low-flux" and "high-flux" boilers[2] were designed with pressure taps at the inlet and exit only. As a consequence, the resulting data[1,3] included losses (of unknown magnitude) associated with flow through an inlet mixing chamber, around exit-end thermowells, and through contractions and expansions at the exit.

An advanced design of the "high-flux" boiler, incorporating an additional pressure tap at the midpoint, was abandoned because of fabrication difficulties; and a test unit of intermediate-flux capability was constructed and installed. This new boiler was designed to provide data on both the heat transfer and the pressure drop; a schematic representation is shown in Fig. 1. The boiler was machined from a 7-ft length of 1/2-in. double extra heavy IPS type 347 stainless steel pipe (0.270-in. inside diameter, 0.839-in. outside diameter). As shown in Fig. 1, the boiler was divided into six 12-in.-long sections which were heated radiantly by individual clamshell heaters of 1 1/4-in. inside diameter. The heated portions were separated by 1 1/2-in.-long gaps in which the wall was

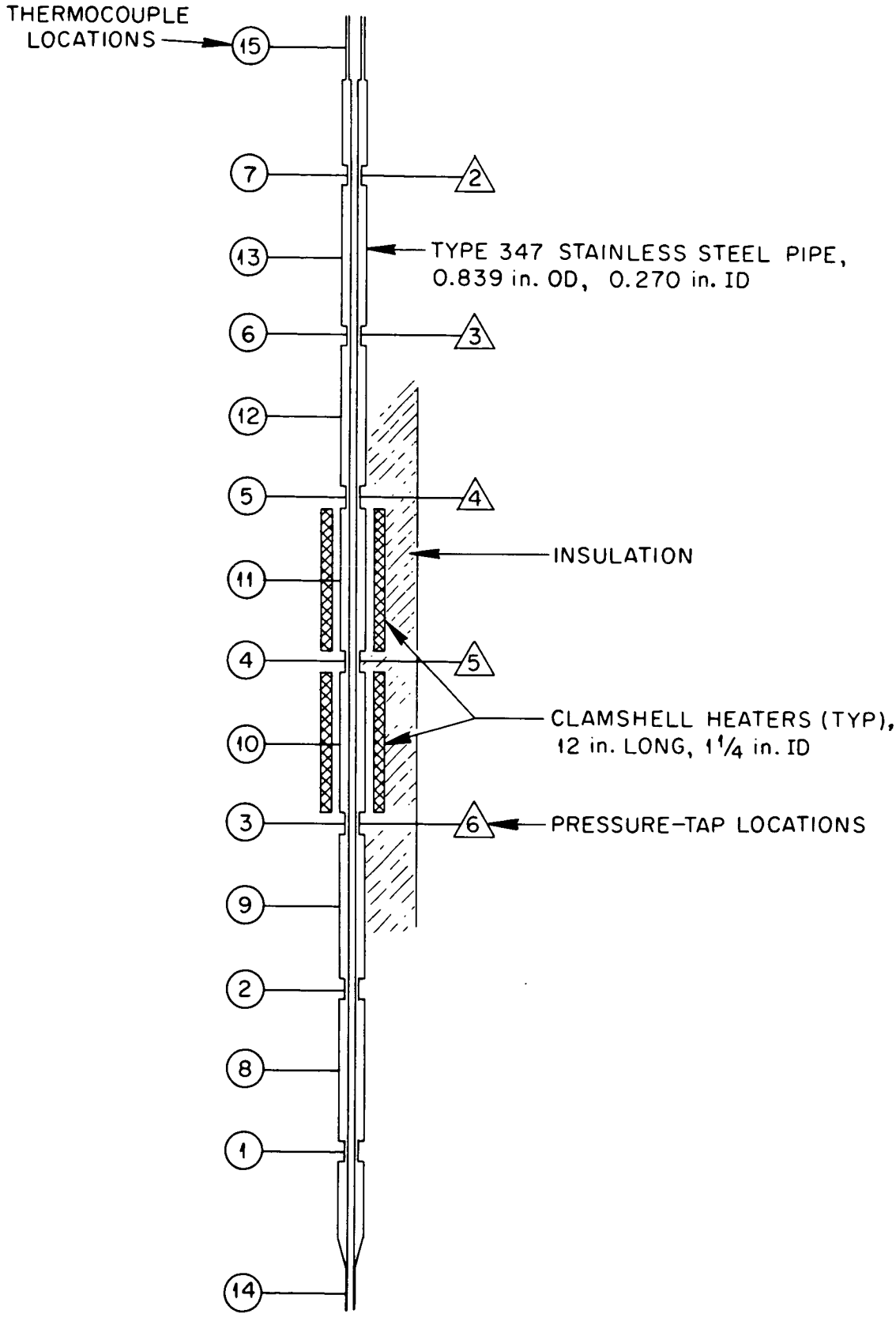


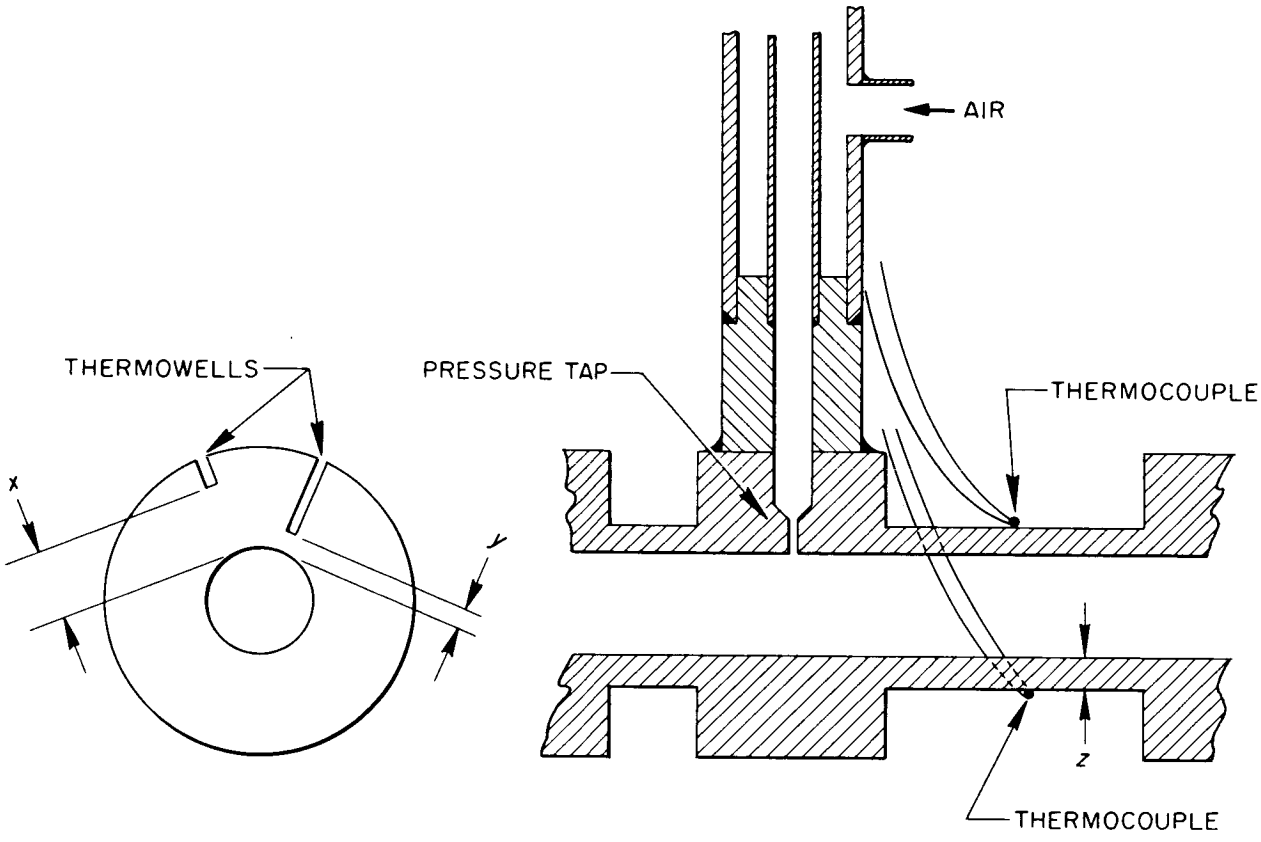
Fig. 1. Schematic of Medium-Flux Boiler Section

thinned from the original 0.285 in. to 0.075 in. Pressure taps (see Fig. 2 for construction detail) were located in the final four gaps and at the boiler exit. The pressures at positions 2, 3, 5, and 6 were measured with Taylor diaphragm-type pressure transmitters having NaK-filled lines and strain-gage signal converters; at position 4, the pressure was determined with a 6-in. bronze Bourdon-tube gage maintained at the calibration temperature of 160°F. Care was taken to insure that the pressure-tap lines leaving the boiler were horizontal and liquid filled. While cooling jackets were provided on all pressure taps, it was found in practice that the normal heat loss was sufficient to assure the absence of vapor in the lines.

A pair of 0.008-in.-diam Pt-Pt 10% Rh thermocouples were also welded to the tube wall in each of the interheater gaps; the leads of these thermocouples were brought out along the pressure-transmitting lines. Fiberfrax insulation in these regions created an essentially adiabatic zone. In addition, tube-wall temperatures were obtained at the midpoint of each heated section by Pt-Pt 10% Rh couples placed in 0.035-in.-diam holes drilled radially into the tube wall; the locations of the bottoms of these wells with respect to the inside tube surface are indicated in Fig. 2. The 8-mil thermocouple wires were threaded through two-hole ceramic insulators (0.031-in. outside diameter) and individually resistance welded to the stainless steel at the bottom of the well. The inside surface temperature was obtained by extrapolation from the temperatures measured at the bottom of the thermocouple wells.

The pressure-measuring system was calibrated at 1000°F over the range 4 to 25 psia by comparison with a precision test gage. During calibration, the liquid potassium was held in the sump tank; and the system was filled with helium. Calibration was effected both before and after each run series. In addition, the electrical part of the system was checked periodically by detaching the strain-gage leads and imposing a standard millivolt signal at this point.

The Taylor devices installed on this loop were found to be unstable, exhibiting significant changes in calibration over a period of time. For example, the output of one transmitter varied over a six-month period by nearly 12%. These changes were always in a positive direction and derive possibly from "aging" of the diaphragms due to prolonged exposure at high temperatures,



THERMOCOUPLE POSITION	WALL THICKNESS (in.)
1–7	$z = 0.075$
8	$x = 0.1210$, $y = 0.041$
9	$x = 0.2005$, $y = 0.051$
10	$x = 0.2146$, $y = 0.018$
11	$x = 0.2070$, $y = 0.054$
12	$x = 0.2106$, $y = 0.033$
13	$x = 0.2040$, $y = 0.021$

Fig. 2. Thermocouple and Pressure Tap Details of Medium-Flux Boiler

occasional imposition (as during calibration) of subatmospheric pressures, and/or corrosion in the potassium environment. While this factor does introduce some uncertainty in the final results, the major effect has been annoyance rather than loss of precision.

The quality at the boiler exit was determined by passing the effluent vapor-liquid mixture through a separator and measuring the flow rates of the resulting vapor (after condensation) and liquid streams both volumetrically in calibrated hold tanks and dynamically by electromagnetic flow meters. Other features of the experimental system have been described previously,[1,3]

EXPERIMENTAL AND CALCULATED RESULTS

The data obtained in the Series D experiments for the axial pressure distribution with boiling potassium flowing through a vertical, circular tube are summarized in Table 1 along with the inlet mass flow, exit quality, and heat input. Results for two typical runs are shown graphically in Figs. 3 and 4. In the first of these (Run D-4, Fig. 3), a low mass flow–high exit quality condition existed; while in the second (Run D-15, Fig. 4), the situation was reversed. Both figures present measured and predicted pressures, fluid temperatures, and calculated qualities as a function of distance from the boiler inlet; the locations of the six boiler heaters are also indicated.

The quality variation along the boiler was calculated from an energy balance which neglected the wall friction and the static head but retained the kinetic energy term. A trial-and-error solution was then effected in which the magnitude of the slip ratio was systematically adjusted to generate an exit quality agreeing as closely as possible with the measured value; a zero inlet quality was assumed. The results are shown by the open circles in the lower portion of Figs. 3 and 4; the measured exit qualities are given by the filled circles. Significant changes in the slip ratio were found to have only minor effects on the calculated exit quality. This result is not surprising in that for the conditions of this experiment the enthalpy term dominates the kinetic energy term in the energy balance. As observed for the

Table 1. Measured and Calculated Pressures for Forced-Convection Boiling of Potassium Within a Vertical Circular Channel

Run No. (Series D)	Inlet Mass Flow (lb/hr)	Exit Quality (wt % vapor)	Total Heater Power (kw)	Measured Boiler Pressure (psia)					Calculated Exit Pressure (psia)	
				PE-6[a]	PE-5	PE-4	PE-3	PE-2	Lockhart-Martinelli	Homogeneous
4	20.5	87.4	5.77	23.3	23.1	22.6	20.8	19.8	19.0	19.9
5A	70.1	19.4	3.84	21.1	21.0	20.4	19.2	17.7	14.4	13.0
6C	76.2	9.95	1.83	16.6	15.8	14.9	13.4	11.9	12.6	11.0
7	72.8	20.1	3.85	25.1	24.1	23.4	20.9	18.1	18.5	17.4
8	64.8	23.5	3.96	23.9	23.1	22.5	19.8	17.4	17.8	16.9
9	62.0	36.9	5.68	30.4	28.7	28.0	24.6	22.1	23.6	23.3
10	55.2	40.4	5.69	29.7	28.1	27.4	24.1	21.7	22.7	22.8
11	49.3	43.3	5.59	27.7	26.5	25.9	22.9	20.7	21.6	21.6
12	43.6	47.3	5.59	26.6	25.2	24.9	22.0	19.9	20.4	20.6
13	51.4	53.0	7.73	34.2	32.5	32.0	28.2	25.7	26.4	27.5
14	56.9	48.7	7.46	35.4	33.5	33.0	28.9	26.3	27.8	28.6
15	63.7	42.2	7.45	37.0	35.0	34.4	30.1	27.2	28.5	29.3

[a]Pressure tap locations, distances measured from boiler inlet: PE-6, 2.156 ft; PE-5, 3.234 ft; PE-4, 4.313 ft; PE-3, 5.391 ft; PE-2, 6.469 ft.

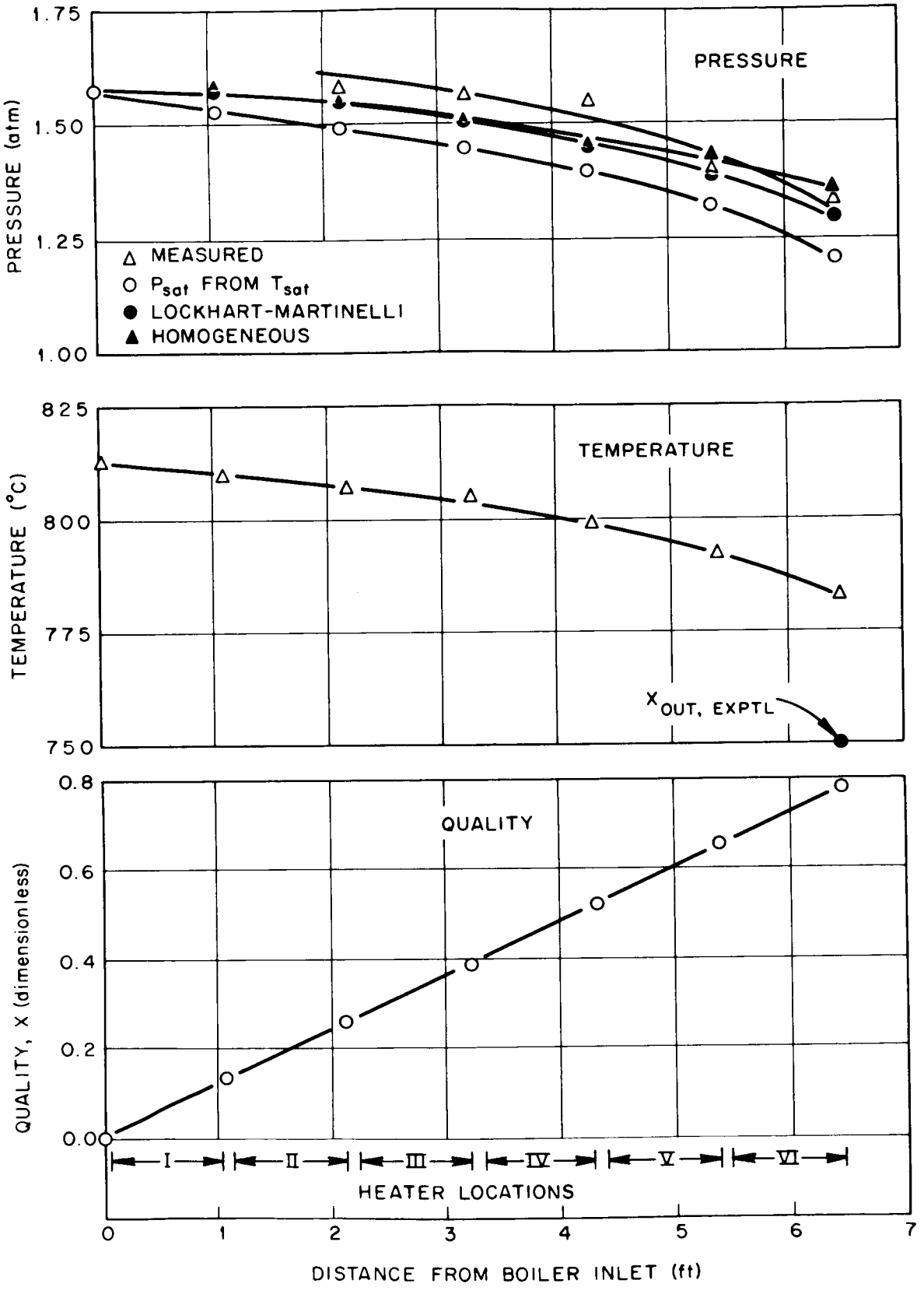


Fig. 3. Axial Pressure, Temperature, and Quality Profiles with Forced-Convection Boiling of Potassium in Vertical, Circular Tubes. Run D-4: W = 20.5 lb/hr; Q/A = 5.18×10^4 Btu/hr·ft^2; $X_{OUT} = 0.874$.

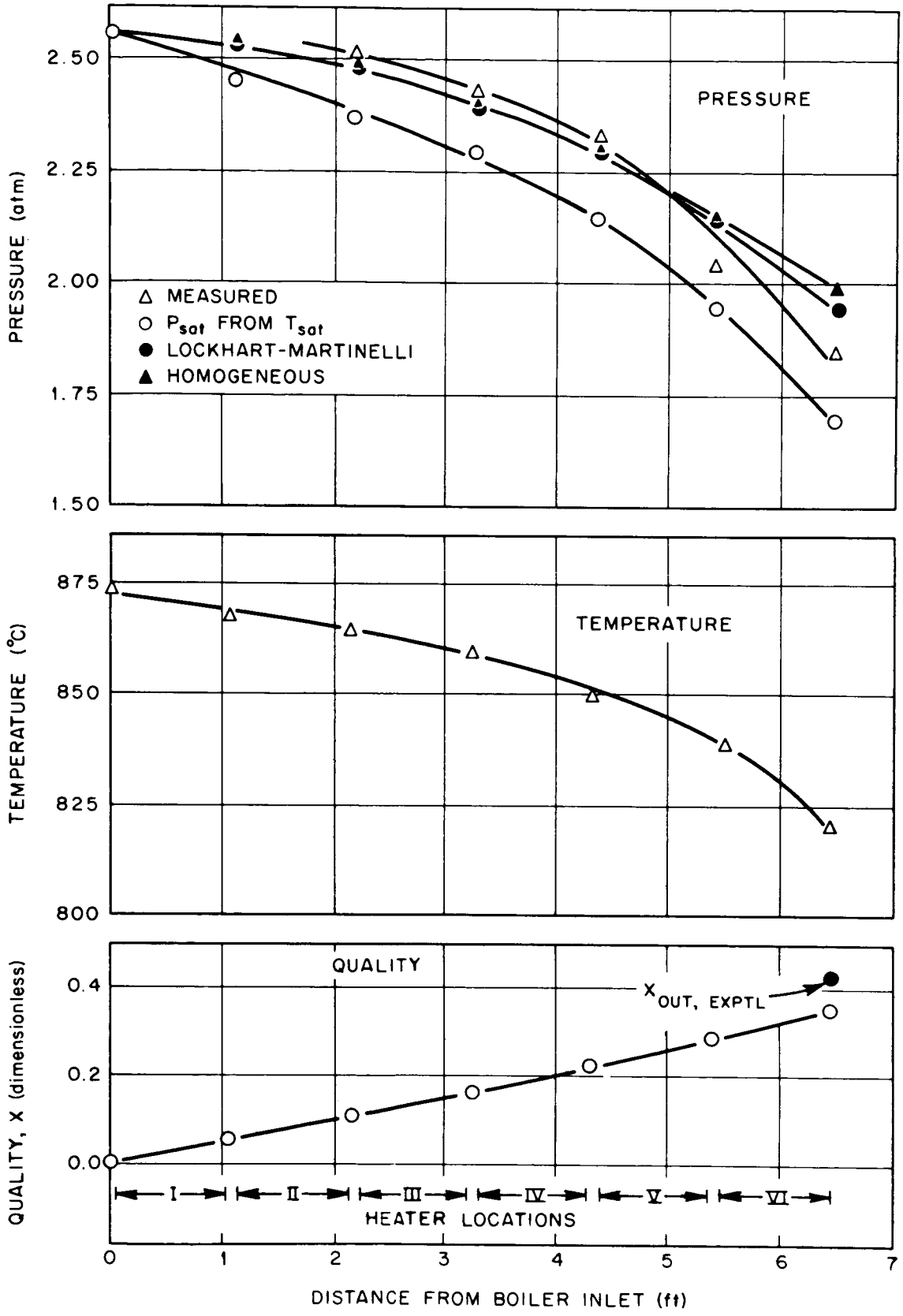


Fig. 4. Axial Pressure, Temperature, and Quality Profiles with Forced-Convection Boiling of Potassium in Vertical, Circular Tubes. Run D-15: W = 63.7 lb/hr; Q/A = 6.77×10^4 Btu/hr·ft^2; $X_{OUT} = 0.422$.

two cases graphed, the calculated exit quality is always somewhat lower than the measured exit quality. Since the slope of the axial quality profile is fixed by the known heat input, the inlet quality could be obtained by extrapolation back from the measured value. The inlet qualities thus obtained were 15% for Run D-4 and 10% for Run D-15. These estimated values are markedly greater than the qualities believed, on a qualitative basis, to have existed at the boiler inlet and may reflect in part errors (on the high side) in the measured qualities due to vaporization between the boiler exit and the measurement station. In any event, the pressure-drop estimations discussed below were based on the calculated qualities without adjustment for the indicated deviation from the measured exit quality.

The central portion of both Figs. 3 and 4 show the fluid temperature distribution along the boiler. The data plotted are wall temperatures measured in the thin-walled (0.075 in.), adiabatic zones (1.5 in. long) between the heaters. It is presumed, under these circumstances, that the wall temperature is essentially the same as the fluid temperature.

Pressures measured at five positions along the boiler are shown by the open triangles in the upper portion of Figs. 3 and 4; as noted in Fig. 1, the first pressure tap (PE-6) was located in the adiabatic zone between the second and third heaters. The data show somewhat more scatter than previously observed in run Series C;[4] this may result from the uncertainties associated with the pressure-measurement system as discussed above in the section on apparatus. An arbitrary smooth curve has been drawn through the data.

The lower pressure curve in both figures gives the saturation pressure (open circles) as derived from the fluid temperature data. The pressure distribution thus derived shows a trend with distance along the boiler that agrees closely with the curve through the measured values but falls significantly and consistently below the latter. This discrepancy in magnitude results in part from the use of the vapor pressure correlation of Lemmon et al.[5] in this analysis; at a given T_{sat}, Lemmon and his co-workers found P_{sat} to be less than the value indicated by other available correlations. Thus, using the equation developed by Ewing et al.,[6] the saturation pressure calculated at position PE-4

in Run D-4 is 1.47 atm; this compares with a value of 1.39 atm calculated from the Lemmon et al. equation and 1.54 atm measured. Similarly, for Run D-15 at the same measurement station, P_{sat} = 2.14 atm according to Lemmon, 2.22 atm according to Ewing, and 2.34 atm measured. The remaining difference between the measured pressure and that calculated from T_{sat} could derive from low temperature readings due to heat loss in the "adiabatic" zone or from a systemic error in the pressure measurements.

For purposes of comparison, the pressure drop along the boiler was also estimated using both the homogeneous and the Lockhart-Martinelli[7] models for the flow. Thus, the filled triangles in Figs. 3 and 4 show the results obtained by assuming the fluid to be homogeneous, while the closed circles give corresponding values obtained by the Lockhart-Martinelli procedure with corrections for changes in the kinetic and gravity heads.

The Blasius friction-factor equation, $f_B = 0.0396\ N_{Re}^{-0.25}$, was used in the homogeneous calculations; while the analogy relation, $f_B = 0.023\ N_{Re}^{-0.20}$, was used in the Lockhart-Martinelli computation. The following further comments are pertinent to the estimation of the pressure drop by the Lockhart-Martinelli procedure:

1. Since the slip ratio was unknown, a value of unity was assumed in the calculations of the kinetic and gravity head corrections.

2. For convenience in the computer calculations, an empirical equation was fitted to the Lockhart-Martinelli parameters; thus,

$$\ln \phi_{\ell tt} = 1.478 - 0.5403 \ln X_{tt} + 0.05194 (\ln X_{tt})^2 + 0.000698 (\ln X_{tt})^3 ,$$

where $\phi_{\ell tt}$ is the square root of the ratio of the total two-phase pressure drop, $(dP/dL)_{TPT}$, to the pressure drop for the liquid phase only, $(dP/dL)_\ell$; and

$$X_{tt} = \left(\frac{1}{x} - 1\right)^{0.9} \left(\frac{\mu_\ell}{\mu_v}\right)^{0.1} \left(\frac{\rho_v}{\rho_\ell}\right)^{0.5} ,$$

x being the mean quality in each heated section. Over the range of the experimental data, $0.01 < X_{tt} < 1.00$, this empirical equation overestimates $\phi_{\ell tt}$; at $X_{tt} = 1.00$, the error is ~5%, and at $X_{tt} = 0.01$, ~10%.

3. Since the pressure was not measured at the boiler inlet, the starting point for the pressure calculations was assumed to be P_{sat} as estimated from the wall temperature measurements. This is probably not an unreasonable assumption in that the fairly long loop section immediately preceding the boiler is essentially adiabatic; and, hence, the wall temperature measured at the end of this region should equal the fluid temperature. The data shown in Figs. 3 and 4 suggest this conclusion.

DISCUSSION

In view of the error discussed above in the evaluation of $\phi_{\ell tt}$, the Series D data have not been presented in the usual graphical form of the pressure-drop ratio versus the Lockhart-Martinelli parameter, X_{tt}. These calculations will be repeated in the near future using a newer, more precise computer procedure for evaluating $\phi_{\ell tt}$. Thus, any comparison of the present data with results obtained with water under similar experimental conditions must be deferred.

The final three columns of Table 1 provide a comparison of measured and calculated exit pressures; in general, the agreement between the tabulated values is good. However, there does not appear to be any consistent trend in these comparisons. Thus, for Run D-4, Lockhart-Martinelli predicts an exit pressure less than measured, while the homogeneous model yields a value greater than measured. In Run D-8, the situation is reversed; while in Run D-15, both calculations indicate exit pressures greater than measured. As discussed above, these comments must be qualified somewhat in respect to the Lockhart-Martinelli calculation. An overestimate in the pressure drop by 15% on the average is indicated; this results in predicted exit pressure which are 3 to 5% low.

ACKNOWLEDGMENTS

The authors acknowledge the contributions of A. I. Krakoviak in the design and construction of the test section, of R. D. Bundy and B. J. Sutton in obtaining the Series D experimental data, and of Dolores Eden for her conscientious typing of the manuscript.

REFERENCES

1. H. W. Hoffman, "Recent Experimental Results in ORNL Studies with Boiling Potassium," pp. 334–350, Proceedings of 1963 High-Temperature Liquid-Metal Heat Transfer Technology Meeting, Vol. I, USAEC Report ORNL-3605, Oak Ridge National Laboratory, November 1964.

2. H. W. Hoffman and A. I. Krakoviak, "Convective Boiling with Liquid Potassium," pp. 19–37, Proceedings of the 1964 Heat Transfer and Fluid Mechanics Institute, W. H. Gredt and S. Levy, editors, Stanford University Press, Stanford, California, 1964.

3. A. I. Krakoviak and H. W. Hoffman, "Boiling Potassium Heat Transfer: Forced-Convection System," pp. 19–20, Studies in Heat Transfer and Fluid Mechanics, Progress Report for Period January 1 – September 30, 1963, H. W. Hoffman and J. J. Keyes, Jr., editors, USAEC Report ORNL-TM-915, Oak Ridge National Laboratory, October 1964.

4. A. I. Krakoviak and H. W. Hoffman, "Boiling Potassium Heat Transfer: Forced-Convection System," pp. 7, 12–15, Studies in Heat Transfer and Fluid Mechanics, Progress Report for Period October 1, 1963 – June 30, 1964, H. W. Hoffman and J. J. Keyes, Jr., editors, USAEC Report ORNL-TM-1148, Oak Ridge National Laboratory, August 1965.

5. A. W. Lemmon et al., "The Thermodynamic and Transport Properties of Potassium," pp. 88–115, Proceedings of 1963 High-Temperature Liquid-Metal Heat Transfer Technology Meeting, Vol. I, USAEC Report ORNL-3605, Oak Ridge National Laboratory, November 1964.

6. C. T. Ewing et al., "High Temperature Properties of Sodium and Potassium, 12th Progress Report for Period 1 July to 30 September 1963," U. S. Naval Research Laboratory Report NRL-6094, June 1964.

7. R. W. Lockhart and R. C. Martinelli, "Prediction of Pressure Drop for Isothermal Two-Phase, Two-Component Flow in Pipes," Chem. Eng. Progr., 45: 39 (1949).

N66 31697

SODIUM BOILING HEAT TRANSFER AND HYDRODYNAMICS

by

Henry Lurie
Atomics International,
Canoga Park, California

(Paper presented by D. Logan)

PRECEDING PAGE BLANK NOT FILMED.

INTRODUCTION

The study of liquid-metal boiling and two-phase hydrodynamics is part of an AI project* whose general objective it is to provide both experimental and analytical information on two-phase flow, hydrodynamic effects, void formation, and pressure generation required in the safety evaluation of sodium cooled reactors. Presented in this report are the results of experiments on the steady-state pool boiling critical heat flux of saturated sodium as a function of pressure, and on the forced convection boiling heat transfer characteristics and the critical heat flux of sodium as functions of pressure, flow rate, and subcooling or quality. Also presented are the steady state two-phase pressure drop and void fraction results for the upflow of sodium in an unheated annulus.

The experimental equipment, the pool boiling experiments, and the initial forced convection tests have been described in several previous Atomics International reports[1,2] and will only be summarized herein. The forced convection critical heat flux data and the two-phase flow experiments will be presented in greater detail in the following pages.

POOL BOILING

A pilot test loop fabricated to develop and test certain critical components of, and as a model for, the larger forced convection loop, was used to obtain additional pool boiling data for sodium. The tests were performed in the boiler-condenser unit of the loop – a 12-in.-diameter pipe section positioned vertically. Heat was supplied to the sodium pool with immersion heaters and removed by vapor condensation at the upper, water cooled plate. The system pressure was adjusted by varying the power input to

* Work sponsored by U. S. Atomic Energy Commission Contract AT(11-1)-GEN-8.

the heaters and establishing equilibrium between the liquid and its vapor. The critical heat flux (CHF) was studied by using specially designed high flux heaters immersed horizontally in the pool through the pipe wall by means of a "Conoseal"* connector. The high flux heater shown in Figure 1 consists of a body assembly, sheath, graphite heating element, boron nitride insulating sleeve, and electrode. A high temperature nickel base alloy was used to braze the body assembly and thermocouples to the sheath. AC power up to 5 kw at 24 volts is supplied to the graphite heating element, with the sodium at the grounded end of the electrode providing a current return path.

In addition to the previous sodium pool boiling data obtained by Mr. Noyes,[1] five additional values for the critical heat flux of sodium under saturated pool boiling conditions were obtained in this series of tests, by using a 1/4-in. OD horizontal, stainless steel heater. The system temperature, and consequently the pressure due to saturation conditions, was slowly lowered while maintaining a constant heat flux on the heater. Actual burnout of the heater occurred in two of the runs. These data together with the previous CHF data are plotted in Figure 2 as a function of the pool pressure; the overall pressure range covered by these data is 0.5 to 8 psia. A straight line (log-log) least square fit of the data was made and is shown as the solid line. The resulting empirical dimensional correlation is

$$\mathrm{CHF} = 534{,}000\ p^{0.17} \ .$$

Although the upward trend of the critical heat flux with pressure is unmistakable, it is considerably lower than that predicted by various theories and correlations derived for other liquids (water and organics). Only a limited amount of data for the CHF of

* Trademark of Aeroquip Corporation

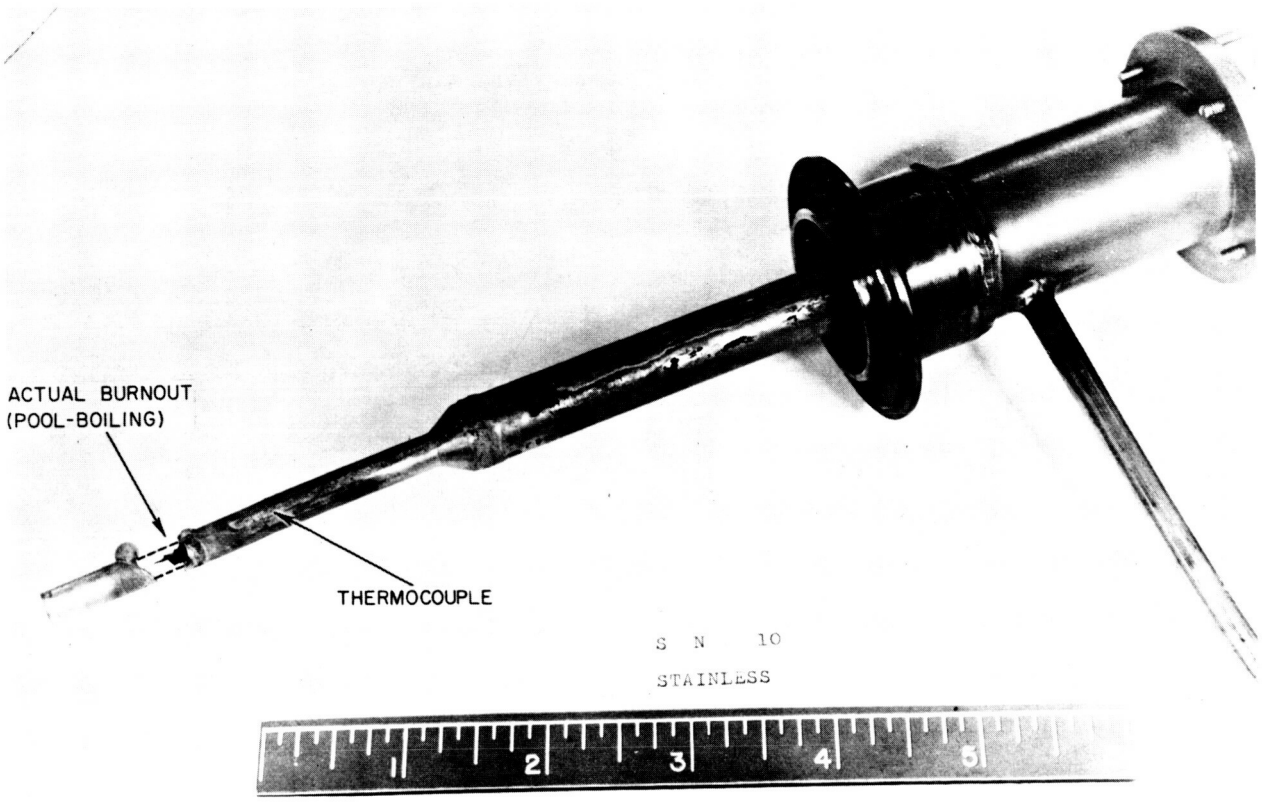


Fig. 1. High Flux Heater

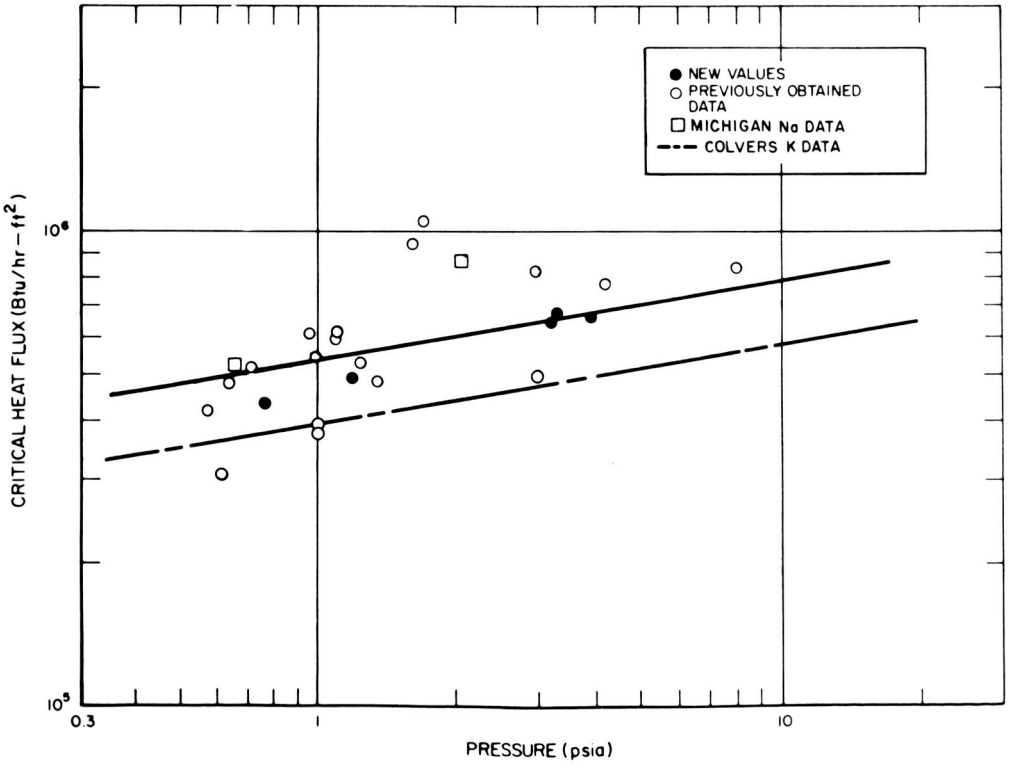


Fig. 2. Critical Heat Flux, Saturated Pool-Boiling

alkali liquid metals is available in the literature. Two values of the CHF for sodium have been reported by Balzhizer, et al.[3] and are shown in the Figure. The data fall in the same range as the current data, though the CHF value at 2 psia falls considerably above the value predicted by the above correlation. The CHF data of Colver[4] for potassium under saturated pool boiling conditions exhibits very little scatter, and his correlation, as seen in Figure 2 exhibits a slope equal to that of the least square fit of the sodium data. That the CHF of potassium is somewhat lower than that of sodium is to be expected from the differences in the physical properties of the two alkali metals.

FORCED CONVECTION BOILING

The forced convection loop used for the forced flow heat transfer and hydrodynamic tests is basically composed of a pump, economizer, boiler, test section, high flux heater, condenser, and subcooler. A detailed description of the loop is given elsewhere[1,2] and only the boiler and test section will be described here. For the first set of experiments at low temperatures and flow rates, a 20-kw preheater was used, with sodium flow upward and across electrical immersion heaters. To obtain higher sodium qualities, flow rates, and temperatures, however, this preheater was replaced by an 80-kw boiler-preheater. This boiler is a pool type with inlet and outlet lines located near the top at opposite ends of the horizontal vessel. It is constructed of a 26-in. long, 12-in.-diameter, stainless steel (type 347) pipe section with end pipe caps. Twenty-five Watlow* immersion heaters extend through, and are seal welded to the bottom of, the vessel. The heaters are attached through specially designed fittings to allow easy replacement of burned out units.

* Watlow Electric Mfg. Co.

The test section shown in Figure 3 is a 1/4-in. by 1/2-in. annular passage, 27 in. long. The inner tube, inserted in the bottom and extending up to the high flux heater, serves as a well for a traveling thermocouple. Under equilibrium two-phase flow conditions, the temperature variation along the test section is an accurate indication of the two-phase pressure drop. The upper end of the test section accommodates the replaceable high flux heaters described above.

Thermocouple wells are provided for sodium bulk temperature measurements, and three taps are located 9, 19, and 26-1/2 in. from the sodium inlet line for pressure determination. A void detector (permanent magnet flowmeter) is located midway between the lower two pressure taps. The void fraction is determined from a comparison between the outputs of this flowmeter and the primary, all liquid, meter at the pump suction.

Sodium flow rates in the test section and in the pump suction line are measured with calibrated permanent magnet flowmeters. Pressures are measured with a sodium manometer in the subcooled flow cases, and are determined from the temperature measurements in the two-phase flow cases. All important temperatures are measured with precalibrated chromel-alumel thermocouples. To protect the high flux heaters from actual physical burnout during critical heat flux experiments, two burnout detectors were used. The detectors were connected in series to the heater power circuit and the activation of either one was sufficient to disrupt the power to the heater. The first detector was dependent on the heater temperature, and the second was dependent on the differential thermal expansion between the heater sheath and the graphite core electrode. A sudden rise in temperature, and a corresponding expansion of the heater electrode, at or just prior to critical heat flux, actuates one or the other of the two detectors.

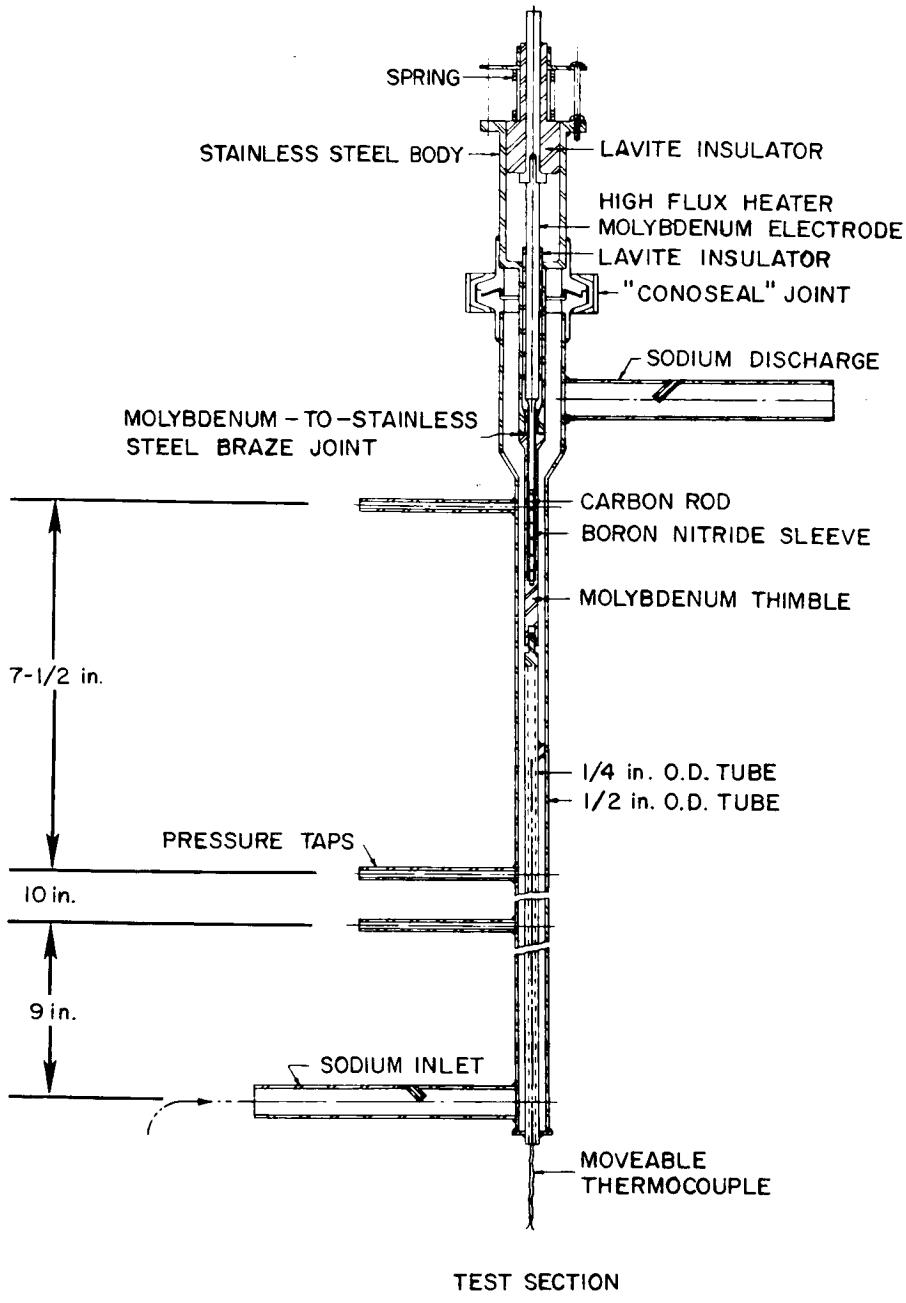


Fig. 3. First Test Section for Two-Phase Loop

The forced convection nucleate boiling data were obtained by using stainless steel and molybdenum sheathed heaters under pressures of 2 to 8 psia. Flow rates varied from 0.6 to 3 gpm (1.3 to 6.7 ft/sec in the test section), with average subcoolings up to 116°F.

The heat transfer characteristics plotted as heat flux vs the surface to sodium temperature difference were represented for each set of conditions by two straight lines; the break at their intersection indicates the change from forced convection to boiling dominated heat transfer. Unlike the familiar boiling curves of other liquids which show nucleate boiling over a wide range of heat fluxes, these data show that convection heat transfer dominates almost to the critical heat flux. Only at these high heat fluxes near the critical value does nucleate boiling seem to dominate the heat transfer mechanism. The surface temperature data confirm this conclusion, for only at these very high heat fluxes were fluctuations in the temperature observed. Figure 4 shows the data for two runs at 2 and 3 gpm. The change from forced convection to boiling dominated heat transfer is seen, as is the increase in the heat flux with flowrate at a constant temperature difference.

A comparison of the forced convection data with the correlation of Dwyer[5] for heat transfer in annuli [$Nu = \delta + \beta(\overline{\psi}Pe)^{\gamma}$] is also shown in Figure 4. The data agree very well with this correlation. The correlation of Lubarsky and Kaufman[6] for heat transfer in round tubes ($Nu = 0.625\ Pe^{0.4}$) is also shown in the figure for comparison.

Critical heat flux for sodium under subcooled forced convection flow was obtained for system pressures of 2 to 8 psia, flow rates of 0.7 to 3 gpm, and subcoolings to 71°F. Under two-phase flow, pressures ranged from 3.6 to 8 psia, flow rates from 0.5 to 1.4 gpm, and qualities from 0 to 14%.

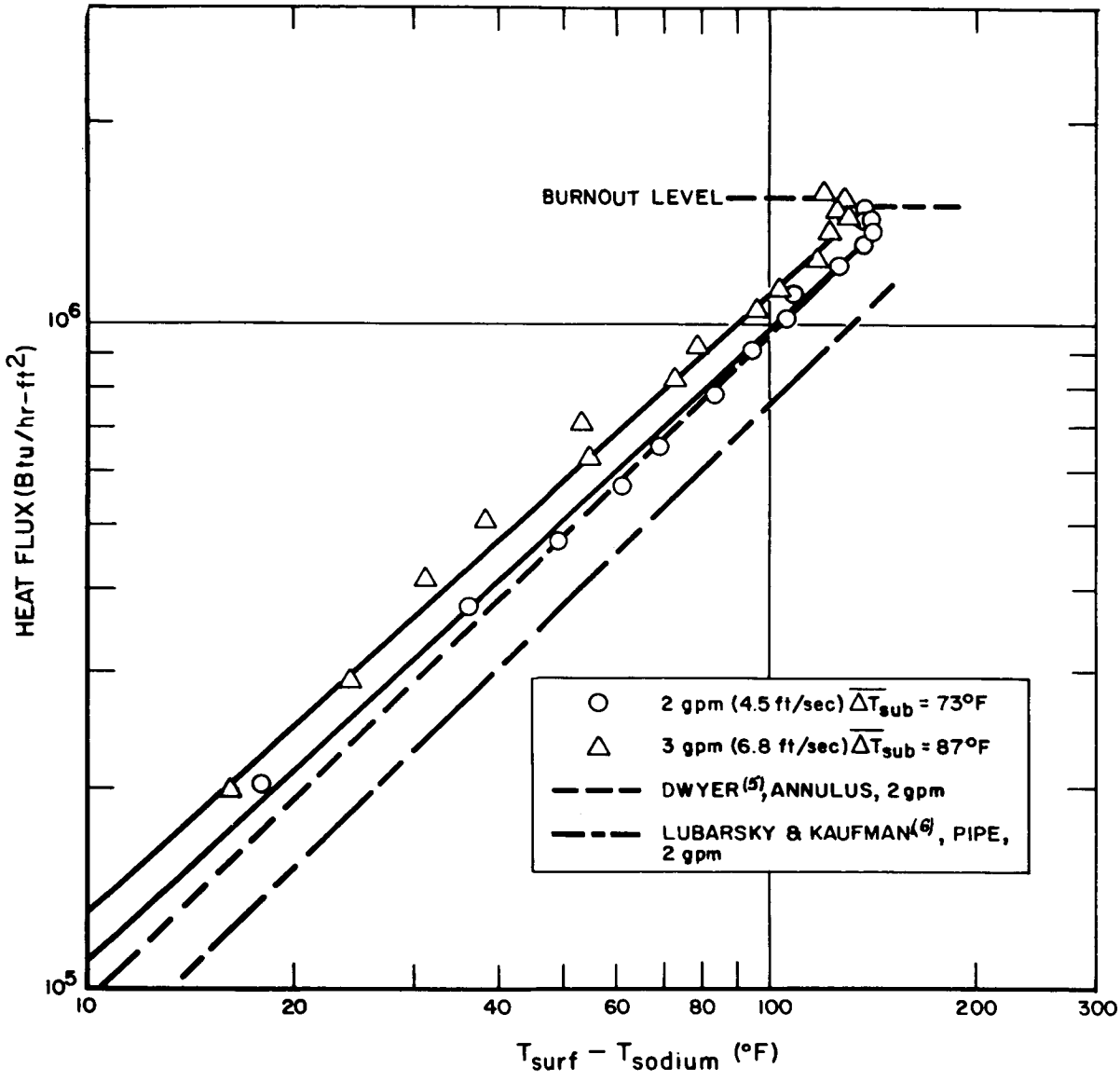


Fig. 4. Sodium Boiling and Critical Heat Flux, Stainless Steel Heater, 2 psia

Many attempts have been made by various investigators to predict the value of the critical heat flux under forced convection flow as a function of pressure, flow, and subcooling or quality, with only limited success. However, it is known from previous experiments reported in the literature that the CHF is a strong function of the coolant velocity, pressure, and its subcooling or quality. Most correlations of data are thus empirical correlations relating the CHF to these parameters.

The method of superposition was employed to correlate the subcooled forced convection data. This method of analysis subdivides a complex mechanism of heat transfer into smaller, more easily solvable problems, and superposes the effects of each one. By this method the CHF is equal to the sum of the CHF under saturated pool boiling conditions and the contributions of the subcooling and forced convection effects[7,8,9]

$$CHF = [CHF]_{\substack{\text{Saturated}\\ \text{pool}\\ \text{boiling}}} + [q/A]_{\substack{\text{Subcooling}\\ \text{effect in}\\ \text{pool boiling}}} + [q/A]_{\substack{\text{Forced}\\ \text{convection}\\ \text{no boiling}}}$$

The effects of the interactions between the various contributions are neglected in this method, but the terms can all be approximated by using established correlations.

Attempts to correlate the sodium data by using this method show that a better correlation is obtained by using the subcooling rather than the total temperature difference values in the forced convection contribution. Figure 5 gives a plot of the CHF as a function of the product $h_c \Delta T_{sub}$. Straight line correlations of the 2 and 5 psia data resulted in the following empirical equations:

$$CHF = 737{,}000 + 1.33\, h_c \Delta T_{sub} \qquad p = 2 \text{ psia}$$

$$CHF = 1{,}080{,}000 + 2.10\, h_c \Delta T_{sub} \qquad p = 5$$

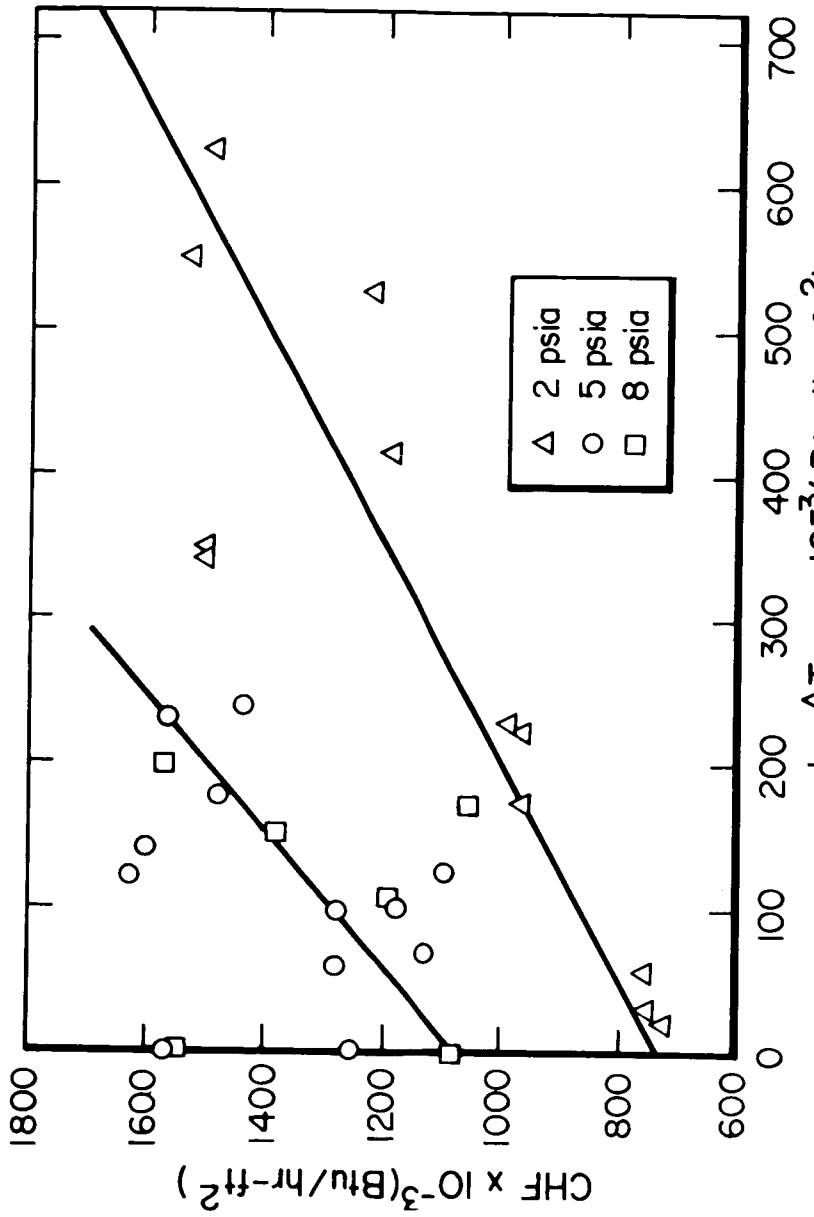


Fig. 5. Critical Heat Flux under Subcooled Forced Convection

On the basis of the superposition method, the constants 737,000 and 1,080,000 Btu/hr ft^2 comprise the total pool boiling contributions to the CHF; i.e., the saturated pool boiling contribution and the subcooling effect under pool boiling. They are, therefore, somewhat higher than the CHF of saturated pool boiling at the respective pressures (600,000 and 700,000 Btu/hr ft^2).

On the basis of the results obtained for other liquids, and on the basis of the sodium pool boiling data,[2] the critical heat flux is expected to increase with the system pressure. Early data obtained at 5 and 8 psia showed considerable scatter with several CHF values lower than corresponding values at 2 psia. This scatter was eliminated at the later stages of experimentation with the conclusion that these lower CHF values were premature; that is, the burnout detector indicated critical heat flux due to a surge or oscillation in temperature even though actual CHF had not been reached. Due to power limitations of the experimental equipment, only a limited range of flow rates and subcoolings could be investigated at these low pressures, and higher pressures could not be reached. The data are sufficient to indicate that the CHF does increase with pressure, but on the other hand, are insufficient to determine the dependence of the slope of the curve on the system pressure.

The critical heat flux under two-phase flow was correlated as a function of the exit quality and pressure as shown in Figure 6. The exit quality and pressure were determined at a point slightly downstream of the high flux heater at the exit of the test section. The CHF is seen to decrease sharply with the increase in quality of the two-phase mixture but increases, as expected, with the system pressure. Attempts to correlate these and the subcooled boiling data in terms of nondimensional parameters have not succeeded as yet. Figure 7 shows a summary of these data as a

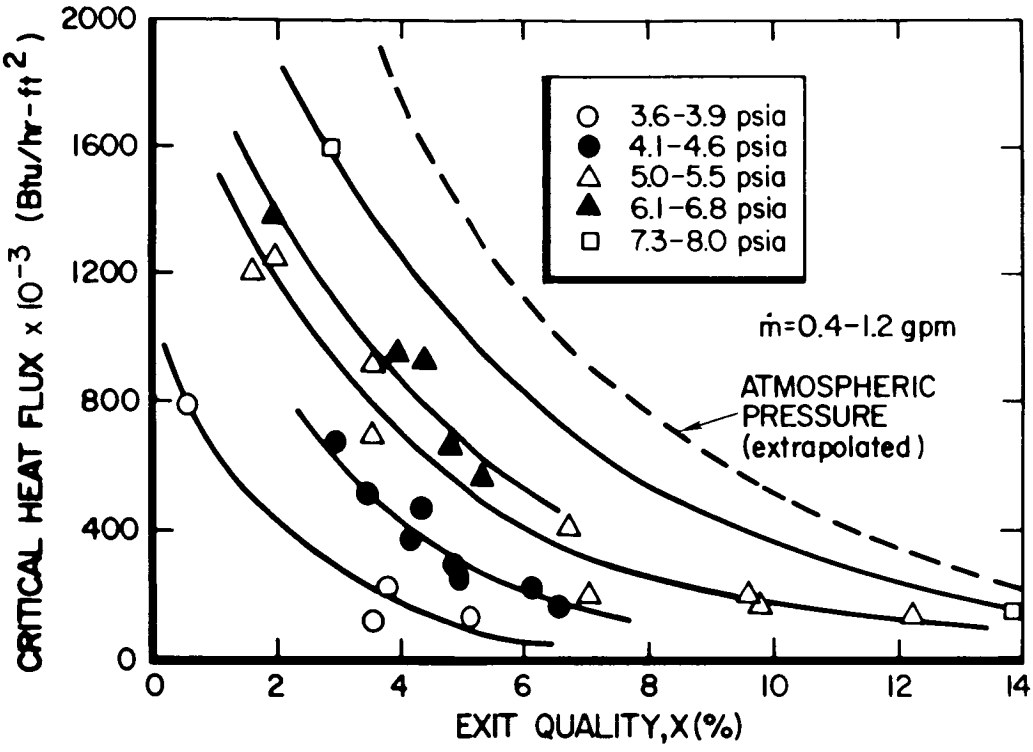


Fig. 6. Critical Heat Flux for Two-Phase Sodium Flow

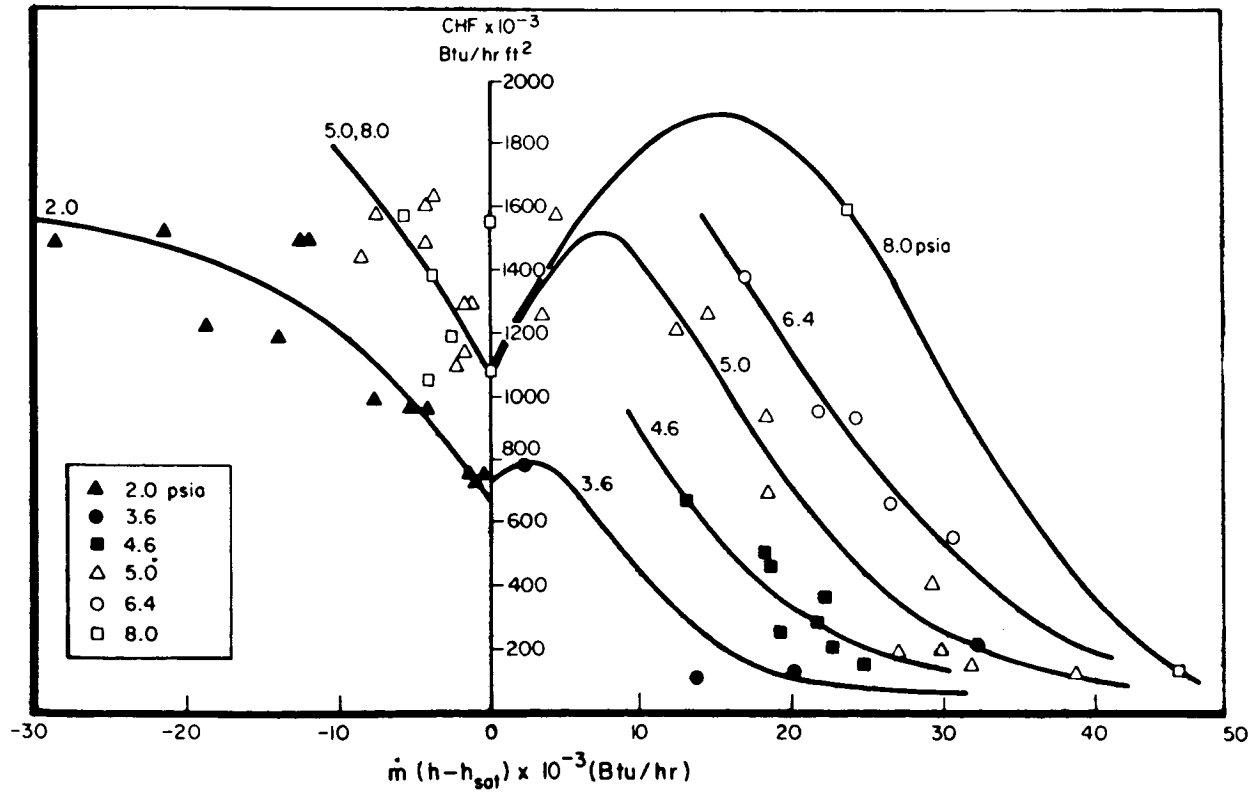


Fig. 7. Critical Heat Flux of Sodium under Forced Convection

function of the dimensional group $\dot{m}(h - h_{sat})$. The flow rate $\dot{m}$ is related to the convective coefficient h_c used in the subcooled data correlation, while the enthalpy difference $(h - h_{sat})$ is proportional to the subcooling or the quality. In the subcooled region ($\dot{m}\Delta h < o$), the CHF is seen to decrease with decreasing flow or subcooling; in the two-phase region ($\dot{m}\Delta h > o$), the CHF first increases then decreases rapidly with increasing flow or quality. This peaking of the CHF curve at low qualities has also been reported in the literature for other liquids, primarily water.

Similar alkali liquid metal data in the low pressure low quality range studied here are not available in the literature. Comparison of these data with other liquid metal critical heat flux data can therefore only be qualitative. Both Hoffman[10] and Fisher, et al.,[11] report critical heat flux data in the high pressure and quality range for potassium and for rubidium and cesium, respectively. Their critical heat flux values, at above-atmosphere pressures and at qualities above 35%, were below 300,000 Btu/hr-ft^2. This seems to be in agreement with the low pressure, low quality sodium data presented in Figure 6.

TWO PHASE HYDRODYNAMICS

A study of the steady state pressure drops and void fractions as a function of absolute pressure, flow rate, and quality was performed for vertical upflow of sodium in the unheated annular test section described earlier. Some flow instabilities were evidenced by oscillations in the bulk fluid temperature, and therefore in the local pressure; however, these fluctuations were kept at a minimum and never exceeded 15°F or approximately 0.3 psia. The quality in the test section was calculated from a heat balance whereas the void fraction was determined from the output of two electromagnetic flowmeters, one reading liquid flow and the other

reading two-phase flow. From electromagnetic flowmeter theory and from a system mass balance, we have:

$$\dot{m}_f = (1 - \alpha) A_o V_f \rho_f$$

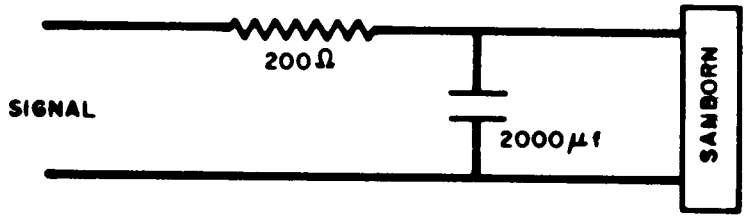
and

$$\alpha = 1 - \frac{V_o}{V_f}(1 - x) \quad .$$

Since E is proportional to V,

$$\alpha = 1 - \frac{E_o}{E_{TP}}(1 - x) \quad .$$

Due to the random void flow past the flowmeter under two-phase flow conditions, the magnetic flowmeter exhibited severe oscillations — so severe, in fact, that accurate readings could not be obtained directly. To overcome this difficulty a filter circuit was attached to the meter output as shown below.



The circuit greatly reduced, and often eliminated, the oscillations; thereby, accurate readings were obtained when using a conventional signal recorder. Calculations and experimental verifications showed that the actual emf measured was the time average of the original oscillating signal. It is expected that a spectrum analysis ("noise analysis") of the flowmeter output may yield very important and interesting information regarding flow characteristics and void distribution. The pressure drop was

determined from the temperature measurements along the inner tube of the annulus on the assumption that thermodynamic equilibrium between the sodium and its vapor existed.

The data, shown in Figures 8 and 9, cover flow rates of 0.3 to 1.8 gpm, pressures of 1.5 to 10 psia, and qualities up to 14%, and are presented as the pressure drop parameter, ϕ_L, and the liquid fraction, R_L, as a function of the Martinelli parameter X_{tt}. The parameter ϕ_L^2 is defined as the ratio of the two-phase frictional pressure drop to the pressure drop that would occur were only the liquid flowing in the pipe. The parameter X_{tt}^2 is defined as the ratio of the liquid pressure drop to the vapor pressure drop, each flowing alone. For both phases in the turbulent regime, assuming $f = C/Re^{0.2}$,

$$X_{tt} = \left(\frac{1}{x} - 1\right)^{0.9} \left(\frac{\rho_g}{\rho_f}\right)^{0.5} \left(\frac{\mu_f}{\mu_g}\right)^{0.1} .$$

The total pressure drop as measured experimentally was corrected for the momentum pressure drop due to sodium vaporization during flow; the resulting frictional pressure drop is the pressure plotted in Figure 8. Over the range of flow rates and pressures covered during the experiment (liquid Reynolds numbers of 6000 to 34,000, and pressures of 1.5 to 10 psia), no additional parametric dependencies could be discerned when the pressure drop ratio was plotted as a function of the parameter X_{tt}. It is therefore concluded that the slight scatter in the data as seen in Figure 8 is due to the experimental variations and errors (especially at the high X_{tt}, low quality region), but most of the data fall between the Lockhart-Martinelli[12] correlations for viscous-viscous and turbulent-turbulent flow.

A comparison between these sodium data and recent potassium

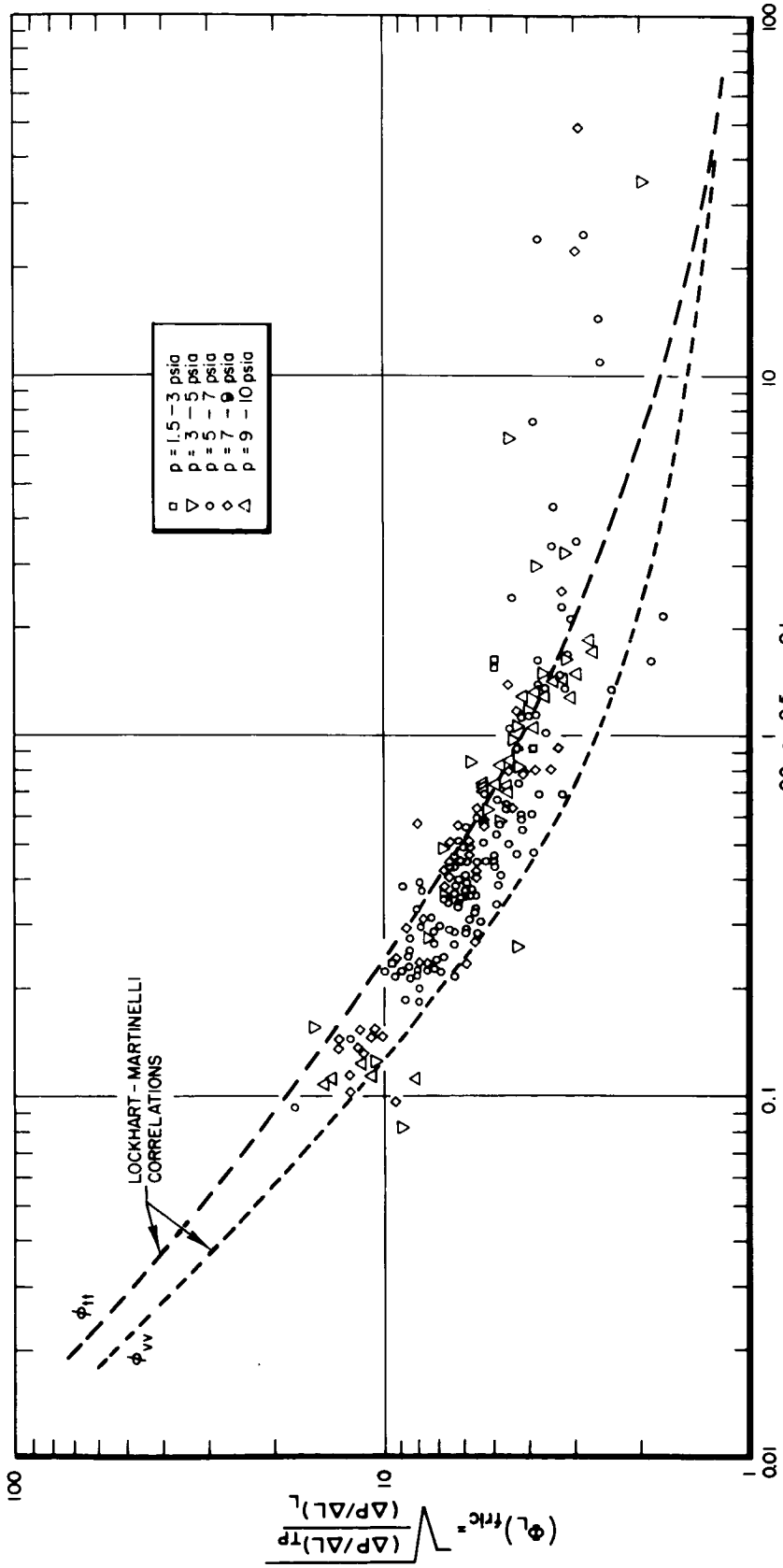


Fig. 8. Two-Phase Frictional Pressure Drop for Vertical Upflow of Sodium

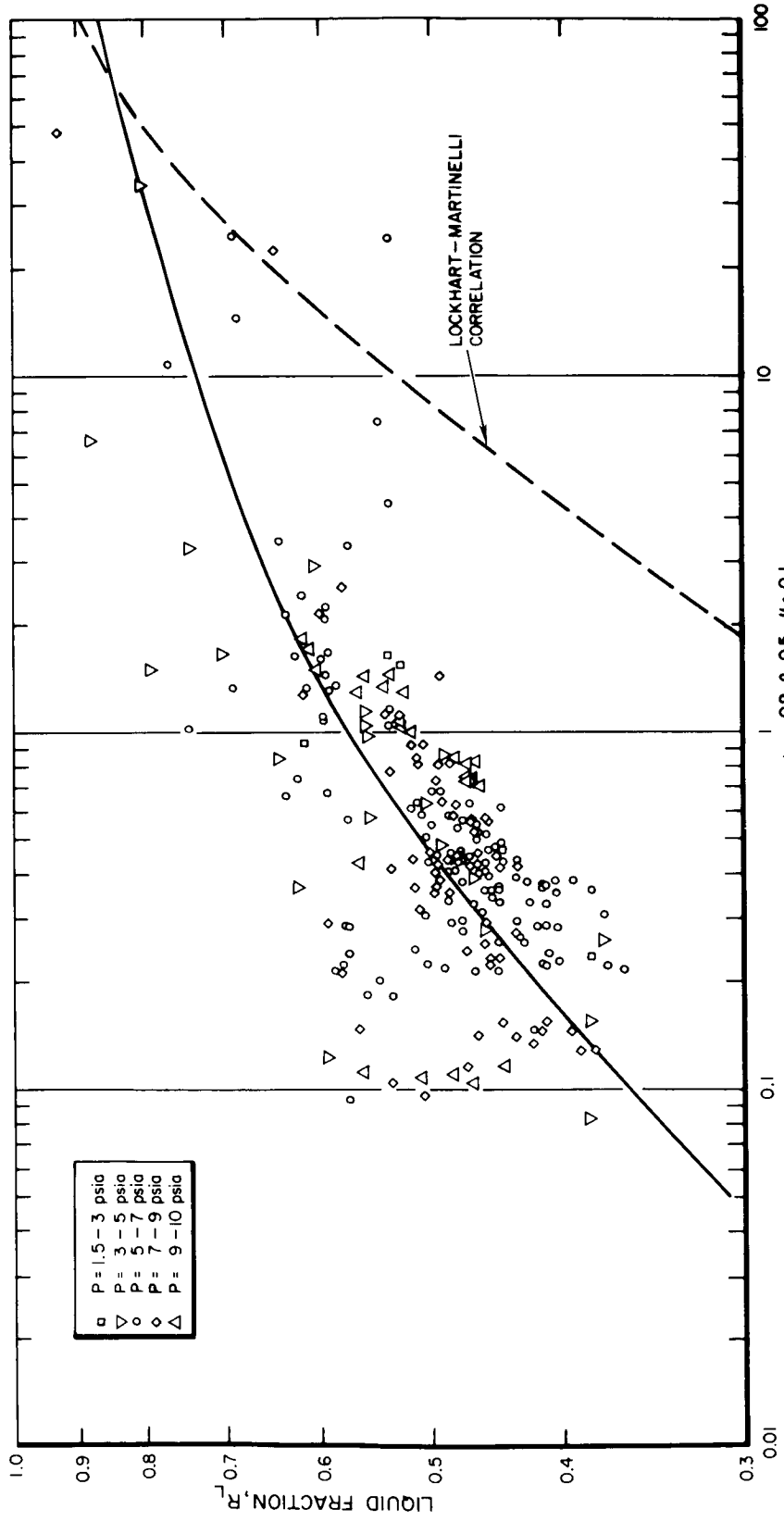


Fig. 9. Liquid Fraction in Vertical Upflow of Sodium

data obtained at the University of Michigan[3] shows excellent agreement. Comparisons with other liquids [13] and with the Lockhart-Martinelli correlation shows slightly lower pressure drops for two-phase alkali liquid-metals than for nonmetallic liquids.

The liquid fraction data in Figure 9 show much more scatter than the pressure drop data discussed above; but again, no parametric dependencies could be established. Again at high values of X_{tt}, a high probable error is introduced in the calculation of the very low quality of the two-phase mixture. The accuracy of the void fraction, on the other hand, is strongly influenced by the severity of the fluctuations in the flowmeter output, caused by the variable distribution of voids in the two-phase mixture as it passes through the magnetic poles of the flowmeter. As the void fraction increases, these fluctuations increase until at high qualities (low X_{tt}) the flowmeter output ceases to be proportional to the velocity because the electrical path within the flowmeter section is sufficiently disrupted by vapor.

A comparison of the sodium and potassium data of Reference 13 is also very good, although the scatter is great in both sets of data. This is an extremely encouraging result, since the sodium data were obtained from the outputs of electromagnetic flowmeters and the potassium data were obtained from gamma-ray attenuation techniques. It is also seen from Figure 9 that the Lockhart-Martinelli correlation is considerably lower than that for alkali liquid metals.

A plot of the sodium slip ratio as a function of the parameter X_{tt} is given in Figure 10. From a system mass balance, the slip ratio is calculated to be

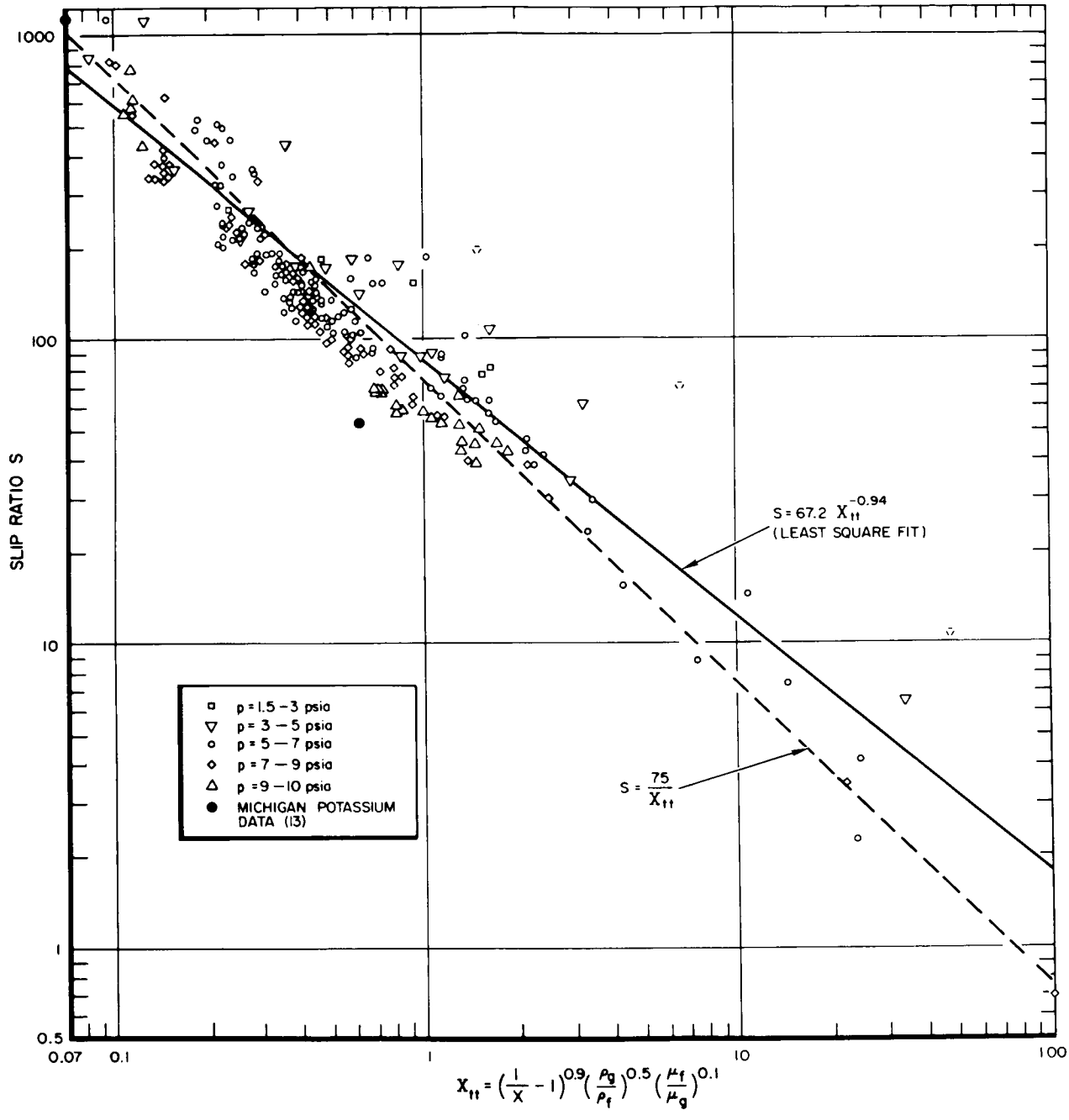


Fig. 10. Slip Ratio in Two-Phase Vertical Upflow of Sodium

$$S = \frac{V_g}{V_f} = \left(\frac{x}{1 - x}\right)\left(\frac{1 - \alpha}{\alpha}\right)\left(\frac{\rho_f}{\rho_g}\right) \quad .$$

A least square straight line fit of the data yields the correlation

$$S = 67.2 X_{tt}^{-0.94} \quad .$$

An approximate correlation of the data is therefore

$$S \cong \frac{75}{X_{tt}} \quad .$$

Only two values of the slip ratio for potassium are given in Reference 13 and they are shown in the figure for comparison. The agreement with the sodium data is very good.

CONCLUSIONS

The primary objective of these studies has been to provide information on two-phase heat transfer characteristics, hydrodynamic effects, void formation, and pressure generation required in the safety evaluation of sodium cooled reactors. The work described herein completes the steady-state phase of the experimental program and has been integrated into the analytical work.

New sodium pool boiling data have been obtained to confirm the variation of the critical heat flux of sodium with pressure and allow the extrapolation to actual reactor conditions. The two-phase forced convection flow data has yielded very useful critical heat flux, pressure drop, and void fraction correlations required for the analytical techniques being developed concurrently. Due to experimental limitations, the data presented here do not cover the complete range of parameters of interest in reactor design, but extrapolation to reactor conditions is possible.

Future work on this program will include the study of the hydraulic stability and dynamics of sodium under two-phase flow,

the investigation of heat transfer under conditions of unstable two-phase flow, and the study of transient void growth and collapse and associated pressures.

NOMENCLATURE

A = flow area

CHF = critical heat flux, Btu/hr-ft^2

E = flowmeter output

h_c = heat transfer coefficient, Btu/hr-ft^2-°F

$\dot{m}$ = flow rate, lb/hr

Nu = Nusselt number

p = pressure, psia

Pe = Peclet number

q/A = heat flux, Btu/hr-ft^2

S = slip ratio

ΔT_{sub} = subcooling, °F

V = velocity

x = quality

X_{tt} = Martinelli parameter

α = void fraction

β, γ, δ = geometry dependent constants in Dwyer's equation

μ = viscosity

ρ = density

$\overline{\psi}$ = average value of the ratio of the eddy diffusivities of heat and momentum

Subscripts

f = liquid phase

g = vapor phase

TP = two phase

o = all liquid flow

REFERENCES

1. R. C. Noyes, "Boiling Studies for Sodium Reactor Safety" Part I, NAA-SR-7909 (August 1963)

2. H. Lurie and R. C. Noyes, "Boiling Studies for Sodium Reactor Safety," Part II, NAA-SR-9477 (October 1964)

3. R. E. Balzhiser, et al., "Investigation of Liquid Metal Boiling Heat Transfer," Third Quarterly Progress Report, University of Michigan (February 1964) IP-05750-9-P

4. C. P. Colver, "A Study of Saturated Pool Boiling Potassium up to Burnout Heat Fluxes," Ph. D. Dissertation, University of Michigan (September 1963)

5. O. E. Dwyer, "Eddy Transport in Liquid Metal Heat Transfer," Brookhaven National Laboratory, BNL-6149 (May 1962)

6. J. G. Knutsen and D. L. Katz, Fluid Dynamics and Heat Transfer, McGraw Hill Book Co., p 466 (1958)

7. N. Zuber, M. Tribus, and J. W. Westwater, "The Hydrodynamic Crisis of Saturated and Subcooled Liquids," International Heat Transfer Conference, Boulder, Colorado (1961)

8. S. Levy, "Prediction of the Critical Heat Flux in Forced Convection Flow," General Electric Co., GEAP 3961 (1962)

9. W. R. Gambill and H. W. Hoffman, "Boiling Liquid Metal Heat Transfer," Space Nuclear Conference, American Rocket Society, No. 1737-61 Oak Ridge National Laboratory (May 1961)

10. H. W. Hoffman, "Recent Experimental Results in ORNL Studies with Boiling Potassium," Proceedings of the 1963 High Temperature Liquid Metal Heat Transfer Technology Meeting, ORNL-3605, Vol 1 (November 1964)

11. C. R. Fisher, L. T. Clark, and J. H. Moskowitz, "Forced Convection Boiling of Rubidium and Cesium Heat Transfer and Pressure Drop," AGN-8099 (February 1964)

12. R. W. Lockhart and R. C. Martinelli, "Proposed Correlation of Data for Isothermal Two-Phase, Two Component Flow in Pipes," Chemical Engineering Progress, Vol 45, No. 1 (January 1949)

13. R. E. Balzhiser, et al., "Investigation of Liquid Metal Boiling Heat Transfer," University of Michigan, Report 05750-19-P (February 1965)

N66 31698

RECENT DEVELOPMENTS IN HEAT TRANSFER AND DEVELOPMENT OF THE MERCURY BOILER FOR THE SNAP-8 SYSTEM*

by

A. J. Sellers

Assistant Senior Engineer, SNAP-8 Division
Aerojet-General Corporation

G. M. Thur

Section Head, SNAP-8 Components
National Aeronautics and Space Administration

and

M. K. Wong

Senior Engineer, Nucleonics Division
Aerojet-General Corporation

(Paper presented by A. J. Sellers)

SUMMARY

The major requirements associated with mercury once-through boilers for space powerplants are repeatable startup and reliable long-term heat-transfer performance without deleterious effects on other system components such as turbines, pumps, and condensers. During the past few years there have been a number of instances where mercury boilers were known to decondition either during startup or after some period of operation. The connotation is that any performance in the direction of providing poorer heat-transfer performance than expected, from either design correlations or some minimum accepted performance, is termed deconditioning, while any trend providing improved performance after initial thermal equilibrium is termed conditioning. This

*The information appearing in this paper is based on work conducted under National Aeronautics and Space Administration Contract NAS 5-417.

PRA/VKC/NASA-L 27 SEPT. 1965

PRECEDING PAGE BLANK NOT FILMED.

condition of performance uncertainty during system startup and endurance operation can cause performance reduction, prevent adequate startup, and precipitate turbine corrosion/erosion.

During the development of the boilers for the SNAP-8 nuclear-electric, Rankine-cycle system, a number of single-tube and full-scale boiler tests were performed (Table 1). The experimental data from these tests were evaluated to determine the validity of proposed semiempirical boiling heat transfer and two-phase flow pressure drop correlations,[1] and boiling conditioning effects. A summary evaluation of these results are:

1. The initial boiler performance characteristics are dependent on the mercury flow passage internal wall surface conditioning state and the thermal and dynamic conditions imposed by the flow passage internal geometry.

2. High-velocity liquid-phase vortex flow at the preheat section end point combined with similar dynamic conditions in the low-vapor-quality section demonstrate excellent boiler conditioning effects when the mercury flow passage is cleaned by established methods prior to mercury injection.

3. The boiling heat-transfer rates obtained from a fully conditioned boiler are in close agreement with the predictions established by the dropwise dry-wall boiling heat-transfer correlations.

4. The two-phase flow pressure drop data are correlated by means of the product (ϕf_v) in terms of a modified Martinelli parameter (λ) as proposed by TRW.[1]

5. The introduction of a tight preheat section plug-insert geometry providing high liquid velocity also improved the boiler performance stability very significantly.

6. Mercury inventory variations were minimized with tight plug-insert geometry.

This paper will describe the test apparatus, operation, and test results of the heat-transfer experiments performed during 1965 at Aerojet-General's Nucleonics Division under NASA Contract NAS 5-417. It was anticipated that the prototype boiler design would have been tested by this writing; however, program delays have prevented these tests.

Superscript numbers in parentheses refer to similarly numbered references listed at the end of the text.

TABLE 1

SUMMARY OF SINGLE-TUBE AND FULL-SCALE BOILER TESTS

Test Item	Containment Material	Plug Section: Plug Length	Plug Section: Wire Size (in.)	Plug Section: Wire Pitch	Overall Length (ft)	Tape Pitch (in.)	Tube ID (in.)	Flow Rate (lb/hr)
1. Single-Tube Tests								
TS 1E-1	316-SS	66-3/4 in.	0.0625	2.5 in.	45	Y=4	0.652	1600
TS 2B								
a.	9Cr-1Mo	10 ft 4 in.	0.105	3 in. for 3 ft 5 in. for 7 ft	60	Y=4	0.902	2600
b.	9Cr-1Mo	10 ft 4 in.	0.135	3 in. for 3 ft 4 in. for 2 ft 5 in. for 5 ft 4 in.	60	Y=4	0.902	2600
CL-3	9Cr-1Mo	5 ft 0 in.	0.049	1.5 in.	57	1.5	0.397	500
CL-4	9Cr-1Mo	5 ft 0 in.	0.048	0.75 in.	57	1.5	.397	500
2. Full-Scale Tests								
-1 SNAP-8 Boiler	9Cr-1Mo	9 ft 9 in.	0.135	3 in. for 3 ft 4 in. for 2 ft 5 in. for 4 ft 9 in.	60	Y=4	0.902	11,200

I. INTRODUCTION

Boiling liquid-metal heat-transfer rates and the associated two-phase flow dynamics of once-through heat exchangers have been the subject of a large number of experimental and theoretical studies during the past decade, particularly since the initiation of the development of various Rankine-cycle SNAP power conversion systems. Difficulties were encountered in achieving rated boiling heat transfer fluxes in NaK-heated once-through mercury boilers. These difficulties were encountered in varying degrees in mercury flow passages made of 316 SS, Haynes-25 and 9Cr-1Mo alloys. Regardless of the material used for the mercury flow passage, some of these boilers demonstrated initial performance characteristics up to design expectations, although the length of the required conditioning period varied. Others did not approach the design expectations after hundreds and even thousands of hours of continuous operation. This was believed to be caused by nonwetting, surface contamination, and/or liquid phase slug formation due to absence of early vortex flow establishment in the flow passage next to the liquid-vapor interface.

Several supporting programs were conducted in conjunction with SNAP-8 boiler development activity to investigate these possible causes. The effects of additives on wetting during mercury pool boiling heat transfer were evaluated.[2] On the basis of the results of this study, rubidium was added to the mercury in amounts up to 860 ppm. The predicted boiling heat-transfer rates were achieved after addition of the Rb in a SNAP-8 full-scale boiler initially operating at a highly deconditioned state for several hundred hours. To investigate the effect of high-velocity liquid-phase vortex flow on the overall boiler performance, a "tight" preheat section plug insert, providing a liquid-phase velocity of 7.0 ft/sec, was initially tested in an experimental boiler originally performing in a deconditioned state. The results showed immediate improvement in obtained boiling heat-transfer rates and the boiler performance stability. The boiling heat-transfer rates as represented by the boiler NaK temperature profile approached the design expectations. The boiler exit pressure fluctuations were reduced to a negligible value. This initial qualitative evidence prompted further investigation of the SNAP-8 boiler design concepts.

II. PURPOSE

The object of this experimental study is to investigate the thermal and dynamic performance characteristics of different once-through boiler plug-insert geometries.* The availability of design data in this area is very limited, yet these data are very important in controlling the thermodynamic behavior of a boiler such as that used in SNAP-8 and similar Rankine-cycle power conversion systems. Since most of these boilers initially exhibit de-conditioned characteristics to some extent, it is of particular interest to investigate the effect of different working-fluid dynamic aspects in the plug-insert section. Initial positive evidence of qualitative value warranted further investigation into this boiler design area.

III. DESCRIPTION OF TEST APPARATUS

A. LOOP DESCRIPTION

A test loop was designed to simulate the SNAP-8 dynamic-cycle conditions for corrosion study. It is a three-loop system consisting of a heated primary circulation NaK loop, coupled through a simulated mercury boiler Rankine-cycle loop which in turn rejects its heat through the condenser to an air-cooled circulating NaK loop. The following operating ranges were used for the boiler plug insert experiment:

NaK Primary Loop

Boiler inlet temperature	1,330°F
NaK flow rate	2,050 lb/hr max
Heater power input	35 kw max

Mercury Loop

Mercury flow	500 lb/hr nominal
Boiler inlet temperature	500°F
Boiler inlet pressure	500 psia max
Boiler outlet pressure	100 psia min

Figure 1 is the flow diagram of the loop and Figure 2 is the schematic arrangement of the loop. The three loop system was constructed to high-vacuum standards.

*Such a geometry consists of a helically wound wire on a solid bar closely fitted and inserted in a mercury tube. The resulting flow passage is of a helical pattern.

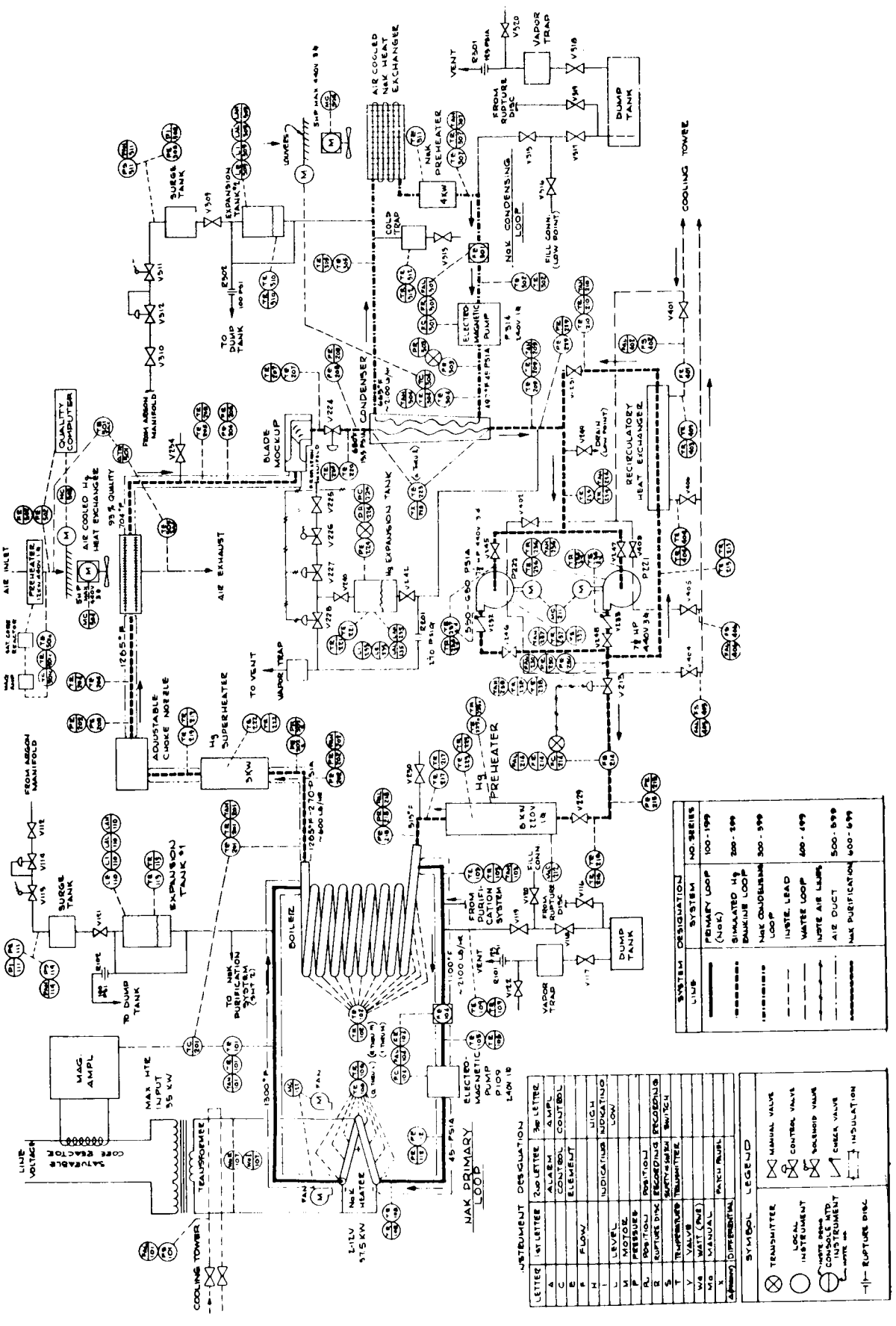


Fig. 1. Flow Diagram - Simulated Mercury Rankine-Cycle Test Loop

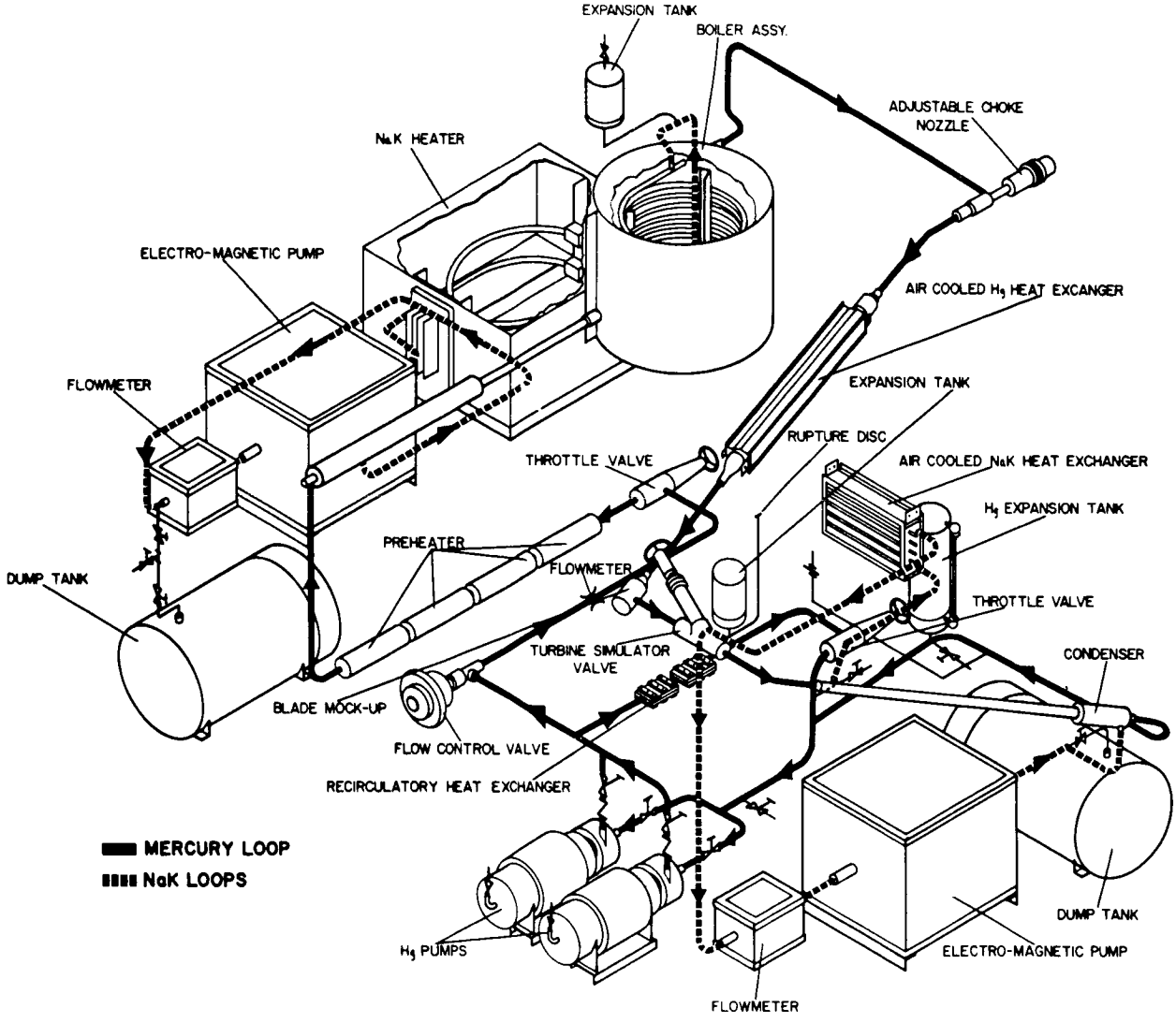


Fig. 2. Layout - Simulated Mercury Rankine-Cycle Test Loop

1. Primary NaK Loop

The NaK primary loop employs a direct resistance heater in which low voltage electrical current is passed through the NaK-carrying tube and the NaK. The heater is coiled with the two grounded leads on the loop side and an insulated low voltage lead at the midpoint of the coil. Since the resistance of each leg is fixed, the power input is varied by controlling the voltage across the terminals. The voltage is regulated with a saturable-core reactor-transformer. An electromagnetic pump maintains the NaK flow which is measured by a magnetic flowmeter. A purification system is employed to reduce and maintain the system oxide level to less than 25 ppm. Other major components in the loop include a level indicator, expansion tank, dump tank, and a cover gas system.

2. NaK Condensing Loop

Major components of the NaK condensing loop consist of a conventional air-cooled finned-tube heat exchanger, a magnetic flowmeter, and an electromagnetic pump. A convection type of cold trap is employed to maintain a low oxide level in the loop.

3. Mercury Loop

The mercury loop uses two Chempump* Model CFHT-7 1/2-65 (one on a standby basis) for pumping the liquid mercury. A venturi flowmeter is used to measure mercury flow rate. Two semistandard valves are used for control purposes and for imposing a resistance between the pump and boiler. An adjustable choked nozzle located downstream of the boiler outlet to regulate boiler outlet pressure, is a convergent-divergent nozzle in which the throat area may be varied with a movable pintle. The mercury vapor is then passed through a desuperheater and a turbine-blade mockup section before entering the condenser. The desuperheater and the blade mockup are not necessary for the boiler experiment, but were originally designed for corrosion study. The NaK-cooled mercury condenser is a counter-flow heat exchanger consisting of three tapered condensing tubes with a straight length for subcooling.

The rest of the mercury loop consists of semiconventional liquid metal components such as bellows-sealed valves, electrical resistance level probes, and a cover gas system.

*Manufactured by Chempump Division of Fostoria Corp., Huntingdon Valley, Penn.

B. BOILER DESCRIPTION

The mercury boiler is once-through counter-flow tube-in-shell heat exchanger in helix form with a protruding inlet and outlet (Figure 3). The mercury flows in the tube and the NaK through the annulus passage. An inlet plug is inserted into the straight part of the protruding mercury inlet section to increase the liquid mercury and low vapor quality helical velocity. A spiral wire vortex-generator is installed in the coiled mercury tube to promote heat transfer. Spacers are used to center the mercury tube in the annulus. The NaK inlet and outlet are located near the ends of the shell. The boiler configuration and geometry are as follows:

Mean helical coil diameter (in.)	18
Helical shell pitch (in.)	1-3/8
Shell size (in.)	1-1/8 OD by 0.083 wall by 9.959 ID
Tube size (in.)	9/16 OD by 0.0832 wall by 0.397 ID
Vortex wire diameter (in.)	0.049
Vortex wire pitch (in.)	1.5
Coil tube length (ft)	55
Straight tube length (ft)	5
Tube material	9Cr-1Mo
Shell material	316 SS

The boiler was installed in a metal tank assembly and insulated with about 6-1/2 in. of fused alumina bubbles. Six 1/2-in.-thick layers of Fiberfrax insulation was affixed to the outside of the boiler supporting tank assembly. The test runs and corresponding plug insert geometries tested are listed in Figure 4.

C. BOILER TEST INSTRUMENTATION

1. Temperature Measurement

The NaK boiler inlet, outlet, and the boiler shell temperatures are measured by 1/16 in. diameter, stainless steel sheathed, MgO insulated thermocouples. These thermocouples have ungrounded junctions, and are attached to the 316 SS tube as shown in Figure 5. The NaK boiler inlet temperature is measured by three thermocouples attached circumferentially at the

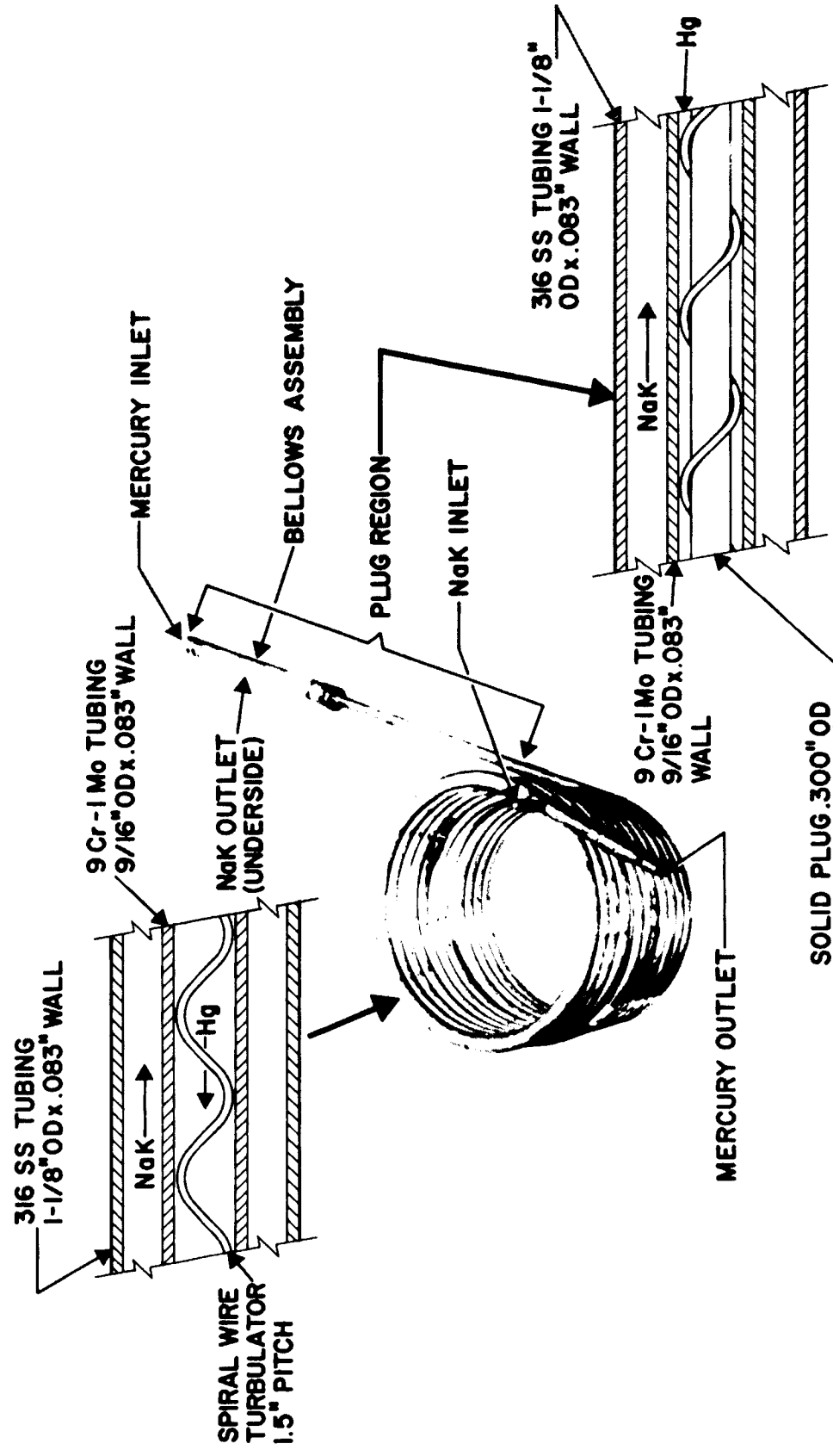


Fig. 3. Mercury Boiler

TEST RUN NO.	PLUG INSERT NO.	L	PREHEAT SECTION					VAPOR SECTION				REMARKS
				W	h	P_1	L_1		P_2	L_2		
		IN.	TYPE[1]	IN.	IN.	IN.	IN.	TYPE[1]	IN.	IN.	INSTRUMENTED	
1	1	--	W	--	--	.75	21	W	.75	36	NO	POOR PERFORMANCE DURING FIRST 660 HR
2	2	6	W	--	--	.125	15	W	.75	36	NO	GOOD INITIAL PERFORMANCE
3	2	6	W	--	--	.125	15	W	.75	36	NO	GOOD RESTART PERFORMANCE
4	1	--	W	--	--	.75	21	W	.75	36	NO	GOOD RESTART PERFORMANCE
5	3	9	M	.033	.048	.125	15	W	.75	36	YES	GOOD PERFORMANCE D = .397" (ASSUMED)
6	4	9	M	.038	.045	.125	15	W	1.50	36	YES	GOOD PERFORMANCE D = .400" (ASSUMED)
7	4	9	M	.038	.045	.125	15	W	1.50	36	YES	GOOD PERFORMANCE PLUG #4 REINSERTED
8	3a	9	W	--	--	.125	15	W	1.50	36	YES	GOOD PERFORMANCE
9	3a	9	W	--	--	.125	15	W	1.50	36	YES	GOOD PERFORMANCE P_{ex} AND P_{in} OSCILLATION
10	3b	6	W	--	--	.17	15	W	1.50	24	YES	GOOD PERFORMANCE REDUCED P_{PL}

1 M = Machined Thread
W = Wire Wound

NOTES: a. All Wire Uses = 0.049 In. Diameter
b. OD of Plugs = 0.0398 in.

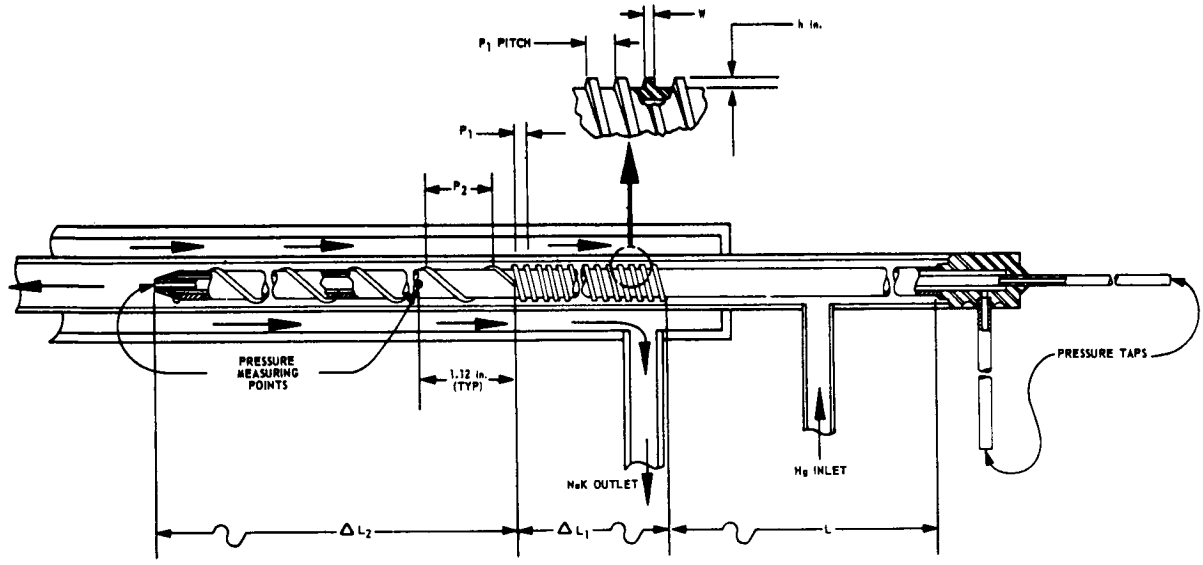


Fig. 4. Plug Insert Geometries Tested

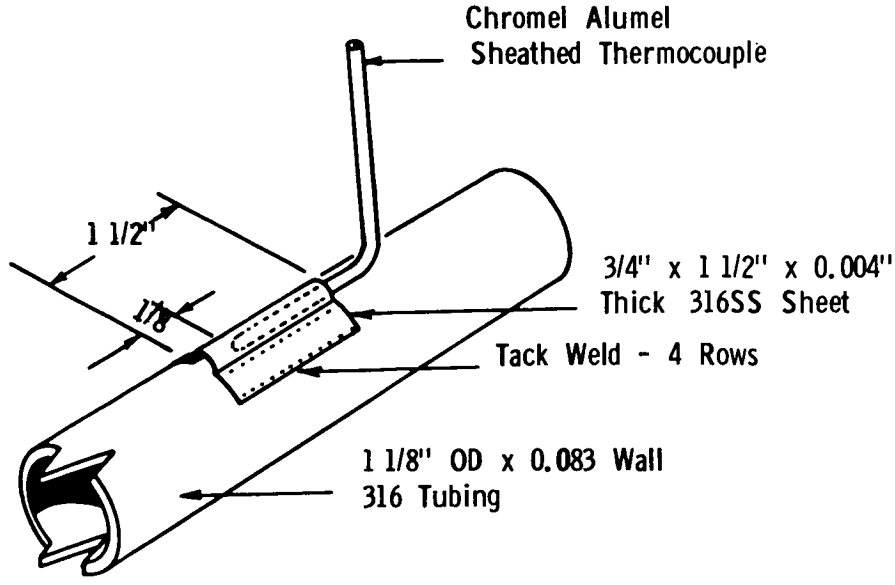


Fig. 5. Thermocouple Installation on Boiler

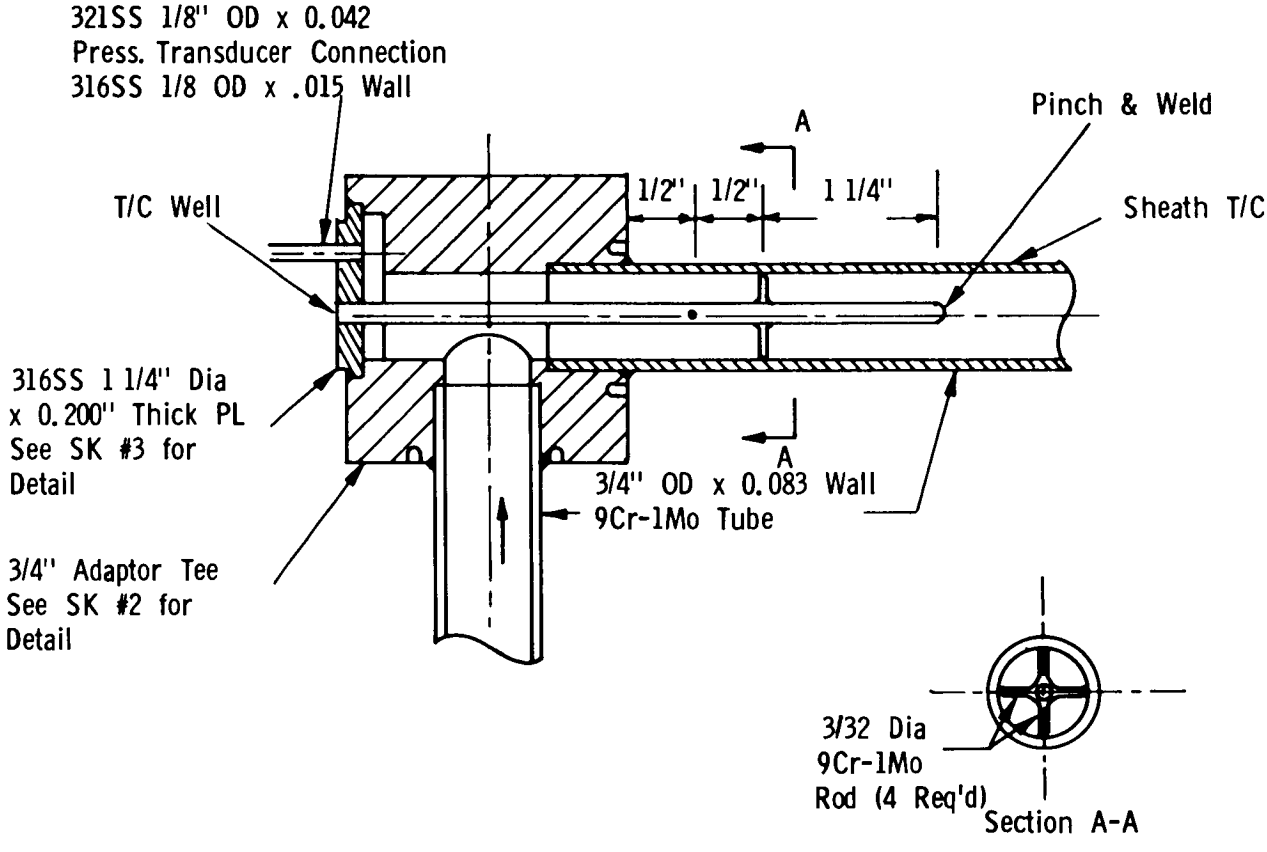


Fig. 6. Mercury Boiler Outlet Immersion Type of Thermocouple

tube 18 in. from the boiler. The boiler outlet temperature is measured by a thermocouple located at about 9 in. from the boiler shell. A total of 24 thermocouples are located along the 60-ft length of the boiler.

The mercury inlet and outlet temperatures are also measured by Chromel-P-alumel 1/16 in. diameter, MgO insulated, stainless steel sheathed ungrounded thermocouples. The boiler inlet thermocouple is welded to the tube wall 10 in. from the boiler inlet. The boiler outlet temperature thermocouple is an immersion type installed as shown on Figure 6, 15 in. downstream of the boiler.

Four Pace 150° reference junctions are used to condition the thermocouple signal. The NaK shell temperatures are recorded on a Leeds and Northrup 24 point 0-1500°F, 12 in. scale strip-chart recorder. The NaK boiler inlet temperature is recorded on a Daystrom Weston 24 point, 150°F-1500°F 4 in.-scale strip-chart recorder. The NaK boiler and the mercury boiler outlet temperature are recorded each on Motorola 2-point, 150°F-1500°F 4-in.-scale strip-chart recorders.

2. Temperature Measurement Accuracy

The thermocouples carry a manufacturers accuracy guarantee of $\pm$ 4°F from 0°F to 530°F, and $\pm$ 3/4% above 530°F. The Leeds and Northrup and Daystrom Weston records are periodically calibrated against a Leeds and Northrup portable potentiometer standard to an accuracy of 1/4% of full scale. The Motorola temperature recorders are set to an accuracy of 1% of full scale, but overall readout accuracy is judged to be approximately 2%.

3. Pressure Measurement

The boiler inlet, outlet, and the two pressure taps in the instrumented plug are measured by 0 to 500 psia range, unbonded type strain gage transducers. Solid state stable bridge supplies provide 6 v,dc excitation to each transducer. The output signal from each transducer is amplified to the desired level and transmitted to the indicators. These pressure readouts are indicated on Motorola 4-in.-scale strip-chart recorders that have a null-balance potentiometer type of movement. In addition, these pressures are also transmitted into a Honeywell Visicorder which is a mirror galvanometer oscillograph using instant trace paper. The Visicorder checks the small-scale

Motorola recorder and indicates the amplitude and frequency of the recorded pressure. Two 10-in.-diameter 0-400 psig, 1/4% accuracy Heise gages are also connected in parallel to the pressure taps of the instrumented plug.

The transducers are calibrated when a new plug insert is installed. Calibration of the transducers is accomplished by applying regulated nitrogen gas at the transducer pressure connection, this pressure is simultaneously monitored on a Bordon tube test gage of traceable accuracy. Several pressure increments throughout the operating range are applied, and the indicator readings recorded. Correction curves are drawn from the results and used to correct subsequent test data. The initial accuracy of each pressure-measuring system is found to be the resolution accuracy of the indicator and is within 1% of full scale.

4. Flow Measurement

An ASME standard venturi flowmeter with the throat diameter of 0.100 in. is used for metering mercury flow. The differential pressure across the flowmeter is parallel to an electronic transducer and a pneumatic transmitter. The electrical output signal from the transducer is then amplified and indicated on a Motorola 4-in. strip-chart recorder. The pneumatic transmitter output signal of 3 to 12 psig is transmitted directly to a 12-in. circular recorder indicator. Periodically, these recorder readouts are calibrated against known mercury flow rates that are within the test run operating range. The calibration flow rate is established by accumulating a given weight of mercury on a scale over a measured time increment. The maximum overall error in weight flow is $\pm$ 4%.

The NaK flow is measured by a permanent magnet flowmeter manufactured by MSA Research Corporation. The flowmeter d-c output is amplified and indicated on a Motorola 4-in. strip-chart recorder indicator. The recorder accuracy is approximately 1% full scale. The overall NaK weight flow accuracy is estimated as $\pm$ 2%.

IV. OPERATION

The pretest preparation[3] includes the instrumentation installation and calibration, mechanical checkout and calibration, and loading of three loops.

A. BOILER STARTUP

The temperature of the NaK in the primary loop is slowly raised to 1150°F, measured at the boiler inlet. Four hours is usually required to reach this temperature. During the heating period, the primary NaK pump is started and flow is slowly increased to a maximum of 2050 lb/hr, and a vacuum of approximately 10 to 20 torr is maintained in the mercury loop to degas the mercury boiler. A dry-ice-in-acetone trap between the mercury loop and vacuum pump collects any mercury or condensable vapors. Upon reaching the NaK temperature of 1150°F, the mercury loop is sealed and the vacuum system is removed. The mercury pump is started initially into a bypass system and then injected into the boiler. The adjustable-choke nozzle is in the fully open position during the hot start. An approximate mercury flow rate of 200 to 350 lb/hr is circulated through the boiler. When the flow is stable, the NaK boiler inlet temperature is slowly increased to the test condition. The mercury system is allowed once more to stabilize. To obtain the desired pressure at the mercury boiler outlet, the adjustable-choke nozzle is gradually closed. Normally, the time elapsed from mercury injection to the first test point is about two hours and, during this period, regular observations are made to monitor the boiler NaK-shell temperature and other test parameters.

B. TEST RUNS

When a test program is designed, the order in which the test points are run is considered carefully since it is desirable to have minimum temperature disruption in the boiler. Once the test point conditions are acquired and the boiler temperature appears stable, it is standard practice to allow the NaK shell temperature profile to remain stable for at least thirty minutes before the data are taken. To further substantiate the data validity, several test points are repeated at the end of the test.

C. SHUTDOWN

For a normal shutdown, the mercury flow into the boiler is first valved off and the primary NaK is allowed to circulate. Power to the heater is shut off as soon as the mercury flow into the boiler is stopped. The NaK flow is continued until the boiler inlet temperature lowers to about 600°F by natural convection. After the boiler cools to room temperature, the vacuum system and cold trap system are connected to the mercury loop, and a vacuum of

15 to 20 torr is maintained until the next startup. If a prolonged shutdown or a plug insert change is scheduled, an argon cover gas of a slight positive pressure is applied and maintained on the mercury loop and boiler at all times.

V. TEST DATA REDUCTION

Test data reduction and analysis are based on the NaK and liquid mercury flow measurements, the boiler NaK and mercury flow terminal temperature measurements, and the boiler NaK-shell-tube surface temperature profile in conjunction with mercury flow passage pressure measurements taken at the boiler inlet and exit. Two additional pressure measurements in the mercury flow passage are obtained by means of internally located pressure taps in the plug-insert section. One is located at the preheat section end point. The other is located at the plug insert vapor section end point. A complete report[4] containing test data recordings used for test data reduction was prepared.

In view of the limited number of mercury flow passage pressure taps, the pressure gradients between P_{Hbi}-P_1, P_1-P_2, and P_2-P_{Hbo} are assumed to be linear. The pressure measurements P_{Hbi}, P_1, P_2 and P_{Hbo} were taken from the pressure taps located at the boiler inlet, preheat section end point, plug insert end point and the boiler exit, respectively. The NaK shell-tube outer surface temperature profile representation is assumed to be identical to the mercury flow passage internal wall temperature profile. This assumption is based on the overall thermal resistance value across the heat flow pass as determined from the test and the analytically determined total resistance across the NaK film and the tube wall. The comparison of these resistances shows that:

$$\left(\frac{1}{U}\right)_{Test} < \left(\frac{r_m}{r_o}\frac{1}{h_N} + \frac{t}{k_w}\right)_{design}$$

which means that (q") test > (q") design. Obviously, the available data on tube wall thermal conductivity and the NaK side file heat transfer coefficient determination method are in error. This consideration implies that the NaK-side film-heat-transfer coefficient is infinite, and the mercury tube wall heat transfer resistance is negligible.

Linear correction of the measured NaK temperature profile was introduced in the excess boiler superheat length. This correction was established from

the heat balance analysis where the net NaK flow and the NaK temperature drop due to the external boiler heat loss were determined. For the average NaK flow rate used in these tests the NaK temperature drop due to external heat loss was approximately 30°F. The boiler NaK shell-tube skin thermocouple temperature measurements at their best are estimated to be of ± 2.5% accuracy with respect to total full-scale indication.

Test data reduction and analytical computations were conducted on the IBM-7094 Model 2 computer. A detailed analytical program[4] for this purpose was prepared.

The main items determined for each test point data set were:

A. Boiler heat balance

B. Plug insert preheat section geometric, dynamic, and thermal parameters

C. Plug insert vapor quality section geometric and dynamic parameters

D. Plug insert section exit vapor quality

E. NaK temperature at liquid-vapor interface

F. NaK temperature in terms of vapor quality

G. Plug insert vapor quality section local boiling thermal and dynamic parameters

H. Unplugged tube vapor quality section local boiling thermal and dynamic parameters

I. Plug insert vapor quality section mean thermal parameters

J. Unplugged tube vapor quality section mean thermal parameters.

VI. DISCUSSION OF RESULTS

The results of the test data reduction are evaluated in the light of proposed drop-wise drywall boiling heat transfer and two-phase flow pressure drop correlations. These correlations are based on mercury nonwetting characteristics which are the principal cause for the dropwise two-phase flow regime in the boiling section. To obtain the predicted boiler performance characteristics in accordance with this design approach, the experimental evidence indicates that the initial physical and/or chemical cleanliness of the wall

surface in the mercury flow passage, prior to mercury injection, is of particular importance. Aside from the thermal and dynamic conditions at the liquid-vapor interface and in the vapor flow quality region, which are necessary to promote effective mercury vaporization, the obtained boiling heat-transfer characteristics, as represented by the NaK temperature profile, can be better or worse than those predicted by the dropwise drywall boiling theory. The boiler performing in accordance to these design expectations is said to be in a conditioned state. The boiler exhibiting better heat-transfer characteristics is said to be in a partially-wetted state; the boiler exhibiting poorer heat-transfer characteristics is said to be in a deconditioned state. When intermittent physical wetting on the mercury flow passage walls occurs, the boiler is said to be in a partially-wetted state. Partial wetting was observed on the plug insert surface when the plug insert was removed from our test boiler after 96 hours of operation. A typical NaK temperature profile for a deconditioned boiler is depicted in Figure 7. The same boiler exhibiting fully-conditioned, or partially-wetted boiler heat-transfer characteristics is shown in Figure 8. The reason for obtaining the boiler NaK temperature profile, as shown in Figure 8, can be attributed to significant changes occurring on the mercury flow passage wall surface. The physical and/or chemical changes occurring on the material surface are only poorly understood, and require further investigation.

Initial test results as depicted in Figures 7 through 13, are of a qualitative nature. They show the effect of the liquid-phase velocity in the boiler preheat section on the overall boiler performance. Figures 7 and 9 depict a typical NaK temperature profile for a deconditioned boiler during the initial test run when the liquid-phase velocity in the helical flow passage was 0.8 ft/sec.

Nonmeasurable improvement in the boiler conditioning effect was observed during several hundreds of hours of operation under a nominal SNAP-8 boiler NaK inlet temperature schedule. The same boiler, when restarted with a revised preheat section plug insert geometry providing a liquid-phase velocity of 6 to 7 ft/sec, exhibited effective mercury flow passage conditioning immediately. Also, the projected NaK temperature profile approached the design conditions very rapidly. Figures 10 and 8 show the progress in conditioning 4 hours and 20 hours after mercury injection, respectively. The boiler

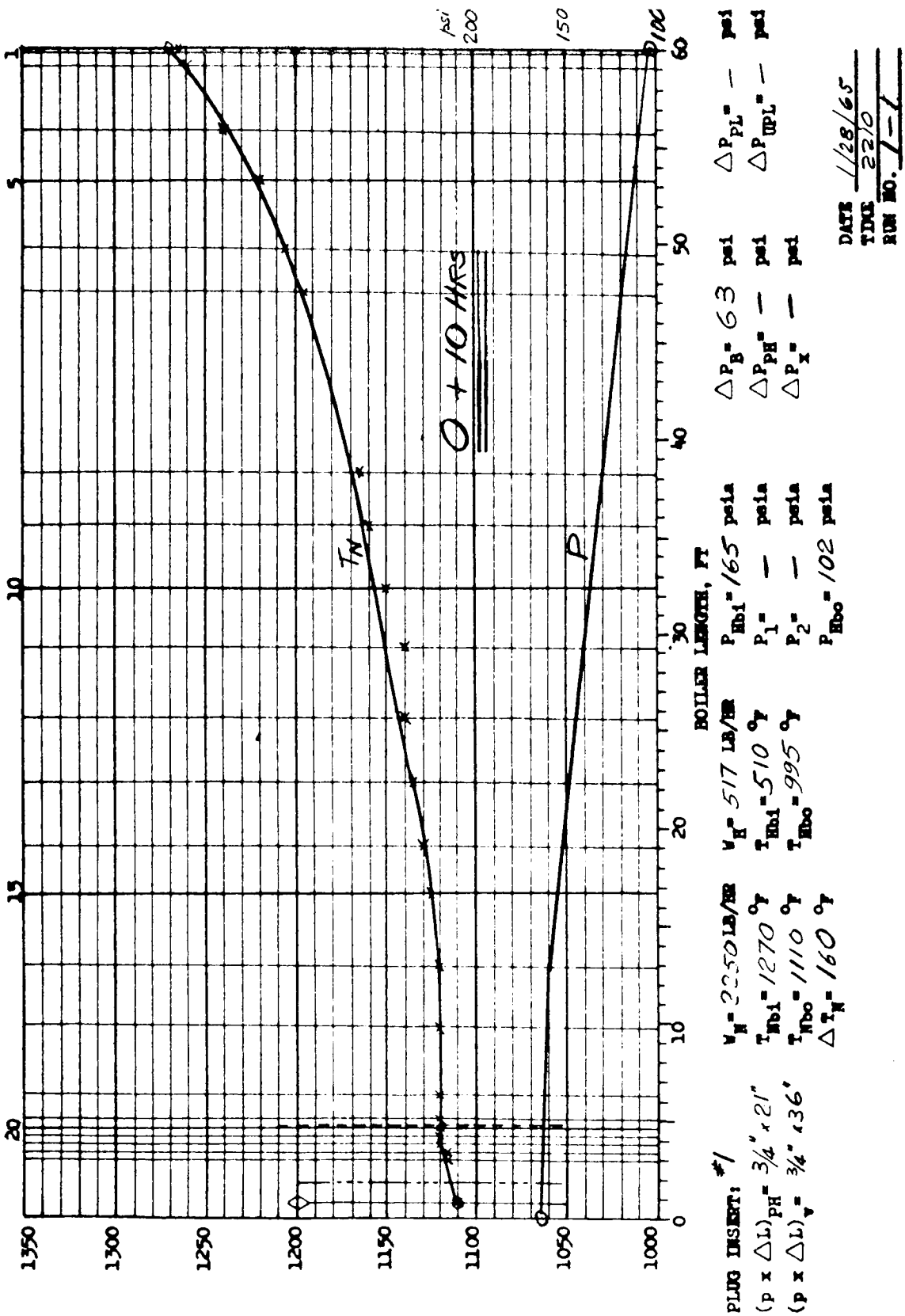


Fig. 7. Boiler NaK Temperature Profile - 0 + 10 Hr

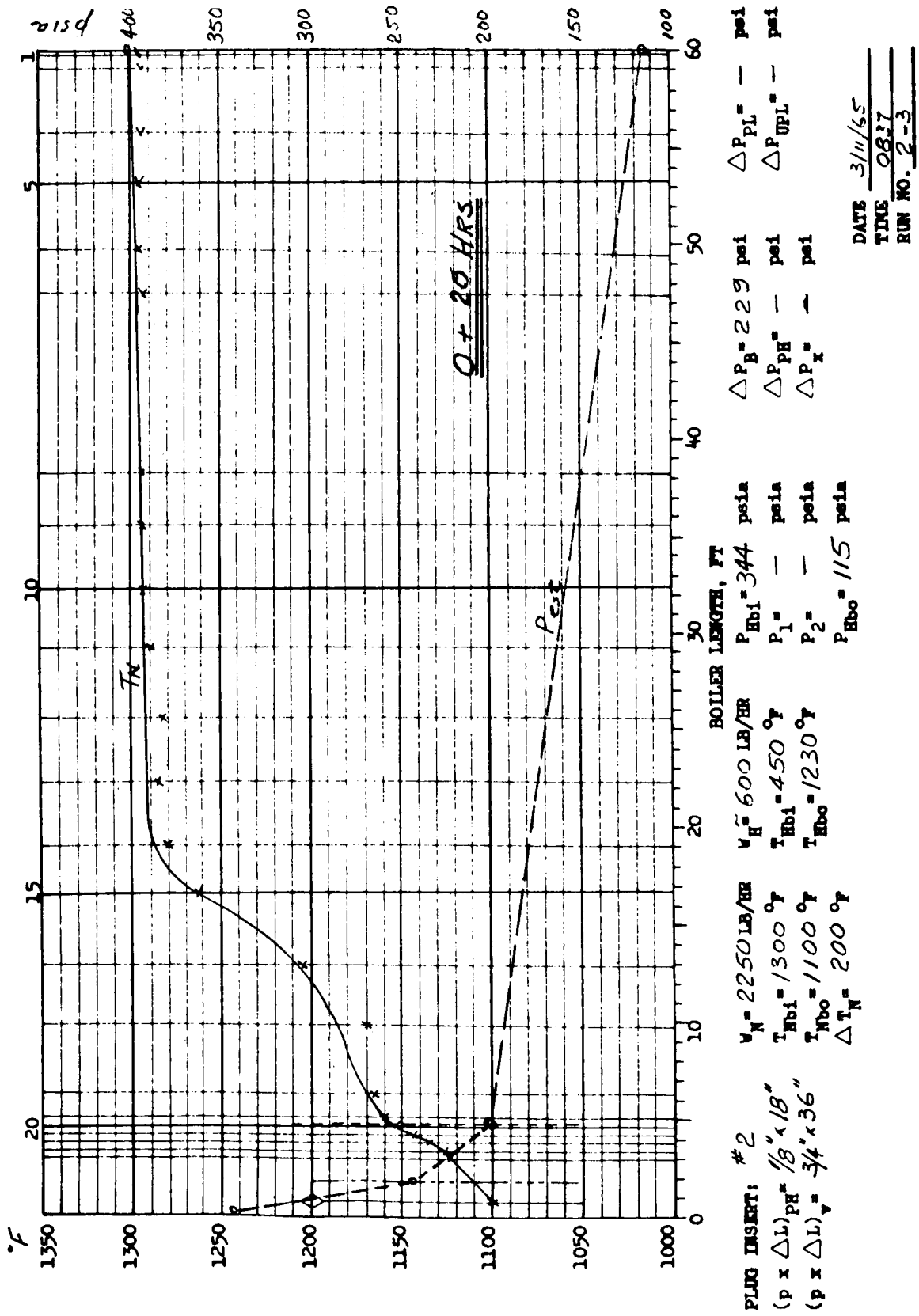
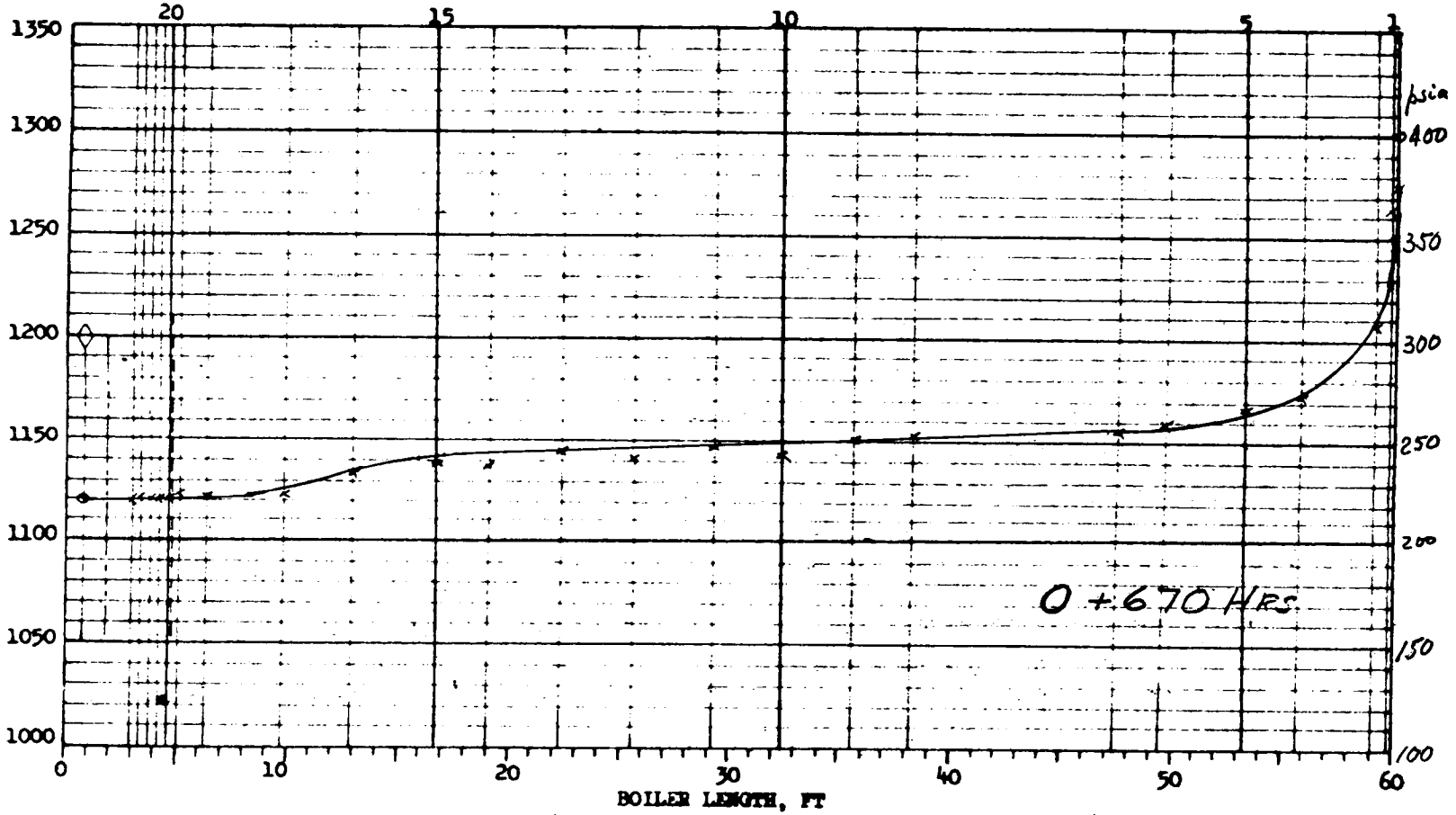


Fig. 8. Boiler NaK Temperature Profile - 0 + 20 Hr



PLUG INSERT:
$W(p \times \Delta L)_{PH}$ = 3/4" x 21"
$W(p \times \Delta L)_{v}$ = 3/4" x 36"

W_N = 2100 LB/HR
T_{Nbi} = 1300 °F
T_{Nbo} = 1120 °F
ΔT_N = 180 °F

W_H = 450 LB/HR
T_{Hbi} = 495 °F
T_{Hbo} = 1180 °F

P_{Hbi} = 300 psia
P_1 = — psia
P_2 = — psia
P_{Hbo} = 260 psia

ΔP_B = 40 psi
ΔP_{PH} = — psi
ΔP_r = — psi

ΔP_{PL} = — psi
ΔP_{UPL} = — psi

DATE 2/24/65
TIME 1600
RUN NO. 1-50

Fig. 9. Boiler NaK Temperature Profile - 0 + 670 Hr

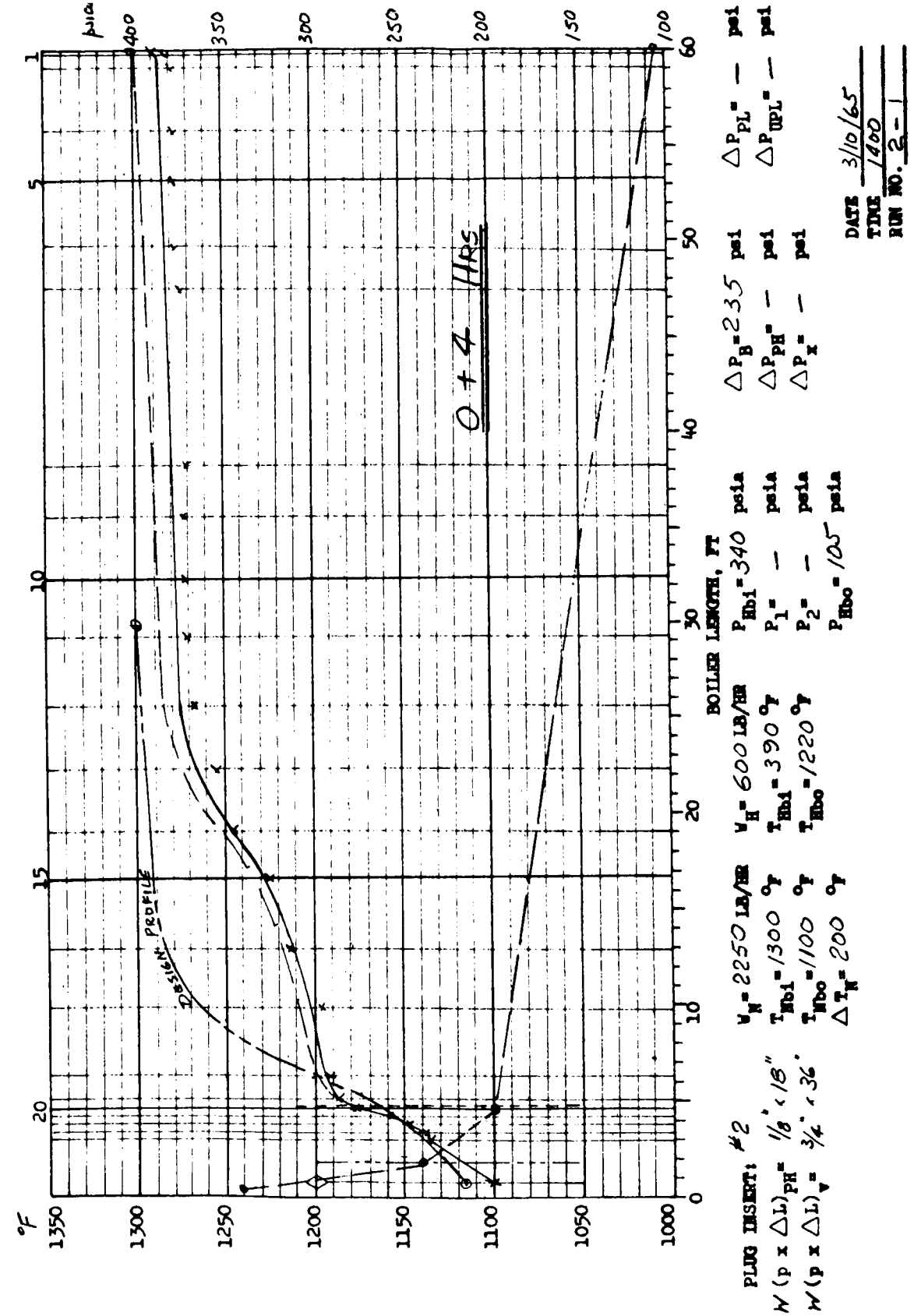


Fig. 10. Boiler NaK Temperature Profile - 0 + 4 Hr

restart (Figure 11) with the same plug insert geometry, did not indicate any boiler performance degradation. A subsequent test run (Figure 12), with the original preheat section plug insert, providing 0.8 ft/sec liquid-mercury velocity, still produced conditioned boiler performance characteristics. This evidence shows that, once the tube surface is in a conditioned or wetted state, the liquid-velocity level in the preheat section is not of particular importance. Examination of the NaK temperature profiles (Figures 11 and 12) and associated test data reveals that the difference between the two plug insert geometries tested can be detected in the slope of the NaK temperature profile and in the boiling termination point. A tight liquid-phase plug insert geometry combined with a similar low vapor quality region seems to be the right design approach for a high-performance once-through boiler. Once the fully conditioned or even wetted mercury flow passage state is established, the boiler can also be operated without a plug insert. This condition is shown in Figure 13, where the slope of the NaK temperature profile reflects boiling heat transfer rates comparable to those obtained with plug inserts. However, in the unplugged boiler this heat transfer is accompanied by excessive oscillations in boiler exit pressure and flow. It is postulated that nucleation sites were developed in the mercury flow passage plug insert regions during previous boiler test runs, when the elevated velocity plug insert geometries were tested. Thus, the boiler inlet and tube section, without a plug insert, was operating under a convective nucleate boiling heat transfer regime.

Test data point sets were prepared,[4] and are representative of the obtained NaK temperature profiles and the associated primary and secondary working fluid operating parameters utilized in the test data reduction program. Typical data point recordings are shown in Figures 14, 15, and 16.

The calculated heat loss values as obtained from the heat balance closure are in the range from 1 to 16% of the total heat input. This discrepancy can be attributed to inaccuracies in temperature measurements or their corrections; e.g., the boiler NaK temperature drop error of $\pm$ 10°F results in a heat loss error of $\pm$ 1.26 kw. The boiler heat loss was also determined on the basis of boiler operation at zero mercury flow and different NaK flow and temperature levels. The estimated heat loss value is 2 to 2.5 kw, or 9 to 10% of the total heat input.

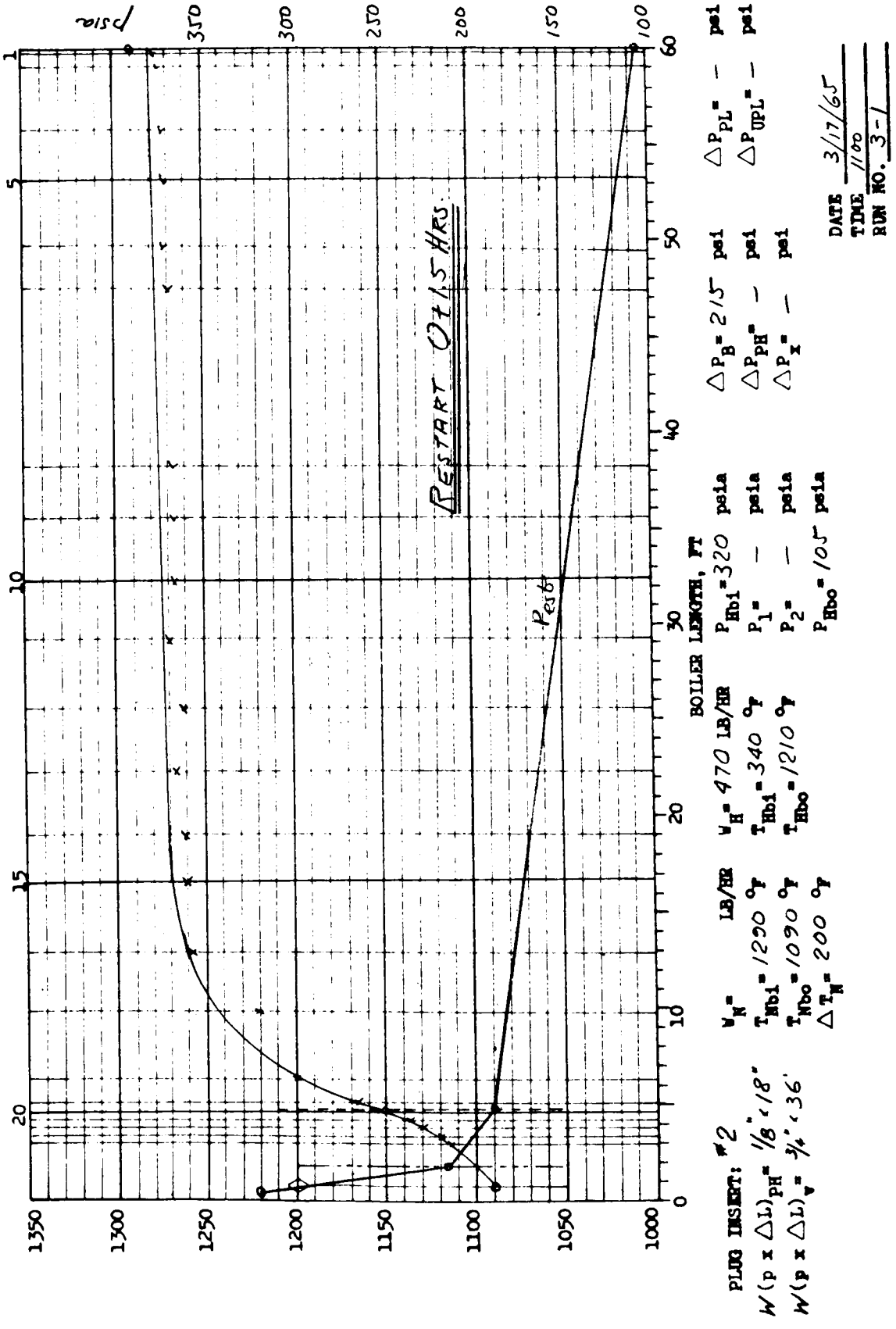


Fig. 11. Boiler NaK Temperature Profile - Restart 0 + 1.5 Hr

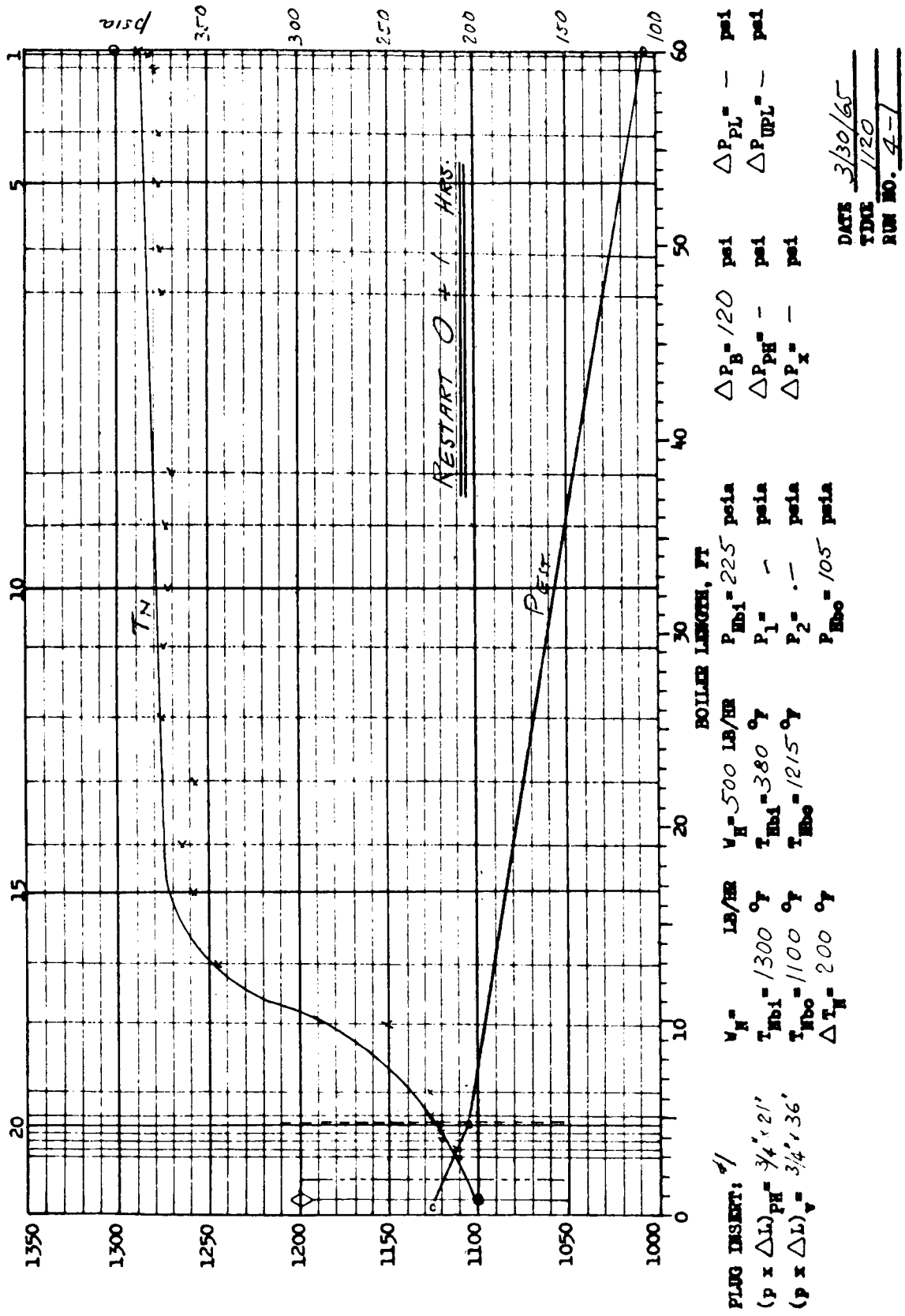


Fig. 12. Boiler NaK Temperature Profile - Restart 0 + 1 Hr

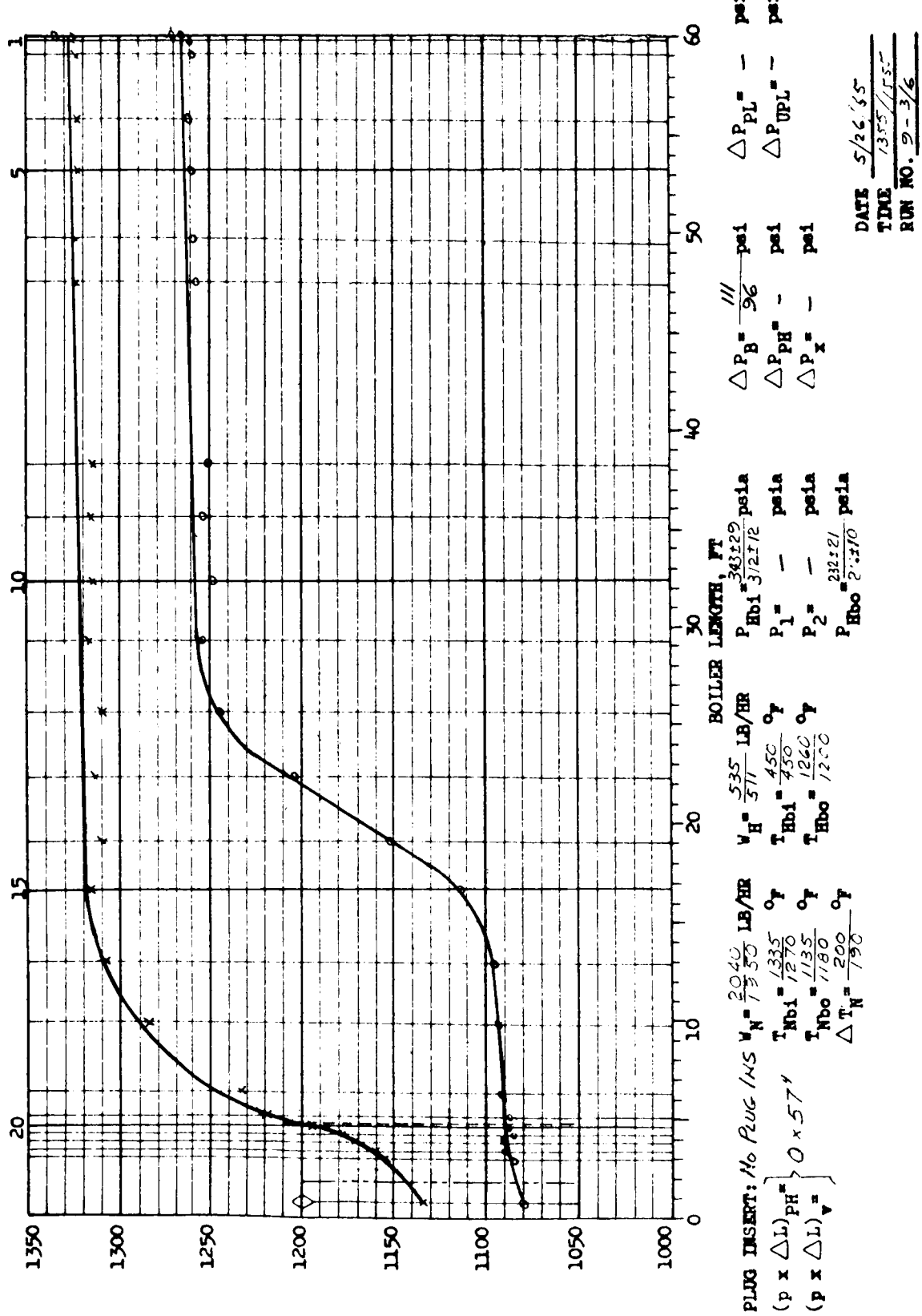


Fig. 13. Boiler NaK Temperature Profile - 0 + 10 Hr

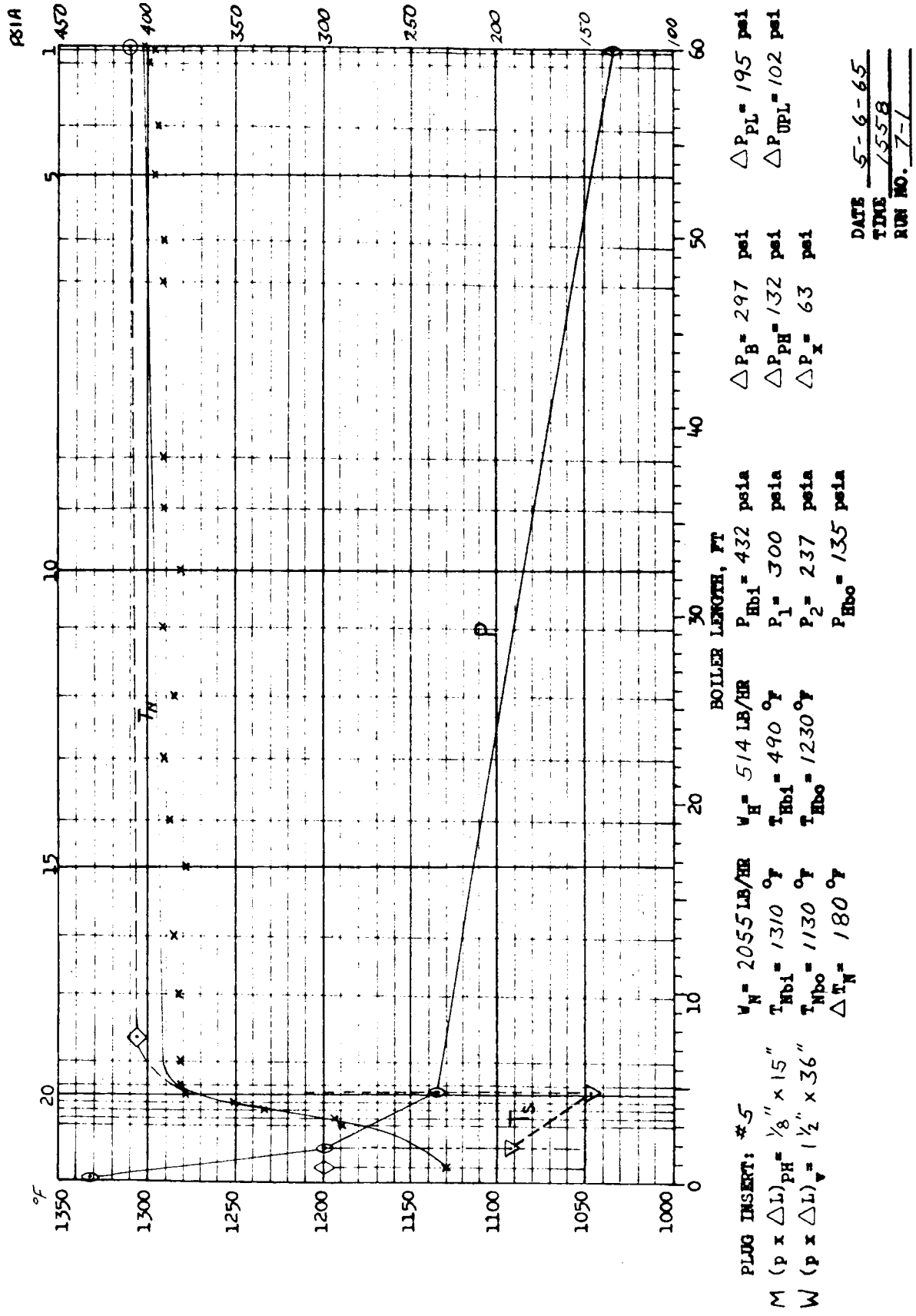


Fig. 14. Boiler NaK Temperature Profile

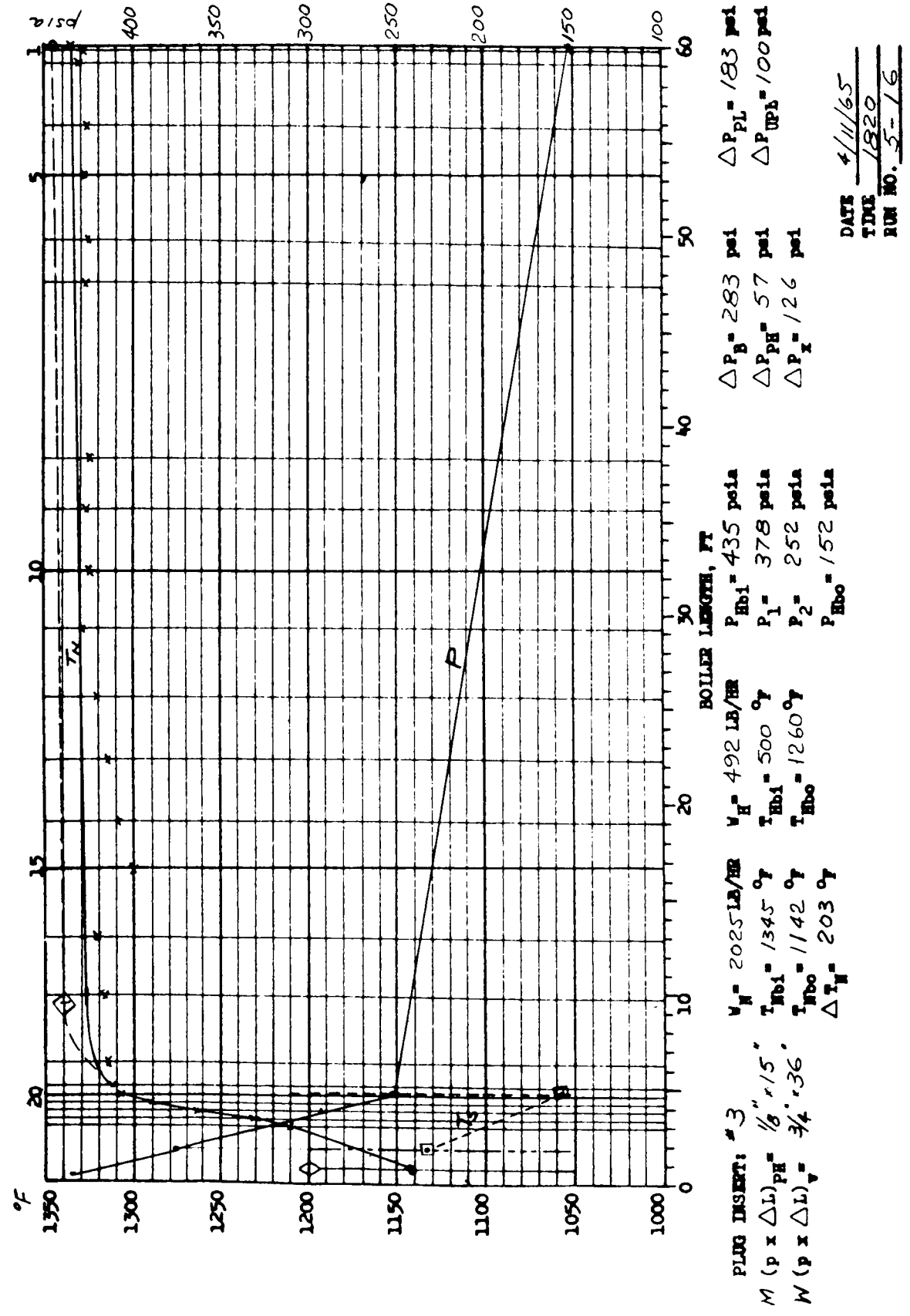


Fig. 15. Boiler NaK Temperature Profile

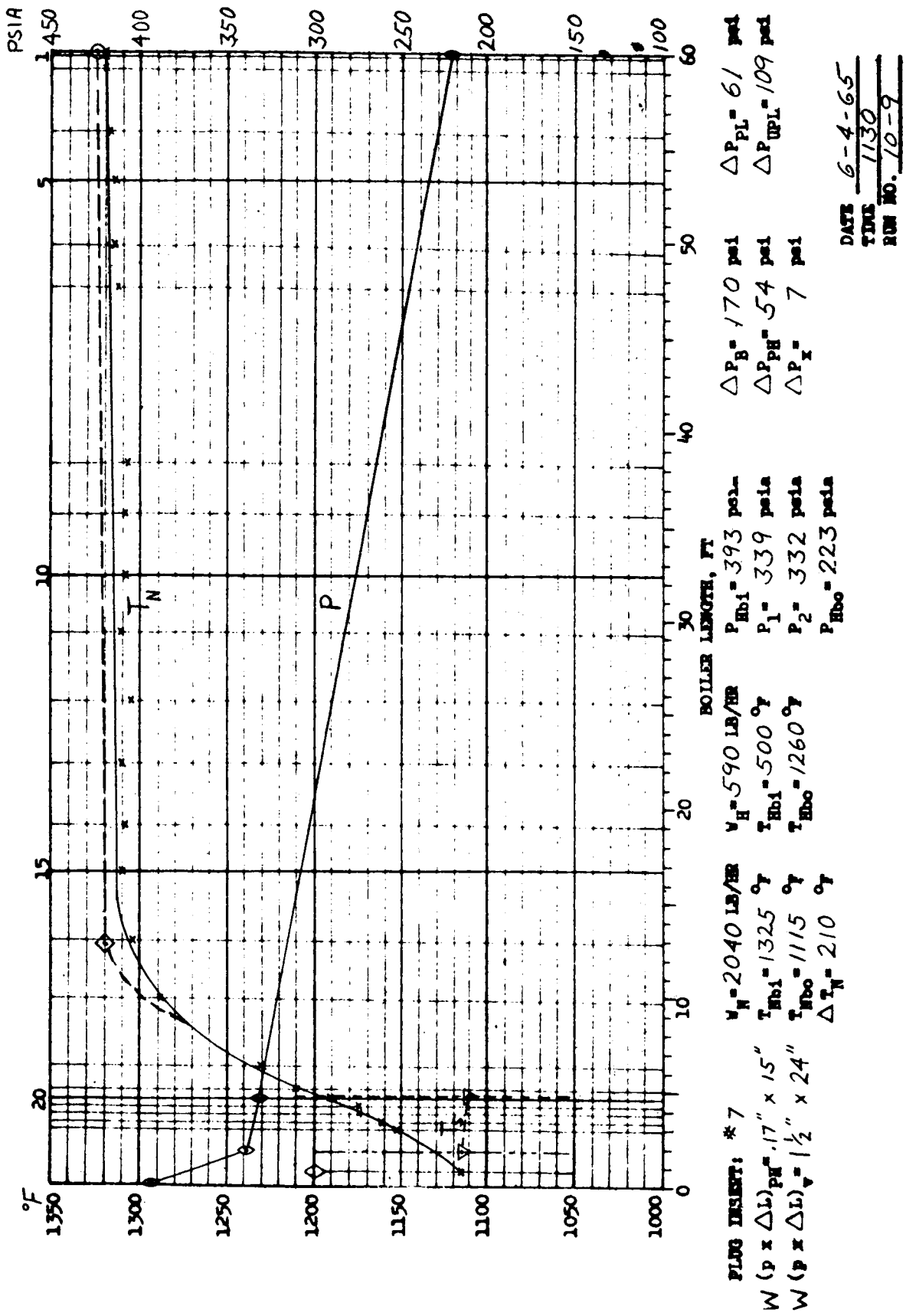


Fig. 16. Boiler NaK Temperature Profile

Similar parametric data-point scatter resulted from the boiler thermal and dynamic test data analysis, which can also be attributed to the inaccuracy of the boiler instrumentation. The most critical areas in this regard are the establishment of the true mercury temperature and pressure conditions in the boiler plug insert section. The point of particular interest is the determination of the liquid-vapor interface location in the boiler. To perform a detailed test analysis in this area, a much more sophisticated instrumentation technique is necessary. A typical and desirable boiler test data representation in conjunction with such an instrumentation is depicted in Figure 17. This representation implies that several mercury flow passage temperature measurements in the preheat (T_{PH}) and low quality vapor section (T_S, T_v) as well as the exact mercury flow pressure (P_{Hg}) and NaK flow temperature (T_N) profiles must be experimentally established. In accordance to this diagram, the liquid-vapor interface location (L_{OO}) is determined when T_{SOO}, T_{NOO} and P_{OO} are projected as the point L_{OO} on the abscissa. Our experimental boiler instrumentation is not providing this type of test data representation. Because of these limitations, the test data evaluation was performed on the basis of several assumptions in conjunction with trial and error methods wherever the available test data were not sufficient to support the analysis.

These assumptions are in the form of corrections in the curvature of the NaK temperature profile and the mercury pressure profile. They are further based on plug insert liquid and low-vapor-quality section calibrations. These calibrations provided pressure-drop data that were utilized to determine the liquid and gas flow frictional pressure drop factors for the different plug insert geometries tested. In making these calibrations, liquid and vapor flow rates were regulated to maintain the same Reynold's number range as that existing in the boiler when operating under normal conditions. The results of liquid flow calibrations are shown in Table 2.

The Darcy type pressure drop correlation for two-phase turbulent flow was used to determine the product ϕf_v, where

$$\phi = \frac{\Delta P_{TP}}{f_v \frac{\Delta L'}{De} \frac{(\bar{x} G)^2}{2 g_c \rho_v}} = \frac{\Delta P_{TP}}{\Delta P_v}$$

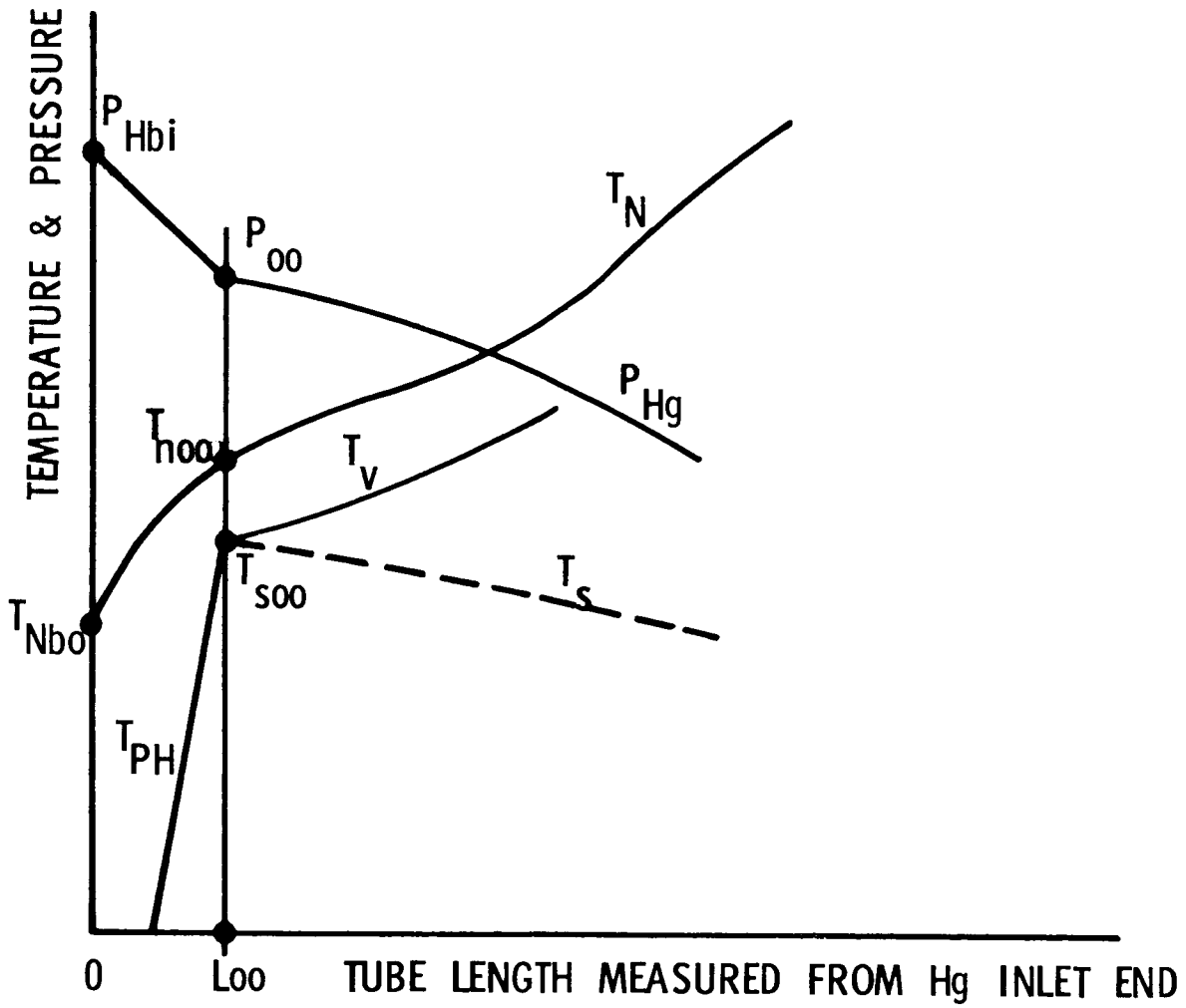


Fig. 17. Typical Boiler Temperature and Pressure Profiles at Mercury End

TABLE 2

BOILER TEST PLUG INSERT FLOW PASSAGE CALIBRATION RESULTS

PLUG INSERT NUMBER	A_c	De	$\Delta L'$	G		μ	ρ	u	W	ΔP	T	Re	f
	ft^2	ft	ft	lbm/sec-ft^2	lbm/hr-ft^2	lbm/hr-ft	lbm/ft^3	ft/sec	lbm/hr	psi	°F		
3 (Run #5)	3.05×10^{-5}	5.24×10^{-3}	12.65	3640	1.31×10^7	2.65	824	4.42	400	27	300	25,900	.00648
	"	"	"	4550	1.64×10^7	"	"	5.53	500	34.8	"	32,600	.00533
	"	"	"	5470	1.98×10^7	"	"	6.63	600	50.3	"	39,000	.00531
5 (Run #6)	2.71×10^{-5}	4.95×10^{-3}	12.81	4110	1.48×10^7	2.71	826	4.97	400	81	280	27,000	.01424
	"	"	"	5130	1.85×10^7	"	"	6.23	500	114	"	33,800	.01281
	"	"	"	6150	2.21×10^7	"	"	7.45	600	156.5	"	40,400	.01223
	"	"	"	7200	2.58×10^7	"	"	8.71	700	205.5	"	47,200	.01172
5 (Run #7)	"	"	"	4110	1.48×10^7	2.81	829	4.96	400	71	250	26,200	.0125
	"	"	"	5130	1.85×10^7	"	"	6.21	500	99	"	32,700	.0110
	"	"	"	6150	2.21×10^7	"	"	7.42	600	128	"	39,200	.0100
6 (Run #8)				4360	1.57×10^7	2.64	824		400	62	300	29,200	.0097
				5450	1.96×10^7	"	"		500	68	"	36,400	.0068
				6530	2.35×10^7	"	"		600	104	"	43,700	.0073
7 (Run #10)				2950	1.16×10^7	2.68	825		450	30	290	24,900	.0163
				3430	1.24×10^7	"	"		500	35.5	"	26,500	.0143
				3780	1.36×10^7	"	"		550	41	"	29,200	.0136
				4120	1.48×10^7	"	"		600	47	"	31,800	.0131
				4470	1.61×10^7	"	"		650	52.5	"	34,400	.0125
3 (Run #5)						1.87	783		400	28.4	800	36,700	
						"	"		500	36.6	"	46,200	
						"	"		600	52.9	"	55,300	
5 (Run #6)						"	"		400	85.5	"	39,100	
						"	"		500	120.2	"	49,000	
						"	"		600	165	"	58,600	
						"	"		700	217	"	68,300	
5 (Run #7)						"	"		400	75.2	"	39,400	
						"	"		500	105	"	49,200	
						"	"		600	135.4	"	58,900	
6 (Run #8)						"	"		400	65.3	"	41,500	
						"	"		500	71.5	"	51,600	
						"	"		600	109.4	"	61,900	
7 (Run #10)						"	"		450	31.6	"	35,700	
						"	"		500	37.4	"	38,000	
						"	"		550	43.2	"	41,800	
						"	"		600	49.5	"	45,600	
						"	"		650	55.3	"	49,300	

The product ϕf_v is correlated in terms of the Martinelli-type parameter

$$\lambda = \left(\frac{\bar{x} \, G \, De}{\mu_v} \right)^{.8} \frac{\mu_v}{\mu_f} \frac{\rho_f}{\rho_v} \frac{\bar{x}}{1 - \bar{x}}$$

which is determined from an incremental local boiling heat transfer analysis. ϕf_v versus λ is plotted separately for plug insert section and unplugged tube section geometries. Figure 18 shows the low vapor quality (up to 15%) pressure drop correlating parameters, when the vapor quality region next to the liquid-vapor interface enters the plug insert preheat section. Figure 19 shows the same correlating parameters for the plug insert vapor quality range from 0 to 80%. The data in Figure 19 were fitted by least squares analysis providing the average curve

$$\phi f_v = e^{4.87} \lambda^{-.674}$$

The average two-phase flow pressure drop factor is determined from the above curve using

$$\phi = \frac{\phi f_v}{f_v}$$

where f_v is obtained from N_2 gas flow tests carried out in a Reynold's number range corresponding to 100% vapor flow. Figure 20 shows a similar plot of data points in the unplugged tube section for the vapor quality range from 20 to 100%. A least squares analysis of the data predicted a curve for best fit given by

$$\ell n \, \phi f_v = 16.06 - 2.224 \, \ell n \, \lambda + .065 \, (\ell n \, \lambda)^2$$

The comparison of two plug insert geometries in regard to their pressure drop in terms of plug insert end point vapor quality is illustrated in Figure 21. Curve 2 as compared to Curve 1 shows that excessive boiler pressure drop may result when the plug insert length is overdesigned. In the case of oversized preheat-section plug insert length and tight-pitch helical flow passage geometry, early vapor generation may occur in the preheat section. Under these conditions the total plug insert pressure drop may reach undesirable proportions (Curves 3 and 4).

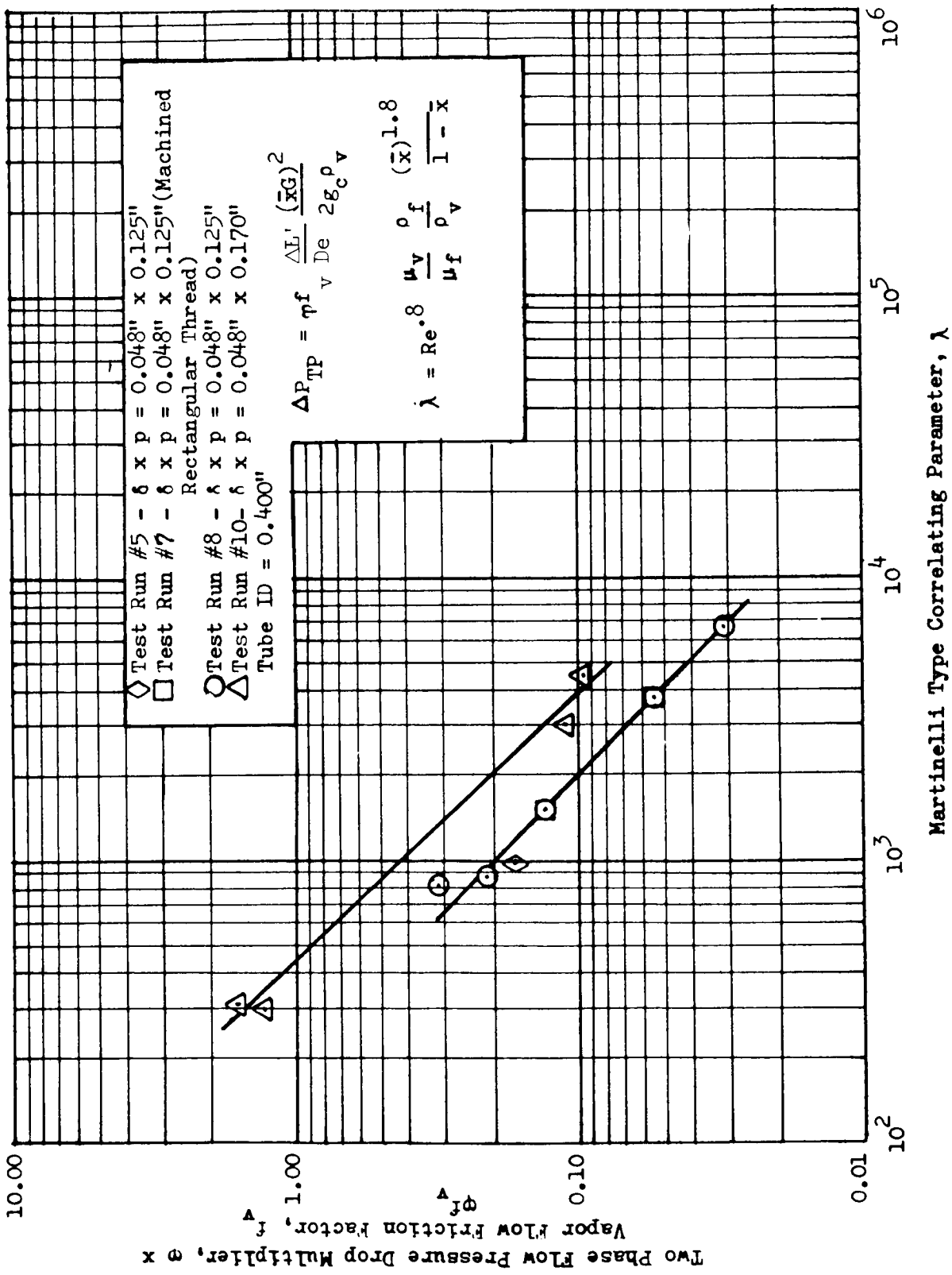


Fig. 18. Two-Phase Flow Pressure-Drop Correlating Parameters in Boiler Plug-Insert Preheat Section

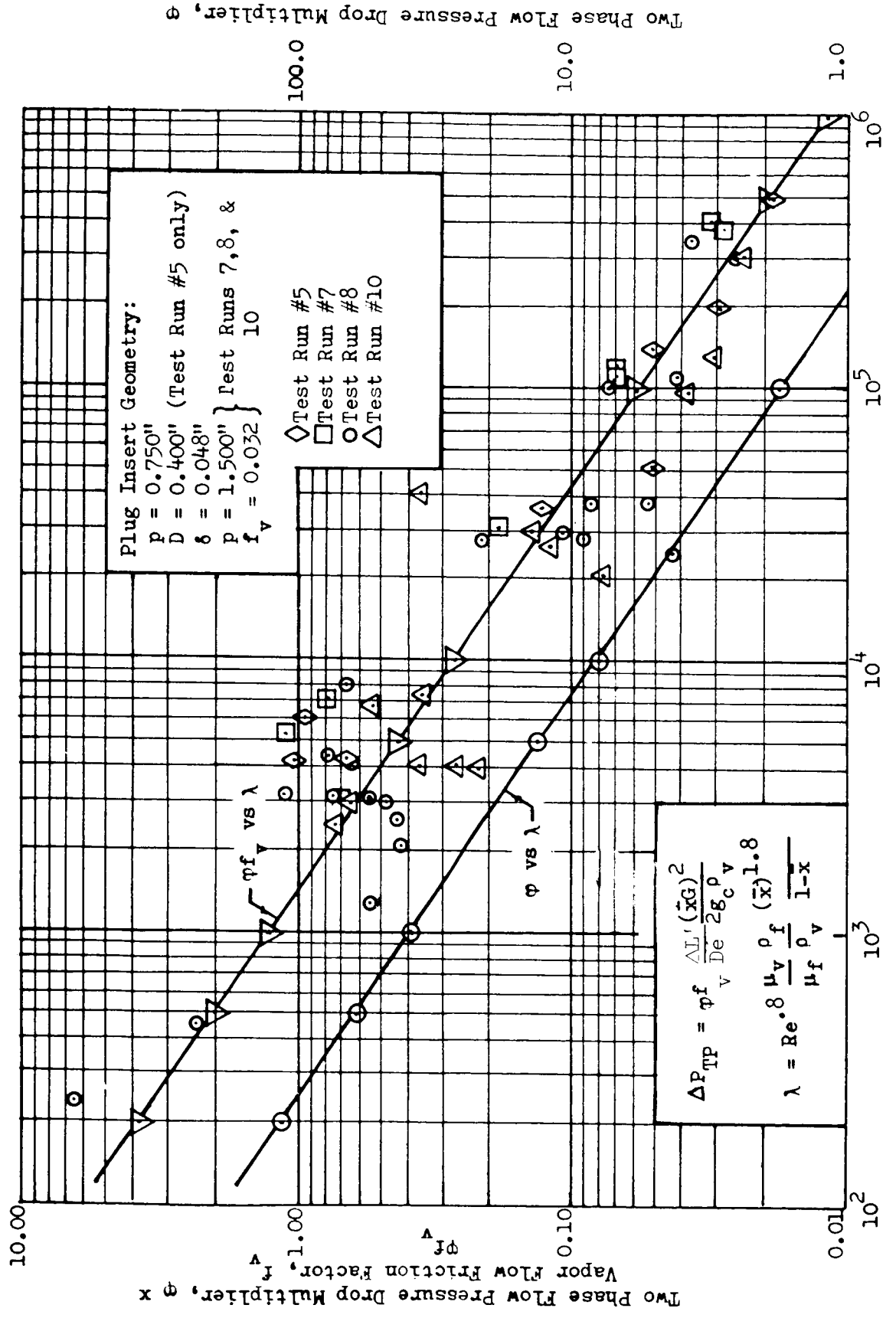


Fig. 19. Boiler Plug-Insert Two-Phase Flow Pressure Drop Correlating Parameters

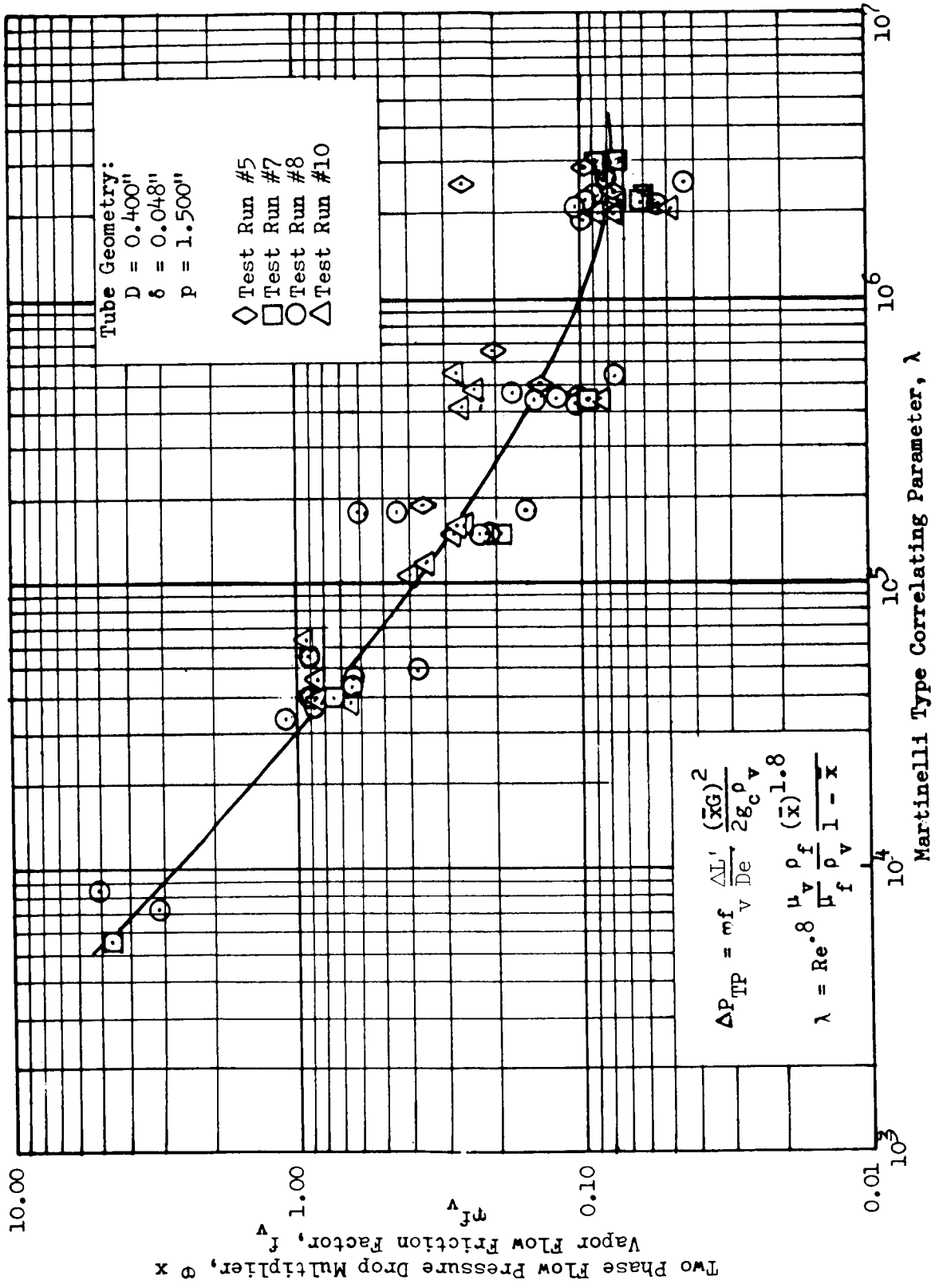


Fig. 20. Unplugged Tube Two-Phase Flow Pressure Drop Correlating Parameters

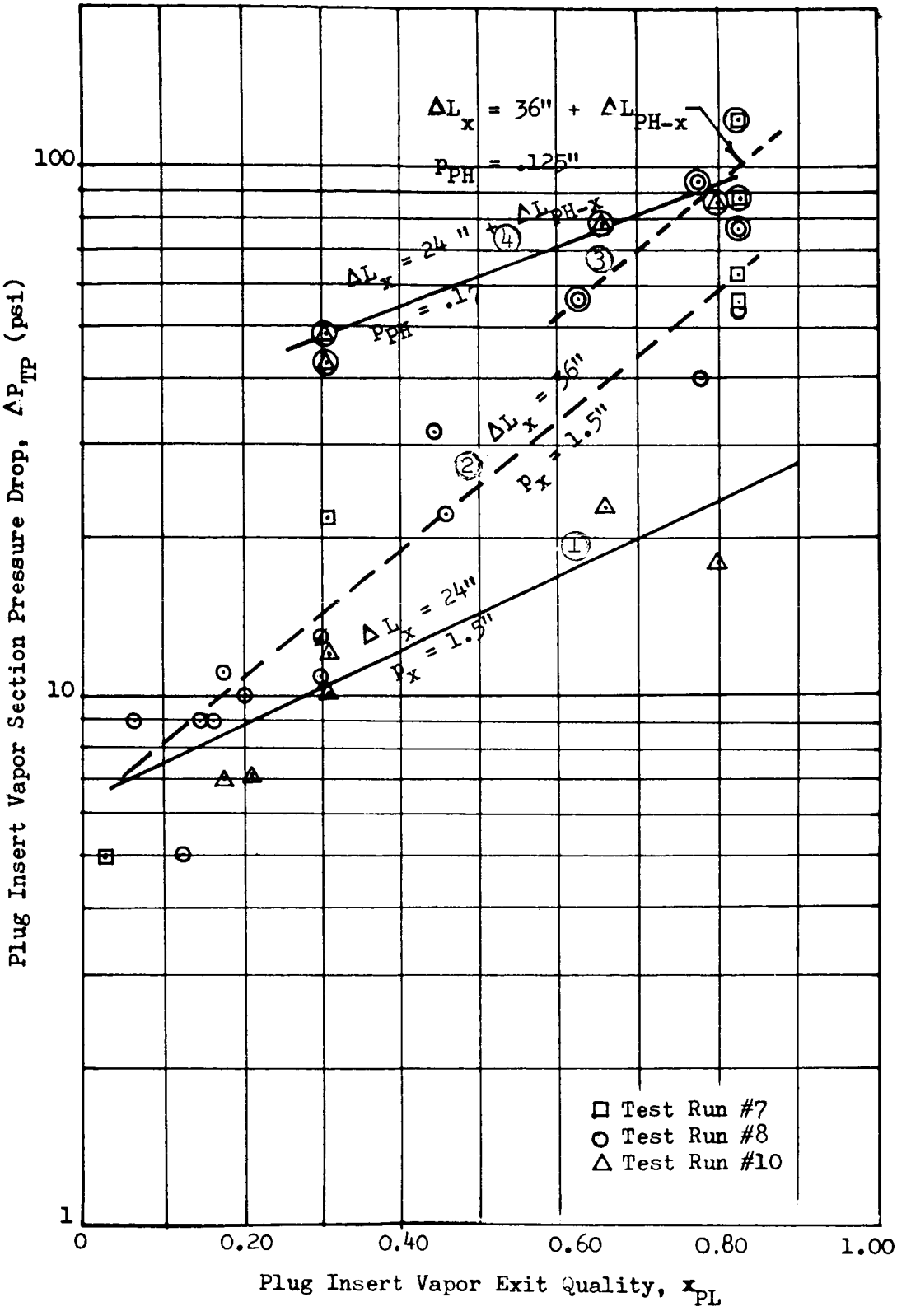


Fig. 21. Plug Insert Vapor Section Pressure Drop versus Plug Insert Vapor Exit Quality

The magnitude of the obtained initial boiling heat fluxes, in terms of the temperature difference at the liquid-vapor interface location, is plotted in Figure 22. In view of the wide scatter of the test data the points can be approximated in the form $q'' = \text{const.}\ \Delta T_{00}$, which is a linear function with a 45° slope. This interpretation would indicate that convection vortex type boiling was induced from the liquid-vapor interface location by the elevated liquid phase velocity.

The vapor quality section thermal and dynamic operating parameters in dimensional and nondimensional form were determined on the basis of local boiling heat-transfer and two-phase flow pressure drop correlations in 20% vapor quality increments. To check out and compare these results with the dropwise dry-wall boiling theory, the obtained local boiling mean temperature difference (ΔT_M) of each quality increment was considered in the light of boiling heat-transfer design correlations for the purpose of determining whether it was in the contact, intermittent contact, or film boiling regime. These results, as well as the results of the analysis of the overall heat transfer in the plug insert section and the unplugged tube vapor section were tabulated.[4]

For each vapor-quality increment ($\Delta x = 0.20$) throughout the length of the boiling section, the calculated mean heat fluxes are plotted in terms of the mean temperature difference between the NaK temperature and the mercury saturation temperature. The mean NaK temperature of each quality increment is determined from the boiler NaK temperature profile. The mercury saturation temperature is determined from the mercury flow passage pressure representation in the same quality increment. Plots of the obtained local boiling heat fluxes at mean vapor qualities of 10, 30, 50, 70 and 90% in terms of mean temperature differences are shown in Figures 23 through 27, respectively. The data scatter display was analyzed by least squares techniques to obtain curves of best fit. The results of this analysis are shown graphically as well as analytically in the figures indicated above.

The results of local boiling heat-transfer representation, as discussed above, are further differentiated into boiling occurring in the plug insert section and boiling occurring in the unplugged tube section. The data points of each quality increment of these sections were considered in the light of different boiling regimes as defined by the dry wall dropwise boiling correlations. These correlations are:[1]

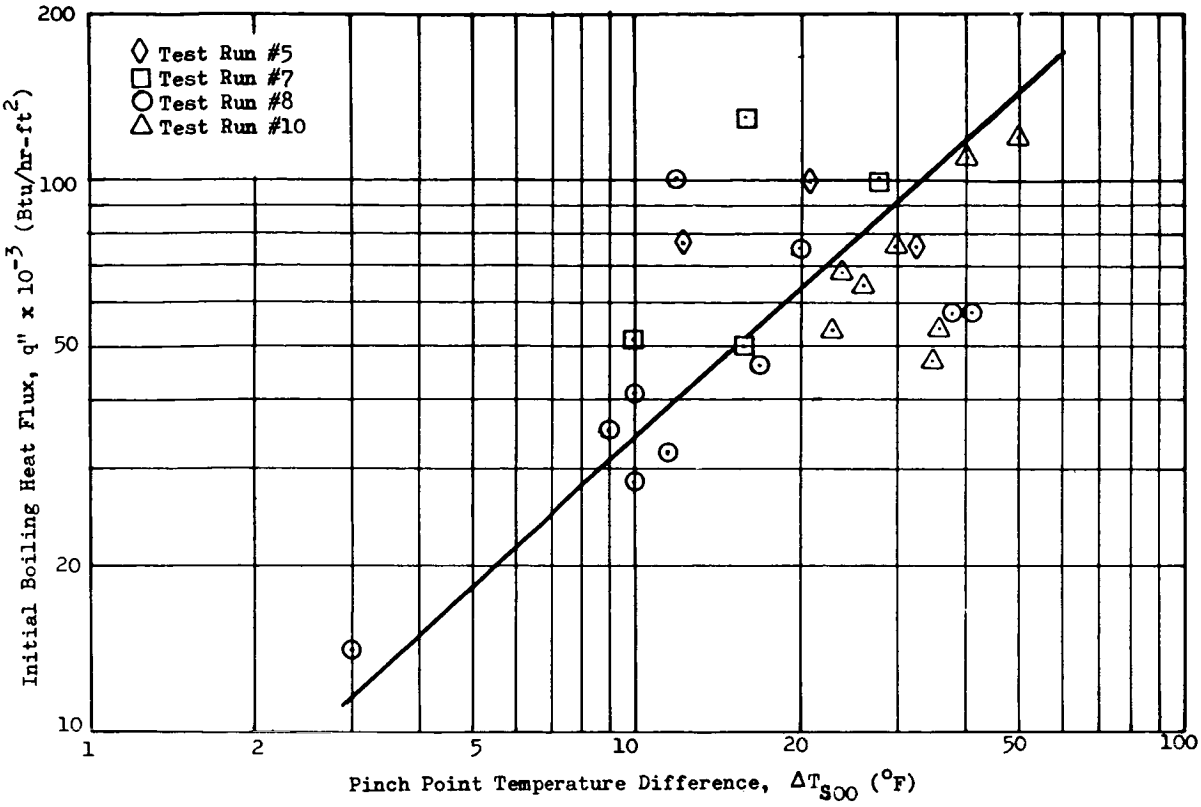


Fig. 22. Initial Boiling Heat Flux versus Pinch-Point Temperature Difference

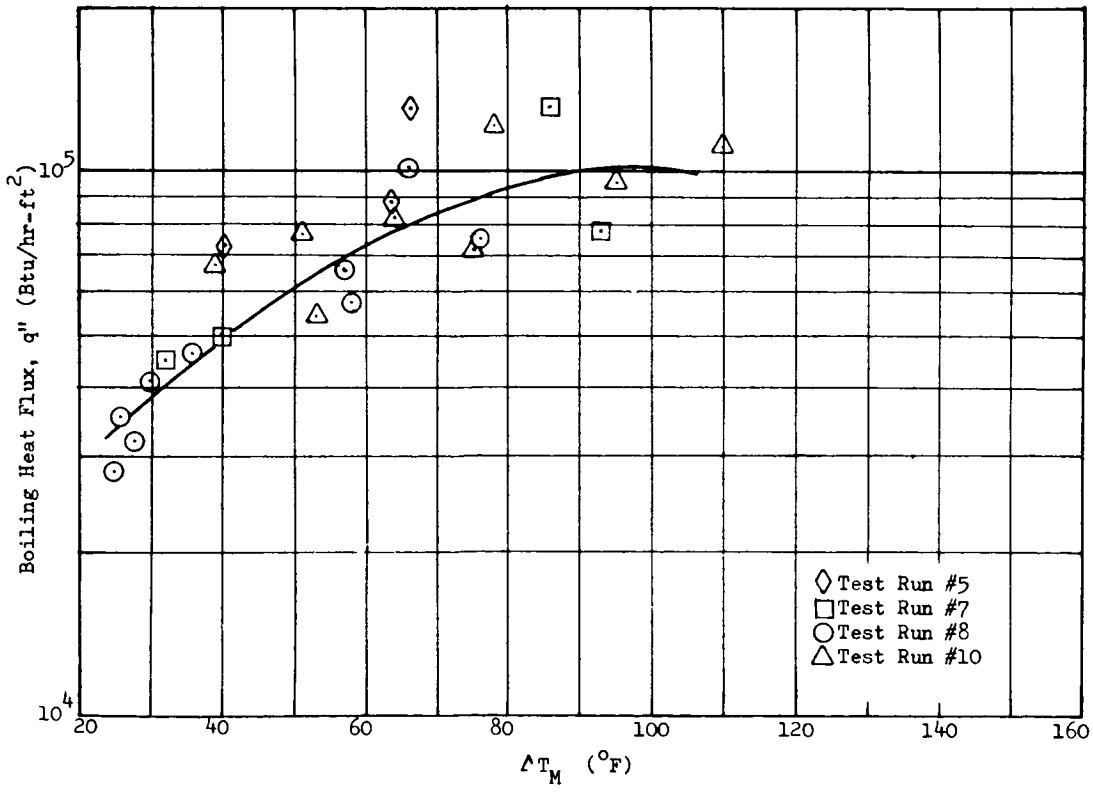


Fig. 23. Local Boiling Heat Flux - 10% Mean Vapor Quality

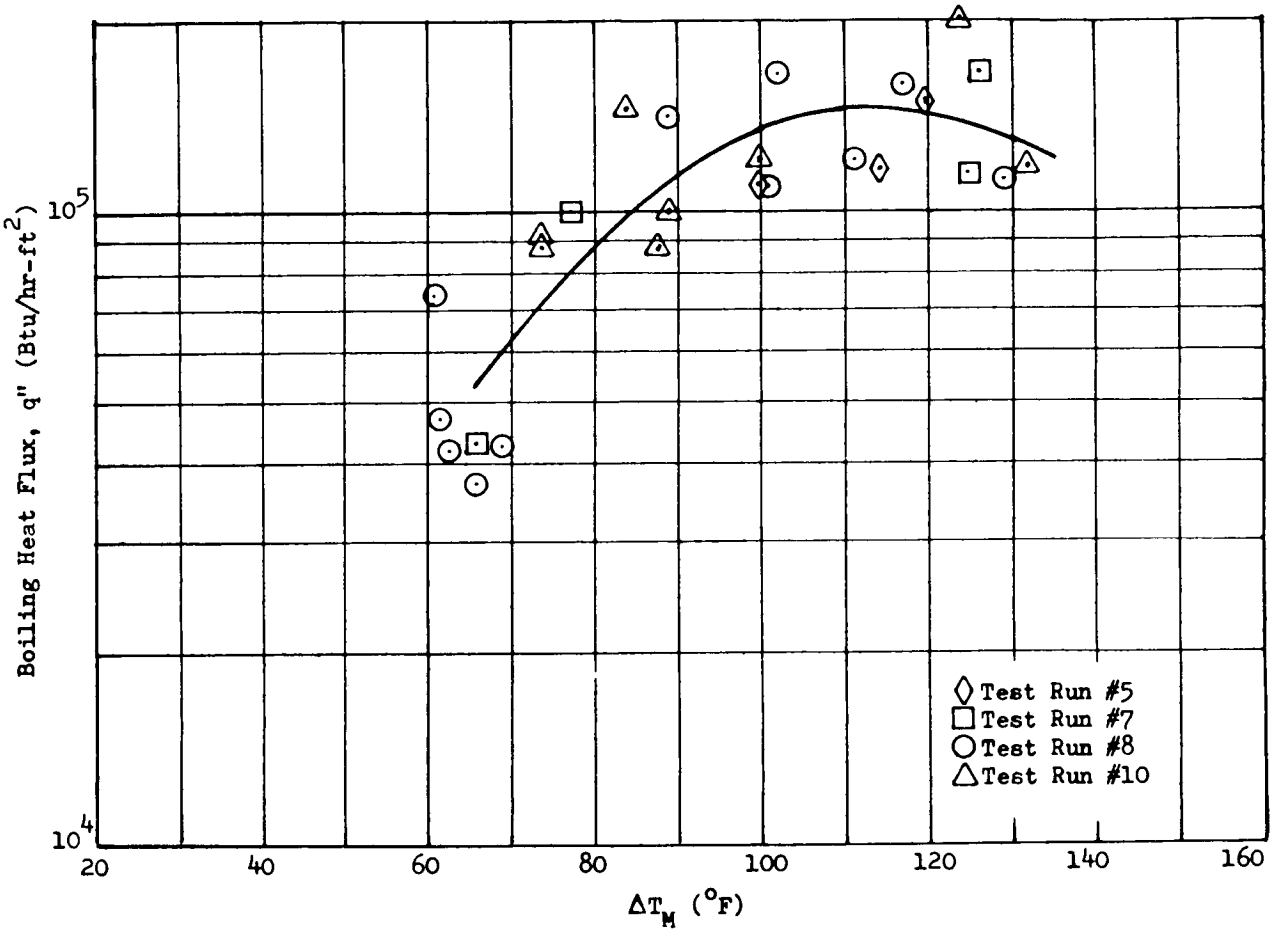


Fig. 24. Local Boiling Heat Flux - 30% Mean Vapor Quality

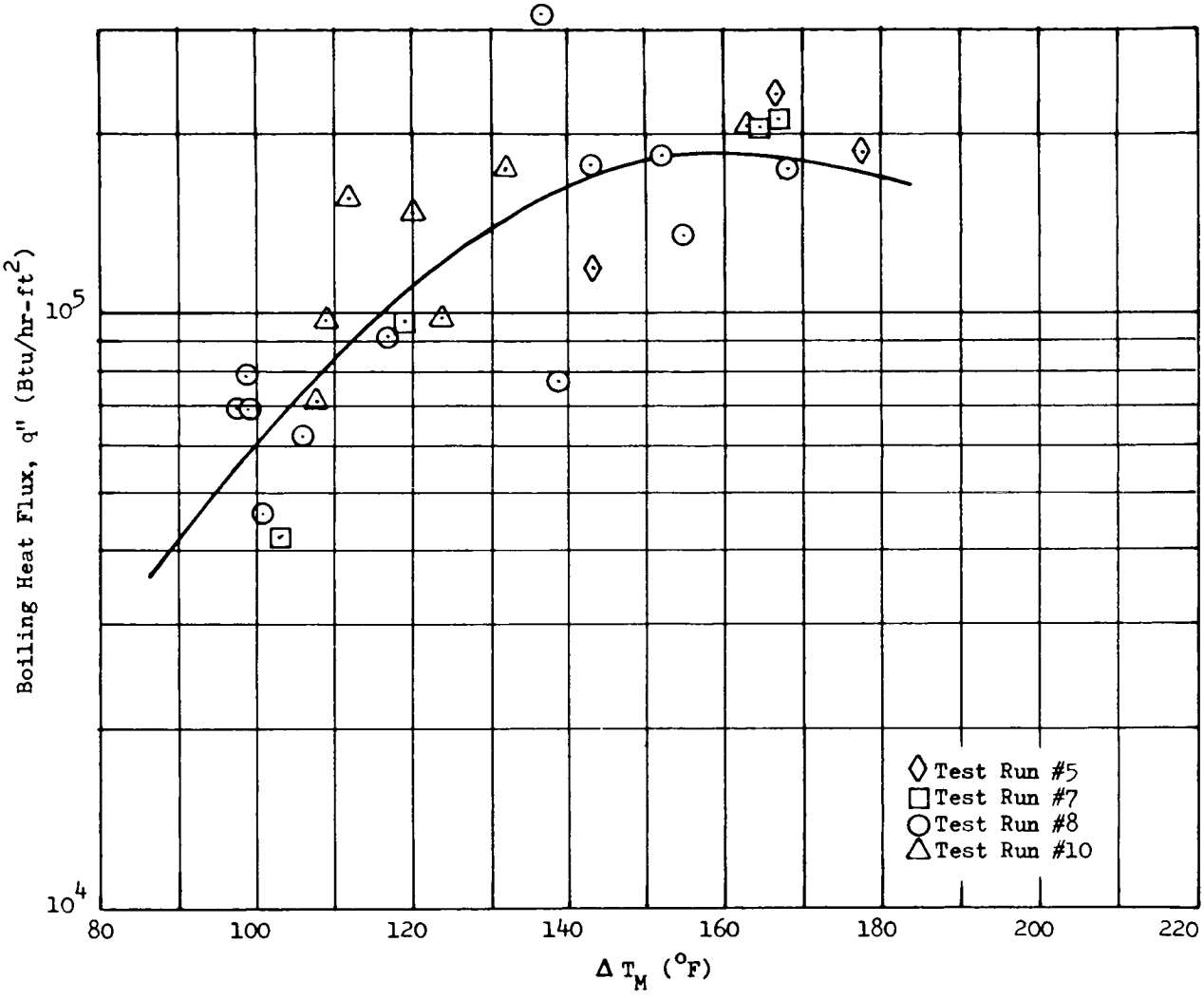


Fig. 25. Local Boiling Heat Flux - 50% Mean Vapor Quality

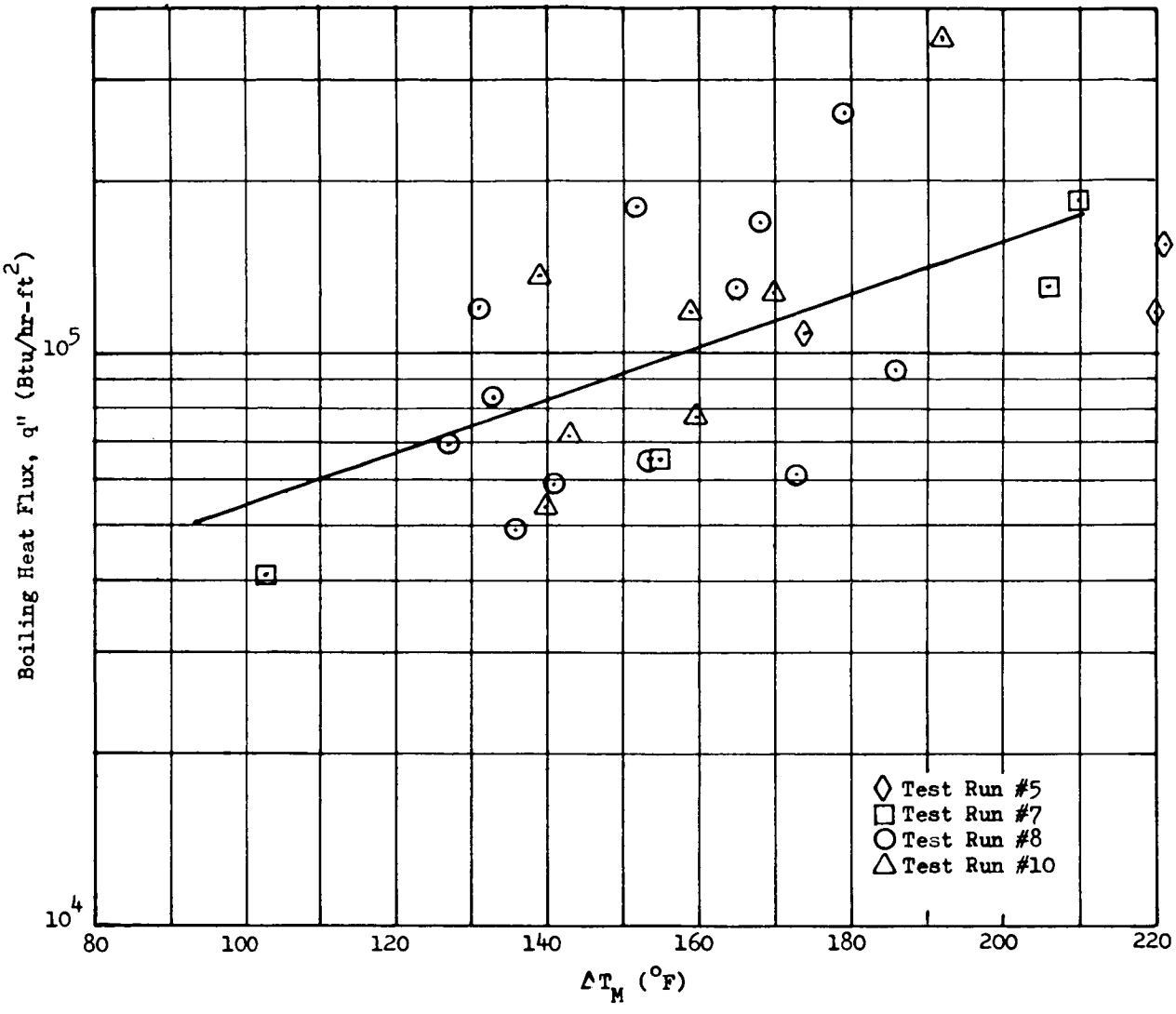


Fig. 26. Local Boiling Heat Flux - 70% Mean Vapor Quality

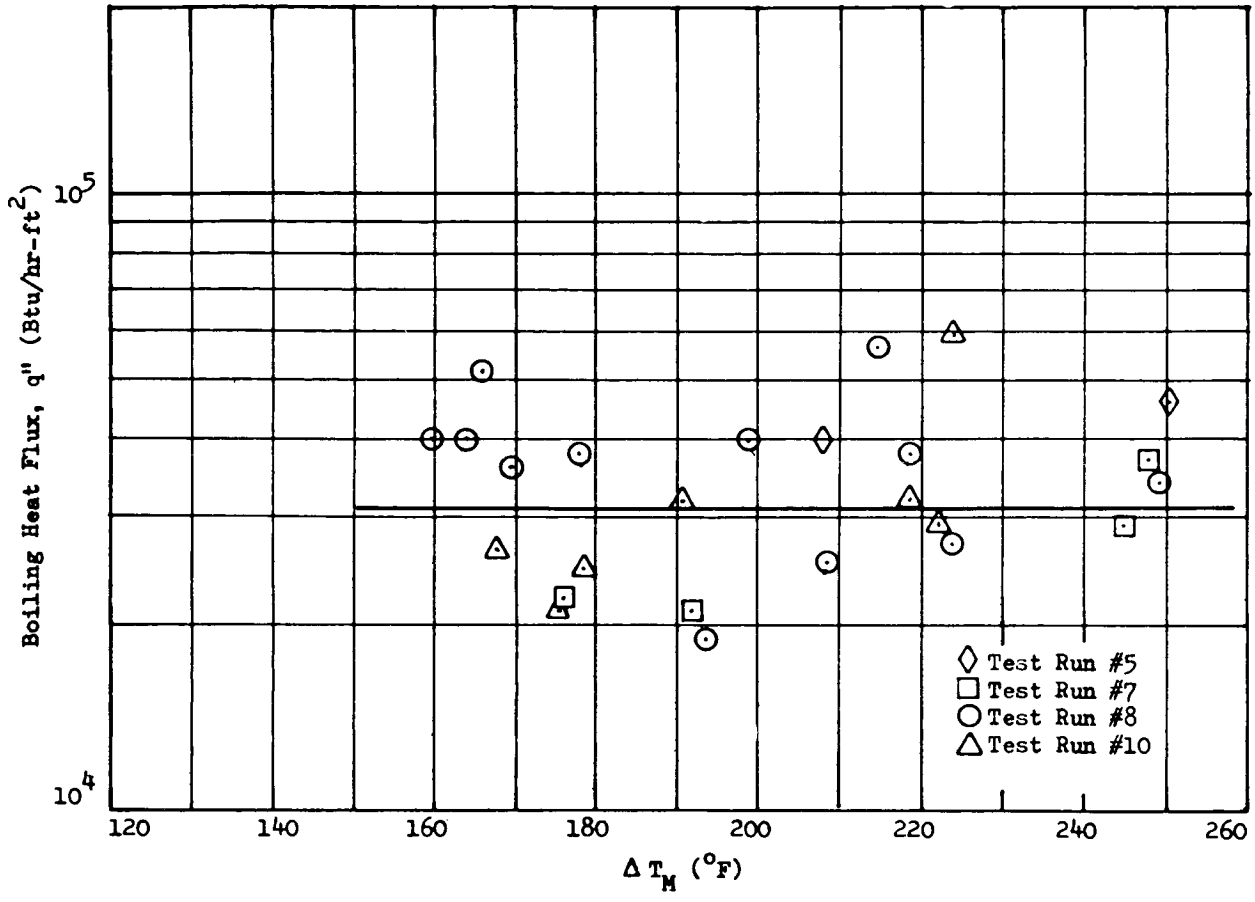


Fig. 27. Local Boiling Heat Flux - 90% Mean Vapor Quality

Contact boiling:

$$Nu_C = \frac{1}{32} Nu_\delta^2 \left(\frac{k_f}{k_v}\right)^2 \left(\frac{D}{\delta_o}\right)^2 \left(\frac{\rho_v}{\rho_f}\right) \frac{(1-x)^{1/3}}{x}$$

Intermittent contact boiling

$$Nu_{IC} = 234\ C^4 \left(\frac{k_v}{k_f}\right)^4 \left(\frac{\delta_o}{D}\right) \left(\tan\alpha \frac{DG}{\mu_v} \frac{h_{fv}\ \mu_v}{k_v\ \Delta T_M}\right)^2 (1-x)^{4/3}\ x$$

Film boiling

$$Nu_F = \frac{6^{1/3}}{4} \left(\frac{D}{\delta_o}\right) \left(\beta^{4/3}\right) \left(\frac{DG}{\mu_v} \tan\alpha \frac{\rho_v}{\rho_f} \frac{h_{fv}\ \mu_v}{k_v\ \Delta T_M}\right)^{2/3} \frac{(1-x)^{2/3}}{x^{1/3}}$$

The boiling regimes are determined by equating $Nu_C = Nu_{IC}$ and $Nu_{IC} = Nu_F$ and solving then for $\Delta T_M = \Delta T_{cr}$ accordingly. These solutions are:

$$\Delta T_{cr-1} = \frac{h_{fv}\ \mu_v\ C^2\ (7488)^{1/2} \left(\frac{k_v}{k_f}\right)^3 \left(\frac{DG}{\mu_v}\right) \tan\alpha\ (1-x)^{1/2}\ x}{k_v \left(\frac{D}{\delta_o}\right)^{3/2} \left(\frac{\rho_v}{\rho_f}\right)^{1/2}}$$

If $\Delta T_{cr-1} > \Delta T_M$ ⟶ use contact boiling regime.

If $\Delta T_{cr-1} < \Delta T_M$ ⟶ calculate ΔT_{cr-2}

$$\Delta T_{cr-2} = C^3 \left(\frac{h_{fv}\ \mu_v}{k_v}\right) \frac{936^{3/4} \left(\frac{k_v}{k_f}\right)^3 \left(\frac{DG}{\mu_v}\right) (\tan\alpha)\ (1-x)^{1/2}\ x}{6^{1/4} \left(\frac{D}{\delta_o}\right)^{3/2} \left(\frac{\rho_v}{\rho_f}\right)^{1/2} \beta}$$

If $\Delta T_{cr-2} > \Delta T_M$ ⟶ use intermittent contact boiling regime

If $\Delta T_{cr-2} < \Delta T_M$ ⟶ use film boiling regime.

The empirical constants taken from Reference 1 are:

	β	C	Nu_δ
$0 < x < 0.4$	0.43	2.3	-
$0.4 < x < 1.0$	1.00	3.0	-
$0 < x < 1.0$	-	-	0.8

These values were used to plot the design curves (q" vs ΔT_M) superimposed on the test data plots. The results of these considerations are depicted in Figures 28 through 36.

Figure 28 shows the test results in relation to the design expectations. The curves $Nu_\delta = 0.54$ and C = 2.0 are derived from the test data and suggest a more conservative design approach in this plug insert mean quality increment.

Figure 29 shows similar comparison of expected and obtained boiling heat fluxes at $\bar{x} = 0.30$ in the plug insert section. The design curves $Nu_\delta = 0.8$ and C = 2.3 are in good agreement with the test results.

Figure 30 shows the heat fluxes obtained at $\bar{x} = 0.30$ in the unplugged tube section. The design curve C = 2.3 as well as the curve derived from test data are in close agreement.

Figure 31 shows the test data at $\bar{x} = 0.50$ in the plug insert section. The design curve $Nu_\delta = 1.26$ derived from the test data is considerably higher than the one used for the design prediction. This may be attributed to the dynamic two-phase flow conditions existing in this mean quality section of the plug insert. The vapor flow helical velocity at $\bar{x} = 0.50$ is in excess of 100 ft/sec. Considerable radial acceleration g forces could, therefore, be induced on the liquid droplets carried by the vapor. Consequently, the contact area of droplets at the tube wall is increased because of droplet deformation or breakup.

Figure 32 depicts the test results at $\bar{x} = 0.50$ in the unplugged tube section. The design prediction curve C = 3.0 and the average curve C = 3.1, as derived from the test data, are, however, in close agreement.

Figure 33 shows test results at $\bar{x} = 0.70$ in the plug insert region. It refers to results similar to those shown in Figure 31. Both cases are accompanied by relatively high pressure drops through the plug insert vapor quality region.

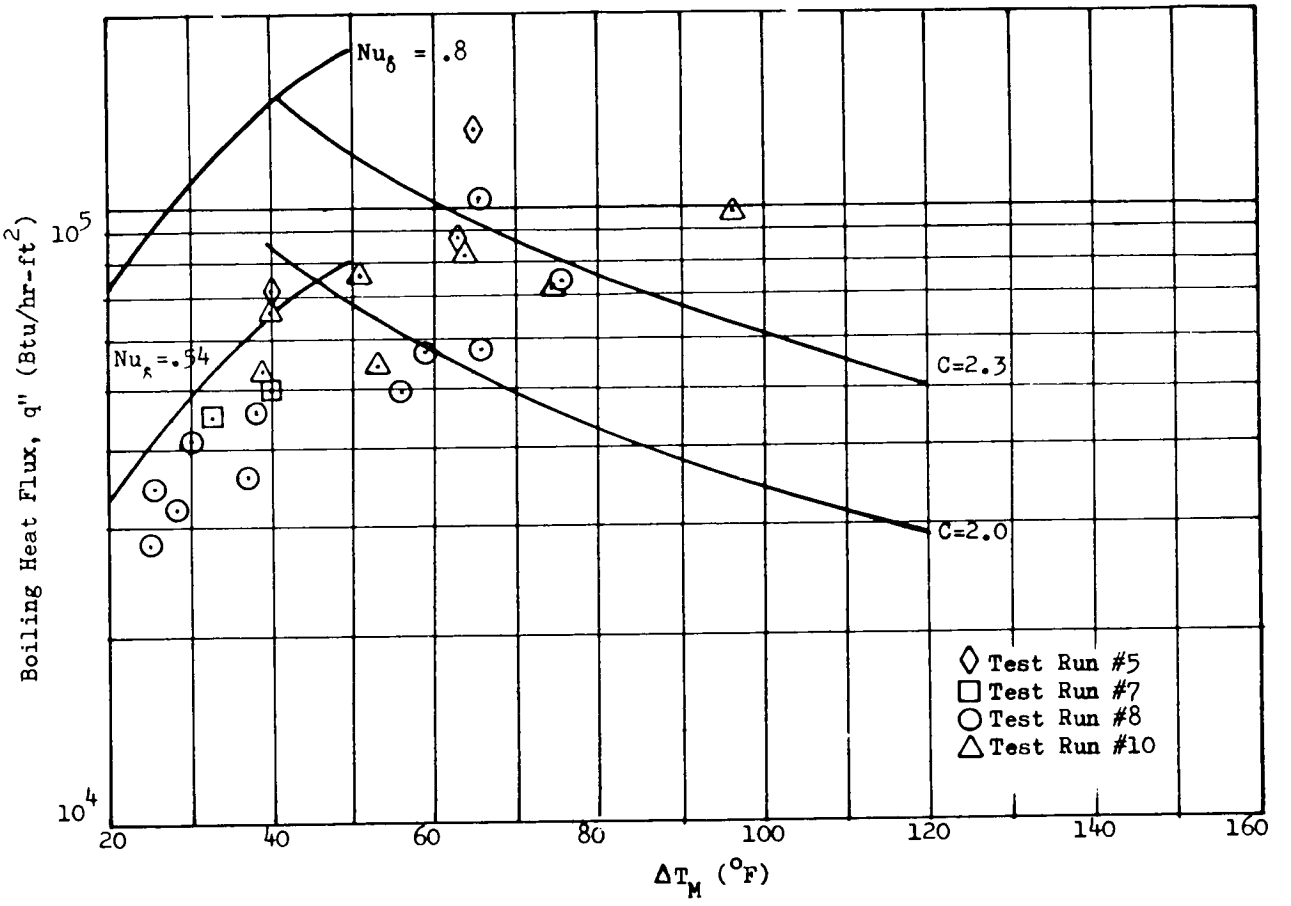


Fig. 28. Local Boiling in Plug-Insert Region - 10% Mean Vapor Quality

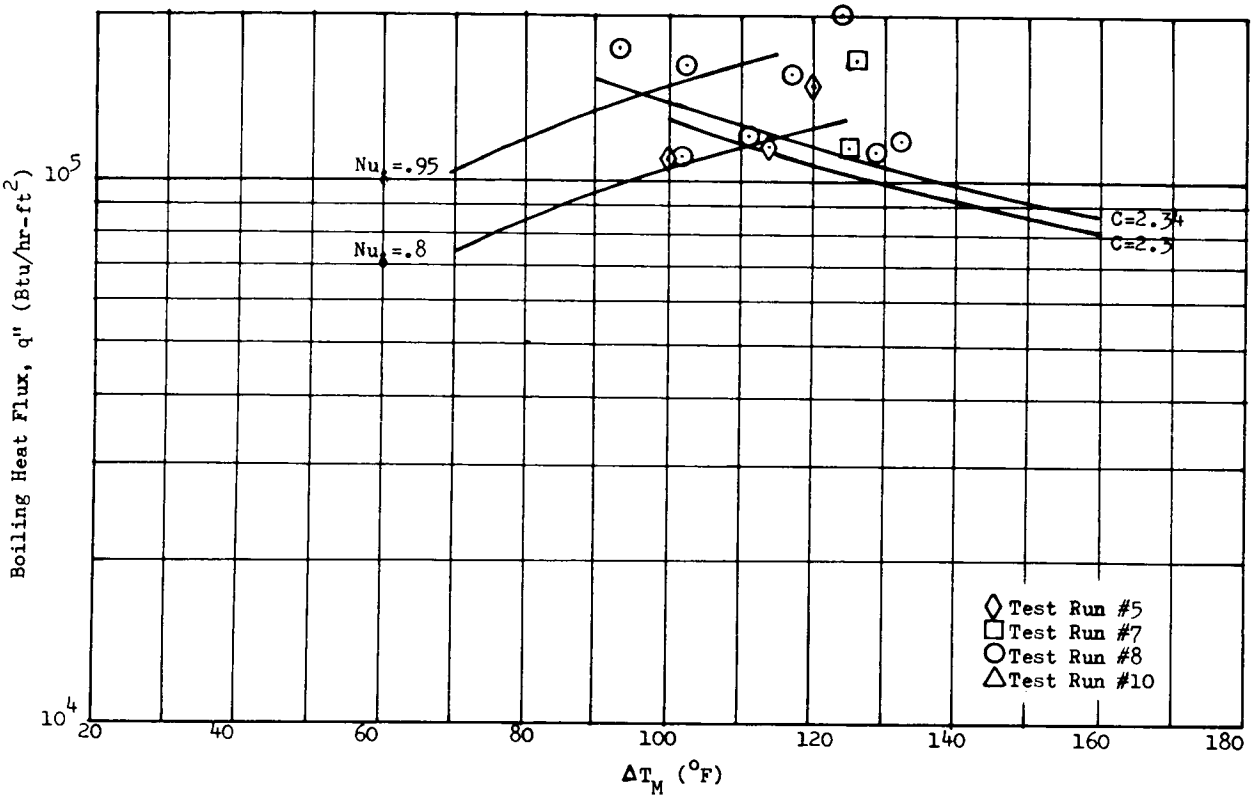


Fig. 29. Local Boiling in Plug-Insert Region - 30% Mean Vapor Quality

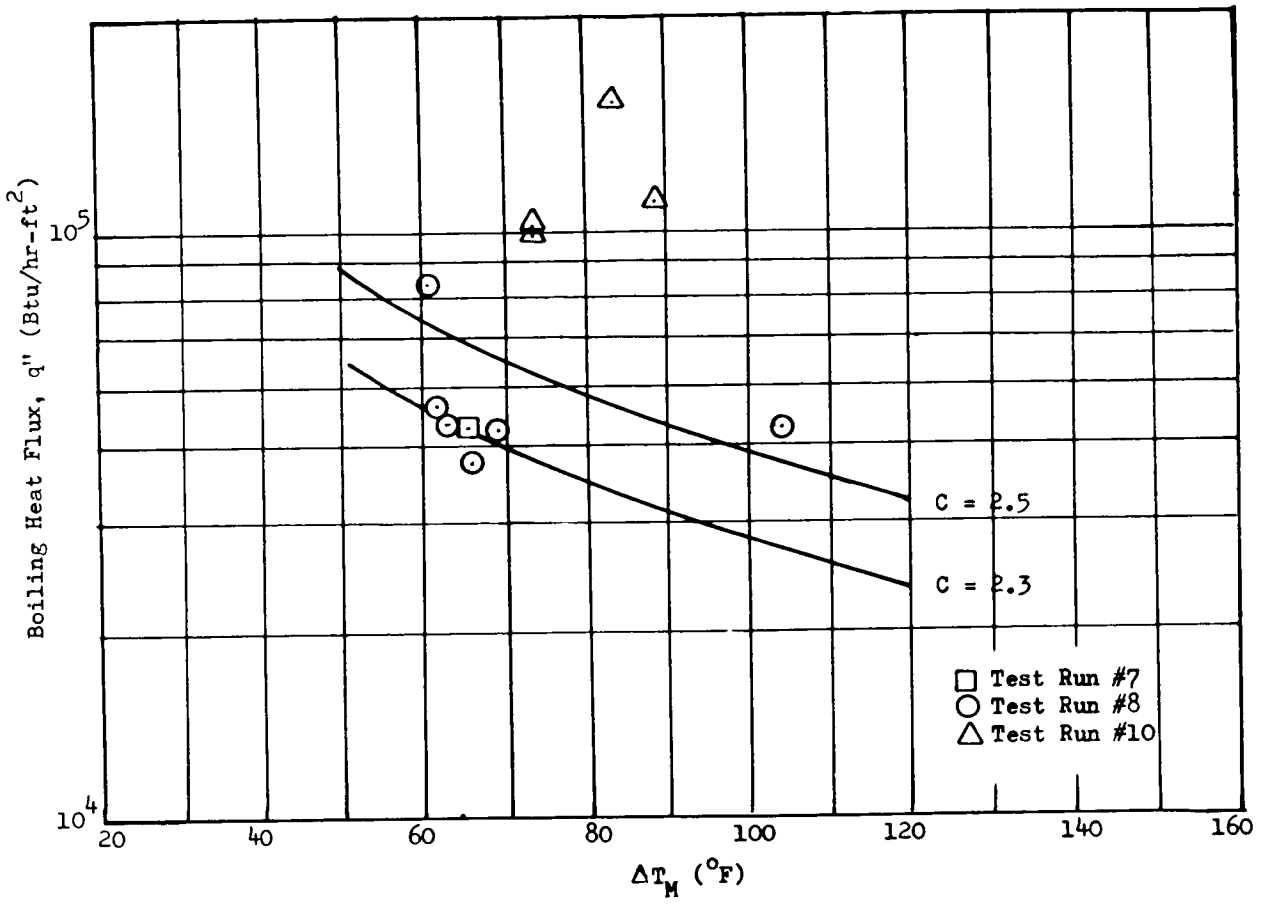


Fig. 30. Local Intermittent Contact Boiling in Unplugged Tube Region - 30% Mean Vapor Quality

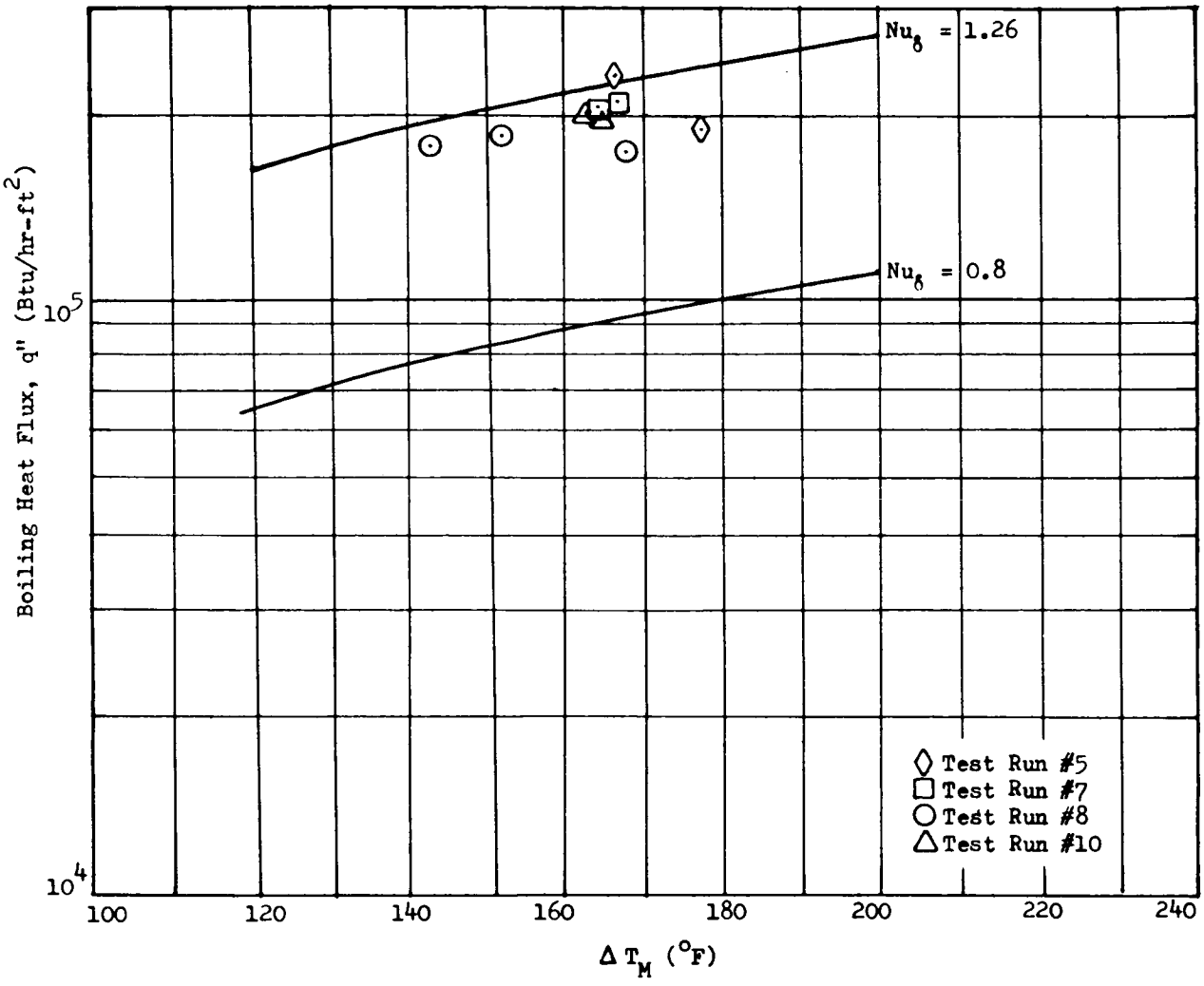


Fig. 31. Local Contact Boiling in Plug-Insert Region - 50% Mean Vapor Quality

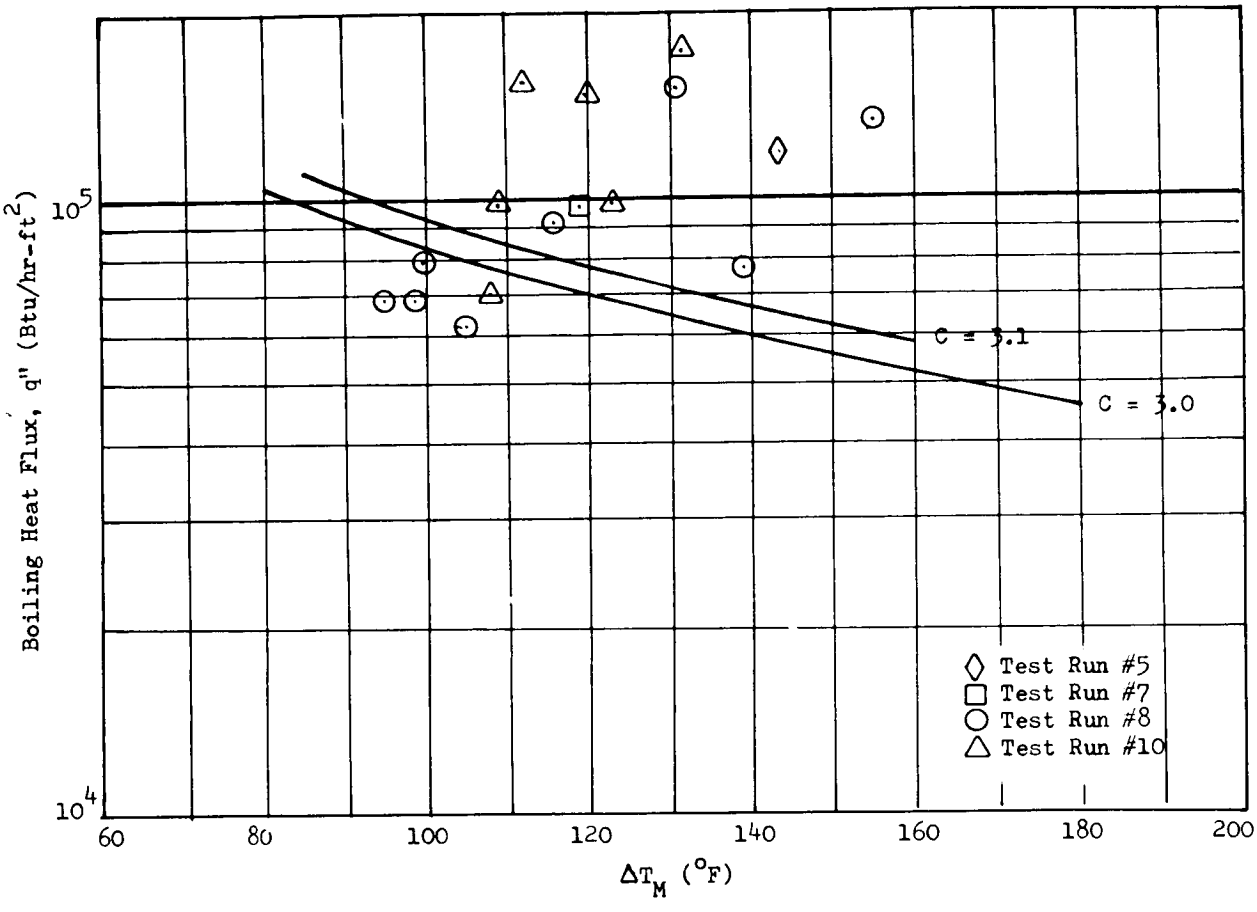


Fig. 32. Local Intermittent Contact Boiling in Unplugged Tube Region - 50% Mean Vapor Quality

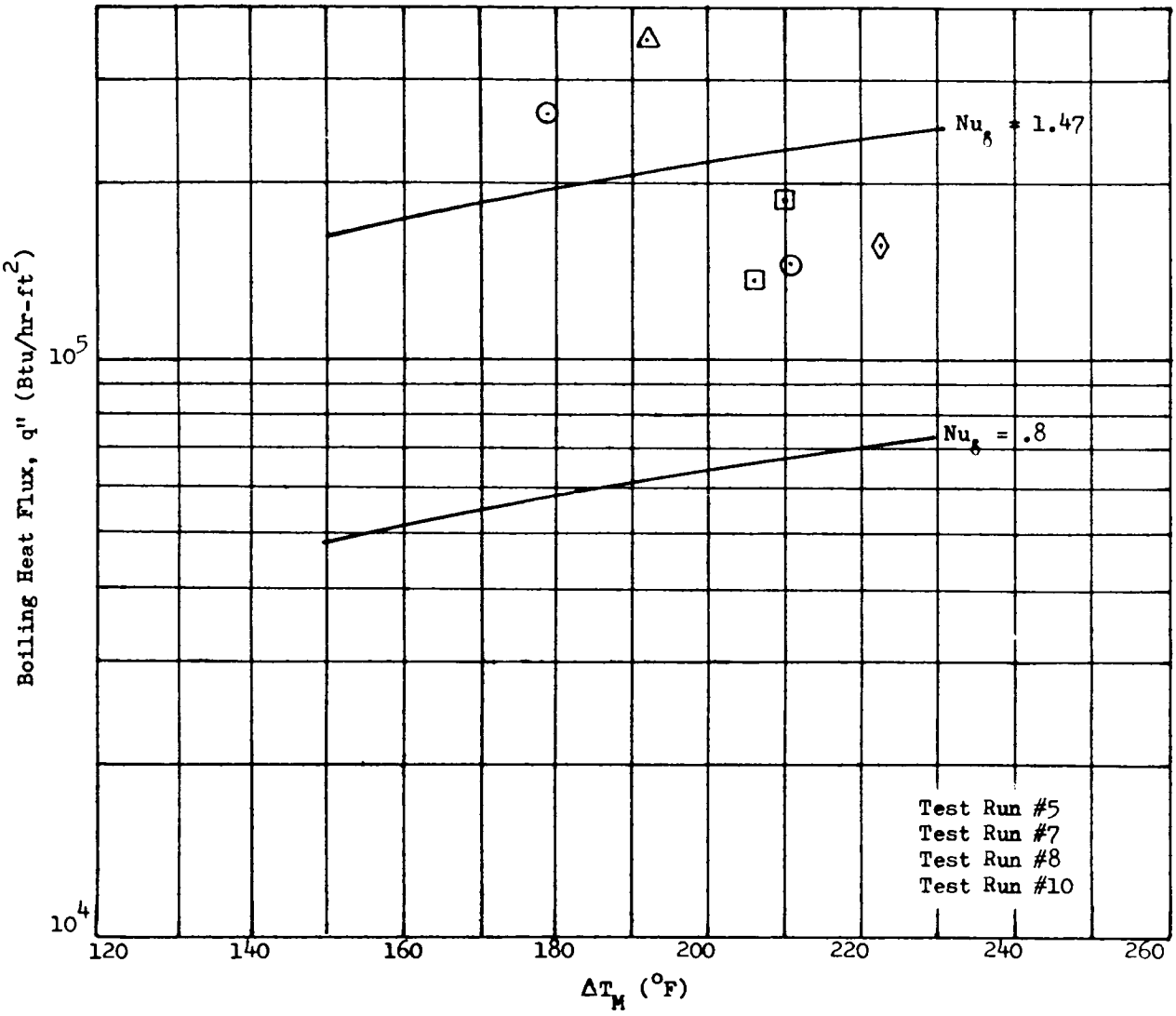


Fig. 33. Local Contact Boiling in Plug-Insert Region - 70% Mean Vapor Quality

Figure 34 provides the results at $\bar{x} = 0.70$ in the unplugged tube section. These heat transfer data can be represented by a local intermittent contact boiling regime at C = 3.6. The design prediction using C = 3.0 is still a good conservative design approach.

Figure 35 shows that test data at $\bar{x} = 0.90$ fall below the expectation of the film boiling regime. This can be explained by test data inaccuracy and error introduced by the estimation of the boiler length at the 100% vapor quality point.

Typical boiling heat flux representations at SNAP-8 operating conditions are shown in Figure 36. These curves indicate that heat-transfer effectiveness and thus the boiler vapor quality section length is dependent on boiler NaK inlet temperature (T_{Nbi}) and the NaK temperature drop (ΔT_N) through the boiler. The minimum boiling length occurs under a high boiler NaK temperature schedule, which is shown by curve A. The maximum boiling length, as shown by the available heat fluxes of curve B, occurs under a low NaK temperature schedule.

VII. CONCLUSIONS

The introduction of a preheat section plug insert providing elevated liquid phase velocity at the liquid-vapor interface location demonstrates significant improvement in the boiler conditioning effect. As shown in Figures 8, 10, and 11, the obtained boiler NaK temperature profiles are approaching the design prediction indicated in Figure 10. It is postulated that high liquid-phase velocities at the liquid-vapor interface significantly reduce or even completely eliminate the convective mercury boiling transition regime between the liquid-vapor interface and the fully established two-phase vortex flow pattern.

The boiler conditioning time is apparently dependent upon the cleanliness of the internal wall surface of the mercury flow passage. To define the surface cleanliness in conjunction with boiler conditioning effect, a better understanding of surface physics and chemistry is needed. Up-to-date experience suggests that tight plug-insert geometries provided in the boiler preheat section, as well as in the low-vapor-quality section are capable of accelerating the boiler conditioning effect by several orders of magnitude when the boiler mercury flow passage is cleaned by established[5] methods prior to mercury injection. This method involves flushing with strong caustic solution, followed by flushing with Alionox detergent solution.

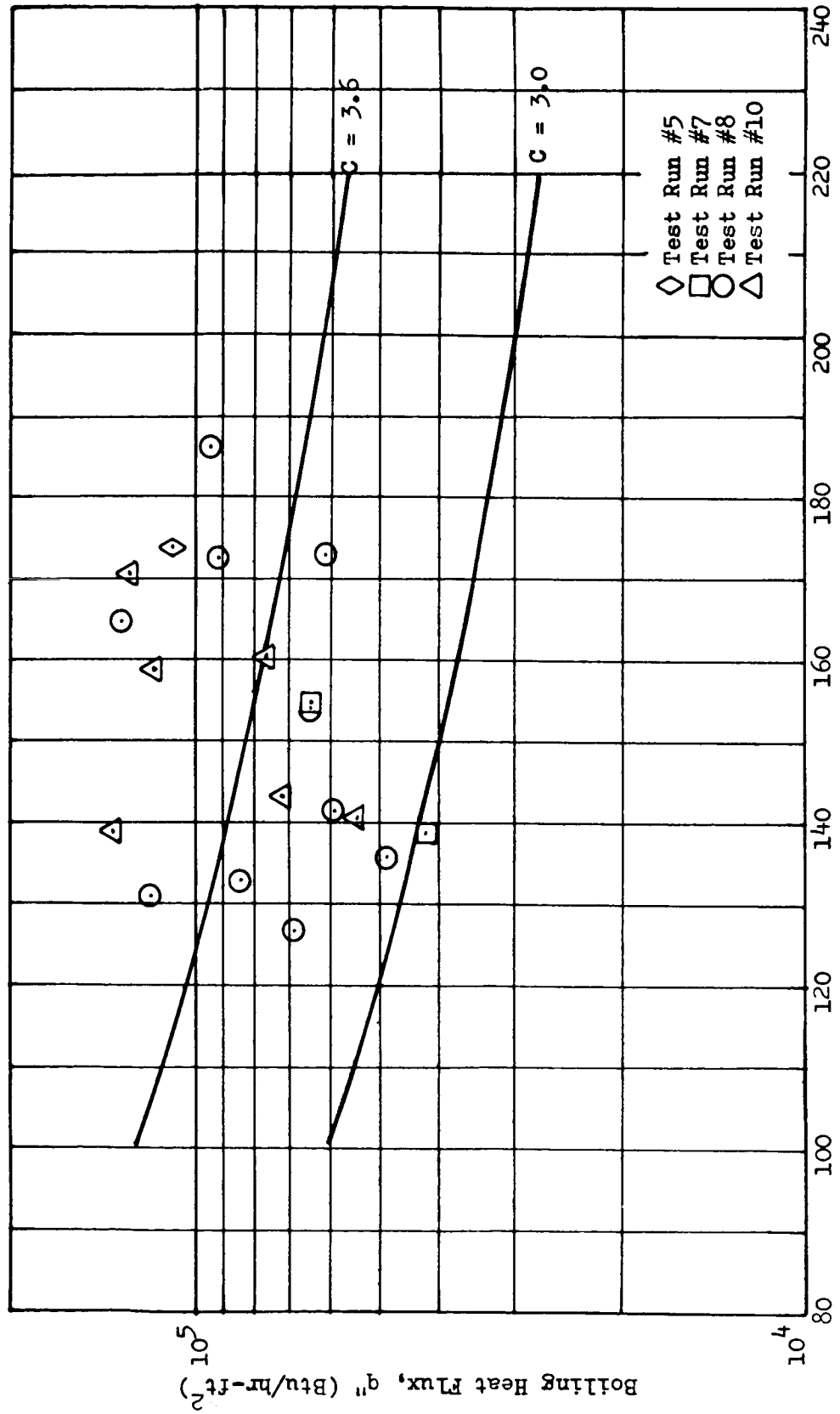


Fig. 34. Local Intermittent Contact Boiling in Unplugged Tube Region - 70% Mean Vapor Quality

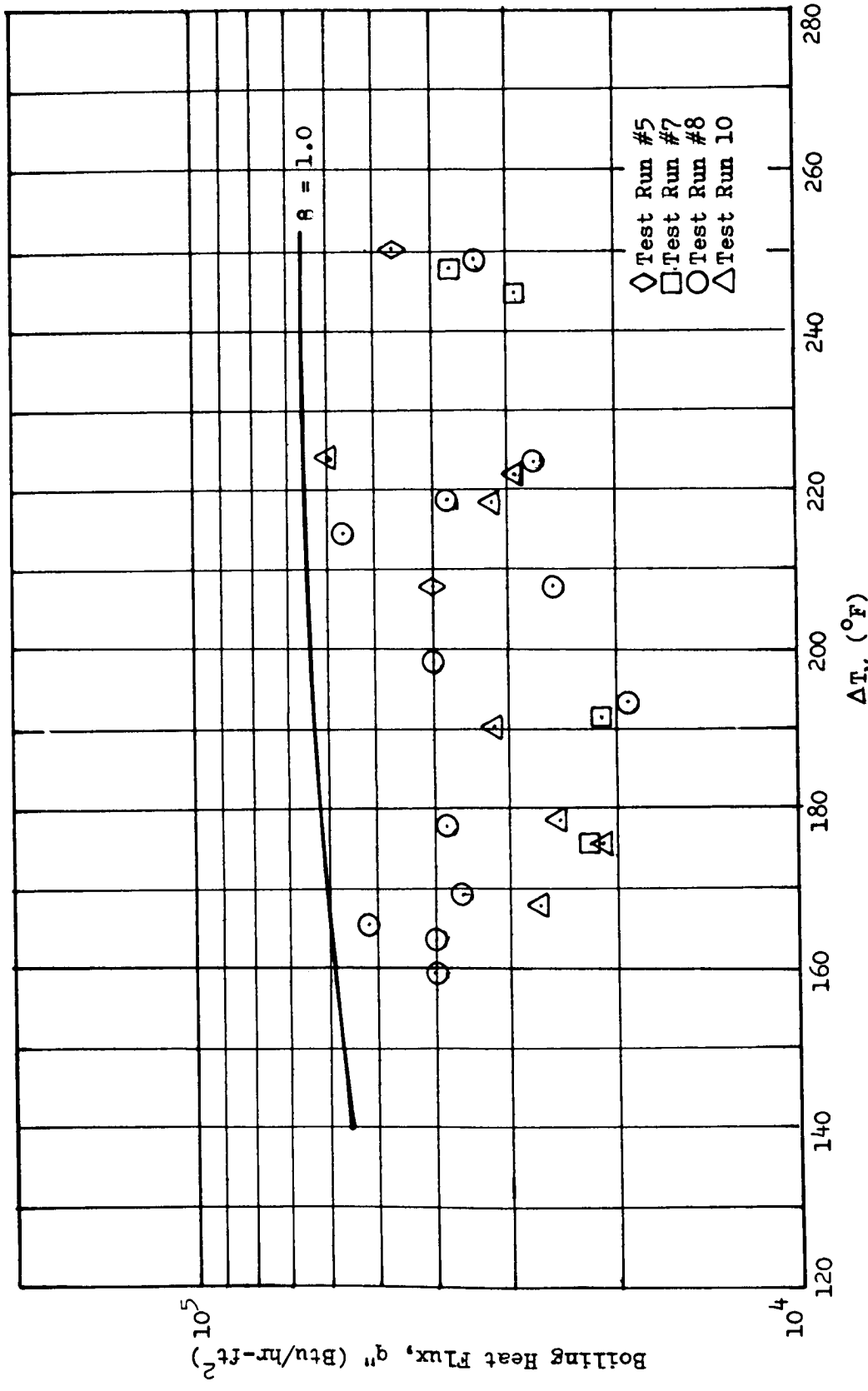


Fig. 35. Local Film Boiling in Unplugged Tube Region - 90% Mean Vapor Quality

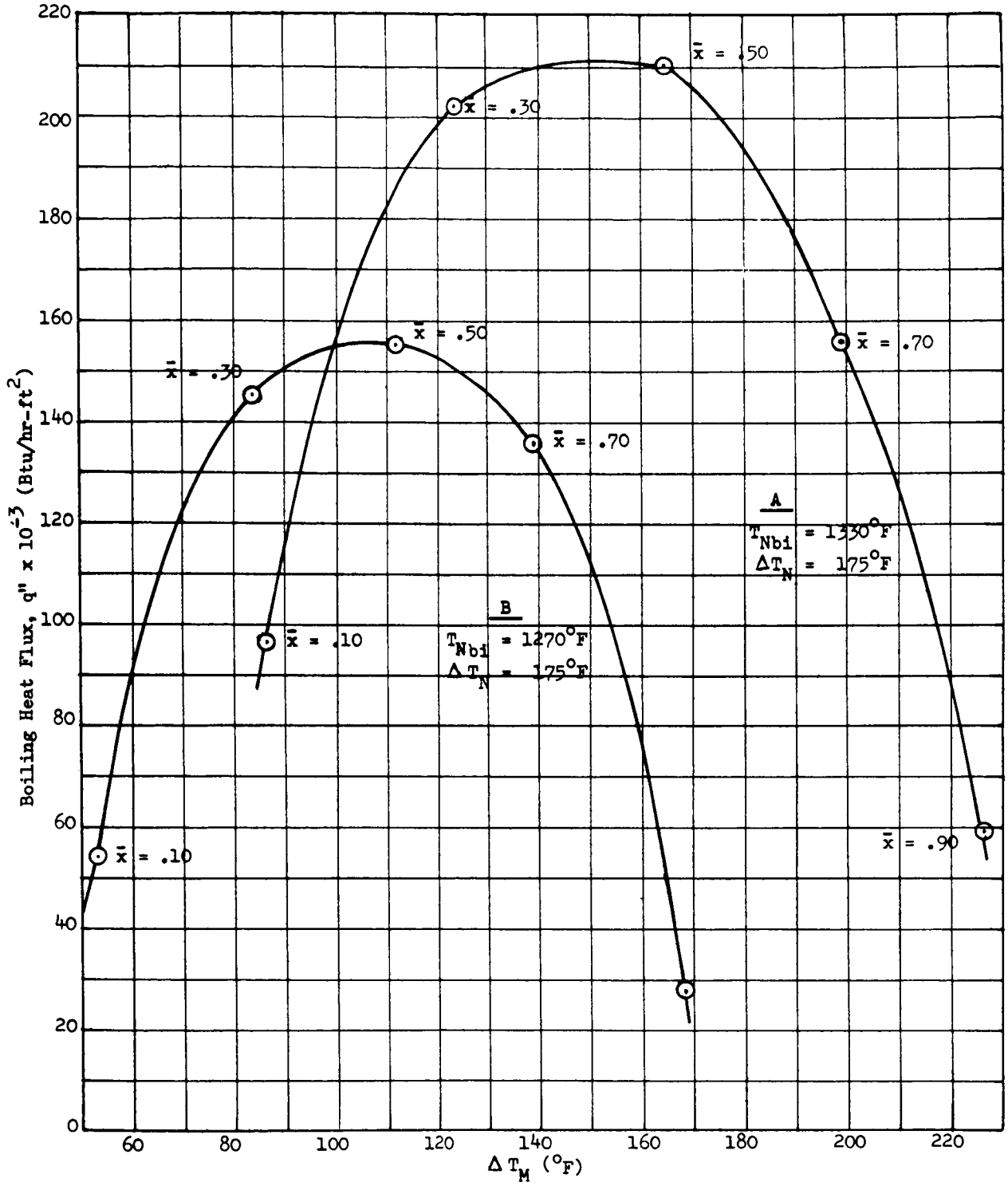


Fig. 36. Typical Boiling Heat Flux Representation throughout the Boiler Vapor Quality Section

The test of two tight preheat section plug-insert geometries providing liquid phase velocities of 4.5 and 6.5 ft/sec at the liquid-vapor interface accordingly resulted in very stable boiler performance. Compared to a loose preheat section plug-insert geometry (u_L = 0.8 ft/sec), the tight plug inserts demonstrate reduction in boiler exit pressure fluctuations by an order of magnitude; e.g., the comparative boiler exit pressure fluctuations are $\pm$10 and $\pm$ 1/2 psia.

Most effective boiling heat transfer was obtained from extended length plug insert geometries where the plug insert end-point vapor quality and vapor-phase velocity were up to 80% and 180 ft/sec, respectively, at high NaK temperature schedules. At low NaK temperature schedules, the same parameters were found to be 45% and 100 ft/sec, respectively. Aside from the high pressure-drop penalty, it is felt that under these dynamic conditions most effective mist or even fog flow can be expected at the plug insert end point and thus the droplet carry-over through the excess superheat length is minimized. It is obvious that high vapor flow velocity (e.g., 180 ft/sec at the plug insert end point) provides high-velocity vapor flow (e.g., 40 ft/sec in the unplugged tube next to the plug insert end point). Thus, effective vortex flow takes place in the unplugged tube. As a result of droplet radial acceleration in this flow regime, the droplets are forced against the tube wall and effectively vaporized.

In accordance with the early vortex two-phase flow establishment definition by means of Weber number $\left(We = \frac{\delta_o \rho_v u_v^2}{\sigma}\right)$, as proposed by Reference 1 (e.g., $\rho_v u_v^2 \geq 142$), a certain vapor phase velocity (u_v) must be obtained to carry droplets of diameter δ_o in the vapor stream. In the case of low liquid-phase velocities (u_L = 0.8 ft/sec) the initial boiling is under the influence of the one g field because of the absence of sufficient liquid and vapor-phase velocity effects. Considerable transition length accompanied by liquid slugging is needed until a fully developed vortex two-phase flow regime $\left(u_v \geq \sqrt{\frac{142}{\rho_v}}\right)$ is established. In the case of elevated liquid phase velocities ($u_L \cong u_v$ = 6.2 ft/sec), the liquid-vapor interface disintegration and initial boiling may take place in a vortex type of flow pattern, where the liquid spheroids are forced against the tube wall thus producing effective initial

vapor generation. This design approach suggests that elevated liquid phase velocities (u_L) at the liquid-vapor interface location initially accelerate the highly deficient vapor phase ($\bar{x} \longrightarrow 0$), simultaneously promoting effective boiling heat transfer rates. The latter in turn do elevate the vapor phase velocity $\left(u_v \longrightarrow u_L \longrightarrow u_{v\text{-}cr} = \sqrt{\frac{142}{\rho_v}} \right)$ causing, finally, the entrainment of liquid drops into the vapor stream. It is postulated that this early vortex two-phase flow boiling regime is desirable for boiler operation in zero- or adverse-gravity environments.

The two-phase flow pressure data, as shown in Figures 18 through 20, are nondimensional, and compare reasonably well with similar data.[1] It is, therefore, felt that these results can be used to evaluate the pressure-drop conditions of other tube sizes and plug insert geometries considered for SNAP-8 and similar Rankine-cycle power conversion systems. Empirically determined gas-flow frictional pressure-drop coefficients are permitting the analysis of two-phase flow pressure drop using the Martinelli parameter for relatively complex flow passage geometries.

The results derived from an analysis of the local boiling heat-transfer test data reveal reasonable agreement with the dropwise dry-wall boiling formulation.[1] The boiling heat-transfer rates can be adequately predicted from proposed semiempirical correlation. The test data comparison with the reference information is shown in Figures 28 through 35. The discrepancies are primarily in the test data areas referring to the plug insert vapor quality section. These discrepancies are caused by the introduction of the helical-flow-passage geometric values into the referenced boiling heat-transfer correlations. These correlations were established for round tubular flow passages with swirl wire in them. The plug insert section flow passage can be analytically treated on the basis of its equivalent or hydraulic diameter only.

The inaccuracies in NaK temperature profile interpretation and in analytical estimates in lieu of test information are the primary reasons for the test data point scatter. The instrumentation deficiencies were particularly felt in the boiler mercury inlet end region. The plot of mercury temperature rise in the preheat section in terms of mercury tube length was not available. Consequently, the true position of the liquid-vapor interface could not be established.

The existing NaK loop flow and heat input capacity placed serious limitations upon the scope of the test objectives. The boiler operation, therefore, was limited to 80% of its design capacity. The test results also show that this boiler is at least twice as long as is necessary.

ACKNOWLEDGMENT

The authors wish to express their appreciation for the assistance of B. E. Farwell, A. R. Herdt, E. F. McDaniel, J. H. Ralphs, and G. R. Redfern, Nucleonics Division, and of M. K. West, SNAP-8 Division, Aerojet-General Corporation.

REFERENCES

1. The SNAP-2 Power Conversion System Topical Report No. 17, Mercury Boiling Research, TRW Report No. ER-4833, October 1964.

2. L. T. Clark and M. F. Parkman, Effects of Additives on Wetting During Mercury Pool Boiling Heat Transfer, ASME, 64-WA/HT-22.

3. M. K. Wong, Corrosion Test Loop Operation Manual, Aerojet-General Nucleonics Report No. AN-SNAP-64-177, 16 February 1964.

4. A. J. Sellers and M. K. Wong, Experimental Investigation of Forced Convection Once-Through Mercury Boiler Performance Characteristics, Aerojet-General Corp. Technical Memorandum No. TM 4933:65-8-311, 3 August 1965.

5. Cleaning of SNAP-8 Power Conversion System Components Prior to Final Assembly - Method II, Aerojet-General Corp. Specification No. AGC-10319/6.

NOMENCLATURE

C	- Constant
D	- Mercury tube diameter
De	- Equivalent tube diameter
f	- Flow friction factor
G	- Specific mass flow
g_c	- Standard acceleration at sea level
h	- Heat transfer coefficient
h_{fv}	- Latent heat
h_N	- NaK side film coefficient
k	- Thermal conductivity
k_w	- Tube material thermal conductivity
$\Delta L'$	- Axial tube length
Nu	- Nusselt number
Nu_δ	- Droplet Nusselt number
P_{Hbi}	- Mercury inlet pressure
P_{Hbo}	- Mercury unit pressure
P_{OO}	- Pressure at liquid vapor interface
P_1	- Preheat section end point pressure
P_2	- Plug insert end point pressure
q''	- Heat flux
Re	- Reynolds number
r_m	- Log mean radius
r_o	- Tube outside radius
t	- Tube wall thickness
ΔT_{OO}	- Temperature difference at liquid-vapor interface
ΔT_{NOO}	- NaK temperature at x = 0
ΔT_{SOO}	- Saturation temperature at liquid-vapor interface
U	- Overall heat transfer coefficient
x	- Vapor quality, vapor weight/total weight
$\bar{x}$	- Mean vapor quality

GREEK SYMBOLS

α	- Swirl wire angle
β	- Nu (actual)/Nu_δ(film-sphere)

GREEK SYMBOLS (cont.)

δ_o - Initial droplet diameter, swirl wire diameter

λ - Martinelli correlating parameter

ρ - Density

ϕ - Two-phase flow pressure drop factor, $\Delta P_{TP}/\Delta P_v$

μ - Viscosity

SUBSCRIPTS

C - Contact boiling

F - Film boiling

IC - Intermittent contact boiling

M - Mean

TP - Two-phase

cr - Critical

f - Liquid at saturation temperature

v - Vapor

N66 31699

X-RAY MOVIE FILM REPORT OF FLOW PATTERNS IN A ONCE-THROUGH FORCED CIRCULATION NaK HEATED MERCURY BOILER

by

R. J. Ziobro
TRW Equipment Laboratories
Cleveland, Ohio

SUMMARY OF FILM PRESENTATION

The films presented offer a visual insight into the two-phase flow liquid metal boiling process at temperatures and pressures where glass equipment cannot be used.

The films were obtained under the Mercury Rankine Program (MRP) as part of the investigation of the boiler conditioning/deconditioning phenomenon.

Figure 1 shows characteristic boiler performance maps of the counterflow once-through forced circulation NaK heated mercury boiler. Curve A represents the design performance based upon heat transfer to non-wetting mercury. (The slope of the NaK temperature curve is proportional to the heat transfer rate.) Curve A is typical of initial performance of a new boiler. Curve B represents boiler performance after the mercury "has become wetting." This is the best performance attainable from the boiler since the NaK film and tube metal resistances now control the heat transfer rate. Curve B is typical of performance attained in a time period ranging from a few hours to a few days after initial operation of a new boiler. Performance between Curves A and B is termed "conditioned." All boilers perform "conditioned" initially and usually return to the "conditioned" state upon subsequent restarts and continue this performance indefinitely. Exceptions have occured upon restart resulting in performance between Curves A and C which is termed "deconditioned." Some form of contamination of the mercury side heat transfer surface, such as by air, water, or oil, during the boiler shutdown period has been evident in cases where the boiler has performed in the deconditioned state.

Visual observations of the "deconditioned" flow pattern were desired to aid in the investigation of causes and in the formulation of equations to enable design for the deconditioned state.

Figure 2 shows the prototype MRP boiler which has four mercury tubes, each tube having swirl wire turbulators throughout the boiling section and plug inserts in the low quality boiling section.

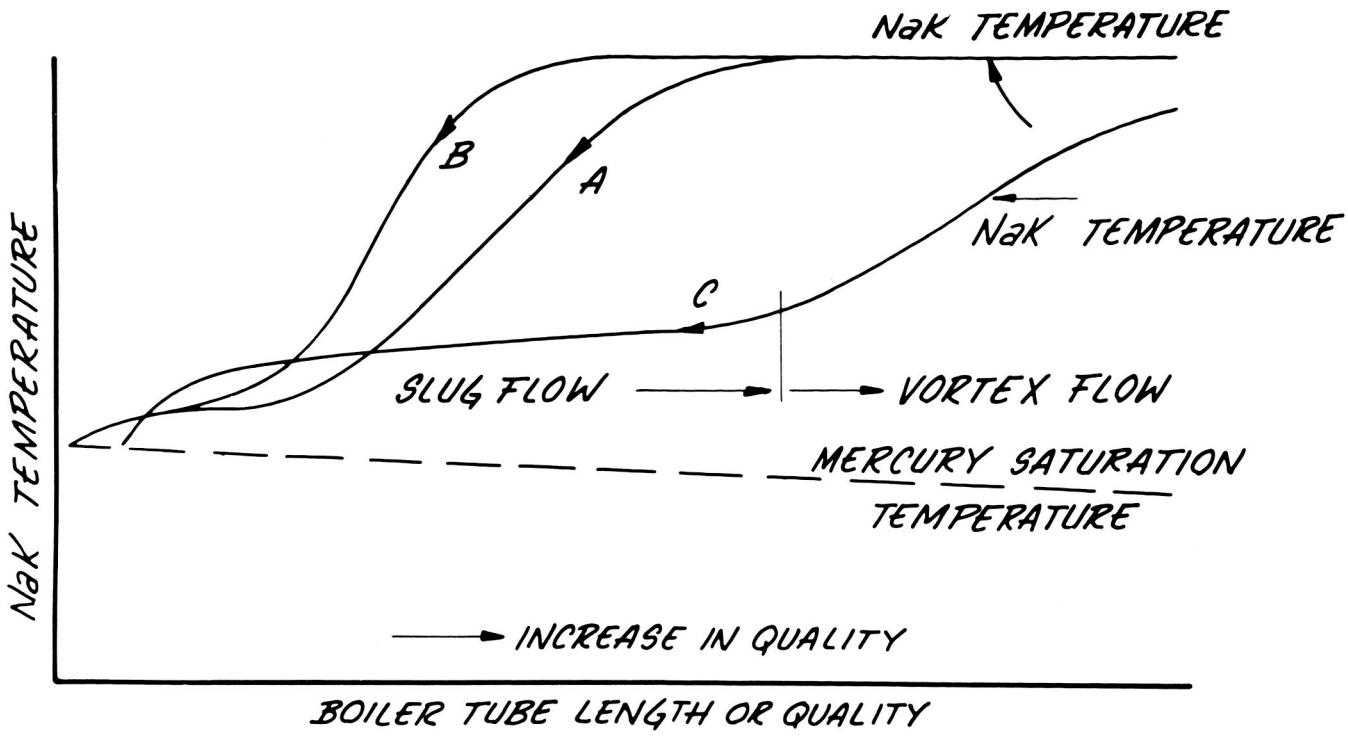


Fig. 1. NaK Temperature Profiles for Three Different Heat Transfer Modes

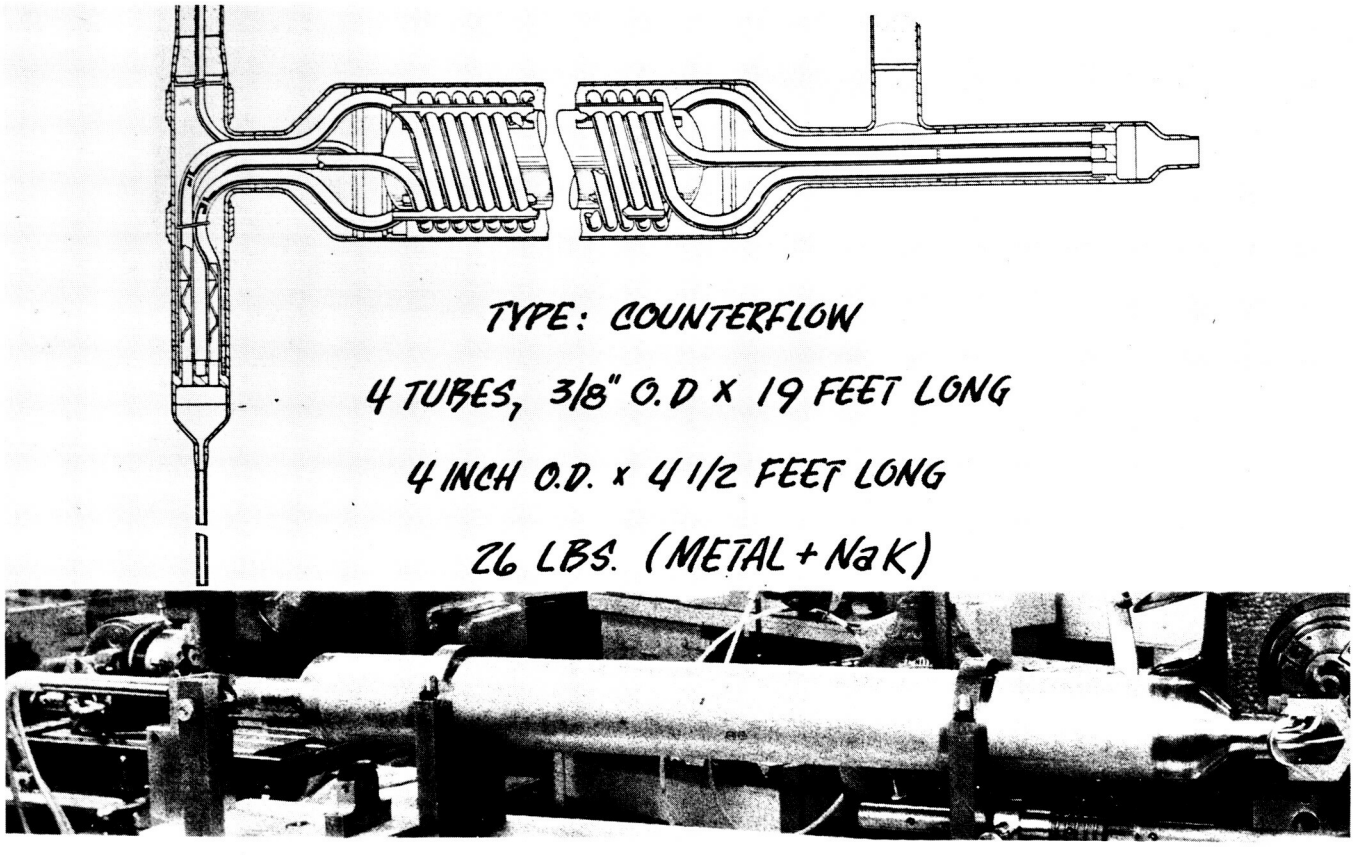


Fig. 2. MRP Model 7 Boiler

The test section for the "deconditioning" studies is shown in Figure No. 3. The single mercury tube has the same length, diameter, and swirl wire turbulator as is found in the prototype boiler. The plug insert is eliminated to exaggerate the deconditioning characteristics. The test section is straight rather than coiled as is the prototype to accommodate the X-ray equipment.

Figure 4 is a schematic of the test rig. Note that the X-ray camera is able to scan the two foot nucleation section and five feet of the low quality boiling zone. Exit qualities up to 80% can be viewed when operating in the "conditioned" state.

Figure 5 is a photograph of the insulated installation of the test section. Mercury flow is horizontal from left to right in the first leg of the test section. Flow is then vertically up to the second leg and then up to the third leg. (See Figure 2 for the three legs.) This Figure shows the travelling dolly to which is attached the image amplifier power supply (below the track), the seven inch image amplifier (closest to the test section) and the Vidicon TV camera (behind the image amplifier).

Figure 6 shows the back side of the test section. The image amplifier power supply is visible. Mounted on this side of the dolly opposite the image amplifier is the Dynamax 60 X-ray source.

Figure 7 shows the 150 KV Westinghouse Industrial X-Ray Generator control and the 17 inch TV monitor screen.

The films were taken with a 16 MM movie camera, 28 frames per second, mounted on a tripod in front of the TV screen.

The films presented traversed the test section seven times. Boiler performance was shown in the conditioned state and in various degrees of "deconditioning."

The significant observation of the deconditioned state is the existence of a slug flow pattern. This flow regime has been defined mathematically in a form suitable for boiler design analysis and performance evaluation.

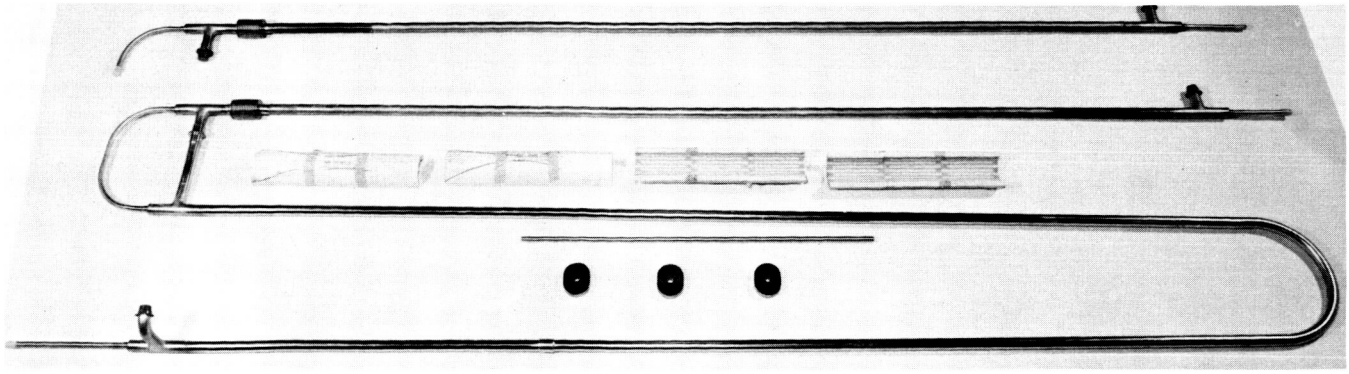


Fig. 3. Single Tube Boiler Nucleation Section and Heaters, and Spare Boiler Inlet Section

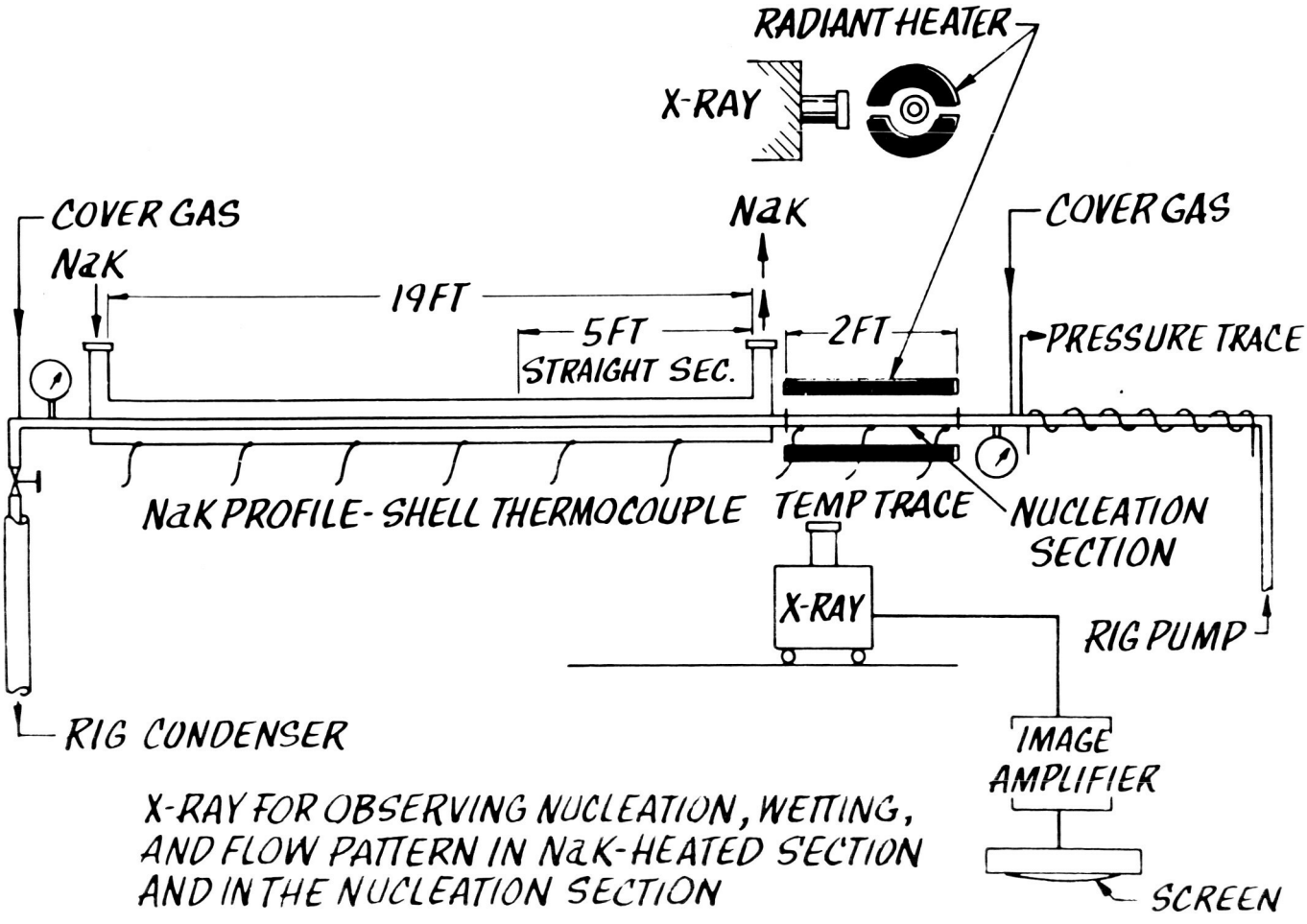


Fig. 4. Schematic Diagram of the Boiler Deconditioning Test Rig

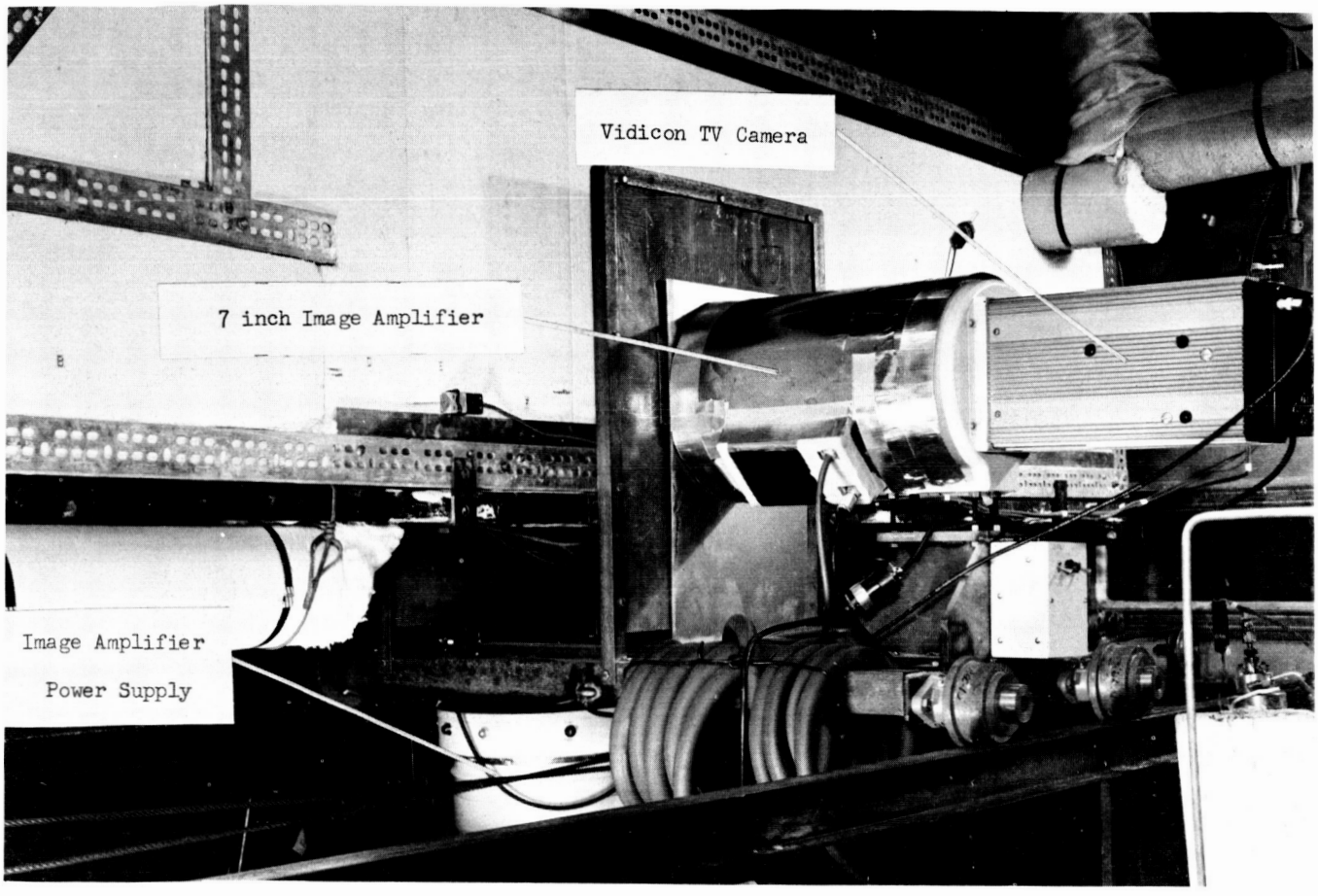


Fig. 5. Test Rig X-Ray Equipment - Front Side

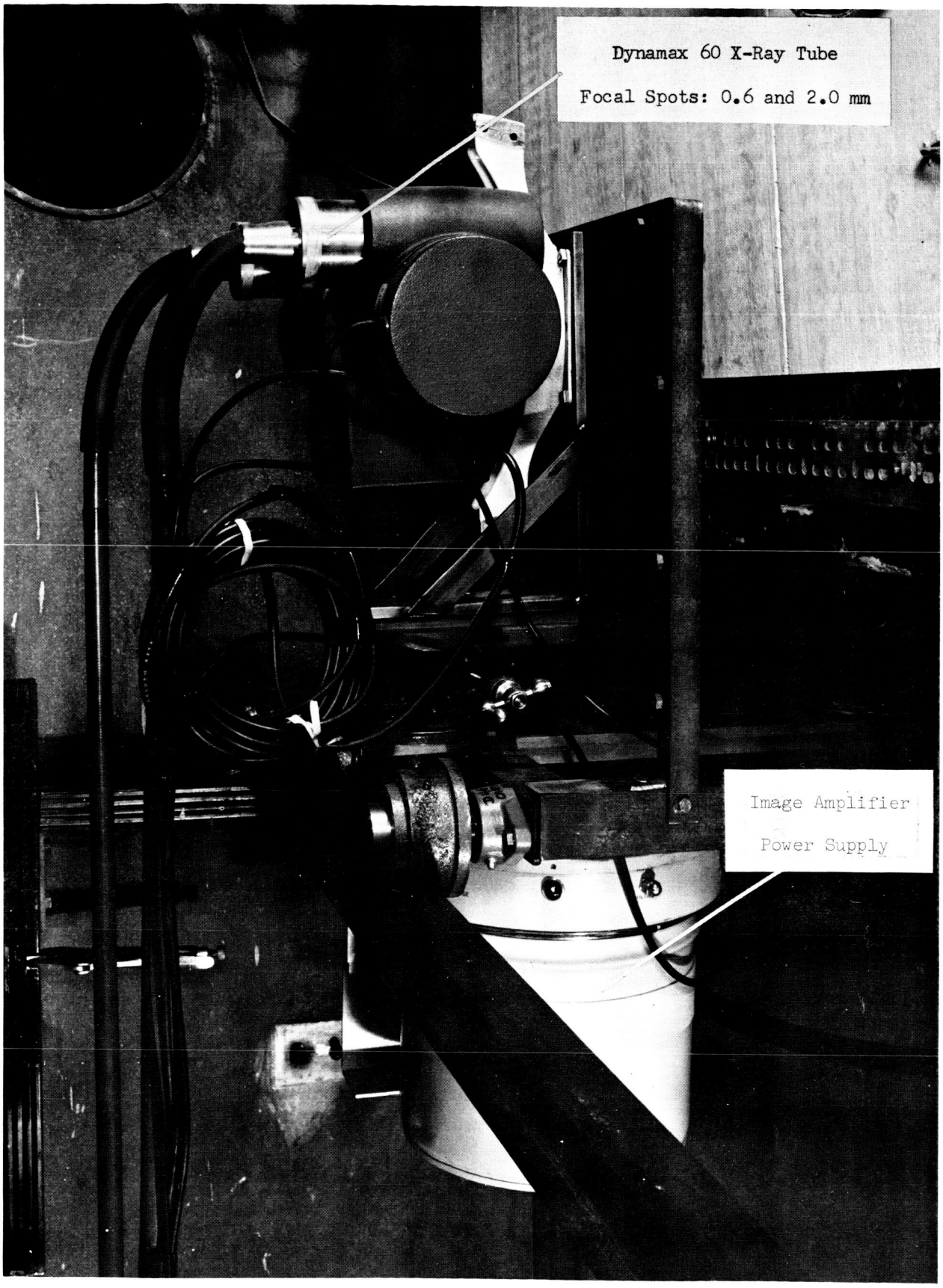


Fig. 6. Test Rig X-Ray Equipment - Back Side

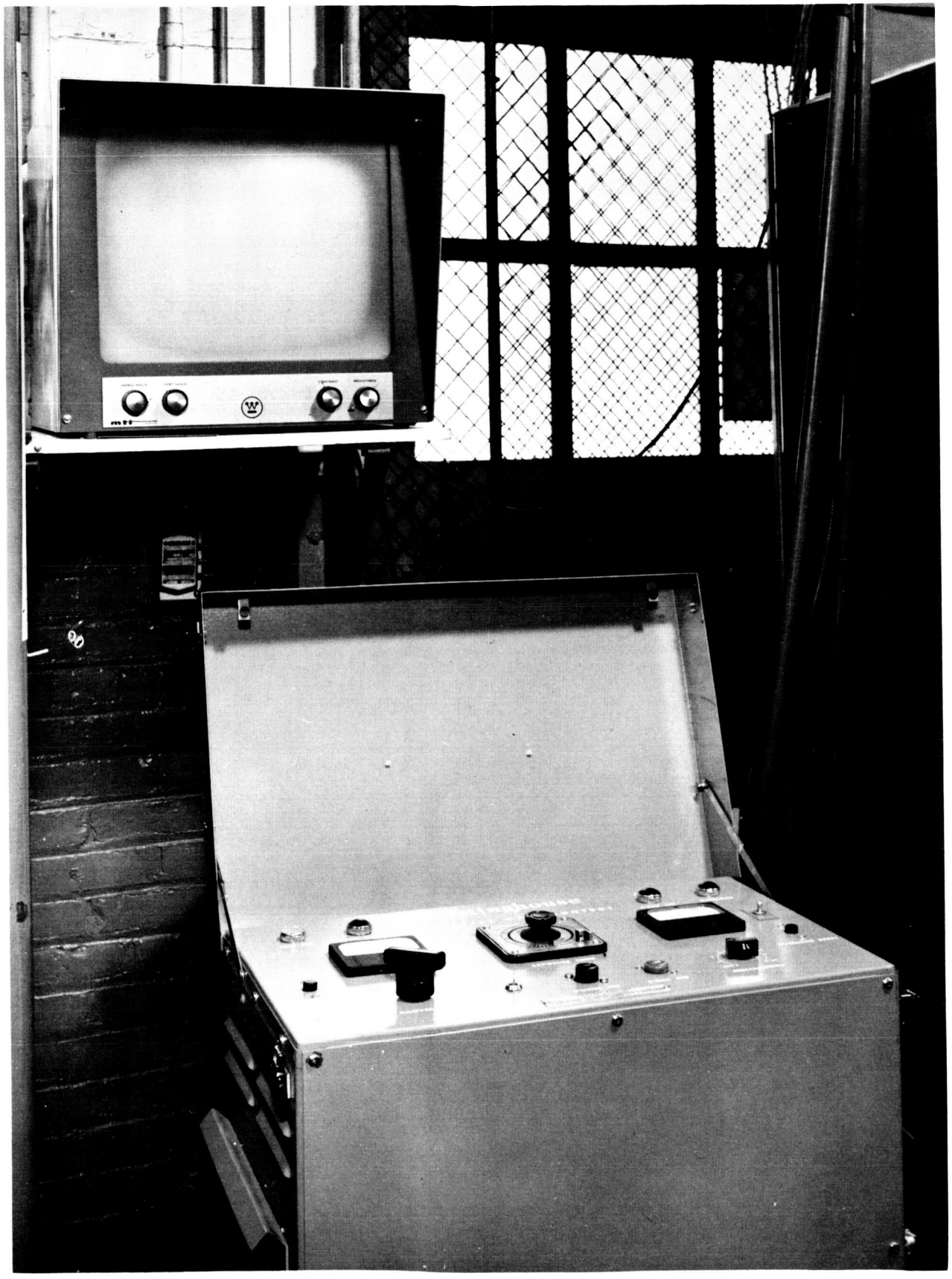


Fig. 7. Westinghouse 150 KV Full-Wave Industrial Control and TV Display Monitor

N66 31700 641

HIGH TEMPERATURE LIQUID METAL INSTRUMENTATION AT ATOMICS INTERNATIONAL FOR: (1) THE SNAP 10A FLIGHT SYSTEM, (2) BOILER CONDITIONING EXPERIMENTS AND MERCURY VAPOR QUALITY MEASUREMENT FOR MERCURY RANKINE SYSTEMS

by

H. H. Hanlin

Atomics International Division of

North American Aviation, Inc.

Canoga Park, California

HIGH TEMPERATURE LIQUID METAL INSTRUMENTATION OF THE SNAP 10A FLIGHT SYSTEM

On April 3, 1965 the first nuclear reactor space power system, SNAP 10A, was placed in an earth orbit and successfully operated for a period of 43 days. This system was designed and developed for the AEC by Atomics International, a division of North American Aviation, Inc. This system utilized a liquid metal, NaK 78, at an average temperature of 1000°F to transport the reactor heat to the thermoelectric converters. Lightweight instrumentation capable of withstanding the launch shock and vibration and operation for 1 year in a space environment was developed to monitor NaK flow rate, pressure and temperature.

Flow Rate Measurement

The thermoelectric powered D.C. conduction pump was utilized to measure flow rate as an integral, auxiliary function. Figure 1 is a photograph of a SNAP 10A pump. Electrodes, AA', were brazed to the throat duct of the pump as shown in Figure 2. High temperature nickel cladded copper lead wire was attached with standard thermocouple grade chromel sockets imbedded into the copper. The fluid in passing through the fringe magnetic field of the pump produces a signal proportional to the fluid flow rate at AA' in accordance with the Faraday principle. Figure 3a plots a typical signal vs flow rate characteristic. The non-zero intercept is due to coupling with the fringe current from the main electrodes of the pump. This effect can be reduced by locating the flow meter electrodes farther down the throat duct from the main electrodes. Signal strength would be reduced however, due to rapid drop-off in the fringe magnetic field. The position selected, approximately 0.25 inches from the main electrodes, provided the best trade-off between decoupling and signal strength. Because of this coupling with pump current, the flow measurement is not independent of the pump characteristics-changes in the pump circuit will cause a change in electrode current and affect the flow meter reading. To minimize this, an additional pair of electrodes,

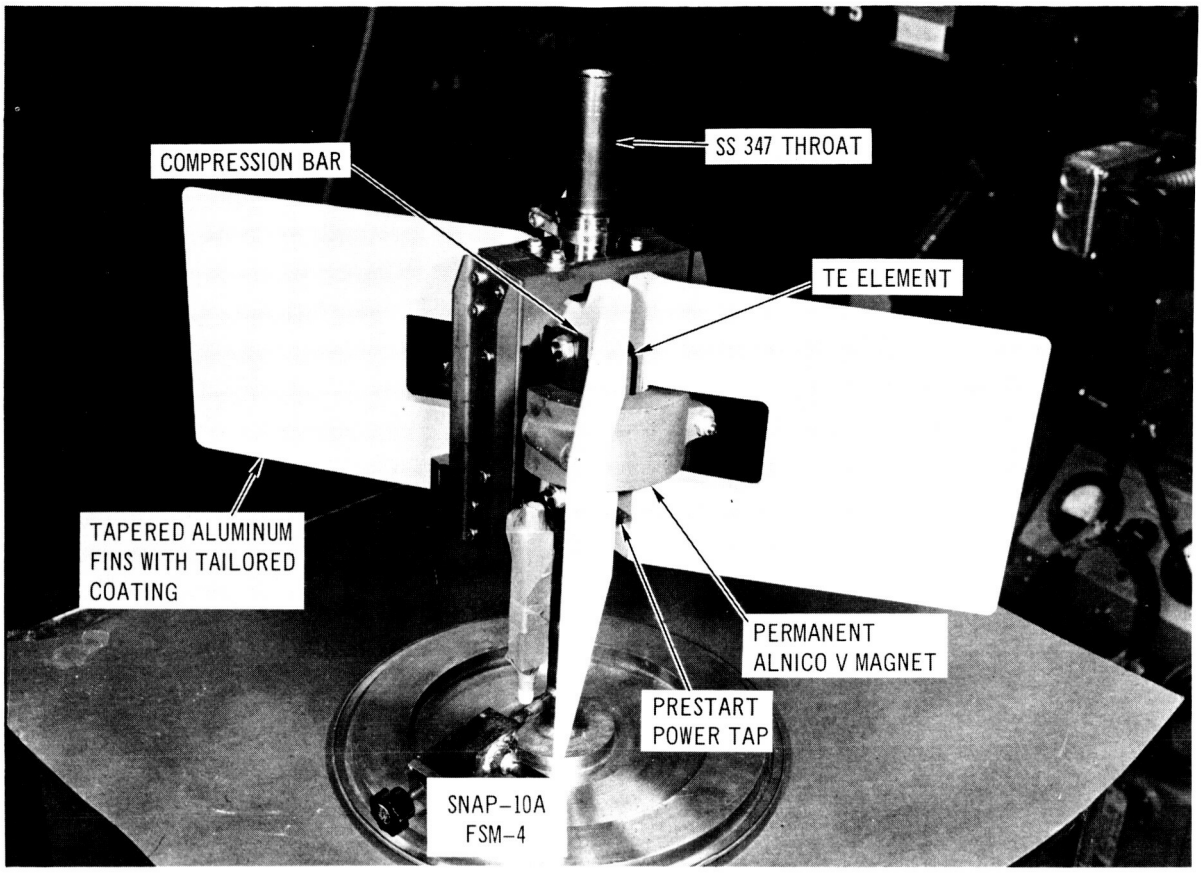


Fig. 1. SNAP 10A TEM Pump

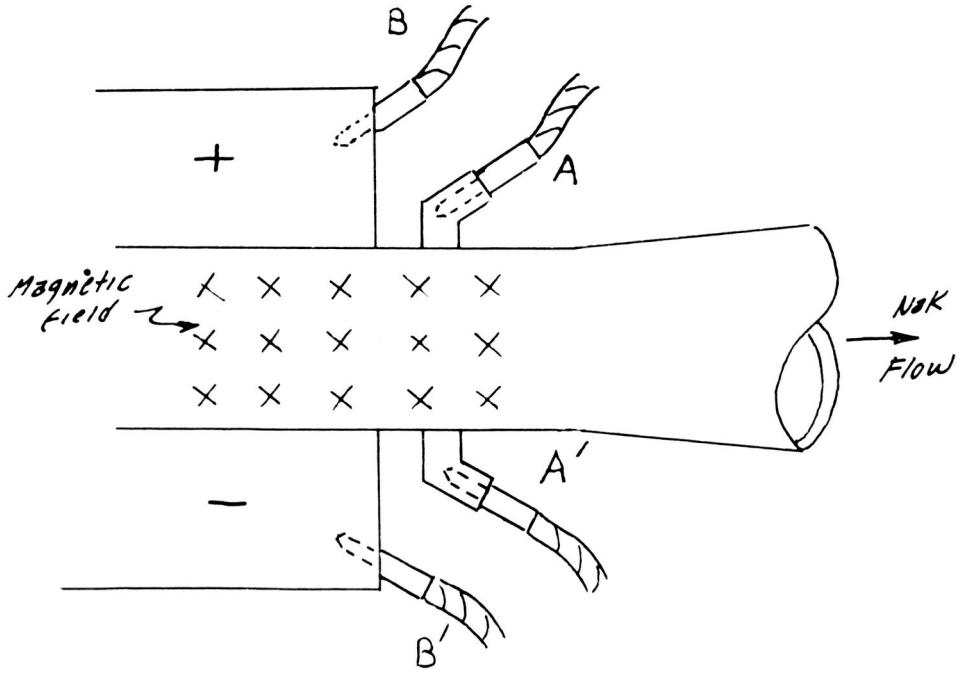


Fig. 2. Flow Meter Electrodes - SNAP 10A TEM Pump

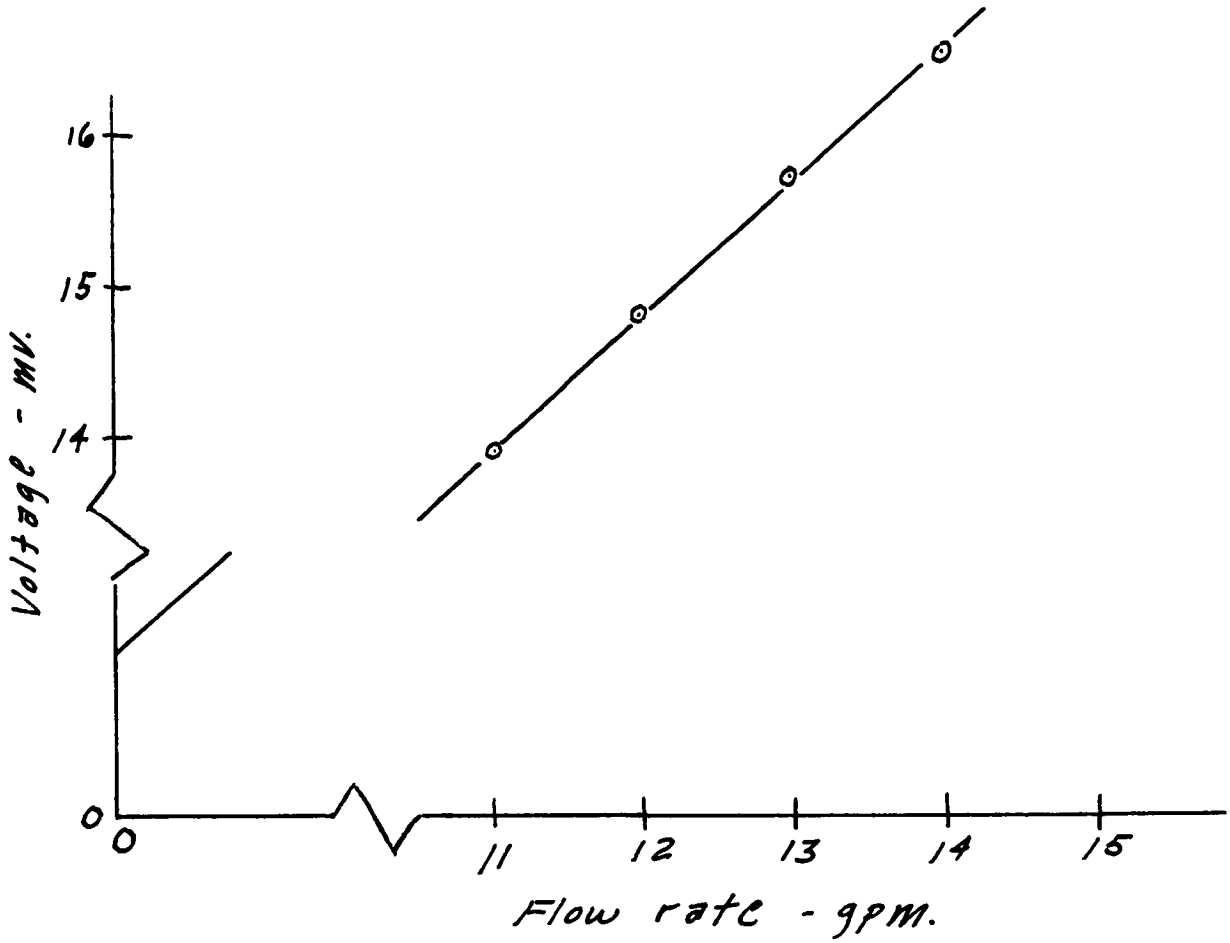


Fig. 3a. Initial Calibration of TEM Pump Flow Meter (SN016)

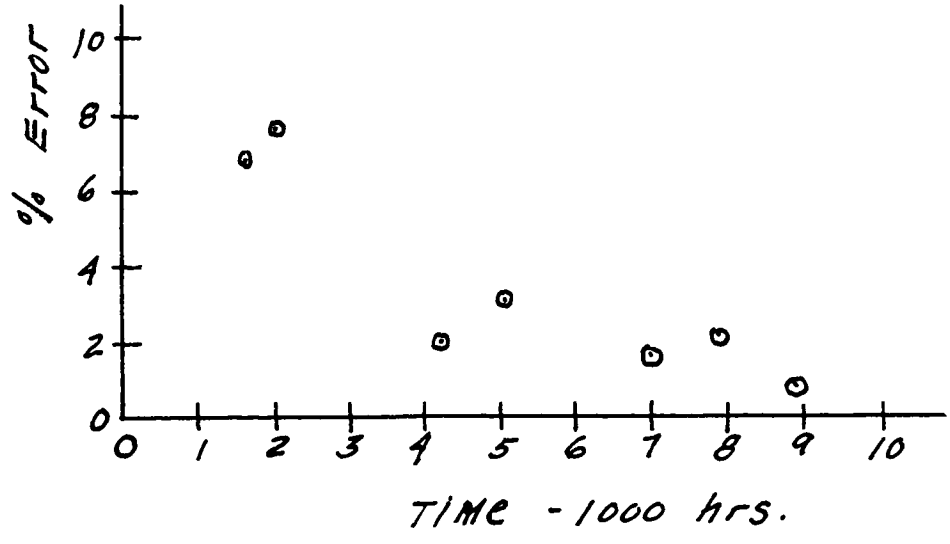


Fig. 3b. Flow Rate Error with Time in Life Test (SN016)

BB' in Figure 2, was placed on the pump. This signal is largely a function of pump current, hence, by monitoring both signals during the flight, each of the two variables, current and flow rate effects, were adequately assessed. Figure 3b plots a typical flow rate error with time as measured during a life test.

Figure 4a plots the signal received from the space system during the 43 day operation. Each point represents an average of 15 minutes of data gathered during an orbit period. As time progressed this parameter was monitored at progressively longer intervals. Figure 4b shows this data converted to gpm taking into consideration the change in fluid temperature with time. No attempt was made to factor in an estimated degradation characteristic. However, final accuracy of this data transmission has been estimated at better than $\pm 10\%$.

Pressure

Liquid metal pressure was indirectly monitored during the SNAP 10A flight primarily to detect and measure leakage in the event it occurred. This was accomplished by measuring the position of the bellows in two expansion compensators. Expansion compensators are required to maintain a constant system pressure in the face of changing liquid metal volume. A 25% volume change is incurred during system startup where the temperature increases from approximately 100°F to 1000°F. Figure 5 is a photograph of the compensator showing the position indicating device installed. Figure 6 shows the elements of the position transducer. The transducer and demodulator convert the mechanical expansion of the bellows into an electrical voltage proportional to the displacement. Readout is achieved by a variable reluctance device whereby a movable magnetic core (armature) is displaced in an a.c. excited magnetic field. This signal was transmitted to a demodulator unit which converted the signal to a 0 to 50 mv d.c. output. The armature, an iron rod, is attached to a clevis which is integral to the top plate of the primary bellows assembly. The demodulator was located in the instrument compartment of the vehicle due to its low operating temperature limitation.

Figure 7 plots transducer output vs bellows deflection of a typical unit during an acceptance test. Gas was used to inflate the bellows; space heaters simulated the temperature profile expected during startup in space. This was estimated to be 750°F at steady state operating conditions. This figure plots one cycle with temperature simulation and two at room

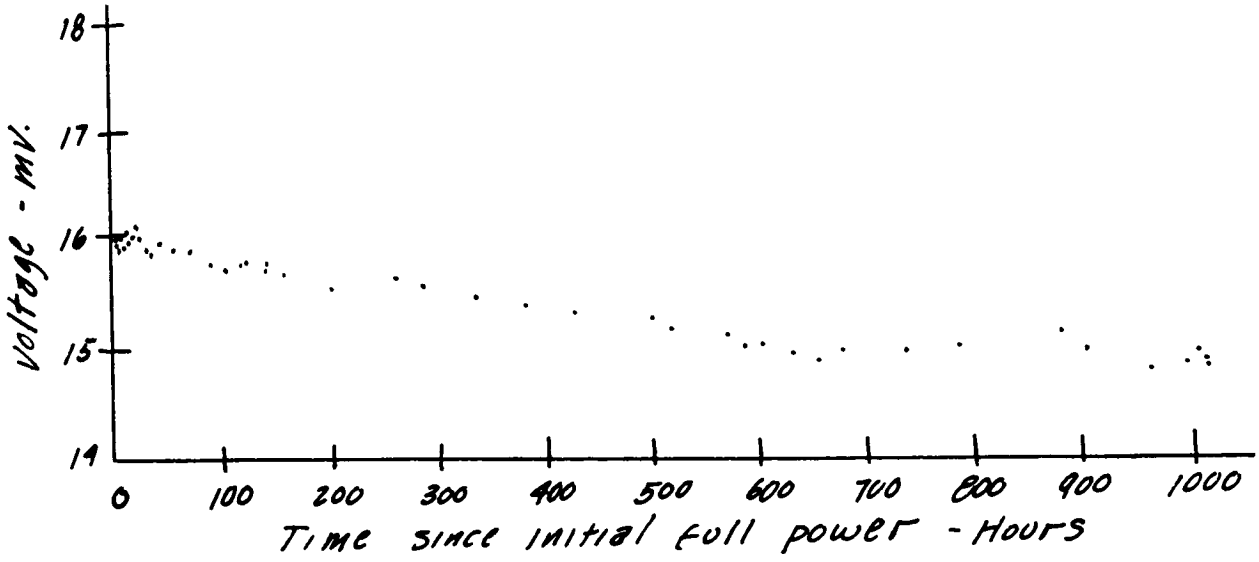


Fig. 4a. Flow Rate Signal Received from SNAP 10A Space System

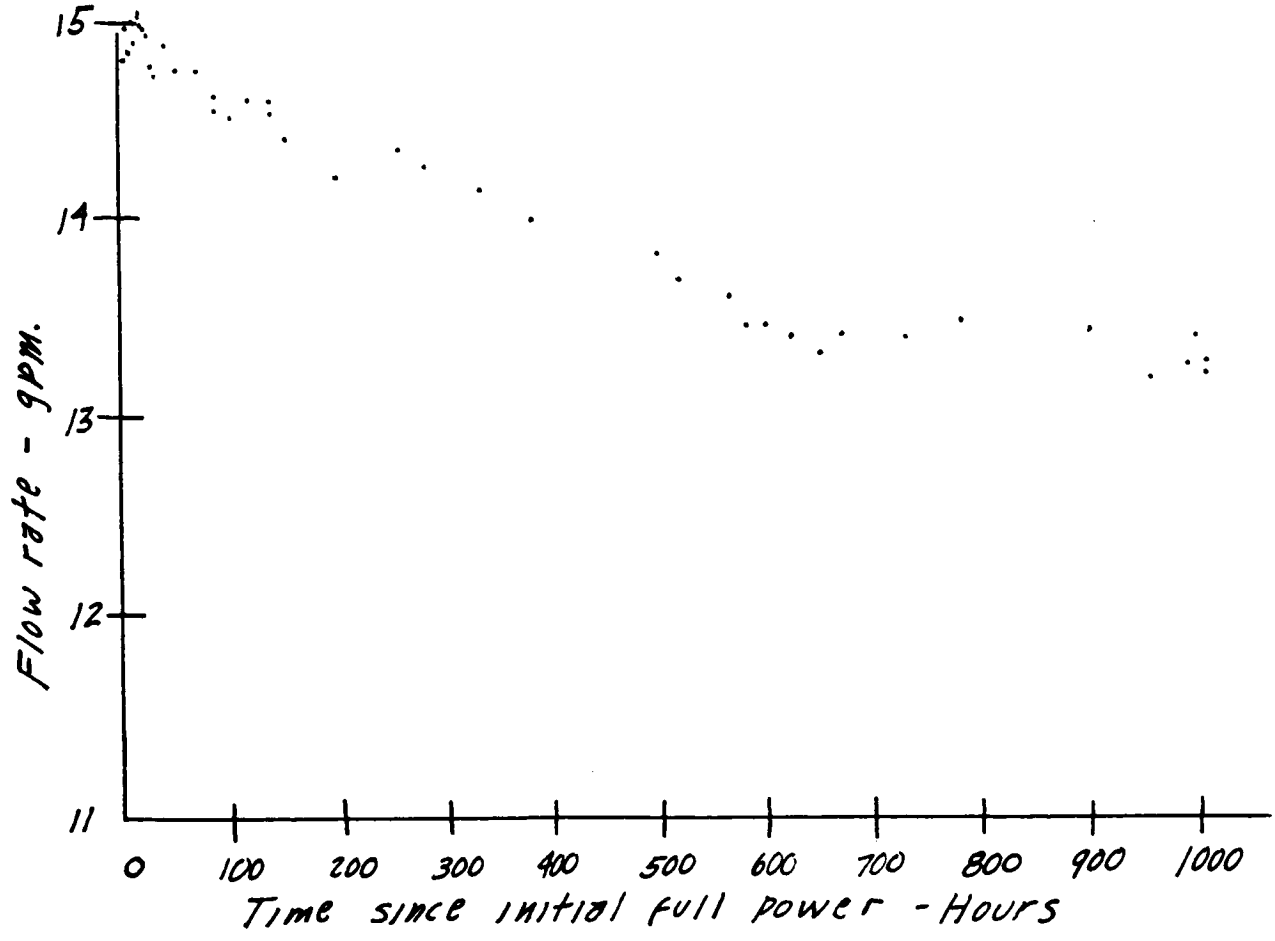


Fig. 4b. Flow Rate Signal Converted to gpm.
Corrected for Temperature Effects

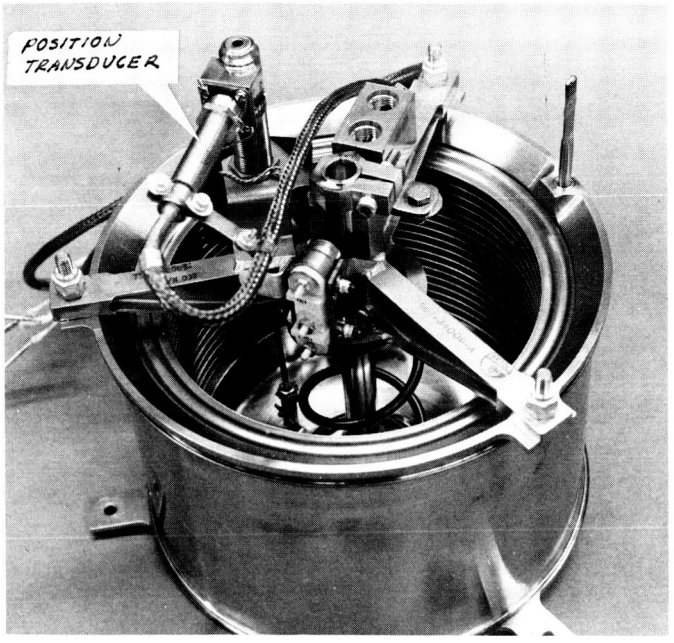


Fig. 5. SNAP 10A Expansion Compensator

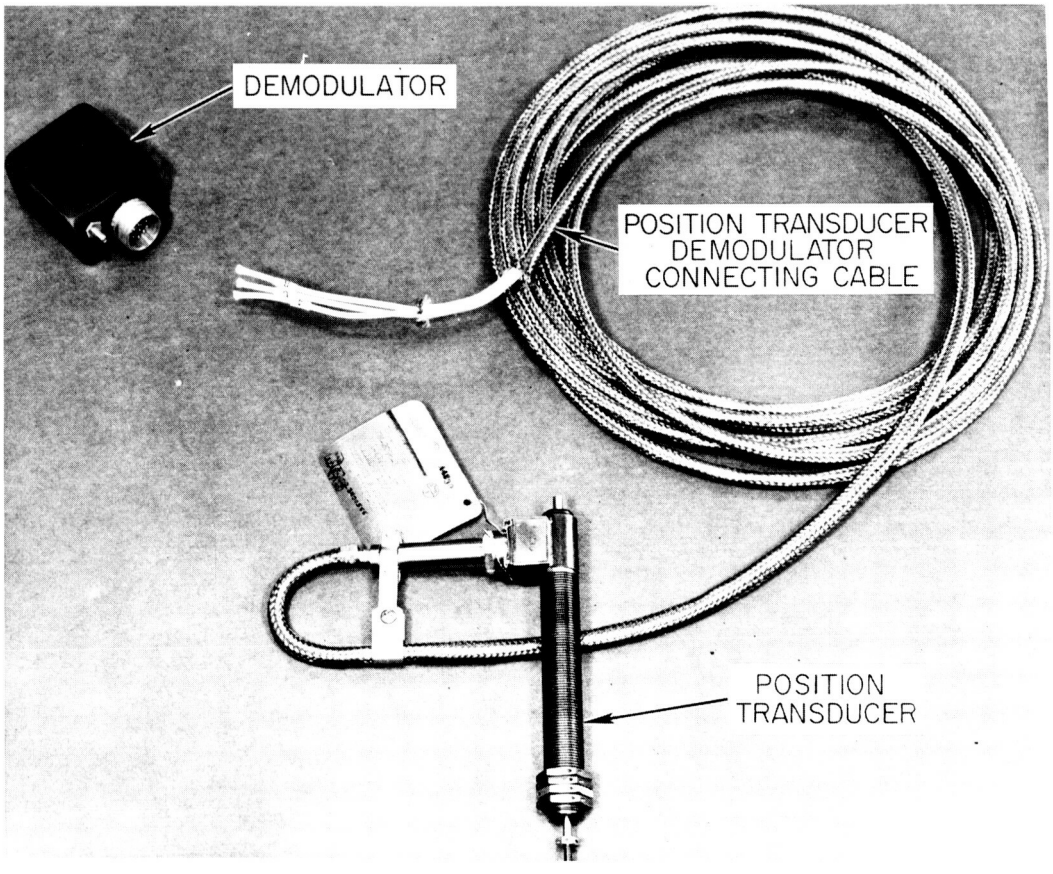


Fig. 6. Position Transducer and Demodulator

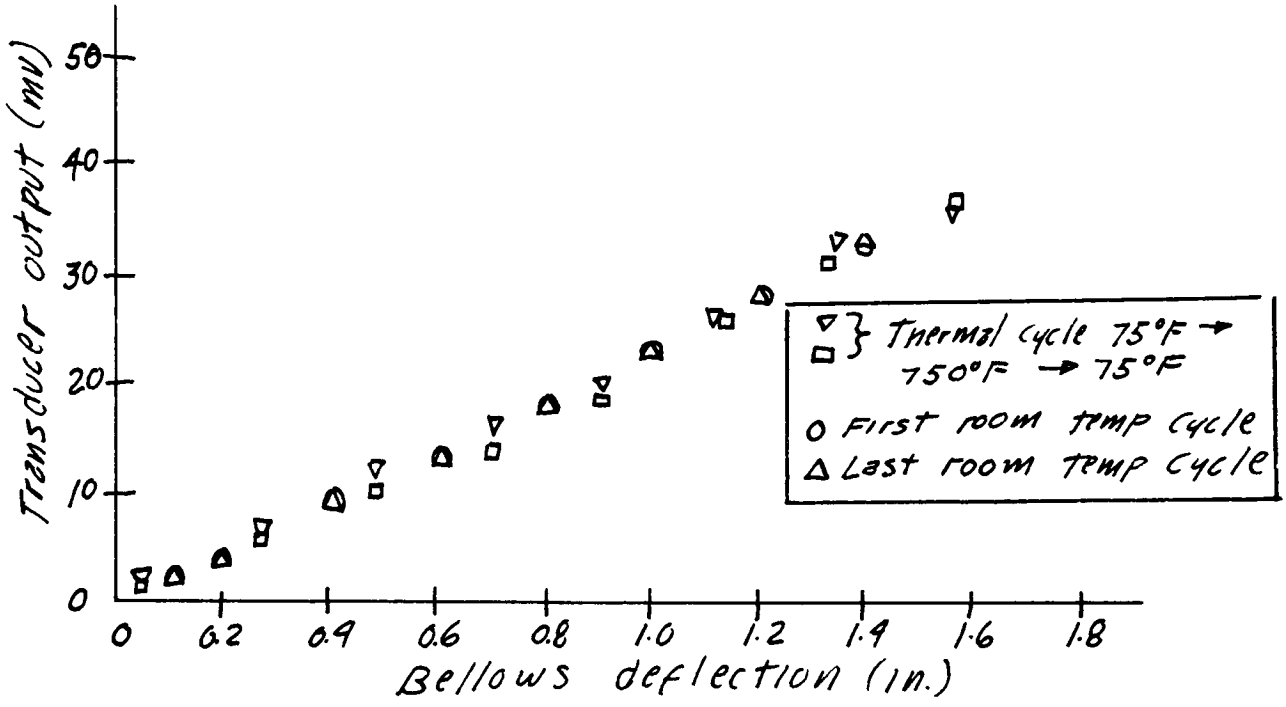


Fig. 7. Position Transducer Output versus Bellows Deflection on ECU 023 during Acceptance Testing

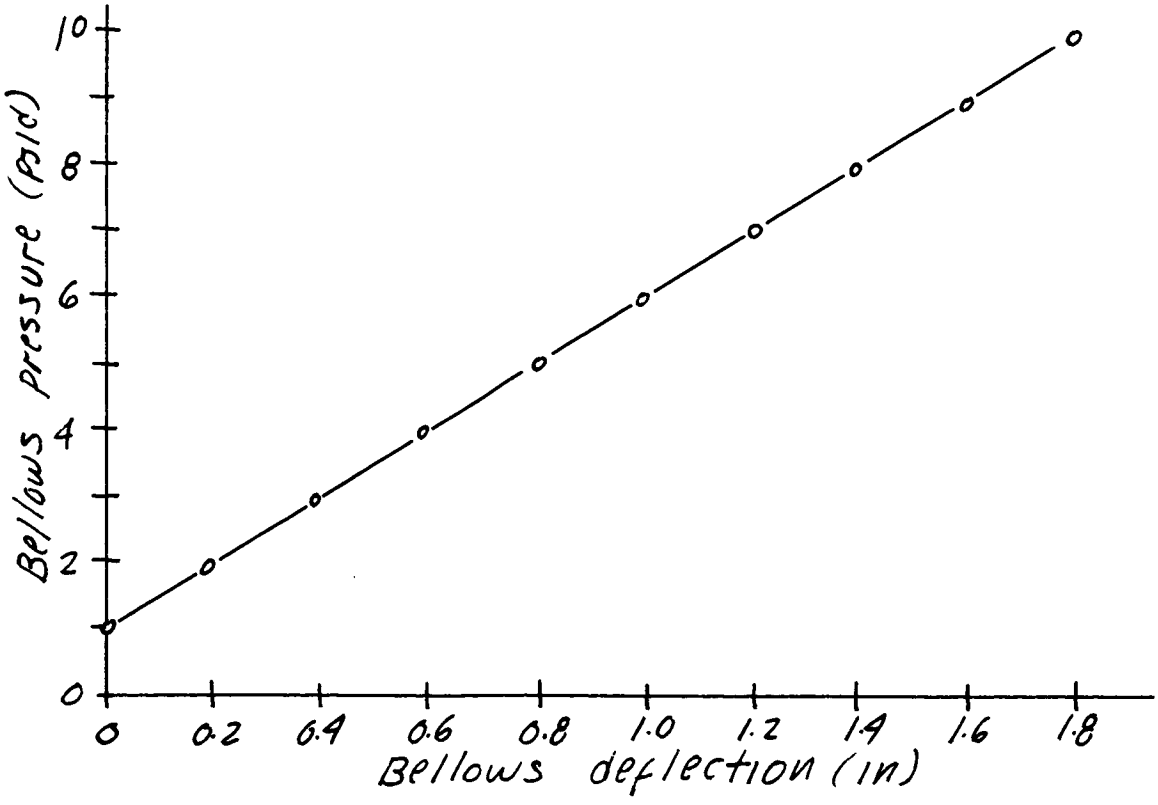


Fig. 8. Ambient Temperature - Pressure Deflection of ECU 023 during Acceptance Testing

temperature conditions. As noted, temperature effects were minimal. Figure 8 plots bellows pressure vs bellows deflection during an acceptance test at ambient conditions on a typical unit. The approximate 1 psi zero offset is due to the loading from the bellows and also from an external spring required to insure minimum positive pressure on the system during all phases of system operation.

Figure 9 plots the data acquired during flight operation of the SNAP 10A system. Temperature at the compensator was not monitored for the flight to avoid possible damage to the thin walled members by attaching temperature sensors. This data has been normalized to 950°F, the average reactor core temperature. With the data in this form, a leak would appear as a deviation in the constant signal readout. Deflection was not converted to pressure at the data reduction center for the flight because pressure was not of primary interest. Pressure would be simply determined from the pressure deflection characteristic for the particular compensator obtained during its acceptance test.

Temperature Measurement

The temperature of the liquid metal at various points in the system was measured with both chromel-constantan thermocouples and resistance type temperature detectors (RTD). Chromel-constantan TC's, rather than the more stable chromel alumel couples, were used because of their greater signal strength. RTD were used where high accuracy was required.

The thermocouples were sheathed in stainless steel and brazed to the system piping. Figure 10 shows a typical installation. The references for the TC's were compensated electronic junctions located in the lower temperature instrumentation compartment of the vehicle.

Figure 10 also shows a typical RTD installation. The sensitive length of the RTD was inserted into the split copper piece brazed to the system piping. A stainless steel bolt (not shown) bolted the copper block leaves together to produce a snug fit. Difference in expansion rates of copper and stainless steel maintained positive contact at the higher system operating temperatures. The Wheatstone bridge network boxes, like the TC reference junctions, were located in the lower temperature instrument compartments. Bridge excitation was 28 volts d.c.

A total of 10 RTD's were installed on the flight system to measure liquid metal temperatures. These included six low range RTD's (0-300°F), monitoring reactor and converter inlet and outlet temperatures during the ascent and pre-startup phases. A primary concern during these phases was

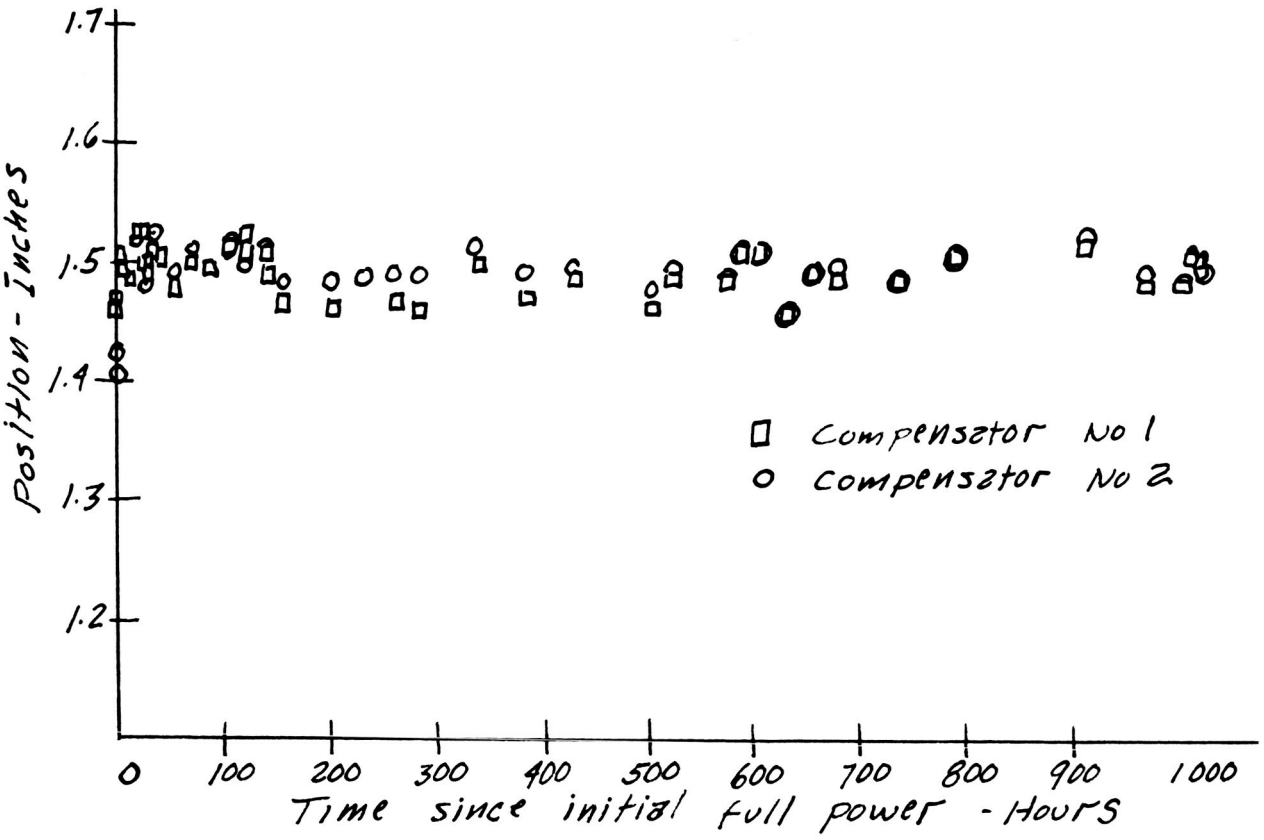


Fig. 9. Compensator Bellows Position versus Operating Time of Flight System

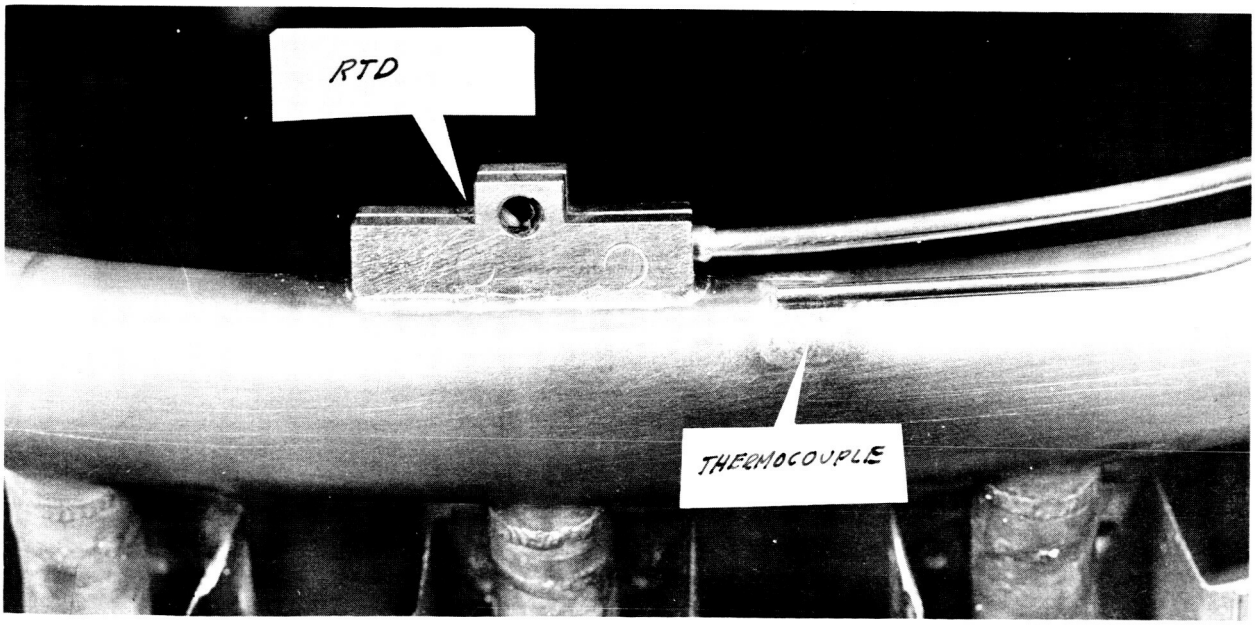


Fig. 10. Typical RTD and TC Installations

the possibility of NaK freezing resulting in plugging in the many converter tubes. The NaK was circulated at approximately 0.5 gpm by the pump during this phase. These low temperature RTD's were turned off after system startup. Four high temperature range (800-1100°F) RTD's measured converter and reactor inlet and outlet temperatures during steady state operation. The RTD's were backed up by TC's in most cases.

Figure 11 plots the reactor inlet and outlet NaK temperatures during the flight. Estimated accuracy of this data is ±10°F. This included a transmission uncertainty of ±3%. No temperature sensor malfunctions were detected, with the possible exception of an erratic heat shield TC, during the entire 43 day system operation.

MERCURY VAPOR QUALITY MEASUREMENT

Mercury vapor quality of at least 97% is required to assure a 10,000 hour life for the Rankine cycle space power systems being developed at Atomics International. A highly accurate (to within 1%) meter is needed to detect quality in this range. Radiation type density detectors, wherein the vapor is the source of radiation, presents a method for obtaining the needed accuracy since accuracy can be made a function of counting time. The major problem with these as with any quality measuring scheme has been that of initial calibration since the vapor properties, pressure and temperature, have been required to be precisely known.

A method[1] of calibration applicable to vapor radiation density detector schemes has been proposed and is being investigated wherein quality measurement to within 1% is possible with vapor flow rate errors of up to 5%, based on vapor temperature and pressure uncertainty. The method is as follows for a tracer detector scheme of the type shown in Figure 12:

1. A reading of the background radiation without mercury vapor flowing is established by taking a total count in a given period of time.
2. The mercury vapor flow with the unknown amount of liquid carry-over is then established and a count taken.
3. A known flow rate of liquid mercury from the remainder of the loop is injected into the calibration tube and another total count taken.
4. The background reading is subtracted from both of the above readings and the quality of the vapor is calculated from the rquat ons derived in the following paragraph.

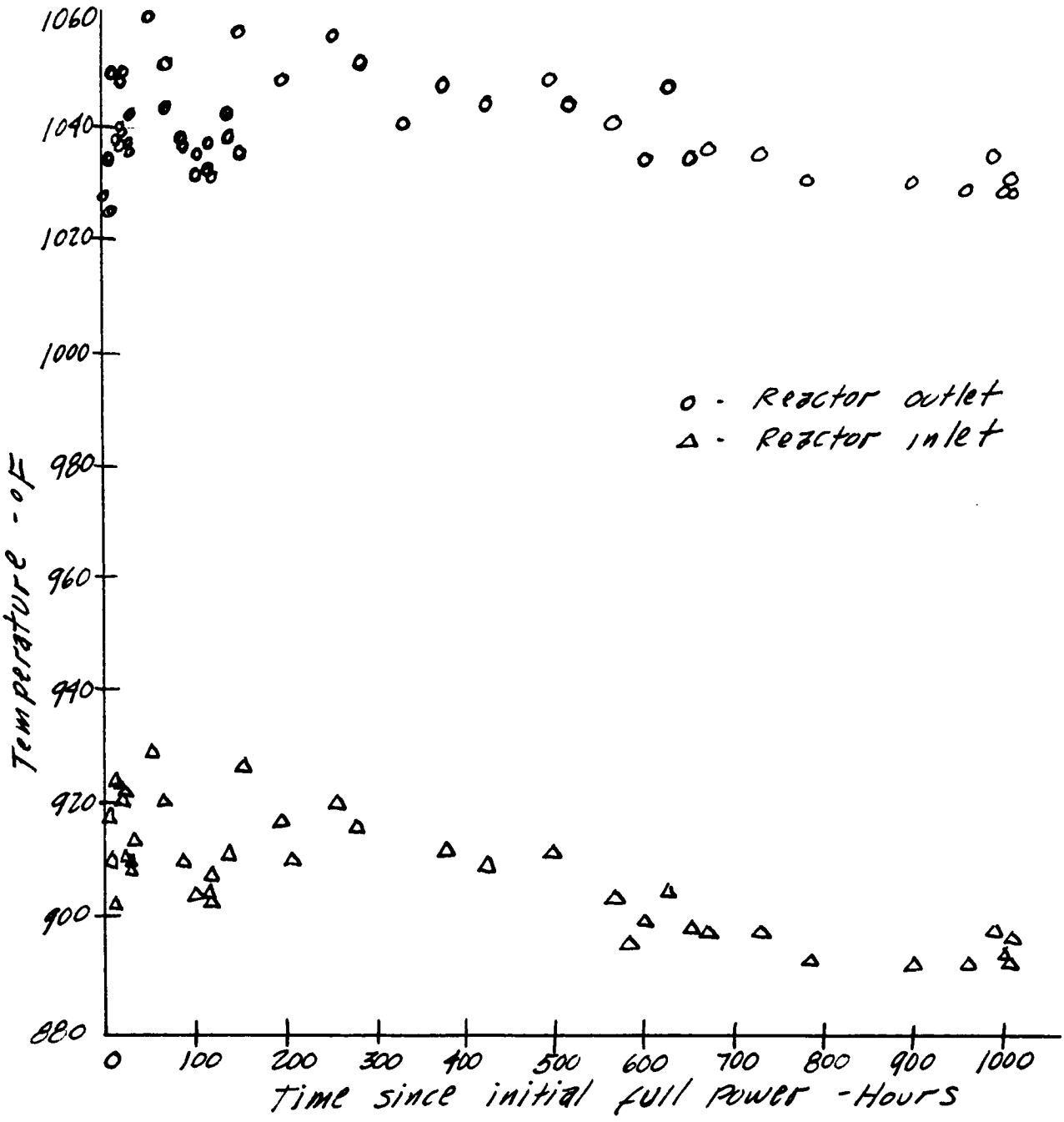


Fig. 11. Flight Data - Reactor Inlet and Outlet NaK Temperatures

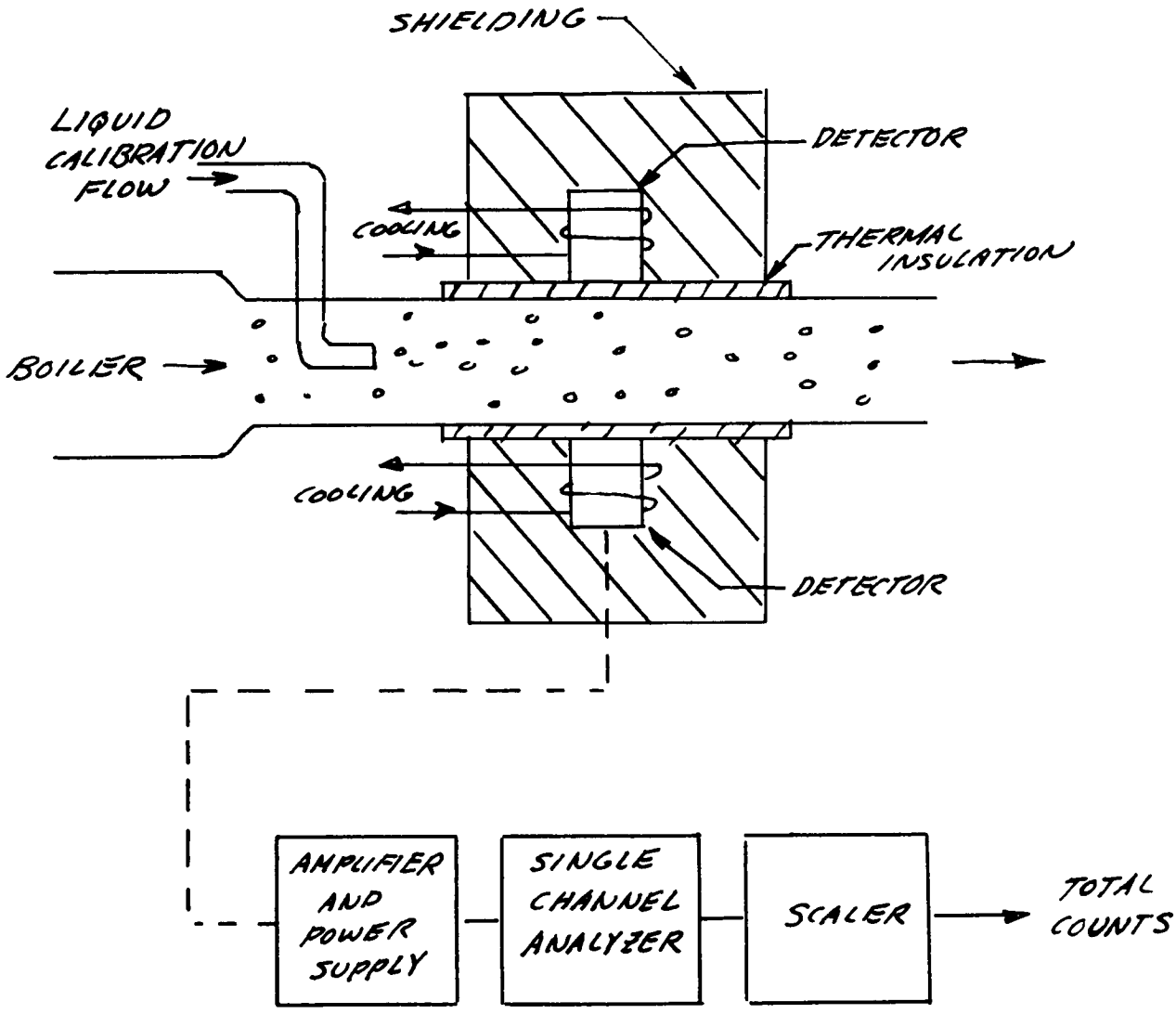


Fig. 12. Vapor Quality Meter Calibration Scheme

Analyses

The total amount of activity in the sensing volume, in terms of disintegrations per minute is given by equation (1)

$$d = (SA)\left[\rho_L V_L + \rho_v V_v\right] \tag{1}$$

where

d = disintegration/min. for mercury in control volume

SA = specific activity of mercury (disintegrations/min/lb)

ρ_L = density liquid

ρ_v = density vapor

V_L = volume of liquid in control volume

V_v = volume of vapor in control volume

This equation can be simplified to the following form:

$$\frac{d}{d_o} = \frac{\rho_L}{\rho_v}(1 - f) + f \tag{2}$$

where

d_o = disintegration/min if sensing volume is all vapor

f = vapor volume fraction = $\dfrac{V_v}{V_{total}}$

V_{total} = total sensing volume

The mercury quality is related to the vapor fraction by the following operation:

$$X = \frac{1}{\frac{\rho_L}{\rho_v}\left(\frac{1-f}{f}\right)\frac{1}{S_R} + 1} \tag{3}$$

X = vapor quality = $\dfrac{\text{Mass flow rate of vapor}}{\text{total mass flow rate}}$

S_R = slip ratio = $\dfrac{\text{velocity vapor}}{\text{velocity of liquid}}$

The slip ratio, S_R, must be determined by a separate experiment or the detector must be located far enough down-stream that the slip ratio approaches unity. This latter approach seems more practical. Combining equations 2 and 3 yields the following:

$$\frac{d}{d_o} = \frac{\frac{\rho_L}{\rho_v}\left(\frac{1}{X} - 1\right) + \frac{\rho_L}{\rho_v}\frac{1}{S_R}}{\left(\frac{1}{X} - 1\right) + \frac{\rho_L}{\rho_v}\frac{1}{S_R}} \qquad (4)$$

If the mercury quality, X, is near unity, and the slip ratio is unity, equation 4 may be approximated as follows:

$$\frac{A}{A_o} = \frac{d}{d_o} = (1 - X) + 1 = (C + 1) \qquad (5)$$

where

C = 1 - X = Carry-over fraction

A = detector count rate (proportional to disintegration rate)

A_o = detector count rate for vapor only

For a quality of 97%, the above equation is approximately 0.1% in error. The device is therefore a linear indicator of mercury quality providing quality is near unity.

Two counts are made, A_1, corresponding to the unknown carry-over condition and A_2, corresponding to the time when a known flow rate of liquid metal is being injected into the calibration tube.

The equations describing these conditions are as follows:

$$C_1 = \frac{\dot{M}_{L_X}}{\dot{M}_{L_X} + \dot{M}_v} \qquad C_2 = \frac{\dot{M}_{L_X} + \dot{M}_{L_C}}{\dot{X}_{L_X} + \dot{M}_{L_C} + \dot{M}_v} \qquad (6,7)$$

$$A_1 = A_o (1 + C_1) \qquad A_2 = A_o (1 + O_2) \qquad (8,9)$$

Subscripts (1) and (2) refer to run number

Run #1 is with no calibration flow

Run #2 is with calibration flow

$\dot{M}_v$ = vapor mass flow rate

$\dot{M}_{L_X}$ = unknown mass flow of liquid due to carry-over

$\dot{M}_{L_C}$ = known liquid calibration flow rate

The unknown carry-over is determined by

$$C_l = \frac{A_l}{A_o} - 1 \qquad (10)$$

A_o, the calibration factor, corresponding to the detector count rate for the vapor only is derived from equations 6-9. An error analysis for this scheme using a set of practical conditions shows that for an assumed 5% error in measuring vapor mass flow rate, an accuracy of $\pm 1\%$ in vapor quantity at 95% can be calculated. This analysis is presented in the appendix. Vapor flow rate would be measured by a venturi flow meter.

Tracer Detector Scheme

The proposed radioactive quality meter uses Hg^{203} disbursed throughout the test loop. Hg^{203} is produced by radiation of natural mercury and has a 48 day half-life. All of the other radioisotopes produced by radiation have shorter half-lives. The radioactive decay of Hg^{203} gives off a .2 mev β particle and a .3 mev γ particle. The proposed quality meter detects this gamma radiation which is given off in approximately 80% of the decays of Hg^{203}. The technique involved is to mix some radioactive Hg^{203} in with the rest of the Hg in the boiler test loop. A gamma detector is then placed on the vapor line from the boiler (Figure 12) so that it sees the mercury within the vapor piping. It is shielded (by lead) from the background radiation and from the rest of the radiation from the mercury loop.

The detector must be cooled since operation of a commercial detector at the vapor temperature ($\sim$1200°F) is not feasible. Insulation must be placed between the detector and piping so as to allow the vapor pipe to run at 1200°F (without condensation) and reduce the heat load on the cooling system. A scintillation detector placed on both sides of a flattened portion of the mercury piping will probably have the best efficiency for counting the gamma radiation. Electronic equipment then records the amount of counts from the scintillator.

X-Ray Fluorescence[2] Scheme

Mercury will re-radiate with characteristic K and L-X rays when excited by ionizing radiation with an energy greater than the binding energy. The probability of radiative de-excitation is called the fluorescence yield. The vapor at a given point in the system piping is irradiated and the fluorescence activity is a precise measure of vapor and entrained liquid density, subject to the same calibration and measurement scheme discussed previously. In this application an X-ray machine would be used as a exciting source since it can be shielded and the beam collimated more easily than a radioisotopic-source. In addition, the exciting energy can be more exactly selected. The detector would be two scintillation detectors at 90° to the incident beam so that the background due to radiation from the beam would be low. The correct signal energy (83.106 KEV) would be selected both by filters and by electronic amplitude selection.

Gamma Backscatter Scheme

The mass of the mercury vapor and entrained liquid in a section of system piping can be measured by the backscattered signal from incident gamma photons. The backscattered signal from mercury within the pipe is reduced first by attenuation of the incident photon in the pipe wall and secondly by attenuation of the backscattered gamma photons in the pipe wall. A preliminary analysis[3] has shown that an adequate signal can be obtained for a Haynes 25 pipe with 028 inch walls-mercury vapor system.

INSTRUMENTATION FOR MERCURY BOILER CONDITIONING EXPERIMENTS[4]

A study program is being carried out to describe fundamental factors influencing boiler conditioning for mercury-systems. This study was initiated when occasional sub-normal performance was observed with several boilers in the Mercury Rankine Program. The study consists of pool boiling experiments to determine the relation between wetting and heat transfer characteristics and to determine factors influencing wetting. Figure 13 is a photograph of the test apparatus. The liquid mercury is contained in the thermally insulated pot. The saturation temperature is varied by an air blower heat exchanger located in the shroud at the top of the pot. A wrap around heater on the pot also controlls system temperature. The heater is inserted into the top of the pot as shown. Figure 14 shows a detailed view of the heater. This high flux heater was specially constructed for this experiment. The heating length consisted of, from center to outside

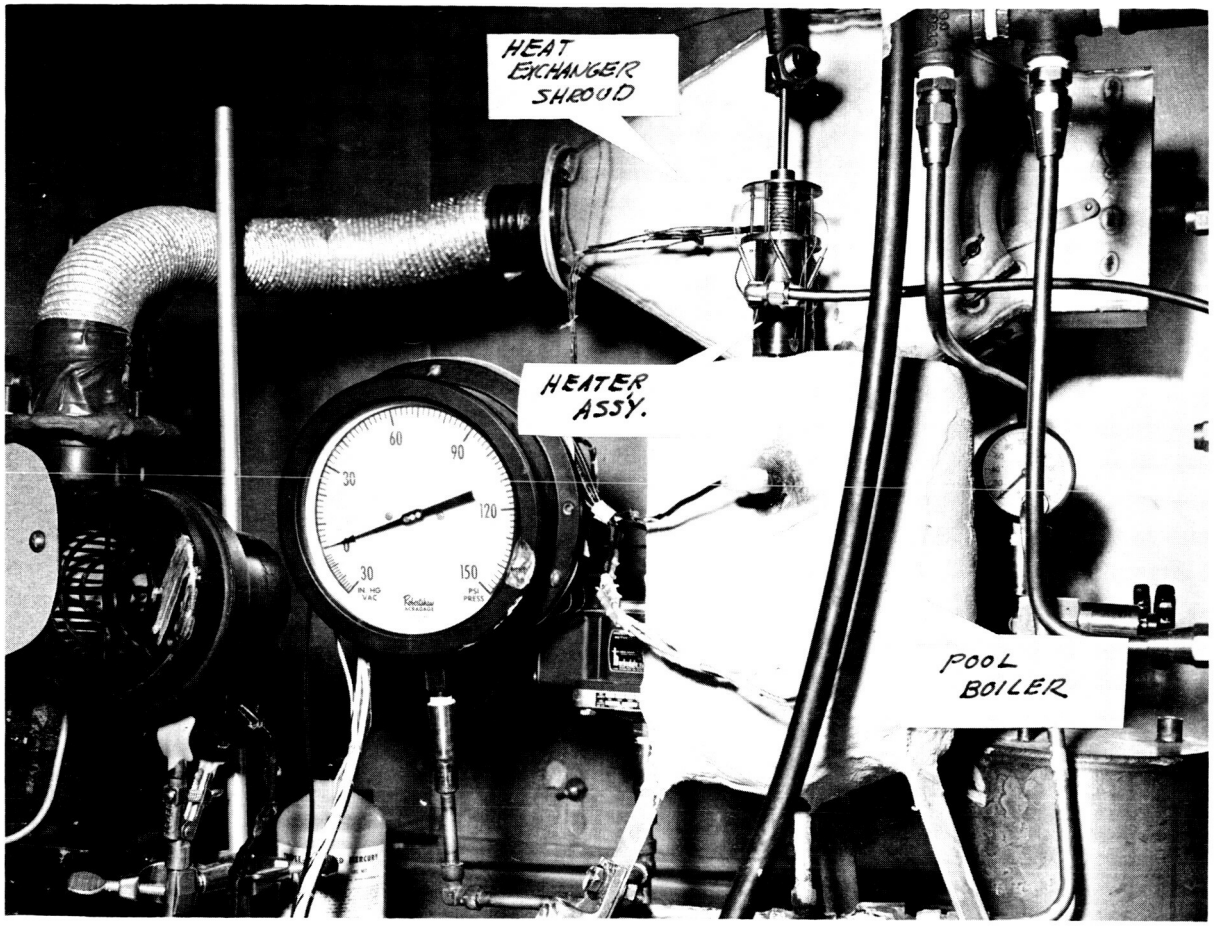


Fig. 13. Pool Boiling Apparatus

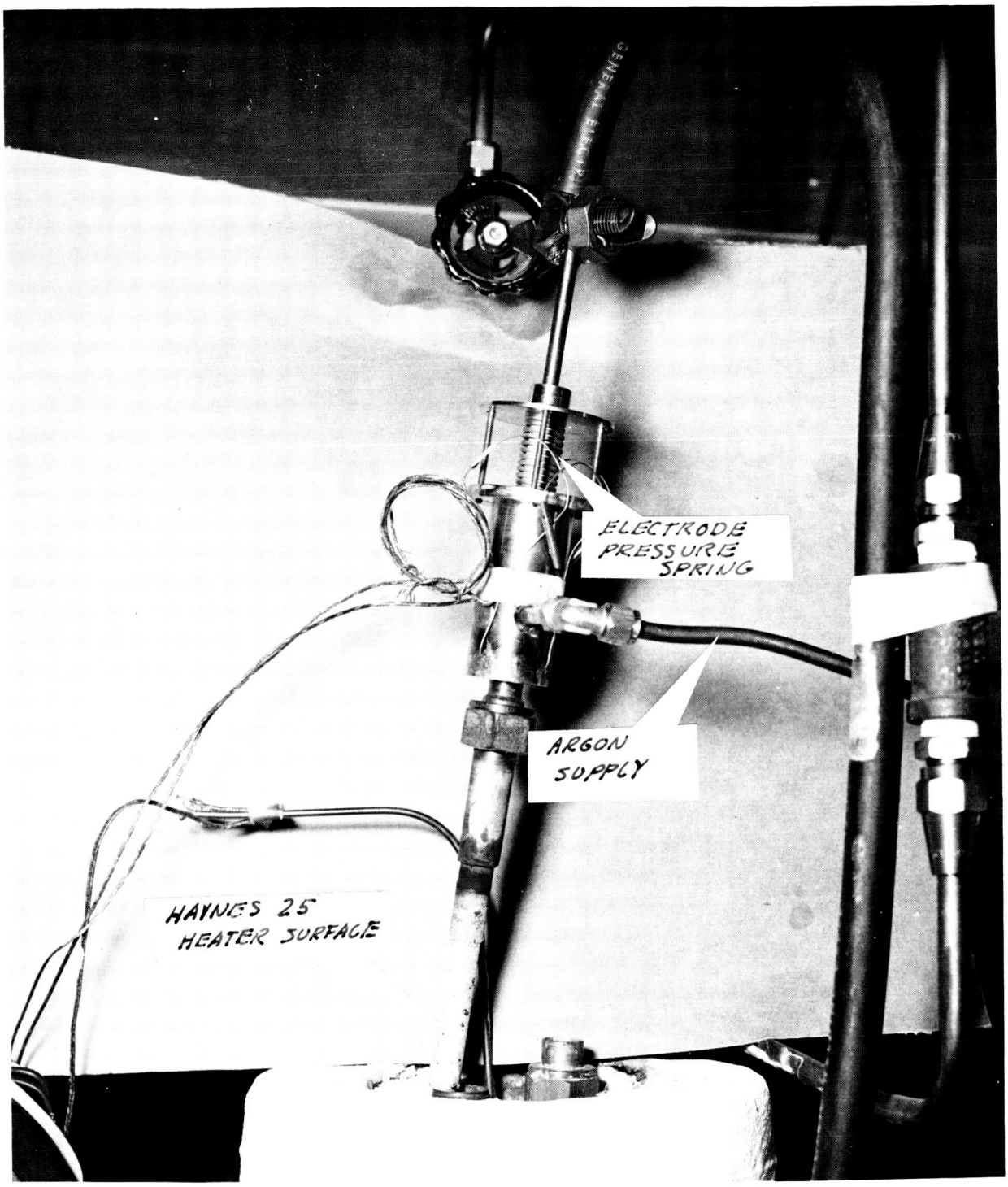


Fig. 14. Pool Boiler Heater Assembly

surface (Figure 15):

Graphite heating element

Boron nitride sleeve

Stainless steel

Copper

Haynes 25 surface

Two thermocouples were recessed in grooves in the stainless steel shell to measure heater temperature. The current lead was pressed against the molybdenum electrode by the spring seen in Figure 14. Argon was used to cool the upper heater assembly.

The Haynes 25 surface of the heater was conditioned by various methods and immersed in the Hg pool. Q/A- ΔT runs at various Hg saturation levels were made for each surface condition. Some surface conditions included:

(1) degreased and cleaned

(2) oxidized

(3) descaled and pickled

(4) oil contaminated

Figure 14 shows a descaled and pickled heater surface immediately after removal from test. Figure 16 shows a Q/A- ΔT result for a degreased and cleaned surface. Figure 17 shows the results for an oil contaminated surface.

Some conclusions from these results and others are that:

1. Exposure of clean Haynes 25 surface at 1200°F to air for a few hours has no deleterious effect on pool boiling heat transfer at a Hg saturation temperature of 950°F for heat fluxes up to at least 200,000 Btu/hr•ft^2.
2. The pool boiling heat transfer for a descaled and pickled Haynes 25 surface is essentially the same as for a degreased and cleaned surface except for an initial period of lower performance for the descaled and pickled surface.
3. The "degreased and cleaned," and "descaled and pickled" surfaces remain wetted when cooled to room temperature after being at 950°F for a period of time.
4. The wetting of a clean Haynes 25 surface is not likely to be uniform.

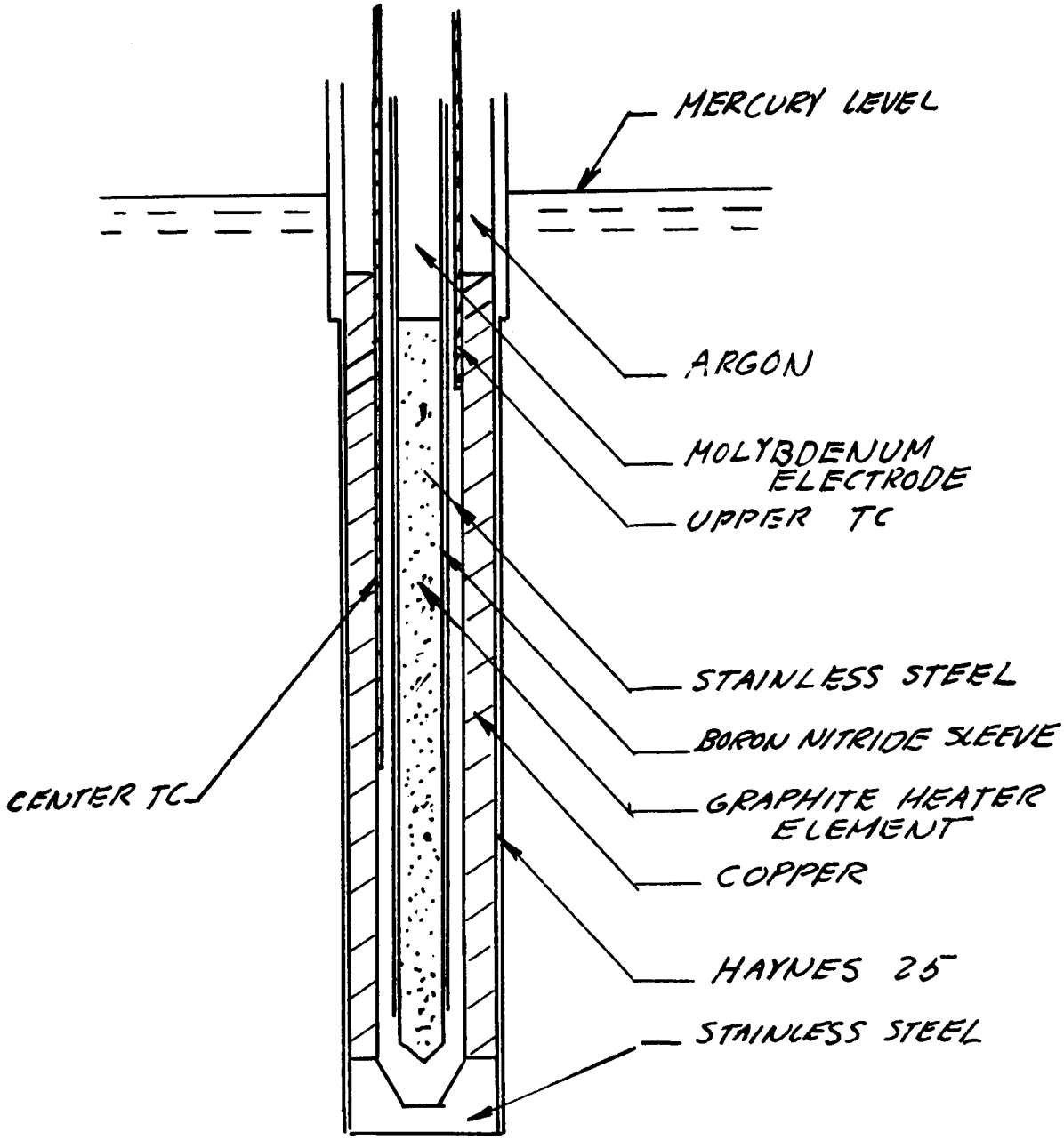


Fig. 15. Sectional View of High-flux Test Heater

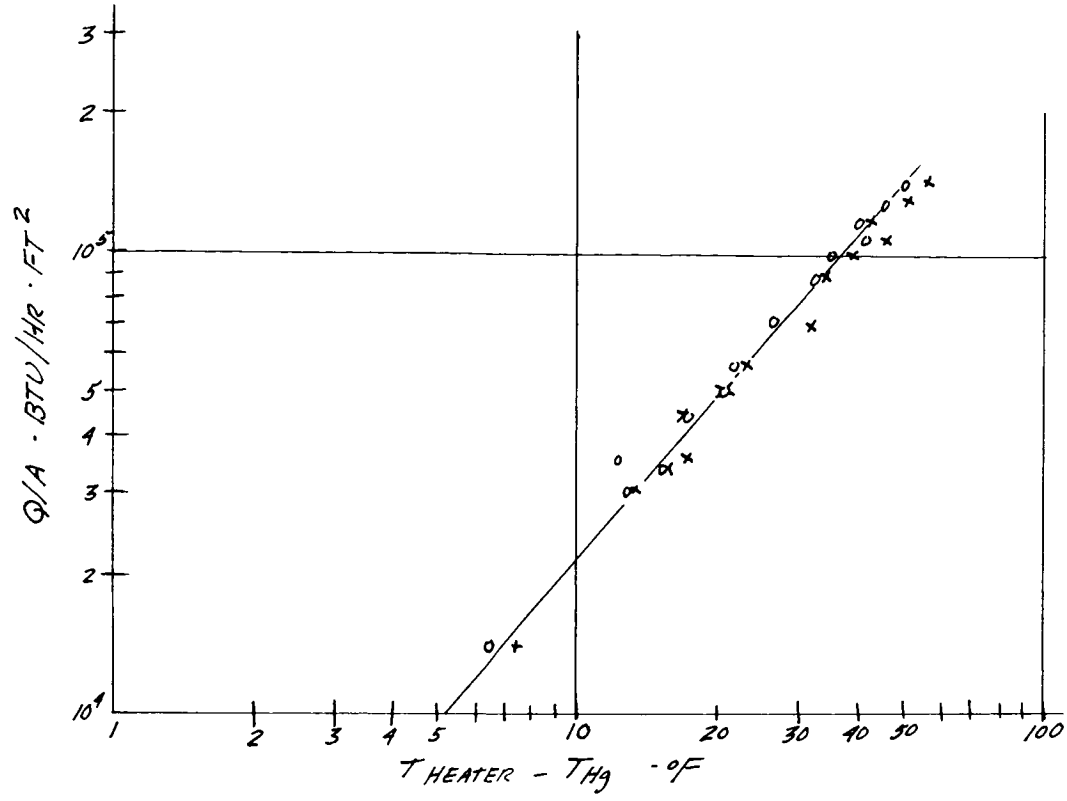


Fig. 16. Q/A versus ΔT Results for Degreased and Cleaned Surface

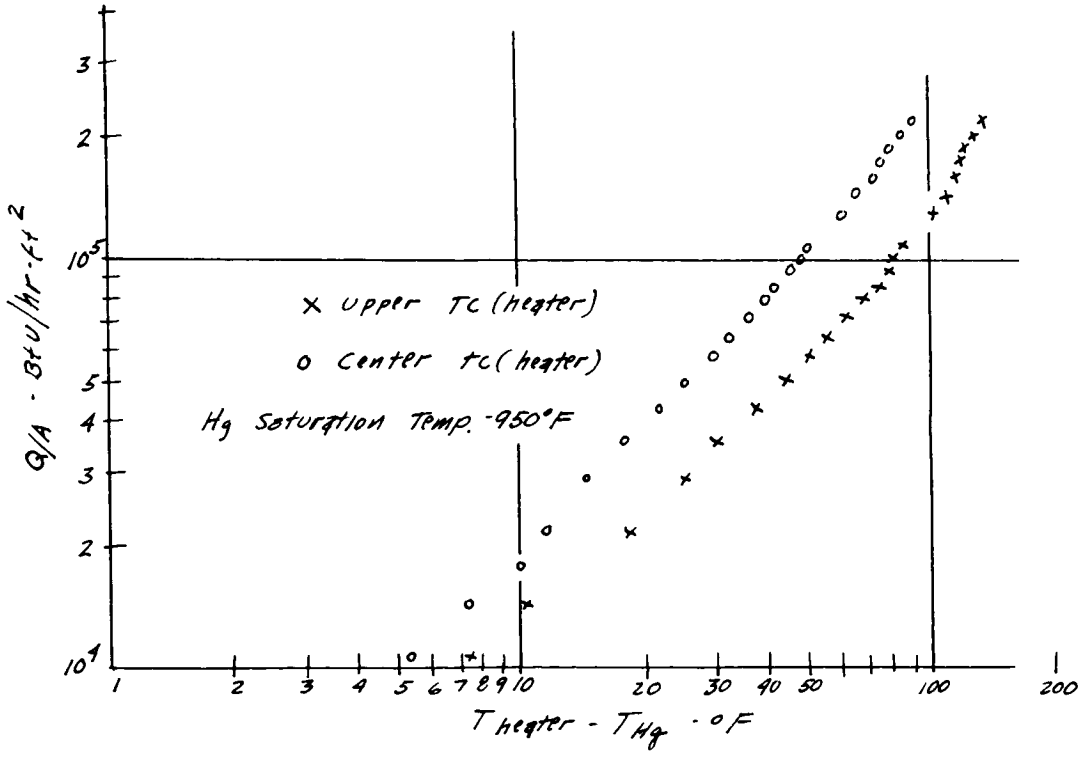


Fig. 17. Q/A versus ΔT Results for Oil Contaminated Surface

5. Contamination of a Haynes 25 surface with even a trace amount of oil will effect a reduction in the pool boiling heat transfer performance of the surface. However, the reduction is fairly small, and restoration of the performance to that of a clean surface with operating time may be possible.
6. Gross contamination of a Haynes 25 surface with oil will effect a drastic reduction in pool boiling heat transfer performance at Hg saturation temperatures greater than 650°F and a moderate reduction at Hg saturation temperatures less than 650°F.
7. A clean Haynes 25 heat transfer surface will not remain clean in an oil contaminated mercury system even when kept completely submerged in the liquid mercury.
8. A direct relationship between degree of wetting and pool boiling heat transfer performance is indicated.

APPENDIX

ERROR ANALYSIS FOR RADIATION TYPE VAPOR QUALITY DETECTOR

The unknown carry-over fraction C_1 is, from equation 10,

$$C_1 = \frac{A_1}{A_o} - 1 \tag{A-1}$$

A_o, the calibration factor corresponding to the activity of the vapor alone is obtained from equations 6-9 as

$$A_o = \left[\frac{1}{8}\frac{\dot{M}_v}{\dot{M}_{L_C}}(A_2 - A_1) + \frac{1}{4}(A_2 + A_1)\right]\left[1 + \sqrt{1 - \frac{\frac{A_1 A_2}{4}}{\left[\frac{A_2 - A_1}{8}\left(\frac{\dot{M}_v}{\dot{M}_{L_C}}\right) + \left(\frac{A_2 + A_1}{4}\right)\right]^2}}\right] \tag{A-2}$$

The error in C_1 is obtained as

$$\frac{\Delta C_1}{C_1} = \left(\frac{1}{1 - \frac{A_o}{A_1}}\right)\sqrt{\left(\frac{\Delta A_1}{A_1}\right)^2 + \left(\frac{\Delta A_o}{A_o}\right)^2} \tag{A-3}$$

$$\frac{\Delta A_1}{A_1} = \frac{2.576}{\sqrt{\text{total counts}}} = \frac{2.576}{\sqrt{100{,}000}} \cong .01 \tag{A-4}$$

$$\frac{\Delta A_o}{A_o} = \left(\frac{A_2 - A_1}{8}\right)\sqrt{\left(\frac{\Delta \dot{M}_v}{\dot{M}_{L_C}}\right)^2 + \left(\frac{\dot{M}_v}{\dot{M}_{L_C}}\right)^2}\left\{1 + \frac{\frac{A_1 A_2}{4}}{\frac{(1 + \sqrt{\ })(\sqrt{\ })}{D}\, D^2}\right\} \tag{A-5}$$

where

$$D = \frac{A_2 - A_1}{8}\frac{\dot{M}_v}{\dot{M}_{L_C}} + \frac{A_2 + A_1}{4}$$

$$\sqrt{\ } = \sqrt{1 - \frac{\frac{A_1 A_2}{4}}{\left[\frac{A_2 - A_1}{8}\frac{\dot{M}_v}{\dot{M}_{L_C}} + \frac{A_2 + A_1}{4}\right]^2}}$$

The following example has been used in order to evaluate the approximate value of this total error:

A_1 = 105,000 counts (after background correction)

A_2 = 113,650 counts (after background correction)

$\dot{M}_v$ = 19 lb/min $\dot{M}_{L_X}$ = 1 lb/min $\dot{M}_{L_C}$ = 2 lb/min

C_1 = .05 C_2 = .1365

$$\frac{\dot{M}_v}{\dot{M}_v} = \frac{\dot{M}_{L_C}}{\dot{M}_{L_C}} = .05 \quad (5\% \text{ error on flow measurements})$$

Using the above, equation (A-2) is used to determine A_o. A_o is found to be 100,000 counts. Using equations A-3, -4 and -5 the total error in carry-over has been determined to be: (A-3), -4 and -5

$$\frac{C_1}{C_1} = .21$$

or

C_1 = (5 $\pm$1)% carry-over

Quality, X, then is

X = 95 $\pm$1%

The accuracy may be improved significantly by mearly taking a larger number of counts.

ACKNOWLEDGMENTS

The information concerning the mercury pool boiling experiments was obtained through Mr. T. T. Shimazaki. The vapor quality detector calibration method was proposed by Mr. E. B. Ash.

REFERENCES

1. AI Internal letter, "A Proposed Mercury Quality Detector," E. B. Ash to D. E. Ellis, February 24, 1965
2. UKAEA Report, "Composition and Coating Thickness Testing Using Radioisotope Techniques," J. R. Rhodes - AERE-R4457
3. AI Internal letter, "Measurements of Mercury Quality in Mercury Rankine Test Systems," L. Baurmash to G. Asanovich, July 30, 1964
4. AI Internal letter, "Contribution to NAA-SR-11491," T. T. Shimazaki to W. W. Velie, June 28, 1965